Hydrodynamics of flexible-body swimming motions

by

Meldon John Wolfgang IV

B.S. in Naval Architecture and Marine Engineering,
Webb Institute of Naval Architecture (1993)

Submitted to the Department of Ocean Engineering
in partial fulfillment of the requirements for the degree of

Doctor of Philosophy in Hydrodynamics

at the

MASSACHUSETTS INSTITUTE OF TECHNOLOGY

June 1999

Author .....
Department of Ocean Engineering
April 8, 1999

Certified by .....
Dick K.P. Yue
Professor of Hydrodynamics and Ocean Engineering
Thesis Supervisor

Accepted by .....
Arthur B. Baggeroer
Ford Professor of Engineering
Chairman, Departmental Committee on Graduate Studies

Hydrodynamics of flexible-body swimming motions

by

Meldon John Wolfgang IV

Submitted to the Department of Ocean Engineering
on April 8, 1999, in partial fulfillment of the
requirements for the degree of
Doctor of Philosophy in Hydrodynamics

Abstract

The performance and agility of fish swimming motions have intrigued both biologists and fluid mechanicians for many years. Both have endeavored to understand the mechanics of fish swimming and to resolve the paradoxical observations surrounding the performance of fish, yet the unsteady hydrodynamics are not well-understood.

In this thesis, the hydrodynamics of the fish-like swimming motions of a flexible-body are examined through numerical simulation. Two- and three-dimensional boundary integral panel methods are developed which can model the steady straight-line swimming and unsteady maneuvering motions of a flexible-body of arbitrary thickness. Multiple, desingularized, infinitesimal wake sheet representation models the nonlinear dynamics of thin shear layer vorticity shed from an arbitrary number of predefined wake separation edges. The integrated performance quantities and the near-body unsteady flow features are corroborated through experimental comparisons. Employing this numeric scheme for a variety of fish forms, the unsteady flow dynamics are resolved in great detail and are found to be much more complex than that predicted by linear theory. In addition, fundamental mechanisms of near-body flow actuation, body-generated vorticity release, and wake vorticity control are found which allow the fish to generate thrust efficiently, to achieve outstanding performance, and to generate large, short-duration maneuvering forces.

Specifically, the straight-line swimming motions of a flexible-body are studied through simulation of several fish geometries. Comparison to classical linear theory highlights the importance of the vortical dynamics in achieving performance and the complexity of the near-body flow patterns. The flow around the body is found to be highly longitudinal through systematic visualization of the body cross-sectional and waterline planes. A body-generated vortex ring structure, created through localized body undulations, actuates the smooth near-body longitudinal flow patterns around much of the fish body, resulting in strong vertical vorticity components bounding the wake thrust jet. Regions of high propulsive efficiency are identified for certain prescribed kinematics, and the performance is found to be strongly dependent on kinematic variation, recoil motions, and geometric modeling choices.

Maneuvering hydrodynamics of fish swimming are studied through the simulation of a 60^o "C"-turn of a Giant Danio. The formation and controlled release of body-generated vorticity through local contortions of the backbone is shown to affect the formation of a turning thrust jet for rapid maneuvering. The interaction body-generated free vorticity and regions of high fluid momentum with the sweeping motion of the tail fin is similarly shown to affect both the strength and direction of the turning jet.

Through simulation of these straight-line swimming and unsteady maneuvering motions, fundamental mechanisms of vorticity control utilized by the fish are identified. Body-generated vorticity released by the body upstream is actuated by the motion of the oscillating tail fin, resulting in complex wake-wake-body interactions for varying kinematics. These interactions may enhance the performance by increasing thrust or increasing efficiency; similarly, large drag forces may be enhanced through constructive interaction of the wakes. Several novel vorticity control modes are elucidated for both straight-line steady swimming and unsteady maneuvering motions.

Mechanisms of near-body flow actuation and vorticity control by the motions of swimming flexible-bodies and oscillating lifting surfaces may have tremendous potential for application to vehicle design and to unsteady maneuvering systems.

Thesis Supervisor: Dick K.P. Yue
Title: Professor of Hydrodynamics and Ocean Engineering

To my parents...

...who taught me to work for what I wanted

Acknowledgments

I would like to extend my sincerest gratitude and appreciation to my advisor, Professor Dick K.P. Yue, who has shown me unconditional support during the past six years. Without his patience and good-natured antagonism, I would never have had the extraordinary opportunity to explore and to develop my professional interests at MIT while concurrently completing this work. Additionally, his insight has proven invaluable to the construction of the framework for this research, which often appeared intractable and enigmatic. I would also like to thank Professor Michael S. Triantafyllou, for his direction and confidence in me, particularly during Professor Yue's sabbatical. His polar opposite management and advisorial style was often a refreshing and energizing complement to Professor Yue's advice, and his encouragement allowed me to pursue multiple publication opportunities throughout the duration of this investigation.

My thesis committee as a whole was instrumental in shaping this work, and the author would likely still be tying up loose ends if not for their suggestions, criticisms, and enthusiasm. Thanks go to Professor Ahmed Ghoniem for his ability to ask the difficult questions which reinforced the relevance of the work within a broader focus and for his genuine interest in this unique problem. Thanks also go to Dr. Franz Hover for his assistance in framing the practical applications of these results and for his discussions on all matters, scientific to editorial. Dominique Jeudy's tireless efforts in assisting with the preparation of various journal submissions also enabled the concurrent completion of this thesis and various other projects in under a decade.

Financial support of the Office of Naval Research under contract N00014-96-1-1141 monitored by P. Purtell, T. McMullen & J. Fein; the Office of Naval Research under grants N00014-89-J-3186 and N00014-93-1-0774 monitored by the American Society for Engineering Education; the Advanced Research Project Agency under contract N00014-94-1-0735; and the Sea Grant Program under grant NA46RG0434 is gratefully acknowledged.

Others who deserve special thanks include Kelli Hendrickson, my kind and resilient office mate who never seemed to notice my moods; Dr. Lenny Imas, who amusingly can be even more hyper-critical than me; Dr. Yuming Liu, for his wisdom and humor; Lian, Xiang, and all of my colleagues in the Vortical Flow Research Laboratory; and all of my former students, who taught me as much as I tried to teach them. My close friendships in and out of MIT during the past six years cannot go unrecognized, as I am certain that their humor and attention kept me from going (more) nuts: Paul, Kris & Jud, Bill, Joe, Spence, Gassman, and Becky - all of you are complete kooks.

Finally, the completion of this thesis would not feel like an accomplishment without the love and support of Danielle. As I write these final chapters, I know that they are introduction to the story of the rest of my life with her. We have so much to look forward to.

Contents

List of Figures

List of Tables

Chapter 1

Introduction

Challenging the paradigm

Two of the most coveted goals of the study of fluid mechanics are (a) the reduction or minimization of fluid drag; and (b) the optimization of thrust production. These two objectives can, however, be integrated to be posed in a more fundamental way. Namely: (c) given a mass or volume, possibly subject to some geometric constraints, minimize the energy required to move it between two points or to follow a specified motion, i.e. speed and path.

Since the pioneering work of Prandtl at the beginning of this century and the understanding of the source of fluid drag in term of departures from ideal flow, namely boundary-layer friction and more importantly flow separation, a strategy for attacking problems (a) and (b) above is developed. Solve (a) first which generally calls for a streamlined and rigid body which minimizes the wake and therefore the drag. In this instance, a flexible body may effectively increase the bluffness. After obtaining an answer to (a), solve (b) to provide the thrust required by (a) to overcome the drag in the most efficient manner, with minimal modifications to the body design consequent of (a). Hundreds of years of engineering have allowed the remarkable achievement of high propulsive efficiencies using a number of steady or quasi-steady propulsion systems, such as sails, propellers, water jets, and oscillating foils. Although the drag and thrust of the body are essentially considered separately, interference effects

associated with coupling of the thrust-production mechanism to the rigid-body, such as effective wake fraction and thrust deduction, promote the iterative design process which continually revisits problems (a) and (b). Indeed, this iterative and sequential approach is *the* strategy for the design of almost all surface and underwater vehicles in the last century.

There are several immediate consequences to the application of this process. First, attempts to minimize the flow disturbance in the design of a marine vehicle result in poor unsteady maneuvering capabilities, which require the generation of large short-duration forces and produce strong wake structures. Second, solving the problem of efficient thrust production is a sophisticated, detailed engineering achievement, while solving the problem of drag minimization or reduction is often still more of an "art" than science.

Observations of natural locomotive systems suggest the possibility of a radically different strategy to the paradigmatic approach described above, namely a synthetic optimization to solve problem (c) directly and to minimize the energy required to move between two points for specified motion and geometric characteristics. The fundamental question posed above is subtle, in that it does not assume the body to be rigid. Looking at fish with long-range, rapid swimming capabilities, such as tuna, this strategy has developed several common characteristics, which dramatically differentiate the motion from the historically-engineered paradigms for marine vehicles. First, the propulsive motion is unsteady and rhythmic, typically with a flexible body. Second, the swimming and maneuvering motions involve the generation and subsequent manipulation of strong energetic vortical structures by the body and in the wake. Finally, the thrust created by the body motion and the resulting drag are *inherently inseparable.* The question here, for example, is not the sophisticated technical question of whether the required mean thrust can be otherwise obtained more efficiently than flapping foils (which, incidentally can be also highly efficient). Rather, the question is whether the energy required by a solution to problem (c) is less than the energy required by a solution to the iterative outcome of (a) + (b), regardless of the specific means used for developing the thrust in problem (b) or the

(mean) thrust part of (c).

The consequence of the development of propulsion systems by fish include dramatically improved maneuvering capabilities over man-made vehicles, as well as the possibility of the reduction of hydrodynamic drag by actively-swimming flexible bodies. This thesis probes the questions posed above by detailed examination of the hydrodynamics of flexible-body fish swimming motions, to understand the fluid dynamic and vorticity control mechanisms which the fish might utilize to decrease the energy expended through locomotion, so that these mechanisms might be applied to man-made propulsion, maneuvering, and hydrodynamic control systems.

1.1 Motivation

Millions of evolutionary years have allowed aquatic creatures to optimize their locomotive skills for their respective roles in a complex underwater ecology. The hierarchy of the predator-prey environment have equipped some of the larger swimmers to realize high swimming speeds, long ranges, and excellent propulsive efficiencies. Others have remarkable rapid maneuvering capabilities, performing 180^o turning motions in less than one body length in under one second, or station-keeping and hovering abilities. An extensive literature base has been developed in the last century in an attempt to quantify these performance assertions, both through experimental observations and measurements as well as detailed approximate analytic or numerical methods. The interdisciplinary interest in the swimming of fish has reached unprecedented levels, with a wealth of contributions to the understanding of the science coming from both fluid dynamicists and marine biologists alike.

Gray [72, 73, 74, 75] documented the motions of the eel and described mechanisms by which the undulations of the backbone contributed to the thrust production. Gray [76] attempted to quantify the performance of swimming dolphin and porpoise through experimental observation of the cetaceans' swimming speed and experimental measurements of the resistance of the cetaceans in a rigid state. By calculating the power required to overcome the drag measured at the observed swim-

ming speed of around 20 knots and comparing that to an estimate of the power generation capabilities of the mammals' musculature, Gray concluded that either the cetacean musculature was capable of producing power at a rate seven times greater than other types of mammalian muscle or that the resistance of the body undergoing swimming motions was seven times less than that of the rigid body resistance. This assertion of the presence of substantial drag reduction in live actively-swimming fish, which has come to be known as *Gray's Paradox*, has remained extremely controversial for over sixty years largely because it is extremely difficult to obtain reliable force measurements from live fish. Recent work by Rome, *et al.* [171] has outlined a methodology that may provide in the near future a definitive answer based on live fish measurements.

Gray's Paradox was the impetus for extensive investigation on the propulsive mechanisms of fish and cetaceans. Several theories emerged to reconcile Gray's Paradox, including turbulence suppression [123], skin friction reduction by means of boundary layer shear stress modification through skin coatings [115, 94], optimized musculature to allow for more efficient energy conversion [171], and control of shed vorticity dynamics [21].

Wu [239] investigated the propulsion characteristics of a flexible 2D plate using an inviscid, linear, potential flow theory. His seminal and elegant work did not consider the dynamics of the shed wake vorticity and did not attempt to validate this theory by comparison to experimental results. Lighthill [125] developed a similar inviscid theory for describing the hydrodynamics of a flat three-dimensional fish body with an arbitrary profile, but his reactive theory does not well describe the three-dimensionality of the flow around the profile or the dynamics of the shed vorticity. Wu [241, 242, 243] reproduced Lighthill's slender body theory results, with consideration of the influence of vorticity shed from separation edges upstream of the inflow into the tail fin. However, for a variety of fish forms, with low aspect ratio bodies and high aspect ratio tails, the basic assumptions of these linear slender body theories are violated. When such methods are employed to predict forces on more realistic fish-like forms, the thrust is overpredicted, given the kinematics of the motion, in comparison

to more comprehensive numerical approximations [97]. Indeed, Lighthill's subsequent conclusions, based on his large-amplitude elongated-body theory [126] application to the observed motions of a live dace *Leuciscus* [16], suggest that the drag of a swimming fish (equal to the thrust produced for steady speed straight-line swimming) is actually higher in the swimming fish by a factor of four than in the rigidly-towed fish.

The propulsive mechanisms utilized by certain fish have been attributed largely to the motions of the airfoil-shaped and often lunate tail, and study of unsteady foil motion, for both the swimming motions of fish and the hovering and flying motions of birds and insects, has provided insights into the details of these dynamics. The linear, ideal flow theory of unsteady foil motions has been studied by a several investigators [215, 239, 241, 242, 243, 127, 40], but as this analytic potential theory employs a linearized body boundary condition and an assumed shape of the wake, the wake dynamics are not allowed to develop. Although nonlinear corrections to this theory have been cited by Lighthill [127] and Chopra [39], the vorticity is assumed to remain on the path traced by the trailing edge, and its self-influence neglected. Lan [121] developed a vortex lattice method which accounts for shed wake influence to investigate numerically the dynamics of pitching and heaving foils and identified regions of high efficiency, and Cheng, *et al.* [36] applied a vortex lattice method for computing the propulsion characteristics of a waving plate. These numerical works again relied on linearized body boundary conditions, and a periodic vorticity distribution in the Trefftz plane. Ellington [53] studied the aerodynamics of hovering insect flight and concluded that the unsteady flow mechanisms play a very important role, including a delay in stall. The large values of lift coefficient were associated with the formation of a leading-edge vortex, which was amalgamated with trailing-edge vorticity for specific parametric combinations [54]. These types of dynamics may be of extreme importance in recovery by the tail of energy released into the fluid through separation and the motions of the fish forebody, as suggested by Lighthill [125]. Many of the analytic and numerical methods developed to study the dynamics of fish propulsion have relied on assumptions of small amplitude motion and of linear behavior of the velocity field surrounding the fish. It is observable that most fish do not utilize small

amplitude tail motions, but rather motions which exceed the limit of classic linear lifting surface theories [204].

Triantafyllou, *et al.* [204] were able to show that a variety of fish and cetacean swim at speeds with a frequency and amplitude of the tail motion which is within a narrow range of Strouhal numbers. This range of Strouhal numbers corresponds to the region of maximum spatial amplification of the thrust jet instability for a two-dimensional flow. This evolutionary predisposition for a fish to swim at a frequency corresponding to the minimum amount of energy lost in the wake for a given momentum is likely no accident, and from an energetics and efficiency standpoint, vorticity control is of key importance for the fish to achieve optimal performance.

Thus, large amplitude oscillation of airfoils has been shown to offer advantages not present in steady conventional propulsors. It was shown, for example, that unsteady motion of airfoils causes very high lift coefficient [80], and can produce propulsive thrust very efficiently [204, 10]. Also, an oscillating foil can be used to alter and reposition oncoming vorticity [114] and recapture energy contained in the eddies of an oncoming flow using vorticity control [68].

Several researchers have attempted to identify the more general mechanisms of vorticity control. Ffowcs-Williams & Zhao [56] and Tokomaru & Dimotakis [202] have shown that efficient flow control can be achieved by unsteady motion of a body in the fluid. In addition, periodic forcing of a flow has been studied by several investigators, with important implications on efficient propulsion [170]. Imposing harmonic rotary oscillations of a cylinder in an oncoming stream can result in a reduction in wake width [196], with maximum influence on the flow when the frequency is close to the Strouhal frequency [202]. Under proper conditions the wake width, and hence the drag, can be reduced substantially. They also make the point that in unforced wakes, the separation points move relatively little, and the natural instability of the flow redistributes the vorticity to create the large scale patterns; whereas in a forced oscillation the separation points move substantially, hence gathering vorticity near the cylinder and releasing it in the wake. Boundary layer turbulence suppression was observed by Taneda [197] in the flow around a flexible plate in an oncoming stream,

as long as the phase speed of the plate's traveling wave c_p exceeds the free stream velocity U. Gopalkrishnan, *et al.* [68] experimentally demonstrated active control of a shear flow by utilization an oscillating foil.

As many fish utilize a sharp trailing edged caudal fin, research on vorticity control by oscillating foils has been particularly revealing. Streitlien [190] developed a numerical method of analyzing the performance of an oscillating foil with nonlinear wake development using a conformal mapping technique. Streitlien, *et al.* [191] used the same numerical technique to show that an oscillating foil in a free stream in the presence of upstream generated vorticity was capable to energy recapture and efficiencies higher that 100%. Anderson, *et al.* [10] employed experimental digital particle image velocimetry techniques (DPIV) to obtain quantitative visualizations of an oscillating foil. This research revealed the mechanisms by which dynamic stall vortices associated with high pitch and heave amplitudes can be manipulated by the kinematics of the foil motion to favorably affect the efficiency of the motion and similarly by which shed vorticity upstream of the oscillating foil can be manipulated to increase or to decrease efficiency.

Several researchers have attempted to visualize the wake of a naturally swimming fish. The problem is quite difficult for several reasons. First, the fish must swim naturally at a given time and position as dictated by the visualization method. The fish should be deeply submerged in unbounded fluid so that walls and the free surface do not affect the flow. Techniques that have been used with moderate success include dye visualization [172, 7] and visualization using a stratified layer [172, 150]. Neither method has elucidated the details of the flow near the body and in the wake. Stamhuis and Videler [186, 187, 188, 189] have utilized experimental particle image velocimetry to capture the flow dynamics around several live swimming organisms and to analyze the energetic makeup of the wake. Anderson [9] used experimental digital particle image velocimetry (DPIV) to visualize the wake behind a swimming danio and identified the active manipulation of shed vorticity by the fish to create a reverse Kármán vortex street in its wake. In addition, mechanisms of regulated bound vorticity release and optimal flow actuation were observed experimentally and

through numerical simulation employing these same experimental data [233, 234]. Müller, *et al.* [153] analyzed the wake of a swimming mullet using similar DPIV techniques and concluded that the manipulation of the wake structure by the continuous swimming motions resulted in high propulsive efficiencies.

One of the most exciting topics in fish swimming hydrodynamics is the fast-start/maneuvering capability of fish. Most fish can turn 180° on a radius considerably less than their body length whereas man-made underwater vehicles require several lengths to execute a 90° turn. Some examples of experimental measurements of live fish maneuvering and starting can be found in Weihs [225, 226], Blake [26], Harper & Blake [81, 82], and Frith & Blake [61]. An excellent review of the literature on fast-start swimming of fish with a wealth of experimental data can be found in Domenici & Blake [51]. A thorough kinematic analysis of unsteady turning and maneuvering motions can be found in Videler [212]. The fish has developed a complex feedback and control system which allows for the conversion of local backbone oscillations into global trajectory changes. A simple robotic mechanism has been used to study fast-start swimming thrust generation elucidates some of the wake dynamics associated with thrust production [5]. Recent work on fish turning visualization and simulation has shed considerable light of the mechanisms of managing body bound vorticity and its subsequent interaction with the oscillating lifting surface of the caudal fin [8, 9, 233, 234]. By examining the near-body flow and the wake produced by the turning motions of certain fish, we may begin to understand some of the mechanisms involved with control of the shed wake vorticity.

Experimental results for the energetic makeup of the swimming fish are hard to obtain, and even when attainable in the laboratory, may not be characteristic of natural environment behavior. As a result, Barrett [18] constructed a robotic underwater flexible hull vehicle in the shape of a tuna with a lunate tail (which have historically been known to achieve high swimming speeds and long ranges) capable of swimming in a straight line on a towing carriage, and on which energetic analysis could be performed. The question addressed by this work was whether unsteady flow control can also lead to overall drag reduction in streamlined bodies, a task that

has proved elusive so far. The development of this robotic mechanism, which can emulate very closely the swimming of the tuna, overcomes the difficulties associated with live fish, because it allows the acquisition of detailed accurate measurements of the hydrodynamic forces on an actively controlled flexible body swimming like a fish. Barrett [19] defined several characteristics as measures of performance, and concluded that over narrow ranges of various swimming parameters, the robot could achieve extremely high efficiencies, and in addition, can experience lower drag than that of the rigid body hull. Repeated precise measurements on the flexible robot have shown that, within a parametric range, drag in an actively swimming vehicle at Reynolds number of about 10^6 can be reduced by 50% or more (up to 70% within the range considered), compared with the value on the same vehicle towed in a rigid–straight configuration. This drag reduction can be attributed only to the effect on the flow of the imposed body flexing in the form of a traveling wave. The mechanisms contributing to this observed drag reduction are attributed to laminarization of the boundary layer and to vorticity control by the tail fin [21].

Using this compendia of experimental data, and drawing from the rich, diverse base of recent literature on fish swimming performance prediction and vorticity control mechanism hypotheses, this thesis will deal with the development and use of a numerical simulation method to explore the mechanisms of vorticity control and flow actuation utilized by swimming fish. Several cases of fish swimming will be examined, using both two- and three-dimensional numerical simulation methods, in an attempt to corroborate experimental observations and measurements and to elucidate the principles of vorticity control hypothesized in previous works more clearly. This numerical method benefits from the advantage that the entire unsteady flow field can be solved and then studied in much detail, an unobtainable luxury when employing experimental DPIV or direct dynamical measurements.

In addition the ability to provide subtle details of poorly understood physics of fish swimming, this numerical method can be employed as a design and optimization tool for practical applications in ocean engineering. The potential for long-range silent propulsion technology is tremendous, and this simulation tool may serve as

a catalyst to the development of this technology as a viable propulsion alternative. The efficiency of this propulsion system can also be seen as an added or exclusive benefit to the stealth features, making this propulsion system attractive to conventional shipping methods in addition to littoral reconnaissance vehicles. Finally, this numerical simulation method may be employed on a more limited scale to investigate the physics of station-keeping and maneuvering, skills which the fish has mastered quite adeptly and which may provide tremendous benefit in a variety of marine and other fluids engineering discipline. Man-made systems aspiring to attain the performance capabilities of fishes may require active vorticity control of this type, in order to generate sustainable minimum energy thrust jets for efficient forward propulsion schemes and to generate large, short-duration localized body forces for maneuvering motions confined to within a fraction of the body length.

1.2 Objectives and canonical problem description

In the present thesis, a numerical methodology is developed to simulate the hydrodynamics surrounding the propulsion of a fish-like body, with attention given to the kinematic mechanisms by which fish control shed wake vorticity and the resulting effects on propulsion and maneuvering. Unlike traditional analytic studies or more recent numerical works, this formulation allows for the satisfaction of the exact body boundary conditions. This numerical methodology will be employed in both two- and three-dimensional canonical problem simulations to study the mechanisms of flow actuation and vorticity control employed by fish in both steady, straight-line swimming as well as rapid maneuvering. Through the simulation of propulsion and maneuvering dynamics, the kinematics of vorticity control and the corresponding unsteady wake dynamics can be examined over a range of parametric values which define the body motion, for use of the simulation method as a optimization tool for flexible-body propulsion design.

To accomplish this thorough investigation, both two- and three-dimensional nu-

merical simulation methods will be developed for the study of the following problems: *(i)* the abrupt starting from rest to some steady horizontal velocity U of a streamlined two-dimensional foil section in an infinite fluid domain, which is allowed to undergo periodic oscillations about its mean nose-tail line in the form of a traveling wave moving from head to tail; *(ii)* the steady forward swimming of a three-dimensional flexible body in a manner similar to the two-dimensional model but with a well-defined fish-like geometry consisting of a streamlined body and a sharp trailing edged 3D foil for a tail; *(iii)* the turning characteristics of a three-dimensional flexible body through the modeling of the turning dynamics of a flexible three-dimensional body in an infinite fluid through a turn angle of $O(\pi/2)$ from a steady-swimming motion to another steady swimming motion, and studying the resulting vortical dynamics associated with this turn. A full summary of each canonical problem is described herein.

1.2.1 Canonical problem *(i)*: 2D straight-line swimming

The investigative focus of this problem is on the dynamics of the vorticity generated by a two-dimensional flexible body undergoing steady, periodic swimming motions and on the associated integrated performance measures of the body dynamics. Such a study might represent the hydrodynamic properties of swimming in the center-plane of an actual high-aspect ratio fish-like body, or more fundamentally, the hydrodynamics associated with the swimming of a flexible high-aspect ratio plate.

The seminal contributions to the two-dimensional inviscid theory of fish swimming by Wu [239, 241] relied on a conformal mapping technique to evaluate the fluid dynamics around a infinitesimally-thin body, and as a result, nonlinear body thickness effects and nonlinear effects of motion amplitude are neglected. More importantly, however, the effects of the shed vortical wake were linearized to a Trefftz plane contribution, obviating wake evolution and shedding nonlinearities.

The study of the stability of two-dimensional thrust [204] and drag [203] jets has revealed that the maximum spatial amplification of the respective convective instabilities is dependent on the Strouhal number St. Thus, the alignment of the two shear layers into regions of large-scale vortical structure of alternative sign, corresponding

to a specific range of Strouhal numbers for the thrust-jet and the drag-jet profiles, minimizes the amount of kinetic energy lost to the wake for a given momentum of the fluid.

The importance of these analyses to fish swimming became clear when a study of the Strouhal number of fish swimming [204] revealed that many species of large, fast-swimming fish all swim within a Strouhal number range corresponding to the maximum spatial amplification of the two-dimensional thrust jet. Thus, fish seem to minimize the energy lost to the production of a vortical wake by swimming at the most efficient Strouhal number, and this further suggests that fish exercise a certain degree of *vorticity control*, where the large-scale vorticity dynamics are two-dimensional in nature.

In order to assess the validity of Wu's two-dimensional theory and to measure the importance of two-dimensional vorticity dynamics in fish swimming, a boundary-integral code is developed for the study of two-dimensional flexible-body swimming. The abrupt starting from rest to some steady horizontal velocity U of a streamlined two-dimensional foil section in an infinite fluid domain, which is allowed to undergo periodic oscillations about its mean nose-tail line in the form of a traveling wave moving from head to tail, is analyzed for a range of Strouhal numbers and waveforms. The effects of viscosity are assumed to be confined to an infinitesimally-thin boundary shear layer along the body and an infinitesimally-thin shear-layer wake. This code, while neglecting viscosity in the evaluation of the momentum equations and thus lending itself to rapid computational analysis, attempts to model the hydrodynamic properties of fish swimming at a high Reynolds number, and may not be accurate for speeds or motions amplitudes where the effects of viscosity are made more prominent through large-scale boundary-layer separation from the body or through creeping flow along the body boundary.

The results from the study of this two-dimensional swimming motion will be compared to the linear theory analytic results of Wu [239], with emphasis on the effects of body motion and wake nonlinearity. While not an accurate representation of the swimming kinematics or of the geometry of a majority of high-speed fish,

this analysis intends to shed light on the effects of the flexible-body motion on the control and development of the resulting thrust-jet wake structure. The correlation of these two-dimensional swimming and wake-development results to three-dimensional swimming properties will be drawn with reference to experiments, literature, and the three-dimensional canonical problems *(ii)* and *(iii)* outlined below.

1.2.2 Canonical problem *(ii)*: 3D straight-line swimming

The investigative focus of this problem is the general fluid physics surrounding steady, periodic swimming motions of a three-dimensional flexible body with fish-like geometry, with emphasis on the analysis of the dynamics of the vorticity generated by separation from the sharp trailing-edges of the body, the near-body flow actuation dynamics affected by the local body motions, and the associated integrated performance measures of the body dynamics. Different fish geometries will be considered, as well as different combinations of parameters defining the fish swimming motions, in order to evaluate the importance of morpnological and kinematic differences between various fish species and motions. Fundamentally similar to the two-dimensional swimming study, this problem's extension to three-dimensions will capture some of the more realistic fish swimming motions and fluid dynamic phenomena and may highlight some of the subtle complexities of three-dimensional vorticity control swimming mechanisms and the subsequent limitations of a two-dimensional analysis.

Three-dimensional theories of swimming performance following the inspiration of Gray [76] have included seminal contributions from Taylor [200], Lighthill [125, 126, 127], Wu [242, 243], and Newman [159, 156]. The later theories of Lighthill and Wu, considered to be *reactive* theories in contrast to the *resistive* theory of Taylor, rely again on linearized body motions and strict assumptions about the body profile. The three-dimensional body is considered to be an infinitesimally-thin plate with a fish-like profile. The motions are considered to be small, as is the rate of change of the body's profile depth. The resulting fluid motions are in the plane of any body section along the length, and the reactive propulsive force results from the change in added mass accelerated by the small body perturbations in the form of a traveling

wave along the body length. Contributions from a wake shed into the fluid by the tail or upstream fins is assumed to come from a linearized Trefftz plane analysis.

In order to couple this reactive theory of fish swimming, a low aspect ratio undulating body, with the unsteady dynamics of the tail, a high aspect ratio oscillating tail, experimental, theoretical, and numerical investigators have endeavored to understand the propulsive mechanisms of oscillating two- and three-dimensional lifting surfaces. Works by Glauert [66], von Kármán & Burgess [215], Scherer [183], Lighthill [126], Chopra [38, 39, 40], Cheng & Murillo [34], McCroskey [149], Koochesfahani [113], Gopalkrishnan [68], Streitlien [190], and Anderson *et al.* [10] form a solid foundation of evidence suggesting that the oscillating lifting surface is an efficient method of producing thrust for propulsive purposes, resulting in high values of lift coefficient, delayed stall, vorticity control and reposition, and energy recapture. Some fish, such as tuna with high-aspect ratio tails, may utilize some or all of these mechanisms in propulsion through oscillation of its caudal fin, and little theoretical work has coupled the mechanisms associated with undulation of a low-aspect ratio body with a high-aspect ratio tail fin.

The development of a unified swimming prediction theory for complex geometries has proved elusive, as simplifying assumptions in the theories have obscured the numerous subtleties of the problem. In order to paint a global picture of the flow as it as affected by the fish motions, flow visualizations [172, 173, 150, 7] have provided qualitative information about the near-body flow in the center-plane depth of the fish, and in more recent works [186, 9, 153], quantitative information through the use of various particle image velocimetry techniques. The limitations of PIV techniques are numerous, not the least of which that these methods yield only partial information about the flow field, i.e. in the plane of the imaging laser. Additionally, the imaging laser may cast shadows which may obscure portions of the only plane of data recorded by the imaging system, particles may flow perpendicularly out of plane, and the behavior of the biological subject is never predictable or precise. Finally, these types of flow visualization, while fundamental to the construction of hypotheses surrounding the fluid control mechanisms utilized by fish to swim efficiently, are insufficient to

predict the dynamical loads on the body in the fluid.

Barrett [19] developed a robotic mechanism, the *RoboTuna*, to enable the direct measurement of dynamical quantities on a flexible swimming fish-like body with predictable, precise, prescribed kinematic characteristics. While the details of the near-body fluid dynamics are not observed on the *RoboTuna* without the aid of dye visualization or PIV techniques, the forces, moments, and powers required to allow the fish to swim through the water are recorded precisely through redundant direct measurements using load cells and force transducers. These measurements have revealed that the fish is able to reduce its hydrodynamic drag below the rigid body drag value within certain ranges of the swimming kinematic parameters. This evidence of drag reduction, in the absence of a unified theory to predict even the swimming performance of fish, let alone the complex fluid dynamics associated with the flexible-body motions for arbitrary geometries, urges the development of a comprehensive numerical simulation capability, heretofore lacking for this problem within a three-dimensional framework.

A three-dimensional boundary-integral code is thus developed for the study of flexible-body fish swimming, in order to corroborate direct dynamical experimental measurements made on the *RoboTuna* and experimental flow visualizations employing DPIV, to assess the validity of Lighthill's three-dimensional slender body theories, and to quantify the importance of three-dimensional vorticity dynamics and vorticity control in fish swimming. The abrupt starting from rest to some steady horizontal velocity U of a streamlined three-dimensional flexible body, with arbitrary fish-like geometry, in an infinite fluid domain is considered. Like the two-dimensional kinematics, the body is allowed to undergo periodic oscillations about its mean nose-tail line in the form of a traveling wave moving from head to tail. The kinematics of the tail are considered to be additional parameters of the motion, allowing for a phase lag between the side-to-side heaving motions of the tail and the pitch angle of the leading edge and for an angle of attack of the tail fin chord with respect to the path traced by its leading edge. These swimming motions are prescribed using seven independent parameters, and the resulting near-body hydrodynamics and the global integrated

dynamical quantities on the body are analyzed for a range of swimming parameters and Strouhal numbers, corresponding to motions for which there is both experimental dynamical and visualization data for comparison.

For the purposes of code development, the effects of viscosity are assumed to be confined to an infinitesimally-thin boundary shear layer along the body and an arbitrary number of infinitesimally-thin shear-layer wakes, to be shed from predefined separation lines at the trailing edges of fins or backbone ridges. In this manner, these simulations attempt to model the hydrodynamic properties of fish swimming at a high Reynolds number, and may not be accurate for speeds or motions amplitudes where the effects of viscosity are made more prominent through large-scale boundary-layer separation from the body or through highly-laminar near-body flows with a large developed boundary layer.

The simulations of straight-line swimming motions will then be employed to study mechanisms of flow actuation and vorticity control for parametric variation of the swimming kinematics and for geometric variation of the body shape and separation line definition. In this manner, the effects of secondary fins, such as thin dorsal, anal, or pectoral fins, on the vorticity dynamics and on the overall performance of swimming can be quantified. The wakes shed by trailing edges of these secondary fins may interact with the vorticity shed from the oscillating caudal fin to enhance or to diminish the efficiency of the propulsive mechanisms, and the correct modeling of these vortical dynamics may be crucial to the accurate resolution of the near-body flow. The phase of the interaction between upstream-shed vorticity and the oscillation of the tail and its impact on swimming performance will be a concentration of this investigation.

The numerical treatment of these secondary lifting surfaces is a non-trivial computational matter. As these fins become smaller and thinner with respect to the rest of the fish body and caudal fin, the stability of the boundary integral solution is jeopardized due to the nature of the computation of the influence coefficients for thick-bodies with tight curvature or sharp corners employing a low-order panel method. For this reason, a mixed-boundary value formulation is developed to allow for the coupled

geometric representation of both thick forms, such as the main body and caudal fin, as well as thin fins, such as the dorsal or anal fins. Thus, the stability problems associated with modeling the thin fins as thick bodies with tight leading-edge curvature are alleviated.

With these computational tools, we can quantitatively assess the performance of straight-line swimming motions over a broad range of geometric and kinematic parameters. Systematic parametric variation investigations will also provide insight into the mechanisms of vorticity control and flow actuation utilized by swimming fish, and visualization of the structure of the complex three-dimensional flow dynamics made possible through direct simulation of the entire flow field will allow for the development of simple models to describe these basic mechanisms in an abstract fashion for application in engineered ocean systems.

1.2.3 Canonical problem *(iii)*: 3D unsteady maneuvering

The investigative focus of this problem is the general fluid physics surrounding unsteady, arbitrary local body motions and time-varying trajectory of a three-dimensional flexible body with fish-like geometry. Significant emphasis is placed on the analysis of the near-body flow actuation dynamics affected by the local body motions, the regulated formation and release and the subsequent control of the dynamics of the body-bound and free wake vorticity, and the associated integrated performance measures of the body dynamics. The turning motion of a small fish, the Giant Danio *Danio malabaricus*, will be examined in detail through numerical simulation, and variations to the fish body geometry and shedding properties will enable evaluation of the various vorticity control mechanisms. Employing a numerical scheme fundamentally similar to the three-dimensional straight-line steady swimming simulation method, this problem's incorporation of arbitrary localized backbone actuation and non-constant trajectory will allow for the study of more complex and natural unsteady fish swimming motions and fluid dynamic phenomena. Additionally, this simulation capability will highlight some of the three-dimensional vorticity control and flow actuation mechanisms employed by fish in achieving outstanding maneuvering

performance.

The turning performance of most species of fish has been observed to be exceptional, with most species of fish being able to affect a complete reversal of trajectory within less than one body length. Additionally, the fast-start acceleration performance of fish in achieving a steady swimming speed from rest has been recorded through a large body of experimental research, with fast-start accelerations of most fish ranging between $3g$ to $7g$ [26], with some notable exceptions, such as the start of a pike *Esox lucius* which has been observed to accelerate at $245m/s^2$ or $25g$ [81], all of which out-perform conventional man-made marine vehicles. While the body kinematics of many turning and starting maneuvers for various species of fish have historically been well-documented [225, 226, 26, 81, 82, 212], the corresponding dynamics of the surrounding near-body fluid has not been analyzed. Weihs [225, 226] extended Lighthill's large-amplitude elongated-body theory [126] to predict the acceleration performance of specific starting and turning maneuvers, but a thorough fluid dynamic investigation to identify the mechanisms responsible for the attainment of remarkable acceleration had heretofore been unattempted. Recent work by Anderson [9] utilized a DPIV flow visualization technique to capture the quantitative near-body flow dynamics in the mid-depth plane of a Giant Danio (*Danio malabaricus*) executing a turning motion, the first time the body kinematics and the corresponding fluid dynamics of a turning motion were simultaneously documented with any degree of precision.

The three-dimensional boundary-integral code which was developed for the study of flexible-body fish swimming is modified to investigate the hydrodynamics of unsteady turning maneuvers. A streamlined three-dimensional flexible body, with arbitrary fish-like geometry, in an infinite fluid domain is considered to start abruptly from rest to perform an imposed unsteady global trajectory. Unlike the three-dimensional swimming kinematics, the localized body undulations about its mean nose-tail line are neither necessarily periodic nor in the form of a traveling wave moving from head to tail. The localized kinematics are also imposed, as are the coupled kinematics of the actuated tail fin which still allow for an angle of attack. Instead of parameters which

analytically describe the imposed swimming motions, the images of experimental data are analyzed at various time steps throughout the turning maneuver in order to gain a time history of both the global trajectory as well as the localized backbone and tail undulations. These backbone and global body trajectories are utilized to derive an analytic approximation to the exact turning motions, employing a series expansion technique with linear additives to account for the non-periodicity of the motion history. The resulting near-body hydrodynamics and the global integrated dynamical quantities on the body are resolved through simulation of the imposed motions, and the hydrodynamic profiles obtained through simulation are compared to those captured using DPIV imaging techniques to assess the validity of our computational technique and modeling assumptions.

Again, the effects of viscosity are assumed to be confined to an infinitesimally-thin boundary shear layer along the body and an arbitrary number of infinitesimally-thin shear-layer wakes, to be shed from predefined separation lines at the trailing edges of fins or backbone ridges. In this manner, these simulations attempt to model the hydrodynamic properties of fish swimming at a high Reynolds number. While these simulations may, in general, not be accurate for motions amplitudes or local backbone trajectories which are extreme or which may cause obvious separation from surfaces other than the predefined trailing edge separation lines, experimental data supports the assertion that the effects of viscosity in the turning motions examined are not exacerbated through large-scale boundary-layer separation from the body or leading edge separation from the lifting surfaces. The Reynolds numbers of the experimental turning motions are within a transition region where the boundary layer can be assumed to be confined to a region close to the body.

The simulation of the unsteady turning motions will then be employed to study mechanisms of flow actuation and vorticity control for geometric variation of the body shape and separation line definition. In this manner, the effects of secondary fins, such as thin dorsal, anal, or pectoral fins, on the vorticity dynamics and on the overall performance of swimming can be quantified. The interaction of secondary wakes shed by trailing edges of thin fins may interact with the body-bound vorticity developed

during backbone flexing and released by the caudal fin in a regulated fashion into the wake to affect the creation of a turning jet and thus vectored body thrusting. The correct modeling of these vortical dynamics may be crucial to the accurate resolution of the near-body flow, as can be validated through comparison to experimental results.

With these computational tools, we can qualitatively and quantitatively assess the performance of unsteady turning and maneuvering motions, as well as the mechanisms of vorticity control and flow actuation utilized by maneuvering fish, Similarly, visualization of the structure of the complex three-dimensional flow dynamics made possible through direct simulation of the entire flow field will allow for the development of simple models to describe these basic unsteady vorticity control mechanisms in an abstract fashion for ocean control system applications.

1.3 Overview of the thesis

The present thesis is organized into seven chapters, five appendices, and a bibliography of both cited and other references. The first chapter, *Chapter 1*, presents a motivation of this work, an argument to justify the problems to be studied, and an outline of the tasks involved in studying the problem. First, previous experimental, theoretical, and numerical research on fish swimming, as well as fields of fluid dynamics whose impact on future fish swimming hydrodynamics research is immediately relevant, are reviewed and discussed. The current research is carefully synthesized from the important contributions of a variety of research disciplines, including biology, fluid mechanics, and control theory, and this synthesis is developed through thorough review of the relevant literature base. Emphasis of the current work is placed on highlighting the dynamics of vorticity interactions with a swimming flexible body and the subsequent impact on swimming performance. The generalized problems of fish swimming to be studied through numerical simulation are then outlined as canonical problems which involve addressing the several fundamental technical and scientific issues relevant to the study of these phenomena through computational analysis. These canonical problems include *(i)* the two-dimensional analysis of steady

swimming motions, *(ii)* the three-dimensional analysis of steady swimming motions, and *(iii)* the three-dimensional analysis of unsteady maneuvering, and the relevant previous research and the formulation of each canonical problem is briefly described.

In *Chapter 2*, the first canonical problem, *(i)* the two-dimensional analysis of steady swimming motions, is studied in detail. The unsteady initial boundary value problem is developed for a streamlined two-dimensional body of arbitrary flexibility in an ideal, irrotational, infinite fluid. The body is impulsively started from rest to a constant translational velocity U, with an infinitesimally-thin, deformable wake sheet separating from a predefined separation point, while undergoing periodic localized backbone undulations in the form of a traveling wave progressing from head to tail down the mean line of the backbone. The solution of the boundary value problem is developed in unsteady boundary integral panel method formulation, with a desingularized discrete vortex representation of the continuous wake sheet shear layer. Systematic convergence, consistency, and stability of the numerical method is shown with respect to panel number, time integration scheme, time step, and desingularization parameter. Attention is given to starting vortex placement and unsteady vortex shedding location and strength computation schemes. The method is further validated through simulation of the steady translation of a rigid foil for a variety of foil geometries, and the steady lift and drag coefficients are compared to experimental and theoretical values.

The two-dimensional method is then employed to investigate the structure of the wake shed by the swimming body, in the shape of a NACA foil cross-section, over a range of parameters defining the parameters of the motion. Attention is given to the structure of the unsteady, deformable wake for swimming motions over a range of Strouhal numbers through variation of traveling wave frequency and amplitude and over a range of wavenumbers. Comparison to the live fish DPIV visualization experiments of Anderson [9] shows good agreement with respect to the developed wake structure. Comparison to the analytic swimming theories of Wu [239] for a two-dimensional waving plate shows some discrepancies for large waveform amplitudes and for high Strouhal numbers, and explanations of these differences are provided.

Finally, the energetics of the wake are analyzed with respect to the Strouhal number of swimming and compared to the stability analysis of Triantafyllou, *et al.* [204]. Extensions of this method to provide predictions of three-dimensional swimming performance are hypothesized.

In *Chapter 3*, the foundations of the numerical method for the study of canonical problem *(ii)* are established. The unsteady initial Dirichlet boundary value problem is developed for a streamlined three-dimensional flexible body in an ideal, irrotational, infinite fluid domain. The body may generate an arbitrary number of desingularized shear layer infinitesimally-thin wake sheets from predefined separation lines along sharp trailing edges or backbone ridges, and the body is impulsively started from rest to a steady translational velocity U while undergoing periodic oscillations in the form of a traveling wave progressing from the nose to the tail along the backbone of the body. For a fish-like body with a thick, distinct caudal fin, seven independent parameters define the kinematics of the swimming motion and caudal fin actuation. The solution of the boundary value problem is developed through unsteady boundary integral formulation. The body is divided into quadrilateral source-dipole panels, and the source-strength on each body panel is set to equal the imposed normal fluid velocity at each panel's collocation point, thus satisfying a Dirichlet body boundary condition and allowing for the determination of the unknown dipole strength distribution. In addition, the unsteady Neumann boundary value problem is developed for thin bodies, such as secondary fins, where the source strength is zero, and the body is comprised of a sheet of dipole panels. The solution is formulated in unsteady boundary integral formulation as well, and the hypersingularity of the self-influence coefficients for the panels is addressed in detail. The coupling of the two initial boundary value problems is then described in detail, and a simple representation of the coupled mixed-boundary value problem solution method is outlined. The geometric descriptions of the fish bodies employed in simulations throughout this research are also outlined. Finally, systematic convergence of the numerical method is presented for a variety of geometries, with respect to panel number, time step, and desingularization parameter, and comparison of the simulation results to published

experimental and numerical data shows excellent agreement.

In *Chapter 4*, an overview of the simulation capabilities of straight-line swimming dynamics is presented, with emphasis on the validation of the code with respect to experimental data of straight-line steady swimming of fish. First, a review of the biological literature is presented, and the many of the common morphological and kinematic features of fish swimming inspire and motivate the issues to be addressed through numerical simulations. Then, both global performance evaluation by comparison with data from the *RoboTuna* as well as detailed unsteady local flow field dynamics by comparison with the DPIV visualization data of a swimming Giant Danio are extensively documented. The comparison of the simulation method to the traditional linear theories of Lighthill [127] qualitatively and quantitatively explores the limitations of the analytic methods in computing both global performance measures as well as local flow dynamics. In addition to the mid-depth waterline plane analysis of the near-body fluid dynamics performed for Giant Danio comparison, sectional flow profiles will be evaluated at discrete times within the swimming cycle, in order to assess the three-dimensional nature of the near-body flow. The three-dimensionality of the near-body flow is not well described by linear theory and has not been observed experimentally, and as such, this analysis may further reveal why the assumptions made in linear theory can never capture the complex dynamics of actual fish swimming and may aid in the development of a model of the actuation mechanisms employed by the fish in controlling the structure and behavior of its near body flow. The predisposition of live fish to swim at Strouhal numbers corresponding to the maximum spatial amplification of a two-dimensional thrust jet will be explored through the assessment of the two-dimensionality and the structural dynamics of the deforming trailing shear layer wakes after steady-state straight-line swimming has been reached. Finally, pressure and vorticity structures will be examined near the body at various time instances during the straight-line swimming cycle, in order to assess the feasibility of lateral line sensing and control algorithm implementation in engineered ocean systems.

The analysis of canonical problem *(iii)*, the dynamics of three-dimensional ma-

neuvering, is presented in *Chapter 5*. The modification of the simulation capabilities to accommodate the unsteady, non-periodic flexible-body motions of maneuvering is outlined for both the three-dimensional and two-dimensional codes, employing series expansions of experimentally-gathered data on the global body trajectory and the localized backbone undulation time history. The case of a turning Giant Danio (*Danio malabaricus*) is presented, and both two- and three-dimensional simulation results for the imposed motions are compared to the experimental DPIV data for a series of discrete times throughout the duration of the turning motion. The geometric and shedding parameter variations, explored in three-dimensional straight-line swimming simulations, are shown to significantly affect the generation of and unsteady structure of the turning thrust jet, and the integrated performance quantities illustrate the dynamical dependence on the morphological modeling assumptions. The literature of turning maneuvers is also subsequently reviewed, and the Giant Danio turn studied in detail in this chapter is shown to be particularly well-suited to this type of unsteady numerical simulation due to its smooth body contortion kinematics and tail leading edge trajectory, which does not appear to cause significant separation in regions other than the trailing edges of its body lifting surfaces. From the literature, other types of turning and starting maneuvers are explored, and the short-comings of the present numerical method are made evident. Based on simulation results which do compare well to experiments, however, a generalized mechanistic maneuvering model is developed to describe the generation of large, short-duration forces for vectored thrust and maneuvering. The details of actuated flow structures, such as streamtubes, low pressure regions, and vortices, at various times during the maneuvering motions reveal the manner in which the body manipulates the near-body flow and shed wake to manage its external loading. A simple model of maneuvering mechanism concludes the chapter, with a discussion of the feasibility of employing a lateral line or other sensing technique for practical application of a maneuvering control system.

The overview of straight-line swimming presented in *Chapter 4* is expanded in *Chapter 6*, which explores in detail the mechanisms of energy recovery employed by fish in straight-line swimming. Whereas the corroboration of our numerical technique

by simulating exact live fish motions and subsequent exploration of the simulated flow fields was the emphasis of the initiation of canonical problem *(ii)*, the focus of this chapter is on the optimization of flow control by fish-like motions, i.e. to explain why the fish swims in the manner in which it has been observed to do. A qualitative overview of the principles of vorticity and flow control mechanisms utilized by fish is straight-line swimming is first presented, to generalize the global picture and to modularize the foci of the detailed investigations to follow, including the generation of bound vorticity and near-body high momentum regions, the principles of controlled release of bound vorticity, the principles of controlled actuation of accelerated fluid, and the principles of energy recovery and its effects on propulsive efficiency.

The details of vorticity control dynamics follows, which reveal the importance of morphology and kinematics on the generation and control of bound and shed vorticity through variation of several parameters, such as separation line definition and body wavelength, which define these swimming attributes. The identification of the main vortical structures is followed by a study of the optimal modes of interaction of this vorticity with the body. Several different variations of kinematic and wake shedding parameters which define these modes are employed to explain why these vorticity-body interactions affect the force distribution around the body and the resulting efficiency of the swimming modes. Following a detailed discussion of these vorticity control dynamics, the details of near-body flow actuation and control are presented in depth. The three-dimensionality of the near-body flow, caused by the actuation of localized body undulations, is explored through examination of the flow structures at different longitudinal and cross-sectional planes around the body at different discrete times during the swimming cycle. This fluid architecture is revealed through visualization of streamlines and regions of high and low pressure. Then, the effects of variation of the geometric modeling parameters on the interactions and behaviors of these unsteady fluid dynamics are explored. The optimization of the interaction modes between the body and these coherent fluid structures is discussed, and the inability of classical swimming theories to predict the complex hydrodynamics of the straight-line swimming motions is emphasized. The chapter concludes with

the development of a simple dynamical model to describe the main vorticity control mechanisms utilized by fish during straight-line swimming. Energy recapture dynamics of the efficient and inefficient modes are discussed, with emphasis on the dependence of the unsteady body load distribution and the resulting wake thrust jet on the kinematic and morphological parameters of the various swimming modes. Finally, methods for using this simple mechanistic swimming model in the development of simple performance prediction tools and unsteady control systems for practical applications are recommended.

Chapter 7 concludes the thesis, with a description of the main contributions of this work to the field of hydrodynamics, and some recommendations are presented for possible future research work in this and related areas. *Appendix A* details some convergence properties of the two-dimensional numeric scheme. *Appendix B* describes preliminary work on the extension of the two-dimensional swimming simulation capabilities to the design of a motion control system. For this work, the simulation capability developed for canonical problem *(i)* is extended to include a rigid body motion time integration scheme, whose formulation and implementation details are included in *Appendix C*. The design of an accurate control system for highly-nonlinear unsteady fluid-structure interactions, such as the case of an oscillating lifting surface with large amplitude motions and shedding a vortical wake, has historically presented tremendous difficulties in application, due to the inability to predict the external unsteady hydrodynamic loads with any precision. Advances in robust adaptive nonlinear control theory makes possible the minimization of performance errors in control of large amplitude motions with highly nonlinear fluid dynamics loads.

To illustrate the effectiveness of this control system design, the oscillatory motions of a two-dimensional lifting surface are examined in a free stream, with its motion constrained to pitch and heave, attached to a spring-damper system, in an attempt to model the effects of a caudal fin attached to the muscles and tendons which store and damp out energy transfered between the external and internal applied loads and the motions of the tail. Tuning physical parameters, such as spring and damping constants, as well as control system parameters, such as adaptation and tracking

error gains, can result in energy absorption from the free stream for motions within a particular range of Strouhal numbers. These preliminary results may provide a useful framework from which to launch a comprehensive investigation into the robust control system design for fluid-structure interaction tuning and simulation-based design.

Appendix D details a proof of dipole panel-vortex ring equivalence, and *Appendix E* details the formulation of a vorticity impulse force calculation scheme, both of interest in the development of three-dimensional panel methods for these flexible-body swimming problems. An extensive bibliography of works referenced and cited throughout the completion of this dissertation can be found the the *Bibliography.*

Chapter 2

Two-dimensional straight-line swimming

2.1 Numerical method formulation & convergence

2.1.1 Unsteady initial boundary value problem

In this chapter, a numerical method is developed to simulate the two-dimensional hydrodynamics surrounding the propulsion of a fish-like body. To achieve this objective, the canonical problem of a streamlined two-dimensional foil section in an infinite fluid domain, abruptly starting from rest to a constant horizontal velocity U is considered. The translating foil section is allowed to undergo periodic oscillations about its mean nose-tail line in the form of a traveling wave moving from head to tail. The fluid is assumed to be inviscid and the free shear layer confined to an infinitesimal vortex sheet, outside of which the flow is irrotational. Aside from the obvious geometric simplifications, the characteristics of real fish swimming at large Reynolds numbers are approximated by assuming that viscous effects are confined to a thin boundary layer and wake region.

The flow, with the exception of the wake, the fluid is assumed to be inviscid and irrotational, as well as incompressible, allowing for the existence of a velocity potential $\Phi(x, y, t)$. Two coordinate systems are defined, an inertial global coordinate system

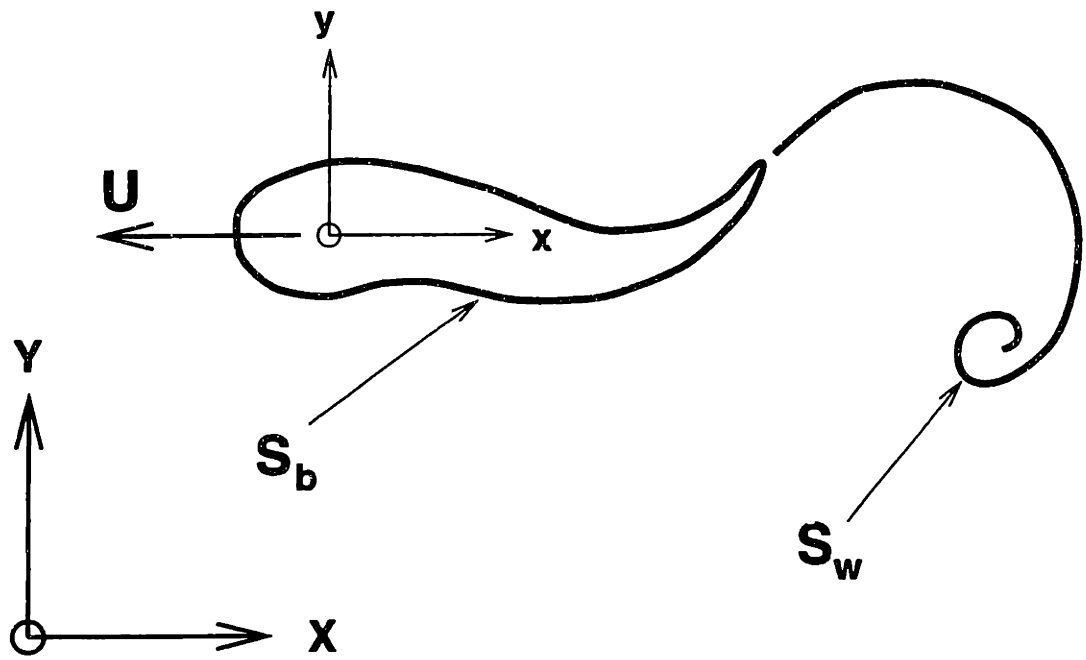

Figure 2-1: Coordinate system convention for the 2D swimming simulations. OXY is an inertial reference frame, while oxy is a body-fixed coordinate system about which mean line undulations are described.

OXY, fixed in space in the fluid, and an local coordinate system oxy, instantaneously fixed in the flexible body, as shown in Figure 2-1. The mean periodic undulations of the body are prescribed with reference to oxy and the global translational and rotational motions of the body are described with respect to OXY. All time and length scales are chosen to be nondimensional with respect to the body length $\ell = 1$. The computational domain is enclosed by three surfaces, the body surface S_b, the shear layer wake S_w, and the far-field boundary S_∞. Because fluid can be described by a harmonic velocity potential Φ, Laplace's equation in the fluid domain governs the conservation of mass:

$$\nabla^2\Phi = 0 \tag{2.1}$$

Further, The total velocity potential $\Phi(x, y, t)$ can be described as the linear superposition of the body perturbation velocity potential $\Phi_b(x, y, t)$ and the wake perturbation velocity potential $\Phi_w(x, y, t)$, both satisfying the Laplace field equation. At any point in time, excluding the initial condition, the strength of the previously-shed wake is known. The shed wake strength is part of the solution of the BVP at previous times,

and thus $\Phi_w(x,y,t)$ is known everywhere at any given time, except for that small portion of wake currently being released into the fluid. As a consequence, the IBVP is formulated and solved for the body perturbation velocity potential $\Phi_b(x,y,t)$. A prescribed body motion gives the no-flux body boundary condition in terms of the body perturbation potential:

$$\frac{\partial \Phi_b(x,y,t)}{\partial n_b} = \{\vec{V}_{body}(x,y,t) - \vec{\nabla}\Phi_w(x,y,t)\} \cdot \hat{n}_b \tag{2.2}$$

A radiation condition requires that the perturbation potential influence decay rapidly to zero in the far field:

$$\vec{\nabla}\Phi_b = 0 \tag{2.3}$$

The unsteady Kutta condition states that the flow must leave the trailing edge smoothly. This condition is a physical restriction which limits velocities and prevents pressure jumps, and it is required to uniquely solve the problem for $\Phi_b(x,y,t)$. To that end, the body perturbation velocity potential jump at the trailing edge (TE) at any time is set to equal the strength of the shed wake perturbation velocity potential.

$$\Delta\Phi_{b_{TE}}(x,y,t) = \Phi_{w_{TE}}(x,y,t) \tag{2.4}$$

2.1.2 Boundary element method

A Green's formulation was considered to solve the problem for the body perturbation velocity potential Φ_b. Green's theorem in three-dimensions can be written:

$$\iiint_V \left[\Phi_1 \nabla^2 \Phi_2 - \Phi_2 \nabla^2 \Phi_1\right] d\tau \;=\; \iint_S \hat{n} \cdot \left[\Phi_1 \vec{\nabla}\Phi_2 - \Phi_2 \vec{\nabla}\Phi_1\right] ds \tag{2.5}$$

This second form of Green's Theorem can be reduced if both Φ_1 and Φ_2 are harmonic functions, satisfying Laplace's Equation, and the left hand side can be set to zero. The expression can then be rewritten:

$$\iint_S \hat{n} \cdot \left[\Phi_1 \vec{\nabla}\Phi_2 - \Phi_2 \vec{\nabla}\Phi_1\right] ds \;=\; 0 \tag{2.6}$$

Considering the two-dimensional simplification of the formulation, this equation can then be changed from a surface integral to a line integral around the boundary, using a two-dimensional version of the divergence theorem:

$$\int_S [\Phi_1 \frac{\partial \Phi_2}{\partial n_b} - \Phi_2 \frac{\partial \Phi_1}{\partial n_b}] \, ds \; = \; 0 \tag{2.7}$$

Then, Φ_1 is equated to the body perturbation velocity potential, Φ_b. Φ_2 is chosen to be the two-dimensional source velocity potential Green's function, $ln|r|$, where r is the distance from observation point (x, y) to any point on the boundary (ξ, η), or $r = \sqrt{(x-\xi)^2 + (y-\eta)^2}$. This choice of Green's function is standard in the development of two-dimensional boundary integral methods in an ideal, irrotational fluid in the absence of a free surface [248, 99]. From Green's theorem, any point can be described in terms of the integral around the boundaries.

$$-\pi \Phi_b(x) f \; = \; - \oint_S (\Phi_b \frac{\partial ln|r|}{\partial n_b}) \, ds \; + \; \int_S (ln|r| \frac{\partial \phi_b}{\partial n_b}) \, ds \tag{2.8}$$

f=0	x: Outside Boundary
f=1	x: On Boundary
f=2	x: Inside Fluid Domain

2.1.3 Numerical implementation

The development of the panel method is a consequence of consideration of the boundaries of the problem. The three boundaries in the problem, the body S_b, the wake S_w, and the boundary at infinity S_∞, are impervious to fluid flux. Through the normal differentiation of the source potential Green's function on the body, the potential distribution on the body can be thought of as a combination of sources and dipoles. Due to the nature of these singularities, whose influence decays as $1/r$ and $1/r^2$, respectively, the boundary at infinity can be shown to have negligible influence; the integration contour at $\vec{x} = \infty$ is thus ignored.

For the unsteady foil problem, the wake strength is a function of space and time

$\Phi_w = \Phi_w(x, y, t)$. The pressure across the wake shear layer is continuous, and the wake surface is a material surface. Thus this infinitesimally-thin wake surface can be represented by a smoothly-varying strength dipole sheet, with the source-strength identically equal to zero. By Kelvin's theorem, as the foil's circulation changes, so does the strength of the shed wake dipole. The unsteady, variable-strength wake is discretized into linear dipole panels each with constant strength ϕ_w. Green's Theorem again allows us to treat a finite-length, linear dipole sheet segment of constant strength as two point vortices, situated at either end of the panel segment, each of circulation strength Γ_v equal to the strength of the dipole sheet ϕ_w, with opposite signs. Proof of this dipole-vortex equivalence can be found in [99]. Thus, the wake can be transformed from a variable-strength dipole sheet into discrete point vortices. Since contributions from the endpoints of adjacent panel determine the strength of any individual vortex, if the two dipole segments have equal strengths, the vortex strength Γ_v will be zero, with positive and negative contributions from each dipole panel. Thus, the strength of the vortices in the wake will be the sum of a positive contribution from one dipole panel and a negative contribution from an adjacent dipole panel.

The remaining computational boundary, the body surface, is subdivided into panels. Linear panels are chosen for ease of geometric description and influence coefficient integration. The body perturbation velocity potential ϕ_b across each panel is assumed to be constant. Higher-order potential distribution descriptions would allow for fewer panels on the body to achieve the same accuracy of the solution, but the computational time required to calculate panel influence coefficients increases with the order of the potential distribution on the panel. Since the foil section is deformable, the influence coefficients must be calculated every time the local body shape changes, so a higher number of panels and constant velocity potential distribution are chosen for simplicity. For simplicity as well as increased accuracy, cosine-spaced panels are chosen, allowing for a smoother velocity potential distribution representation in geometric regions of strong velocity gradients, such as the leading and trailing edges. While in general the spacing and length of each panel may arbitrary, cosine-spaced panels with cosine-spaced collocation points often exhibit faster convergence behav-

ior [95].

The body perturbation velocity potential ϕ_b at each panel collocation point can then be found in terms of the perturbation potentials at all of the other panels, as can be seen by modifying equation (2.8):

$$-\pi \cdot \phi_b(x_i) + \sum_{\substack{j=1 \\ j \neq i}}^{k} \phi_b(x_j) \cdot Q_{ij} = \sum_{j=1}^{k} \frac{\partial \phi_b(x_j)}{\partial n_b} \cdot P_{ij} \tag{2.9}$$

where 'k' is the number of panels and where

$$P_{ij} = \int_j^{j+1} ln|r_{ij}| \, ds \tag{2.10}$$

$$Q_{ij} = \int_j^{j+1} \frac{\partial ln|r_{ij}|}{\partial n_{b_j}} \, ds \tag{2.11}$$

$$r_{ij} = \sqrt{(x_i - x_j)^2 + (y_i - y_j)^2} \tag{2.12}$$

A linear system of equations results for ϕ_b at each panel. A discrete form of the no-flux kinematic boundary condition at each panel can be found by modifying equation (2.2):

$$\frac{\partial \phi_b(x_i)}{\partial n_b} = \{\vec{V}_{body}(x_i) - \sum_{v=1}^{nv} \vec{\nabla}\Gamma_v \frac{\theta_i}{2\pi}\} \cdot \hat{n}_b \tag{2.13}$$

This normal velocity is set to be equal to the panel source strength, a Dirichlet boundary condition of specifying the potential on the boundary. The source strength normal velocity given above in equation (2.13) is comprised of contributions from the imposed velocity of the body and the velocities induced at each panel by the shed wake sheet, represented by nv discrete vortices, each of strength Γ_v.

Now the body perturbation potential and the strength of the shed wake dipole sheet, equal to the circulation about the foil, can be found by solving the linear system of equations and applying the Kutta condition. The Kutta condition states that the fluid must leave the trailing edge smoothly, in the case of a cusped trailing edge, tangentially. The strength of the shed shear layer Γ is prescribed to be equal to the jump in the body perturbation velocity potential between the top and bottom

surfaces of the foil's trailing edge, preventing infinite velocities at the trailing edge point. A modified Morino Kutta condition [95] is utilized which accounts for the projection of the potential jump at the trailing edge from the panel collocation points to the actual trailing edge point by accounting for the potential associated with the local body velocity $\vec{V}_b$:

$$\Gamma = \phi_{b_{top}} - \phi_{b_{bottom}} + \vec{V}_b \cdot \vec{r}_{te} \tag{2.14}$$

At any time, the strength of the shed dipole Γ is unknown and is solved for in the system of equations for ϕ_b. Thus, the first wake panel is treated as a ϕ_b panel for the boundary element evaluation, and the boundary integral is resolved around a new contour containing the first wake panel. Then, the strength of the shed vortex in the wake is equal to the contribution of the wake dipole from the previous time step and the oppositely signed contribution from the endpoint vortex of the new wake dipole. Thus, it can be easily deduced that the strength of the shed vortices is zero for a steadily translating foil with an infinitely-long wake, that is, a starting-vortex infinitely-far away and inducing no normal velocity on the foil.

Rewrite in a linear system for ϕ_b:

$$-\pi\phi_b(x_i) + \sum_{\substack{j=1 \\ j\neq i}}^{k} \phi_b(x_j)Q_{ij} + \Gamma Q_{iw} = \sum_{j=1}^{k} \frac{\partial \phi_b(x_j)}{\partial n_b} P_{ij} + \frac{\partial \Gamma}{\partial n_b} P_{iw} \tag{2.15}$$

where

$$P_{ij} = \int_j^{j+1} ln|r_{ij}|\, ds \tag{2.16}$$

$$Q_{ij} = \int_j^{j+1} \frac{\partial ln|r_{ij}|}{\partial n_{b_j}}\, ds \tag{2.17}$$

$$r_{ij} = \sqrt{(x_i - x_j)^2 + (y_i - y_j)^2} \tag{2.18}$$

$$\Gamma = \phi_b(x_1) - \phi_b(x_k) + \vec{V}_b \cdot \vec{r}_{te} \tag{2.19}$$

$$P_{iw} = \int_{S_w} ln|r_{iw}|\, ds \tag{2.20}$$

$$Q_{iw} = \int_{S_w} \frac{\partial ln|r_{iw}|}{\partial n_w}\, ds \tag{2.21}$$

$$\frac{\partial \phi_b(x_j)}{\partial n_b} = \{\vec{V}_b(x_j) - \sum_{v=1}^{nv} \vec{\nabla}\Gamma_v \frac{\theta_j}{2\pi}\} \cdot \vec{n_b} \tag{2.22}$$

It can be shown that $P_{iw}\ \partial\Gamma/\partial n_b$ vanishes, and the system of equations for ϕ_b can be rewritten in the final expanded form:

$$-\pi\phi_b(x_i) + \sum_{\substack{j=1 \\ j\neq i}}^{k} \phi_b(x_j)Q_{ij} + (\phi_b(x_1) - \phi_b(x_k))Q_{iw} = \sum_{j=1}^{k} \frac{\partial \phi_b(x_j)}{\partial n_b} P_{ij} + (\vec{V}_b \cdot \vec{r}_{te})Q_{iw} \tag{2.23}$$

or in simple matrix form for unknown ϕ_b:

$$[Q]\{\phi_b\} = [P] \tag{2.24}$$

The unsteady problem can be solved at each time step, and the solution of the above linear system of equations yielded ϕ_b and Γ, where Γ is the strength of the shed wake dipole element and is representative of the foil's total circulation. The first wake dipole sheet is then redefined as two vortices, one at the foil's trailing edge, and another at the convected location of the shed wake.

Thus, given any discretized wake and the position of a new shed vortex, a boundary integral equation can be solved to find the body perturbation potential and the foil's circulation, from which, the strength of the new shed vortex and the total fluid velocity field can be found. The vortices comprising the wake are convected by the velocity fields resulting from the body perturbation velocity potential and by the influence of every other vortex by the two-dimensional form of the Biot-Savart law.

An interesting problem remains, however, and that is the determination of the location of the new shed vortex. An accurate representation of the wake is desirable, especially in this problem, where strong transient effects in the wake may make huge differences in fish propulsive forces and efficiencies. Unfortunately, the velocity directly at the trailing edge *point* is not well defined, and thus the trajectory of the wake (or the point vortex representations of the wake) as it is shed is not well defined either.

Different vortex shedding solutions were investigated in reference to this problem. Concentrated point vortex representations of the total wake, including theory developed by Brown and Michael [31], Rott [175], and Graham [69] were considered, but ultimately rejected as one-point representations of the wake were not considered desirable in a problem whose solution is heavily dependent on unsteady wake dynamics. Also, most of the concentrated point vortex theory is based on a similarity solution, or an asymptotic expansion of the complex potential about a separation point in a conformally-mapped plane, which is both mathematically tedious for an unsteady problem and inextensible to three dimensions. A discretized wake was chosen, as has been outlined earlier, because of advantages in wake visualization and because the strength of the shed vortices is not a function of time.

There are problems with discretized vortex shedding, including randomness and instability of the singular solution if the vortices become to close [11, 12, 180, 181], a lack of a suitable shedding criterion [58], the difficulty in flow representation near the shedding edge [71, 108]. Randomness as a highly numerical problem, however, can be alleviated in a number of ways. First, amalgamation of vortices can be employed to replace two close vortices with one vortex giving an equal contribution in the far field or to replace the inner spiral of an infinitely wound spiral vortex sheet by a single core vortex surrounded by a finite-winding-number discretized vortex sheet [165, 91, 209, 210]. Also, vortices becoming too close in a spiral can be dealt with by either a continuous redistribution of vorticity in the spiral [146].

As far as determining a suitable shedding location, Maskell [145] theorized that the flow must leave the trailing edge parallel to the upper or lower surface depending on the sign of the shed vorticity. However, this procedure would lead to interpolative and iterative simulations, as the sign of the shed vorticity would not be known a priori and the location of the shed vortex would have an influence on the solution of the problem of determining the sign of the shed vorticity itself. Sarpkaya [179] in 1975 generalized the Maskell shedding criterion for a cusped trailing edge. By fitting a circular arc through the trailing edge and the previously shed vortex, and approximating this shape as the wake trajectory, a new shed vortex could be placed along this circular

arc, and the problem could be solved from there. Streitlien [190] analytically solved the problem of a mappable, analytic foil shape, with a cusped trailing edge, heaving and pitching in the complex plane, and shedding a discretized vortex wake using this technique. As a result, this method was adopted for the two-dimensional numerical method, and during the development of the code, only foils with cusped trailing edges were employed. When the numerical code was adapted to foil's with non-cusped trailing edges, to save the additional computational time which would result from the implementation of an iterative Maskell scheme, a modified Sarpkaya criterion was developed, in which the circular arc is fit through the trailing edge point, tangent to the mean line of the foil, and the previously-shed vortex. Any inaccuracies which result from this approximation are likely to be small, as the trailing edge included angles utilized in these analyses have been small.

Finally, this unsteady method, which employs a complex shedding criterion based on previously-shed vorticity, is not completely described without treatment of the location of the starting vortex. For both experimental investigations and numerical simulations of impulsively-started flows, starting vortex location data and prediction algorithms have been poorly documented in the literature. Rott [175] developed an expression for the starting vortex location for unsteady, separated flow based on asymptotic expansions in a conformally-mapped plane, which is not easily applicable to this problem. Many propeller codes fit an unsteady wake onto a known steady wake geometry [105, 107]. An unsteady method employing a flexible body will not be able to know the shape of the wake a priori, so this type of treatment may not be wholly accurate when the deformation of the unsteady wake is important. A first estimate placed the starting vortex for an impulsively-started flow around a fixed Joukowski foil of chord $c = 1$ exactly the distance downstream equal to the free stream velocity $U = 1$ times the time step dt. This produced a reasonable looking wake. The dynamics of the wake were studied as the time step was decreased and are presented in Figure 2-2, and it was found that the center of vorticity seemed to converge to a position closer to the trailing edge as the time step was decreased. Streitlien [190] estimated that the location of the starting vortex was three-quarters of the same distance downstream

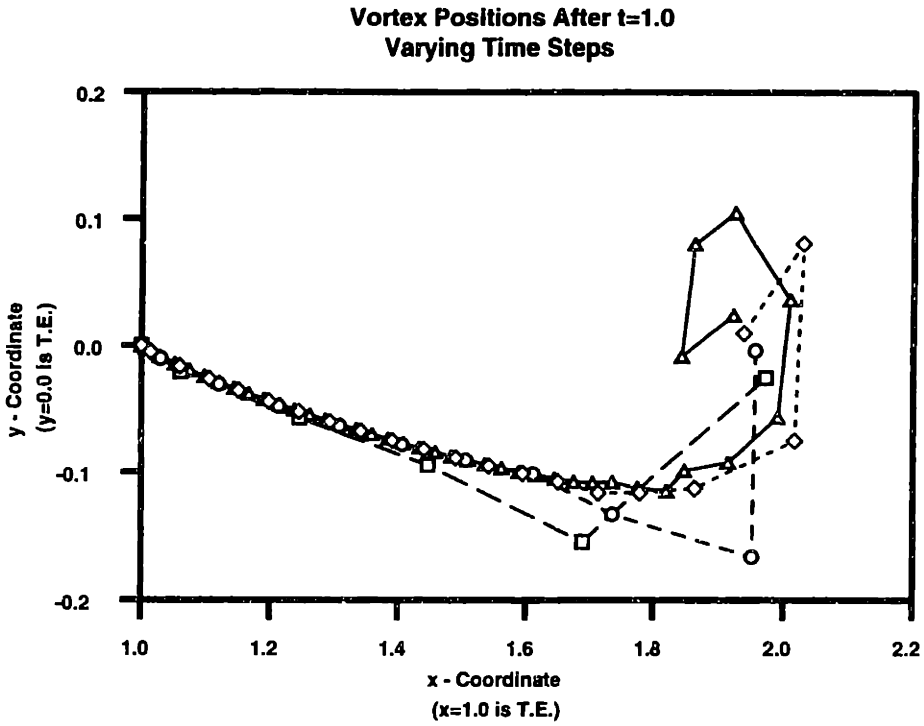

Figure 2-2: Convergence of the starting vortex spiral for various values of the time step dt for the impulsively-started flow U around a Joukowski foil of chord length c with cusped trailing edge. Starting vortex is placed a distance Udt directly downstream of the trailing edge. The simulation is run to nondimensional time $Ut/c = 1.0$ for various time steps shown above: $\square$ $dt = 0.2$; $\circ$ $dt = 0.1$; $\diamond$ $dt = 0.05$; $\triangle$ $dt = 0.025$.

at the trailing edge angle, not directly downstream. These two methods were then compared for various values of the time step as shown in Figure 2-3, and the method of Streitlien seemed to converge to a location slightly closer to the trailing edge point than the method of placing the vortex directly downstream at a distance of Udt. As a result, Streitlien's estimate was adopted for the two-dimensional unsteady foil code.

A fourth-order Runge-Kutta scheme was utilized in the numerical code for time integration. The boundary-integral equation must be solved as intermediate steps in the time integration. The nature of the Runge-Kutta time integration scheme is such that the velocity at several intermediate temporal locations must be found before the final convection can be carried out. Each time the vortices are convected to an intermediate location, a new induced velocity must be found at this location for each vortex, based on the strengths of all other vortices and the gradient of the body perturbation potential. If the boundary value problem is not solved as an intermediate

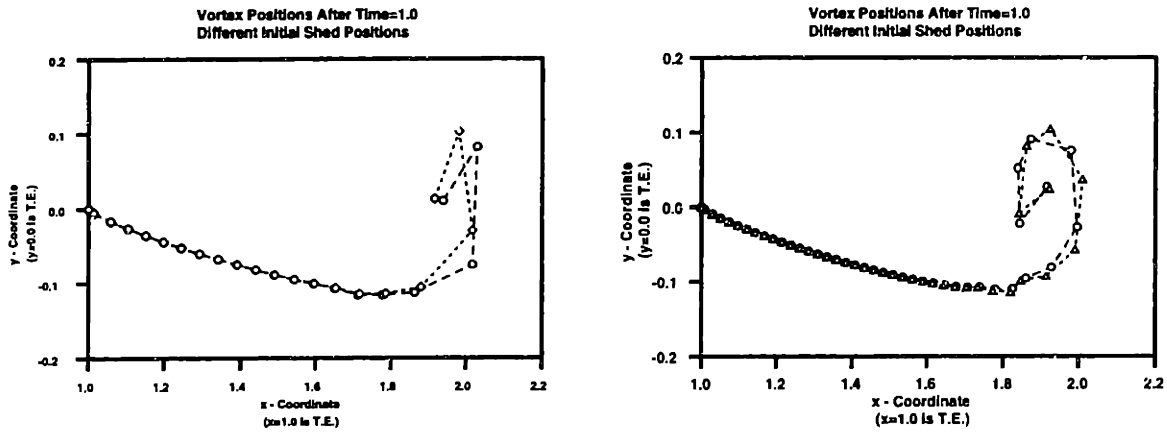

(a) $dt = 0.05$ (b) $dt = 0.025$

Figure 2-3: Convergence of the starting vortex spiral for various starting vortex placement schemes for two values of the time step dt for the impulsively-started flow U around a Joukowski foil of chord length c with cusped trailing edge. Vortex placement schemes are identified by symbols: $\circ$ starting vortex is placed a distance Udt directly downstream of the trailing edge; $\diamond$ Streitlien (1994). The simulation is run to nondimensional time $Ut/c = 1.0$ for two time steps shown above: (a) $dt = 0.05$ (b) $dt = 0.025$.

step, the boundary conditions on the foil and in the wake are likely to be violated by this new flow condition, and the induced velocities would thus be wrong. Therefore, at each intermediate Runge-Kutta step, the boundary value problem is solved, a new vortex is shed, and the new induced velocities are computed at each intermediate vortex location. Then, the shed vortex is removed, and the vortices return to their original locations for the next intermediate step. At the final stage of convection, the vortices are moved from their original locations at the fourth-order Runge-Kutta velocity to the new locations, and the problem is solved again with one vortex shed in the wake. The problem becomes even more complicated when the body has an associated unsteady motion, either imposed or found through time integration of the rigid body equations of motion, as the new body location must be found at each intermediate Runge-Kutta step. The net result of implementing this higher-order scheme is approximately the same computational load as an Euler time integration scheme. Although a larger time step can be used, the intermediate boundary value problem solution requires the same number of computational time steps. Nonethe-

less, the fourth-order Runge-Kutta scheme results in less wake instability and higher accuracy, as validated by a Richardson extrapolation scheme.

2.1.4 Desingularization

Over the course of a simulation, the total number of body panels k is constant, but a wake of time-varying strength represented by discrete point vortices of constant circulation is continually shed from the sharp trailing edge of the flexible foil body to satisfy the Kutta condition. As a result, the total number of wake vortices nv increases with time. These discrete vortices are a representation of the thin shear layer produced over the body and separated from the trailing edge. These free vortices are capable of sustaining no normal stress, like the freely-deformable material wake sheet. Thus, these wake vortices are allowed to deform under their self-induced and body-induced perturbation velocities.

The wake vortices are convected after the solution of the boundary value problem for ϕ_b at each time step using a fourth-order Runge-Kutta time integration scheme. The velocity field which convects these vortices [23] is obtained from a two-dimensional version of a desingularized version Biot-Savart law. The desingularization technique employed eliminates the infinitesimal vortex sheet singularity and the associated Kelvin-Helmholtz instability [116, 117, 181], which is eliminated by viscosity in a real fluid. The inclusion of the desingularization is a necessity in the prevention of nonlinear energy transfer to the highest wavenumber modes and of simulation breakdown or in non-physical solution growth caused by the numerical instabilities.

A wake vortex of strength Γ comprising is assigned core radius δ_w, such that the velocity $\vec{v} = [\dot{x}, \dot{y}]$ induced at $\vec{x} = [x, y]$ by this vortex at $\vec{\zeta} = [\xi, \eta]$ can be expressed by a two-dimensional desingularized Biot-Savart velocity field:

$$\dot{x} = -\frac{\Gamma}{2\pi} \frac{y - \eta}{r^2 + \delta_w^2} \tag{2.25}$$

$$\dot{y} = \frac{\Gamma}{2\pi} \frac{x-\xi}{r^2+\delta_w^2} \tag{2.26}$$

$$r^2 = (x-\xi)^2 + (y-\eta)^2 \tag{2.27}$$

As $\vec{x}$ approaches the vortex center $\vec{\xi}$, r approaches zero, and the velocity field expressed by (2.25) and (2.26) approaches a finite limit. All of the vortices are thus convected by the velocity fields induced by every other vortex in the wake, as well as by the velocity field induced by the ϕ_b of the body panels. Similarly, the body doublet panels are desingularized by the same technique, which arbitrary body desingularization radius δ_b. When vortices impinge on body elements such as might occur during starting or turning motions, non-physical free wake vortex acceleration is thus avoided. Without this body desingularization, free wake vortices interacting with flexing body panels may convect inside the body.

2.1.5 Integrated quantities

The body surface velocities are found through taking the gradient of the velocity potential ϕ_b at each time over the surface of the body. Two different methods were explored for finding these velocity components on a surface of arbitrary curvature, a finite-difference method and a surface parametization gradient method. First, a one-sided, two-point finite-difference scheme was developed in the normal $\hat{n}$ and tangential $\hat{\tau}$ directions along the body surface to find $\partial\phi_b/\partial\tau$. This tangential velocity is then transformed into its x and y components to get the velocity $\vec{\nabla}\phi_b$ at each panel. A three-point central finite-difference scheme was similarly developed in the normal and tangential reference frame for find the tangential body velocity and consequently $\vec{\nabla}\phi_b$. The second method employed involved the surface parametization of the velocity potential ϕ_b and the x and y coordinates of each panel collocation point. The velocity potential ϕ_b at a given panel, as well as the x and y collocation point coordinates, were parametized using Lagrange polynomials employing three-nodes. Lagrange interpolation was then used to find the derivatives of the functions in terms of the parametric variables. In this manner, the parametizations can be related through a Jacobian

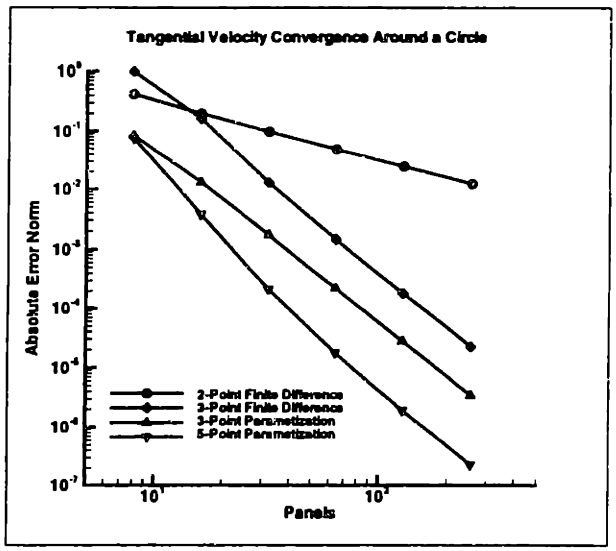

Figure 2-4: Convergence of various tangential velocity determination schemes for the steady flow about a circular cylinder section. The maximum error at any panel with respect to the potential flow solution for the velocity distribution of the flow around a cylinder is shown as a log function of the body panel number. Two-point and three-point finite difference schemes in the normal and tangential directions are compared with three-point and five-point Lagrangian polynomial surface parametization schemes.

transformation, and the x and y derivatives of ϕ_b at each panel collocation point are easily obtained. This method can be extended to Lagrange polynomials of arbitrary order, but three-point and five-point parametizations were considered for this investigation. The convergence properties of these tangential velocity determination schemes is shown in Figure 2-4, which compares the various schemes for determining the surface velocities of the flow around a sphere, whose potential distribution was found using this panel method. It can been seen that the 5-point parametization converges robustly for large numbers of surface panels, and will thus be considered for the remainder of this two-dimensional investigation.

Given the surface velocity $\vec{\nabla}\phi_b$ distribution around the body, the pressure p can be found at each panel. The force $F(\vec{x},t)$ on the body is found at any time by integration of the unsteady pressure $p(\vec{x},t)$ around the body. The corresponding rotational moment $M(\vec{x},t)$ about the body's time-dependent center of mass $\vec{X}_m(\vec{x},t)$ is also found. The instantaneous pressure $p(\vec{x},t)$ is found by employing the unsteady

Bernoulli equation for potential flow:

$$p(\vec{x},t) = -\rho\frac{\partial\phi_b}{\partial t} - \frac{1}{2}\rho\vec{\nabla}\phi_b\cdot\vec{\nabla}\phi_b \tag{2.28}$$

The force and moment on the body are given by

$$F(\vec{x},t) = \oint_{S_B} p\hat{n}_b\,dl \tag{2.29}$$

$$M(\vec{x},t) = \oint_{S_B} p(\vec{r}\times\hat{n}_b)\,dl \tag{2.30}$$

where $\hat{n}_b$ is the body normal vector, dl is the counterclockwise integration contour on the external body surface, and $\vec{r}$ is the local vector between the center of mass of the body $\vec{X}_m(\vec{x},t)$ and the body surface. The discrete form of the above equations for a body with k panels, each with constant pressure distribution p_i across each panel, can be written

$$F(\vec{x},t) = \sum_{i=1}^{k} p_i\hat{n}_{bi} \tag{2.31}$$

$$M(\vec{x},t) = \sum_{i=1}^{k} p_i(\vec{r}_i\times\hat{n}_{bi}) \tag{2.32}$$

The rate of work done by the body producing this motion, or power into the fluid $P(\vec{x},t)$, can be found by integrating the product of the local force and the local velocity $\vec{v}_b$ around the body.

$$P(\vec{x},t) = \oint_{S_B} p\hat{n}_b\cdot\vec{v}_b\,dl \tag{2.33}$$

This is useful for computing propulsive efficiency η, defined at the ratio of forward swimming speed U times the mean component of $F(\vec{x},t)$ in the direction of swimming, or thrust $\bar{T}$, to the mean power input to the fluid $\bar{P}$, averaged over a complete steady-state swimming cycle. It is simply written

$$\eta = \bar{T}U/\bar{P} \tag{2.34}$$

It is interesting to note that the power input to the fluid $P(\vec{x},t)$ should exactly equal the rate of change of kinetic energy in the fluid. However, for this formulation, one cannot exactly compute the kinetic energy $E(t)$ in the fluid due to the singular nature of the discrete vortices which are used to represent the shear layer wake, which is normally given by:

$$E(t) = \frac{1}{2}\rho \iiint_V \vec{\nabla}\phi \cdot \vec{\nabla}\phi \, dV = \frac{1}{2}\rho \iint_S \phi \hat{n} \cdot \vec{\nabla}\phi \, dS \tag{2.35}$$

Batchelor [23] Eq. (7.2.8) describes the total kinetic energy of a fluid in terms of the vorticity distribution as

$$E(t) = \rho \iiint_V \vec{v} \cdot (\vec{x} \times \vec{\omega}) \, dV \tag{2.36}$$

where $\vec{\omega}$ is the vorticity distribution in the fluid, and $\vec{v}$ is the resulting velocity field, and $\vec{x}$ is the position vector. Substituting potential flow definitions for the velocity and vorticity vectors in terms of a velocity potential, we can rewrite the kinetic energy as

$$E(t) = \rho \iiint_V \vec{\nabla}\phi \cdot (\vec{x} \times (\vec{\nabla} \times \vec{\nabla}\phi)) \, dV \tag{2.37}$$

Using the two-dimensional form of the divergence theorem,

$$E(t) = \rho \iint_S \phi \hat{n} \cdot (\vec{x} \times (\vec{\nabla} \times \vec{\nabla}\phi)) \, dS \tag{2.38}$$

Due to the contributions from the contours around the actual vortices, this integral is singular as well. Therefore, the only measure of the kinetic energy of the fluid is the time integration of the power required to produce the body motion, or the total work done by the body.

2.1.6 Convergence and consistency

Steady problem

Convergence of the code for the solution of a steady problem was first assessed. The boundary value problem was solved once in the manner described above by assuming that the wake was of constant strength and extended to the boundary at S_∞, where the influence of the "starting" vortex was considered negligible. No desingularization technique was employed.

The steady-state circulation around a Joukowski foil was first found and compared to the analytic value of the circulation [1]. In addition, the circulation calculated by the code was compared to calculations from a similar steady-flow panel code used in conventional propeller section calculations, PAN2D [139]. The errors in the calculated circulations with respect to the analytic solution were determined using both codes over a range of panel numbers, for both a Joukowski profile and a NACA 65A section, and these errors are presented below in Tables 2.1 and 2.2. Log plots of the errors for the Joukowski profile and the NACA 65A profile are given in Figure 2-5.

The steady-state lift force was then found for a varying number of panels, and convergence of the lift on the foil section for an increasing number of panels k is shown in Figure 2-6. In Figure 2-6(a), the force is calculated by both pressure integration over the body surface and through the use of the Kutta-Joukowski theorem [1, 23, 105], and both methods show identical convergence properties for an evenly-spaced, centrally-collocated panel distribution. The lift coefficient on the foil section was compared to its analytic value of $C_L = 8\pi r_c \cos\alpha_c \sin\alpha_c$, where α_c is the angle of the stagnation point in the conformally-mapped circle plane with reference to the circle center of radius r_c and the direction of uniform flow [1]. In Figure 2-6(b), pressure integration is used to find the steady lift about the same Joukowski foil section for both evenly-spaced, centrally-collocated panels and cosine-spaced, cosine-collocated panels.

Panels k	Γ_p	PAN2D	Error Γ_p	Error PAN2D
10	-0.6220648	-0.6218283	0.4968609	0.4970522
20	-0.7559584	-0.7562110	0.3885649	0.3883606
40	-0.9253088	-0.9265477	0.2515907	0.2505887
60	-1.0038163	-1.0068482	0.1880922	0.1856400
80	-1.0483540	-1.0540045	0.1520692	0.1474990
100	-1.0770998	-1.0861975	0.1288189	0.1214606
140	-1.1122913	-1.1308742	0.1003553	0.0853251
180	-1.1333108	-1.1649714	0.0833544	0.0577466
220	-1.1475034	-1.1959014	0.0718751	0.0327297
280	-1.1620539	-1.2446224	0.0601063	0.0066768

Table 2.1: Convergence of the steady circulation about a Joukowski profile (conformal transformation parameters: $a = 0.5$, $x_c = -0.05$, $y_c = 0.1$. See [1] for details.) at an angle of attack $\alpha = 0.0$ with an increasing number of body panels k. Actual values of the circulation (left) and the absolute errors (right) with respect to the analytic circulation are given, for both the present method Γ_p and for PAN2D. Panels are evenly-spaced of equal length with central collocation points. Analytic value of the circulation is $\Gamma_a = -1.2363674$.

Panels k	Γ_p	PAN2D	Error Γ_p	Error PAN2D
10	-0.7670391	-0.7670694	0.2995076	0.2994800
20	-0.9396297	-0.9397055	0.1418907	0.1418214
40	-1.0279356	-1.0281149	0.0612460	0.0610823
60	-1.0547221	-1.0550061	0.0367835	0.0365241
80	-1.0668209	-1.0672160	0.0257343	0.0253735
100	-1.0735423	-1.0740437	0.0195961	0.0191382
140	-1.0806895	-1.0814165	0.0130689	0.0124051
180	-1.0844138	-1.0853685	0.0096678	0.0087959
220	-1.0867006	-1.0878928	0.0075794	0.0064906
280	-1.0888538	-1.0904063	0.0056130	0.0041952

Table 2.2: Convergence of the steady circulation about a NACA 65A profile ($t/c = 0.20$, $m/c = 0.15$) at an angle of attack $\alpha = 0.0$ with an increasing number of body panels k. Actual values of the circulation (left) and the absolute errors (right) with respect to the analytic circulation are given, for both the present method Γ_p and for PAN2D. Panels are cosine-spaced in length with cosine-spaced collocation points. Analytic value of the circulation is $\Gamma_a = -1.095$.

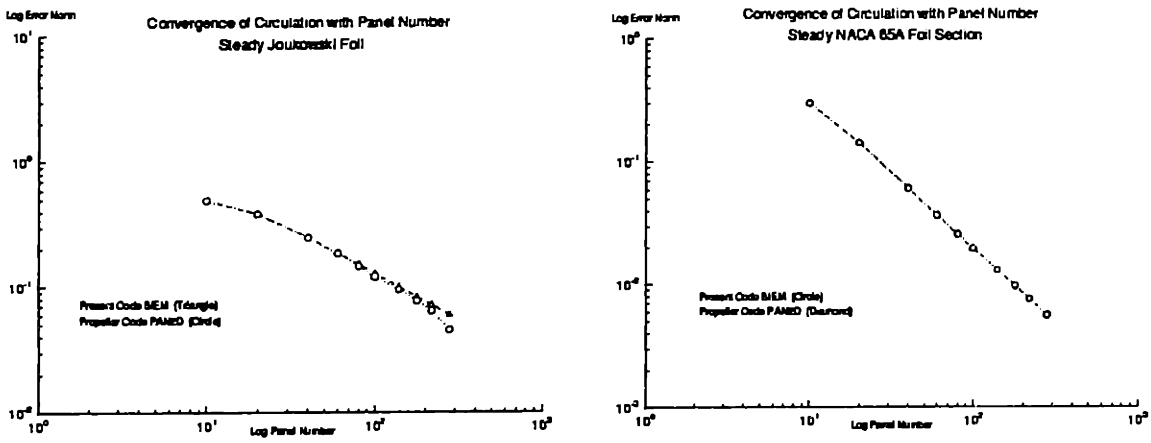

(a) Joukowski profile

(b) NACA 65A profile

Figure 2-5: Convergence with panel number k of the steady circulation about (a) a Joukowski profile (conformal transformation parameters: $a = 0.5$, $x_c = -0.05$, $y_c = 0.1$. See [1] for details.) and (b) a NACA 65A profile ($t/c = 0.20$, $m/c = 0.15$). Each profile has an angle of attack $\alpha = 0.0$. The absolute error norm in the steady circulation value with respect to the analytic solution is shown as a log function for of the number of body panels. The present method is compared with steady propeller analysis code PAN2D predictions.

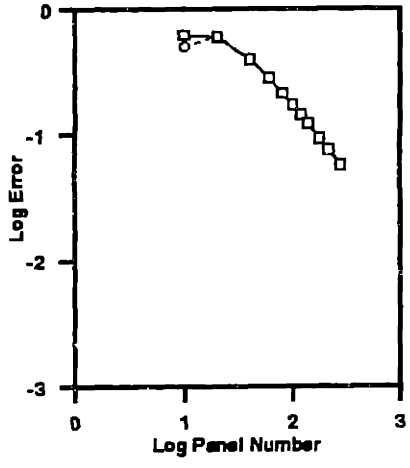

(a) Different force techniques

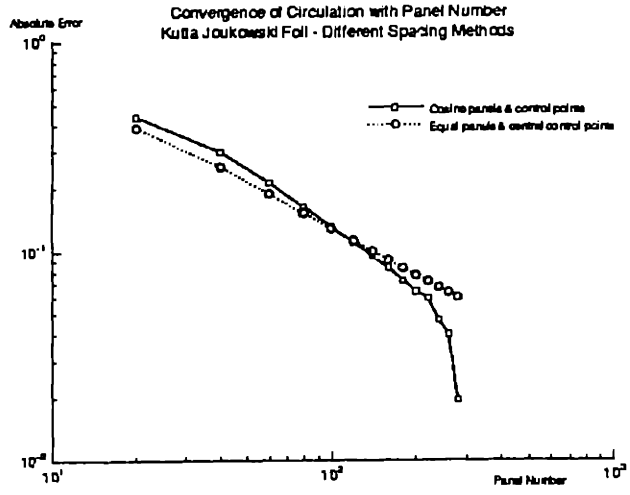

(b) Different panel spacings

Figure 2-6: Convergence of the lift coefficient about a steady Joukowski profile (conformal transformation parameters: $a = 0.5$, $x_c = -0.05$, $y_c = 0.1$. See [1] for details.) with angle of attack $\alpha = 0.0$. The error in the steady-state lift in comparison to analytic solution is shown: (a) for both pressure integration (□) and Kutta-Joukowski theorem (○) as a log function of the number of body panels, employing evenly-spaced, centrally-collocated panels; (b) for both a cosine-spaced panel distribution with cosine-spaced collocation points (□) and an evenly-spaced, centrally-collocated panel distribution (○), employing pressure integration to find the force.

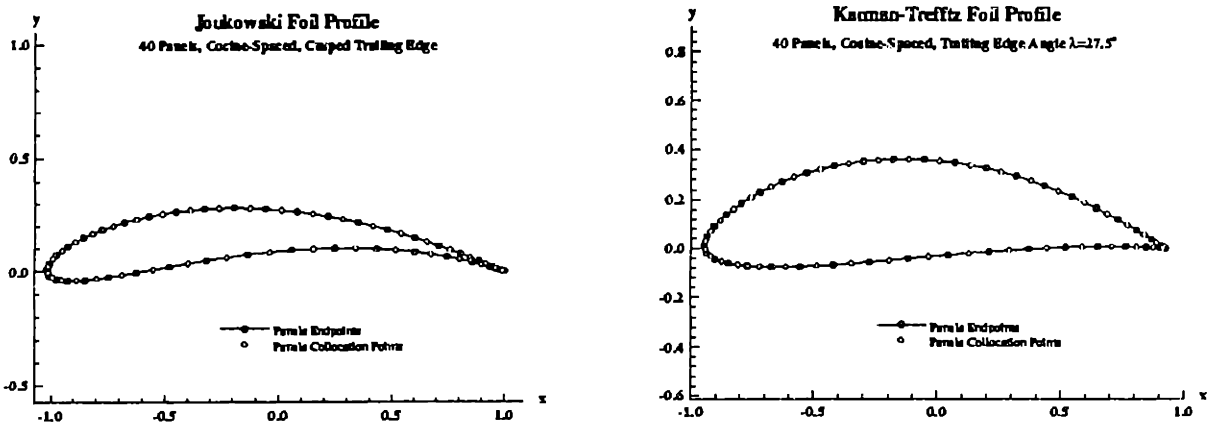

(a) Joukowski foil profile

(b) Kármán-Trefftz foil profile

Figure 2-7: Sample profiles of the two-dimensional foil shapes used in computational method convergence tests. The panel endpoints and collocation points are shown for (a) a Joukowski foil with a cusped trailing edge and (b) a Kármán-Trefftz foil with a finite-angle trailing edge.

Unsteady problem

The unsteady code was validated numerically and visually by simulating impulsively-started flow around fixed Joukowski and Kármán-Trefftz foils [41, 71], shown in Figure 2-7. The simulations were allowed to run to a nondimensional time of $Ut/c = 100$, based on a free stream speed $U = 1$ and chord length $c = 1$.

Details of the convergence and consistency tests are included in *Appendix A*. Subtle issues concerning the desingularization of the method can cause a unique instability for small trailing edge angles if not properly addressed, and the time integration scheme is also of critical importance in maintain solution stability. This numerical instability is caused by the proximity of the shed wake dipole to the smallest trailing edge panels. If this panel is too small, or its trailing edge panel neighbors are too small, the size of the corresponding influence coefficients approaches machine accuracy and the influence coefficient matrix becomes poorly conditioned, leading to a numerical solution error. Contributing to this instability is the trailing edge geometry as well, as this sharp corner places two panels in very close proximity, with an angular rotation in positive-conventions on the order of π. In an attempt to minimize error,

these convergence tests employing a conventional LU-decomposition scheme serve to *identify ranges of computational parameters which minimize error* in the numerical simulation. As the convergence tests in *Appendix A* show a smooth increase in error as time step is reduced for all fixed values of all other parameters, a simple instability criterion or Courant number does not exist which separates the convergent from the non-convergent simulations. For all subsequent investigations employing this two-dimensional technique, parameters were slightly varied near the chosen computational operating point to ensure a consistent and accurate solution.

In general, small values of desingularization radius δ_w were employed with moderate panel numbers k and time step sizes k for a Runge-Kutta time integration scheme of fourth order. Finite angle trailing edge geometries were exclusively used, with Joukowski profiles yielding consistent results for only steady flow cases. Specifics of the choices are included with all computational results contained herein. Visual verification of the unsteady wake dynamics was as expected, as the starting vorticity rapidly coiled the initial wake into a tight spiral winding.

2.2 Straight-line swimming results

2.2.1 Body motions

A two-dimensional foil profile, consistent with that of an actual fish mid-body waterline section, is considered. For many species of fish, a NACA 0012 or 0016 section is a close approximation of the maximum-width waterline unstretched section, in terms of both aspect ration and the location of maximum body thickness along the length, ignoring details of the pectoral fins and caudal peduncle [26, 212, 47, 48, 214]. For that reason, a NACA 0016 section is chosen as the body profile for this investigation. A wave form is is fitted to the mean line, hereafter referred to as backbone, which closely approximates that of *tunniform* locomotion, where the wave passing down the backbone has a monotonically increasing amplitude from the wave-form source, near the head of the fish, to the trailing edge. In addition, *tunniform* propulsion confines

most of the motion of the body to rear portion of the fish. This type of motion, is a more evolved form of *carrangiform* motion, which is characterized by a linearly varying wave amplitude from the head to the tail of the fish, and of the even more primitive *anguilliform* motion, which is characterized by a constant backbone-wave amplitude from the head to the tail of the fish, and it has been adopted by the tuna and similar predator fishes for long-ranging food-finding and cruising, as well, as high burst speeds capability [72, 76, 198, 200, 124, 127, 47, 49, 50, 48, 19].

Barrett [18, 19] completed his work on the construction of a robotic tuna, *Robo-Tuna* and has detailed the research into the backbone motion of the tuna. He had chosen a propagating sine wave with an amplitude envelope which has both linearly-varying and quadratically-varying components. This motion very closely represents that of motion of live tuna as detailed by Dewar [47, 48], but is limited to a quadratic amplitude for robotic control simplification. The smooth, amplitude-modulated traveling wave moving along the length of the body has a phase speed $c_p = \omega/k$, which is in general different from the swimming speed U. In this description, $k = 2\pi/\lambda$ is the wavenumber, corresponding to the wavelength of the backbone perturbation λ, and ω is the circular frequency of oscillation. The transverse amplitude of the backbone motion $y(x)$ gradually increases along the length, such that the primary propulsive motions are confined to the afterbody region. For comparison purposes, his waveform is chosen as the basis for the flexible foil undulation. A full discussion of fish swimming characteristics will be given in *Chapter 4*, and due to the obvious morphological differences between a flexible foil section and a live fish with an articulated tail, a simple waveform representation is both desirable and of fundamental scientific interest. The imposed transverse motion $y(x,t)$, with x measured from the nose, has the form:

$$y(x,t) = a(x)\sin(kx - \omega t) \tag{2.39}$$

where $a(x)$ is the amplitude envelope, given the form of a quadratic function:

$$a(x) = c_1 x + c_2 x^2 \tag{2.40}$$

where c_1 and c_2 are adjustable parameters, detailed in [21]. Dimensionless parameter c_1 is selected as an independent, while c_2 is chosen to achieve a specific value of the double-amplitude of motion, denoted by A, along the length of the body and, primarily, at the trailing edge. The proper frequency scaling of data is thus achieved by maintenance of a constant non-dimensional Strouhal number St, based on the wake Strouhal law [207, 204] observed in live fish, where St is given by:

$$St = fA/U \tag{2.41}$$

where f is the frequency of oscillation and A is the total average lateral excursion of the trailing edge separation point.

This motion is adopted for the purpose of this investigation, and the straight-line swimming characteristics at a constant speed U of a flexible-body foil section can now be described. At an initial time t_0 the body shape is prescribed in an otherwise still fluid. The body is then impulsively moved forward with velocity U and the backbone motion of the fish is prescribed by the waveform equation (2.39). At any time, the boundary integral equation is solved for the strength of the unsteady shed wake, and motion of the wake is convected in time using the fourth-order Runge-Kutta method. Again, at each intermediate step in the time integration process, the new backbone shape must be computed, and a vortex must be shed to satisfy the Kutta condition, but the body is always returned to the original unperturbed position, and the original number of vortices comprise the wake before the following intermediate time step.

2.2.2 Typical wake profiles

For the unsteady prescribed swimming motions described above, vorticity is released into the wake in the form of discrete vortices through separation from the oscillating trailing edge. This vorticity originated from the undulations of the body, which produces bound vortices, and the propagation of the traveling backbone wave moves these bound vortices to the trailing edge of the foil where these vortices are released into the wake. Over a cycle, the loading on the body oscillates periodically, manifested

in the changing strength of the wake vortices released throughout the swimming cycle as the backbone wave progresses towards the trailing edge. In this section, the unsteady dynamics of the developing wake structure are examined for the prescribed backbone waveform motions, and the mechanisms of the thrust jet formation are studied with respect to a variety of prescribed body motions.

The swimming motions were studied for a range of Strouhal numbers St. For a given swimming speed U, the Strouhal number was varied by varying the tail oscillation frequency f over the range of St to be considered. The double-tip amplitude of the tail A was generally held fixed around 0.2ℓ, a typical lateral tail excursion for many species of swimming fish [26, 212, 47, 48]. Strouhal numbers St of interest were typically within the range $0.1 < St < 0.4$, as many of the interesting physical phenomena of thrust and drag wake jet instability occur within these ranges [203, 207, 204]. Specifically, this range of Strouhal numbers correspond to the regions of maximum spatial amplification of the thrust jet instability ($St \sim 0.3$), indicating minimum wasted energy in the wake for a given amount of fluid momentum.

The body motions for prescribed for a Strouhal number $St = 0.2$ are shown in Figure 2-8. Note that the scales in x and y directions are not consistent, exaggerated to illustrate the subtleties of the backbone waveform kinematics. Swimming kinematic parameters for this run: $\lambda/\ell = 0.95$, $c_p/U = 0.95$, $A/\ell = 0.2$. The run is simulated for several $O(20)$ periods of the motion using a foil with $k = 100$ body panels, a time step size of $dt = 0.05$, and a desingularization radius $\delta_w = 0.02$. The resulting wake shedding dynamics are illustrated in Figure 2-9; note that the scales in the x and y directions are now equal. Each position in Figure 2-9 corresponds to the numbered backbone shapes illustrated in Figure 2-8. With a phase speed c_p slightly less than the swimming speed U, the crests of the backbone wave appear to move slightly forward in Figures 2-8 and 2-9, in the direction of straight-line swimming. If the wave speed c_p was equal to U, the crests would appear stationary in the inertial reference frame.

Examining the vortex shedding dynamics of Figure 2-9, in Position 1, the trailing edge begins to move downwards from the extreme lateral excursion during the half-cycle. As the foil section begins to acquire a circulation from the local backbone

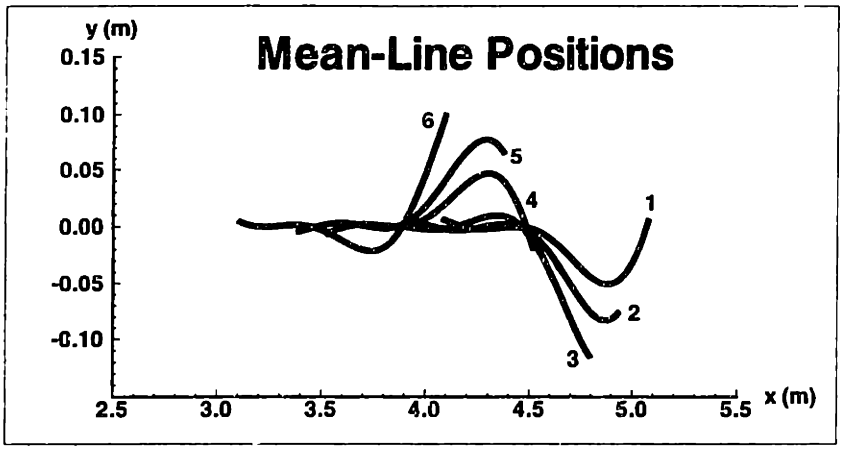

Figure 2-8: Body backbone profiles over an oscillation cycle for 2D straight-line swimming motions of a flexible foil at Strouhal number $St = 0.2$. Other kinematic parameters of the motion: $\lambda/\ell = 0.95$, $c_p/U = 0.95$, $A/\ell = 0.2$.

undulation and the forward translation at speed U, vortices with positive circulation are shed into the wake. As can be seen in the subsequent frame of Position 2, the continuation of the downward stroke towards the bottom extreme lateral excursion produces more positive vorticity is released into the wake, strengthening the clockwise circulation around the body. In Position 3, the trailing edge is at the extreme downwards lateral excursion, with the load on the body stabilizing and vortices of zero strength being shed into the wake. Also in this frame, clockwise vorticity (blue) shed during the previous half cycle begins to tighten into a spiral. The center of this clockwise vorticity spiral is roughly along the centerline of the foil's stretched-straight mean line. In Position 4, the trailing edge begins to move upwards, away from the extreme bottom lateral excursion, releasing clockwise vorticity into the wake which was clockwise body-bound circulation during the previous half-cycle shown as Positions 1–3. In Position 5, the trailing edge continues to move upwards and release more clockwise vorticity into the wake, as the body acquires a counterclockwise circulation. In Position 6, the swimming cycle is complete, with the trailing edge at the extreme upwards lateral excursion. The clockwise vorticity has been entirely released into the wake as the counterclockwise body circulation strength stabilizes with the extreme backbone perturbation. Again, the counterclockwise vorticity released into the wake during the previous half-cycle can be seen to tighten into a spiral, with the center of

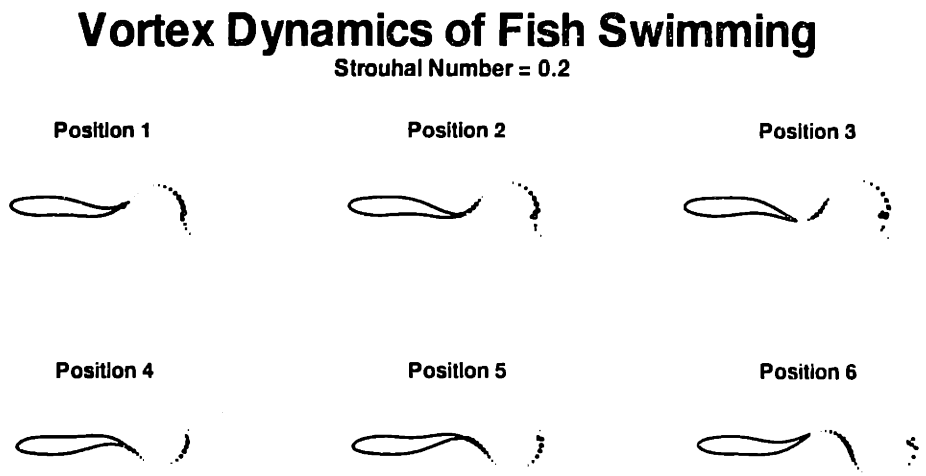

Figure 2-9: Wake generation profiles over an oscillation cycle for 2D straight-line swimming motions of a flexible foil at Strouhal number $St = 0.2$. Position numbers correspond to those backbone shapes illustrated in Figure 2-8. Size of the vortices and the color range are scaled to the magnitude and sign of the circulation Γ. Red vortices indicate a counterclockwise (positive) circulation, and the blue vortices indicate a clockwise (negative) circulation. Green vortices have no circulation. Circulation range $\Gamma = [-0.025, 0.025]$. Kinematic parameters of the motion: $\lambda/\ell = 0.95$, $c_p/U = 0.95$, $A/\ell = 0.2$. Numerical parameters for the simulation: $k = 100$, $dt = 0.05$, $\delta_w = 0.02$.

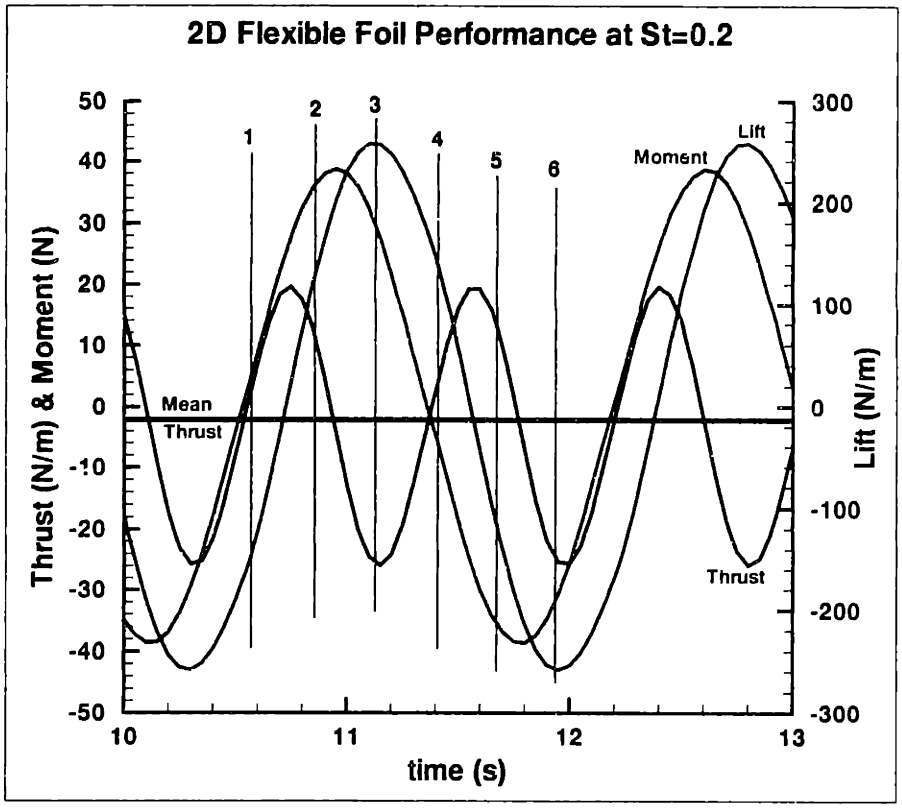

Figure 2-10: Time record of body forces and moment over an oscillation cycle for 2D straight-line swimming motions of a flexible foil at Strouhal number $St = 0.2$. Thrust (black), lift (red), and rotational moment (blue) are shown. The corresponding times in the swimming cycle for body positions shown in Figures 2-8 and 2-9 are indicated with labeled vertical green markers. Other kinematic parameters of the motion: $\lambda/\ell = 0.95$, $c_p/U = 0.95$, $A/\ell = 0.2$.

the spiral roughly on the centerline of the foil's stretched-straight mean line. A time record for the forces and moment on the foil during the swimming cycle are shown in Figure 2-10. Each position of Figures 2-8 and 2-9 is labeled on 2-10 at the corresponding time during the cycle. The peaks in the lift force on the body are shown to correlate well to the vortex wake shedding pattern seen in Figure 2-9 and discussed above. A slight steady-state drag is realized for this case.

Similar body motions for prescribed for a Strouhal number $St = 0.3$ are shown in Figure 2-11. Again, note that the scales in x and y directions are not consistent, exaggerated to illustrate the subtleties of the backbone waveform kinematics. Swimming kinematic parameters for this run: $\lambda/\ell = 0.95$, $c_p/U = 1.1$, $A/\ell = 0.2$. The run is simulated for several $O(20)$ periods of the motion using a foil with $k = 100$ body

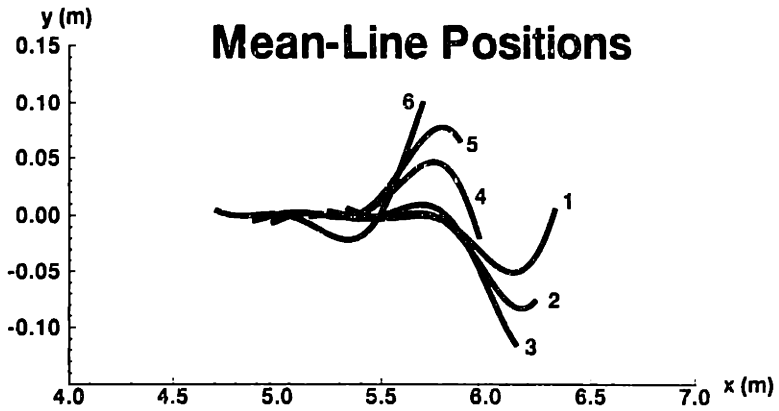

Figure 2-11: Body backbone profiles over an oscillation cycle for 2D straight-line swimming motions of a flexible foil for Strouhal number $St = 0.3$. Other kinematic parameters of the motion: $\lambda/\ell = 0.95$, $c_p/U = 1.1$, $A/\ell = 0.2$.

panels, a time step size of $dt = 0.05$, and a desingularization radius $\delta_w = 0.02$. The resulting wake shedding dynamics are illustrated in Figure 2-12, with equal scales in the x and y directions. Each position in Figure 2-12 corresponds to the numbered backbone shapes illustrated in Figure 2-11. With a phase speed c_p now slightly greater than the swimming speed U, the crests of the backbone wave appear to move slightly backwards in Figures 2-11 and 2-12, opposite to the direction of straight-line swimming. This condition of wave speed c_p being greater than U, is necessary for the generation of thrust for a symmetric body in an inviscid flow [239, 241, 197, 9] which can be elucidated by a detailed look at the vortex generation dynamics and comparison to the $St = 0.2$ case.

Examining the vortex shedding dynamics for Strouhal number $St = 0.3$ shown in Figure 2-12, in Position 1, the trailing edge begins to move downwards from the extreme lateral excursion during the half-cycle. As the foil section begins to acquire a circulation from the local backbone undulation and the forward translation at speed U, vortices with counterclockwise (positive) circulation are shed into the wake. At this point during the swimming cycle, which is analogous to the body shape in Position 1 for Strouhal number $St = 0.2$ in Figure 2-9, much more positive vorticity has been shed into the wake for $St = 0.3$ than for $St = 0.2$, entirely due to the difference in the c_p/U for these two Strouhal numbers. As can be seen in the subsequent

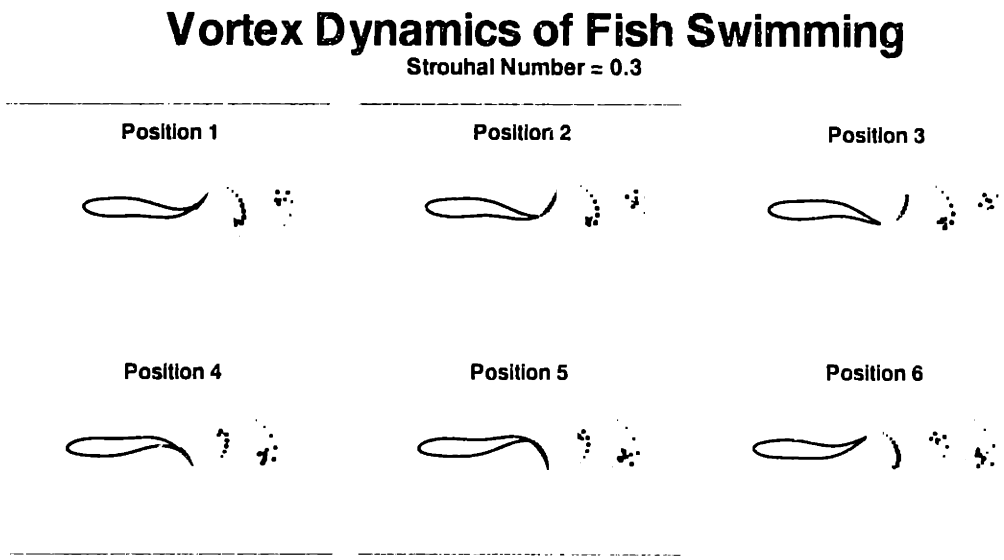

Figure 2-12: Wake generation profiles over an oscillation cycle for 2D straight-line swimming motions of a flexible foil at Strouhal number $St = 0.3$. Position numbers correspond to those backbone shapes illustrated in Figure 2-11. Size of the vortices and the color range are scaled to the magnitude and sign of the circulation Γ. Red vortices indicate a counterclockwise (positive) circulation, and the blue vortices indicate a clockwise (negative) circulation. Green vortices have no circulation. Circulation range $\Gamma = [-0.02, 0.02]$. Kinematic parameters of the motion: $\lambda/\ell = 0.95$, $c_p/U = 1.1$, $A/\ell = 0.2$. Numerical parameters for the simulation: $k = 100$, $dt = 0.05$, $\delta_w = 0.02$.

frame of Position 2, the continuation of the downward stroke towards the bottom extreme lateral excursion produces more positive vorticity is released into the wake. As the strength of this counterclockwise vorticity shed into the wake diminishes, however, the clockwise circulation around the body stabilizes sooner for $St = 0.3$ than for $St = 0.2$. In Position 3, the trailing edge is at the extreme downwards lateral excursion. The circulation around the body begins to diminish, however, due to the local motions of the traveling backbone wave, and the body begins to shed its clockwise vorticity into the wake. Also in this frame, clockwise vorticity (blue) shed during the previous half cycle begins to tighten into a spiral. The center of this clockwise vorticity spiral is slightly below the centerline of the foil's stretched-straight mean line. In addition, counterclockwise vorticity (red) shed during the previous cycle begins has fully tightened into a spiral, and the counterclockwise vorticity just released near the trailing edge begins to curl up into a loose spiral, with the centers of these spirals slightly above the centerline of the foil's stretched-straight mean line.

In Position 4 of Figure 2-12, the trailing edge begins to move upwards, away from the extreme bottom lateral excursion, and continues to release clockwise vorticity into the wake which was body-bound circulation during the previous half-cycle shown as Positions 1–3. In Position 5, the trailing edge continues to move upwards, and the release of clockwise vorticity into the wake subsides as the body acquires a strong counterclockwise circulation. In Position 6, the swimming cycle is complete, with the trailing edge at the extreme upwards lateral excursion, with the clockwise vorticity entirely released into the wake. The peak counterclockwise body circulation strength now begins diminish with the propagation of the backbone wave perturbation, as the release of counterclockwise vorticity initiates. Again, the counterclockwise (red) vorticity released into the wake during the previous half-cycle can be seen to tighten into a spiral, with the center of the spiral slightly above the centerline of the foil's stretched-straight mean line. Similarly, the clockwise vorticity just released into the wake begins to tighten into a spiral, while the clockwise vorticity released into the wake during the previous cycle has formed a tight spiral, both slightly below the centerline of the foil's stretched-straight mean line. The net result of the offset

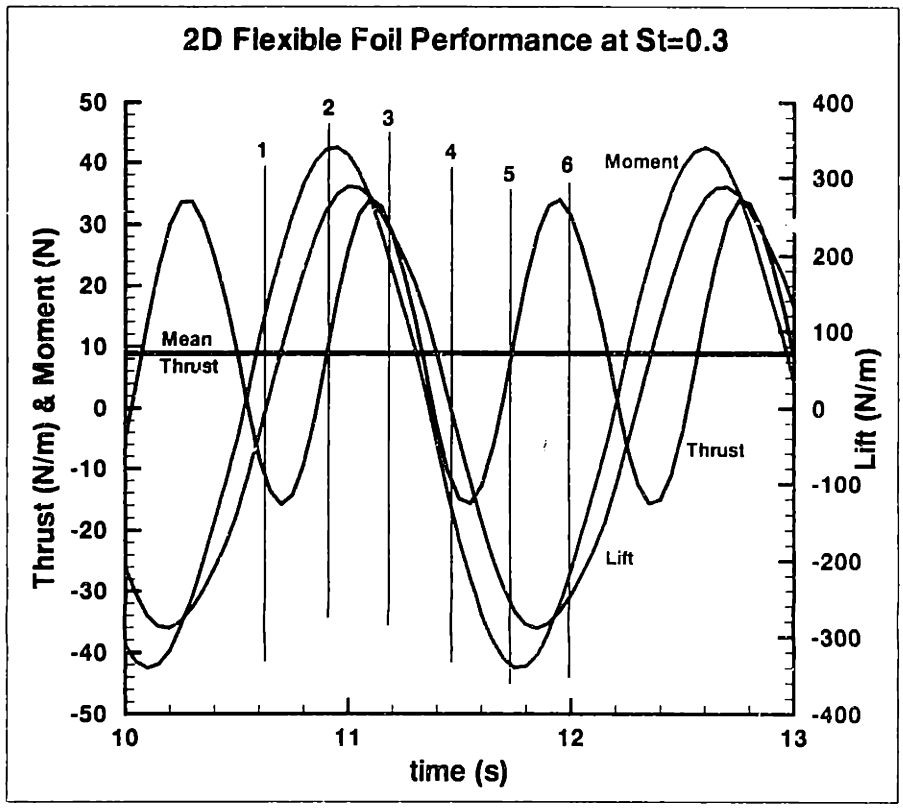

Figure 2-13: Time record of body forces and moment over an oscillation cycle for 2D straight-line swimming motions of a flexible foil at Strouhal number $St = 0.3$. Thrust (black), lift (red), and rotational moment (blue) are shown. The corresponding times in the swimming cycle for body positions shown in Figures 2-11 and 2-12 are indicated with labeled vertical green markers. Other kinematic parameters of the motion: $\lambda/\ell = 0.95$, $c_p/U = 0.95$, $A/\ell = 0.2$.

counter-rotating vorticity patches is a jet of fluid opposite the direction of straight-line swimming, manifested through the stable reverse Kármán vortex street seen through the discrete representation of the wake.

A time record for the forces and moment on the foil during the swimming cycle are shown in Figure 2-13. Each position of Figures 2-11 and 2-12 is labeled on 2-13 at the corresponding time during the cycle. The peaks in the lift force on the body are shown to correlate well to the vortex wake shedding pattern seen in Figure 2-12 and discussed above. A steady-state thrust is realized for this case.

2.2.3 Comparison with linear theory

Swimming plate theory explained

The forces on the flexible foil found by the present simulation method are compared to the reactive theory of fish propulsive mechanisms described by Wu (1961,1971) [239, 241]. The forces provided by the simulation compare well with the linear theory results for limited ranges of the motions considered, and discrepancies between the results of the two theories are explained.

Wu (1961) utilizes an analytic method to estimate the thrust and power coefficients on a two-dimensional swimming plate of negligible thickness whose motion is characterized by a progressive wave which travels down the chord of the plate from nose to tail, while the plate moves forward at some speed U. The wave originates at the nose of the plate and is simple periodic with an arbitrary amplitude expressed in powers of the body length coordinate. Wave amplitude h and wave slope along the body length $\partial h/\partial x$ are assumed to be very small compared to the body length. Perturbation velocities $[u, v]$ caused by the unsteady waving motion are small with respect to steady swimming velocity U. Euler equations are linearized with respect to U; these govern the conservation of momentum of the fluid, in terms of an acceleration potential ϕ.

A vortex sheet is assumed to be shed from the plate, forming a vortex wake, and the tangential component of velocity across this surface need not be continuous, although the pressure must be. The pressure need not be continuous across the plate. Because the acceleration potential ϕ is described in terms of a linear function of the pressure p, and has singularities only along the body boundary, it is chosen as the quantity of interest in the analysis, over the complex velocity w which has discontinuities on the plate, and across the wake. Also, because the acceleration potential can be shown to satisfy Laplace's equation, the existence of an acceleration stream function ψ can be defined by the Cauchy-Riemann equations, giving rise to a complex acceleration potential $f(z,t) = \phi(x,y,t) + i\psi(x,y,t)$ where $z = x + iy$.

The body boundary condition on the plate in linearized with respect to the steady

velocity U, i.e. the perturbation velocities are neglected, and it is applied at the mean position of the plate $y = \pm 0$, along the entire length of the plate. This condition is applied to the complex acceleration potential $f(z,t)$. The body boundary condition requires v and ψ to be even in y, and thus the u and ϕ are odd in y. From this, $\phi(x,0,t) = 0$ outside the region of the plate $|x| > 1$. A Kutta condition is applied to the trailing edge of the plate, limiting the complex potential there to be finite. A radiation condition is imposed which states that the complex potential f goes to 0 as z goes to ∞, and the complex velocity w must go to 0 at the upstream ∞, or $z \to -\infty$.

Employing linearized body boundary conditions and neglecting the influence of the dynamics of the shed vorticity in the wake, the thrust produced by the body as well as the energy lost to transverse motions and thus the total power can be be expressed in terms of Bessel functions, after some algebraic manipulation involving the conformal transformation of the complex acceleration potential $f(z,t)$ for the linearized flow past a flat plate into the flow past a circular cylinder. The details of these straightforward expansions can be found in Wu (1961) [239]. The phase difference between the various components of the waveform is arbitrary between powers of the body length, but if the phase difference is taken to be zero, then the thrust coefficient C_T and wasted energy coefficient C_E can be expanded for a quadratic amplitude waveform described by equation (2.39) as:

$$C_T/2\pi = c_0^2 T_1 + c_1^2 T_2 + c_0 c_1 T_3 - c_0 c_2 T_4 \tag{2.42}$$

$$C_E/2\pi = c_0^2 E_1 + c_1^2 E_2 + c_0 c_1 E_3 - c_0 c_2 E_4 \tag{2.43}$$

where c_1 and c_2 are the amplitude coefficients from the waveform equation (2.40), and c_0 any constant-amplitude waveform component along the backbone such that $a(x) = c_0 + c_1 x + c_2 x^2$. The various amplitude-dependent components can be expressed in terms of Bessel functions of the wavenumber k and the reduced frequency $\sigma = \omega \ell / 2U$

for chord ℓ as

$$T_1 = \Omega\Omega_* + QQ_* \tag{2.44}$$

$$T_2 = \Omega'\Omega'_* + Q'Q'_* \tag{2.45}$$

$$T_3 = Q\Omega' + Q_*\Omega'_* - \Omega Q' - \Omega_* Q'_* + \sigma^2\{J_0 J'_1 - J_1 J'_0\} \tag{2.46}$$

$$T_4 = \Omega\Omega''_* + \Omega_*\Omega'' + QQ''_* + Q_* Q'' \tag{2.47}$$

$$E_1 = [F - (F^2 - G^2)]\{N_0^2 + N_1^2\} \tag{2.48}$$

$$E_2 = [F - (F^2 - G^2)]\{(N'_0)^2 + (N'_1)^2\} \tag{2.49}$$

$$E_3 = 2[F - (F^2 - G^2)]\{N_0 N'_1 - N_1 N'_0\} \tag{2.50}$$

$$E_4 = 2[F - (F^2 - G^2)]\{N_0 N''_0 + N_1 N''_1\} \tag{2.51}$$

where all derivatives are partials taken with respect to k, and where F and G are the real and imaginary parts, respectively, of the Theodorsen function of the reduced frequency, $C(\sigma) = F(\sigma) + iG(\sigma)$. Other components are defined in terms of $J_0(k)$ and $J_1(k)$ as follows:

$$\Omega(\sigma, k) = (\sigma - k)\{F(\sigma)J_0(k) + G(\sigma)J_1(k)\} \tag{2.52}$$

$$\Omega_*(\sigma, k) = \Omega(\sigma, k) + kJ_0(k) \tag{2.53}$$

$$Q(\sigma, k) = (\sigma - k)\{(1 - F(\sigma))J_1(k) + G(\sigma)J_0(k)\} \tag{2.54}$$

$$Q_*(\sigma, k) = Q(\sigma, k) + kJ_1(k) \tag{2.55}$$

$$N_0(\sigma, k) = (\sigma - k)J_0(k) \tag{2.56}$$

$$N_1(\sigma, k) = (\sigma - k)J_1(k) \tag{2.57}$$

The quadratic backbone wave form envelope thrust coefficient components T_i are shown in Figure 2-14 as function of reduced frequency σ for various wavenumbers k. As can be seen, positive contributions to the thrust occur when the reduced frequency exceeds a certain threshold for a given wavenumber k. This threshold corresponds to

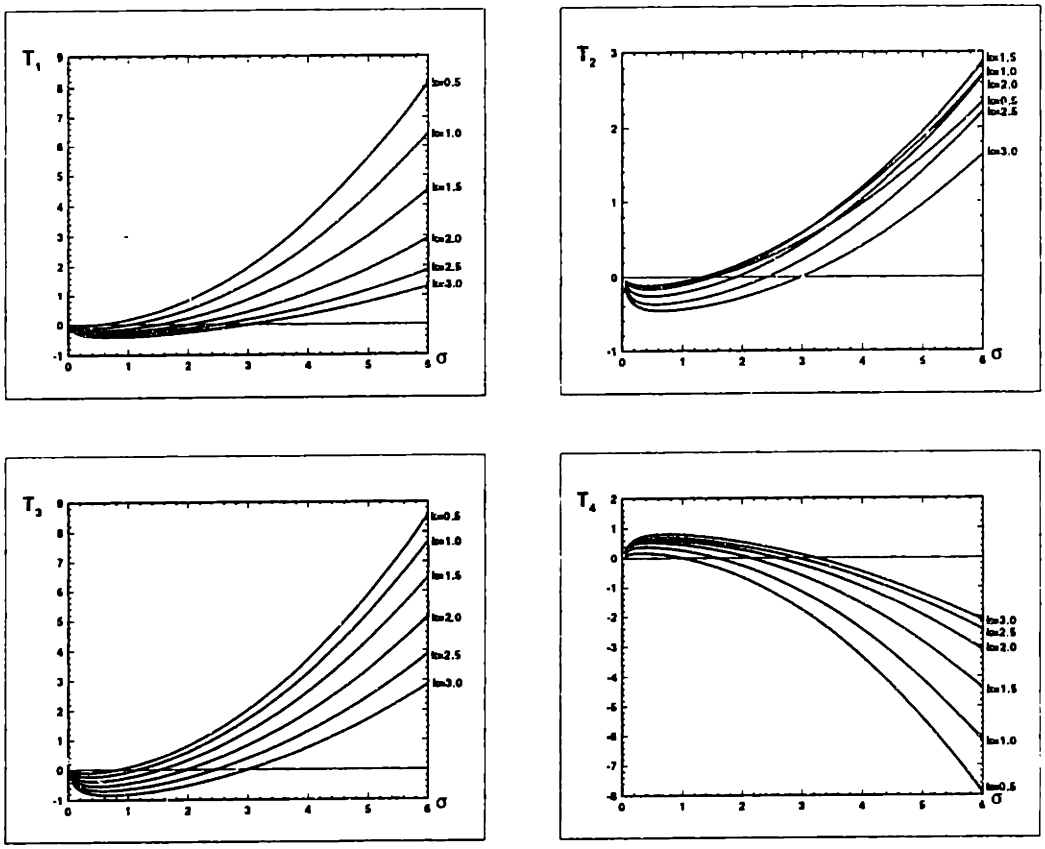

Figure 2-14: Thrust coefficient T_i components as a function of reduced frequency σ for various values of wavenumber k for Wu's flat plate swimming theory [239]. Components for quadratic amplitude waveform envelope shown.

the point at which the speed of the backbone wave c_p exceeds the swimming speed U. These plots are similar to those given as Figures 1–4 in Wu (1961) [239] but are specific to the case of a quadratic amplitude envelope considered in this investigation.

Given thrust coefficient C_T and the wasted kinetic energy coefficient C_E, the power coefficient can be easily expressed as just

$$C_P = UC_T + C_E \tag{2.58}$$

or expanded for the quadratic amplitude backbone wave form envelope as

$$C_P/2\pi = c_0^2 P_1 + c_1^2 P_2 + c_0 c_1 P_3 - c_0 c_2 P_4 \tag{2.59}$$

with the various components of the power coefficient expressed as $P_i = UT_i + E_i$.

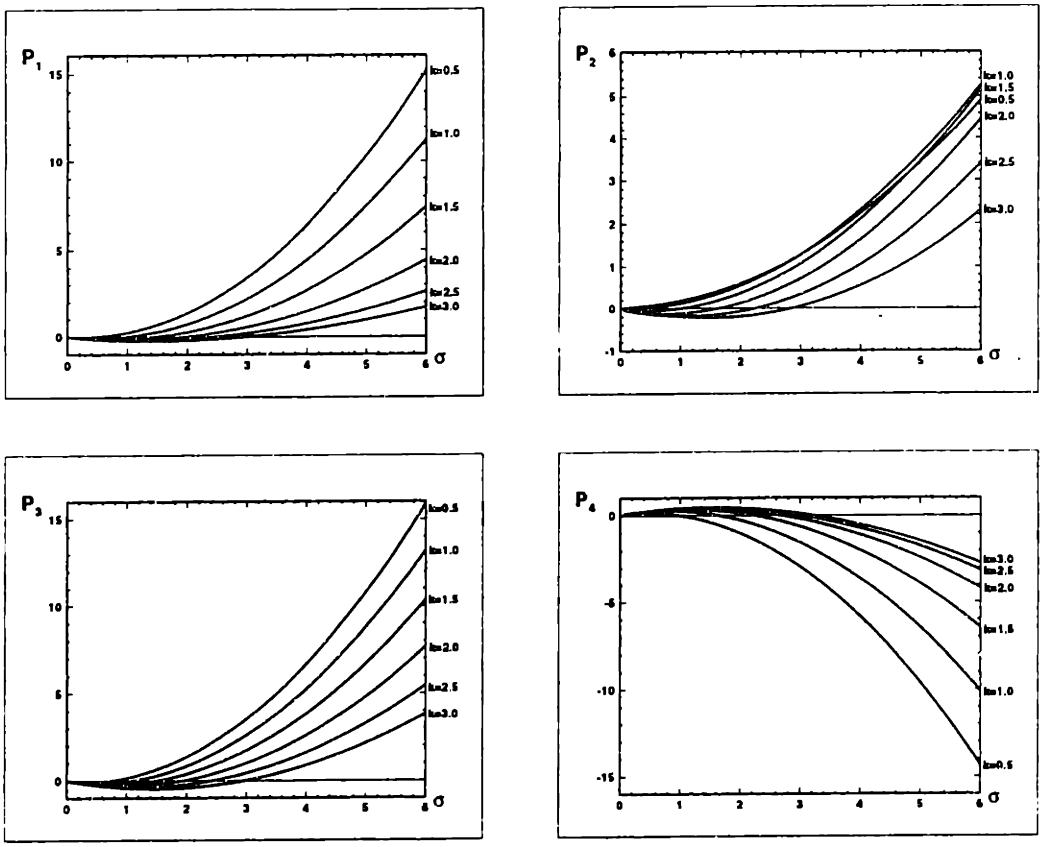

Figure 2-15: Power coefficient components P_i as a function of reduced frequency σ for various values of wavenumber k for Wu's flat plate swimming theory [239]. Components for quadratic amplitude waveform envelope shown.

The quadratic backbone wave form envelope power coefficient components P_i are shown in Figure 2-15 as function of reduced frequency σ for various wavenumbers k. Again, positive contributions to the power consumed occur when the reduced frequency exceeds a certain threshold for a given wavenumber k, i.e. when the speed of the backbone wave c_p exceeds the swimming speed U. This figure is similar to Figures 5–6 of Wu (1961) [239] but is specific to the quadratic amplitude envelope case considered herein.

Comparison results

To quantify the linear behavior of our numerical method for small amplitude tail oscillations, a small constant-amplitude case of a traveling wave is utilized to compare the numerical boundary integral method to the theoretical approximate solution of

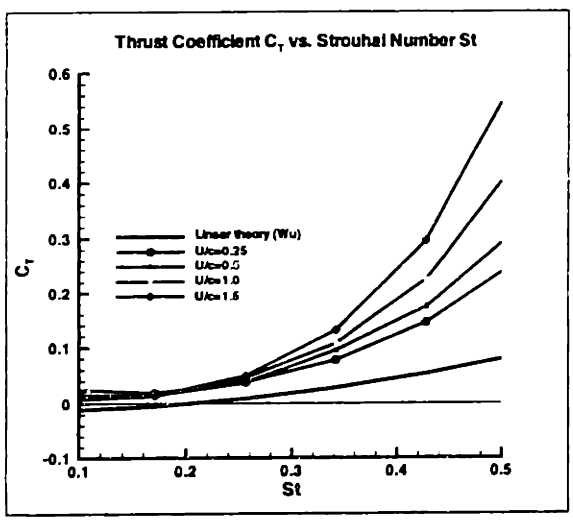

(a) Thrust coefficient C_T

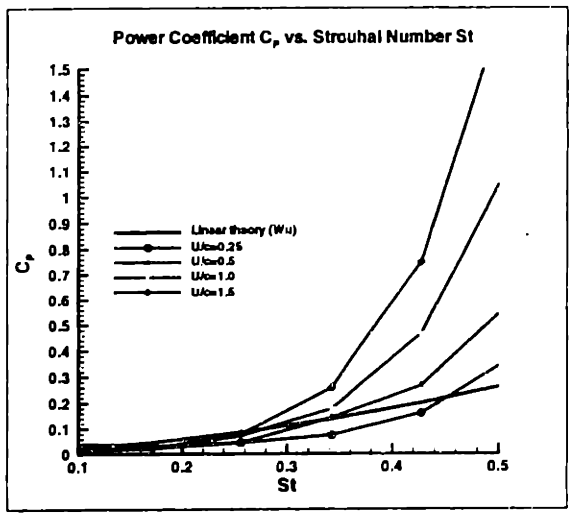

(b) Power coefficient C_P

Figure 2-16: Two-dimensional straight-line swimming performance versus Strouhal number St. Shown: (a) thrust coefficient C_T versus St; (b) power coefficient C_P versus St. In both cases, comparison between the present method for increasing values of swimming speed U/ℓ and Wu's linear flat plate swimming theory [239] is shown for a constant amplitude waveform envelope.

Wu. The thickness of the flexible foil NACA section is reduced to ten percent of the chord length, to minimize the effect of thickness on the wake development and propagation. The comparison of thrust coefficient C_T is shown in Figure 2-16(a) as a function of the Strouhal Number, for various values of the swimming speed U. Similarly, the power coefficient comparison is shown in Figure 2-16(b). As can be seen, the present boundary integral element method compares well with the linear theory for low Strouhal numbers. Strouhal number is varied by increasing ω. Thus, for any value of Strouhal number St, the reduced frequency is kept constant when ω is increased for curves of increasing U. It is clear that the low frequency cases are more in agreement with the linear theory, which is the limit case of zero frequency and zero Strouhal number. This Figure 2-16 illustrates the limitations of linear theory when moderate or large frequencies characterize the motion.

The increase in frequency of the trailing edge beat for a given maximum lateral excursion causes the wake dynamics to heavily influence the loading on the foil. The vortices shed into the wake are stronger, and as a result, their evolution dynamics

are more significant to the pressure field around the body. This periodic unsteady wake profile trailing behind the flexible foil rapidly winds into packets of vorticity which evolve into a complex reverse Kármán vortex street. These strong vortices, shed closer to the body as the frequency increases, induce strong near-field velocities which affect the local body unsteady circulation distribution, as shown in Figures 2-9 and 2-12. The strength of this shed wake is further enhanced by the increased thrust coefficient for a given Strouhal Number over an increasing swimming speed U range shown in Figure 2-16.

These vorticity dynamics can be further inferred from Figure 2-17. The dependence of the thrust-power ratio on the Strouhal number is clearly evident from this plot. Although the thrust coefficient C_T and power coefficient C_P each displayed similar monotonically increasing behavior with the Strouhal number, which was in agreement with the trends predicted by linear theory, the same cannot be said for the thrust-power ratio, which shows peak performance at a low Strouhal number, as opposed to the monotonically increasing C_T:C_P ratio with increasing Strouhal number of the linear prediction [239]. This behavior, consistent over a range of Strouhal numbers St for different values of the swimming speed U/ℓ, must be entirely the result of the wake vorticity dynamics and their interaction with the undulating body. These conclusions are consistent with the predictions and findings of many experimental and computational investigations of oscillating foil thrust generation and performance [203, 113, 207, 204, 68, 10].

The comparison of thrust coefficient C_T is shown in Figure 2-18(a) as a function of the Strouhal Number, for various values of the maximum trailing edge double amplitude h/ℓ. Similarly, the power coefficient comparison is shown in Figure 2-18(b). As can be seen, the present boundary integral element method compares well with the linear theory for low Strouhal numbers. Strouhal number is varied by increasing ω while keeping U constant. Thus, as the Strouhal number St increases with ω, the reduced frequency similarly increased but is not affected by kept increasing h/ℓ. It is clear that the low amplitude cases are more in agreement with the linear theory, which is the limit case of zero amplitude. This Figure 2-18 illustrates the limitations

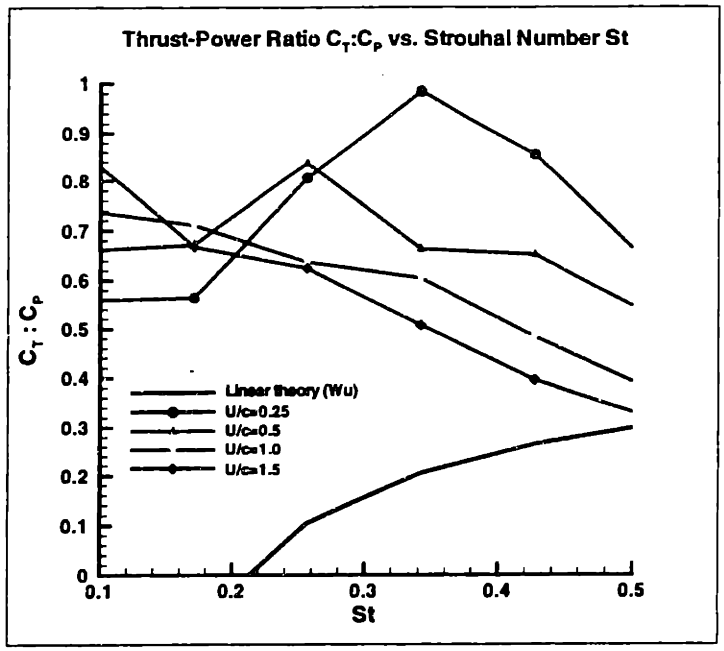

Figure 2-17: Two-dimensional straight-line swimming performance versus Strouhal number St. Thrust-power ratio C_T:C_P shown versus St. Comparison between the present method for increasing values of swimming speed U/ℓ and Wu's linear flat plate swimming theory [239] is shown for a constant amplitude waveform envelope.

of linear theory when moderate or large amplitudes characterize the motion.

The increase in amplitude of the tail beat brings about an increased width of the wake. The periodic unsteady wake profile trailing behind the flexible foil rapidly winds into packets of vorticity which evolve into a complex reverse Kármán vortex street. This vortical structure influences the performance on the foil propulsion by generating a jet of fluid which is countered by increased momentum imparted to the fish form. This is evidenced by the increased thrust coefficient for a given Strouhal Number over an increasing amplitude range shown in Figure 2-18.

These vorticity dynamics can be similarly inferred from Figure 2-19. Again, the dependence of the thrust-power ratio on the Strouhal number is clearly evident from this plot. The thrust-power ratio C_T:C_P shows a peak performance at a low Strouhal number, defying the linear theory which would predict a monotonically increasing C_T:C_P ratio with Strouhal number. This behavior, consistent over a range of Strouhal numbers St for different values of the tail beat double amplitude h_o/ℓ, must be entirely the result of the wake vorticity dynamics and their interaction with the undulating

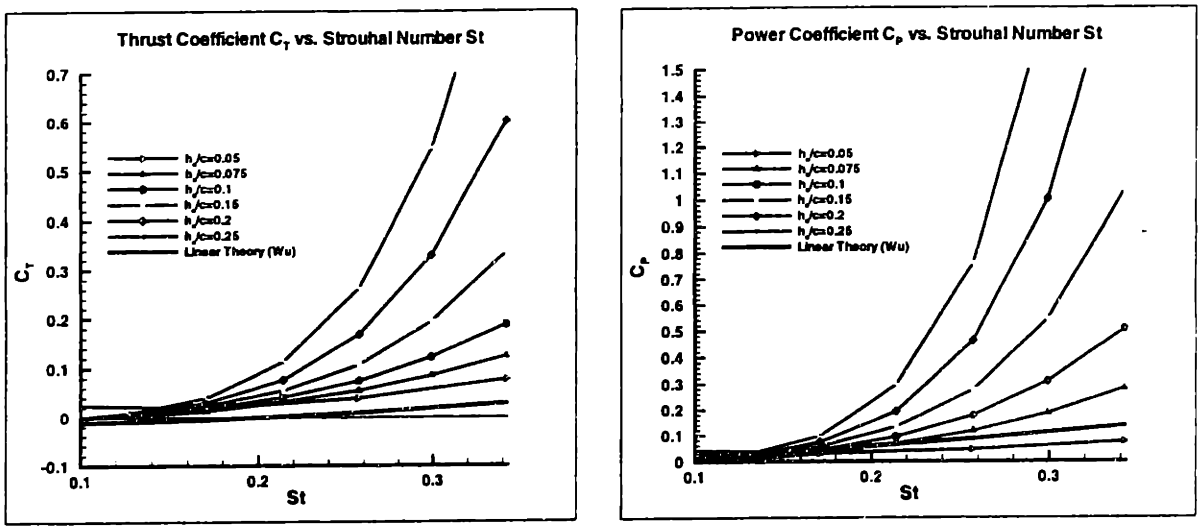

(a) Thrust coefficient C_T

(b) Power coefficient C_P

Figure 2-18: Two-dimensional straight-line swimming performance versus Strouhal number St. (a) Thrust coefficient C_T versus St (b) Power coefficient C_P versus St. In both cases, comparison between the present boundary element method for increasing tail beat amplitudes h_o/ℓ and Wu's linear flat plate swimming theory [239] is shown for a constant amplitude waveform envelope.

body.

The integrated dynamics of the undulating foil over a range of Strouhal numbers, for systematic parametric variation of the swimming speed and the tail beat width, show complex dependence on the behavior of the nonlinear deforming wake. The linear theory does not predict either of these trends, as the thrust and power coefficients are simply functions of the reduced frequency σ and the wavenumber k. These comparisons show how small trailing edge amplitudes and frequencies reduce nonlinear wake effects. The further effects of more moderate choices of frequency and amplitude on the swimming performance and the wake dynamics are discussed in the following section.

2.2.4 Strouhal number dependence of wake dynamics

The motion of the flexible foil is simulated over time for the traveling-wave backbone motion and a steady forward velocity, and the resulting wake is examined. By varying

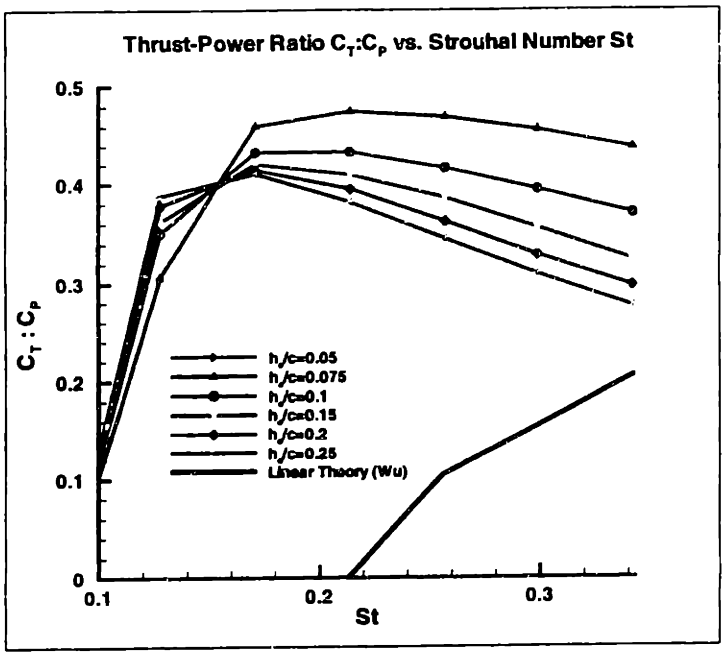

Figure 2-19: Two-dimensional straight-line swimming performance versus Strouhal number St. Thrust-power ratio C_T:C_P shown versus St. Comparison between the present method for increasing values of tail beat amplitude h_o/ℓ and Wu's linear flat plate swimming theory [239] is shown for a constant amplitude waveform envelope.

the parameters governing the backbone motion, the overall structure of the wake changes, and the influence of the geometry of the shear layer on the body causes the propulsive forces to vary as well, as evidenced by the discussion of the previous section. Triantafyllou, *et al.* (1993) [204] showed through stability analysis and experimentation on flapping foils, that the optimal Strouhal Number for oscillating foils in terms of propulsive efficiency was found to be in the range of 0.25 to 0.35, corresponding to the frequency of maximum spatial amplification of the thrust jet instability. Varying the Strouhal number of the flexible foil is proposed to exhibit this same wake structural dependence, and defining regions of Strouhal Number will govern the propulsive forces on the flexible foil for fish-like motions of moderate frequency and amplitude.

The amplitude envelope of the local foil undulating motion, defined by equation (2.40), is chosen to yield an amplitude of 10% of the chord ℓ, such that the total lateral excursion of the tail to be $A/\ell = 0.2$. The thickness of the body section is chosen to be 16% of the chord ℓ. Although several different combinations of linear and

quadratic amplitude terms were employed to yield this total lateral excursion magnitude, typically the linear term was kept small, contributing about 25% of the total lateral excursion at the trailing edge or $c_1 x_{te}/\ell = 0.05$. This combination of amplitude magnitude terms yields maximum tail amplitudes typical of most *carrangiform* swimmers [57, 47, 19]. In addition, the backbone wavelength λ is fixed at a length slightly longer than the chord ℓ, also typical of most *carrangiform* swimmers. With this amplitude fixed, the swimming motion is simulated over a range of Strouhal numbers St by increasing the frequency of the tail beat amplitude. This results in an increasing c_p/U for increasing St.

Figure 2-20 graphically illustrates the dependence on the wake dynamics on the Strouhal number of swimming. For all three cases between $St = 0.05$ and $St = 0.25$ the reverse Kármán vortex street thrust jet wake structure is clearly evident, as $c_p/U > 1$. As the St increases, the strengths of the wake vortices and thus the thrust jet increase as well. The proximity of the strong wake structures to the flexing body becomes increasingly prominent as the Strouhal number increases, further affecting the local flow and circulation about the undulating foil, and thus its load profile.

As previously discussed, many fish swim with a backbone wavelength λ which is slightly greater than the body length ℓ. The two-dimensional flexible-body swimming numerical method is employed to investigate the dependence of the swimming performance on the backbone wavelength. Figure 2-21 shows the thrust and power expenditures of the undulating foil as functions of the backbone wavenumber k for two different values of the backbone wave frequency. Again, the total trailing edge lateral excursion amplitude is $A/\ell = 0.2$. The qualitative trends and quantitative values observed in this figure are in good agreement with those reported by other investigations of wavy plate swimming performance dependence on the wavelength of the backbone wave [36]. A peak in the thrust and power generated by the motions is evidenced at a wavenumber $k \approx 3 - 4$, corresponding to a backbone wavelength $\lambda \approx 1.5 - 2\ell$. For slightly higher wavenumbers, where the wavelength is decreasing to the body length $\lambda \to \ell$, the thrust-power ratio begins to climb, until the wavelength λ becomes less than the body length ℓ at $k > 2\pi$ and the thrust begins to diminish

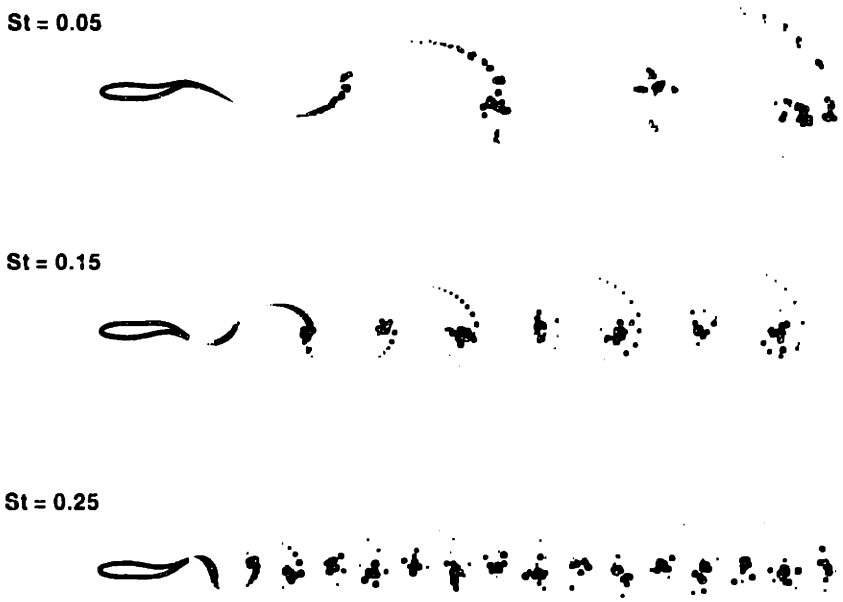

Figure 2-20: Wake profiles for 2D straight-line swimming simulations of a flexible foil. A range of Strouhal numbers are shown: $St = 0.05$ (top), $St = 0.15$ (middle), $St = 0.25$ (bottom). Strouhal number is varied by fixing A/ℓ and λ/ℓ and increasing c_p/U. Size of the vortices and the color range are scaled to the magnitude and sign of the circulation Γ. Red vortices indicate a counterclockwise (positive) circulation, and the blue vortices indicate a clockwise (negative) circulation. Green vortices have no circulation. Circulation range $\Gamma = [-0.02, 0.02]$. Numerical parameters for the simulations: $k = 100$, $dt = 0.05$, $\delta_w = 0.02$.

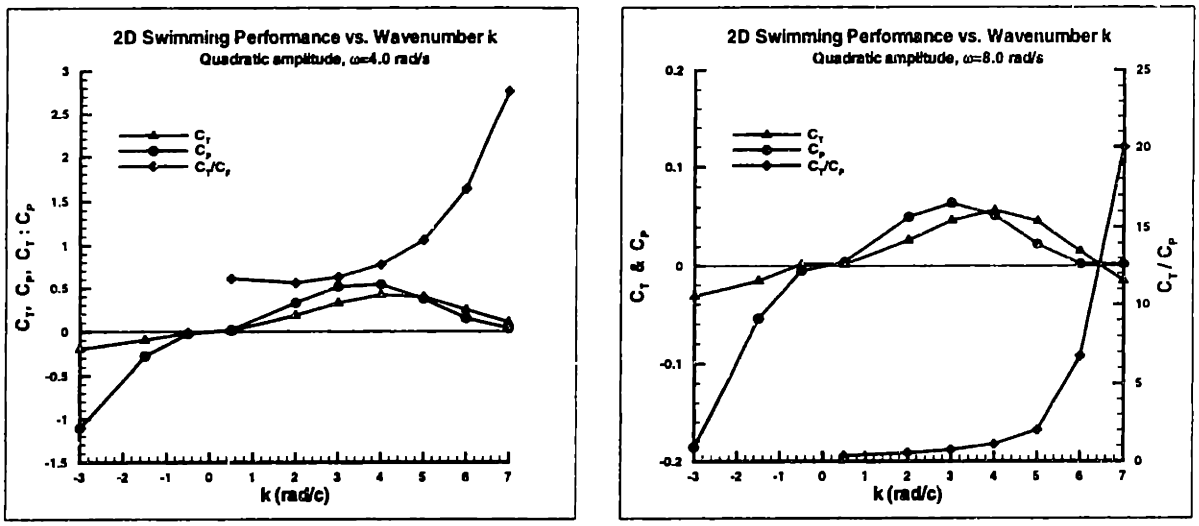

(a) $\omega = 4.0\ rad/s$ (b) $\omega = 8.0\ rad/s$

Figure 2-21: Two-dimensional straight-line swimming performance versus backbone wavenumber k. Thrust coefficient C_T, power coefficient C_P, and thrust-power ratio C_T:C_P shown for backbone wave frequencies (a) $\omega = 4.0\ rad/s$ and (b) $\omega = 8.0\ rad/s$. A quadratic amplitude waveform envelope is employed.

significantly.

Finally, the performance of the swimming motions over a range of Strouhal numbers for various values of the swimming speed U/ℓ for the quadratic amplitude backbone wave form is examined. Thrust coefficient C_T and power coefficient C_P are shown in Figure 2-22 as functions of Strouhal number St for different values of U/ℓ (U/c where c is the chord). In addition, the linear theory prediction employing Wu's theory for the quadratic amplitude waveform is also shown for comparison purposes. The agreement between the linear theory and the present numerical method is good for low swimming speeds. In fact, the linear theory may overpredict the thrust generated during steady straight-line swimming for low U. However, for large U/ℓ, the predicted forces on the swimming flexible foil are much higher than predicted by the linear theory, due to the effects of nonlinearly deforming vorticity in the wake discussed previously.

The effects of these wake-body interactions are again evident from the dependence of the thrust-power ratio C_T:C_P on the Strouhal number St, shown in Figure 2-23.

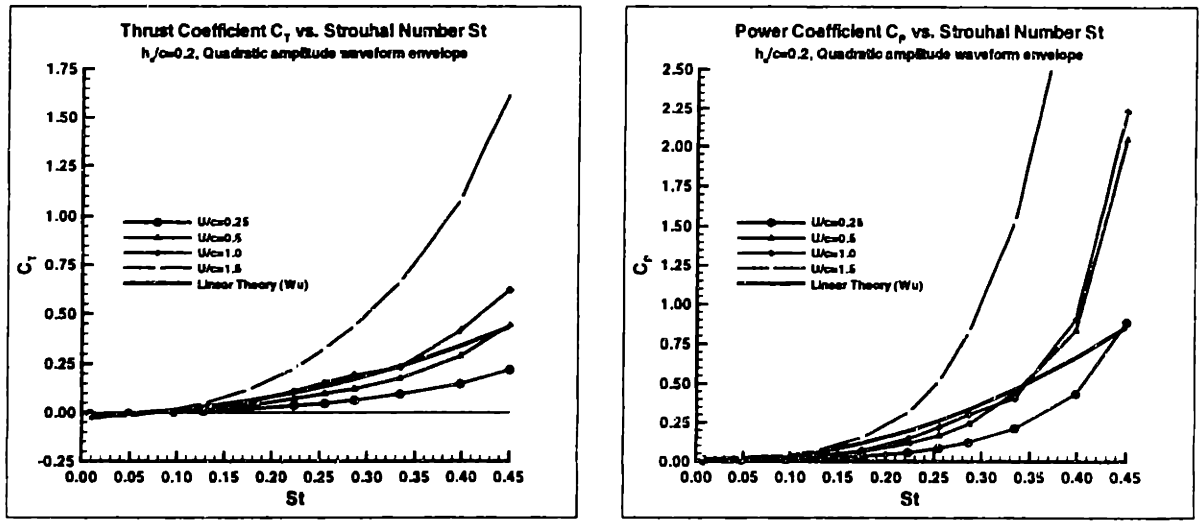

(a) Thrust coefficient C_T vs. St

(b) Power coefficient C_P vs. St

Figure 2-22: Two-dimensional straight-line swimming performance versus Strouhal number St. (a) Thrust coefficient C_T versus St (b) Power coefficient C_P versus St. In both cases, comparison between the present boundary element method for increasing swimming speeds U/ℓ and Wu's linear flat plate swimming theory [239] is shown for a quadratic backbone waveform amplitude envelope.

The thrust-power ratio C_T:C_P shows a peak performance at a low Strouhal number. In this case, the linear theory predicts a monotonically decreasing C_T:C_P ratio with Strouhal number for positive values of thrust and power coefficient. This behavior, consistent over a range of Strouhal numbers St for different values of the swimming speed U/ℓ, must be entirely the result of the wake vorticity dynamics and their interaction with the undulating body.

To further quantify the effect of the wake dynamics on the swimming performance, the momentum of the thrust jet is studied as a function of the Strouhal number. As the strength of the vorticity shed from the foil increases as the Strouhal number increases, the momentum of the thrust jet must be nondimensionalized for meaningful comparison. To do this, the width of the thrust jet is considered a measure of the amount of wasted energy in the wake for a given momentum present due to the rotational motion produced by the vortex street. This non-dimensional wake width is found simply by determining the integrated moment of the vorticity magnitude in the wake about the axis of straight-line swimming ($y = 0$) and dividing by the integrated

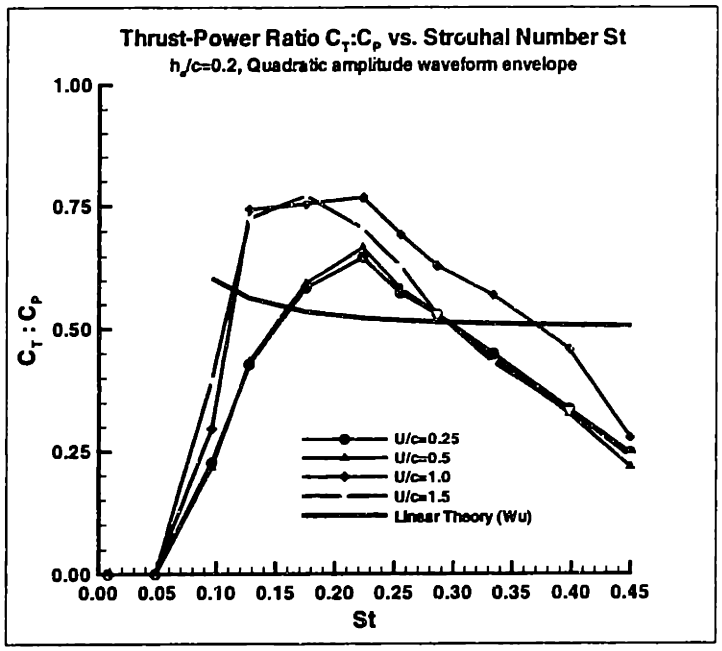

Figure 2-23: Two-dimensional straight-line swimming performance versus Strouhal number St. Thrust-power ratio $C_T : C_P$ shown versus St. Comparison between the present method for increasing swimming speeds U/ℓ and Wu's linear flat plate swimming theory [239] is shown for a quadratic backbone waveform amplitude envelope.

magnitude of all wake vorticity:

$$\Psi_w = \frac{\int\int_{wake} y_v^2 \omega_z^2 \, dxdy}{\int\int_{wake} \omega_z^2 \, dxdy} \tag{2.60}$$

For a discrete vortex representation of the wake with nv vortices each of strength Γ_v, this can be expressed

$$\Psi_v = \frac{\sum_{i=1}^{nv} y_{v_i}^2 \Gamma_i^2}{\sum_{i=1}^{nv} \Gamma_i^2} \tag{2.61}$$

Using the quadratic backbone waveform amplitude envelope to produce a trailing edge lateral excursion of $A/\ell = 0.2$, results for the variation in thrust coefficient C_T and power coefficient C_P as functions of Strouhal number St displayed above in Figure 2-22 are reexamined from the standpoint of wake dynamics. The non-dimensional wake width Ψ_v over the range of Strouhal numbers is determined for the various swimming speeds considered U/ℓ. At each Strouhal number, the wake width was then averaged over the range of swimming speeds examined, and Figure 2-24 shows the non-dimensional thrust jet wake width Ψ_v as a function of the Strouhal

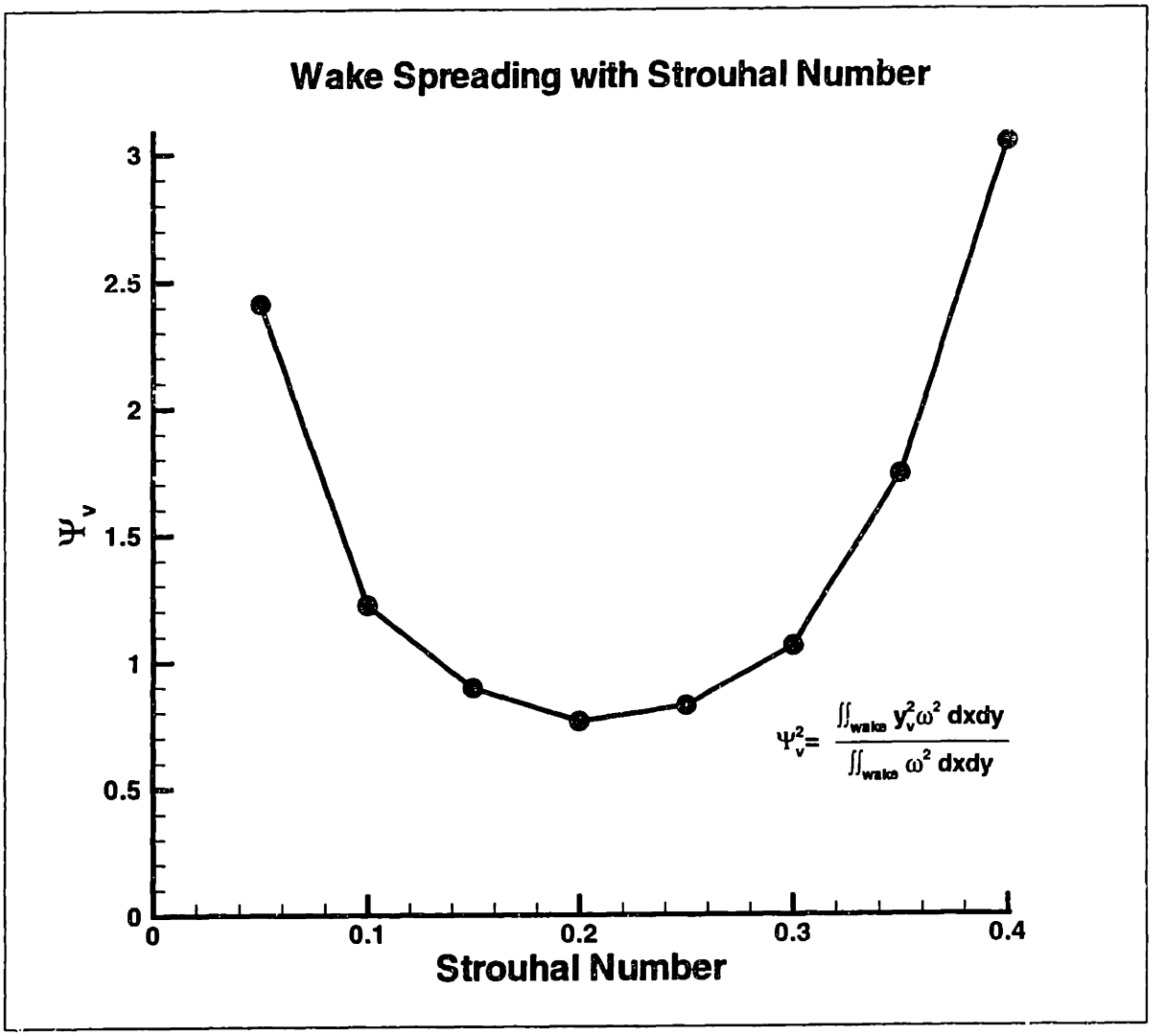

Figure 2-24: Two-dimensional straight-line swimming non-dimensional thrust jet wake width Ψ_v as a function of Strouhal number St.

number.

A clear minimum in the wake width Ψ_v is evident for Strouhal numbers between $St = 0.15$ and $St = 0.3$. This is in general agreement with theoretical wake width Orr-Sommerfeld stability analyses [203, 204], and corroborates the assumption that the nonlinear wake evolution dynamics are of key importance in obtaining superior propulsive performance utilizing fish-like swimming motions and mechanisms.

2.3 Discussion

The two-dimensional computational method has elucidated some important scientific principles in the study of flexible-body fish-like swimming dynamics. In addition, several numerical issues have been identified relevant to the application of unsteady panel methods to discrete vortex representations of continuous deforming shear layer wakes.

A source-dipole based panel method was chosen for this problem due to its extensibility to three-dimensions. In addition, flat panels with constant perturbation potential distributions were chosen to reduce computational time, which is necessarily greater for this flexible-body problem due to the requirement of recalculating geometric influence coefficients at every time instant. A desingularized discrete vortex representation of the wake was employed to enable the removal of the singularity associated with the infinitesimal dipole surface representation of the shear layer at high Reynolds number. All of these choices, however, revealed a unique convergence behavior of the numerical method. While the systematic variation of numerical parameters such as panel number, desingularization radius, and time step demonstrated the consistency of the numerical method, the convergence of the simulations to analytic solutions was affected greatly by the geometric representation. Specifically, the geometry of the section shape, the size and distribution of the trailing edge panels, and the size of the newly-shed wake panel and its proximity to the trailing edge were the largest contributing factors to the divergence of the solution as the numerical parameters were systematically decreased to approach the continuous solution. A specific Courant of CFL number [89, 90] at which the solution began to diverge was not identified; rather, the solution exhibited gradual decay in the accuracy as the continuous solution was approached. However, the numerical method compared well to classical panel method results, and additionally, for more moderate choices of geometric representation and discrete numerical parameters, the solution error was often minimal. The selection of a non-cusped trailing edge was determined to be a primary contributor to promoting solution accuracy. For this reason, the convergence tests

performed on the two-dimensional computational method may seem extensive; however, these tests enabled the identification of parametric ranges in which the solution was considered to be most accurate. In addition, the lessons learned from these extensive two-dimensional convergence tests alleviated the need to perform such extensive convergence testing in three-dimensions should the same phenomena be encountered, where the computational time associated with each simulation is often over an order of magnitude larger.

The lack of literature on the study of two-dimensional flexible-body fish-like swimming prompted the comparison of the present method to the seminal works of Wu [239, 241]. More recent two-dimensional computational works [184, 135] do not devote a tremendous effort to the corroboration of Wu's method or challenge the assumptions on which his studies were based. Using a thin body section to reduce the effects of thickness on the development of the near-body flow and the resulting wake structure, the dependence of vorticity dynamics on the realized performance of the swimming motions was shown in be of key importance. Variation of the kinematic parameters defining the motion over a range of Strouhal number or reduced frequency illustrated the peak performance of the swimming flexible-foil section at a low Strouhal number, unlike the monotonic increase with Strouhal number predicted by linear theory for a constant-amplitude traveling backbone wave. These results were consistent over the range of Strouhal number considered for various fixed values of both the trailing edge total lateral excursion as well as the speed of the swimming motion.

Application of the method to examining more moderate fish-like motions for thicker bodies, such as those which might be found in live fish, further corroborated these results. A peak performance was found at a low Strouhal number for a quadratically-varying backbone traveling wave envelope, unlike the monotonic decrease with Strouhal number predicted by the linear theory for this wave form. To understand the dependence of the performance realized on the observed wake structure, the nondimensional wake width was shown to have a minimum with this same range of low Strouhal number, exhibiting wake spreading as the Strouhal number was

increased or decreased from this range. This is in general agreement with theoretical results, and explains how a swimming fish may exploit the natural wake instabilities to enhance its own performance for a given wasted energy imparted to the wake.

Some discussion to the short-comings of this numerical method cannot be avoided. This computational technique has proven to be useful for the study of the problems discussed herein. In addition, it is certainly useful for the study of a host of additional scientific problems, including the performance of pitching and heaving rigid foil sections [66, 183, 22, 149, 207, 2, 190, 245, 68, 46, 10, 169] and the control of foil motions for the possible extraction of energy from a flow [244, 28, 80, 191, 193]. Preliminary work on this type of control problem is described herein in *Appendix B* for the rigid body time integration of the unsteady foil, derived in *Appendix C*. Limitation of this method in addressing these problems include the absence of leading-edge separation modeling, which has show to be fundamental in the generation of large lift coefficients for thrust production [53, 54, 207, 9, 10, 134, 217], and the applicability of the trailing edge shear layer separation model or similar well-defined separation lines [140, 25].

Thus, while this two-dimensional method may be used to elucidate the hydrodynamic mechanisms of several types of lifting surface problems, the application of this method for use in the elucidation of the complex propulsive mechanisms employed by fish is less straightforward. Many of the fish which realize high swimming speeds, long duration swimming ranges, and reported outstanding performance are all a subclass of *carrangiform* swimmers, namely *tunniform* swimmers, whose motions are characterized by extreme tail motions confined to the rear-third of the body length with a rigid fore-body. This in itself would not preclude the present method from simulation of the problem if it were not for the morphology of these same fish, which are all characterized by a low-aspect ratio rigid body, a dramatic reduction in body depth anterior to the tail in a peduncle region, and a high-aspect ratio lunate tail. It is from the motion of the tail that the *tunniform* swimmers produce the majority of their propulsive forces. Thus, while the present method may be useful for the study of the flow around a rigid oscillation of a section of this high-aspect ratio lunate tail, three-dimensional effects such as those suggested by Lighthill [124, 125, 126] would

be obscured, as would interaction of the oscillating tail motions with vorticity shed from upstream via anterior fins such as the dorsal or from a backbone shedding ridge, such as is found on bluefin tuna *thunnus thynnus*. For these reasons, the extension of this study of the hydrodynamics of fish-like swimming motions to three-dimensions will be the focus of the subsequent chapters in this thesis.

Future extension to the present method could include the study of oscillating rigid-foil or flexible-foil sections as described above. Additionally, it would be interested to utilize the method for the study of multiple wake shedding bodies. Most relevant to the present study of fish swimming would be the study of a flexible upstream undulating foil section shedding a wake, which interacts with an oscillating rigid foil section downstream. In this manner, the in-plane vorticity dynamics which the *tunniform* swimmers, with backbone shedding ridges and high-aspect-ratio large-lateral-excursion tails, exploit might be studied with the intention of investigating the spacing, frequency, and phase of the multiple-body motions. Additionally, with the reduced computational load of this method over a three-dimensional method, problems such as fish schooling, counter-rotating propulsor blade sections and multiple wing flutter could be examined. Finally, the rigid-body equations of motion could be implemented with the inclusion of a parametric viscous drag dependence.

Chapter 3

Three-dimensional numerical method

3.1 Unsteady initial boundary value problem

A computational tool for investigating swimming characteristics of a three-dimensional flexible body with arbitrary motions and geometry is developed, as an extension of the two-dimensional investigation of the hydrodynamics of flexible-body propulsion described in *Chapter 2*. The formulation of this numerical method for thick bodies is analogous to the formulation presented for two-dimensions, so many of the details will be omitted for brevity.

We consider as a canonical problem the abrupt starting from rest to a constant velocity U of a streamlined flexible body geometry undergoing prescribed undulations about its mean line, with arbitrary distribution of sharp-trailing-edged fins. The viscous effects are assumed to remain confined to a thin boundary layer around the streamlined body regions and thin shear layer wakes which are shed from the sharp trailing edges of the body continuously as time proceeds. The fluid is assumed to be inviscid and incompressible. With the exception of the wake regions, the fluid is assumed to be irrotational as well, allowing for the existence of a velocity potential $\Phi(\vec{x}, t)$. We define two coordinate systems, an inertial global coordinate system $OXYZ$, fixed in space in the fluid, and an local coordinate system $oxyz$, instanta-

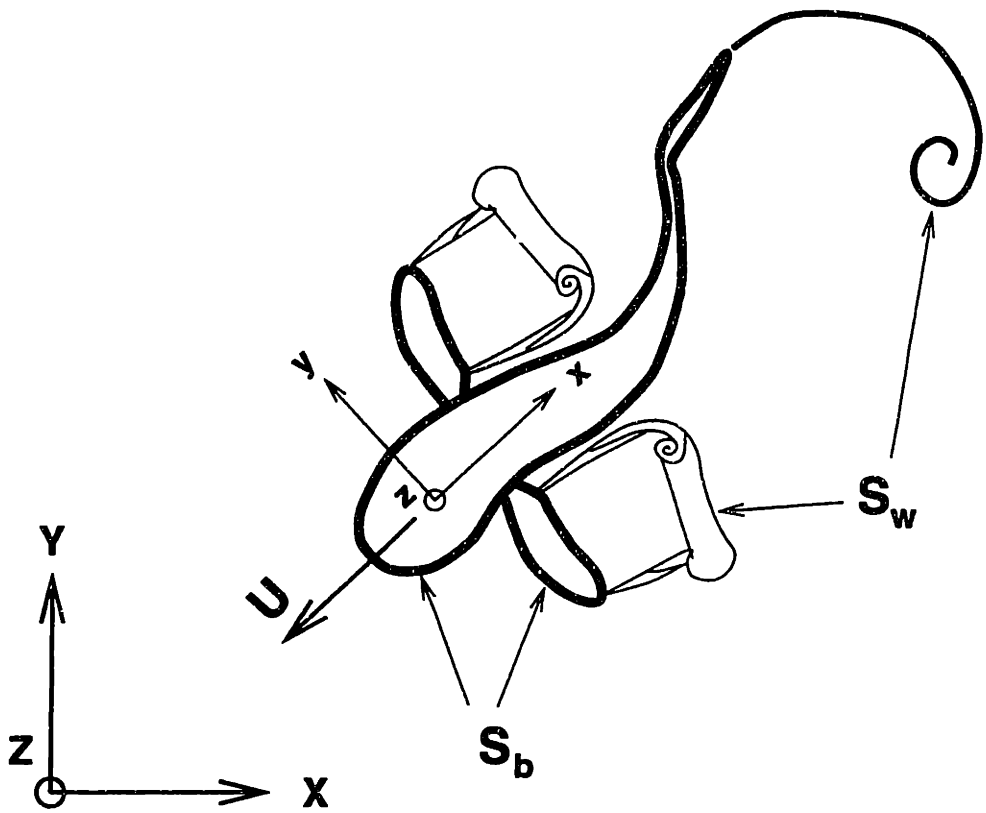

Figure 3-1: Coordinate system convention for the straight-line swimming problem (top view). $OXYZ$ is an inertial reference frame, while $oxyz$ is a body-fixed coordinate system about which mean line undulations are described.

neously fixed in the flexible body and orthonormal to the stretched-straight mean line and body section plane. The mean periodic undulations of the body are prescribed with reference to $oxyz$ and the global translational and rotational motions of the body are described with respect to $OXYZ$. Figure 3-1 details the coordinate systems used in the problem. All time and length scales are chosen to be nondimensional with respect to the body length $\ell = 1$.

We consider the computational domain to be enclosed by three types of surfaces, the body surfaces S_b, infinitesimally thin wake sheet surfaces S_w, and a far-field boundary at infinity S_∞. All of the bounding surfaces of the domain are thus written $S = S_b + S_w + S_\infty$. Laplace's equation for the velocity potential $\Phi(\vec{x}, t)$ governs the conservation of mass of the fluid, and the unsteady Bernoulli equation describes the pressure everywhere in the field. The velocity potential can be further described by the linear superposition of a body perturbation velocity potential $\Phi_b(\vec{x}, t)$ and a wake

perturbation velocity potential $\Phi_w(\vec{x},t)$, each satisfying the Laplace field equation. At any time other than the initial condition, the strengths of all previously-shed wake sheets are known, so the wake perturbation velocity potential $\Phi_w(\vec{x},t)$ is known everywhere except on the newly-shed portions of the wake surfaces. Thus, the boundary value problem is formulated for the body perturbation velocity potential $\Phi_b(\vec{x},t)$.

The prescribed body motions $\vec{V}_b(\vec{x},t)$ gives the no-flux body boundary condition in terms of the body perturbation potential for a body normal vector $\hat{n}_b$:

$$\frac{\partial \Phi_b(\vec{x},t)}{\partial n_b} = \left\{ \vec{V}_b(\vec{x},t) - \vec{\nabla}\Phi_w(\vec{x},t) \right\} \cdot \hat{n}_b \tag{3.1}$$

A radiation condition is imposed such that the velocity potential $\Phi(\vec{x},t)$ influence decay rapidly to zero in the far field. Thus at S_∞ we require:

$$\vec{\nabla}\Phi(\vec{x},t) = 0 \tag{3.2}$$

The prescribed motion of the body forces the area of the shed wakes to increase, as an unsteady Kutta condition is applied to the sharp trailing edges of the body to enforce smooth tangential flow separation. The strength of this newly-shed portion of the wake sheet is unknown. At any time, however, we can set the strength of the shed wake velocity perturbation potential to the jump in the body perturbation potential between the upper and lower surfaces near the trailing edge (TE) [95, 99, 107, 105].

$$\Phi_w(\vec{x},t)|_{TE} = \Delta\Phi_b(\vec{x},t)|_{TE} \tag{3.3}$$

3.2 Panel method implementation

A Green's formulation was considered to solve the problem for the body perturbation velocity potential Φ_b. Green's theorem in three-dimensions can be written:

$$\iiint_V \left[\Phi_1 \nabla^2 \Phi_2 - \Phi_2 \nabla^2 \Phi_1 \right] d\tau = \iint_S \vec{n} \cdot \left[\Phi_1 \vec{\nabla}\Phi_2 - \Phi_2 \vec{\nabla}\Phi_1 \right] ds \tag{3.4}$$

where V is the entire fluid domain enclosed by surfaces S. This second form of Green's Theorem can be reduced if both Φ_1 and Φ_2 satisfy Laplace's Equation to eliminate the left hand side:

$$0 = \iint_S \left[\Phi_1 \cdot \frac{\partial \Phi_2}{\partial n} - \Phi_2 \cdot \frac{\partial \Phi_1}{\partial n} \right] ds \tag{3.5}$$

Then, we equate Φ_1 to the body perturbation potential, $\Phi_b(\vec{x}, t)$, and we equate Φ_2 to the three-dimensional harmonic Green's function, $1/|r|$, where r is the distance from observation point x to any point ξ on the boundary, $r = |\vec{x} - \vec{\xi}|$. Thus, from Green's theorem, we can see that the body perturbation velocity potential $\Phi_b(\vec{x}, t)$ at any point can be described in terms of the integral around the boundaries of the contributions to the perturbation velocity potential. If this point $\vec{x}$ is on the boundary, equation (3.5) can be written:

$$2\pi\Phi_b(\vec{x}, t) = \iint_S \Phi_b(\vec{x}, t) \frac{\partial(1/|r|)}{\partial n} ds - \iint_S \frac{1}{|r|} \frac{\partial \Phi_b(\vec{x}, t)}{\partial n} ds \tag{3.6}$$

The influences of the singularities which appear as sources and dipoles in the integrands of (3.6) decay with the distance r from the singularity as $1/r$ and $1/r^2$, respectively. Thus, the boundary at infinity S_∞ can be shown to have negligible influence.

The unsteady wake strength is a function of space and time $\Phi_w(\vec{x}, t)$. The pressure across the wake shear layer is continuous and the wake surface is a material surface and can thus be represented by a smoothly-varying strength dipole sheet. By Kelvin's theorem, the total circulation of the fluid domain for the impulsive motion problem must remain constant. Thus, as the foil's circulation changes, so does the strength of the shed wake dipole. At any time, the strength of the entire wake is known, and thus the strength of $\Phi_w(\vec{x}, t)$ is known, except for the recently-shed shear layer which is smoothly directed off of specified separation edges. The unknown strength of the newest portion of the wake sheet is addressed through the Kutta condition as previously described by (3.3). Thus, the body perturbation velocity potential $\Phi_b(\vec{x}, t)$ and the change in circulation of the various wake-shedding lifting surfaces of the body can be written in terms of surface integrals over the body surface S_b and the wake

sheet surface S_w.

Representation of the time-dependent continuous potential distributions over the body and wake surfaces is developed in discrete form. The body and the wake are each divided into quadrilateral panels. The source-dipole distribution representing the body is approximated as piecewise constant over each body panel, and similarly the dipole distribution representing the thin shear layer wake is approximated as piecewise constant over each wake panel. The collocation point for each panel is approximated as the geometric center of the panel. Body grid is generated with higher panel densities in regions of presumed rapid potential variation and in regions with complex geometric considerations, such as large curvature or lifting surface tips, to reduce panel skew and to increase accuracy with respect to the unsteady, continuous velocity potential distribution.

At any time t, the body perturbation velocity potential at each panel collocation point $\phi_b(\vec{x},t)$ can then be found in terms of the perturbation potentials at all of the other panels, as can be seen by modifying (3.6):

$$-2\pi\phi_b(\vec{x}_i,t) \; + \; \sum_{\substack{j=1 \\ j\neq i}}^{k} \phi_b(\vec{x}_j,t)Q_{ij} \; = \; \sum_{j=1}^{k} \frac{\partial\phi_b(\vec{x}_j,t)}{\partial n_b} P_{ij} \tag{3.7}$$

where k is the total number of body panels and where

$$P_{ij} \; = \; \iint_j \frac{1}{r_{ij}}\, ds \tag{3.8}$$

$$Q_{ij} \; = \; \iint_j \frac{\partial(1/r_{ij})}{\partial n_{b_j}}\, ds \tag{3.9}$$

$$r_{ij} \; = \; |\vec{x}_i - \vec{x}_j| \tag{3.10}$$

A linear system of equations results for $\phi_b(\vec{x},t)$, the body perturbation velocity potential over each panel. However, the strength of the most recently shed wake panels $\phi_w(\vec{x}_{TE},t)$ is unknown at this point, not addressed in the above system of equations (3.7). This unknown can be absorbed into the system of equations for $\phi_b(\vec{x},t)$

by the introduction of a discrete form of the Kutta boundary condition (3.3).

$$\phi_w(\vec{x}_{TE}, t) \;=\; \phi_b(\vec{x}_{TE}, t)|_{top\ panel} - \phi_b(\vec{x}_{TE}, t)|_{bottom\ panel} \tag{3.11}$$

Therefore, we can describe the perturbation velocity potential of the new wake panels in terms of the body perturbation velocity potential $\phi_b(\vec{x}, t)$. A Morino correction term is added to the approximation for $\phi_w(\vec{x}_{TE}, t)$ to account for the trailing edge panel collocation points situation slightly offset from the separation line [95, 107, 105, 166]. So, the influence coefficients for the $\phi_b(\vec{x}, t)$ at these panels adjacent to the trailing edges of the body contain influence terms from the recently shed wake panels, due to an extension of the boundary integral limits to include the rows of new wake panels for incorporation of the discrete Kutta boundary condition (3.3).

A no-flux kinematic boundary condition on the body surface (3.1) gives the normal velocity at each panel. This normal velocity is comprised of contributions from the imposed velocity of the body $\vec{V}_b$ at each panel and the velocities induced at each panel by the dipole-sheet approximation to the free wake structures, which has further been represented by a discrete collection of individual wake panels with piecewise constant perturbation velocity potentials $\phi_w(\vec{x}, t)$. The source strength σ at each panel is thus equated to this panel normal velocity, a Dirichlet condition for the source potential prescription on the boundary. We can write this boundary condition in its discrete form:

$$\sigma = \frac{\partial \phi_b(\vec{x}_j, t)}{\partial n_b} = \left\{ \vec{V}_b(\vec{x}_j, t) - \sum_{m=1}^{nw} \vec{\nabla} \phi_{wm}(\vec{x}_j, t) \right\} \cdot \hat{n}_b \tag{3.12}$$

where nw is the total number of wake panels of known strength. Thus, we rewrite in the linear system (3.7) for $\phi_b(\vec{x}, t)$:

$$-2\pi\phi_b(\vec{x}_i, t) \;+\; \sum_{\substack{j=1 \\ j \neq i}}^{k} \phi_b(\vec{x}_j, t) Q_{ij} \;+\; \phi_w(\vec{x}_{TE}, t) Q_{iw} \;=\; \sum_{j=1}^{k} \sigma P_{ij} \tag{3.13}$$

where the influence coefficients Q_{iw} are integrals over the new wake panels S'_w adjacent to the trailing edges $\vec{x}_{TE}$. The influence coefficients are found using standard panel

integration techniques [86, 87, 248, 158].

$$Q_{iw} = \int\int_{S'_w} \frac{\partial(1/r_{iw})}{\partial n_w} ds \tag{3.14}$$

$$r_{iw} = |\vec{x}_i - \vec{x}_{TE}| \tag{3.15}$$

The discrete forms of the Kutta condition (3.11) and the kinematic body boundary condition (3.12) can be employed to arrive at a simple system of linear equations for $\phi_b(\vec{x}, t)$ at any given time t which is expressed from (3.13) in the general form:

$$[\tilde{Q}] \{\phi_b\} = [\tilde{P}] \tag{3.16}$$

At each time step, this linear system of equations is solved to find $\phi_b(\vec{x}, t)$ and $\phi_w(\vec{x}_{TE}, t)$ through use of an iterative scheme. $\phi_w(\vec{x}_{TE}, t)$ is representative of the change in the total circulation of the body lifting surfaces. While the number of body panels k is constant, the total number of wake panels nw increases with time, as a wake of time-varying strength is continually shed from the trailing edges of the body. The numeric scheme is temporally integrated using a fourth-order Runge-Kutta scheme.

3.3 Thin fins: Mixed-initial boundary value problem

Three-dimensional geometries chosen for this investigation of fish-swimming dynamics are consistently composed of a main body, with smoothly-varying elliptical cross sections, and a tail fin, with rounded leading and sharp trailing edges. Occasionally, however, additional fins are modeled to investigate the effects of a more accurate geometry representation. Modeling these fins as finite-thickness lifting surfaces with rounded leading and sharp trailing edges becomes impractical as the fins become smaller and thinner with respect to the main body. As the angle between adjacent panels at the leading edge approaches 2π, the resulting square-root singularity desta-

bilizes the source distribution influence coefficient matrix P_{ij} [99].

The addition of thin fins to the main body and caudal fin arrangement is accomplished through the utilization of vortex lattice surfaces [120, 121, 36, 99, 96, 97], and coupling the solution algorithm of the source-dipole method to the vortex lattice method [166, 142]. A surface of zero-thickness is discretized into a grid of planar quadrilateral elements. This grid forms a network of dipole panels, which can be represented by a lattice of linear, constant-strength vortex segments. The doublet jump strength across each panel $\phi_b(\vec{x}, t)$ is assumed to be constant.

The source strength σ distribution across each panel on the thin surface is set identically to zero. A zero-normal velocity Neumann boundary condition is thus applied at each thin panel's collocation point x_f with normal $\hat{n}'$.

$$\frac{1}{2}\frac{\partial \phi_b(\vec{x}_f, t)}{\partial n'} = \vec{V}_B \cdot \hat{n}' \tag{3.17}$$

The application of this boundary condition results in a set of equations for a geometry with both thin fins and thick bodies, where the doublet jump strength ϕ_b across any thin fin panel at x_f can be expressed as

$$-2\pi\frac{\partial \phi_b(\vec{x}_f, t)}{\partial n'} + \sum_{\substack{j=1 \\ j\neq f}}^{kf} \phi_b(\vec{x}_j, t) Q_{fj} + \sum_{m=1}^{kb} \phi_b(\vec{x}_m, t) Q_{fm} = \sum_{m=1}^{kb} \frac{\partial \phi_b(\vec{x}_m, t)}{\partial n} P_{fm} - \sum_{n=1}^{kw} \phi_w(\vec{x}_n, t) Q_{fn} \tag{3.18}$$

where kb, kf and kw are the total number of body, thin fin, and wake panels, respectively, and the influence coefficients are expanded as

$$Q_{fj} = \int_{fins} \frac{\partial^2 (1/r)}{\partial n \partial n'} dS_j \tag{3.19}$$

$$Q_{fm} = \int_{body} \frac{\partial^2 (1/r)}{\partial n \partial n'} dS_m \tag{3.20}$$

$$Q_{fn} = \int_{wakes} \frac{\partial^2 (1/r)}{\partial n \partial n'} dS_n \tag{3.21}$$

$$P_{fm} = \int_{body} \frac{\partial (1/r)}{\partial n'} dS_m \tag{3.22}$$

The vortex lattice solution algorithm requires the differentiation of equation (3.6) an additional time to apply the Neumann boundary condition when the panel source strength is zero. The details of the development of this higher-order algorithm are analogous to those presented herein for a source-dipole panel method and thus will not be discussed. However, it should be mentioned that some care must be taken in the geometric modeling of these thin fins not to use a fine panel mesh density, as a hypersingularity present in the self-influence coefficient Q terms can destabilize the numerical algorithm for very fine discretizations [193]. The size of the thin fin panels should be on the order of the largest body panels to minimize the matrix condition number.

Otherwise, these integrations of the second normal derivative of a doublet influence across a particular panel are performed by standard vortex-lattice algorithm. For constant potential jump distributions over a quadrilateral geometry, the hypersingularity requires no special treatment for the typical grid discretizations applied in these simulations. For more complex geometries and potential jump distributions, and for boundary collocation, removal of the hypersingularity is essential, and can be achieved through various numerical and analytic techniques, including Hadamard finite part approximations and robust limit evaluation [144, 143, 79]. For fine grid discretizations in these simulations, the hypersingular kernel is desingularized in a manner similar to the shed dipole sheet approximation to the wake, with a numerical core radius δ_b applied to the discrete vortex line segments which define the four corners of a panel with constant doublet strength potential jump [116]. Proof of constant-dipole panel and vortex ring equivalence is found in *Appendix D*. The core desingularization technique applied in cases of fine grid discretizations is discussed in the following subsection 3.4.

The remaining equations in the system are expressed as above (3.13). Combined, total mixed boundary-value problem consists of a set of matrix equations for the ϕ_b on the body geometries ϕ_{bb} and the ϕ_b jump across the thin fin geometries ϕ_{bf}, as well

as the strength of the unsteadily shed wake. In general form, the system is expressed

$$\begin{bmatrix} Q_{11} & Q_{12} \\ Q_{21} & Q_{22} \end{bmatrix} \begin{Bmatrix} \phi_{bb} \\ \phi_{bf} \end{Bmatrix} = \begin{bmatrix} P_1 \\ P_2 \end{bmatrix} \tag{3.23}$$

A wake equivalent to that described in the previous section is shed from the trailing edge as time progresses, as prescribed by a Kutta condition. The Kutta condition for the thin wing states that the change in circulation around the lifting surface section must equal the change in vorticity shed into the wake, in accordance with Kelvin's theorem which states that the change in total circulation for the entire fluid domain must be zero:

$$\frac{D\Gamma}{Dt} = 0 \tag{3.24}$$

so the strength of the newly-shed doublet panel is equal to the strength of the thin fin trailing edge panel doublet at the previous time step, $t - dt$. For the steady case, the wake doublet strength approaches a constant, as expected. The coupling of these two types of surface representation allows for the simulation of complex bodies undergoing unsteady arbitrary flexing motions.

3.4 Desingularization

Over the course of a simulation, the total number of body panels k is constant and may be comprised of both thick geometries and thin fins. Wakes of time-varying strengths are continually shed from the sharp trailing edges of the various lifting surfaces on the body to satisfy the Kutta condition, and as a result, the total number of wake panels nw increases with time. These material surface wakes are representations of the thin shear layers produced by separation and are freely-deformable, capable of sustaining no normal stress. To that end, the free vorticity in the wakes is allowed to deform under its self-induced and body-induced perturbation velocity influence.

After the solution of the boundary value problem for ϕ_b is obtained at each time step, the wake panel endpoints are convected using a fourth-order Runge-Kutta time

integration scheme. The velocity field which convects these wake panels obtained from a desingularized version Biot-Savart law. The desingularization technique employed [116, 117] eliminates the infinitesimal vortex sheet singularity and the associated ill-posedness. The inclusion of the desingularization is necessary to prevent nonlinear energy transfer to the highest wavenumber modes and simulation breakdown, in addition to non-physical solution growth caused by the numerical instabilities.

A wake vortex element of strength Γ comprising the side edge of one quadrilateral doublet panel is assigned core radius δ_w, such that the velocity $\vec{v}$ induced at $\vec{\xi}$ by this vortex element anywhere can be expressed by the desingularized Biot-Savart law

$$\vec{v}(\vec{\xi}) = \frac{\Gamma}{4\pi} \oint \frac{\vec{s} \times \vec{r}}{r^3 + \delta_w^3} dl \tag{3.25}$$

where $\vec{s}$ is the tangent vector to the vortex element, $\vec{r}$ is the vector with magnitude r from the vortex element to the field point $\vec{\xi}$, and the path of integration is along the length of the vortex element. As $\vec{\xi}$ approaches the vortex, r approaches zero, and the velocity field expressed by (3.25) approaches a finite limit.

Similarly, the body doublet panels are desingularized by the same technique, with arbitrary body desingularization radius δ_b. This desingularization assists in stabilizing the solution algorithm for coupled mixed boundary value problems with bodies of fine mesh discretizations. Additionally, when upstream-shed vorticity impinges on downstream body elements, non-physical free wake acceleration and deformation is avoided. These impinging wake panels pass around the outside of the body surface, often tangentially, convected by the body surface normal and tangential velocities. Without this body desingularization, free wake panels interacting with flexing body panels may convect inside the body.

To further prevent wakes from penetrating the body surface upon numerical time integration, the location of the wake after convection is cross referenced with the body volume, and any panels which may have penetrated the body are removed to lie outside the body adjacent to the panel closest to where the wake had been convected. This artificial wake convection is necessary to achieve an accurate solution of the

boundary value problem at each time step and is a consequence of the assumption that the wake can be represented by a continuous dipole sheet. This assumption may also restrict the complexity of the wake dynamics which may be simulated, as wakes are never allowed to break and cannot be severed by the motion of a passing tail fin. However, the dynamics of upstream-shed wakes are far more significantly affected by the strength of the wake shed from the caudal fin in this work, and artificial repositioning of vorticity which may penetrate the body in the simulations is not found to be prohibitive to revealing interesting wake interaction phenomena. A more complete representation of the wake might include the representation of a the vorticity field by free vortex particles or elements [110, 111, 112, 180, 231, 232, 181]. The numerical challenges associated with the implementation of these types of schemes, including increased computational time, vorticity field diverge, and vortex line stretching, continuity and vorticity redistribution, were deemed of great interest but beyond the scope of the present investigation.

3.5 Integrated quantities

At each time step, we find the velocity and force distribution over the body panels. Once the unknown body perturbation velocity potential ϕ_b is known on each panel, the surface velocity on each panel can be found by spatial differentiation of ϕ_b over the body. A five-point central difference numerical scheme calculates the tangential velocity at each panel in a local panel coordinate system parametized by arc length along orthogonal grid axes. This tangential surface body velocity is transformed to the global reference frame using information about the instantaneous body normal vector $\hat{n}_b$ at that panel. Surface velocities at edge or corner panels are calculated similarly using a three-point one-sided difference in the local panel reference frame.

The pressure coefficient c_p at each surface panel can then be found by employing the unsteady Bernoulli equation.

$$c_p = \frac{-1}{U^2}(\vec{\nabla}\phi_b \cdot \vec{\nabla}\phi_b + 2\frac{\partial \phi_b}{\partial t}) \tag{3.26}$$

The partial derivative $\partial\phi_b/\partial t$ is found by taking the material derivative of ϕ_b at each panel using a temporal second-order backward difference technique and subtracting the convective term arising from the imposed motions of the unsteady flexing body. The force F_b is found by integrating the pressure on each panel over the body.

$$F_b = \frac{1}{2}\rho U^2 \oint_b c_p \hat{n}_b \, dS \tag{3.27}$$

For the geometries considered in this fish swimming hydrodynamics investigation, the tail is modeled a finite-thickness high aspect ratio foil, and the leading edge suction acting on the tail fin is resolved through direct pressure integration over the body.

Whereas for thick bodies, the pressure is calculated on only one side of each panel, for thin fin surfaces, the total force realized is directly related to the pressure jump between the upper and lower surfaces of the fin. The lower surface velocities are calculated for the thin fins, and the pressure coefficient c_{p_l} on the lower surface is determined. The total force on the thin fin portion of the body is then

$$F_{b_{\text{thin}}} = \frac{1}{2}\rho U^2 \oint_b (c_p - c_{p_l})\hat{n}_b \, dS \tag{3.28}$$

The thin fin representation of body geometry lacks a robust method of determining the leading edge suction force, however. Several investigators [120, 121, 96, 97] present the case of a three-dimensional lifting surface undergoing periodic sinusoidal oscillations, for which the leading-edge suction force can be described in closed form. For a thin fin producing nonperiodic motions, however, such as those realized during maneuvering and turning, this method proves inapplicable. For this reason, great care is taken in this work to utilize thin fin surfaces whose leading edge is contiguous with its intersection line on the body, thus eliminating the exposure of the leading edge to oncoming flow. In this way, only normal forces are sustained, and thrust may only be produced through inclination of the flexing fin. However, for the purpose of modeling the relatively minor leading-edge suction forces which may arise, the methodology of Lan [120, 121] is used to compute the leading-edge singularity parameter C_s for arbitrary leading edge sweep angle Λ, measured from the perpendicular to the inflow.

The leading edge suction force on highly-swept thin fins is categorically neglected due to the singular behavior at the leading edge angle approaches a direction parallel to the incoming flow ($\Lambda \rightarrow 90^o$). C_s is set equal to the upwash from bound vorticity at the leading edge (LE), subtracting the effect of imposed perpendicular motions.

$$C_s N_c \sqrt{\tan^2 \Lambda + 1} = \sum (\text{upwash}_{\text{LE}}) - \vec{V}_b(\vec{x}_{le}, t) \cdot \hat{n}_{b_{le}} \tag{3.29}$$

where N_c is the number of bound vorticity segments contributing to the upwash at the spanwise location. The upwash is found through evaluation of the Biot-Savart terms as previously described. Then sectional leading-edge suction force coefficient c_t is instantaneously given by

$$c_t = \frac{\pi C_s^2}{2 \cos \Lambda_l} \tag{3.30}$$

which is numerically integrated over the length of the thin fin to determine the total leading edge suction force. Again, for highly-swept thin fin configurations, this suction force is ignored.

The power transmitted to the fluid by the motions of the body P_b is the product the local force and the local imposed body velocity.

$$P_b = \frac{1}{2} \rho U^2 \oint_b c_p \hat{n}_b \cdot \vec{V}_b \, dS \tag{3.31}$$

or in the case of a thin fin

$$P_{b_{\text{thin}}} = \frac{1}{2} \rho U^2 \oint_b (c_p - c_{p_l}) \hat{n}_b \cdot \vec{V}_b \, dS \tag{3.32}$$

For a geometry with a number of thick-bodies and thin fin surfaces, the total force F_b and the total power delivered to the fluid P_b may be, in general, quite complex time record, even for sinusoidal transverse motions. We can instantaneously decompose the total force into a sideforce L_b, which should have a zero temporal mean, and a longitudinal force T_b, which in general should have a non-zero mean value of thrust or drag for a mean swimming speed U in the absence of skin frictional drag

modeling. Any hydrodynamic buoyancy force Z_b is neglected for level swimming and maneuvering, and should ordinarily vanish at all time for top-bottom geometric symmetry. The mean value of thrust generated over one period for harmonic body undulations is denoted $\bar{T}_b$. Similarly, the mean power transmitted to the fluid over a period of harmonic body motion is denoted $\bar{P}_b$. This allows us to measure the classical hydrodynamic propulsive efficiency η for swimming speed U as

$$\eta = U\bar{T}_b/\bar{P}_b \tag{3.33}$$

Performance measures will be addressed in further detail in the appropriate context. Another method which can be used to obtain a prediction of the force on the unsteady body shedding a wake is the vorticity impulse method [128, 133], described briefly in *Appendix E*. It is especially of interest in comparing the force calculated through simulation to the force estimated from two-dimensional flow visualization techniques, such as DPIV.

3.6 Convergence & consistency

To assess the validity and consistent performance of the numeric scheme and to identify ranges of operating parameters for further simulation, a series of systematic convergence tests were performed for a variation of the typical simulation parameters which approach the continuous solution. A convergence of the integrated quantities was assessed for three types of forces: *(i)* added mass forces; *(ii)* steady lifting forces; *(iii)* unsteady lifting and added mass forces.

Added mass forces

The unsteady potential flow about non-lifting streamlined bodies is examined through the simulation of the flow about accelerating ellipsoids, of which a sphere is a special case. Figures 3-2 and 3-3 show the relative maximum error in the force on the two bodies as functions of the panel number k for different simulation time step sizes dt.

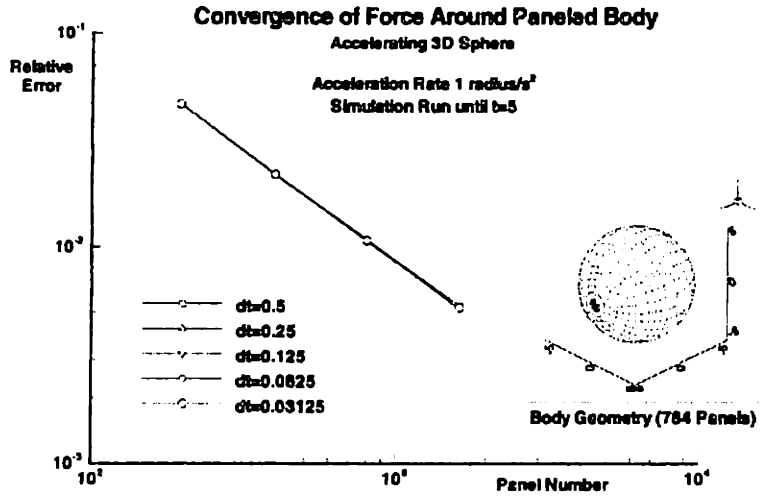

Figure 3-2: Convergence of the three-dimensional numerical method. The error in the added mass force on an accelerating sphere is shown as a function of panel number k for various values of the time step dt.

Without the generation of an unsteadily-deforming wake surface, the panel method shows good convergence properties to the continuous representation of the solution as the panel number k is increased. As the time step size dt size decreases, the solution shows equivalent performance, as the unsteady velocities in the problem are increasing at a constant rate irrespective of the time step size dt. Additionally, the geometric influence on the convergence properties of the two ellipsoids is negligible for the two special cases considered.

The ability to simulate unsteady added mass forces is confirmed through the study of an oscillating sphere in an unbounded fluid domain. The sphere is forced to move in a side-to-side motion, such that the excursion length to one side from the central starting point is equal to the radius of the sphere. The sphere motion is impulsively-started, and this initial condition can be seen to have an affect on the accuracy of the integrated force, depending on the time-step chosen, shown as a time record in Figures 3-4 and 3-5 for $k = 196$ and $k = 1620$ body panels, respectively. The theoretical solution is shown as a bold line, while records for different time steps are

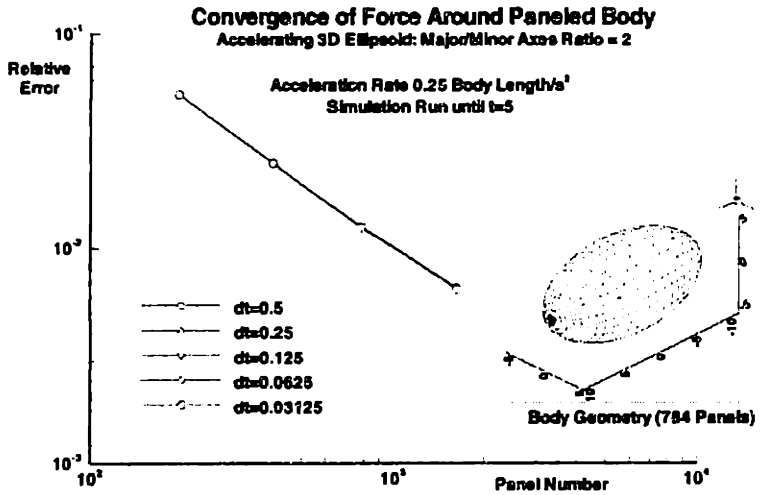

Figure 3-3: Convergence of the three-dimensional numerical method. The error in the added mass force on an accelerating ellipse (major-minor axis ratio = 2:1) is shown as a function of panel number k for various values of the time step dt.

made clear in the figure legend. Since a backward-differencing technique used to find the instantaneous body velocity distribution at each panel, for large values of the time step dt the computed body velocity is less accurate. As all of the force on the sphere arises from the unsteady Bernoulli pressure term, poor approximations to the panel velocities result in errors in the convective term $\vec{v}\cdot\vec{\nabla}\phi$, which must be subtracted from $d\phi/dt$ to get the unsteady $\partial\phi/\partial t$ term. These errors manifest themselves in the time record as temporal phase lags in the force record, which are ameliorated for decreasing time step size dt, approaching the continuous solution. This behavior is as expected and emphasizes the importance of time step size dt selection for time integration for reasons other than the Courant condition of maintaining fluid excursions of less than the smallest panel length during time stepping [89, 90].

The maximum error at any point during the oscillation cycle for the time records shown in Figures 3-4 and 3-5 is shown as a function of time step size dt in Figure 3-6. The method sees good convergence as the time step is decreased for various numbers of body panels k. Similarly, this maximum relative error in the unsteady force

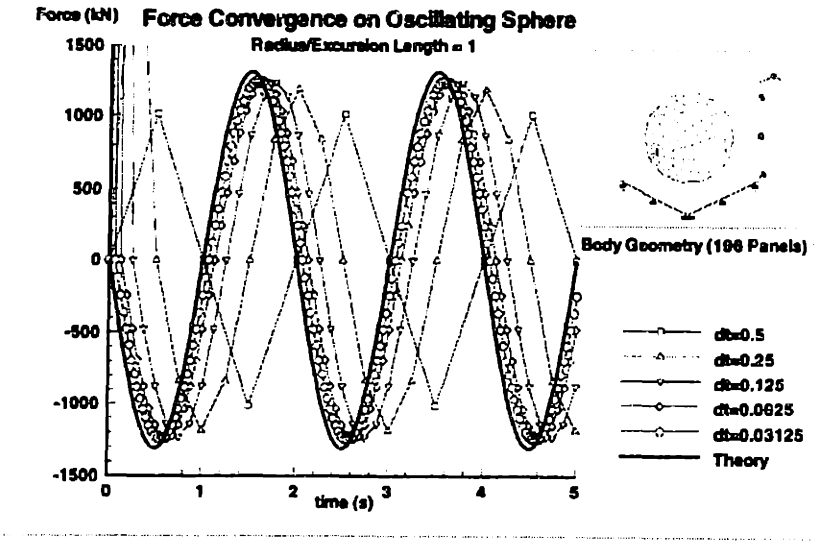

Figure 3-4: Performance of the three-dimensional numerical method showing the effects of the initial condition. The unsteady added mass force on an oscillating sphere is shown as a function the time for $k = 196$ panels. Theoretical value [157] is shown for comparison. Impulsive start initial condition affects the phase of the force.

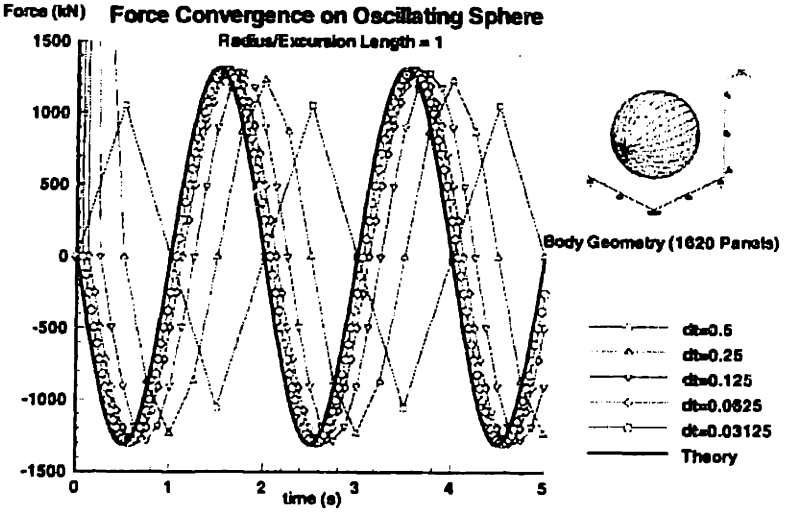

Figure 3-5: Performance of the three-dimensional numerical method showing the effects of the initial condition. The unsteady added mass force on an oscillating sphere is shown as a function the time for $k = 1620$ panels. Theoretical value [157] is shown for comparison. Impulsive start initial condition affects the phase of the force.

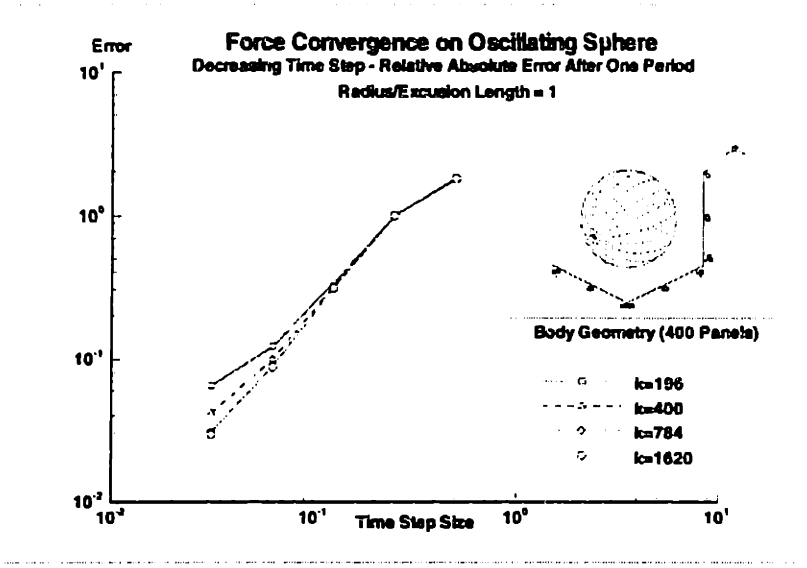

Figure 3-6: Convergence of the three-dimensional numerical method. The error in the unsteady added mass force on an oscillating sphere is shown as a function the time step dt for various values of the panel number k.

compared to the theoretical solution is shown as a function of the number of body panels in Figure 3-7 for various values of the time step size dt. The error curves are relatively flat, as the maximum error in the force distribution typically occurred at the instances of maximum force, caused more by the temporal phase lag than the approximation inaccuracies inherent to a sparse panel representation. These convergence tests confirmed the validity of using the numerical panel method scheme to simulate the flow around and integrated performance of a body undergoing unsteady motions in an unbounded, inviscid fluid with the absence of shed wake surfaces.

Steady lifting forces

With the accuracy of the numerical method to compute unsteady added mass forces proven, the effects of the wake representation model on the performance prediction capabilities of the method needed to be assessed. The ability of the method to predict the unsteady lifting forces arising from the shedding of a thin shear layer wake was validated by simulating impulsively-started motion of a finite-aspect ratio foil at a

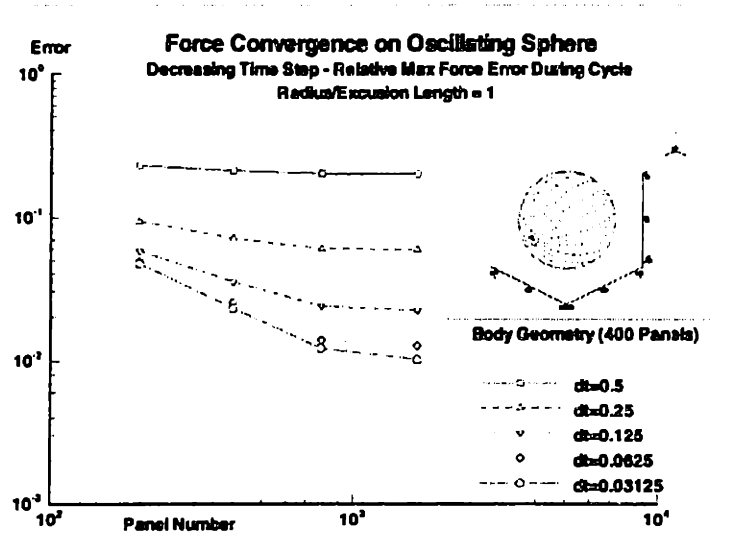

Figure 3-7: Convergence of the three-dimensional numerical method. The error in the unsteady added mass force on an oscillating sphere is shown as a function the panel number k for various values of the time step dt.

small angle of attack to a speed U, in a fluid otherwise at rest. A sample simulation result showing the evolution of the starting wake and the unsteady record of the developing lift force is shown in Figure 3-8. After the foil has translated a distance of approximately ten chord lengths c, the lift on the foil approaches steady-state, as evidenced by the convergent strength of the shed dipole sheet which is revealed through superimposed color contours on the wake computational grid. Simulation parameters for this simulation: $k = 400$ body panels, time step $dt = 0.02$, wake desingularization radius $\delta_w = 0.05$, and body panel desingularization radius $\delta_b = 0.01$.

Convergence of the numerical method was confirmed by varying the time step size dt and the number of panels k around the foil, in addition to the aspect ratio AR and the desingularization parameter δ_w for the wake, and comparing the steady lift coefficient to the experimental values illustrated in Figure 17-5 of Hoerner (1985). The validity of both the source-dipole method and the vortex-lattice method was assessed with separate convergence trials.

For a thick uncambered foil of high aspect ratio $AR = 12$ with a NACA 0012

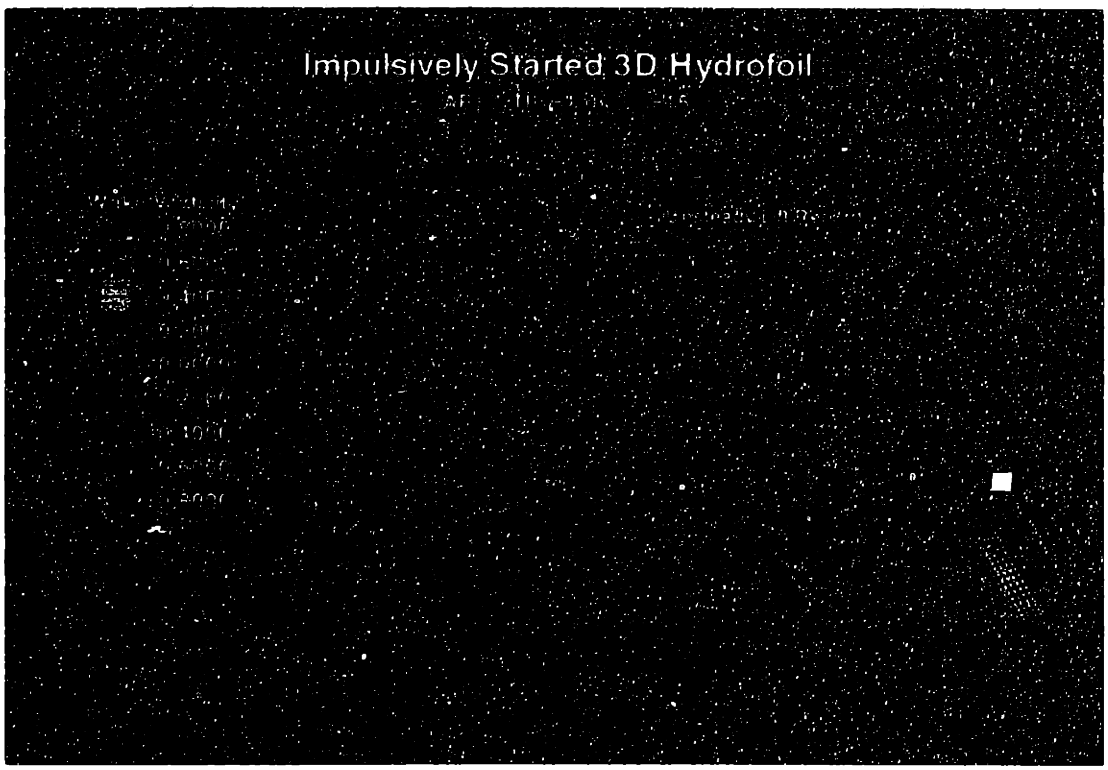

Figure 3-8: Wake profile and unsteady lift record about an impulsively-started foil at an angle of attack $\alpha = 16^o$ with aspect ratio $AR = 7.0$. Wake dipole strength is shown in color contours superimposed on the wake computational grid showing the evolution of the wake vorticity and the development of steady-state wake strength.

		$dt = 0.2$	$dt = 0.1$	$dt = 0.05$
k		400	400	400
δ_w	$(1/c)$	0.05	0.05	0.05
δ_b	$(1/c)$	0.01	0.01	0.01
α	(deg.)	10	10	10
C_L	(computation)	0.8099	0.8149	0.8256
C_L	(Hoerner)	0.862	0.862	0.862
Error	(%)	6.04	5.46	4.22

Table 3.1: Convergence of the three-dimensional numerical method showing lift coefficient on an impulsively-started foil after time $Ut/c = 40.0$ for decreasing time step dt. NACA 0012 foil section with aspect ratio $AR = 12$.

		$k = 100$	$k = 200$	$k = 400$	$k = 800$
dt		0.1	0.1	0.1	0.1
δ_w	$(1/c)$	0.05	0.05	0.05	0.05
δ_b	$(1/c)$	0.01	0.01	0.01	0.01
α	(deg.)	10	10	10	10
C_L	(computation)	0.6001	0.7761	0.8149	0.8441
C_L	(Hoerner)	0.862	0.862	0.862	0.862
Error	(%)	30.4	9.97	5.46	2.08

Table 3.2: Convergence of the three-dimensional numerical method showing lift coefficient on an impulsively-started foil after time $Ut/c = 40.0$ for increasing panel number k. NACA 0012 foil section with aspect ratio $AR = 12$.

profile, sample convergence results are given in Tables 3.1, 3.2, and 3.3, for variation of the numerical simulation parameters dt, k, and δ_w, respectively. Simulations were run to a nondimensional time $Ut/c = 40.0$ for a chord length c. As can seen in the tables, decent convergence properties are obtained as the continuous solution is approached. While the decrease in the time step dt and the increase in the panel number k are characterized by steadily decreasing error, the variation of the wake desingularization radius δ_w is shown to have little effect on the solution accuracy, since the desingularization radii considered are still fairly small and since the wake dynamics have reached a steady-state behavior in the vicinity of the foil.

The effects of changing the aspect ratio AR of the foil be seen by comparing

		$\delta_w = 0.1$	$\delta_w = 0.05$	$\delta_w = 0.025$	$\delta_w = 0.01$
k		400	400	400	400
dt		0.1	0.1	0.1	0.1
δ_b	$(1/c)$	0.01	0.01	0.01	0.01
α	(deg.)	10	10	10	10
C_L	(computation)	0.8141	0.8149	0.8152	0.8153
C_L	(Hoerner)	0.862	0.862	0.862	0.862
Error	(%)	5.56	5.46	5.43	5.42

Table 3.3: Convergence of the three-dimensional numerical method showing lift coefficient on an impulsively-started foil after time $Ut/c = 40.0$ for decreasing wake panel desingularization radius δ_w. NACA 0012 foil section with aspect ratio $AR = 12$.

		$k = 100$	$k = 200$	$k = 400$	$k = 800$
dt		0.1	0.1	0.1	0.1
δ_w	$(1/c)$	0.05	0.05	0.05	0.05
δ_b	$(1/c)$	0.01	0.01	0.01	0.01
α	(deg.)	10	10	10	10
C_L	(computation)	0.4131	0.6156	0.6871	0.7180
C_L	(Hoerner)	0.748	0.748	0.748	0.748
Error	(%)	44.8	17.7	8.14	4.01

Table 3.4: Convergence of the three-dimensional numerical method showing lift coefficient on an impulsively-started foil after time $Ut/c = 40.0$ for increasing panel number k. NACA 0012 foil section with aspect ratio $AR = 6$.

Table 3.4, showing the convergence of the steady-state lift with panel number k for a foil of aspect ratio $AR = 6$, to Table 3.2, showing the convergence for a foil of aspect ratio $AR = 12$, for the same simulation parameters. Although the errors between the experimentally measured lift and the simulation results are considerable for low numbers of panels, the errors decrease rapidly as the number of panels increases. This increase in steady lift coefficient error for a decreased aspect ratio foil with a low panel number can be attributed to the poor representation of the potential variation near the foil tips for low panel numbers.

The convergence properties of the vortex-lattice method are similarly assessed. For an infinitesimally thin foil of high aspect ratio $AR = 12.0$, sample convergence

		$dt = 0.2$	$dt = 0.1$	$dt = 0.05$
k		200	200	200
δ_w	$(1/c)$	0.05	0.05	0.05
δ_b	$(1/c)$	0.01	0.01	0.01
α	(deg.)	10	10	10
C_L	(computation)	0.7854	0.8043	0.8311
C_L	(Hoerner)	0.862	0.862	0.862
Error	(%)	8.91	6.69	3.58

Table 3.5: Convergence of the three-dimensional vortex-lattice numerical scheme showing lift coefficient on an impulsively-started foil after time $Ut/c = 40.0$ for decreasing time step dt. Thin foil with aspect ratio $AR = 12$.

		$k = 50$	$k = 100$	$k = 200$	$k = 400$
dt		0.1	0.1	0.1	0.1
δ_w	$(1/c)$	0.05	0.05	0.05	0.05
δ_b	$(1/c)$	0.01	0.01	0.01	0.01
α	(deg.)	10	10	10	10
C_L	(computation)	0.6433	0.7830	0.8043	0.8231
C_L	(Hoerner)	0.862	0.862	0.862	0.862
Error	(%)	25.4	9.16	6.69	4.51

Table 3.6: Convergence of the three-dimensional vortex-lattice numerical scheme showing lift coefficient on an impulsively-started foil after time $Ut/c = 40.0$ for increasing panel number k. Thin foil with aspect ratio $AR = 12$.

results are given in Tables 3.5, 3.6, and 3.7, for variation of the numerical simulation parameters dt, k, and δ_w, respectively. Simulations were run to a nondimensional time $Ut/c = 40.0$ for a chord length c. As can seen in these tables, good convergence is obtained as the continuous solution is approached. Again, while the decrease in the time step dt and the increase in the panel number k are characterized by steadily decreasing error, the variation of the wake desingularization radius δ_w is shown to have little effect on the solution accuracy.

However, the convergence properties of the variation of the body desingularization radius δ_b exhibit interesting phenomena. For an infinitesimally thin foil of high aspect ratio $AR = 12.0$, convergence results are given in Tables 3.8 and 3.9, for variation

		$\delta_w = 0.1$	$\delta_w = 0.05$	$\delta_w = 0.025$	$\delta_w = 0.01$
k		200	200	200	200
dt		0.1	0.1	0.1	0.1
δ_b	$(1/c)$	0.01	0.01	0.01	0.01
α	(deg.)	10	10	10	10
C_L	(computation)	0.8003	0.8043	0.8086	0.8053
C_L	(Hoerner)	0.862	0.862	0.862	0.862
Error	(%)	7.16	6.69	6.19	6.58

Table 3.7: Convergence of the three-dimensional vortex-lattice numerical scheme showing lift coefficient on an impulsively-started foil after time $Ut/c = 40.0$ for decreasing wake panel desingularization radius δ_w. Thin foil with aspect ratio $AR = 12$.

of δ_b for $k = 100$ and $k = 200$ body panels, respectively. Simulations were run to a nondimensional time $Ut/c = 40.0$ for a chord length c. As can seen in these tables, good convergence is obtained as body desingularization radius δ_b is decreased until a critical threshold is surpassed, at which point the error begins to increase. The rate of the error increase as δ_b becomes too small is exacerbated by increasing the number of panels, which can been seen by comparison of the two tables. This error is caused by the singularity in the self-influence coefficient determination for the doublet distribution in the flat panel, whose self-induced velocities become unbounded as the collocation point of the panel approaches the bounding vortex rings as the panel size decreases.

While the wake desingularization radius δ_w selection has little influence on the integrated performance of the foil, it influences the wake behavior strongly, and proper selection of a δ_w is crucial to eliminating the wake singularity and preventing non-physical, unsteady wake behavior. In contrast, the proper selection of the body desingularization δ_b is critical to obtaining good predictions of integrated performance but is found to have little influence on the modeled behavior of the wake dynamics.

Unsteady lifting and added mass forces

The validity of the predictions obtained by the three-dimensional computational scheme for the unsteady forces on a moving body shedding a thin shear layer wake in

		$\delta_b = 0.1$	$\delta_b = 0.05$	$\delta_b = 0.01$	$\delta_b = 0.005$	$\delta_b = 0.001$
k		100	100	100	100	100
dt		0.1	0.1	0.1	0.1	0.1
δ_w	$(1/c)$	0.05	0.05	0.05	0.05	0.05
α	(deg.)	10	10	10	10	10
C_L	(computation)	0.6131	0.6943	0.7830	0.7921	1.104
C_L	(Hoerner)	0.862	0.862	0.862	0.862	0.862
Error	(%)	28.9	19.5	9.16	8.11	28.1

Table 3.8: Convergence of the three-dimensional vortex-lattice numerical scheme showing lift coefficient on an impulsively-started foil with $k = 100$ panels after time $Ut/c = 40.0$ for decreasing body panel desingularization radius δ_b. Thin foil with aspect ratio $AR = 12$.

		$\delta_b = 0.1$	$\delta_b = 0.05$	$\delta_b = 0.01$	$\delta_b = 0.005$	$\delta_b = 0.001$
k		200	200	200	200	200
dt		0.1	0.1	0.1	0.1	0.1
δ_w	$(1/c)$	0.05	0.05	0.05	0.05	0.05
α	(deg.)	10	10	10	10	10
C_L	(computation)	0.5892	0.7643	0.8043	0.8112	1.343
C_L	(Hoerner)	0.862	0.862	0.862	0.862	0.862
Error	(%)	31.6	11.33	6.69	5.89	55.2

Table 3.9: Convergence of the three-dimensional vortex-lattice numerical scheme showing lift coefficient on an impulsively-started foil with $k = 200$ panels after time $Ut/c = 40.0$ for decreasing body panel desingularization radius δ_b. Thin foil with aspect ratio $AR = 12$.

an unbounded fluid is assessed by comparing to some results from the literature for an oscillating foil. The performance of an oscillating foil has been studied theoretically, computationally and experimentally by many investigators for both two-dimensional flows [66, 215, 183, 22, 149, 207, 2, 190, 245, 68, 46, 10, 169] and three-dimensional flows [38, 120, 127, 39, 40, 100, 121, 103, 27, 98, 28, 36, 137, 96, 97]. However, for large amplitudes and rotational motions of the foil, the physics is not well-understood. Recently, Sverdrup [193] surveyed the literature and comprehensive explored the parametric space of performance using a linearized vortex lattice method, comparing his results to the literature when applicable.

The numerical study of the performance of oscillating three-dimensional propulsors involves the correct modeling of a variety of physics under the imposed simulation conditions, including the unsteady trailing edge separation models, leading edge vortex production and manipulation, boundary layer control, wake dynamics and stability, and wake-body interactions. A complete investigation of the application of this three-dimensional panel method to simulating these physics was deemed beyond the scope of the current research objectives. However, it is necessary to understand how this method compares to linearized numerical approximations which have been used to simulate the problem in the past.

The kinematics of the oscillating foil in pitch and heave are characterized by the reduced frequency ν and the feathering parameter θ, which can be expressed

$$\nu = \frac{\omega c}{U} \tag{3.34}$$

$$\theta = \frac{|\alpha| U}{\omega H} \tag{3.35}$$

where ω is the frequency of the foil oscillation, c is the chord length, U is the translational velocity, α is the maximum angle of attack to the direction of motion, and H is the heave amplitude. The reduced frequency ν and the feathering parameter θ completely describe the motion, and both are related to the Strouhal number, which

written in the variables of the present investigation appears as

$$St = \frac{H\omega}{\pi U} \tag{3.36}$$

but the feathering parameter θ is more a measure of the local angle of attack of the foil relative to the incoming flow at the leading edge and does not explicitly consider the width of the wake. Similarly, the reduced frequency ν is more a measure of the number of oscillation cycles within a given spatial frame of reference relative to the foil chord length; this ratio is irrespective of the heave amplitude H and thus the wake width and Strouhal number St.

The heave $h(t)$ and pitch $a(t)$ motions are prescribed as sinusoidal functions, with an arbitrary phase lag ϕ between pitch and heave, such that

$$h(t) = H \sin(\omega t) \tag{3.37}$$

$$a(t) = \alpha \sin(\omega t + \phi) \tag{3.38}$$

The selection of the location of the pitching axis greatly affects the performance of the foil [126, 127, 38, 39, 40, 121, 193]. However, Lighthill [126] found that the best performance could be obtained when the pitching axis was closest to the trailing edge of the foil. For that reason, the investigative comparisons contained herein utilize a trailing edge pitch point.

The flow dynamics for two sample simulations employing a large heave amplitude are shown in Figures 3-9 and 3-10. The geometric and kinematic parameters of the motion chosen are identical to those employed by several other investigators [121, 96]. However, due to the nonlinear nature of the computational method, the wake is allowed to deform and affect the performance of the foil. A thick foil is used in all simulations, with a NACA 0012 section profile and an aspect ratio of $AR = 7$. The feathering parameter $\theta = 0.8$ and the reduced frequency $\nu = 0.75$. The heave amplitude H employed for the two simulations shown is equal to the chord length c. This large amplitude motion amplifies the effects of the nonlinear deformation of the

wake and is likely outside of the linear parameter range on which the assumptions of linearized vortex-lattice theory is predicated, such as developed by Lan [121] and Kagemoto [96]. For these heave amplitudes and kinematic parameters, the maximum angle of attack realized during the motion is $\alpha = 34.38^o$, which would likely cause unsteady leading edge separation in a reality. These properties are the subject of ongoing experimental research [9, 10, 169]. The performance of the foil for the kinematic parameters ν and θ chosen was found by Lan [121] to be extremely sensitive to the to the phase angle between pitch and heave ψ. Although the angle of attack realized by the foil in the simulations shown is likely to exceed the range of validity for the computational method chosen, the wake evolution is shown for two different phase angles between pitch and heave, $\phi = 0^o$ in Figure 3-9 and $\phi = -30^o$ for Figure 3-10. The wake dynamics are quite significant for this moderate heave amplitude and significantly affect the performance of the foil motions.

The performance of the oscillating foil of aspect ratio $AR = 7.0$ over a range of phase angles ϕ is examined for comparison to Lan [121] and Kagemoto [96]. Figure 3-11 shows the dependence of the thrust coefficient on the phase angle ϕ between pitch and heave. The thrust coefficient found by the present numerical method employs two different amplitudes of the heave motion $H/c = 1$ and $H/c = 0.1$. The latter heave amplitude results in a maximum angle of attack of the foil $\alpha = 3.438^o$, which is well within a range where leading edge separation will be negligible for the prescribed kinematic parameters of the motion of feathering parameter $\theta = 0.8$ and reduced frequency $\nu = 0.7$. The thrust coefficient dependence on ϕ for the two heave motions are then compared to the linear results of Lan [121] and Kagemoto [96]. Linear approximations assume a heave amplitude $H/c = 1.0$ based on chord c. Comparison of the thrust coefficients from the linear and the two heave amplitudes is made possible through the normalization of the thrust coefficient in the normal manner by the square of the heave amplitude [125].

The thrust found by the present numerical method for small heave amplitudes $H/c = 0.1$ is smaller than the vortex-lattice prediction, but good qualitative comparison reveals the sensitivity of the phase angle ϕ on the performance. This reduction in

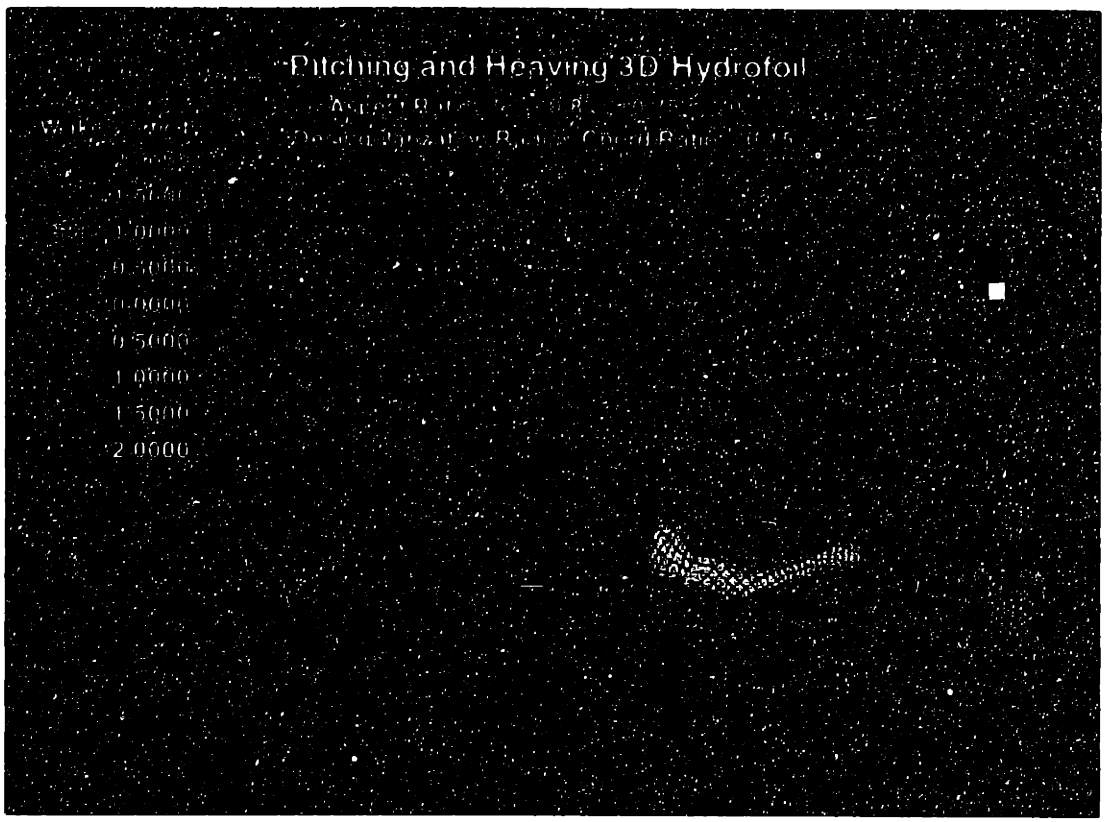

Figure 3-9: Wake evolution behind an impulsively-started oscillating foil of aspect ratio $AR = 7.0$. Motion is characterized by feathering parameter $\theta = 0.8$, reduced frequency $\nu = 0.7$, and phase angle between pitch and heave $\phi = 0^o$. Heave amplitude H is equal to chord length c. Wake dipole strength is shown in color contours superimposed on the wake computational grid showing the unsteady wake evolution.

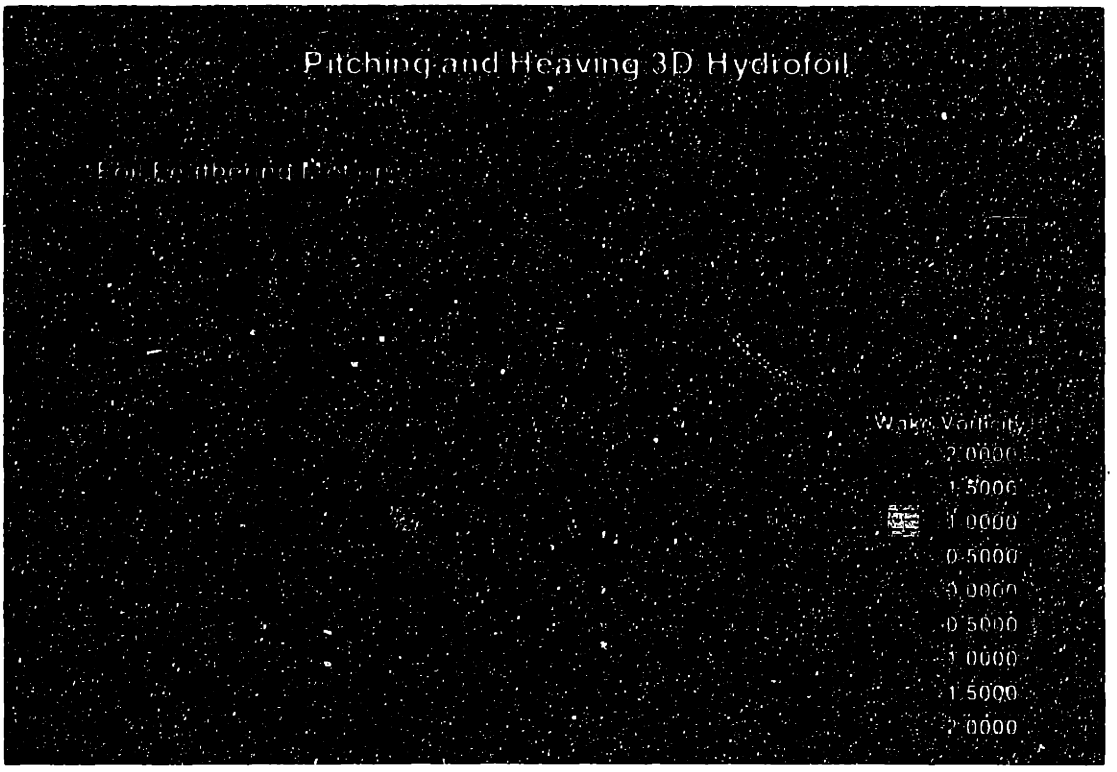

Figure 3-10: Wake evolution behind an impulsively-started oscillating foil of aspect ratio $AR = 7.0$. Motion is characterized by feathering parameter $\theta = 0.8$, reduced frequency $\nu = 0.7$, and phase angle between pitch and heave $\phi = -30^o$. Heave amplitude H is equal to chord length c. Wake dipole strength is shown in color contours superimposed on the wake computational grid showing unsteady wake evolution.

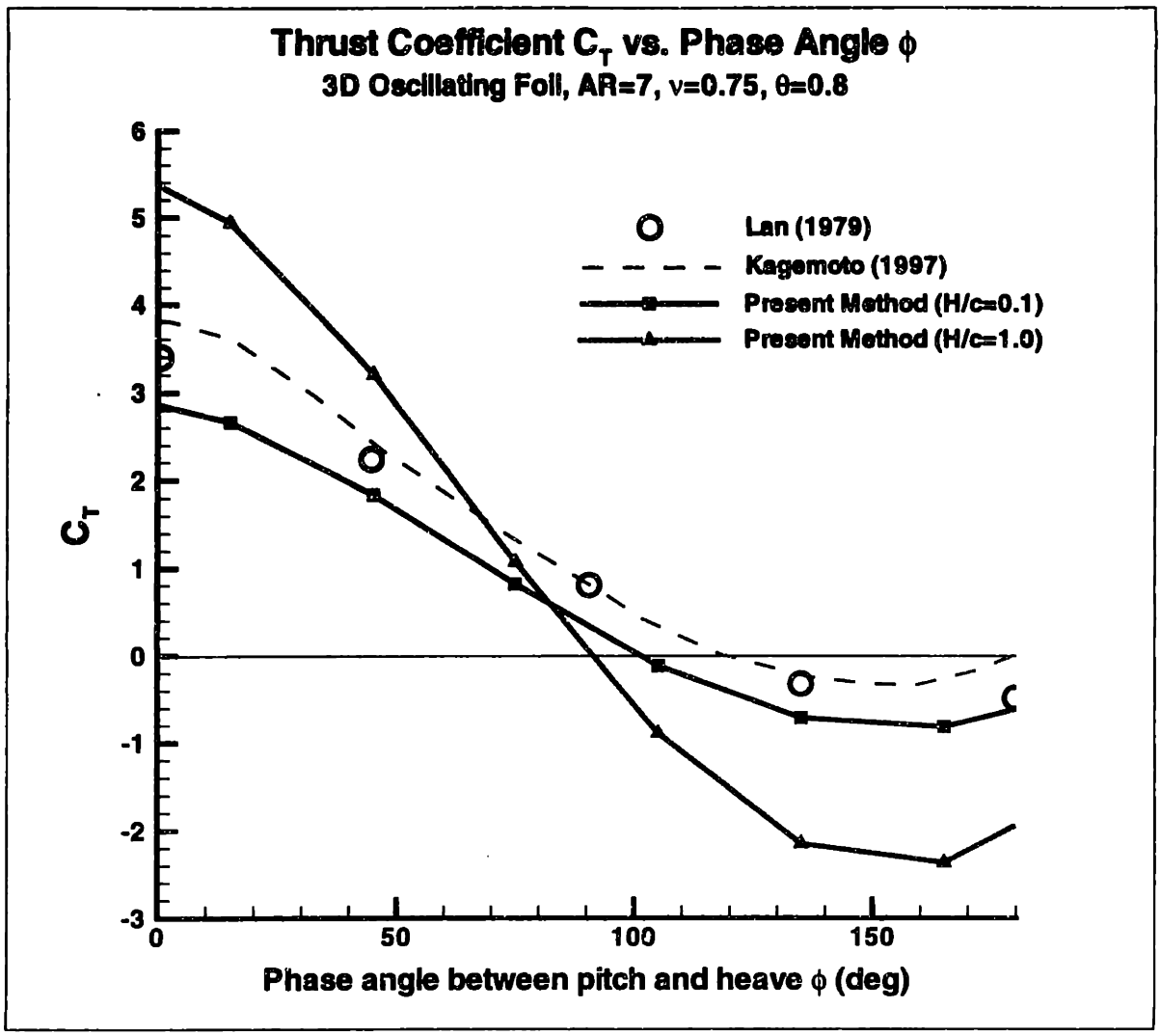

Figure 3-11: Thrust coefficient of an oscillating foil of aspect ratio $AR = 7.0$ as a function of the phase angle ϕ between pitch and heave. The thrust coefficient found by the present numerical method using two different amplitudes of the heave motion is compared to the linear results of Lan [121] and Kagemoto [96]. Motion is characterized by feathering parameter $\theta = 0.8$ and reduced frequency $\nu = 0.7$. Linear approximations assume a heave amplitude $H/c = 1.0$ based on chord c. The thrust coefficient found by the present method is normalized with respect to the heave amplitude.

thrust coefficient can be explained by the reduction in the strength of the leading edge singularity for a thicker foil, reducing the component of thrust arising from leading-edge suction. The effects of the large amplitude motion on the performance, shown dramatically with visual confirmation of the strong wake deformation in Figures 3-9 and 3-10, can be easily seen from Figure 3-11. The behavior of the thrust coefficient follows the same trends, but is much larger than the linearly predicted force at low phase angles and predicts a large drag force for phase angles which merely predicted a small drag force with the linear methods. For low positive values of generated thrust coefficient, such as those realized at a phase angle of around $\phi = 90^o$, a high efficiency is also obtained, which is consistent with both oscillating foil theory [126] and experiments [10].

The dependence of the performance of the foil on large amplitude motions in a comparison to the performance predictions from linearized methods was not attempted within the scope of this work. These convergence tests merely served to lay the foundation for the application of this numerical method to the simulation of complex flexible body problems with multiple coupled thin and thick geometries shedding an arbitrary prescribed number of thin shear layer wakes undergoing periodic and nonperiodic motions. The proper selection of numerical simulation parameters is crucial to the success of the following investigation, which explores the hydrodynamics of fish-like swimming motions.

Chapter 4

Overview of straight-line swimming

4.1 The morphology of fish swimming

In this section, the characteristics of various fish body shapes and of fish swimming kinematics are described, which supports the choices made in the modeling of the fish swimming motions through numerical simulations. In addition, a brief overview of how existing research on fish swimming performance measurements and flow visualizations corroborate the use of this numerical simulation method to study the hydrodynamics of fish swimming.

Several excellent review references have been compiled over the last century which catalogue the hydromechanics of fish swimming and the related morphological characteristics associated with the various types of swimmers [84, 77, 127, 7, 26, 212, 214]. Most of these studies have been inspired by the observed performance and agility of many species of fish, and the motivation for uncovering the hydrodynamic propulsive mechanisms has been greatly influenced by Gray's works [72, 76] and the mystery of *Gray's paradox*.

A survey of the comparative biomechanics of a large number of steady straight-line swimmers reveals three basic types of fish motions [29], and fish which swim with any of these types of motion generally have certain common morphological characteristics [214].

- *Anguilliform* swimmers: These fish swim with an eel-like motion, characterized

by large lateral excursions over the length of the body, which undulates with a constant amplitude traveling wave progressing from the head to the tail. The body cross section is generally elliptical with minimal variation in depth along the body length. Secondary fins are usually small if present. Examples include eels, sea snakes, and tadpoles.

- *Carangiform* swimmers: The motion of these fish is characterized by traveling wave progressing from the head to the tail, which grows in amplitude towards the tail. The lateral excursions are not as extreme as in *Anguilliform* locomotion in comparison to the body length. The body depth varies gradually over the length, with a tapering region just anterior to the caudal fin (tail) known as the caudal peduncle. Secondary fins are usually present, including dorsal, anal, ventral, and pectoral fins. The use of these fins varies among species. Examples include trout, salmon, and the Giant Danio.

- *Thunniform* swimmers: These fish are within a subclass of *Carangiform* swimmers which confine their motions to the posterior portion of the body. The motion of these fish is characterized by traveling wave progressing from the head to the tail, which grows dramatically in amplitude just anterior to the caudal peduncle. The main portion of the fish body appears relatively stiff by comparison. In addition, the body depth varies dramatically over the length, with an ellipsoidal body and a high aspect ratio tail connected through an extremely narrow caudal peduncle. Secondary fins are usually present, including dorsal, anal, ventral, and pectoral fins, but often these fins are retractable to become flush with the body and are typically used during maneuvering. These *Thunniform* swimmers are among the most high-performance swimmers, capable of high-speed, long-range swimming and excellent maneuverability. Examples include predator species such as tuna and marlin.

How these swimming motions actuate the surrounding flow to affect efficient execution of the straight-line swimming and maneuvering motions is the subject of the current investigation. This work will concentrate on examining the hydrodynamical aspects of both *Carangiform* and *Thunniform* swimming, due to the observed performance reported by previous investigators and the availability of published research on which to base comparison. In addition, the hydrodynamics and vorticity control mechanisms associated with these types of motions may be exploited in a variety of fluid dynamic engineering applications, such as exploratory AUVs, surface and underwater vessel propulsion, and control systems for station-keeping and maneuvering.

4.2 Linear theory

Several analytic approaches have been developed to predict fish-like swimming performance. The two classes of three-dimensional analytic swimming theories are *resistive* and *reactive*. The resistive theories developed by Taylor [198, 199, 200] are applicable for large amplitude motions at low Reynolds numbers, such as those used in flagellar propulsion and some forms of *Anguilliform* motion. Resistive motions are thought to be of low efficiency with viscous forces dominating the performance. The *reactive* theories developed by Lighthill [124, 125, 126, 127] and Wu [242, 240] are for large amplitude motions are higher Reynolds numbers. Reactive theories are for high efficiency motions, where added mass forces dominate the performance.

The two seminal contributions in this field come from Lighthill, in his slender body theory [125], followed by his extension of this to motions of large amplitude [126]. Both theories consider three-dimensional, infinitesimally-thin bodies. The lateral motion of the backbone undulations in slender body theory is limited to much less than the order of the body length. The forces on the fish can be reevaluated for large-amplitude motion of the backbone by employing the large-amplitude elongated body theory. While no assumption is made about the maximum height of the body-cross section, the longitudinal variations in cross-sectional properties, and such as the body depth or the lateral water momentum per unit length, must be slow on the scale of the cross-sectional height. The thrust generation mechanism is the shedding of lateral water momentum through the vertical trailing edge acting with a lateral force on the wake.

When appropriate, the predictions afforded by the slender body theories for the various motions and geometries considered in the course of this investigation will be presented for comparison purposes. First, to better understand the assumptions, limitations, and consequences of employing these linear theories, they will be explained in detail herein.

4.2.1 Lighthill's slender body theory

The general form of the slender body theory is developed for *Anguilliform* motions, although extensions to *Carangiform* and *Thunniform* swimming will be discussed. The morphological characteristics which will make this theory applicable include a slender body with slowly-varying cross-section depth, a sharp trailing edge at the tail, and a constant amplitude traveling wave over the length of body. The body is assumed to be straight-line swimming in an ideal fluid, seeing a free stream of mean speed U, with small-amplitude slowly-varying undulations along the backbone and a small body inclination angle to the streamwise direction.

The amplitude of the lateral backbone undulations $h(x,t)$ is given with respect to the location x along the stretched straight length l of the fish. The velocity of the fluid perpendicular to the backbone due to the undulations can be written:

$$w(x,t) = \partial h(x,t)/\partial t \; + \; U \, \partial h(x,t)/\partial x \tag{4.1}$$

The added mass of fluid at any fish cross-section of depth $s(x)$ can be written:

$$m(x) \approx 1/4\pi\rho s^2 \tag{4.2}$$

describing the area of a circle which perpendicularly circumscribes the cross section, which is shown to be valid for a variety of cross-sectional shapes for large backbone wavelengths. Then, the lateral fluid momentum per unit length can be described as $m(x)w(x,t)$, which results in a force Z on the fluid per unit length from the time rate of change of this momentum:

$$Z \; = \; [D]m(x)w(x,t) \; = \; \Big(\frac{\partial}{\partial t} + U\frac{\partial}{\partial x}\Big)m(x)w(x,t) \tag{4.3}$$

where $[D]$ is the material derivative. The rate at which the fish does work on the

fluid, or the amount of power E required to produce the motions can be expressed as

$$E = \int_0^l Z\frac{\partial h}{\partial t}dx = \int_0^l \frac{\partial h}{\partial t}[D]m(x)w(x,t)dx \tag{4.4}$$

which can be manipulated through the definition of the material derivative to yield

$$E = \int_0^l \Big(\frac{\partial}{\partial t}\Big(mw\frac{\partial h}{\partial t}\Big) + U\frac{\partial}{\partial x}\Big(mw\frac{\partial h}{\partial t}\Big)\Big)dx - \int_0^l mw\frac{\partial w}{\partial t}dx \tag{4.5}$$

Rearranging this above expression and integration of the second term on the right hand side yields

$$E = \frac{\partial}{\partial t}\int_0^l \Big(\frac{1}{2}mw^2 - Umw\frac{\partial h}{\partial x}\Big)dx + U\Big[mw\frac{\partial h}{\partial t}\Big]_{x=l} \tag{4.6}$$

This is the expression derived by Lighthill [125], and a physical interpretation of the right hand side terms of this equation aid in the understanding of the application of the theory. The first two terms represent the rate of energy exchange between the water and the body of the fish which fluctuates in time and over the length of the fish: the first term represents energy fluctuations in the vertical and lateral directions; the second term is affected by energy fluctuations in x also. The third term represents the rate of work involved in shedding lateral momentum into the wake. Thus, the linear theory allows for energy associated with x momentum arising from small lateral perturbations on a slightly-sloped body surface.

The power into the fluid E can also be expressed in terms of the thrust P, in an inertial reference frame where the fluid is at rest at S_∞:

$$E = UP + U\Big[\frac{1}{2}mw^2\Big]_{x=l} + \frac{\partial}{\partial t}\int_0^l \Big(\frac{1}{2}mw^2\Big)dx \tag{4.7}$$

Again, a physical interpretation of the right hand side terms of this equation elucidates the physics. The first term is simply the rate of work done in producing useful thrust. The second term is the rate of kinetic energy shed into the wake at the trailing edge at the swimming velocity U. The final term is the rate of the kinetic energy fluctuations

over the body. This term has a time mean of zero. The thrust can then be found by using the previous two forms of E:

$$P = \left[mw\frac{\partial h}{\partial t} - \frac{1}{2}mw^2\right]_{x=l} - \frac{\partial}{\partial t}\int_0^l \left(mw\frac{\partial h}{\partial x}\right)dx \tag{4.8}$$

and the efficiency $\eta = U\bar{P}/\bar{E}$ can then be easily written, noting that the time averages of the integral quantities in the expressions for P and E are zero:

$$\eta = 1 - \frac{1}{2}\frac{\overline{\left[w^2\right]_{x=l}}}{\overline{\left[w\partial h/\partial t\right]_{x=l}}} \tag{4.9}$$

A trade-off is immediately obvious. The mean thrust $\bar{P}$ is entirely dependent on w. For good efficiency, however, $w \ll \partial h/\partial t$.

It is difficult to understand physically what the terms in the equation for P mean. Lighthill's (1970) [125] explanation is not terribly clear, so for that reason, the expression can be easily derived from a first principles control volume argument for the conservation of moment. The control volume bounding control surfaces include the body, a surface Π perpendicular to the body's trailing edge, and a semi-spherical contour at S_∞. In this manner, as can be seen in Figure 4-1 the wake shed by the body is excluded.

The conservation of momentum can be reduced to

$$[X, Z] = -\int\int\int_V \partial/\partial t(\rho\vec{v})dV - \int\int_\Pi \rho\vec{v}(\vec{v}\cdot\hat{n})dS + \int\int_\Pi p\vec{n}dS \tag{4.10}$$

where X and Z are the thrust and side forces on the fish, and p and $\vec{v}$ are the pressure and the velocity of the fluid. The fluid momentum per unit length of the fish is rewritten

$$\rho\vec{v} = mw\left[-\frac{\partial h}{\partial x}, 1\right] \tag{4.11}$$

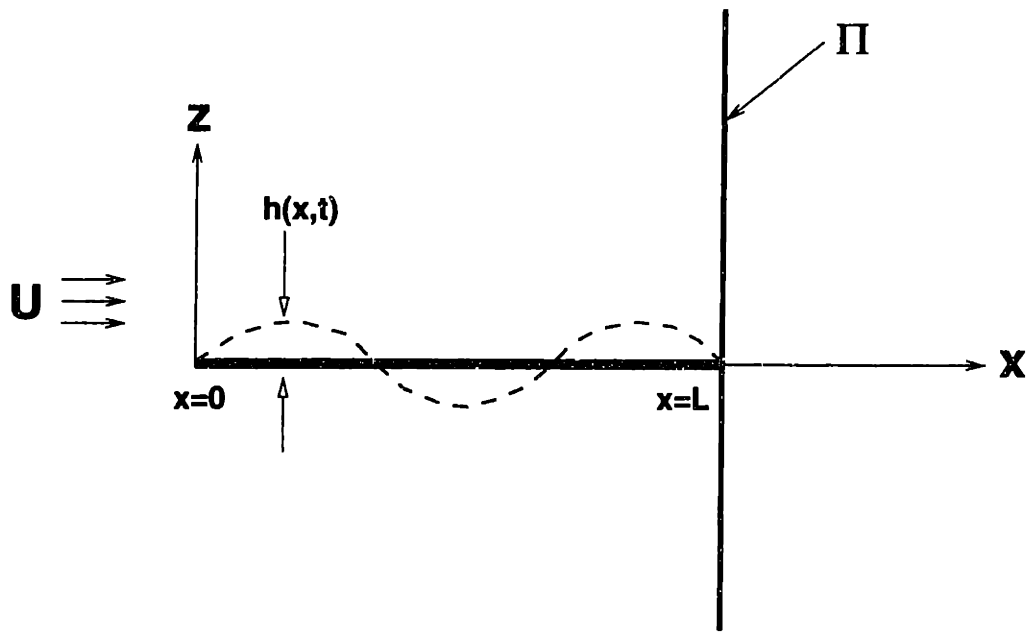

Figure 4-1: Control volume schematic for Lighthill's slender body theory derivation.

and employing the divergence theorem, Equation (4.10) becomes

$$[X, Z] = -mwU\Big[-\frac{\partial h}{\partial x}, 1\Big]_{x=l} - \frac{d}{dt}\int_0^l mw\Big[-\frac{\partial h}{\partial x}, 1\Big]dx + \int\int_\Pi p\vec{n}dS \qquad (4.12)$$

The pressure can be evaluated over the trailing surface of the control volume Π using unsteady Bernoulli Equation:

$$-\frac{p}{\rho} = \frac{\partial \phi}{\partial t} + \frac{1}{2}|\vec{\nabla}\phi|^2 + C(t) \qquad (4.13)$$

The $\partial\phi/\partial t$ term will give no contribution to the pressure integral, since the potential ϕ is odd in z. In addition, the time constant in Bernoulli's equation can be written in a frame of reference fixed at the trailing edge of the fish

$$C(t) = -p_\infty - \frac{1}{2}\rho w^2 \qquad (4.14)$$

Thus, the velocity of the fluid at any section along the fish length can be written

$$\vec{\nabla}\phi = \Big[\frac{\partial \phi}{\partial y}, \frac{\partial \phi}{\partial z} + w\Big]. \qquad (4.15)$$

so that the quadratic terms on the right hand side of the unsteady Bernoulli equation appear as

$$\frac{1}{2}\rho\Big\{w^2-\Big(\frac{\partial\phi}{\partial y}\Big)^2-\Big(\frac{\partial\phi}{\partial z}\Big)^2\Big\}=\rho w\Big(\frac{\partial\phi}{\partial z}+w\Big)-\frac{1}{2}\rho\Big\{\Big(\frac{\partial\phi}{\partial y}\Big)^2+\Big(\frac{\partial\phi}{\partial z}+w\Big)^2\Big\} \quad (4.16)$$

After some straightforward algebra, these quadratic terms can be expressed in terms of the total momentum mw and kinetic energy $1/2mw^2$ per unit length in $(\partial\phi/\partial y, \partial\phi/\partial z + w)$:

$$p = w(mw) - \frac{1}{2}mw^2 = \frac{1}{2}mw^2 \quad (4.17)$$

Then, integration of the resultant pressure p across the Π plane yields

$$X = \Big[mwU\frac{\partial h}{\partial x} - \frac{1}{2}mw^2\Big]_{x=l} + \frac{d}{dt}\int_0^l mw\frac{\partial h}{\partial x}dx \quad (4.18)$$

which can be rewritten for the thrust P upon employing the definition for w and noting that a negative X indicates positive thrust P

$$P = \Big[mw\frac{\partial h}{\partial t} - \frac{1}{2}mw^2\Big]_{x=l} - \frac{d}{dt}\int_0^l mw\frac{\partial h}{\partial x}dx \quad (4.19)$$

This expression describes contributions to the thrust resulting from momentum convection, wake generation (felt as a pressure), and unsteady momentum transfer by the body.

With the derivation of the thrust term complete, we consider the hydrodynamics of the thrust generation mechanisms. The transfer of momentum into the wake, representing wasted energy, takes the form of a vortex sheet. The slender body theory assumes that perturbation velocities at the trailing edge are two-dimensional, a consequence of the assumption that the velocity potential can be described at discrete sectional locations as an elliptic potential distribution from complex mapping. In addition, the linear theory neglects the roll-up of the free vortex sheet, and it induces the same two-dimensional cross-flow as the body section when it was shed from the trailing edge.

Streamwise vortices separate from the trailing edge, and spanwise (depthwise) are assumed to maintain solenoidal quality of the vorticity field, as the strength of the sheet changes with w. The rate of rotation of the vortex sheet about the trailing edge depth is assumed to be $-\partial w/\partial x$, which is the rate of twisting lateral momentum mw of the trailing edge section into the x direction. This affirms the conclusion that the total rate of change of momentum in the wake is $1/2mw^2$ at $x = l$.

The slender-body theory has conditional extensions for a variety of morphological variations found on real fish. Both Lighthill [125], Wu [242, 243] and Newman [159, 156] allow for the inclusion of multiple fins, upstream of the oscillating tail, shedding multiple vortex sheets into the wake. The same assumptions of conformally-mapped sectional potential variations apply for the multiple wake configurations. The backbone wave traveling down the spine at a speed slightly higher than the swimming speed is needed for thrust, but as the wakes are shed, they are convected at the swimming velocity. Thus, if the fins are closely separated, the vortex sheet strength will maintain the dynamics of one continuous fin, possibly also reducing skin friction drag. For large separations, consideration must be given to the value of lateral momentum which was shed at an upstream fin when it intercepts the downstream fin in the integrals for Z side force on the body per unit length. The phase of this encounter may affect the swimming performance. Similar analysis shows that multiple fins can produce more useful thrust without an increase in wake energy.

Similar extensions to the slender body theory are made for *Carangiform* swimming motions, which are characterized by a slender body with slowly-varying cross-section depth and a sharp trailing edge, producing a traveling wave confined to the posterior half of the body with increasing traveling wave amplitude towards tail. Thus, smaller anterior fins are assumed no longer to shed a strong vortex wake. From the gradual necking of the main body before the tail fin common to most *Carangiform* swimmers, it is assumed that increased lateral motions cause vortices to be shed from the upper and lower sharp edges of the slender body's depth. This vortex shedding causes an increase in the kinetic energy in the water along the body and at the trailing edge. These vortices additionally create some force on the body, whose value is

approximated as a function of w and s, and the total momentum finally shed at the trailing edge of the tail must be found by considering all previously shed vortices from upstream lateral motions. The morphological and performance consequences of this *Carangiform* motion provided by the extended slender body theory include:

- Increased momentum shed into the wake from increased motions indicates an increase in wasted energy.
- Because of the vortices shed by lateral motions, the increase in wasted energy is not outweighed by increased thrust production from the trailing edge.
- Decreasing the vortices shed from the body through increased lateral motions reduces wasted wake energy.
- Decreasing the depth of the body in the posterior region where the motion amplitude is increasing, followed by a rapid increase in depth at the tail is advantageous in decreasing wasted wake energy, as well as side forces which are shown to produce lateral recoil motions.
- Consequence of this necking of the body anterior to the tail is an increase in angular recoil about the center of mass of the fish, as the side force is concentrated at the trailing edge.
- Increasing the rotational moment of inertia of the forward portion of the body by increasing its mass and its depth to counter this recoil moment is advantageous.
- Thus, fish employing *Carangiform* swimming motions generally have a large forward body, a reducing after section before the tail, and a large trailing edge depth.

Similar extensions to the slender body theory are made for lunate-tail swimming or *Thunniform* swimming motions, which are characterized by a body with large tail with sharp trailing & rounded leading edge producing a traveling wave confined to a small posterior portion of the body with sharply increasing traveling wave amplitude towards tail. Due to the dramatic necking before the tail and the extreme lateral excursions of the caudal fin, a slight modification to the *Carangiform*-modified slender body theory is inapplicable. Thus, linearized two-dimensional potential theory of pitch and heave motions of tail cross-sections is employed to find the thrust and efficiency. The vortex sheet shed from the tail is assumed two-dimensional in nature,

and the ignored streamwise vortices would tend to decrease the efficiency by introducing additional wake kinetic energy. Through this analysis, it can be shown that based on the assumptions, the thrust and efficiency are found to be dependent on the pitch point b and the feathering parameter θ for varying reduced frequency σ, defined in *Chapter 3*. Higher efficiency η can be realized for larger values of θ, and higher values of thrust for a given θ for values of b closer to the trailing edge.The morphological and performance consequences of this *Thunniform* motion provided by the lunate tail swimming theory include:

- Minimum wasted wake energy occurs at a pitch point b_o which is three-quarters of the length of the chord from the leading edge.
- The thrust increases for increasing pitch point position from the leading edge, so that the maximum η occurs for a pitch point between b_o and the trailing edge.
- Moving the pitch point of the foil close to the trailing edge increases the component of thrust arising from leading edge suction and decreases the component arising from redirection of lateral momentum.
- This phenomena increases for decreasing θ.
- Eventually, leading edge separation will induce stall in the physical system, which is not considered in this model.
- The optimal caudal fin shape would have tapered ends with a trailing edge practically vertical to achieve a constant pitch axis. The leading edge would be bowed as a result.
- The scooping out of the fin near the center may reduce skin friction drag without effecting the wake significantly.
- Factors affecting the validity of the analysis include the three-dimensionality of the flow, the nonlinearities of the amplitude and foil thickness, and the nonlinearities of the vortex wake deformation.

4.2.2 Lighthill's large amplitude elongated body theory

An extension to the generalized slender body theory is developed for large-amplitude *Anguilliform* and *Carangiform* motions by Lighthill (1971) [126]. Again, the morphological characteristics which will make this theory applicable include a slender

body with slowly-varying cross-section depth, a sharp trailing edge at the tail, and a constant amplitude traveling wave over the length of body. The body is assumed to be straight-line swimming at a mean speed U in an ideal fluid. Additionally, the backbone is assumed to be inextensible of length l.

The coordinates along the backbone of the fish (x, z) are described in terms of its arc length a from the trailing edge and fluctuate with time t. The velocity of any point on the backbone $[\partial x/\partial t, \partial z/\partial t]$ has components tangential u and normal w to the backbone, so that

$$u = \frac{\partial x}{\partial t}\frac{\partial x}{\partial a} + \frac{\partial z}{\partial t}\frac{\partial z}{\partial a} \tag{4.20}$$

$$w = \frac{\partial z}{\partial t}\frac{\partial x}{\partial a} - \frac{\partial x}{\partial t}\frac{\partial z}{\partial a} \tag{4.21}$$

Backbone inextensibility is expressed as

$$\left(\frac{\partial x}{\partial a}\right)^2 + \left(\frac{\partial z}{\partial a}\right)^2 = 1 \tag{4.22}$$

The fluid momentum vector per length of fish can then be written

$$mw\left[-\frac{\partial z}{\partial a}, \frac{\partial x}{\partial a}\right] \tag{4.23}$$

where m is defined as sectional added mass as in slender body theory.

To derive the forces acting on the fish body, a control volume is then chosen in the same manner as for slender body theory, shown in Figure 4-2. In this case, the plane Π is perpendicular to the trailing edge which may be at any angle to $z = 0$. Thus, the plane Π fluctuates in time at a slope of $-\partial x/\partial z$ at $a = 0$.

The pressure along Π is given by $p = 1/2mw^2$ as before. Similar to slender body theory, the forces in the x and z direction $[P, Q]$ on the fish can be written:

$$[P, Q] = \left\{-mwU\left[-\frac{\partial z}{\partial a}, \frac{\partial x}{\partial a}\right] + \frac{1}{2}mw^2\left[\frac{\partial x}{\partial a}, \frac{\partial z}{\partial a}\right]\right\}_{a=0} - \frac{d}{dt}\int_0^\ell mw\left[-\frac{\partial z}{\partial a}, \frac{\partial x}{\partial a}\right]da \tag{4.24}$$

Utilizing the inextensibility condition and the definition of velocity w in terms of its

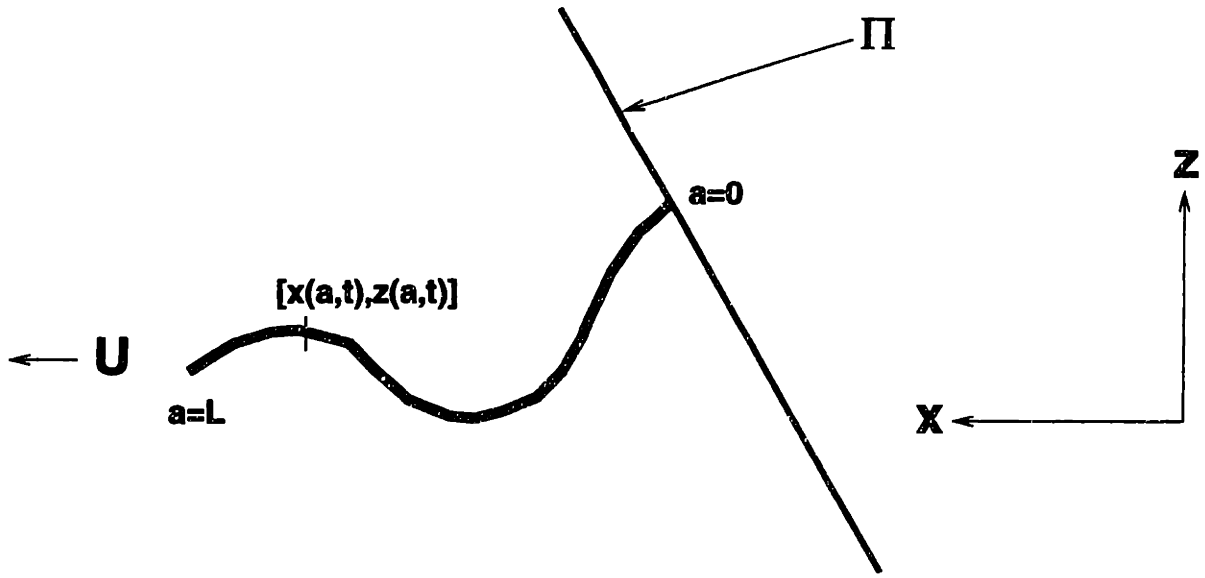

Figure 4-2: Control volume schematic for Lighthill's large amplitude elongated body theory derivation.

large-amplitude components:

$$[P,Q] = \left\{ mw\left[\frac{\partial z}{\partial t}, -\frac{\partial x}{\partial t}\right] - \frac{1}{2}mw^2\left[\frac{\partial x}{\partial a}, \frac{\partial z}{\partial a}\right]\right\}_{a=0} - \frac{d}{dt}\int_0^\ell mw\left[-\frac{\partial z}{\partial a}, \frac{\partial x}{\partial a}\right]da \quad (4.25)$$

Investigation of the performance of the swimming motions for large amplitudes reveals that high mean thrust is realized for large $\partial z/\partial t$ at $a = 0$, and w need not be as small desired for the slender body theory approximation, since negative mean thrust correlation with w^2 is reduced by the trailing edge slope $\partial x/\partial a$. In addition, the time dependent thrust along the body is found to generally be out of phase with the time dependent thrust produced by the trailing edge, smoothing out the total thrust time profile in *Carangiform* motion. Sideforce implications change little from the slender body theory, such that for *Carangiform* motion, recoil is minimized for large cross-sectional depth in the anterior regions of the body, a contraction region just before the tail, and a large tail fin with a sharp trailing edge. The energy wasted by shedding a thin shear layer into the wake is reduced from slender body theory prediction, proportional to $1/2mw^2\partial x/\partial a$. However, streamwise vorticity and downwash effects are not considered which would increase wake kinetic energy and reduce thrust, respectively. These conclusions would indicate that the large amplitude

elongated body theory will predict higher efficiencies and thrust than the generalized slender body theory.

Lighthill [126] utilized this large amplitude swimming theory to predict the performance of live fish by extracting data from published sketches of caudal fin movement during straight swimming of a dace [16]. The local velocity perpendicular to the trailing edge w at $a = 0$ was determined from the data, as was the trailing edge angle $\partial x/\partial a$. Using this information, the thrust at each discrete time was estimated using the large amplitude elongated body theory. The contribution to the thrust from the quadratic w term was negligible, the majority of the mean thrust coming from $mw\partial z/\partial t$. This mean thrust coefficient was compared to the predicted drag coefficient for a similar body at Reynolds number $O(10^5)$, and was found to be four times higher (*Lighthill's paradox*).

Lighthill's [126] findings of increased drag in swimming fish are in direct contradiction of Gray's Paradox [76]. Yet, many of the limitations in the application of large amplitude elongated body theory may account for these discrepancies, including the neglect of three-dimensional effects, form drag and its possible suppression [197, 196, 170, 56, 202], wake dynamics and wake-body interactions. Thus, it seems quite possible that a combination of these effects may have contributed to the overestimation of the thrust by the large amplitude linear theory and the overestimation of the associated steady swimming drag of the actual fish. However, these slender body theories until recently have remained the paradigm for the analytic performance prediction for fish swimming motions. In addition, they have been modified to account for a number of kinematic and morphological specificities, including rapid starting and maneuvering [225, 226]. They have been recognized to overpredict the thrust on more realistic fish-like forms [211] because basic assumptions of the linear slender body theory are violated.

4.3 Steady swimming of a bluefin tuna

4.3.1 Experimental evidence

In this section, our investigation of fish-like swimming addresses the second canonical problem, the simulation of three-dimensional straight-line swimming motions using the computational method developed and described in detail in *Chapter 3*. As the hydrodynamic propulsive mechanisms between various aquatic species may vary, the subject of this investigation is the bluefin tuna (*Thunnus thynnus*). This predator species of ocean fish travels great distances spanning oceans in search of food and has been reported to maintain high swimming speeds, with outstanding maneuvering and burst speed generation. Additionally, the tuna was the subject of a comprehensive engineering construction project and hydromechanical study employing a robotic mechanism. Barrett [18, 20, 19, 21] developed a robotic flexible-hull underwater vehicle shaped like a tuna, the *RoboTuna*, on which precise, repeatable direct dynamic measurements could be performed. Photographs of a live tuna and the RoboTuna can be found in Figures 4-3.

The robotic mechanism has length $L = 1.25\ m$ and consists of a streamlined main body capable of flexing and a propulsive tail-fin. The outer shape of the vehicle in its position at rest is an exact replica of the shape of a bluefin tuna, including the caudal and two smaller attached fins. A schematic of the tuna taxonomy is shown below in Figure 4-4 for reference. The robotic mechanism is tested in the Ocean Engineering Testing Tank Facility at MIT in a water tank with dimensions 35 m long by 2.5 m wide by 1.25 m deep. The robot is connected to an overhead carriage through a streamlined strut so it can be towed at constant speed. It was towed at mid-depth to avoid interference effects with the free surface and the bottom. Complete details of the geometry, construction, calibration, and operation of the *RoboTuna* can be found in Barrett (1994, 1996) [18, 19].

Direct experimental dynamical measurements of the energetic makeup and efficiency of live swimming fish are difficult to obtain and may not be characteristic of natural behavior. The development of the *RoboTuna*, which can emulate very closely

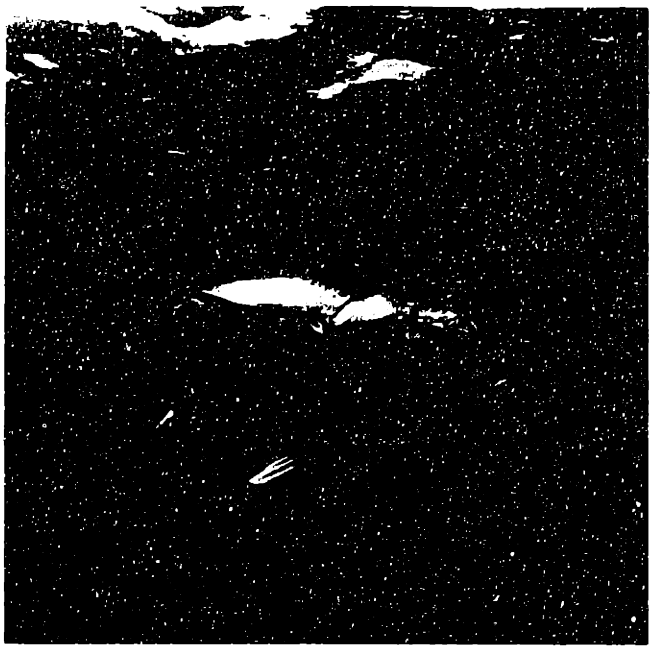

(a) Bluefin Tuna

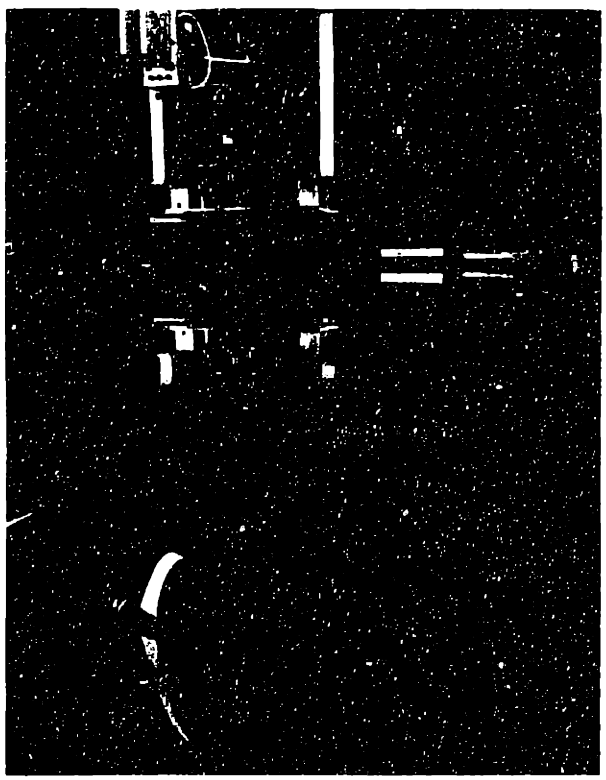

(b) *RoboTuna*

Figure 4-3: Photographs of (a) a live bluefin tuna and (b) the *RoboTuna*.

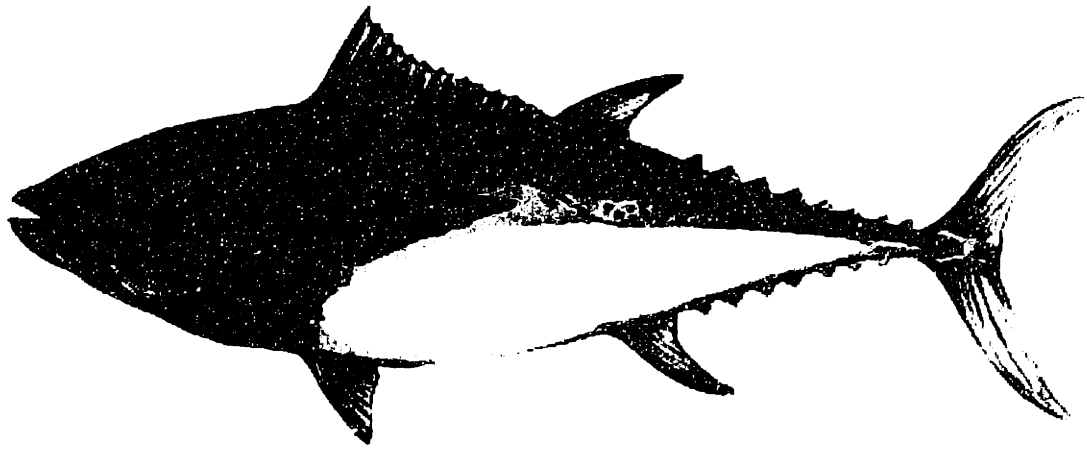

Figure 4-4: Taxonomic schematic of the tuna, showing the arrangement of secondary fins and the finlets on the contraction region of the dorsal and ventral ridges. The secondary fins are retractable, which may decrease straight-line swimming resistance.

the swimming of the tuna, overcomes the difficulties associated with live fish, however, because it allows the acquisition of detailed accurate measurements of the hydrodynamic forces on an actively controlled flexible body swimming like a fish. Repeated precise measurements on the flexible robot have shown that, within a parametric range, drag in an actively swimming vehicle at Reynolds number of about 10^6 can be reduced by 50% or more (up to 70% within the range considered), compared with the value on the same vehicle towed in a rigid–straight configuration. This drag reduction can be attributed only to the effect on the flow of the imposed body flexing in the form of a traveling wave [21].

The motion was initially selected to resemble the tuna motions observed in live tuna [57, 47, 48]. The motion was curve-fitted so as to be purely sinusoidal and to consist of a smooth amplitude-modulated traveling wave along the length with constant phase speed, $c_p = \omega/k$, which may in general differ from swimming speed U. The imposed transverse motion $y(x,t)$, in a body-fixed coordinate system with x measured starting from the edge of the second link and positive towards the tail, has the form:

$$y(x,t) = a(x)\sin(kx - \omega t) \tag{4.26}$$

where $k = 2\pi/\lambda$ is the wavenumber, corresponding to wavelength λ, ω is the circular frequency of oscillation, and $a(x)$ is the amplitude envelope, given as:

$$a(x) = c_1 x + c_2 x^2 \tag{4.27}$$

where c_1 and c_2 are adjustable parameters. c_1 is independent, while c_2 is chosen to achieve a specific value of the double-amplitude or total lateral excursion of the motion, denoted by A, at the tail fin's junction to the body. The distance x is measured from the edge of the second link, which is rigidly attached to the towing strut, positive towards the tail, and is non-dimensionalized by the body length. Typically, the phase speed $c_p = \omega/k$ is larger than the forward speed U, while the wavelength λ is close in value to the body length.

Various motions were studied by Barrett [19], and utilization of a genetic algorithm [67] allowed for the optimization of apparent drag reduction during conditions of self-propulsion by varying the kinematic parameters, chosen originally from parametric kinematic data presented in Dewar [47].

The experimental results suggest that significant reduction in body drag is achievable through fish-like propulsion. The power expended by the motors and the mast force are the principal measured quantities which prove drag reduction. While the mast force is governed by viscous mechanisms, one may expect that, in the absence of large form-drag, the power is principally influenced by inviscid mechanisms; and hence could be calculated fairly accurately by inviscid numerical methods, provided the vorticity shed from sharp trailing edges (such as the tail fin) is properly modeled and accounted for. In order to check this hypothesis and hence further elucidate the principal flow mechanisms, the inviscid computational model is employed to simulate the flow kinematics and forces around the three-dimensional *RoboTuna* geometry under the same conditions used in the experiments.

4.3.2 Numerical modeling

To develop the numerical model of the *RoboTuna*, we consider the geometry of the robotic hull, as described in Barrett (1994, 1996) [18, 19]. Computational forms are chosen to include the major load bearing portions of the geometry, including the body and the caudal fin, but excluding the smaller lifting surfaces such as the dorsal and anal fins, as well as the strut which connects the *RoboTuna* to the overhead carriage. The tail is assumed to generate the largest wake, and the primary separation line is chosen to be the trailing edge of the tail. Although the *RoboTuna* does possess a smaller dorsal and anal fin, because separation is not promoted all along the backbone by the construction of a backbone ridge, the modeling of additional vorticity shedding from separation lines upstream of the caudal fin is neglected.

The body sections are elliptical with a major to minor axis ratio of $AR = 1.5$, where the major axis corresponds to the height of the body. A curvefitting technique is used to determine the profile shape of the body with $\ell = 1.0$, and is given simply by:

$$z(x) = \pm 0.305 \tanh(6x + 1.8) \quad \text{for} \quad -0.3 \leq x \leq 0.1 \tag{4.28}$$

$$z(x) = \pm(0.15 - 0.152 \tanh(7x - 3.15)) \quad \text{for} \quad 0.1 \leq x \leq 0.7 \tag{4.29}$$

The caudal fin is is assumed to have chordwise sections of NACA 0016 shape, to allow for efficient resolution of leading edge suction forces. The caudal fin leading edge and trailing edge profiles for the semi-span are also determined through a curvefitting technique, and are given simply by:

$$x(z)_{LE} = 39.543z^3 - 3.685z^2 + 0.636z \tag{4.30}$$

$$x(z)_{TE} = -40.74z^3 + 9.666z^2 + 0.07 \tag{4.31}$$

where $0 \leq z \leq 0.15$. The leading edge of the tail at midspan intersects the posterior end of the body's contraction region. The entire body length is then scaled to $\ell = 1$. The numerical grid in the region of the caudal peduncle, where the body and tail

intersect, is artificially smoothed. This simplification allows for rapid repanelization of the structured grid and ease of relative panel motion. The differences in the peduncle contraction region between the numerical form and the actual *RoboTuna* are assumed to have a small effect on the hydrodynamic similitude, as this region sustains a small hydrodynamic load and serves to transmit force from the oscillating tail to the center of mass of the body while minimizing the hydrodynamic recoil associated with tail loading moments about the center of mass [124, 125, 127].

We study through simulation the problem of this body starting from rest to reach a constant horizontal velocity U while undergoing periodic undulations about its mean line. A thin shear layer wake is continuously shed from the trailing edge of the caudal fin only as time proceeds. The computational geometry includes the body, employing $O(2,000)$ panels, and the caudal fin, employing $O(1,000)$ panels. The motion of the body is prescribed to be identical to that of the flexible, fish-like robot, as described by (4.26) and (4.27). The tail follows the path of the caudal peduncle but can be pivoted with oscillatory angular motion of arbitrary amplitude and arbitrary phase angle with respect to the lateral motion, resulting in a nominal angle of attack α.

The simulation starts with the body in a flexed position, and the caudal fin wake is shed continuously in time as the fish begins to move. Several periods of the motion are simulated to eliminate transients associated with initial conditions, and to achieve steady-state wake structure, motions and forces. The effects of the initial wake structure on the flow are damped out quickly, and steady-state behavior of integrated quantities is evident typically after one period of the motion. The time step depends on the Strouhal number and the frequency of the backbone wave, and is typically chosen as $dt = 0.05$. The wake generally contains up to $O(8,000)$ panels at the conclusion of the simulation. A typical simulation result is shown in Figure 4-5, where the evolving wake structure is evident. The numerical simulations employed $1,500$ body panels, $1,290$ tail panels, and produced 40 wake panels per time step for 250 time steps, totaling $10,000$ panels at the simulation's conclusion. The time step was chosen to be $dt = 0.05$ with a desingularization radius of $\delta = 0.025$. The evolving wake structure behind the fish in Figure 4-5 compares well qualitatively with dye

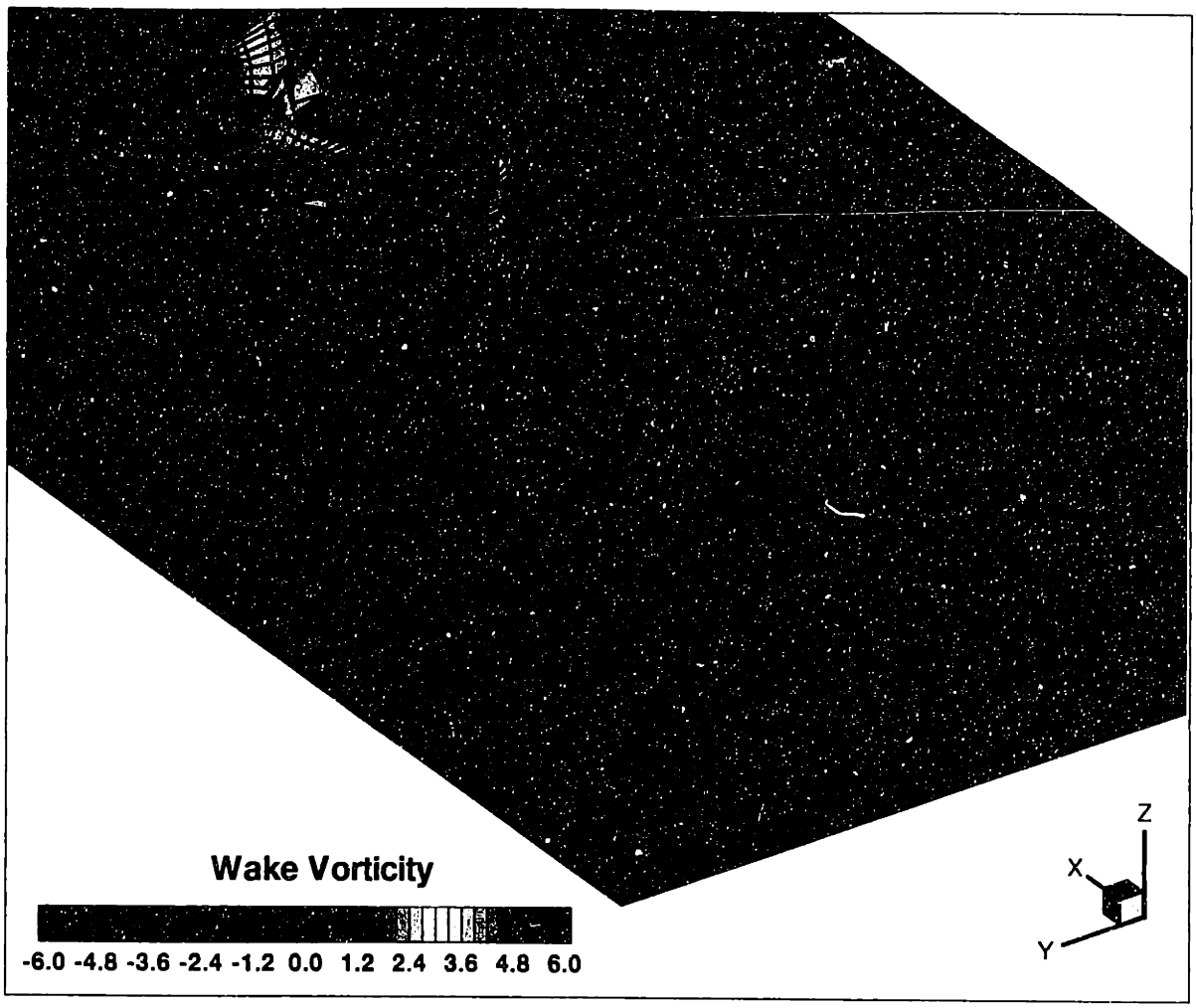

Figure 4-5: Numerical simulation results for the *RoboTuna* geometry showing the evolving straight-line swimming wake structure. Strouhal number $St = 0.182$. Run parameters: $U = 0.656$ BL/s, $\omega = 6.278$ rad/s, $\lambda = 0.936$ BL, Double tip amplitude $A = 0.120$ BL, $\alpha = 24.8^o$, Tail phase$= 80^o$. Body length is denoted as $BL = 1.066$ m from head to caudal peduncle.

visualization experiments performed in the wake of the flexible robot, such as those illustrated in Triantafyllou and Triantafyllou (1995) [206].

Sample time records of the forces on the body and the power delivered to the fluid for the imposed body motions simulated in Figure 4-5 can be seen in Figures 4-6 and 4-7. The transient effects of the impulsive motions are seen at the outset of the force records, where some spikes are evident. However, the transient effects of the starting wake vorticity on the performance are minimal, as evidenced the force time records, which show an approach to steady-state oscillations in the lift and thrust force

after one or two complete periods of the motion. Figures 4-6 and 4-7 also illustrates the separate contributions of the main body and the caudal fin to the total thrust, sideforce, and power delivered to the fluid. It can be seen that the tail sustains the majority of the thrust and sideforces. The magnitude of the thrust produced by the low aspect ratio oscillating body is minimal, less than 10% of the steady-state thrust coming from the oscillating caudal fin motions, and the sideforce peak magnitude sustained by the body is approximately 30% of the peak sideforce sustained by the tail.

4.3.3 Results and comparisons

Quantitative comparison between the experimental measurements and the numerical simulations of expended power can be made directly. As mentioned above, the simulations are made for an inviscid fluid and no comparison of forces can be made; however, in the absence of substantial separation or form drag it is expected that the power estimates should be sufficiently close. The effects of upstream vorticity shed by the body on the flow dynamics around the caudal fin are not modeled in this simulation, due to the smooth nature of the synthetic robotic mechanism skin without predetermined separation edges and to the small size of the secondary dorsal or anal fins. These dynamics may be important for other geometric configurations, as vorticity control may account for $5-15\%$ of the recovered energy [68] and will be addressed further in this investigation elsewhere.

Input parameters for four experimental runs and corresponding numerical simulations can be found in Table 4.1. The numerical simulations employed $1,500$ body panels, $1,290$ tail panels, and produced 40 wake panels per time step for 250 time steps, totaling $10,000$ panels at the simulation's conclusion. Again, the time step was chosen to be $dt = 0.05$ with a desingularization radius of $\delta = 0.025$.

Power time histories for both the experimental runs and the numerical simulations can be found in Figures 4-8 and 4-9. For the first pair of records in Figure 4-8, Run 1, 47.7% drag reduction was experimentally realized at a Strouhal number of 0.182. The second pair of records in Figure 4-8, Run 2, 47.8% drag reduction was experimentally

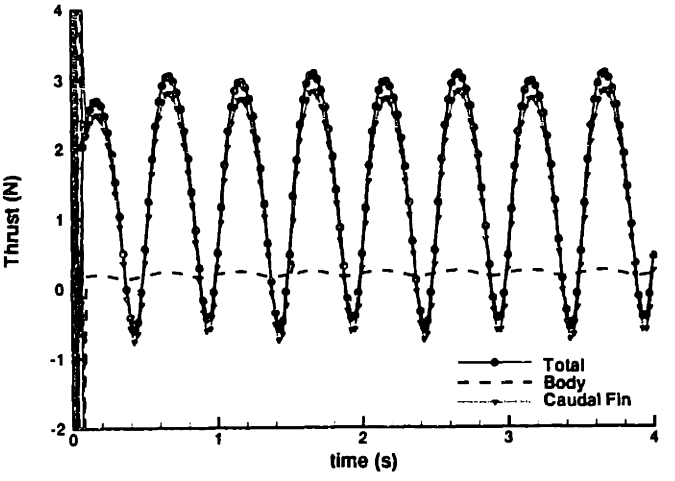

(a) Thrust

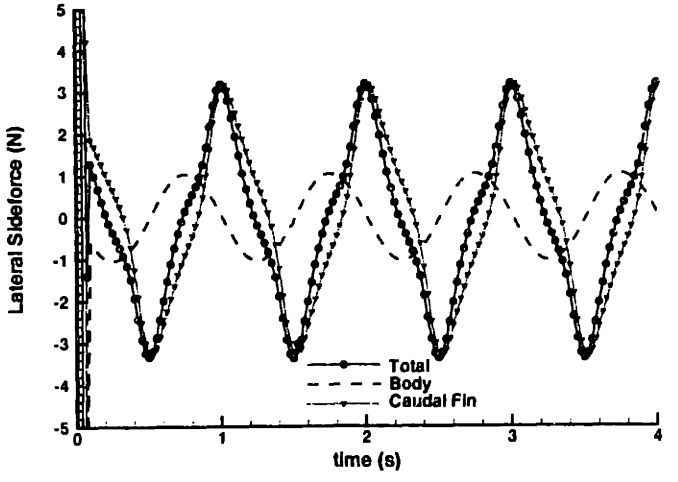

(b) Lateral Sideforce

Figure 4-6: Numerical simulation results of the integrated quantities for the *Robo-Tuna* geometry straight-line swimming motions. The total quantity (—•—), body contribution (- - -), and caudal fin contribution (··▼··) to the (a) thrust force and (b) lateral sideforce, are shown for the imposed motions. Initial condition of impulsive-start is evident from force spikes at $t = 0.0$. Kinematic parameters are identical to those of Figure 4-5.

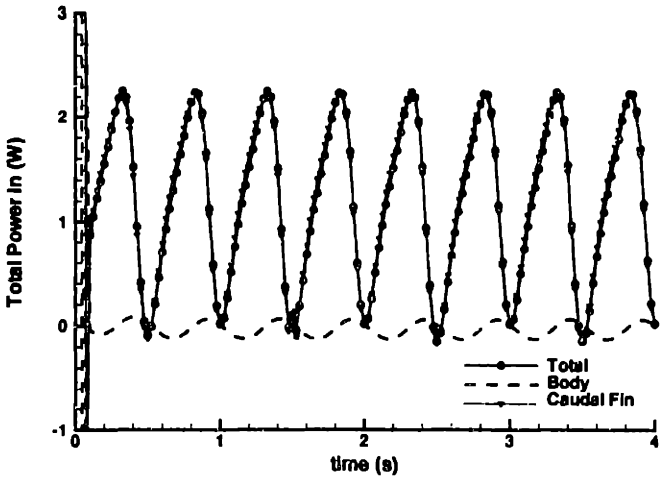

Figure 4-7: Numerical simulation results of the power delivered to the fluid for the *RoboTuna* geometry straight-line swimming motions. The total quantity (—•—), body contribution (- - -), and caudal fin contribution (· · ▼ · ·) to the power are shown for the imposed motions. Initial condition of impulsive-start is evident from force spikes at $t = 0.0$. Kinematic parameters are identical to those of Figure 4-5.

Barrett Run Code		Run 1 j705_03	Run 2 j702_06	Run 3 z702_01	Run 4 j706_06
Strouhal number St	(–)	0.182	0.198	0.273	0.353
Swimming speed U	(BL/s)	0.656	0.656	0.656	0.656
Tail circular frequency ω	(rad/s)	6.278	6.830	8.095	7.767
Wavelength λ	(BL)	0.936	0.936	1.081	1.321
Tip double amplitude A	(BL)	0.120	0.120	0.139	0.187
Angle of attack α	(deg.)	24.8	19.0	21.0	19.0
Tail phase of pitch & heave	(deg.)	80.0	97.7	97.7	97.7
Drag reduction (experiment)	(%)	47.7	47.8	47.9	43.8
Mean power input (experiment)	(W)	1.07	1.08	2.04	3.71
Mean power input (computation)	(W)	1.15	1.29	1.68	3.05
Mean power input difference		7.48%	19.4%	17.6%	17.8%
Peak power input (experiment)	(W)	2.04	1.99	3.88	5.81
Peak power input (computation)	(W)	2.30	2.20	3.04	6.06
Peak power input difference		12.7%	10.7%	21.6%	4.43%
Mean computed thrust	(N)	1.50	1.67	2.12	3.93
Peak computed thrust	(N)	2.88	3.02	4.42	5.61
Computed propulsive efficiency	η	91.4%	90.4%	88.4%	90.1%

Table 4.1: Parameters for four cases for comparison between experimental results and numerical simulations. Body length $BL = 1.066\ m$ from head to caudal peduncle.

realized at a Strouhal number of 0.198. Run 3 at a Strouhal number of 0.273 and Run 4 at a Strouhal number of 0.353 experimentally achieved drag reductions of 47.9% and 43.8%, respectively shown as the top and bottom pairs of records in Figure 4-9. The time records compare well qualitatively, revealing a second harmonic in the time history of the power expended. For all four runs, the numerically computed propulsive efficiency was around 90%.

Quantitative agreement for these cases is good under the assumptions made. The exact timing among the links of the experimental device was found to affect the overall power time record and may be a cause of deviation due to the flexibility of the experimental apparatus. Also, natural resonances in the mechanical system and mechanical losses are expected to cause some deviations between theory and experiment. Despite the simplifications made through the choice of the numeric scheme, and the unmodeled mechanical behavior and losses, the difference in the mean power between theory and experiment is less than 20% in three of the cases and 7.5% for Run 1.

Barrett [19] produced over 400 runs with the *RoboTuna* in his experimental investigation. A genetic algorithm technique was employed to optimize the selection of the kinematic parameters and their variation over a series of tests. These kinematic parameters would be varied in an attempt to produce the greatest apparent reduction in hydrodynamic drag from the rigid body drag. In addition, the optimization process would attempt to maintain a condition of self-propulsion, such that the mean force between the undulating *RoboTuna* and its supporting strut was negligible, as only in this manner can meaningful information concerning drag reduction be extracted.

During the optimization process, Barrett [19] utilized sample groups with varied kinematic parameters and compared their performance against each other. These sample groups, or generations, were then modified in a subsequent series of tests, trading and modifying their kinematic parameters in an attempt to produce better performance results. Rather than attempt to run simulation cases for all 400 or so of existing experimental datasets, an optimization series was utilized as the basis for simulation input parameters. Simulation results for the `j-series` of runs is presented

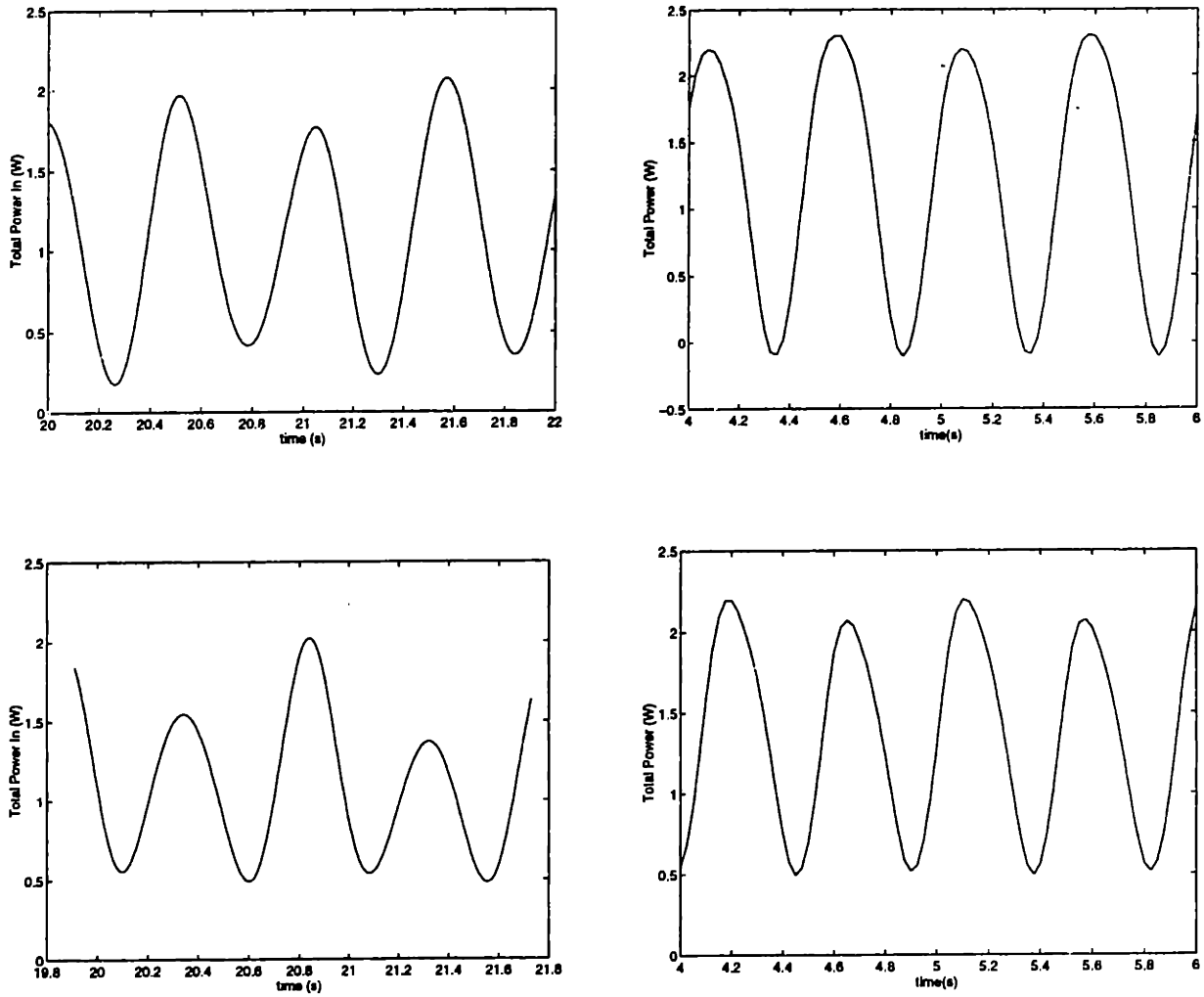

(a) Experimental

(b) Computational

Figure 4-8: Total power into the fluid for straight-line swimming. The mean power deviation between the (a) experimental (from Barrett, *et al.* (1999) [21]) and the (b) numerical time history power records is for Run 1 (top): 7.48% and for Run 2 (bottom): 19.4%.

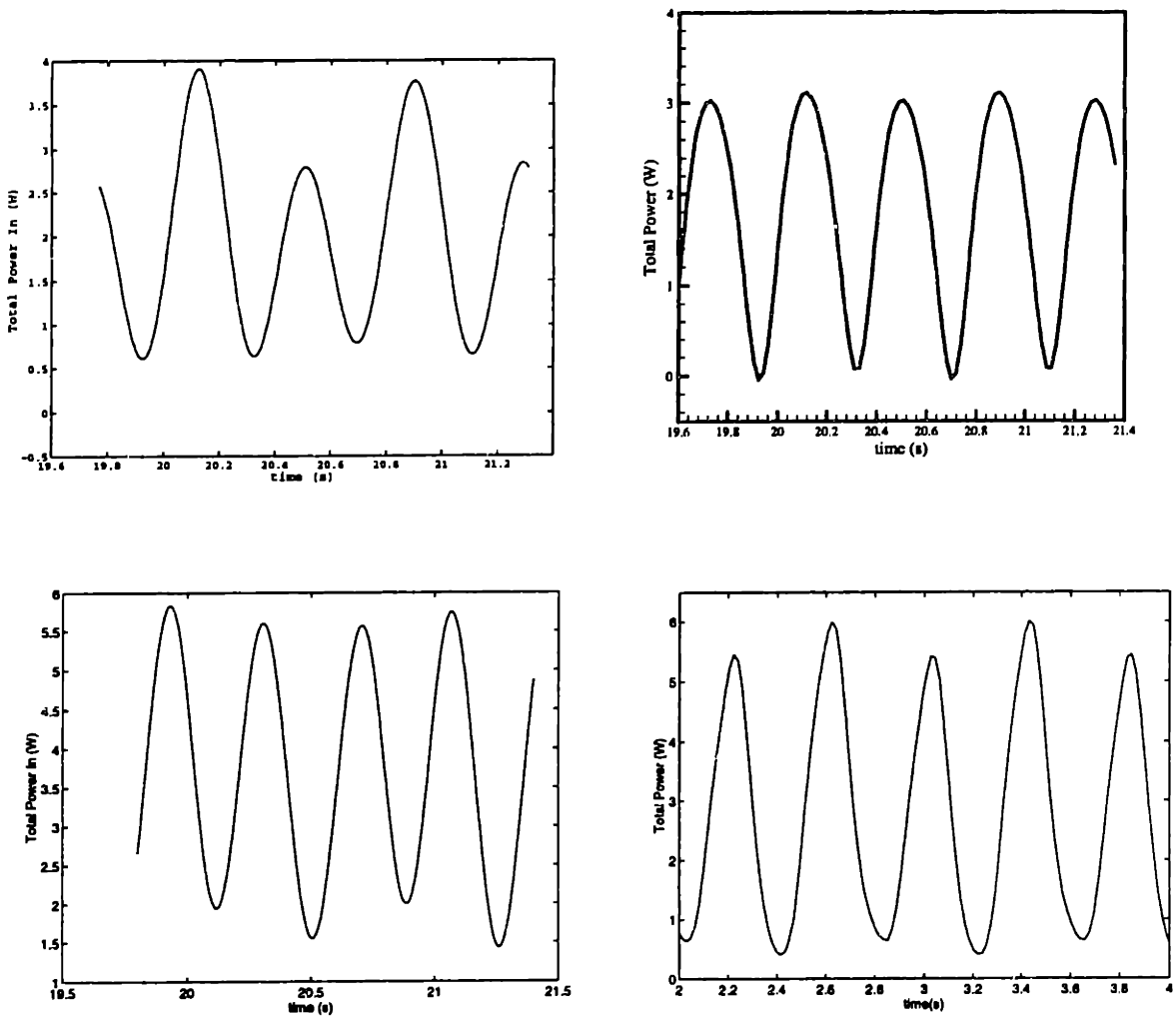

(a) Experimental

(b) Computational

Figure 4-9: Total power into the fluid for straight-line swimming. The mean power deviation between the (a) experimental (from Barrett, *et al.* (1999) [21]) and the (b) numerical time history power records is for Run 3 (top): 17.6% and for Run 4 (bottom): 17.8%.

in Tables 4.2 and 4.3. Tables 4.2 details the kinematic parameters of each case in the optimization series. The initial generation can be recognized as the grouping of ten cases at the top, or the `j701_` generation. Subsequent generations are numbered similarly as `j70x_` where `x` is the generation number. The optimization series typically utilized 10 cases in each generation, but for later generations, only good experimental data was retained, limiting the number of tests shown to 50. The last two cases from the `z-series` were randomly selected from the experimental data pool whose apparent drag reduction exceeded at certain threshold.

This more thorough investigation of experimental cases through simulation did not produce results which were consistently as good as those presented in Figures 4-8 and 4-9. The computed mean power into the fluid found through simulation compares to the experimental value to within 25% slightly over 30% of the time for the 50 cases presented. In several cases, the simulated mean power is more than double the experimental measurement, and in 3 cases, the mean power delivered to the fluid is negative, indicating power absorption and drag. The mean values of the computed thrust are presented in Table 4.3, and in 6 cases, drag is realized. For thrust producing cases, propulsive efficiencies range from 25% to 90%. Those cases which show good comparison to experiment for mean power expenditure and additionally show high propulsive efficiencies have been presented earlier in Figure 4-8 and 4-9.

However, poor comparison between the experimental records and the numerical simulation may be revealing in itself. The assumptions inherent to the computational model obviate understanding of viscous mechanisms contributing to the performance, such as boundary layer amplification, unsteady bluff body separation. Additionally, drag wake creation by the oscillating tail through choice of feathering kinematics can be obtained, but leading edge vorticity effects, such as stall and oscillation half-cycles which shed two sets of spanwise vorticity structures instead of one, are not capable of being handled through simulation. As a result, poor comparison between the experimental and simulation mean power expenditures suggests that viscous forces are not insignificant. Those cases which additionally realize significant drag amplification or drag reduction in the experiments can attribute the performance or lack thereof to

Barrett Run Code	U (BL/s)	α (deg)	A (BL)	λ (BL)	ϕ (deg)	c_1 (-)	c_2 (1/BL)	k (rad/BL)	ω (rad/s)
j701_01a	0.6562	1.4	0.158	1.461	95.4	0.00153	0.18502	4.2995	4.322
j701_01b	0.6562	11.5	0.134	1.316	77.0	0.00236	0.15501	4.7748	3.137
j701_03	0.6562	11.5	0.134	1.316	77.0	0.00236	0.15501	4.7748	3.137
j701_04	0.6562	25.4	0.104	1.295	90.8	0.00166	0.12030	4.8502	15.052
j701_05	0.6562	27.3	0.120	0.936	97.9	0.00294	0.13693	6.7102	10.693
j701_06	0.6562	19.0	0.187	1.125	97.7	0.00099	0.22023	5.5851	4.356
j701_08	0.6562	8.2	0.166	1.191	88.1	0.00095	0.19550	5.2760	9.042
j701_09	0.6562	10.8	0.140	1.439	80.0	0.00364	0.16064	4.3675	5.342
j701_10	0.6562	27.1	0.143	1.098	90.1	0.00395	0.16327	5.7238	3.400
j702_01a	0.6562	28.4	0.134	1.316	90.0	0.00236	0.15501	4.7748	9.534
j702_01b	0.6562	28.4	0.134	1.316	90.0	0.00236	0.15501	4.7748	9.534
j702_01c	0.6562	27.1	0.140	1.439	90.1	0.00364	0.16064	4.3675	3.463
j702_01d	0.6562	10.8	0.143	1.098	80.0	0.00395	0.16327	5.7238	5.244
j702_02	0.6562	11.5	0.120	0.936	77.0	0.00294	0.13693	6.7102	3.518
j702_04	0.6562	19.0	0.120	1.316	97.7	0.00236	0.13866	4.7748	6.789
j702_05	0.6562	27.3	0.187	1.125	97.9	0.00376	0.21597	5.5851	3.960
j702_06	0.6562	19.0	0.120	0.936	97.7	0.00294	0.13693	6.7102	6.830
j702_09	0.6562	10.8	0.143	1.180	80.0	0.00395	0.16327	5.3268	5.244
j702_10	0.6562	27.1	0.140	1.439	90.1	0.00364	0.16064	4.3675	3.463
j703_01	0.6562	28.4	0.134	1.316	90.0	0.00236	0.15501	4.7748	10.088
j703_02	0.6562	28.4	0.134	1.316	75.5	0.00236	0.15501	4.7748	9.534
j703_05	0.6562	27.3	0.120	0.936	97.9	0.00294	0.13693	6.7102	6.209
j703_06	0.6562	19.0	0.187	1.320	97.7	0.00376	0.21597	4.7584	4.356
j703_07	0.6562	24.8	0.174	1.098	80.0	0.00400	0.19954	5.7238	4.317
j703_09	0.6562	19.0	0.187	1.125	97.7	0.00376	0.21597	5.5851	4.356
j703_10	0.6562	27.3	0.120	0.936	97.9	0.00294	0.13693	6.7102	6.209
j704_04	0.6562	19.0	0.120	0.936	97.7	0.00215	0.13814	6.7102	6.830
j704_05	0.6562	27.3	0.187	1.320	92.7	0.00376	0.21597	4.7584	3.960
j704_06	0.6562	19.0	0.120	0.936	97.7	0.00294	0.13693	6.7102	6.830
j704_08	0.6562	24.8	0.133	1.002	80.0	0.00400	0.15079	6.2689	5.285
j705_01	0.6562	24.8	0.144	1.320	80.0	0.00376	0.16412	4.7584	5.226
j705_02	0.6562	4.6	0.174	1.098	97.7	0.00400	0.19954	5.7238	4.697
j705_03	0.6562	24.8	0.120	0.936	80.0	0.00294	0.13693	6.7102	6.278
j705_04	0.6562	19.0	0.174	1.098	97.7	0.00400	0.19954	5.7238	4.697
j705_05a	0.6562	19.0	0.120	1.470	97.7	0.00294	0.13693	4.2730	6.416
j705_05b	0.6562	19.0	0.120	1.470	97.7	0.00294	0.13693	4.2730	6.416
j705_06	0.6562	19.0	0.187	1.320	99.1	0.00376	0.21597	4.7584	4.356
j705_07	0.6562	19.0	0.174	1.098	97.7	0.00222	0.20228	5.7238	4.697
j706_01	0.6562	24.8	0.187	1.320	80.0	0.00376	0.21597	4.7584	4.004
j706_02	0.6562	6.4	0.120	0.936	97.7	0.00294	0.13693	6.7102	6.830
j706_06	0.6562	19.0	0.187	1.320	97.7	0.00376	0.21597	4.7584	7.767
j706_07	0.6562	19.0	0.120	0.936	78.9	0.00294	0.13693	6.7102	6.830
j708_08	0.6562	24.8	0.187	1.264	80.0	0.00376	0.21597	4.9723	4.004
j709_08	0.6562	24.8	0.187	1.320	80.0	0.00839	0.20884	4.7584	4.004
j710_02	0.6562	24.8	0.187	1.264	91.9	0.00376	0.21597	4.9723	4.004
j710_06	0.6562	24.8	0.187	1.320	80.0	0.00236	0.21812	4.7584	3.168
j710_09	0.6562	12.3	0.187	1.320	80.0	0.00236	0.21812	4.7584	4.004
z702_01	0.6562	21.0	0.139	1.080	97.7	0.00042	0.16391	5.8202	8.095
z706_06	0.6562	28.9	0.101	1.216	89.8	0.00372	0.11375	5.1675	6.371

Table 4.2: Kinematic parameters for a genetic algorithm optimization series of *RoboTuna* straight-line swimming simulations. Body length is denoted by $BL = 1.066\ m$ from head to caudal peduncle.

Barrett Run Code	St (-)	Percent Drag Reduction	$\bar{P}_{in}$ Exp. (W)	$\bar{P}_{in}$ Comp. (W)	Error (%)	$\bar{T}$ Comp. (N)	η (%)
j701_01a	0.166	-82.8	1.17	-0.12	110.5	-1.22	-
j701_01b	0.102	-282.9	4.58	-0.45	109.9	-0.92	-
j701_03	0.102	2.7	0.65	-0.45	169.3	-0.92	-
j701_04	0.379	-157.2	3.70	0.23	93.8	-3.65	-
j701_05	0.310	46.0	2.79	3.99	43.0	4.23	74.3
j701_06	0.198	44.7	1.25	0.79	37.1	0.82	73.0
j701_08	0.365	-200.3	5.79	4.08	29.5	-0.72	-
j701_09	0.182	15.8	1.46	2.41	64.5	2.55	74.2
j701_10	0.118	-9.8	0.91	1.69	85.0	0.60	24.8
j702_01a	0.310	46.0	4.44	4.89	10.1	5.19	74.3
j702_01b	0.310	40.6	4.44	4.89	10.1	5.19	74.3
j702_01c	0.118	-8.9	0.86	3.21	273.2	2.86	62.2
j702_01d	0.182	21.4	1.30	1.77	36.8	1.82	72.0
j702_02	0.102	-0.4	0.64	2.96	361.2	2.40	56.9
j702_04	0.198	44.0	1.31	1.66	27.4	1.88	79.2
j702_05	0.180	45.3	1.18	1.33	12.9	1.52	79.9
j702_06	0.198	47.8	1.08	1.29	19.4	1.67	90.4
j702_09	0.182	4.4	1.35	1.83	36.1	1.61	61.5
j702_10	0.118	1.5	0.87	1.69	95.2	0.88	36.4
j703_01	0.328	-31.3	5.70	6.81	19.6	5.29	54.4
j703_02	0.310	-2.9	5.70	6.54	14.7	5.76	61.7
j703_05	0.180	45.4	1.13	1.77	57.3	2.00	79.0
j703_06	0.198	45.8	1.45	2.07	42.7	2.47	83.8
j703_07	0.182	45.2	1.22	1.93	58.2	2.49	90.1
j703_09	0.198	44.3	1.26	1.68	33.6	2.04	84.9
j703_10	0.180	28.2	1.12	2.67	137.1	2.65	69.5
j704_04	0.198	42.6	1.11	0.83	25.1	1.02	86.3
j704_05	0.180	45.1	1.30	0.94	27.3	1.23	91.4
j704_06	0.198	45.4	1.12	1.55	38.6	1.50	67.7
j704_08	0.170	39.6	1.16	1.71	47.0	1.93	79.1
j705_01	0.182	40.3	1.33	1.83	37.8	2.29	87.4
j705_02	0.198	-62.6	1.28	0.11	91.2	-0.12	-
j705_03	0.182	47.7	1.07	1.15	7.5	1.50	91.4
j705_04	0.198	45.0	1.34	1.47	9.3	1.53	73.2
j705_05a	0.186	42.3	1.20	1.78	48.5	2.29	90.1
j705_05b	0.186	28.3	1.18	1.92	62.9	2.14	78.1
j705_06	0.198	27.1	1.44	0.97	33.0	1.07	77.7
j705_07	0.198	45.0	1.36	1.66	22.3	2.08	87.4
j706_01	0.182	46.0	1.31	1.67	26.8	1.89	79.4
j706_02	0.198	8.1	0.88	1.08	22.8	0.38	24.9
j706_06	0.353	43.8	3.71	3.05	17.8	3.93	90.1
j706_07	0.198	45.1	1.28	1.99	55.7	2.19	77.0
j708_08	0.182	46.0	1.26	1.59	26.2	2.00	88.2
j709_08	0.182	46.1	1.32	1.42	7.4	1.66	81.5
j710_02	0.182	46.1	1.29	1.19	7.6	1.45	85.5
j710_06	0.144	38.7	1.01	1.38	37.0	1.50	76.0
j710_09	0.182	23.7	1.10	1.30	17.6	1.38	74.2
z702_01	0.273	47.9	2.04	1.68	17.6	2.12	88.4
z706_06	0.156	67.6	0.87	1.23	41.1	1.43	81.3

Table 4.3: Performance results for a genetic algorithm optimization series of *RoboTuna* straight-line swimming simulations. Comparison between experimental and computational methods is given in percent absolute mean error. Body length is denoted by $BL = 1.066\ m$ from head to caudal peduncle.

either *(i)* unsteady boundary layer effects of relaminarization or widespread separation or *(ii)* unsteady vorticity control mechanisms caused by the oscillation kinematics of the caudal fin.

The simulation tool is useful, however, in determining the mechanisms by which the fish can reduce its drag for cases which show good comparison. In addition, for cases which do not compare well, the three-dimensional numerical method can illustrate the unsteady lifting and potential flow features and structures which might promote the dominance of viscous and turbulent behavior. This is easily accomplished through visualization, and a more thorough investigation of the visualization of fluid structures and their manipulation by the undulations of the body can be found in *Chapter 6.*

4.3.4 Effects of recoil - Imposed periodic sway

The real bluefin tuna does not swim in a perfectly straight line. It undergoes both periodic yawing and swaying motions, which are a result of the moment produced about the fish center of mass by the oscillating lifting surface of the tail. These oscillatory motions of the center of mass in the lateral direction are manifestations of the recoil forces and represent one source of energy loss [223, 224]. Thus, a reduction in these motions is desirable to maintain swimming efficiency [242, 243, 125, 127].

For the *RoboTuna* comparisons, the motion of the body is imposed in a straight-line because the basic purpose is to corroborate numerical predictions of the dynamical measurements against experimental results. However, Dewar [47] notes that the tuna body lateral undulations are not insignificant, total double amplitude of the excursion up to 4% of the body length. To investigate the effect of imposing periodic lateral motions on the performance, a periodic sway motions was imposed on the *RoboTuna* simulations, for cases which exhibited exceptional comparison and swimming performance. The sway motion was of the form:

$$y(t) = a_s \sin(\omega t + \epsilon) \tag{4.32}$$

Barrett Run Code		Run 1 j705_03	Run 2 j702_06	Run4 j706_06
Strouhal number St	(–)	0.182	0.198	0.353
Swimming speed U	(BL/s)	0.656	0.656	0.656
Tail circular frequency ω	(rad/s)	6.278	6.830	7.767
Wavelength λ	(BL)	0.936	0.936	1.321
Tip double amplitude A	(BL)	0.120	0.120	0.187
Angle of attack α	(deg.)	24.8	19.0	19.0
Tail phase between pitch & heave	(deg.)	80.0	97.7	97.7
Numerical sway frequency ω_y	(rad/s)	6.278	6.830	7.767
Sway double amplitude A_y	(BL)	0.1	0.1	0.1
Drag reduction (experiment)	(%)	47.7	47.8	43.8
Mean power input (experiment)	(W)	1.07	1.08	3.71
Mean power input (computation w/ sway)	(W)	1.52	4.12	4.47
Mean power input difference (w/ sway)		42.1%	281%	17.0%
Peak power input (experiment)	(W)	2.04	1.99	5.81
Peak power input (computation w/ sway)	(W)	4.36	7.85	9.82
Peak power input difference (w/ sway)		114%	294%	69.0%
Mean computed thrust (w/ sway)	(N)	1.72	2.43	5.07
Peak computed thrust (w/ sway)	(N)	3.33	4.73	8.66
Computational propulsive efficiency η_y	(%)	79.2	41.3	79.5

Table 4.4: Parameters for three simulation cases from Table 4.1 with additional imposed periodic sway motion. Comparison between experimental results and numerical simulations is also given. Body length denoted as BL.

where a_s is the amplitude of the sway motion, constant over the length. The phase parameter ϵ is chosen specific to the initial conditions of the motion simulated, such that the maximum excursion to one lateral side is 90° out of phase with the lateral oscillations of the tail, maintaining the amplitude of lateral tail oscillation and thus the Strouhal number St.

Three cases are considered, with kinematics identical to cases presented in Table 4.1. The amplitude of the sway motion was chosen to be $a_s = 0.05\ BL$, such that the total sway excursion was 10% of the body length, far exceeding that of actual tuna. This sway amplitude exaggeration is intended to promote the deconstructive hydrodynamic effects of recoil. Results of the simulations and comparison to the constrained straight-line motions of the *RoboTuna* are presented in Table 4.4.

The three power time histories for both the experimental runs and the numerical simulations with the imposed sway motions can be found in Figure 4-10. Run 1, Run 2, and Run 4 power time histories are shown as the top, middle, and bottom pairs of records, respectively. Although the qualitative behavior is similar between experiment and simulation, the quantitative comparison is relatively poor, with a much larger power expenditure found through simulation with the imposed sway motions than realized experimentally with the *RoboTuna*. This is in good agreement with the theoretical and biological observations that increased lateral motions result in increased energy wasted and reduced efficiency. The performance consequences of excessive recoil motions may have tremendous impact on further experimental application of fish-like propulsion systems.

4.3.5 Linear theory comparison

Many of the analytic and numerical methods developed to study the dynamics of fish propulsion have relied on assumptions of small amplitude motion and of linear behavior of the velocity field surrounding the fish. It is observable that most fish do not utilize small amplitude tail motions, but rather motions which exceed the limit of classic linear lifting surface theories [26, 212, 204]. Triantafyllou, *et al.* (1993) were able to show that a variety of fish and cetacean swim at speeds with a frequency and large amplitude of the tail motion which is within a narrow range of Strouhal numbers. This is borne out by Videler & Hess (1984) [213], who showed that two species of pelagic predators with large tail beat amplitudes exhibited high Froude propulsive efficiencies, close to the maximum propulsive efficiency of an actuator disk.

Likewise, the use of linear theory to estimate the performance characteristics of the *RoboTuna* is certainly suspect. However, for the sake of completeness, the predictions afforded by classical analytic theory may elucidate some expected behavior, although the experimental performance of the *RoboTuna* and the corresponding numerical simulation performance predictions certainly do not show a simple relationship to the variation of a few kinematic parameters.

Both Lighthill's large amplitude elongated body theory and Lighthill's slender

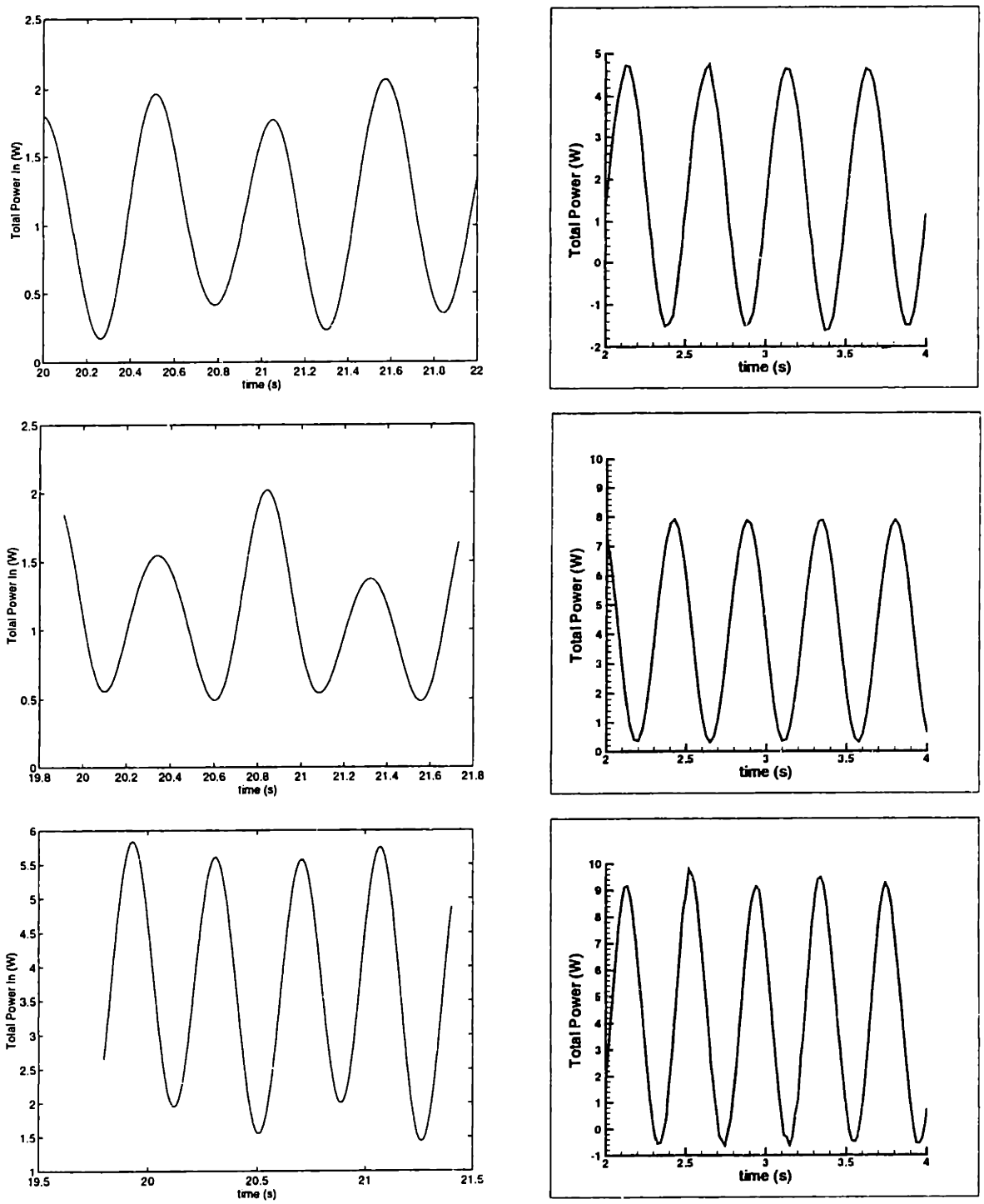

(a) Experimental

(b) Numerical

Figure 4-10: Total power into the fluid for straight-line swimming. Experimental power results for the straight-line motion are presented with power results for simulation with imposed periodic sway motion for performance comparison. The mean power deviation between the (a) experimental (from Barrett, *et al.* (1999) [21]) and the (b) numerical time history power records is for Run 1 (top): 42.1%, for Run 2 (middle): 281%, and for Run 4 (bottom): 17.0%.

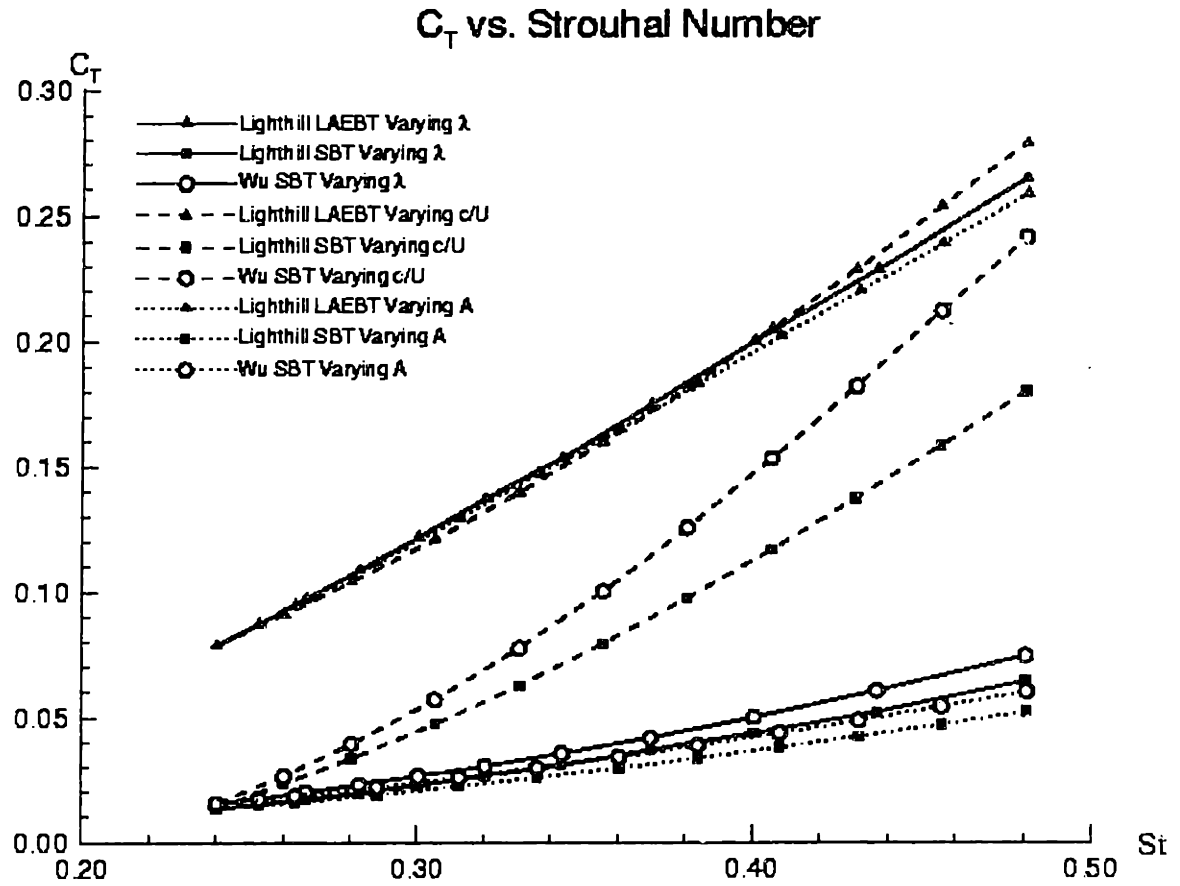

Figure 4-11: Thrust coefficient C_T vs. Strouhal number St for the *RoboTuna* geometry profile and prescribed kinematics. Various linear theory approximations are employed for comparison: Lighthill's large amplitude elongated body theory (▲); Lighthill's general slender body theory (■); Wu's 2D swimming plate theory (o). The behavior of thrust coefficient C_T differs depending on the manner of parametric variation of the Strouhal number St, i.e. by varying: backbone wavelength λ (solid); phase speed of backbone wave c_p/U (dashed); tail beat amplitude (dotted).

body theory are employed to predict the thrust generated by the tuna motion over a range of Strouhal numbers. For comparison, Wu's 2D theory is similarly employed. The Strouhal number is increased over a narrow range by varying three kinematic parameters, one at a time, keeping the other two fixed, namely the backbone wavelength λ, the phase speed of the backbone motion c_p/U, and the tail beat amplitude A. The kinematic parametric dependence of the thrust coefficient variation with Strouhal number St can be seen in Figure 4-11.

The three-dimensional theories of Lighthill require that the profile shape of the

fish be known, so that the rate of change of sectional added momentum can be calculated. The *RoboTuna* computational geometry profile, given by Equations (4.28) and (4.29) were utilized to find the rate of change of the body depth along the length. Similarly, the quadratic backbone amplitude envelope utilized in the experiments and numerical simulations was employed to describe lateral motion of the tail beat A. The rate of variation of the thrust coefficient with Strouhal number is closely dependent on the kinematic parameter varied. Varying the phase speed of the backbone wave c_p/U provokes the most dramatic increase in thrust coefficient with Strouhal number. It should be noted that if the amplitude envelope increase was linear instead of quadratic, the variation of the thrust coefficient by varying amplitude A or wavelength λ would be identical for all three theories.

As expected, Lighthill's large amplitude elongated body theory yields the largest thrust predictions over the range of Strouhal numbers considered. However, the monotonic behavior of the performance with Strouhal number is not corroborated by the experimental measurements or the numerical simulations, and the validity of its applicability is dubious. The reasons for these differences likely include the numerous nonlinearities of the physical problem mentioned previously, such as vorticity dynamics and viscous phenomena, underlining the limitations of the linear theory.

4.4 Steady swimming of a Giant Danio

4.4.1 Visualization of live fish swimming

Several researchers have studied through visualization the wake of a naturally swimming fish. Techniques which have been used with moderate success include dye visualization [172, 7] and visualization using a stratified layer [172, 150]. Neither method has elucidated all the details of the flow near the body and in the wake. Stamhuis and Videler [186] utilized experimental particle image velocimetry to capture the flow dynamics around several live swimming organisms and to analyze the energetic makeup of the wake. Anderson [9] used experimental digital particle image

velocimetry (DPIV) to visualize the wake behind a swimming Giant Danio (*Danio malabaricus*) and identified the active manipulation of shed wake vorticity to create a reverse Kármán vortex street. Müller, *et al.* [153] analyzed the wake of a swimming mullet (*Chelon labrosus* Risso) using similar DPIV techniques and concluded that the manipulation of the wake structure resulted in high propulsive efficiencies. Ames [8] demonstrated that shallow water effects cause stronger shedding of body-generated vorticity further upstream from the body through flow visualization with live fish, more clearly elucidating the qualitative mechanics of swimming.

Whenever possible, the results obtained by the present numerical method will be compared to flow visualizations obtained through the use of DPIV. A brief description of the DPIV experimental technique and its limitations is included herein for background.

DPIV explained

Particle image velocimetry has been shown to be the method of choice for flow visualization around live fish. DPIV was first introduced by Willert and Gharib [230] for flow measurement and visualization. A fluid domain is filled with neutrally buoyant flourescent particles, and a laser sheet illuminates a plane of the flow. A video camera then takes pictures of the flow looking down on the plane in rapid succession, such that sequential images are not separated by more than a very short time dt. The images are then compared, and relative particle displacements are analyzed to approximate the velocity field through the plane. With DPIV, an entire two-dimensional velocity field can be measured at one instant in time, with simultaneous flow visualization. Using DPIV, one experiment is required to map an unsteady flow, whereas with other single point methods, we would have to do many experiments with many probes and considerable post-processing to accomplish the same goal. The DPIV method derives from the analog flow measurement techniques of laser speckle velocimetry (LSV) and particle image velocimetry (PIV).

The DPIV algorithm is applied to two images of the flow separated by small time dt, and small subsets of image data (interrogation windows) are compared at

the same location in each image by computing the spatial cross correlation. When the particle images match well, the cross correlation function is sharply peaked, and the location of the peak marks the displacement of the particle image pattern. The algorithm is then applied throughout the images to obtain the entire flow field. For a complete discussion of general DPIV capabilities and limitations, see Willert and Gharib [230]. Unique problems arise in the use of DPIV to visualize flows around moving, deformable bodies. As the fish swims and boundaries move, interrogation windows cross boundaries and contain spurious image data. This biases the cross correlation peak towards the displacement of the boundary, resulting in spurious displacement data for the fluid near the boundary. A complete discussion of the near-body DPIV techniques we employ, including their capabilities, limitations, and validation, can be found in Anderson [9]. Further, while the fish in the experiments conducted by Stamhuis and Videler [186], Anderson [9], and Müller, *et al.* [153] showed no adverse reaction to either the laser light sheet or the particles seeding the fluid, Ames [8] has developed a novel imaging system using organic particles which fluoresce at a non-visible wavelength, which can then be imaged with an infra-red filter on the camera. This technique has great potential for improving the flow visualization testing conditions on the fish to those which would ensure more natural swimming behavior.

4.4.2 Experimental evidence

Anderson [9] developed novel near-body flow visualization techniques using digital particle image velocimetry (DPIV), which were employed to study the flow around swimming fish. In this manner, the wake features of steadily swimming fish may be resolved well in a mid-body plane, as described by Müller, *et al.* (1997), for a continuously swimming mullet (*Chelon labrosus* Risso). These DPIV techniques were used to study the steady straight-line swimming motions of the Giant Danio, whose morphology is pictured in Figure 4-12. Several fish were used with varying lengths between 5 and 10 cm. The maximum span of the caudal fin was approximately 23 percent of the body length. Whenever possible, data will be presented normalized

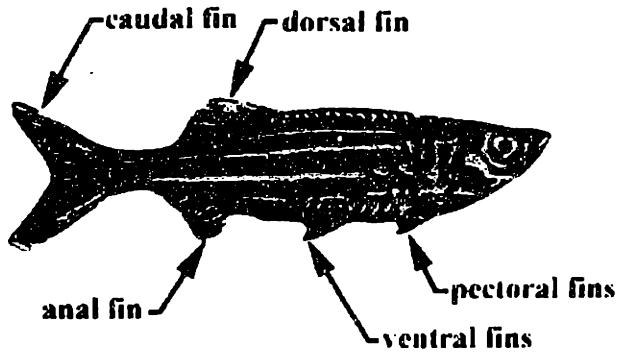

Figure 4-12: Morphology of the Giant Danio (*Danio malabaricus*). Taken from (Anderson (1996) [9].

with respect to fish body length, hereafter denoted as ℓ.

Several steady straight-line swimming cycles of the Giant Danio were captured and studied using DPIV. Figure 4-13 summarizes the experimental apparatus for DPIV implementation in the experiments. As illustrated in Figure 4-13, the fish was confined in a layer of fluid ($\approx$ 3 *cm* thick) between the free surface and a highly permeable screen comprised of a steel wire grid (2.5 cm openings) and a fine nylon mesh ($\approx$ 3 mm openings). The clearance between the fish and the screen and free surface was not formally measured but was estimated to be 3 mm. The screen confined the fish yet allowed fluid to pass through it. The screen was approximately 25 *cm* from the tank bottom. The flow in the horizontal symmetry plane of the fish was revealed by orienting the laser light sheet at the mid-depth of the confinement layer. The horizontal mid-plane of the fish is illuminated from the side and imaged from above. In general, the light sheet illuminated the fish at the caudal fork; however, in some instances slight bending of the caudal fin caused the tips of the tail to be illuminated. One particularly clear case is presented where the fish swam directly away from the light source, thus revealing the flow on both sides of the body and in the wake without shadows. For this case, the fluid ahead of the fish was nearly stationary and all motion can be attributed to the motion of the fish. Velocities very near the body boundary are not shown in the following results because the image of the fish itself contaminates the flow image data. Spurious data are directly removed, and adjacent data are treated specially to avoid inclusion of contaminated data in

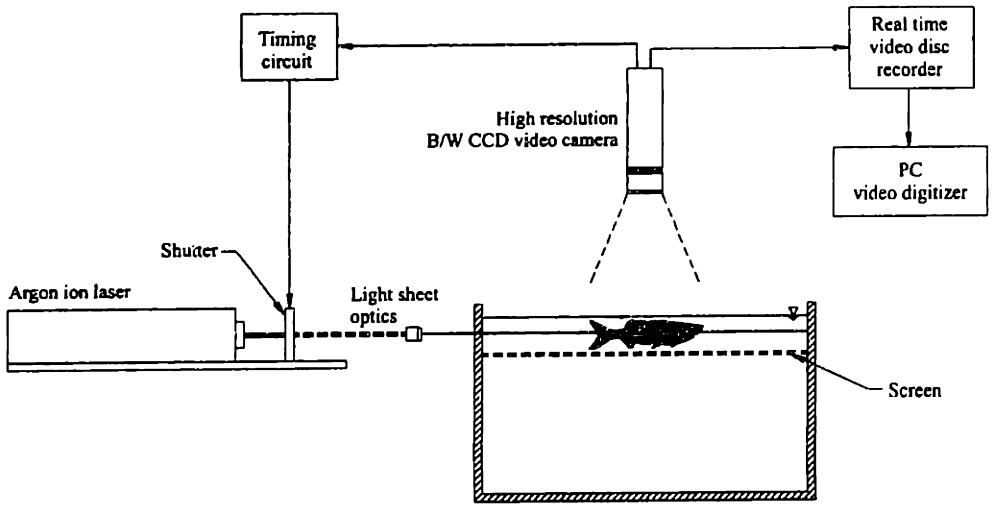

Figure 4-13: Schematic diagram of experimental DPIV apparatus. A 51 x 25 x 28 cm glass tank, was seeded with small (20-40 μm diameter), neutrally buoyant fluorescent polymer spheres. A planar slice of the flow approximately 3 mm thick was illuminated with a 6 watt Argon-ion laser connected to a fiber optic cable and light sheet optics. Taken from Wolfgang, *et al.* (1999) [233].

the smoothing filter and calculations of vorticity and circulation.

Figure 4-14 (from Wolfgang, *et al.* 1999 [233]) shows the velocity field and vorticity contours adjacent to and in the wake of the fish while steadily swimming straight at 8.9 cm/s (1.1 body lengths per second), a normal swimming speed for the Giant Danio. The fish was swimming roughly at a constant mean velocity for the duration of the cycle captured, traveling steadily from one end of the tank to the other. As a result, any acceleration or deceleration of the body occurred well before or after the images shown in Figure 4-14, so the flow features are typical of steady-state motion. Nearly one swimming cycle is shown with the successive data sets separated by approximately 0.22 T, where T is the period of the tail oscillation. The figures show the fish body exactly as it appears in the first image of each image pair except that it is colored uniformly for clarity. Slight variations in the body image exist due to the fact that in some cases the caudal fork is illuminated by the laser sheet while in other cases the caudal fin tips are illuminated.

At the start of the swimming cycle, along the top of Figure 4-14, the fish tail is

in the maximum downward position. A clockwise vortex is forming with its center near the tip of the tail as a result of shed body-generated vorticity associated with the body undulation. The vortex is already well formed although at this point the tail has not begun its upward motion. Subsequent upward tail motion will contribute same-signed vorticity to this vortex. Immediately below the fish and slightly anterior to the tail, the flow follows the upward velocity of the body. Slightly upstream of this position at approximately the mid-body of the fish, longitudinal flow towards the tail marks the formation of the next bound counterclockwise vortex.

In the second set of plots of Figure 4-14, the tail has moved upward, and the new clockwise vortex is now clearly visible in the wake. The region of longitudinal flow has moved rearward and upward with the tail motion. In the third pair of plots in Figure 4-14, the tail is in its maximum position ready to begin the downstroke. The flow on the upper side of the fish follows the body motion downward which defines the circular flow that becomes the next counterclockwise vortex. The bottom of Figure 4-14 shows this new vortex in the wake as well as the next clockwise vortex forming along the body. The swimming cycle then concludes with the tail in the maximum downward position and the next clockwise vortex positioned at the tail tip, ready to be shed on the upstroke.

The closed circular contours shown in Figure 4-14 indicate concentrated vortices arranged in a jet pattern. Body bound vorticity can not manifest itself, as that would require processing of the velocity field through the body of the fish. The wake organizes into a stationary reverse Kármán street: vortices align in a staggered pattern such that the net wake produces a jet flow. The maximum velocity along the centerline of the jet is approximately 90% of the average velocity of the fish. The flow adjacent to the fish is strongly influenced by the body undulation as demonstrated by the clockwise flow at approximately three quarters of the body length from the nose. This clockwise flow is the beginning of the next vortex destined to be shed by the tail into the wake. The new "vortex" is formed well *before* encountering the tail. The increasing lateral motion of the posterior body region augments the circulation and strengthens the vortex before it is shed into the wake, just before and at the

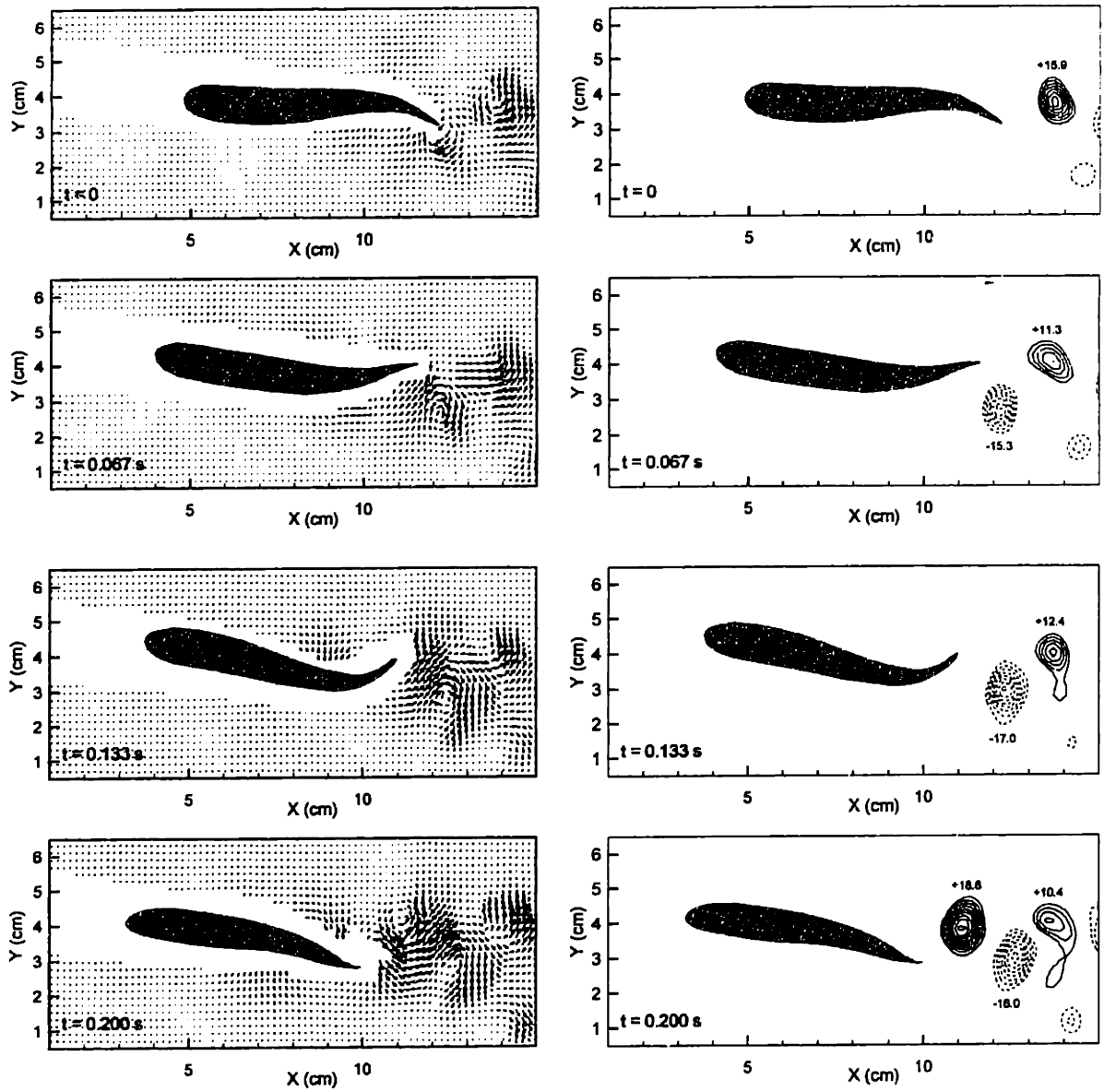

Figure 4-14: Velocity field (left) and vorticity contours (right) during straight, steady swimming of the Giant Danio. Each arrow represents one cross correlation calculation with the length indicating the relative magnitude of the velocity. The maximum velocity shown is approximately 8 cm/s. Vorticity contours range from -5.0 to -20.0 and $+5.0$ to $+20.0$ in $\pm 1.67\ s^{-1}$ increments. Kinematic parameters of the straight-line swimming motion: swimming speed $U = 1.1\ \ell/s$; tail beat frequency $f = 3.3\ Hz$; tail tip double amplitude $A = 0.16\ \ell$; backbone wavelength $\lambda = 1.1\ \ell$; Strouhal number $St = 0.45$. Taken from Wolfgang *et al.* (1999) [233].

peduncle. The tail manipulates this vorticity through repositioning and shedding of additional vorticity.

4.4.3 Numerical modeling

To develop the numerical model of the danio body, we consider the geometry of the actual fish, as shown in Figure 4-12. Computational forms are chosen to include the major load bearing portions of the geometry, including the body, the caudal fin, and the smaller lifting surfaces such as the dorsal and anal fins.

The viscous effects of the fluid are assumed to be confined to a thin boundary layer near the body and a thin shear layer wake. As a result, it is reasonable to assume that the near-body viscous effects on the body are small in comparison to the effects of unsteady vorticity generated by separation, such as that which would occur at the sharp trailing edge of the various fins. The tail is assumed to generate the largest wake, and a primary separation line as chosen to be the trailing edge of the tail. Although the danio possesses a large dorsal fin, a large anal fin, and smaller ventral and pectoral fins, these edges are treated differently in the following cases. It is obvious from the experimental evidence that the tail realizes the greatest unsteady motion amplitudes, which would sustain the largest unsteady lifting forces and generate the strongest vorticity structures; however, the influence of vorticity shed upstream on the tail by secondary lifting surfaces on the flow around the tail, the total wake structure, and the force on the body is unclear.

Lighthill (1975) hypothesized that if the gap between the dorsal and caudal fins, any vorticity shed from dorsal or ventral lifting surfaces would behave much differently than a fin bridging the gap between the two fins, and the spatial phase between the tail and the dorsal fin motions may result in recovery of upstream energy shed. Streitlien *et al.* (1996) showed this type of energy recovery through simulation of an oscillating two-dimensional foil in a stream with regions of distributed vorticity, as shed by an upstream bluff body.

For this reason, two different geometries are chosen. The first geometry, hereafter called Body I, includes the main portion of the body and the caudal fin, as shown in

the top portion of Figure 4-15. The body sections are assumed to be elliptical with a major to minor axis ratio of $AR = 2.2$, where the major axis corresponds to the height of the body. A curvefitting technique is used to determine the profile shape of the body with $\ell = 1.0$, and is given simply by:

$$z(x) = p(x) \pm 0.305 \tanh(6x + 1.8) \quad \text{for} \quad -0.3 \leq x \leq 0.1 \tag{4.33}$$

$$z(x) = p(x) \pm (0.15 - 0.152 \tanh(6.3x - 3.08)) \quad \text{for} \quad 0.1 \leq x \leq 0.7 \tag{4.34}$$

$$p(x) = 0.195 * \tanh -(3.0 + x/1.5) + 0.195 \tag{4.35}$$

The caudal fin is is assumed to have chordwise sections of NACA 0016 shape, to allow for efficient resolution of leading edge suction forces. The caudal fin leading edge and trailing edge profiles for the semi-span are also determined through a curvefitting technique, and are given simply by:

$$x(z)_{LE} = 39.543z^3 - 3.685z^2 + 0.636z \tag{4.36}$$

$$x(z)_{TE} = -40.74z^3 + 9.666z^2 - 0.15z + 0.1075 \tag{4.37}$$

where $0 \leq z \leq 0.15$. The leading edge of the tail at midspan intersects the posterior end of the body's contraction region. The entire body length is then scaled to $\ell = 1$. The numerical grid in the region of the caudal peduncle, where the body and tail intersect, is artificially smoothed. This simplification allows for rapid repaneliza-tion of the structured grid and ease of relative panel motion. Again, the differences in the peduncle contraction region between the numerical form and the actual danio are assumed to have a small effect on the hydrodynamic similitude, as this region sustains a small hydrodynamic load and serves to transmit force from the oscillating tail to the center of mass of the body, as well as to minimize hydrodynamic recoil forces [124, 125, 127]. Recent work by Kagemoto [96] shows that the fish morphology is optimized through this necking peduncle region to minimize the recoil forces

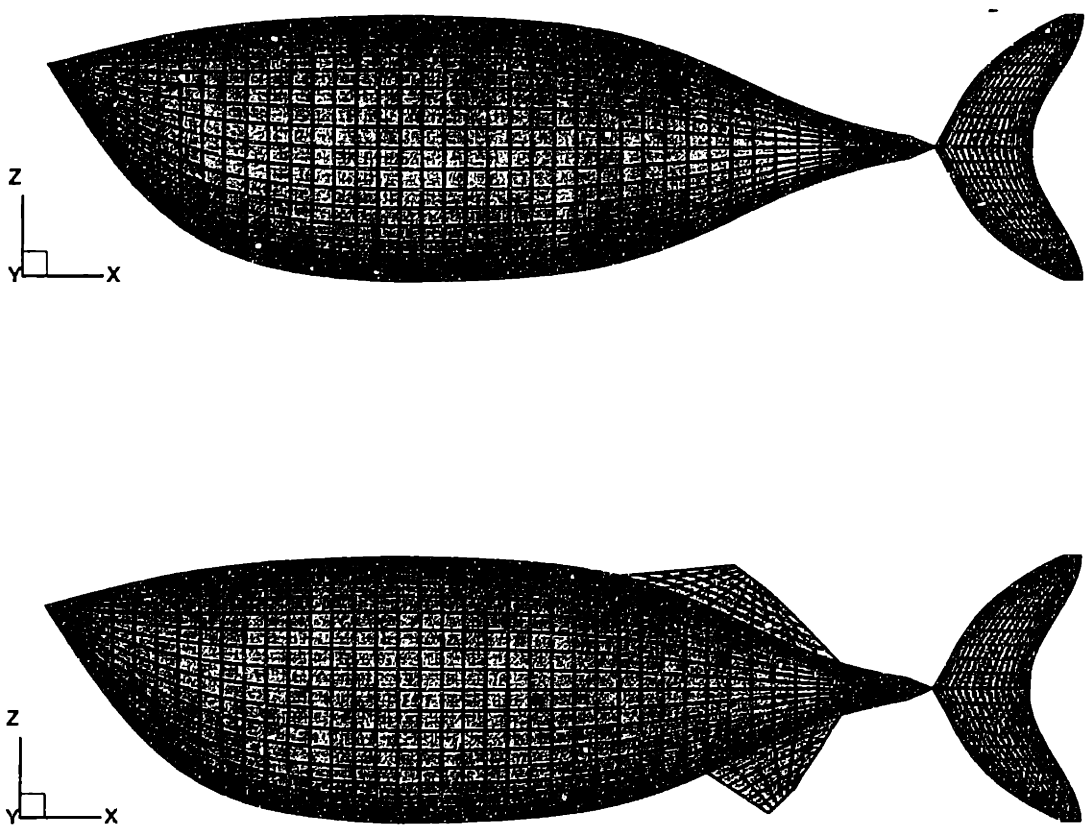

Figure 4-15: Computational forms chosen for a Giant Danio: Body I - caudal fin only (top), Body II - caudal, dorsal, and anal fins (bottom).

and maximize the propulsive efficiency for *Carangiform* swimming motions. Additional geometric differences between the numerical body representation and the live danio include the omission of the anal and dorsal fins, and the smaller ventral and pectoral fins. The smaller ventral and pectoral fins are assumed to have minimal effect on propulsion and may be important to affect maneuvering and are neglected in this analysis. The roles of anal and dorsal fins in propulsion are investigated by implementation of two different wake shedding schemes.

The trailing edge of the caudal fin is assumed to be the single wake producing edge on the fish in the first wake shedding scheme, hereafter referred to a scheme A. Upstream shed vorticity is assumed to have a negligible influence on the flow into the caudal fin, the downstream wake structure, and the total force on the fish. Scheme A is illustrated in Figure 4-16. The second shedding scheme, scheme B, also illustrated in Figure 4-16, models the vorticity shedding from the trailing edge by defining separation lines along the dorsal and ventral contraction regions anterior to the caudal peduncle. These separation lines are fixed along these midbody profile axes, and it is assumed that for straight-line swimming of moderate tail excursion, the dynamics of backbone-shed vorticity will not differ greatly from the dynamics of the vorticity shed from the actual dorsal and anal fins.

A second geometry, shown in the bottom of Figure 4-15 and hereafter referred to as Body II, was developed to model the dorsal and anal fins, requiring the implementation of a third wake shedding scheme, scheme C, also shown in Figure 4-16. The fins are attached to the body, roughly along the axes of the ventral and dorsal separation lines found in scheme B for Body I, and are modeled as zero-thickness vortex-lattice lifting surfaces. These fins remain attached to the body along the same axes but are allowed to flex with the prescribed motion of the body. Each fin is assumed to shed a vortex wake from its trailing edge.

Shown in Figure 4-17 is a typical straight-line swimming case employing the three different shedding schemes, revealing the nonlinear wake sheet deformations and interactions. Figure 4-17(a) is an example of shedding scheme A, with clean separation of the main wake from the trailing edge of the caudal fin and with a lack of body-wake

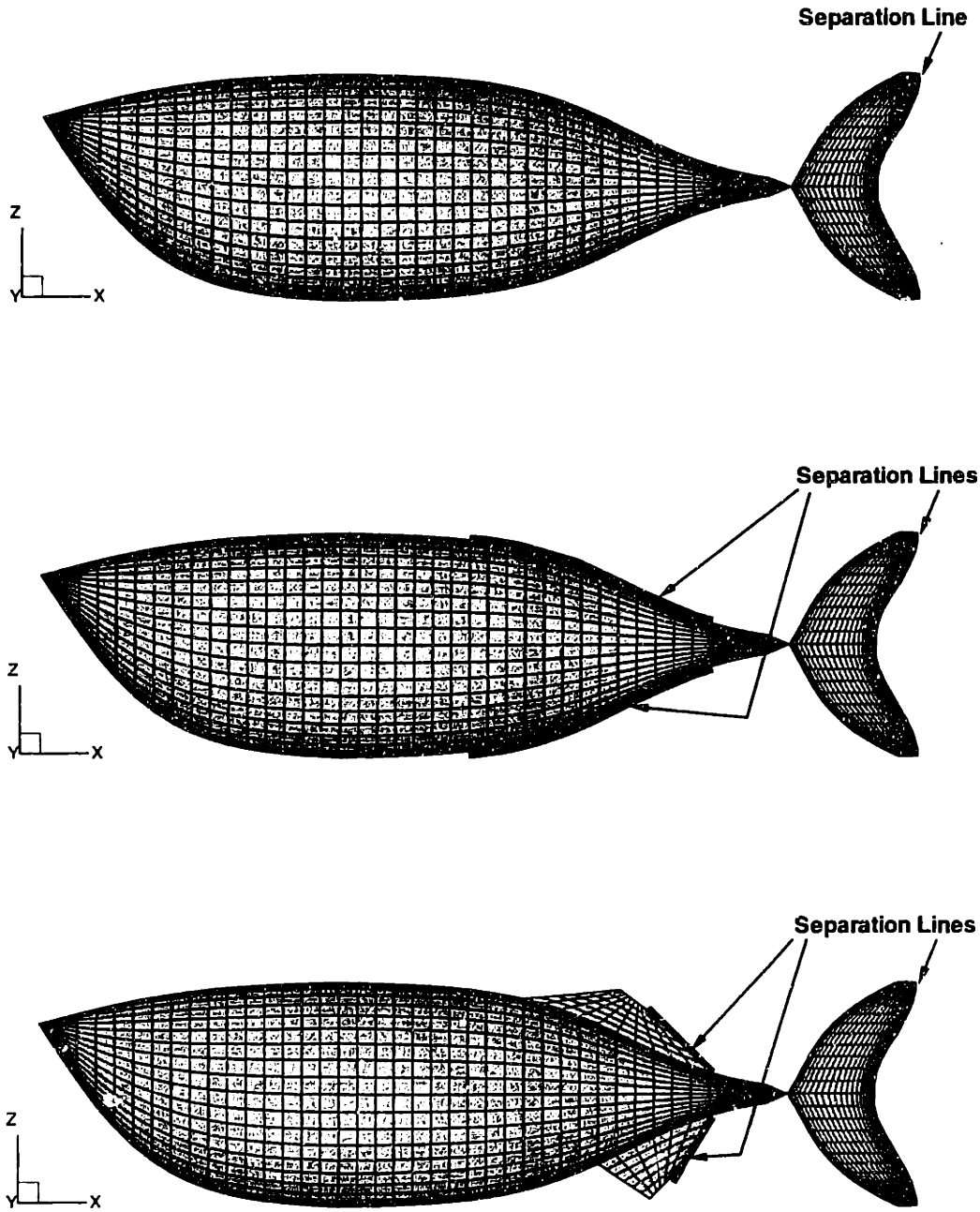

Figure 4-16: Various wake separation schemes chosen for the computational forms chosen for a Giant Danio: Scheme A - caudal fin shedding only (top); Scheme B - dorsal and ventral separation lines with cadual fin shedding (middle); Scheme C - dorsal, anal, and caudal fin separation (bottom).

interactions. The wake rolls up behind the tail, forming a reverse Kármán vortex street structure and thrust jet, under the self-influence of the shed vorticity and the body perturbation velocity influence as well. Vorticity strengths reveal the structure of the vortex rings comprising the thrust jet. Figure 4-17(b) reveals the wake interactions resulting from shedding scheme B under straight-line swimming conditions. The dorsal and ventral shedding regions produce wakes, whose strengths oscillate due to the unsteady body undulations. These wakes then tightly roll-up before reaching the leading edge of the caudal fin, through the influence of oscillating body perturbation velocities and the self-influence of the shed vorticity. Figure 4-17(c) clearly demonstrates the effects of modeling the thin dorsal and anal fins as vortex-lattice lifting surfaces with clearly defined trailing edges. While the thin fin trailing edges are not entirely vertical, they are closer to the leading edge of the caudal fin, which reduces the roll-up effects seen in Figure 4-17(b), and which allows the thin fin wake sheets to interact more cleanly with the caudal fin wake.

4.4.4 Imposed motion description

The kinematic history of the Giant Danio straight-line swimming motions is obtained from the experimental sequence of images taken over several swimming cycles using DPIV, such as in Figure 4-14. From this information, we derive the analytic representation for the swimming motions. It is observed that the Giant Danio motion generally resembles a *carangiform* motion. *Carangiform* swimmers possess tapering tails of medium length which terminate in a well-defined caudal fin. The *carangiform* motion is characterized by a smooth, amplitude-modulated traveling wave moving along the length of the fish backbone with a phase speed $c_p = \omega/k$, which is in general different from the swimming speed U. In this description, $k = 2\pi/\lambda$ is the wavenumber, corresponding to the wavelength of the backbone perturbation λ, and ω is the circular frequency of oscillation. The transverse amplitude of the backbone motion $y(x)$ gradually increases along the length, such that the primary propulsive motions are confined to the tail region.

Based on the experimental observations made of the Giant Danio using DPIV,

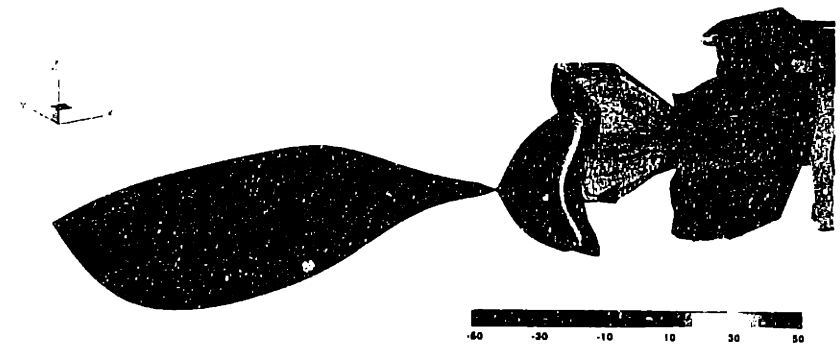

(a) Shedding scheme A

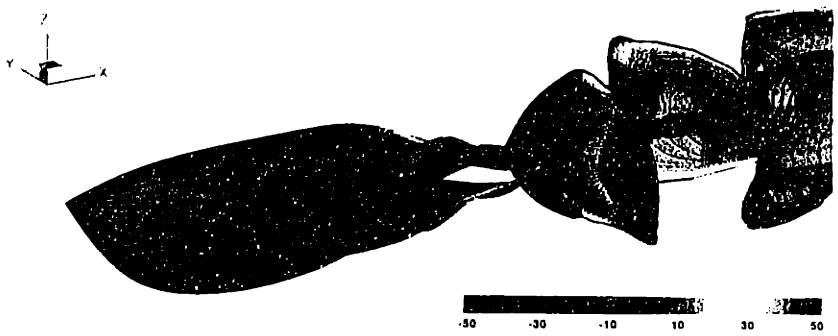

(b) Shedding scheme B

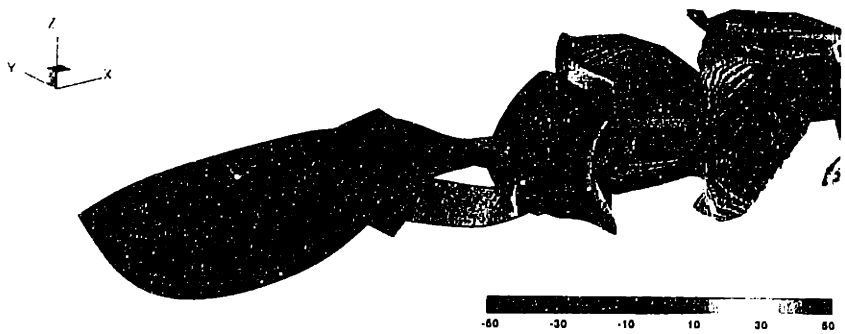

(c) Shedding scheme C

Figure 4-17: Employing the various shedding models to reveal the wake structure behind the computational danio geometry during straight-line swimming simulation.

which are discretized from Figure 4-14, the analytic description of the motion was curve-fitted to be purely sinusoidal and to consist of a smooth amplitude-modulated traveling wave along the body length with constant phase speed, $c_p = \omega/k$ for a constant swimming speed U. The imposed transverse motion $y(x,t)$, with x measured from the nose, has the form:

$$y(x,t) = a(x)\sin(kx - \omega t) \tag{4.38}$$

where $a(x)$ is the amplitude envelope, again given the form of a quadratic function with c_1 and c_2 are adjustable parameters, as described previously. Dimensionless parameter c_1 is selected as an independent, while c_2 is chosen to achieve a specific value of the double-amplitude of motion, denoted by A, along the length of the body and, primarily, at the tail. These parameters, obtained from the discretizations of the DPIV data of Figure 4-14, are used to develop the imposed motion description for the computational inviscid model. We chose to impose the measured motion because the basic purpose is to corroborate numerical predictions of the detailed flow against experimental results. Then, numerical results are used to investigate the details of the flow development that cannot be easily observed in the experiment.

4.4.5 Flow profile comparison

Both Body I and Body II are employed to investigate the straight-line swimming of the Giant Danio as obtained during the experimental DPIV runs. The kinematic parameters which prescribe the motion are those calculated from experimental DPIV images, specifically: swimming speed $U = 1.1\ \ell/s$; tail beat frequency $f = 3.3\ Hz$; tail tip double amplitude $A = 0.16\ \ell$; backbone wavelength $\lambda = 1.1\ \ell$; Strouhal number $St = 0.45$; phase angle between pitch and heave of the tail motion $\phi = 95^o$; and tail angle of attack $\alpha = 6^o$.

Figure 4-18 illustrates the flow patterns is relation to the three-dimensional computational geometry kinematics of Body I. The streamtraces reveal the two-dimensional velocity components in the mid-plane of the body, sectioning the caudal fin at midspan,

contoured by the strength of the dynamic pressure coefficient components. While the velocity vectors in this plane, in general, may have three-dimensional vertical components, careful analysis reveals that the flow is strongly two dimensional in most regions along the body at this depth for all separation schemes and body geometries. Shedding scheme B is chosen for display in the figure 4-18 for clarity, although the wake sheet structure is absent in this representation, to give a visual correlation between the caudal fin and flexible body kinematics with the prominent in-plane flow features.

Focusing on the midbody plane flow dynamics, the in-plane flow properties are replotted for Body II and separation scheme C, due to the improved geometric similarity with that of the live Giant Danio. Figures 4-19 through 4-22 highlight many of prominent features developing during the course of a straight-swimming period. Figure 4-19 illustrates the midbody plane velocity vectors and streamlines at eight discrete intervals over the swimming cycle. Velocity vectors densely grid the plane, scaled in size by the magnitude of the local velocity, so that far from the fish they may appear as points. In-plane streamlines are superimposed on the velocity vector grid to clarify the direction and the structure of the flow perturbations. Although the streamlines in this representation are continuous, the magnitude of the fluid velocity drops off greatly in this reference frame as the distance from the fish body increases. While the velocity vectors in this plane, in general, may have three-dimensional vertical components, careful analysis reveals that the flow is strongly longitudinal in most regions along the body at this depth for all separation schemes and body geometries. While the flow around the top and bottom of the fish body has strong three-dimensional behavior, sectional plane profiles along the body length show that the flow in the mid-plane is entirely longitudinal and has no vertical components. The complexity of the flow at other depths will be addressed in Section 4.5.

The color contours of the velocity vectors in Figure 4-19 are correlated to the sign and magnitude of the vertical vorticity component ω_z. The red vorticity indicates a clockwise or positive circulation, and the blue vorticity indicates a counterclockwise or negative circulation. The green areas are irrotational. Details of the wake

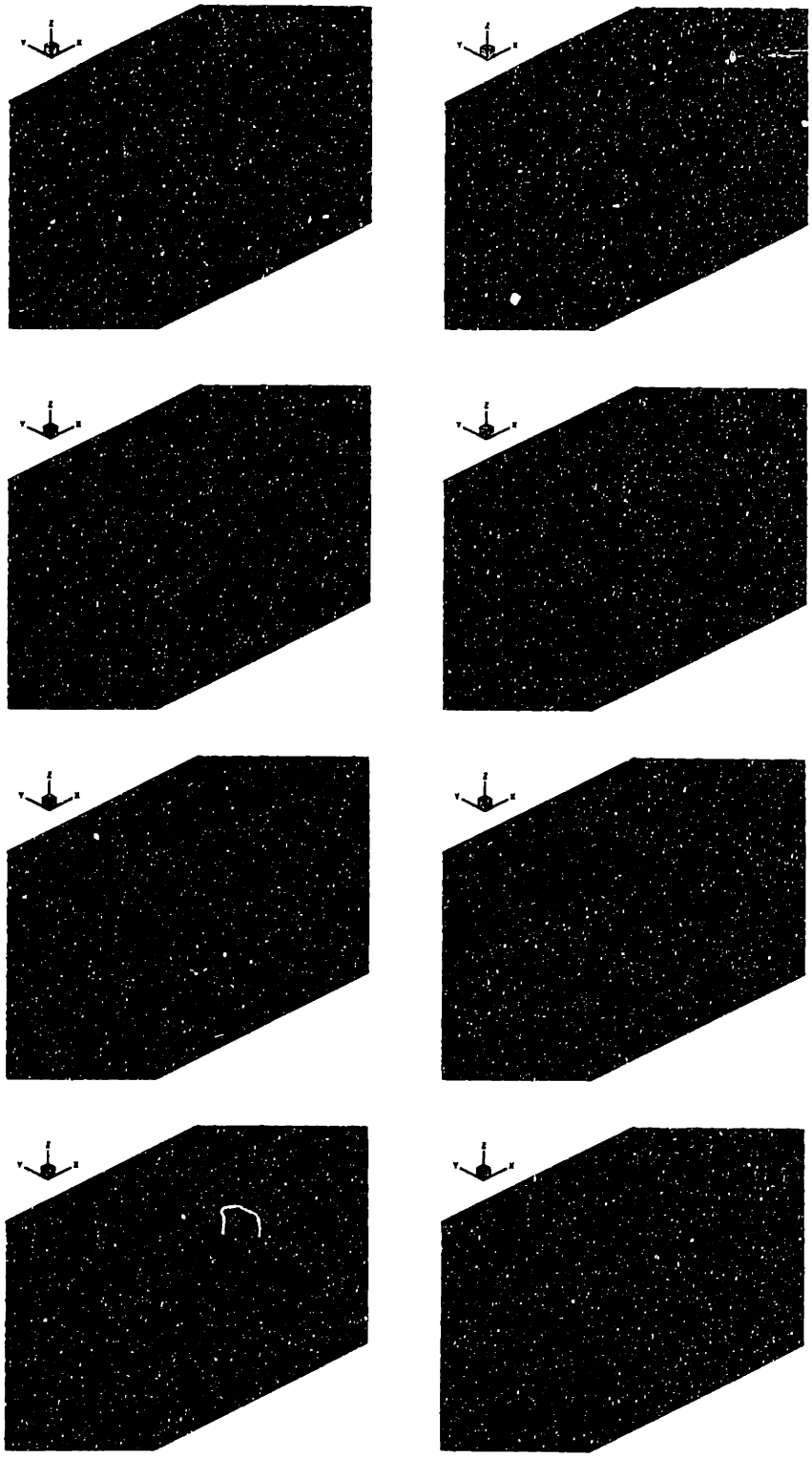

Figure 4-18: Mid-plane depth $z = 0.5H$ flow profiles for one period of the fish swimming motion. In-plane velocity streamlines (black) are superimposed on velocity vectors. Velocity vectors are scaled in size by velocity magnitude and in color by dynamic pressure coefficient (Range:[0 (green),2 (red)]). Sequence is shown top to bottom, first left then right column, at intervals of $T/8$.

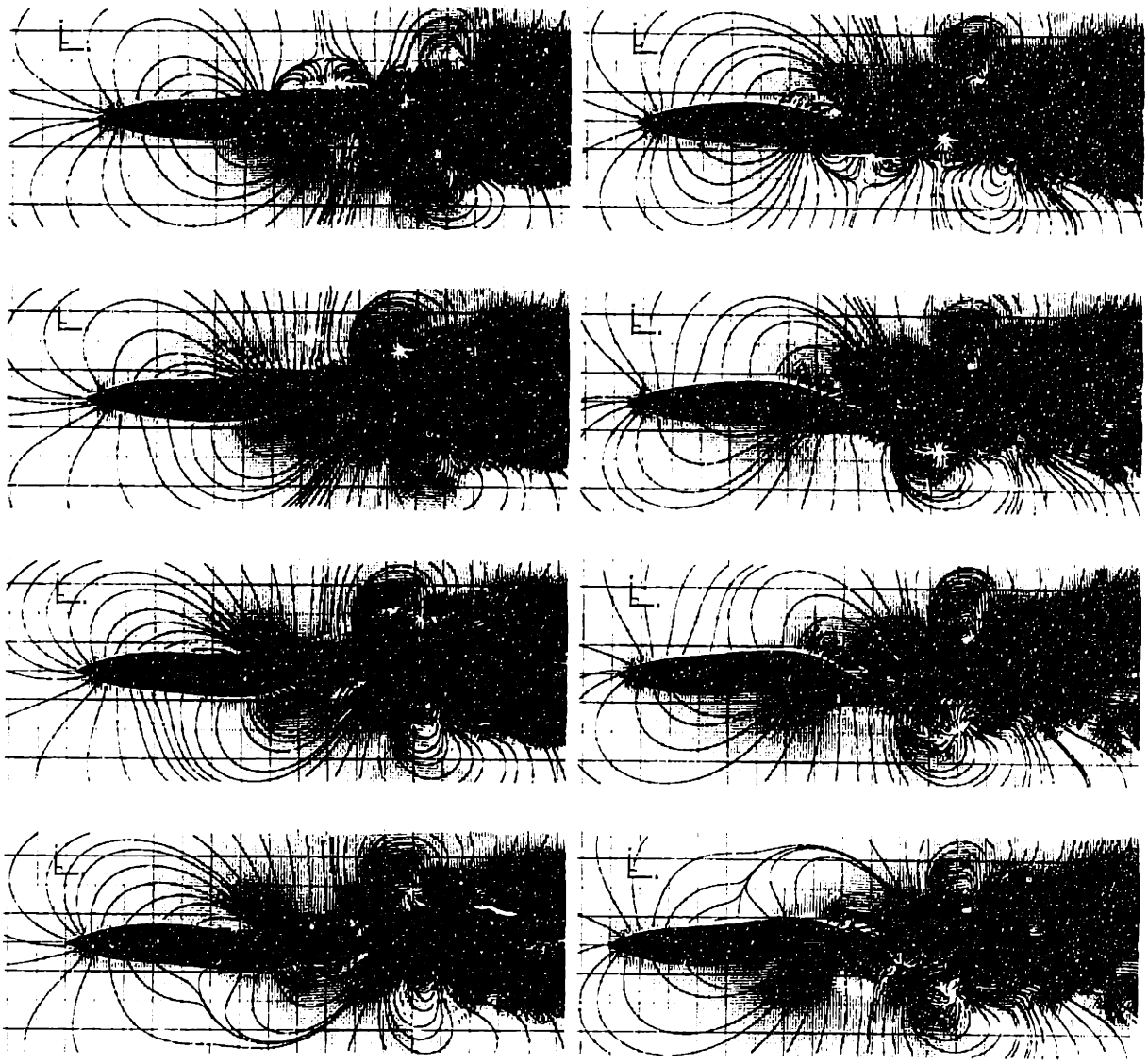

Figure 4-19: Mid plane depth $z = 0.5H$ flow profiles for one period of the fish swimming motion viewed from above. In-plane velocity streamlines (black) are superimposed on a dense velocity vector grid. Velocity vectors scaled in size by velocity magnitude and scaled in color by vertical vorticity ω_z contours (Range:$[-10s^{-1}, 10s^{-1}]$). Red vorticity indicates clockwise rotation, blue vorticity indicates counterclockwise rotation, and green regions are irrotational. Sequence is shown top to bottom, first left column, then right column, at intervals of $T/8$.

structure dynamics and the developing thrust jet are evident also in figure 4-20, which shows the wake vorticity contours ω_z over the swimming cycle. These vorticity contours compare favorably with the experimental results shown previously in Figure 4-14, with similar wake strength and developing wake dynamics. The formation of a steady thrust jet is evident through the unsteady dynamics of the oscillating caudal fin, continuously shedding and manipulating wake vorticity of oscillating strength. Streamline trajectories are determined using a fourth-order Runge-Kutta spatial integration with linear interpolation between grid points. The absence of small-scale turbulent fluctuations in the numerical representation of the fluid dynamics obviates the need for higher-order integration and interpolation schemes. The rectangular grid relevant length is $d\ell = 0.01$ based on the body length $\ell = 1$.

Figure 4-21 illustrates the thrust jet region and the near body flow dynamics by correlating the perturbation velocity vector magnitude with the dynamic pressure contours at regular intervals over the swimming cycle. Figure 4-22 similarly illustrates the dynamic pressure contours only over the course of the swimming cycle. Both Figures show the thrust jet region and the near body flow dynamics by showing the dynamic pressure contours at midbody depth, at regular intervals over the course of the swimming cycle. The dynamic pressure contours reveal low pressure regions formed upstream, along the midsection region and contraction region of the fish body length, which are then manipulated by the oscillation of the afterbody. Specifically, the controlled actuation of the caudal fin intercepts these low pressure regions as they progress posteriorly in the local body frame of reference and pass in the region on the inside of the maximum lateral excursion of the caudal fin. As the caudal fin is swept to the other side through the low pressure region, the separation from the sharp trailing edge of the caudal fin contributes to the formation of a reverse Kármán vortex street. This vorticity control and production interaction mechanism contributes to the efficient production of the thrust jet comprising the wake of the straight-line swimming motions, evident from the contours of dynamic pressure or momentum in the fluid from Figures 4-21 and 4-22.

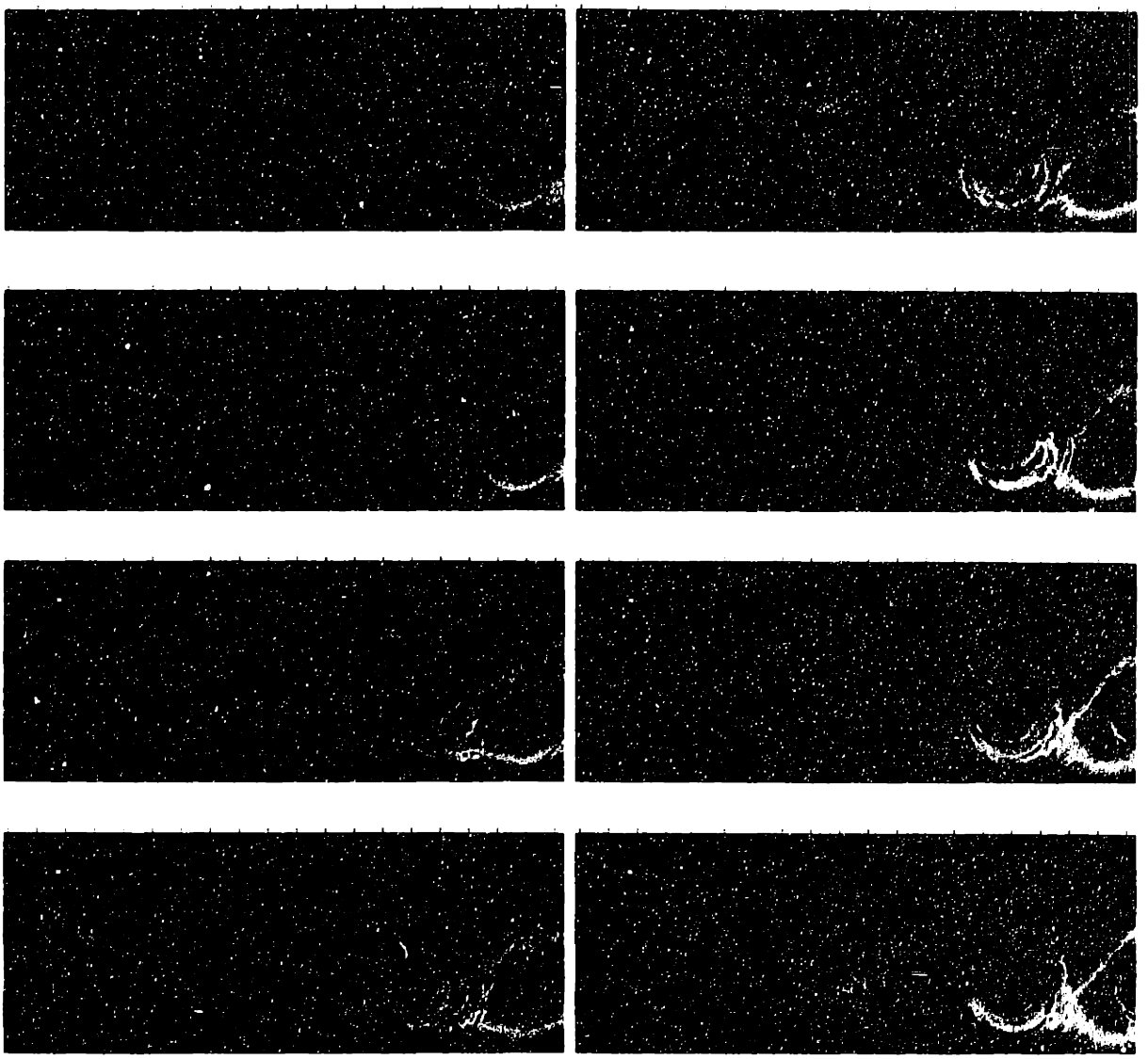

Figure 4-20: Mid plane depth $z = 0.5H$ flow profiles for one period of the fish swimming motion viewed from above. Vertical vorticity ω_z contours shown only (Range:$[-10s^{-1},10s^{-1}]$). Red vorticity indicates clockwise rotation, blue vorticity indicates counterclockwise rotation, and green regions are irrotational. Sequence is shown top to bottom, first left column, then right column, at intervals of $T/8$.

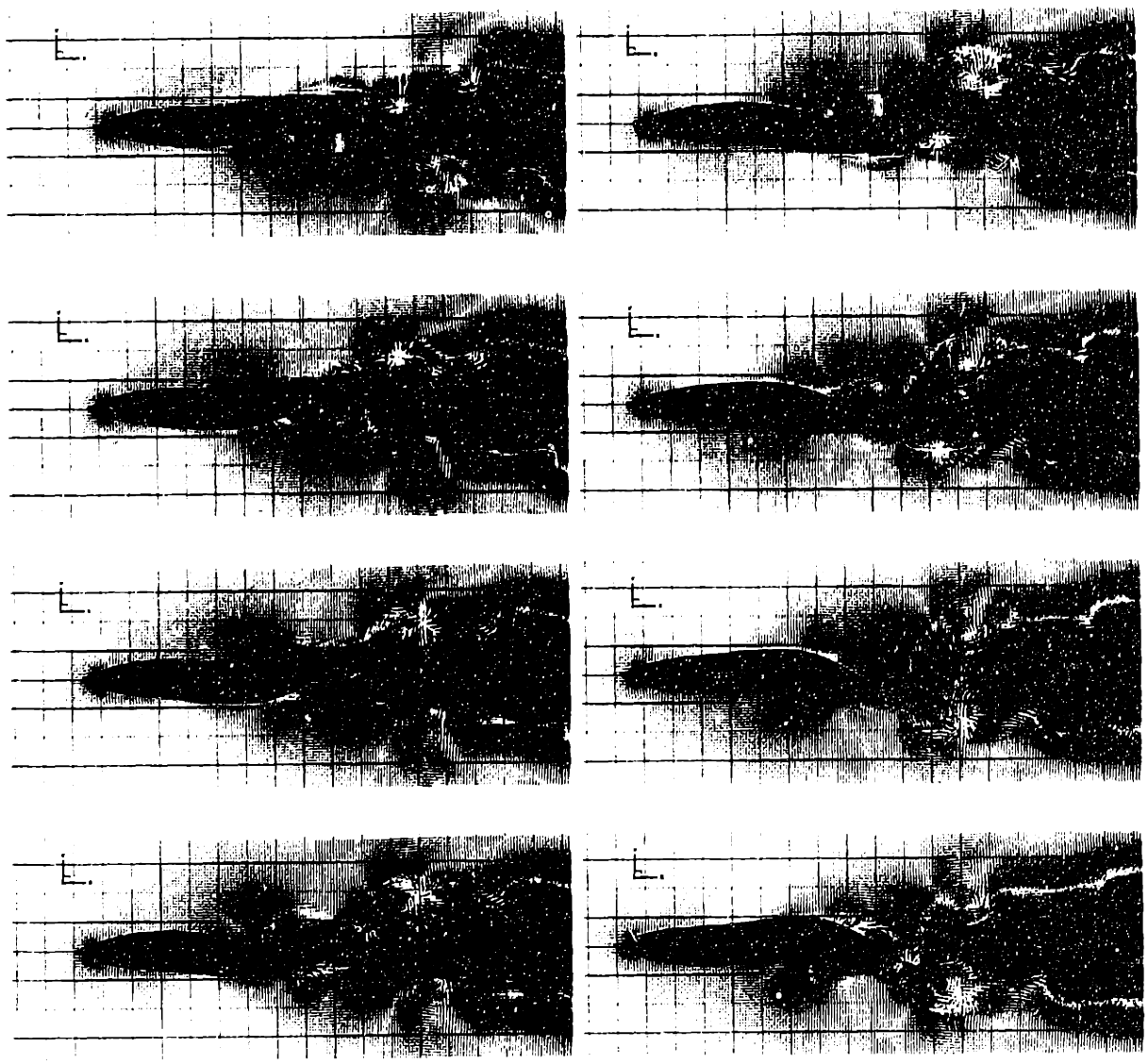

Figure 4-21: Mid plane depth $z = 0.5H$ flow profiles for one period of the fish swimming motion viewed from above. Velocity vectors are shown, scaled in size by velocity magnitude and in color by dynamic pressure coefficient contours (Range:[0,2]). Blue regions are high pressure, and the red regions are low pressure, clearly revealing the wake thrust jet. Numerical desingularization of the rolled up wake structures allows for the vortex cores bounding the thrust jet to be easily identified. Sequence is shown top to bottom, first left column, then right column, at intervals of $T/8$.

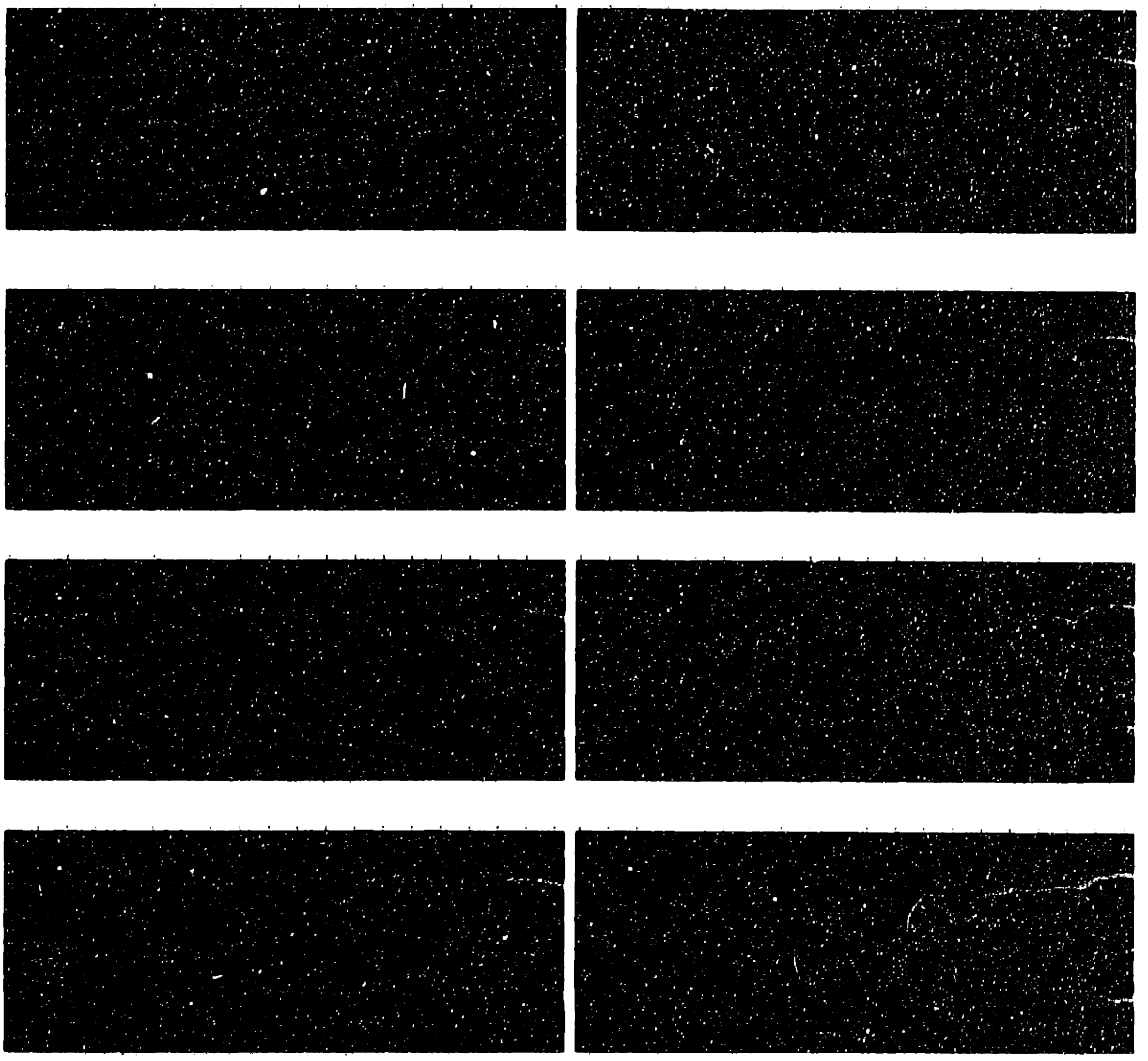

Figure 4-22: Mid plane depth $z = 0.5H$ flow profiles for one period of the fish swimming motion viewed from above. Dynamic pressure coefficient contours shown only (Range:[0,2]). Blue regions are high pressure, and the red regions are low pressure, clearly revealing the wake thrust jet. Numerical desingularization of the rolled up wake structures allows for the vortex cores bounding the thrust jet to be easily identified. Sequence is shown top to bottom, first left column, then right column, at intervals of $T/8$.

4.4.6 Discussion

Comparison between the experimental data and the numerical simulation results shows good quantitative and qualitative agreement. The wake Strouhal numbers (St) clearly support the conclusions of Triantafyllou, *et al.* (1993) [204]. Wake vortex strength and placement compare well, with thrust jet width of approximately 1.3 times the maximum body width. Maximum computed numerical vorticity strengths are within 20% of experimental values. Simulation results reveal that the side forces are distributed evenly between the tail and the main body, while the tail sustains over 90% of the longitudinal force. A detailed close-up given in Figure 4-23 elucidates complex processes of bound vorticity release and thrust wake formation. The near-body and wake streamline patterns near the trailing edge separation line of the caudal fin show qualitatively similar features.

Comparisons between the experimental and simulation results illustrate the formation mechanisms of the wake thrust jet region and the near body flow dynamics through the sequence of mid-body depth images over the straight-line swimming cycle showing vorticity and velocity features manipulated by the body. Vorticity contours in the wake and near the body reveal the formation of bound vorticity which is propelled toward the tail through localized body undulation. Controlled actuation of the tail fin trajectory and attitude releases this body-bound vorticity in a favorable manor to form a reverse Kármán vortex street in the wake. In addition, the dynamic pressure contours and the velocity vectors reveal low pressure regions formed upstream, along the midsection region and contraction region of the fish body length, which are then manipulated by the oscillation of the afterbody to contribute to the strength of the thrust jet formed by the reverse Kármán vortex street. Specifically, the controlled actuation of the caudal fin intercepts these low pressure regions as they progress posteriorly in the local body frame of reference. These low pressure regions pass from the outside of the contraction region to the inside of the caudal fin just prior to the moment of maximum lateral excursion of the caudal fin and align with the average thrust jet profile. As the caudal fin is swept to the other side through this

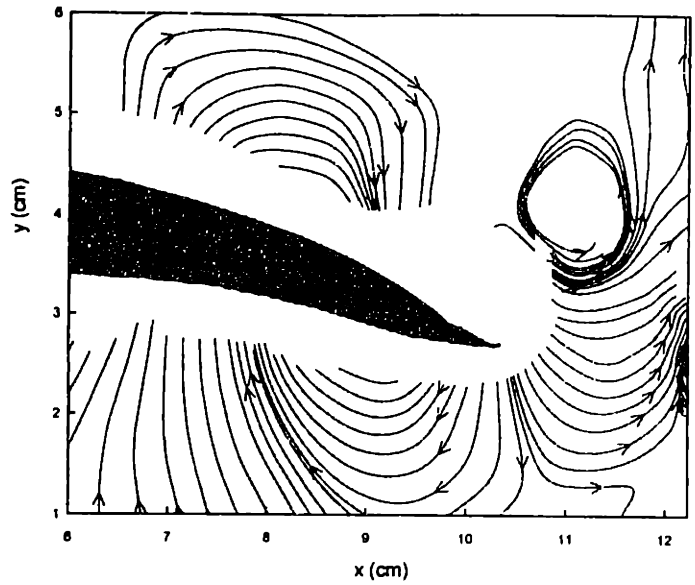

(a) DPIV

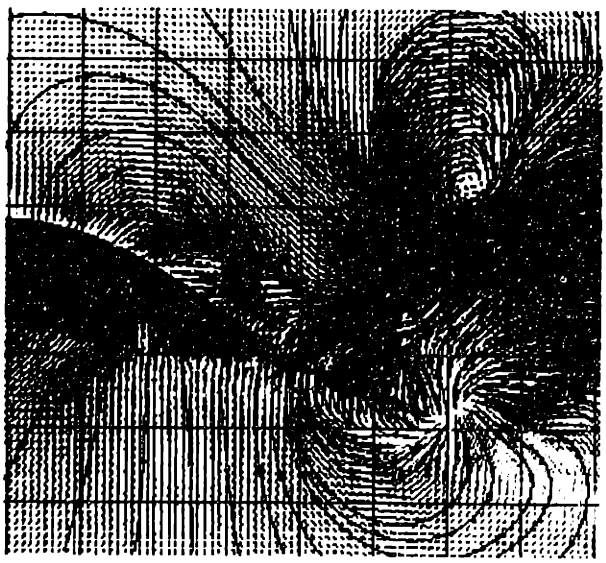

(b) Computation

Figure 4-23: Close-up of the separated and near-body flow near the tail of the Giant Danio during straight-line swimming. Magnification of near-body streamlines illustrate the effect of body-bound and free vorticity on the adjacent flow. (a) DPIV experimental data shows the in-plane velocity streamlines near the trailing edge, revealing the large wake vortex and the body-bound vorticity near the trailing edge. (b) Numerical simulation results for the same instant superimpose streamlines (black) on a dense in-plane velocity vector grid. Velocity vectors are scaled in size by velocity magnitude and in color by ω_z (Range:$[-10s^{-1},10s^{-1}]$).

region of high fluid momentum, additional separation results from the sharp trailing edge of the caudal fin passing through the low pressure region and further contributes to the formation of a reverse Kármán vortex street. This vorticity control and production interaction mechanism contributes to the efficient production of the thrust jet comprising in the wake of the straight-line swimming motions.

4.5 Numerical simulation of near-body planar flow profiles

Classical swimming models which attempt to predict the performance of the swimming motions of fish often fall short of arriving at consistent conclusions, due to assumptions which inadequately model the near-body flow around the undulating body. Wu [239] utilized two-dimensional theory to analyze the swimming motions of a swimming plate; however, the validity of this linear approximation in describing the flow dynamics associated with a complex three-dimensional fish body, especially those with a low aspect ratio lifting body attached to a high aspect lifting tail, is questionable. Lighthill's three-dimensional linear theory recognizes the importance of upstream vorticity shedding in affecting the overall performance of the fish, citing the reduced frequency and the profile geometry as of key importance in improving swimming efficiency and increasing generated thrust, although the modeling of near-body flow dynamics is neglected. Employing either of these theories tends to predict higher forces and power requirements for steady straight-line fish swimming than predicted by Gray [76].

The manner in which the two- and three-dimensional theories arrive at a solution for the velocity potential involves conformal mapping techniques to describe the flow at any one section along the fish depth or length, respectively. Figure 4-24 illustrates the near-body flow pattern predictions consequent of employing the two-dimensional swimming theory of Wu or the three-dimensional slender-body theory of Lighthill. In figure 4-24(a), the actuated flow is assumed to travel along streamlines laterally

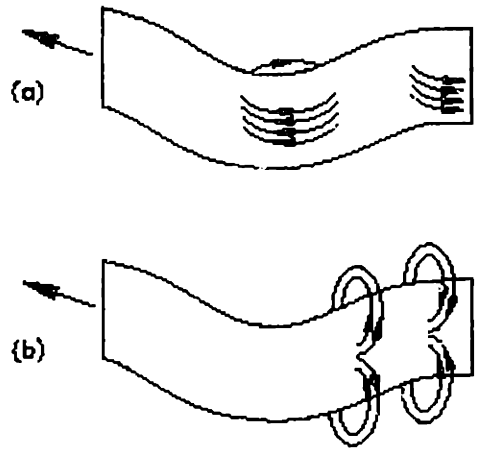

Figure 4-24: Depiction of near-body velocities in straight-line swimming as modeled by the classical swimming theories: (a) two-dimensional swimming plate theory of Wu (1961) [239]; (b) three-dimensional slender-body theory of Lighthill (1975) [127]. Figure from Anderson (1996) [9].

away from the fish and parallel to the direction of swimming, and hereafter this flow pattern is referred to as "longitudinal". The flow patterns shown in figure 4-24(b), hereafter referred to as "transverse", assume the fluid travels laterally away from and sectionally around the depth extremes of the geometry. Through systematic visualization of numerical simulations of the Giant Danio swimming motions performed in Section 4.4, the flow around actual fish is shown to be neither simply "longitudinal" nor "transverse", as predicted by Wu's 2D or Lighthill's 3D theories, respectively. Such simplifications obviate understanding of fluid actuation and control mechanisms. Rather, combinations of "longitudinal" and "tranverse" flow features are prevalent along the length of the fish body, at all points during the swimming cycle.

4.5.1 Waterline cuts

The investigation of the near-body flow commences with a look at the in-plane streamline profiles at different heights z (measured from the top of the maximum backbone depth) over the fish body depth D. Figures 4-25 through 4-28 demonstrate the flow patterns is relation to the three-dimensional computational geometry kinematics of

Body I. The streamtraces reveal the two-dimensional velocity components at the mid-depth plane of the body $z/D = 0.5$, sectioning the caudal fin at midspan, and at an upper-body plane $z/D = 0.2$, which passes through the backbone shedding region for shedding scheme B, which is employed in these simulations. The velocity vectors are scaled in size by the velocity magnitudes, such that far away from the fish in this inertial reference frame, these vectors may appear as points. The velocity vectors again are contoured by the strength of the dynamic pressure coefficient components, red indicating low pressure and green indicating high pressure.

Figures 4-25 through 4-28 compare the mid-depth and upper-body flow planes at many sixteen times over the entire period of the swimming motion. From examination of the unsteady streamline patterns, it is clear that the near-body flow over much of the body length is in-plane and quite "longitudinal" in appearance. However, the confluence of streamlines in regions at certain time instances suggest a strong three-dimensional flow component, particularly visible in the upper-body planes. This out-of-plane flow component is "transverse" in nature, corresponding to cross-flow over the top of the body resulting from the actuation by the progressive backbone wave.

Looking at the streamline patterns in the wake, it is clear that the vertical vorticity ω_z shed into the wake is strong over much of the depth of the fish. This is in agreement with the observations of Triantafyllou *et al.* (1991, 1993) [207, 204] that many species of fish are predisposed to swim at a Strouhal number St corresponding to the maximum spatial amplification of the two-dimensional thrust jet instability. The near-body streamlines indicate the presence of body-generated vorticity components which are released into the flow along the backbone ridge through separation scheme B. However, this vorticity tends to roll-up before it enters the tail, due to large cross-flow perturbation velocities and due to its own self-influence, confusing the plotted streamline patterns.

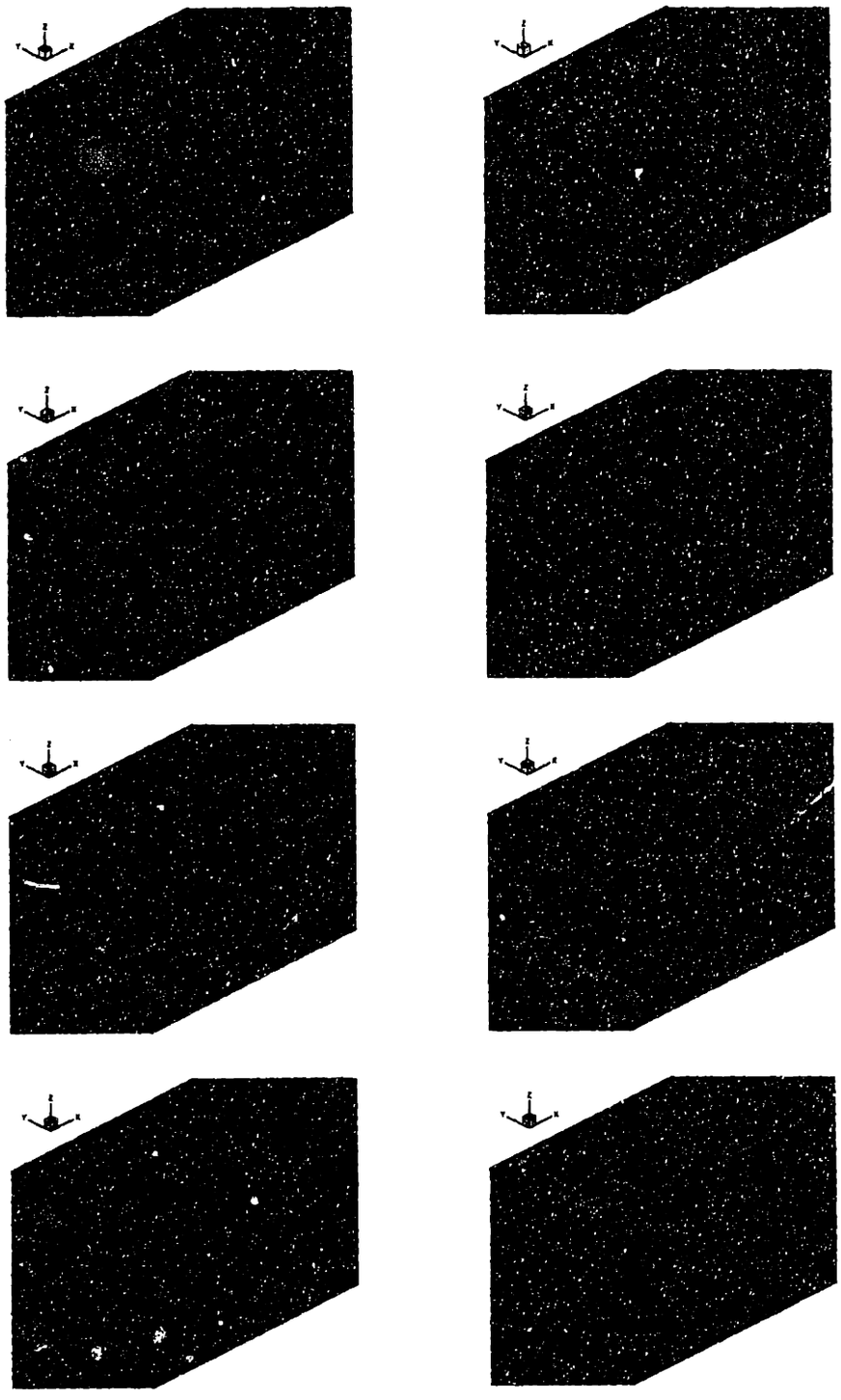

Figure 4-25: Flow profiles for one-quarter period of the Giant Danio swimming motion. Two cuts at different depth planes z over total body depth D: mid-plane depth $z/D = 0.5$ (left), upper-body depth $z/D = 0.2$ (right). In-plane velocity streamlines (black) superimposed on velocity vectors, which are scaled in size by magnitude and in color by dynamic pressure coefficient (Range:[0 (green),2 (red)]). Sequence shown top to bottom at intervals of $T/16$ for $t = 0$ to $t = 3T/16$.

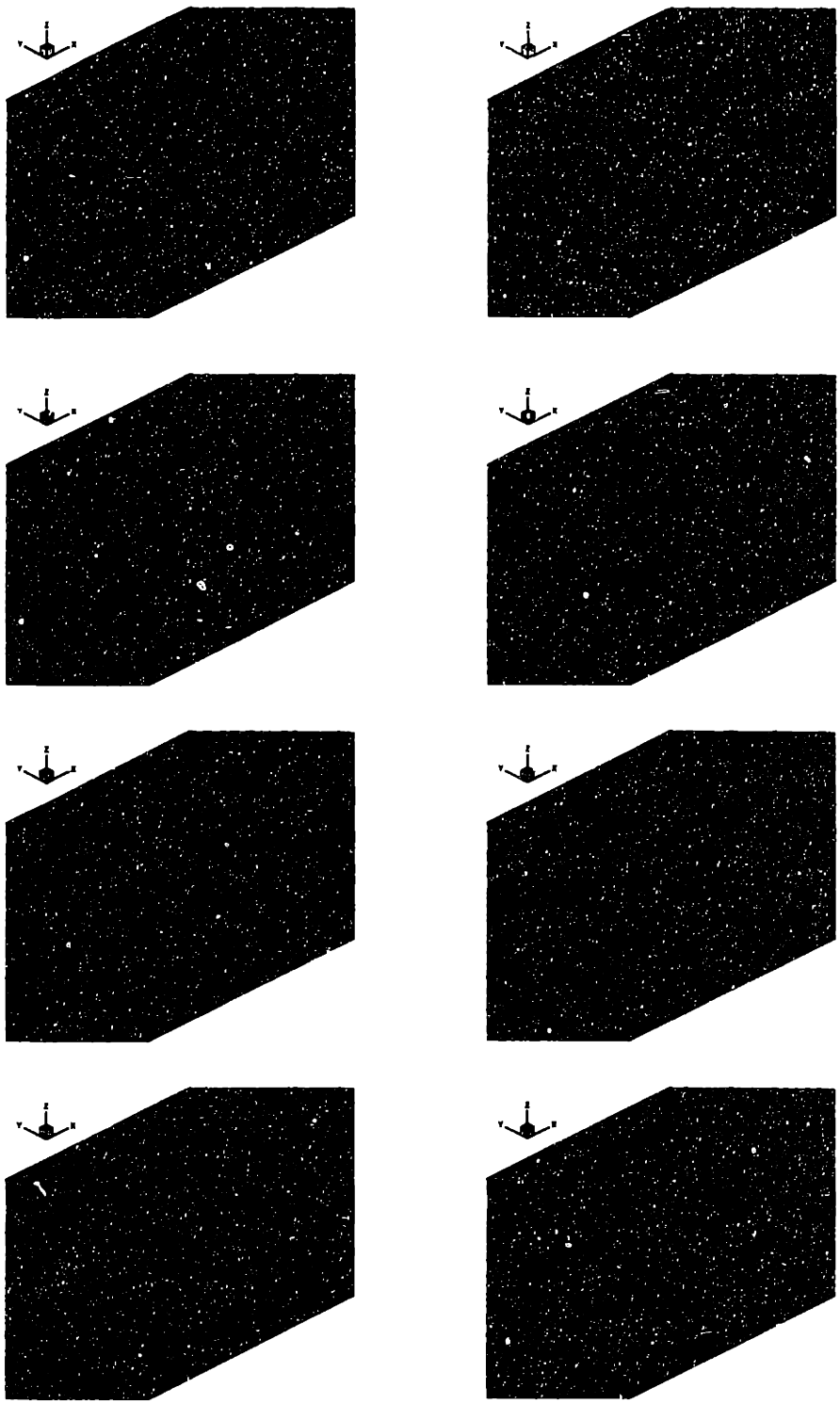

Figure 4-26: Flow profiles for one-quarter period of the Giant Danio swimming motion. Two cuts at different depth planes z over total body depth D: mid-plane depth $z/D = 0.5$ (left), upper-body depth $z/D = 0.2$ (right). In-plane velocity streamlines (black) superimposed on velocity vectors, which are scaled in size by magnitude and in color by dynamic pressure coefficient (Range:[0 (green),2 (red)]). Sequence shown top to bottom at intervals of $T/16$ from $t = T/4$ to $t = 7T/16$.

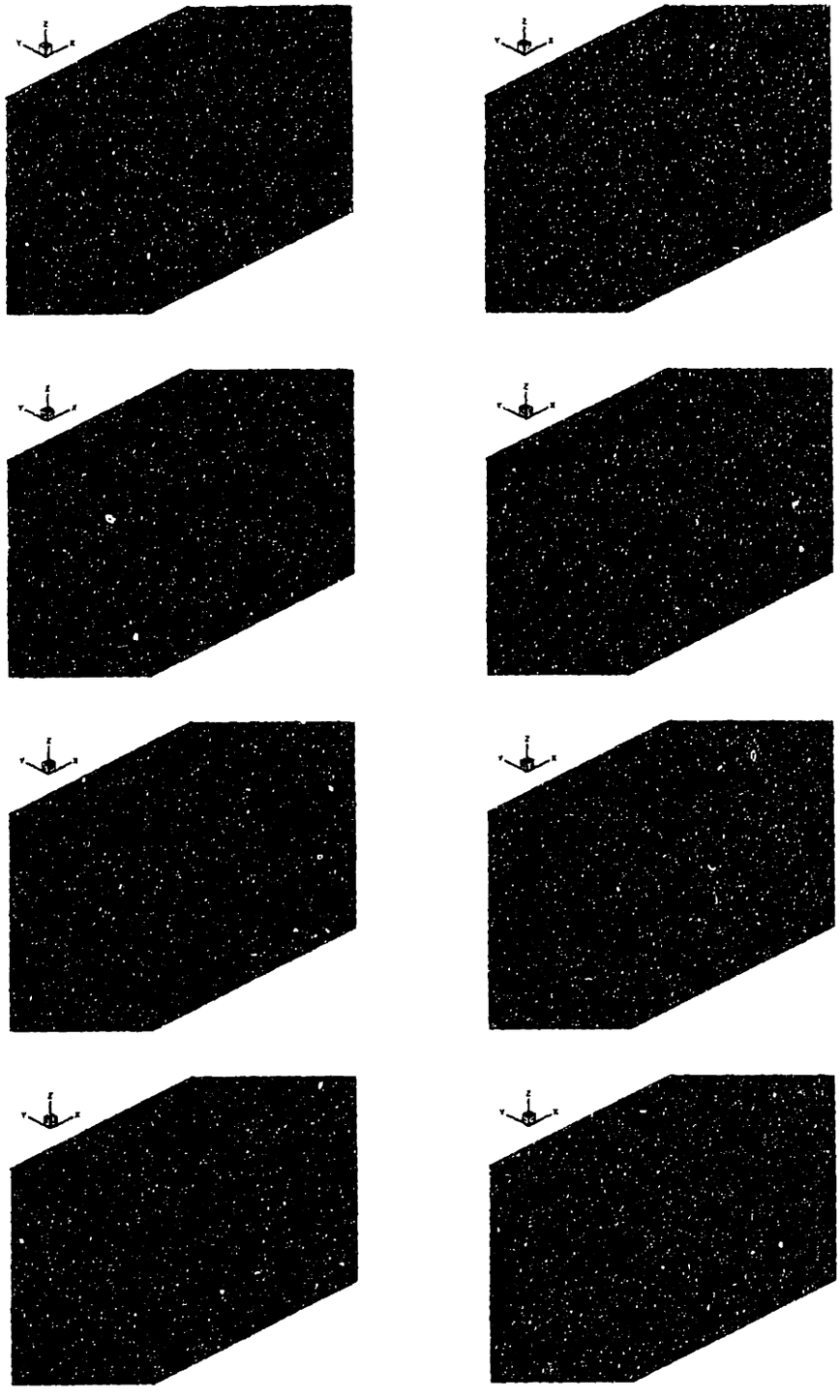

Figure 4-27: Flow profiles for one-quarter period of the Giant Danio swimming motion. Two cuts at different depth planes z over total body depth D: mid-plane depth $z/D = 0.5$ (left), upper-body depth $z/D = 0.2$ (right). In-plane velocity streamlines (black) superimposed on velocity vectors, which are scaled in size by magnitude and in color by dynamic pressure coefficient (Range:[0 (green),2 (red)]). Sequence shown top to bottom at intervals of $T/16$ from $t = T/2$ to $t = 11T/16$.

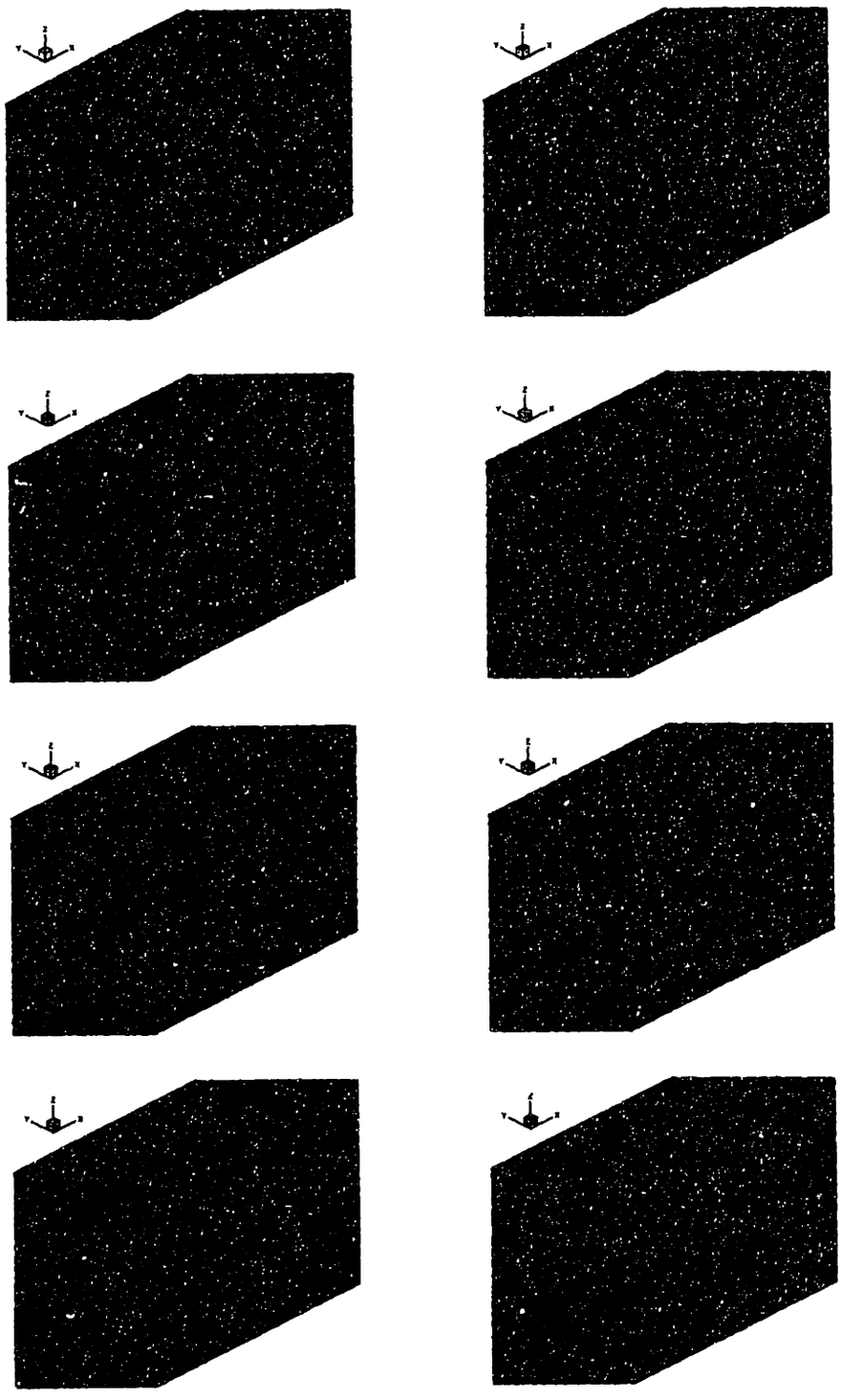

Figure 4-28: Flow profiles for one-quarter period of the Giant Danio swimming motion. Two cuts at different depth planes z over total body depth D: mid-plane depth $z/D = 0.5$ (left), upper-body depth $z/D = 0.2$ (right). In-plane velocity streamlines (black) superimposed on velocity vectors, which are scaled in size by magnitude and in color by dynamic pressure coefficient (Range:[0 (green),2 (red)]). Sequence shown top to bottom at intervals of $T/16$ from $t = 3T/4$ to $t = 15T/16$.

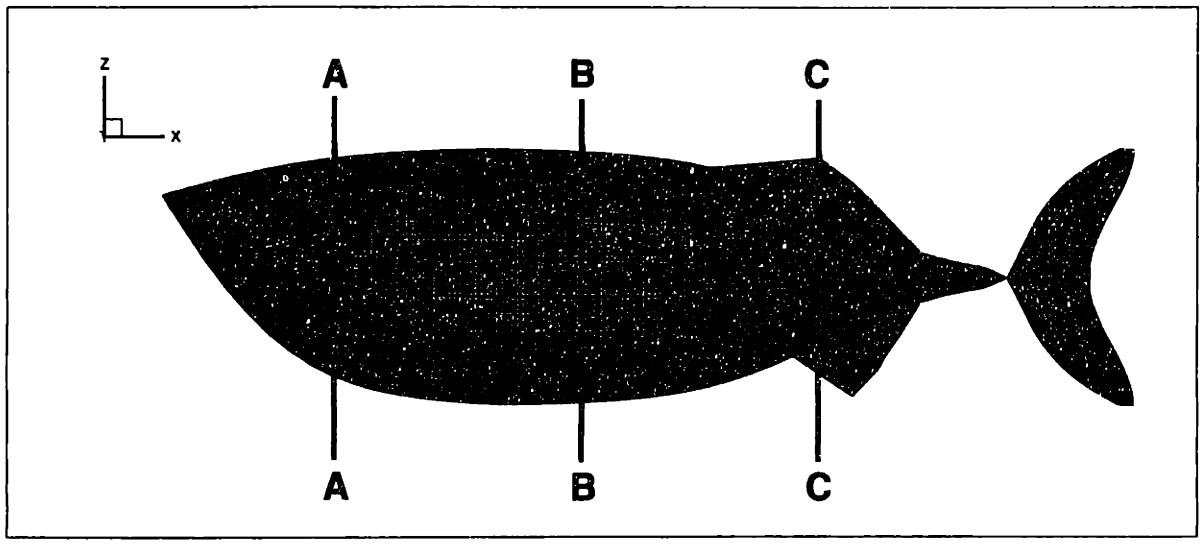

Figure 4-29: Location of sectional cuts along the length of the Giant Danio during straight-line swimming.

4.5.2 Sectional cuts

The near-body flows for the straight-line swimming motions of Section 4.4, employing Body II and separation scheme C for their geometric implications on multiple wake interactions and improved performance. Figure 4-29 illustrates the three locations which were chosen to examine the sectional flows dynamics. The first section, Cut AA, is located near the head where the sectional area of the body is increasing. The second section, Cut BB, is located along the length at the fish midbody, where the sectional area is constant. Cut CC, the final cut, is positioned in the contraction region near the caudal peduncle at the peak of the dorsal fin and through the leading edge of the anal fin where the anal fin depth is increasing.

Figures 4-30 and 4-31 illustrate the near-body flow at the three sectional cuts during one-half period of the swimming motion, at intervals of $T/8$. In-plane streamlines are superimposed on vector plots of the sectional flow, contoured by the strength of the longitudinal vorticity ω_x. In addition, a top view at each time step is provided for visual correlation with the sectional flows. These top views are the same as shown in figure 4-19, with the in-plane streamlines superimposed on velocity vectors contoured by the strength of the vertical components of vorticity ω_z. The details of the section

flows during the second half of the period are omitted for brevity but can be described as mirror images of the flow patterns for corresponding body positions during the first half of the cycle. The top view image of the streamline patterns defines the "upstroke" or "downstroke" conventions included in the detail descriptions of the flow features, and the sections are viewed looking forward from tail to head and similarly define the "right" or "left" conventions.

The details of the sectional flows during at the discrete time intervals are described herein. At the initial time $t = 0$ in the cycle, near-body flow at the head is laterally displaced away from the body over much of the depth by the backbone wave motions of increasing amplitude. The midbody upstroke, in the top view convention, combines "longitudinal" patterns to the right with convergent "transverse" streamlines to the left. A highly "longitudinal" flow pattern emerges in the contraction region during the upstroke of the tail. At $t = T/8$, the near-body "longitudinal" flow pattern at the head is again prevalent, while the midbody downstroke reveals a "transverse" sectional flow pattern. The contraction region deceleration results in a complex mixed flow pattern with "transverse" flow around the thin fins from the left and "longitudinal" streamlines to the right from midbody influence. At $t = 2T/8$, near-body "longitudinal" flow patterns at the head are sustained, and likewise, the midbody downstroke again produces a "transverse" sectional flow. As the contraction region reverses undulation direction, "longitudinal" streamlines to the left of the body and fins combine with a weakly "transverse" flow from bound vorticity generated upstream. Finally at $t = 3T/8$, the near-body "longitudinal" flow pattern at the head shows with slight "transverse" influence as the head changes undulation direction to the right. The midbody deceleration sustains "transverse" streamline pattern, as the contraction region downstroke produces a highly "transverse" sectional flow pattern around the thin fins, with the affects of the change in rotational direction of the bound vorticity apparent.

To summarize, at Cut AA, near-body flow dynamics at the head reveal a "longitudinal"-type actuation, as fluid is displaced laterally over the depth. At Cut BB, near-body flow dynamics at mid-section reveal combined "longitudinal" and "transverse" actu-

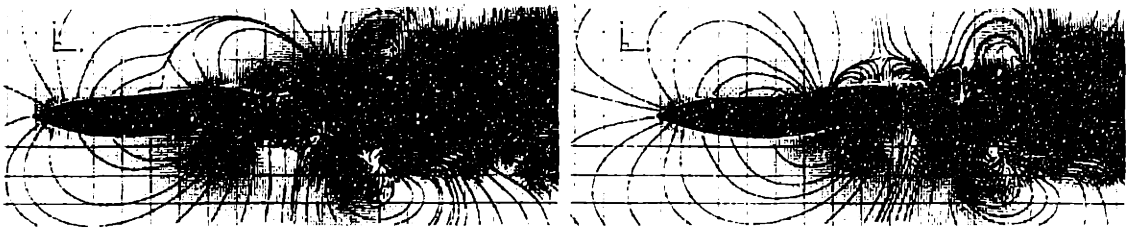

(a) $t = 0$: Top View (b) $t = T/8$: Top View

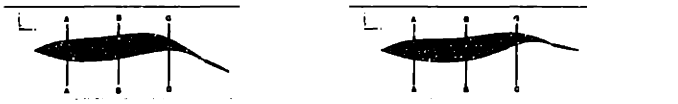

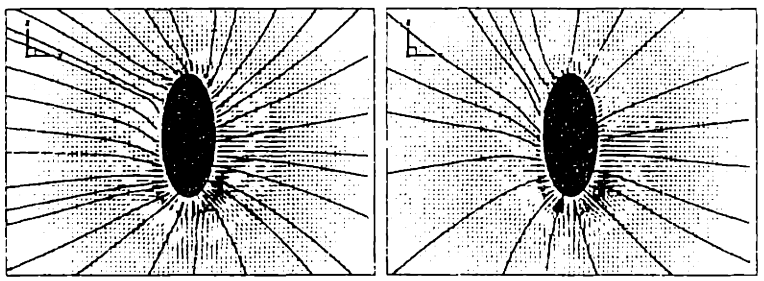

(c) $t = 0$: Cut AA (d) $t = T/8$: Cut AA

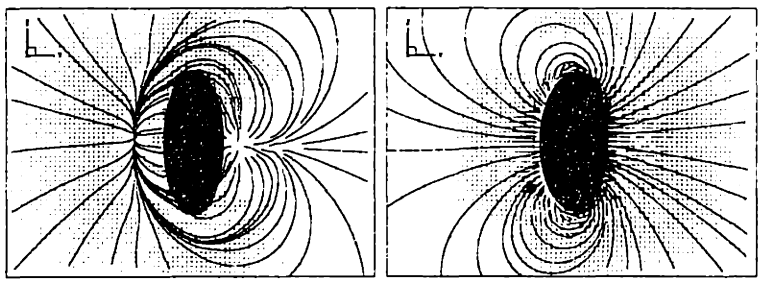

(e) $t = 0$: Cut BB (f) $t = T/8$: Cut BB

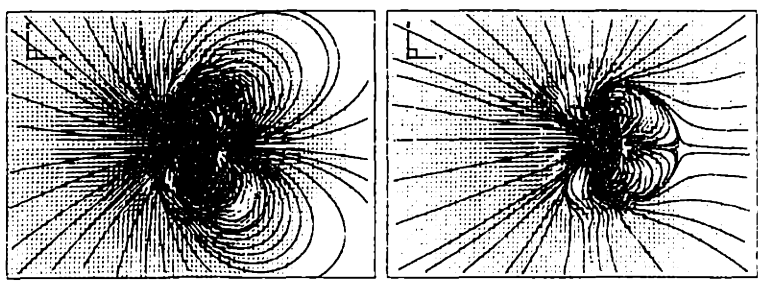

(g) $t = 0$: Cut CC (h) $t = T/8$: Cut CC

Figure 4-30: Sectional flows at $t = 0$ and $t = T/8$ during the straight-line swimming cycle of the Giant Danio. Streamlines of the planar fluid velocities are superimposed on velocity vectors. Color contours are scaled by vertical ω_z vorticity (-10 s^{-1} to 10 s^{-1}) in top views, and by longitudinal ω_x vorticity (-1 s^{-1} to 1 s^{-1}) in sectional views. Section views are looking from tail to head.

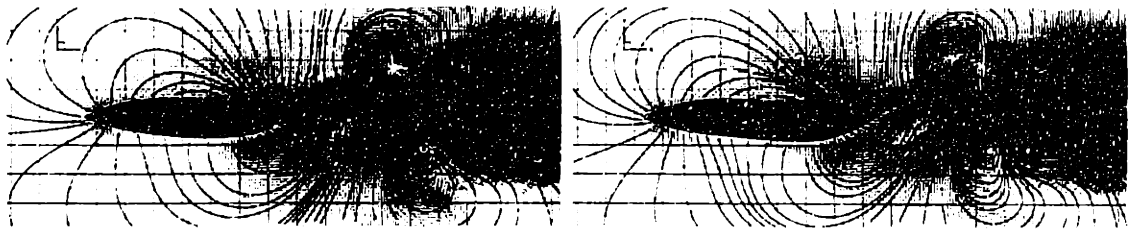

(a) $t = 2T/8$: Top View (b) $t = 3T/8$: Top View

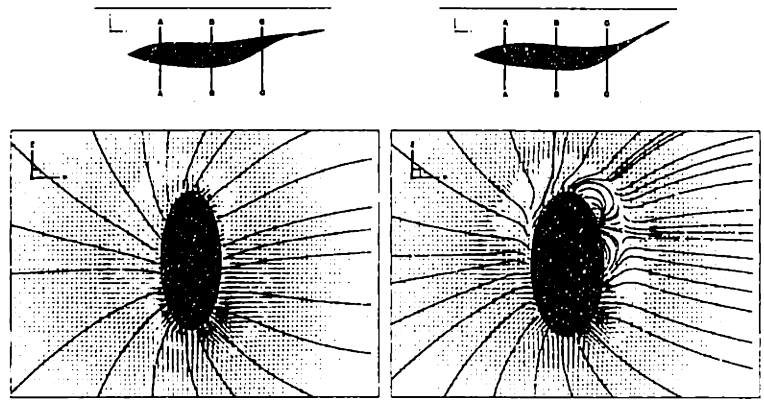

(c) $t = 2T/8$: Cut AA (d) $t = 3T/8$: Cut AA

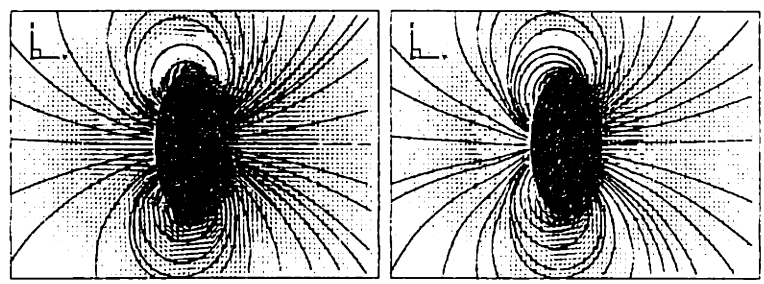

(e) $t = 2T/8$: Cut BB (f) $t = 3T/8$: Cut BB

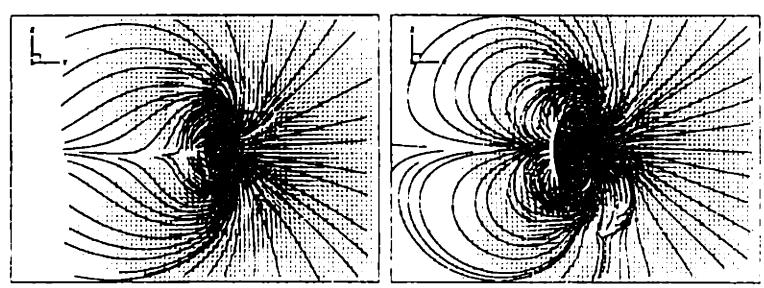

(g) $t = 2T/8$: Cut CC (h) $t = 3T/8$: Cut CC

Figure 4-31: Sectional flows at $t = 2T/8$ and $t = 3T/8$ during the straight-line swimming cycle. Streamlines of the planar fluid velocities are superimposed on velocity vectors. Color contours are scaled by vertical ω_z vorticity ($-10\ s^{-1}$ to $10\ s^{-1}$) in top views, and by longitudinal ω_x vorticity ($-1\ s^{-1}$ to $1\ s^{-1}$) in sections. Section views are looking from tail to head.

ation patterns, as fluid is directed laterally away and sectionally around the body. Near-body flow dynamics around Cut CC in the contraction region also reveal a complex "longitudinal"/"transverse" actuation pattern, as thin fins bound vorticity strength grows along the length of the fish. The transverse three-dimensionality of the flow is strongest near the upper and lower edges of the fish, and longitudinal flow patterns dominates over much of the body depth. This description is in agreement with the quantitative findings of vortex lattice theory [36], which has be used to predict the swimming performance of low-aspect-ratio swimming plates whose performance is somewhere between the estimates of the two-dimensional theory and slender body theory.

From this evidence, it can be seen simplified modeling of near-body flow dynamics may underestimate performance measures such as efficiency and overestimate the thrust and power required for swimming, and hence the drag on an undulating body [243, 159, 156], supported by evidence of drag reduction on the RoboTuna [21]. Through systematic numerical simulations, the near-body flow around actual fish during straight-line steady swimming is shown to be mechanized by complex combinations of "longitudinal" and "transverse" actuation patterns, which assist in the efficient manipulation of the ambient fluid to form a thrust jet by shedding bound vorticity into the wake.

4.6 Mechanistic model of straight-line swimming

This section synthesizes the many computational results and observations provided in this chapter to improve the understanding of the fish-swimming model, based on the simulated motions of live fish or the *RoboTuna*. In *Chapter 6*, the effects of variation of the kinematic and geometric parameters utilized in this chapter on the performance of fish swimming motions and the dynamics of the near-body flow and vorticity structures will be examined in detail.

Figure 4-32 summarizes the development and control of vorticity by the flexible body undulation during the swimming cycle. This model simplifies the complex

three-dimensional nature of the near-body flow, but accurately portrays the dominant features of the mid-depth plane flow and principal mechanisms involved in manipulation of the large-scale two-dimensional vorticity features in the wake. In Figure 4-32(a), counterclockwise-rotating (positive) bound vorticity moves towards tail tip as the upward stroke of the tail nears its maximum excursion. New clockwise-rotating (negative) bound vorticity develops in the midbody region of the fish length, due to the commencement of downward midbody motion. Two zones of strong low pressure exist along the fish body. L_1, on the outside of the upward stroke of the contraction region, passes over the leading edge of the tail fin as the tail reaches its maximum upward excursion, aligning with the thrust jet inside the maximum stroke of the tail. L_2 forms in the midbody region as the next trough of the backbone wave progresses posteriorly from the head.

Figure 4-32(b) illustrates the shedding of the positive bound vorticity into the wake, while negative bound vorticity is fully developed in the contraction region and along the tail, due to the local body contortion and coordinated downward caudal peduncle motion. The low pressure region L_1 is now contributing fully to the momentum in the wake, and as the trailing edge of the tail fin passes through L_1, the strength of the shed positive vorticity is reinforced. The low pressure region L_2 progresses tangentially along the body towards the tail through the contraction region as the midbody completes its downward stroke. Additionally, the downward stroke completion of the midbody contributes to the formation of new positive body-bound vorticity in the midbody.

In Figure 4-32(c), the downward stroke of the tail is nearly complete, and low pressure region L_2 now passes over the leading edge of the tail from the outside of the contraction region to align with the momentum in the wake. Negative vorticity is poised at the trailing edge of the tail for release into the wake, while new positive body-bound vorticity is fully formed in the contraction region of the body. Additionally, a new low pressure region L_3 forms in the midbody region, as the crest of the next backbone wave progresses posteriorly from the head.

Figure 4-32(d), negative vorticity is shed into wake, and the trailing edge of the

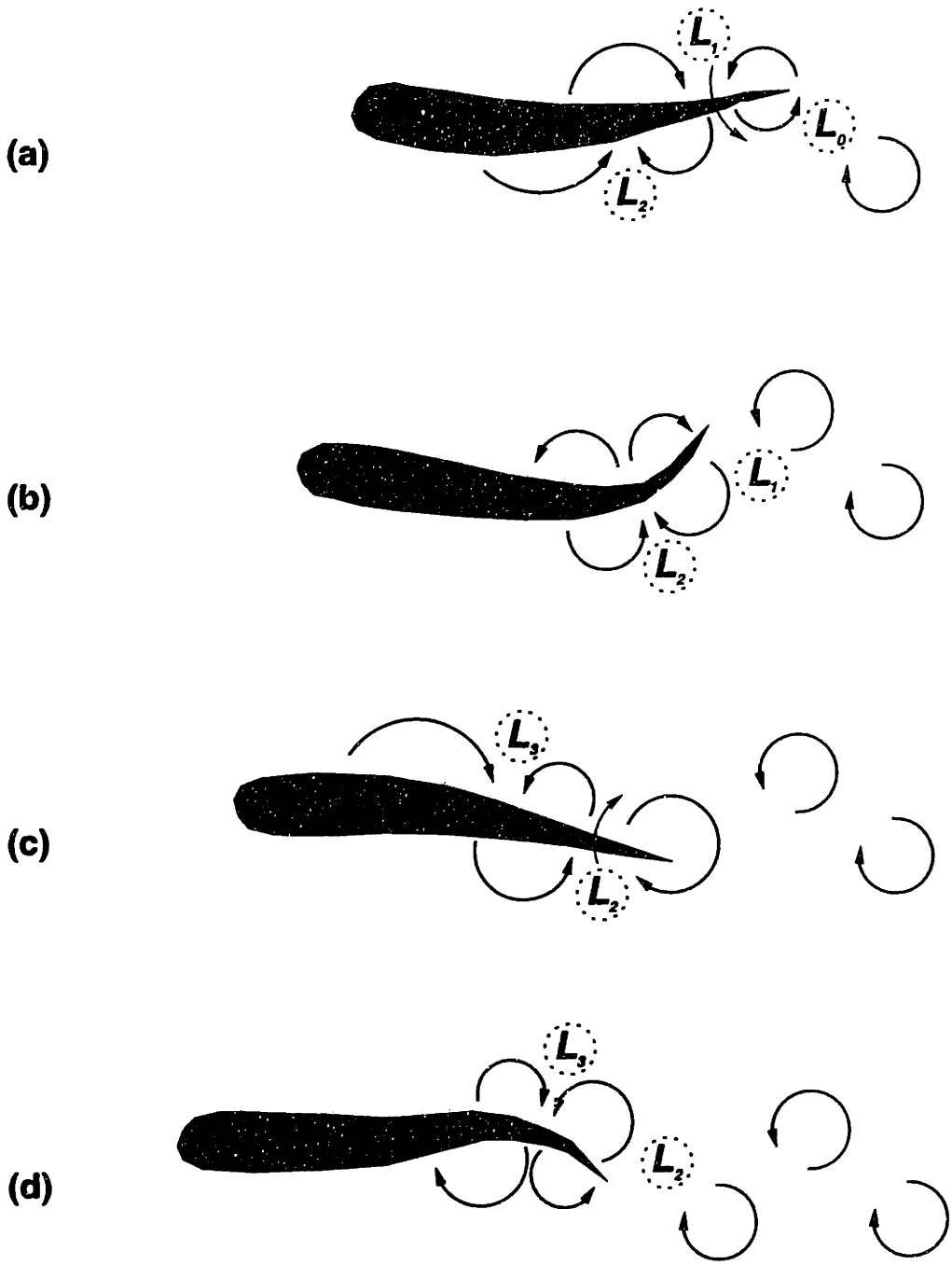

Figure 4-32: Body-bound and wake vorticity development and near body flow dynamics during one cycle of straight-line swimming motions. Circled L indicates a region of low pressure which is manipulated by the body and tail to contribute to the formation of the reverse Kármán vortex street thrust jet.

tail passes through L_2 region during its upstroke, reinforcing the strength of the negative vorticity shed into the wake. Positive bound vorticity is fully developed in contraction region and around the tail, due to the local undulation of the body and the coordinated upward stroke of the caudal peduncle. Similarly coordinates with the conclusion of the upstroke of the midbody, new negative body-bound vorticity begins to form in the midbody region, and low pressure region L_3 progresses posteriorly towards the tail. Thus, the cycle concludes and returns to the picture shown in Figure 4-32(a), and the alternating-sign free vorticity in the wake pairs to form a thrust jet, in a convective instability corresponding to the Strouhal number of swimming.

It is evident that the thrust jet formation by the motion of swimming fish is actuated by optimal release of body motion-generated bound vorticity. This mechanism of regulated bound vorticity shedding results in efficient reverse Kármán vortex street formation during straight-line swimming.

Chapter 5

Dynamics of three-dimensional maneuvering

Fish can turn 180° on a radius considerably less than their body length, whereas man-made underwater vehicles require several body lengths to execute a similar turn. Experimental measurements of live fish maneuvering and starting can be found in Weihs [225, 226], Blake [26], and Harper and Blake [81, 82]. A thorough kinematic analysis of unsteady turning and maneuvering motions can be found in Videler [212], and a recent review of fast-starting capabilities of fish can be found in Domenici and Blake [51]. The three-dimensional numerical method of *Chapter 3* and *Chapter 4* is modified to simulate transient fish-like motions, such as turning and maneuvering. Detailed results for the near-body flow dynamics around a live fish executing unsteady, rapid turning motions are presented, which compare the simulation results to experimentally observed fish turning motions. By examining the near-body flow and the wake produced by the turning motions of fish, the concepts of vorticity shedding and manipulation by the tail are extended to explain fish maneuvering performance. Through precise body actuation, the fish regulates the formation and controlled release of body-generated vorticity, resulting in the production of a pair of counter-rotating vortices and hence a thrust jet. Thus, the fish is able to rapidly direct its generated thrust and achieve its desired trajectory.

5.1 Turning of a Giant Danio

5.1.1 Experimental evidence

The flow patterns around a swimming Giant Danio (*Danio malabaricus*) performing a 60° turn were captured on video using DPIV by Anderson (1996) [9]. Some of the velocity field data are missing due to fish shadows. In Figure 5-1, horizontal slices of the flow are obtained with the camera looking vertically down. The laser is located at the top of each figure. The fish begins the maneuver coasting downwards; then it rapidly contorts its body into a tight "C"-curve and subsequently recoils to resume straight-line swimming in a direction 60° towards the right as viewed by the fish from the starting direction. A total of 13 images were taken during the turn, at 0.0667 second intervals, for a total of 0.8 seconds. The backbone mean line positions of the fish were obtained from each image graphically, by manual discretization of the backbone at each time into twenty equal arc length segments. The backbone locations were later used to analyze the trajectory of the fish for numerical simulation. The fish intersected the laser plane at mid-body depth for the duration of the turn.

The DPIV results for this maneuver are shown in Figure 5-1. The region immediately below the fish is in its shadow, so these data have been removed [9]. Before arriving at the position shown in Figure 5-1(a), the fish completed a turn originating in the upper left corner of Figure 5-1(a). Residual vorticity from these movements remains above and to the left of the fish. In Figure 5-1(b), the fish has completed its straight-line swimming motions and begins to bend, moving its head towards the new swimming direction with the tail moving in the opposite sense, forming a characteristic "C"-shape. The fluid motion follows that of the contorting body, moving directly towards the fish on the concave side of the body and directly away from the fish on the convex side of the body, at the points of maximum curvature.

In Figure 5-1(d), we see the flow organize into two circular-like flows, one centered at the tail and one near the head, as the tightening of the body into a "C"-shape nears completion. In Figure 5-1(e), the tail begins to move towards the right of the viewed image, shedding in the wake the already-formed counter-clockwise vortex. At this

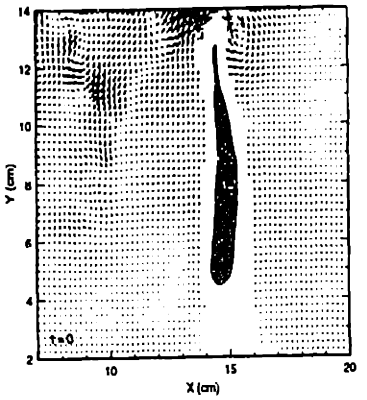

(a) t=0.0s

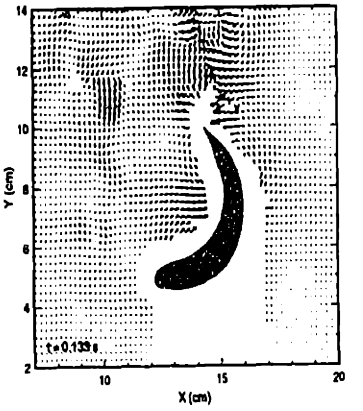

(b) t=0.133s

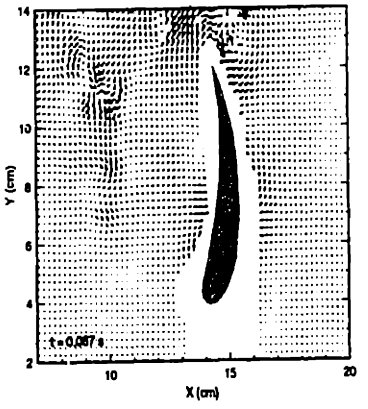

(c) t=0.067s

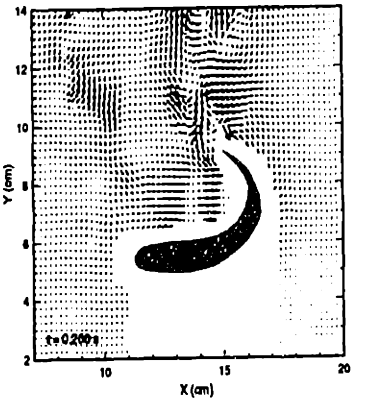

(d) t=0.200s

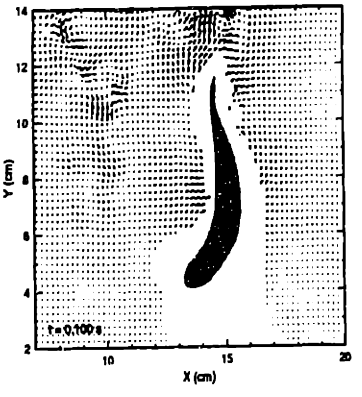

(e) t=0.133s

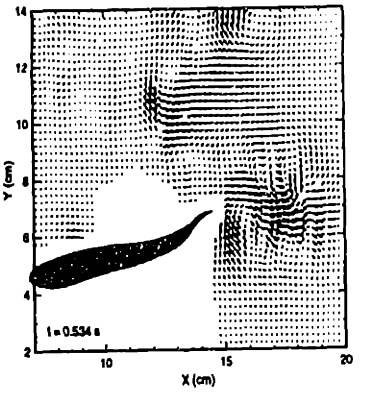

(f) t=0.534s

Figure 5-1: Experimental velocity fields captured using DPIV in the wake of a turning Giant Danio. Six images are shown during the course of the maneuver, detailing the formation of a "C"-shape through local body contortion and the generation of a strong pair of counter-rotating vortices which provide the large transient force needed for turning. Taken from Wolfgang, *et al.* (1999) [233].

instant, the effect of bound vorticity near the head is obscured due to light reflection from the body. The next several frames are not presented due to body reflections which obscure a large portion of the flow. However, analysis of the video record shows that during the stroke of the tail, sweeping downwards as the fish body heads to the left, the counterclockwise vortex sheds into the wake. During the stroke of the tail which sweeps back upwards as the fish continues moving to the left, the clockwise vortex initially associated with the front region of the body moves posteriorly and sheds in the wake.

The net result is shown in Figure 5-1(f): a strong vortex pair forms which provides a jet directed slightly downward and to the right. The vortices in this pair are packets of counter-rotating large-scale wake vorticity, and Figure 5-2 shows the vorticity contours at the same instant. The asymmetric shapes of the contours of the two vortices which make up the turning jet are due to the unsteady, non-periodic body motions and velocity. Additional vorticity shown in this figure, but not labeled with contour strength values, was created by the fish before the initiation of the turning maneuver. The entire turning sequence, from a coasting position to steady swimming 60^o to the right as viewed by the fish from the starting trajectory, takes slightly more than half a second.

The vortices comprising the jet have average nondimensional circulation which is almost 50% greater than the typical wake vortex strength for steady straight-line swimming. The core radius of the jet vortices is more than double that of those produced in straight swimming. The jet is 0.34 ℓ wide, with maximum jet velocity of $u_j \approx U$ oriented approximately 60^o to the *left* of the initial starting position as seen by the fish [9]. Interestingly, the fish velocity after the turn is roughly the same as the jet velocity. Also, the direction of the jet is roughly in the direction required by horizontal momentum balance. Three-dimensional effects are significant, and the vigorous motion of the fish somewhat disrupts the two-dimensional planar results. After completing the turn, the fish begins to swim steadily at $U = 1.5\ \ell/s$.

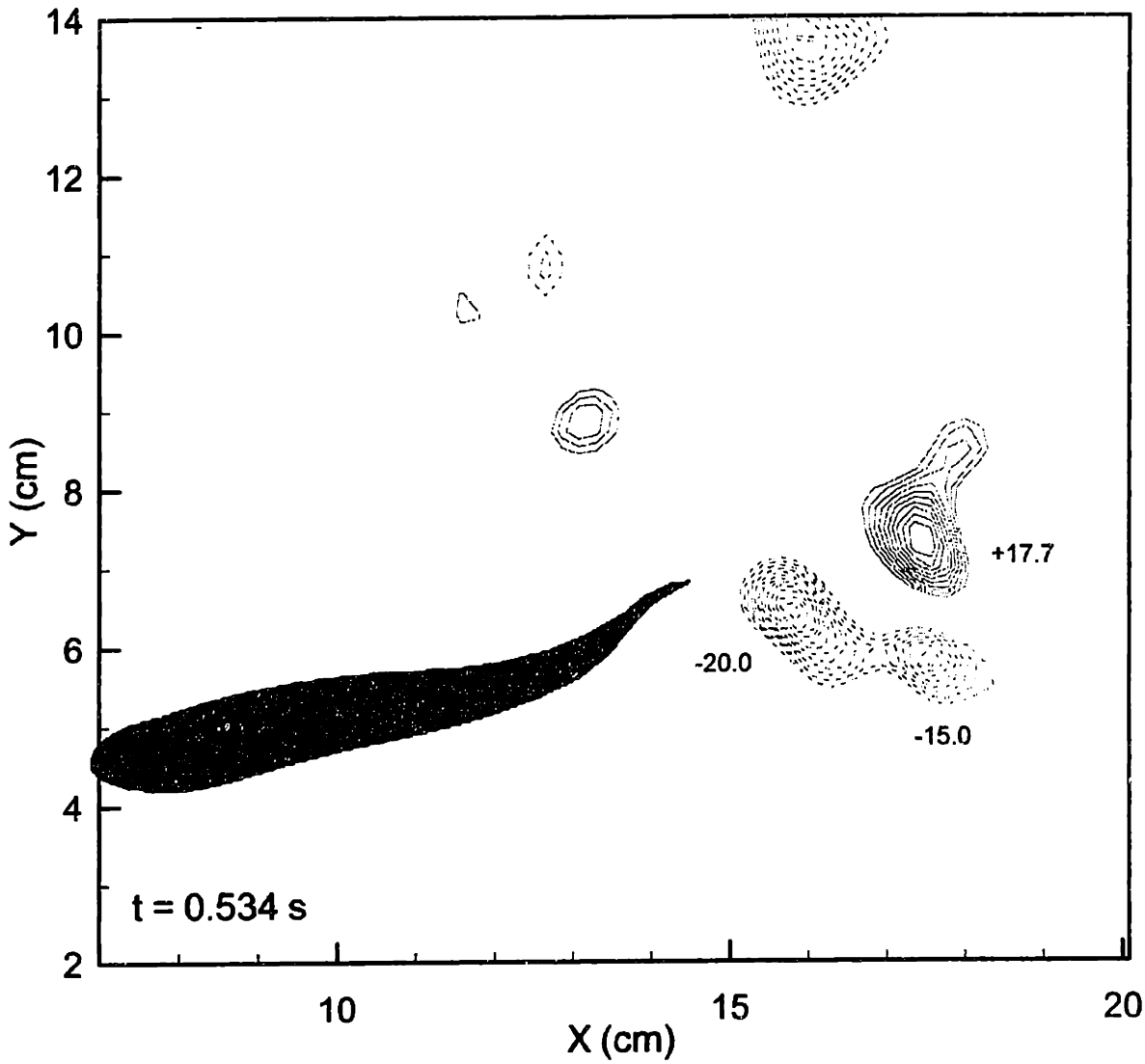

Figure 5-2: Vorticity contours in the wake of a turning fish. Solid lines denote positive vorticity, dashed lines negative vorticity. Contour values are as follows: 6.7 to 16.9 s^{-1} and -6.7 to -20.0 s^{-1} in 1.03 s^{-1} increments. Unlabeled vorticity contours are remnants of prior turning motions and the cessation of straight-line swimming motions. Taken from Wolfgang, *et al.* (1999) [234].

5.1.2 Numerical modeling

The body motions observed in live fish are imposed on the computational fish model, including its tail flapping as well as its trajectory. As the shape and position of the fish were only known at thirteen time steps during the maneuver, an accurate wake picture could not be produced if these thirteen positions were the sole simulation input with such a large time differential between body positions. An interpolative scheme was necessary to arrive at the location of the fish at intermediate time steps, from which the fish turn could be simulated.

Figure 5-3 details the coordinate systems used in the problem. The $OXYZ$-coordinate system is global and fixed. The $oxyz$-coordinate system is a coordinate system whose origin is fixed at the nose of the fish. The x-axis always passes through the tail of the fish. Thus, the flexing motion of the fish can be described in a local coordinate system, while its trajectory can be described in the global coordinate system. The z-coordinates of the fish body depth were assumed to be invariant as the plane of the laser sheet intersected the fish at a mid-body depth for the duration of the turning motion.

The thirteen fish images were then analyzed as follows. First, the position of the nose in the global coordinate system was recorded as a function of time, serving as the origin of the $oxyz$-coordinate system. The angle θ which the $oxyz$-coordinate system made with the global coordinate system was also recorded as a function of time, by constructing the x-axis through the fish tail at each time interval.

A periodic motion was assumed for the local flapping motion of the fish. As the fish had a fairly uncambered mean line shape at both the first time step and the last time step of the fish turn, it was assumed that the local shape of the fish mean line at the extrapolated time of 0.8667 seconds would be equal to the original mean line shape. In this way, the local x and y coordinates of the mean line, as well as the thickness distribution h, could be expanded as Fourier sine series as functions of time. Additionally, as the local y-coordinate and the thickness are always zero at the nose and tail, these could be expanded as Fourier sine series as functions of backbone arc

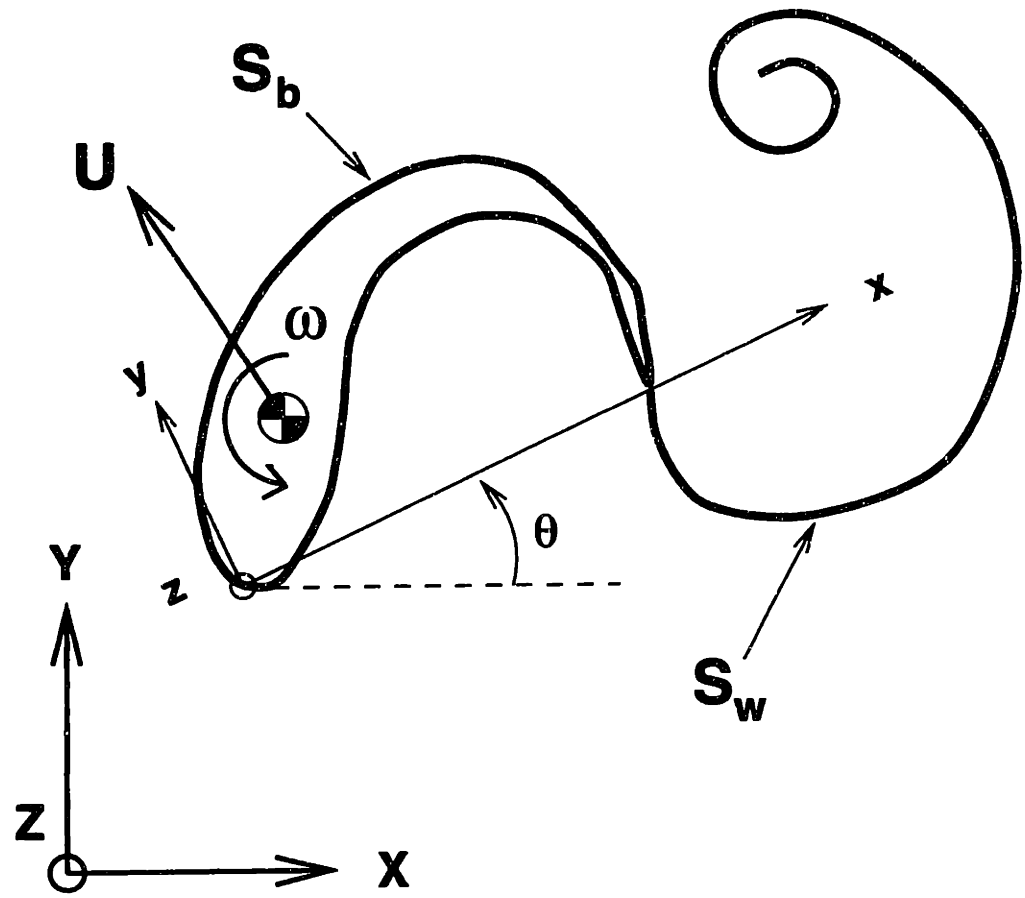

Figure 5-3: Coordinate system convention for the maneuvering problem (top view). Local unsteady body motions are described with respect to the body-fixed $oxyz$ coordinate system, and the body trajectory is described with respect to an inertial reference frame $OXYZ$.

length, while the local x-coordinate could be expanded as a linear function plus a Fourier sine series as a function of backbone arc length. Thus, the local behavior of the backbone can be found at any time during the simulation.

Thus, at each time step, the local coordinates can be expanded as Fourier sine series in arc length s, where t_p is the total number of arc length segments:

$$x(s) = \left(\frac{s}{t_p}\right)L_o + \sum_{n=1}^{\infty} B_n \sin\left(\frac{n\pi s}{t_p}\right) \tag{5.1}$$

$$y(s) = \sum_{n=1}^{\infty} A_n \sin\left(\frac{n\pi s}{t_p}\right) \tag{5.2}$$

$$h(s) = \sum_{n=1}^{\infty} C_n \sin\left(\frac{n\pi s}{t_p}\right) \tag{5.3}$$

In this way, the complex local shapes of the mean line are accommodated, whereas a functional description such as $y = f(x)$ for the expansion would suffer from multi-valued violations at discrete times. Then, given these expansions at each time step, we wish to link them through an expansion in time, where t_s is the total number of original time steps. For each of mode in the spatial expansion of x, y, and h, a periodic shape in time exists if we extrapolate to one more time step where all parameters return to their original values, and thus, the coefficients can be expanded as functions of time:

$$A_n(t) = A_n|_{t=0} + \sum_{m=1}^{\infty} A_{nm} \sin\left(\frac{m\pi t}{t_s}\right) \tag{5.4}$$

Thus, the equations which describe the flapping motion of the fish in the local coordinate system as functions of arc length and time become:

$$x(s,t) = \frac{s}{t_p}L_o(t) + \sum_{n=1}^{N}\left\{B_n|_{t=0} + \sum_{m=1}^{M} B_{nm} \sin\left(\frac{m\pi t}{t_s}\right)\right\} \sin\left(\frac{n\pi s}{t_p}\right) \tag{5.5}$$

$$y(s,t) = \sum_{n=1}^{N}\left\{A_n|_{t=0} + \sum_{m=1}^{M} A_{nm} \sin\left(\frac{m\pi t}{t_s}\right)\right\} \sin\left(\frac{n\pi s}{t_p}\right) \tag{5.6}$$

$$h(s,t) = \sum_{n=1}^{N}\left\{C_n|_{t=0} + \sum_{m=1}^{M} C_{nm} \sin\left(\frac{m\pi t}{t_s}\right)\right\} \sin\left(\frac{n\pi s}{t_p}\right) \tag{5.7}$$

$$L_o(t) = L_o|_{t=0} + \sum_{m=1}^{M} L_m \sin\left(\frac{m\pi t}{t_s}\right) \tag{5.8}$$

where N and M are the number of Fourier sine modes in space and time, respectively.

The coefficients are found by Fourier transform of the discretized fish mean line data at each time step. Thus, the behavior of the local mean line can be found at any time within the parameters of the simulation, and an large number of time steps can be employed to simulate the 0.800 second fish turn.

Given the behavior of the fish in the local coordinate system, the orientation of the local coordinate system within the global frame of reference is assessed. Although obviously not periodic, the location and inclination of the local coordinate system origin in the global coordinate frame is determined by a related method. Originally, a least-squares fit polynomial of arbitrary order was chosen to describe the X and Y positions of the origin of the oxy-coordinate system in time, and likewise for the angle of incidence, θ. However this approximation resulted in spurious trajectories, especially at the temporal extremes of the simulation, which increased in magnitude with the order of least-square polynomial chosen. Greatly improved accuracy is achieved by expansion of the deviation of the X, Y, and θ in terms of a Fourier sine series, again of arbitrary order P, with the subtraction of a linear term which forces the coordinates to zero at either end of the simulation period. Superposition of the linear term and the Fourier sine series expansion yields the trajectory and inclination of the local coordinate system within the global reference frame.

$$\theta(t) = \theta|_{t=0} - \frac{t}{t_s}\left(\theta|_{t=0} - \theta|_{t=t_s}\right) + \sum_{p=0}^{P} C_{\theta p} \sin\left(\frac{p\pi t}{t_s}\right) \tag{5.9}$$

$$X(t) = X|_{t=0} - \frac{t}{t_s}\left(X|_{t=0} - X|_{t=t_s}\right) + \sum_{p=0}^{P} C_{Xp} \sin\left(\frac{p\pi t}{t_s}\right) \tag{5.10}$$

$$Y(t) = Y|_{t=0} - \frac{t}{t_s}\left(Y|_{t=0} - Y|_{t=t_s}\right) + \sum_{p=0}^{P} C_{Yp} \sin\left(\frac{p\pi t}{t_s}\right) \tag{5.11}$$

where the coefficients $C_{\theta p}$, C_{Xp}, and C_{Yp} are found in the usual manner using the discretized mean line global location and inclination information. Simulations were

found to result in optimal reproduction of the experimentally observed motions when ten Fourier sine modes for both temporal and spatial expansion of the local mean line behavior and for the temporal expansion of the local coordinate system global trajectory were employed.

Given the position of the mean line (backbone) at a large number of intermediate time steps, the full three-dimensional body can be described at each time step. As the backbone deforms, the sectional planes are assumed to remain orthogonal to the backbone, and it is also assumed that the body volume is fixed. Therefore, an additional boundary condition must be applied to this numerical method, that the volume of the body must be constant. Thus, the body is scaled at each time so that the integral of the total normal velocity around the body must be zero:

$$\oint_{S_b} \vec{\nabla}\phi_b \cdot \hat{n}_b \;=\; 0 \tag{5.12}$$

From this analytic description of the motion, we can produce a simulation of an arbitrary number of time steps, and the difficulties in accurately reproducing the body motion and the resulting wake are alleviated with a sufficient number of time steps in the simulation. Figure 5-4(a) shows the experimental backbone trajectory and flexing behavior of the Giant Danio during the turn as discretized from the DPIV images. The computational backbone trajectories to be imposed over the simulation length are also shown in Figure 5-4(b), employing fifty intermediate time steps of information.

The viscous effects of the body are again assumed to be confined to a thin boundary layer near the body and in a small wake described by shear layers. The Reynolds number of the Giant Danio before and after the turning motion are approximately $R_e = 10400$ and $R_e = 11000$, respectively. At this Reynolds number, we would expect the boundary layer to be laminar or within a transition region, as illustrated by experimental data of drag coefficient for axisymmetric streamlined bodies with varying ℓ/d ratios found in Figure 6.22 of Hoerner (1965) [92]. It is reasonable to assume that the near-body viscous effects on the body are small in comparison to

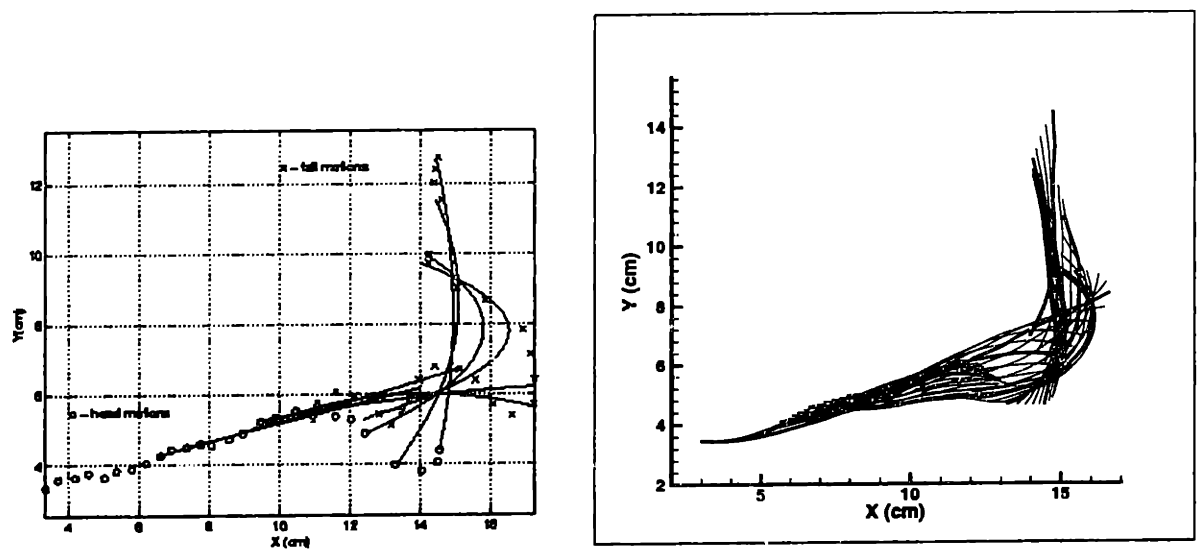

(a) DPIV

(b) Computation

Figure 5-4: Trajectory of maneuvering fish. (a) Experimental data: the 'o' and 'x' marks indicate head and tail motions, respectively, and the curves represent a few of the body backbone positions. The starting position is vertical with the head pointing downwards. The fish contorts its body into a tight curve, then recoils to resume swimming to the left. (Figure from Anderson (1996) [9].) (b) Simulation input: the fish mean line trajectory is shown during the numerical simulation at intervals of $dt = 0.02s$. Bold backbone lines are superimposed every $0.1s$ for clarity.

the effects of unsteady vorticity generated by separation, such as that which occurs at the sharp-trailing edges of the body which generates a wake. Again, the tail is assumed to generate the largest wake, and a primary separation line is chosen to be the trailing edge of the tail. The large dorsal and anal fins are also included in the course of this investigation, to examine the influence of upstream-generated vorticity on the flow around the tail, the overall wake structure, and the generated unsteady body forces.

Thus, the body shape can be described at each time step, and the imposed normal velocities at each panel midpoint are known; hence the boundary integral equation can be solved to find the solution of the unsteady boundary value problem at each time step, as described previously.

5.1.3 Numerical results and comparisons

The turning motion of the Giant Danio is simulated using the method described above for Body II and Separation Scheme C, described in detail in *Chapter 4*. It was observed in the experiments that the near-tail flow dynamics are affected by the motions of the dorsal and anal fins during the maneuver. These interactions are less apparent during straight-line swimming with reduced dorsal and anal fin lateral motions and may be of secondary importance. As a result, the accurate modeling of the geometry during the turning maneuver was deemed crucial to resolving the flow dynamics around the tail and around the dorsal and anal fins with their large excursions.

The simulation time step size $dt = 0.01$ was chosen to be small enough to describe the details of the motion completely and to resolve wake-body dynamics and wake self-interactions. Fourier expansions of the mean line shapes in the local coordinate system reference frame employ fifteen temporal modes and ten spatial modes. Similar expansions of the local coordinate system trajectories within the global coordinate system employ ten temporal modes. Numerical desingularization parameters for the wake and body were chosen to be $\delta_w = 0.02$ and $\delta_b = 0.025$, respectively, based on a body length of $\ell = 1.0$, selected through a convergence process ensuring optimal

stability of the numeric solution.

In order to eliminate the influence of any starting vorticity shed by the caudal, dorsal, and anal fins during the impulsive start of the numerical simulation, a ramping-up time interval was added to the initial portion of the simulation. The initial conditions of the simulation are such that the fish mean line is locally perturbed to assume the shape of the Giant Danio at the start of the turning maneuver. The global position of the geometry is such that it translates at a constant velocity, equal to the velocity at the start of the turning maneuver. At the conclusion of the ramping-up time interval, the position, velocity, and shape of the geometry is identical to that of the Giant Danio at the initial frame of the experimental DPIV data. The total simulation length of 160 time steps thus modeled the 0.800 second turning maneuver, with 0.800 seconds of initial coasting motion before the turn was initiated to eliminate unwanted starting vorticity dynamics.

Results of the simulation are shown in Figures 5-5 and 5-6. These are taken at 0.100 second intervals, shown from $t = 0.000$ seconds at the start of the turning maneuver roughly until the turn is completed at $t = 0.700$ seconds. These frames are representative of time steps $t_s = 80$ to $t_s = 150$ at 10 time step intervals.

The sequence of images shown in Figure 5-5 detail the two-dimensional flow patterns around the turning fish in a plane at mid-body depth on the fish. Velocity vectors densely grid the plane, scaled in size by the magnitude of the local velocity, so that far from the fish, these can appear as points. In-plane streamlines are superimposed on the velocity vector grid to clarify the direction and the structure of the flow perturbations. The individual velocity vectors making up the grid are also scaled in color by the value of the vertical component of vorticity ω_z. The red vorticity indicates clockwise (positive) circulation, and the blue vorticity indicates counterclockwise (negative) circulation. The green areas are irrotational. In the initial plots of the sequence, at the extreme top of the fluid plane there is residual vorticity resulting from the starting motions in the simulation. This is caused by the translation of the Giant Danio geometry from the top of the frame into its starting position. The turning maneuver produces additional vorticity which is largely unaffected by

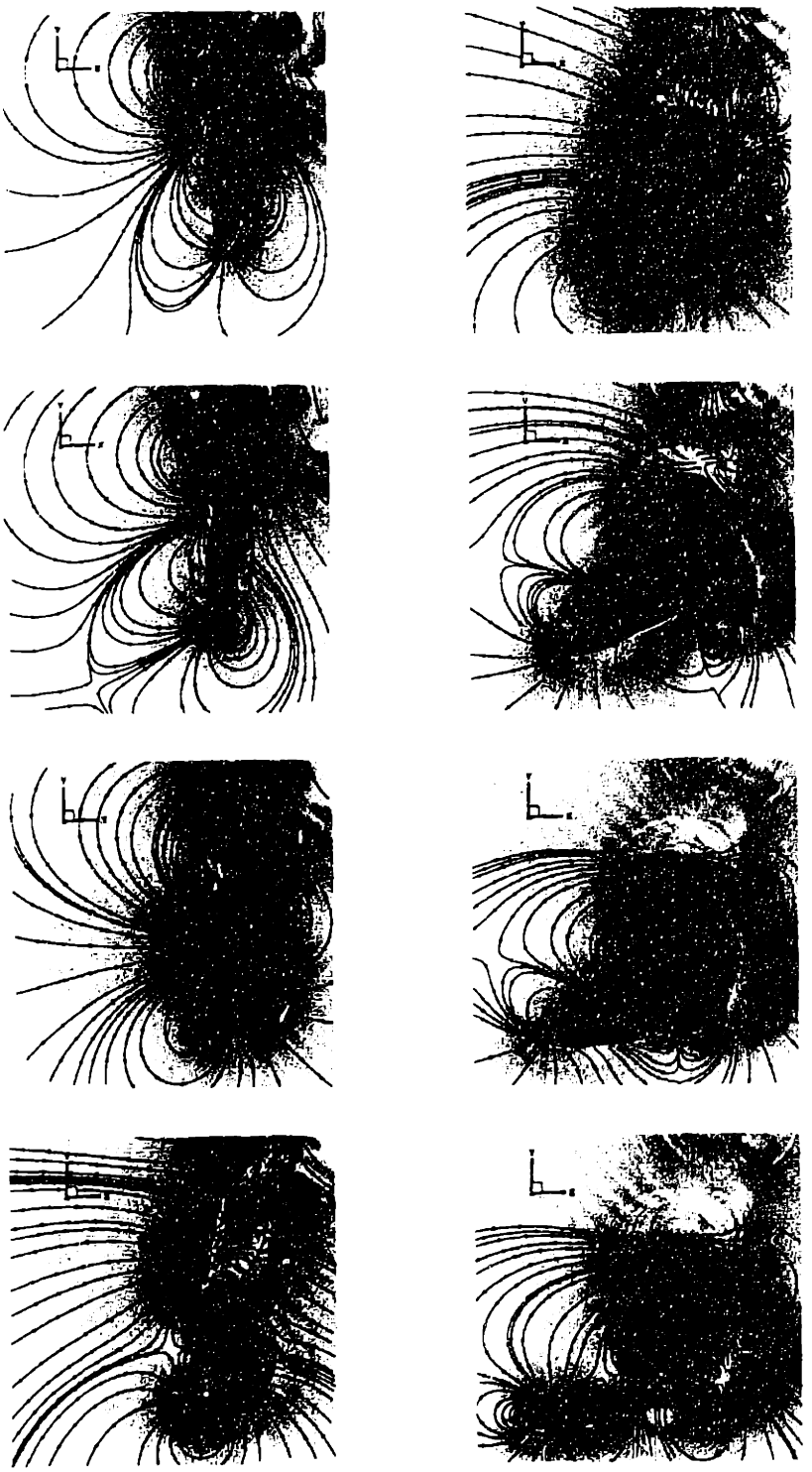

Figure 5-5: Mid-depth plane $z = 0.5H$ flow profiles during the unsteady turning motion, viewed from above. In-plane velocity streamlines (black) are superimposed on a dense velocity vector grid. Velocity vectors scaled in size by magnitude and in color by vertical vorticity ω_z contours (Range:$[-20s^{-1},20s^{-1}]$). Red vorticity indicates clockwise rotation, blue vorticity counterclockwise rotation, and green regions are irrotational. Sequence is shown top to bottom, first left then right column, at intervals of $dt = 0.1\ s$, from $t = 0.0\ s$ to $t = 0.7\ s$ of the original experiment.

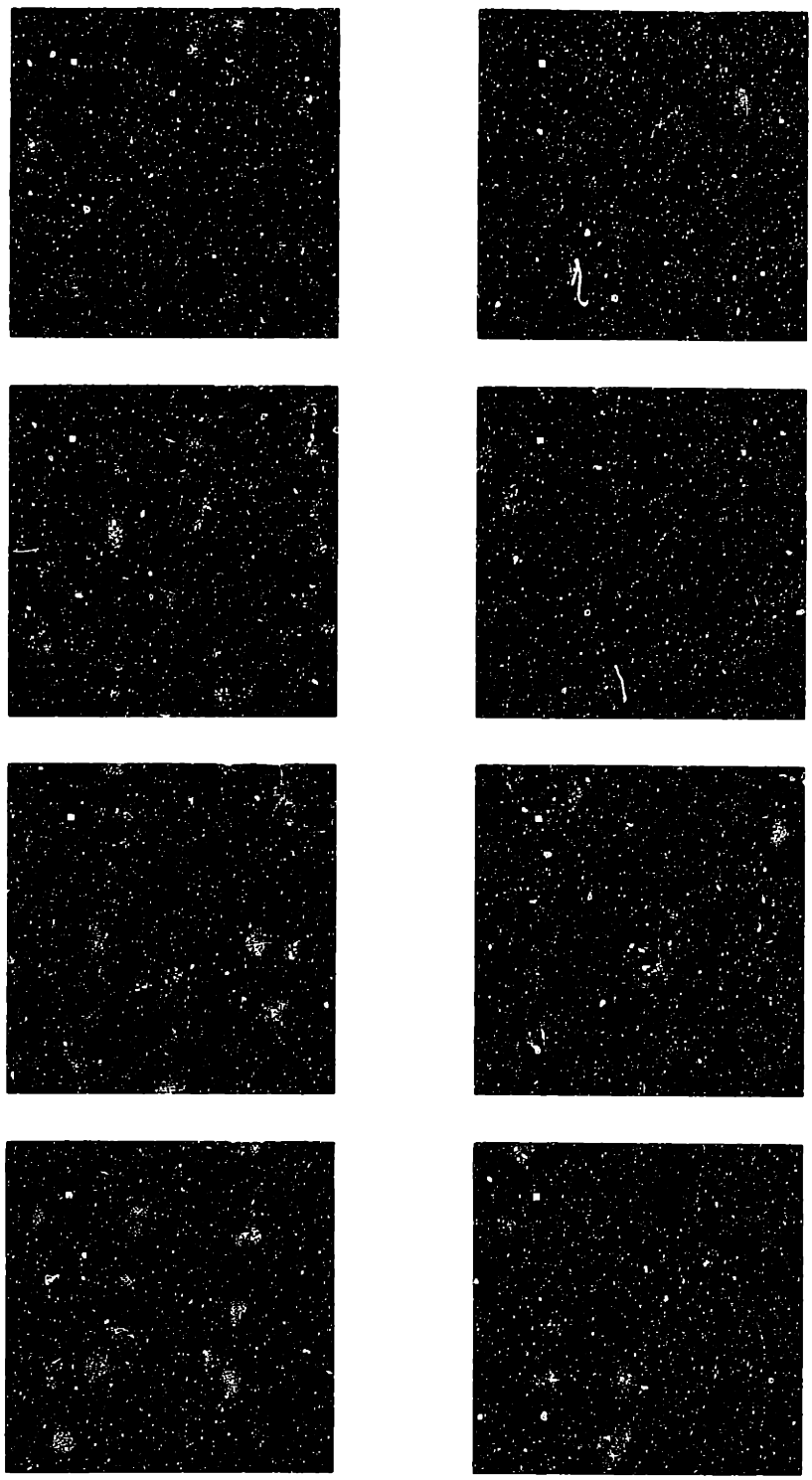

Figure 5-6: Mid-depth plane $z = 0.5H$ flow profiles during the unsteady turning motion viewed from above. Dynamic pressure coefficient contours shown (Range:[0,3]). Blue regions are high pressure, and the red regions are low pressure, revealing the formation of a turning-assisting jet. Sequence is shown top to bottom, first left then right column, at intervals of $dt = 0.1\ s$, from $t = 0.0\ s$ to $t = 0.7\ s$ of the original experiment.

the decaying starting vorticity.

The sequence of images shown in Figure 5-6 illustrates the evolution of dynamic pressure contours during the turn. Blue regions indicate high dynamic pressure, whereas the red regions are low dynamic pressure areas. From both Figures 5-5 and 5-6, it can be seen that as the fish contorts itself into a tight "C"-shape, the flow is organized into three circular patterns, around the head, the midbody, and the tail fin, respectively. As the fish begins to sweep its tail towards the reader's right, the tail fin sheds positive vorticity, as negative bound vorticity moves from the contraction region towards the tail. A large low pressure region coming from the left of the body crosses over to the right, passing over the tail and eventually pairing with the previous vortex to form a strong jet which turns the fish. The negative vorticity in the contraction region moves posteriorly to the tail during the downstroke, and a new low pressure region is formed below the fish. This negative vorticity is released into the wake during the subsequent follow-through upstroke, as the second low pressure region passes over the leading edge of the tail fin. As the tail concludes its upstroke and passes through the second region of high fluid momentum, it recovers energy from the jet through the enhanced separation from the trailing edge of the tail, reinforcing the negative vorticity which is being shed into the wake and resulting in additional loading on the tail which propels the body forward.

5.1.4 Two-dimensional turning simulation results

The two-dimensional computational method developed in *Chapter 2* was similarly modified to accommodate the simulation of arbitrary unsteady maneuvering motions. Again, the mean line local undulations were represented by temporal and spatial Fourier expansions about the instantaneous nose-tail line from the experimental data, and the trajectory of the global coordinate system was similarly represented through temporal Fourier series expansions. The desingularized point vortex representation to the wake dipole sheet was retained, and a fourth-order Runge-Kutta time integration scheme was employed. The shape of the foil section was prescribed to be similar to the three-dimensional geometry thickness distribution at the mid-depth plane. It

should be noted that the articulated tail is not modeled, and the two-dimensional section tapers in the afterbody to a finite-angled trailing edge at a distance from the nose corresponding to the mid-span of the caudal fin.

In the wake of the turning motion of the two-dimensional foil section, a turning thrust jet is clearly visible in Figure 5-7. The red point vortices induce a counter-clockwise fluid rotation and the blue point vortices induce a clockwise fluid rotation. Two large patches of counter-rotating vorticity make up the thrust jet which is transporting fluid to the right of the figure and slightly downward. Again, the strong fluid turning jet is oriented approximately 60° to the *left* of the initial starting position as seen by the foil section, and the foil velocity after the turn is roughly the same as the jet velocity. Also, the direction of the jet is roughly in the direction required by horizontal momentum balance.

In addition, another jet is evident at the top of the image, transporting fluid upward and slightly to the left; this jet, however, is likely the manifestation of the initial conditions of the simulation as the ramping-up time imposed was much less. However, a small jet was produced during the three-dimensional simulations as the body ceased its straight-line swimming motions and commenced the backbone contraction; this small jet produced during the three-dimensional simulation did not retain the strong vertical vorticity components as time progressed and the wake began to roll-up. The second jet at the top of Figure 5-7 is a result of the combination of these two factors, the initial condition and starting vorticity shed reinforcing the strength of this jet produced at the outset of maneuvering.

The wake at the conclusion of the two-dimensional turning motion shown in Figure 5-7 compares well quantitatively to the experimental vorticity field observed through DPIV around the live fish in Figure 5-2, as well as qualitatively. The total circulation of the two counter-rotating patches of discrete desingularized point vortices is of the same order of magnitude at the circulation of the experimentally observed patches, with total patch circulation magnitudes of approximately 40 cm^2/s each. This two-dimensional simulation corroborates the observations that the near-body flow around the fish is largely two-dimensional. Additionally, the excellent compari-

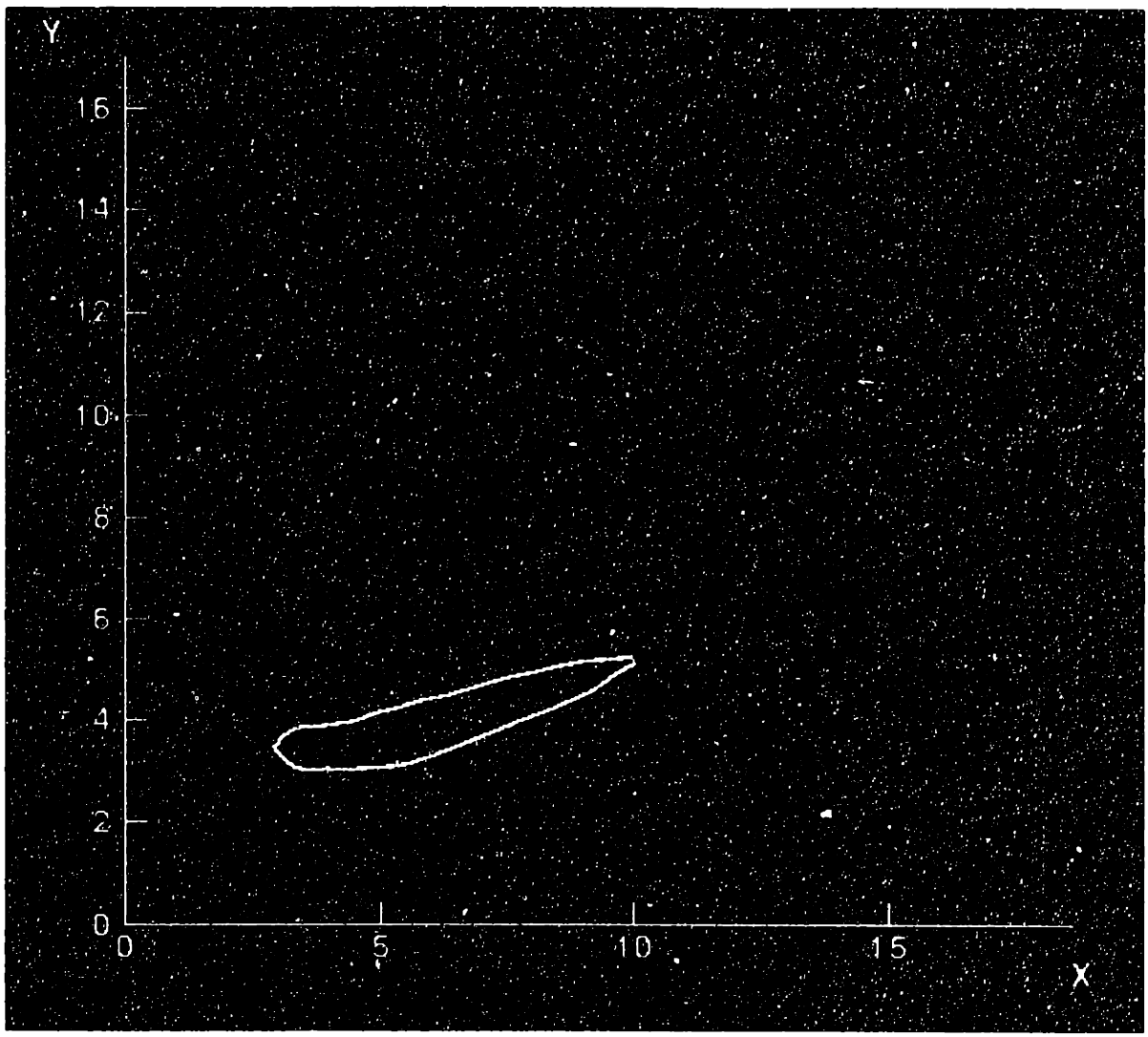

Figure 5-7: Wake visualization behind the turning motions of a two-dimensional flexible foil with a thickness distribution along the backbone comparable to the Giant Danio width at the mid-depth plane. Turning motions prescribed are identical to those imposed in three-dimensions, although the absence of the articulated tail should be noted. Size of the desingularized point vortices and the color range are scaled to the magnitude and sign of the circulation Γ. Red vortices indicate a counterclockwise (positive) circulation, and the blue vortices indicate a clockwise (negative) circulation. Green vortices have no circulation. Circulation range $\Gamma = [-1, 1]$. Desingularization radius $\delta_w = 0.02\ \ell$ where ℓ is the foil section unstretched chord length.

son of thrust jet patch circulations in the mid-depth plane observed in the experiment and simulation to the two-dimensional point vortex description of the wake suggests that the strongest wake structures shed by the tail in the three-dimensional simulations behave as the manifestations of the two-dimensional thrust jet instability.

5.1.5 Body forces during turning

The dynamics of the maneuver are shown in Figure 5-8, as obtained through the three-dimensional simulation of the motions with Body II and Separation Scheme C. In the top of the figure, the force on the fish body during the turn is depicted as a function of time, projected along the X and Y components of the global coordinate system. In the bottom plot of Figure 5-8, the fluid force acting on the fish center of mass at each time step of the simulation is shown, with the mean line curves of the fish backbone superimposed on the plot every four time steps.

The forces are moderately large at the outset of the maneuver, as the fish halts the oscillatory motions of straight-line swimming. The reducing-amplitude backbone undulations release residual body-bound vorticity into the wake, and cause a small lateral force oscillation. The force magnitude increases sharply, however, as the fish begins to contort into a tight curve and the body is forced downwards and to the right. Then, as the fish sweeps its caudal fin downwards, the direction of the force abruptly changes while its magnitude stays approximately constant, forcing the fish to the left and slightly upwards. This recoiling force which occurs during the tail's downstroke redirects the center of mass of the fish body to travel along the desired path to the left, or 60^o to the right of the original swimming direction as seen by the fish. This abrupt redirection of the body force is accomplished through the manipulation of the body-generated vorticity through its controlled release from the upstream fins to interact with the strong vorticity shed from the caudal fin. The body forces gradually subside as the turn is completed and straight-line swimming commences again, with the forces on the body primarily being lateral lift forces with a component in the direction of forward steady straight-line swimming, countering any viscous force which the fish must overcome. Thus, it is evident from the vector time history that the strong,

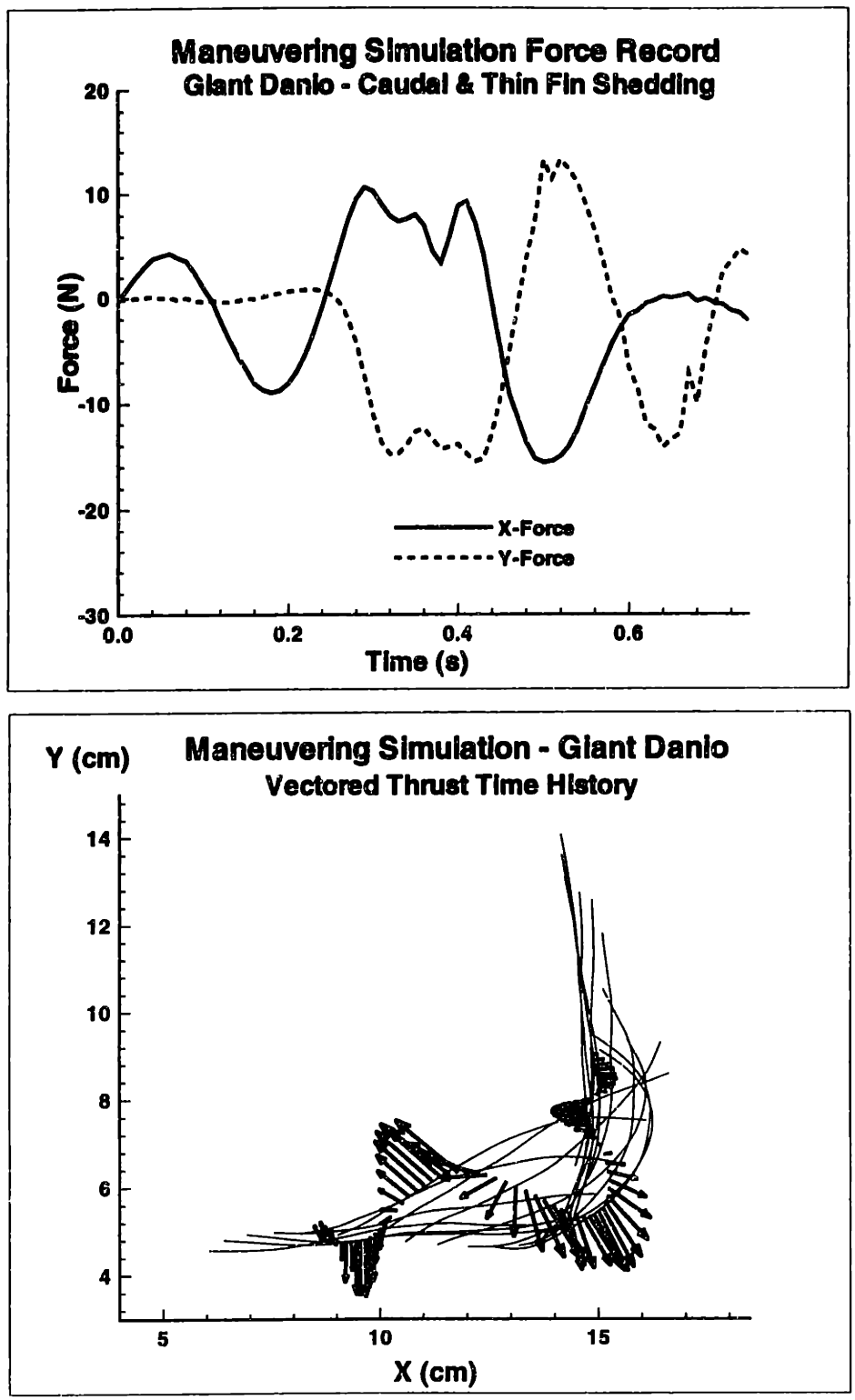

Figure 5-8: Force time history for the turning Giant Danio simulation. The top plot shows the X (—) and Y (- - -) components of the force on the fish body center of mass in a global reference frame as a function of time. Below, the force vectors acting through the center of mass are shown as a function of position at every time step during the maneuver. Body mean line locations are superimposed on the vector plot at 4 time step intervals.

rapidly-changing forces on the body allow it to turn over a short distance relative to its length.

5.1.6 Mechanism of turning thrust jet formation

The simulation was performed for all three separation models: Separation Schemes A and B for Body I, and Separation Scheme C for Body II. The subsequent choice to present data for Separation Scheme C in detail, shown in Section 5.1.3, was made after evaluation of the wake profiles produced by each computational geometry and their respective comparisons to the experimental images obtained through DPIV. The comparative evaluation was based on both the structure and interaction of the unsteadily-deforming wake sheets (computational validity) and the mid-body streamline and vorticity patterns observed in the flow (model validity). The flow patterns observed near the completion of the turn after the formation of the turning thrust jet are presented in Figure 5-9 below.

As can be seen in Figure 5-9, the structure of the turning jet is significantly influenced by the wake shedding scheme implemented. For simple caudal fin wake shedding seen in Figure 5-9(a), a strong jet is formed by the two large counter-rotating vortices which transports fluid to the right, opposite the direction of swimming. However, the position of the blue vortex inducing a counterclockwise fluid rotation is much farther above and to the left of the same patch of vorticity observed in the experimental DPIV wake profiles. The placement of this vortex was found to be sensitive to interactions of the caudal fin dipole sheet with upstream-shed vorticity, investigated with other separation schemes. The flow profiles in the wake look clean, with wake dynamics and interactions confined to the self-induced roll-up of the two strong jet vortices. As small jet to the left can be seen between the large patch of positive (blue) vorticity and the small patch of red vorticity directly above it. This smaller jet is also seen to be influenced by the upstream-shed vorticity wake-wake interactions, and its existence can be seen through examination of the experimental records in Figures 5-1 and 5-2. While this simple wake shedding model certainly produces a nice clean result, the comparison with experimental data is poor compared to separation schemes which

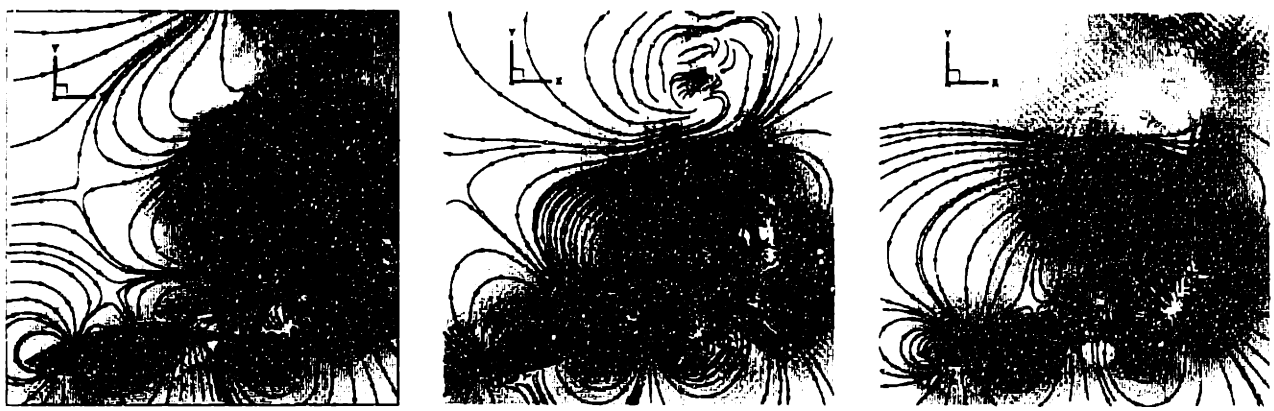

(a) Separation Scheme A (b) Separation Scheme B (c) Separation Scheme C

Figure 5-9: Wake profiles at the conclusion of the turning motion of the Giant Danio for three wake separation models: (a) Body I, Separation Scheme A; (b) Body I, Separation Scheme B; (c) Body II, Separation Scheme C. Mid-depth plane $z = 0.5H$ flow profiles shown viewed from above. In-plane velocity streamlines (black) are superimposed on a dense velocity vector grid. Vectors scaled in size by magnitude and in color by vertical vorticity ω_z contours (Range:$[-20s^{-1},20s^{-1}]$). Red vorticity indicates clockwise rotation, blue vorticity counterclockwise rotation, and green regions are irrotational. Time $t = 0.7$ s of the original experiment is shown.

consider the effects of upstream-shed vorticity and their subsequent interactions with vorticity shed from the caudal fin.

In Figure 5-9(b), a backbone ridge and caudal fin shedding scheme is employed. The strong turning thrust jet can be seen in the wake of the fish, with the counter-rotating patches of positive and negative vorticity forcing fluid to the right and slightly downwards. The location of the vortices which comprise the thrust jet compares well with the experimental data, although the strength of the wake vorticity is diminished from that realized in Figure 5-9(a) and in the experimental data presented in Figure 5-2. The effects of the interactions of the backbone-shed wakes with the caudal fin wake can be seen in the center of the thrust jet, where the instantaneous in-plane streamline patterns appear confused, but the overall dipole-like jet structure is evident. These wake-wake interactions are caused by the two horizontal vortex tubes, which are formed as the backbone-shed wakes roll-up tightly shortly after being shed due to the extreme backbone motions, which initiate circular out-of-plane velocity patterns which affect the roll-up of the caudal fin wake. In this manner, vertical vorticity ω_z is turned to become more horizontal ω_x or ω_y, and diminishes the strength of the in-plane vorticity comprising the thrust jet as it is seen in Figure 5-9(b). It should also be noted that the presence of the small jet to the left at the top of the flow plane is more evident with the adoption of this shedding model, as observed in the experiments, although the strength of this jet is actually much smaller than the large turning thrust jet and merely appears stronger due to the confluence of a large number of computed streamlines between the vortices which bound the jet.

In Figure 5-9(c), a dorsal, anal, and caudal fin shedding scheme is employed. The strong turning thrust jet can again be seen in the wake of the fish, with the counter-rotating patches of positive and negative vorticity forcing fluid to the right and slightly downwards. The location of the vortices which comprise the thrust jet again compares well with the experimental data, and now the strength of the wake vorticity is comparable to that realized in the experimental data presented in Figure 5-2 (although still slightly diminished from the vorticity shed into the wake from caudal fin shedding scheme in Figure 5-9(a)). The effects of the interactions of the backbone-

shed wakes with the caudal fin wake can again be seen in the center of the thrust jet, where the instantaneous in-plane streamline patterns appear confused, but the overall dipole-like jet structure is evident. The streamline patterns seen in this wake are slightly cleaner than those observed with the backbone ridge shedding scheme, as the two thin fin wakes do not roll-up into two horizontal vortex tubes, and the circular out-of-plane velocity patterns are diminished. It should also be noted that the presence of the small jet to the left at the top of the flow plane is still evident with the adoption of this shedding model, as observed in the experiments, with the strength of this jet still much smaller than the large turning thrust jet.

This thin fin shedding scheme produces the best comparisons to experimental results, and the interactions of body-generated vorticity can be seen to have a significant influence on the mechanisms of the thrust jet formation. This regulated-release of body-generated vorticity by upstream thin fins affects the flow around the caudal fin as the body contorts itself into a "C"-curve and through the propulsive stroke, such that the loading profile on the tail is not significantly altered until the propulsive stroke begins. Without the influence of upstream-shed vorticity, the near-body flow is significantly altered in the following manner. As the fish body begins to contort into a "C"-curve, circular flows emerge around different regions of the body. The presence of upstream shed wakes between the mid-body region and the tail contribute to the pattern of these circular flows, such that the flow around the leading edge of the articulated caudal fin is diminished. In this way, vorticity shed by the caudal fin during the contortion phase of the turn is strongly influenced by the body-generated vorticity, and the overall change in circulation of the tail is reduced. Without the presence of these wake regions between the mid-body and the tail, body contortion dramatically increases the leading edge cross-flow, inducing a rapid change in body circulation as vorticity is shed into the wake from the caudal fin trailing edge. This rapid dumping of caudal fin-generated vorticity into the wake positions the first vortex of the thrust jet farther above and to the left of where it is experimentally observed and where simulations with upstream wake shedding models predict. As the propulsive stroke begins, the first vortex is left behind in the model with caudal shedding only. How-

ever, during the propulsive strokes of upstream-shed wake simulations, the circulation around the tail gradually changes during the downstroke due to the influence of the upstream wakes.

These mechanisms of vortex placement based on the interaction of the tail with upstream-shed vorticity can also be observed experimentally through the additionally visualizations of a Giant Danio performing a "C"-turn presented in Ames (1998) [8], where the circulation around the tail is seen to be strongly influenced by the circular flows generated by the extreme localized undulations of the body. Further, these visualizations highlight the manner in which wake vorticity left in the turning thrust jet affects the near-body flow in the mid-body and contraction regions of the fish, not just the tail, corroborating the importance of the upstream-shed wakes from the dorsal and the anal fins on the flow around the caudal fin, in the region between the trailing edges of the body fins and the leading edge of the caudal fin, and in the subsequent turning thrust jet.

5.1.7 Discussion

Figure 5-10 summarizes the development and control of vorticity by the flexible body deformation during the turning maneuver. In Figure 5-10(a) the fish ceases its straight-line swimming undulations, and in Figure 5-10(b) the fish initiates its backbone curve. In the center of the body, a pair of oppositely-signed bound vortices develop, due to the midbody translation to the right and the opposite motion of the head and tail. The acceleration of the fluid in the midbody region forms a low pressure region L_1 to the left of the body. In Figure 5-10(c) local contortion of backbone into "C"-shape is complete, and the pair of body-generated oppositely-signed bound vortices separate slightly as the counterclockwise bound vorticity moves toward the tail fin. The low pressure region L_1 also moves posteriorly through the contraction region.

Straightening of the body in a wave-like motion commences in Figure 5-10(d), which releases counterclockwise vorticity into the wake by separation from the trailing edge of the caudal fin. The low pressure region L_1 passes over the leading edge of

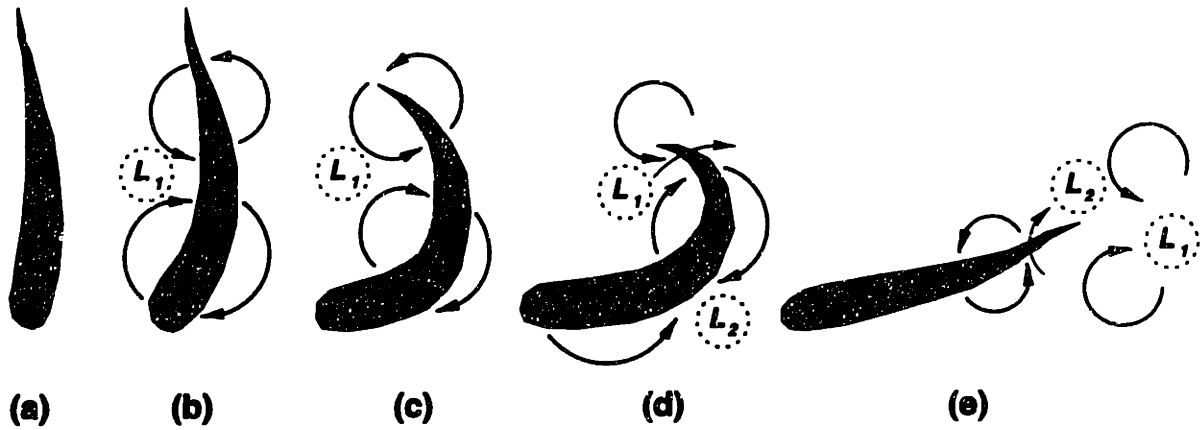

Figure 5-10: A descriptive model summarizing body-generated and wake vorticity control mechanisms used during the fish turning maneuver. Circled L indicates a region of low pressure which is manipulated by the body and tail to reinforce the formation of the turning thrust jet.

the tail, and the body recovers energy as the tail is swept through this area of high fluid momentum and additional trailing edge separation contributes to the formation of counterclockwise vorticity. The clockwise vorticity progresses posteriorly with the straightening of the backbone, and the induced counterclockwise flow around the head as the forebody of the fish makes a slight downward motion forms a low pressure region L_2 below the midbody region. As straightening continues, the clockwise bound vorticity travels down the length of the body towards the tail and is released into the wake with the completion and reversal of the downward sweep of the caudal fin trailing edge. Similarly, low pressure region L_2 passes in front of the leading edge of the tail fin at the maximum excursion of the downstroke, and contributes to the formation to the turning jet as the tail sweeps upwards through the low pressure region and the production of clockwise vorticity is reinforced. Resumption of straight-line swimming motions completes the release of strong clockwise vorticity into the wake, as shown in Figure 5-10(e), which then pairs with the counterclockwise vorticity to form a turning jet in the wake. The rapid formation of this thrust jet accomplishes the turning of the fish. It is remarkable that no uncontrolled vorticity appears to be shed during the turning process.

This model greatly simplifies the complex three-dimensional nature of the near-

body flow, but accurately portrays the dominant features of the mid-depth plane flow and principal mechanisms involved in manipulation of the large-scale two-dimensional vorticity features in the jet wake which affects the turning dynamics. Thus, control of bound vorticity and wake formation by the body and the tail fin for thrust vectoring to perform turning maneuvers is achieved through large localized backbone and tail actuation, enabling efficient manipulation of near-body flows and empowering the generation of large, short-duration maneuvering forces.

5.2 Fast-starting of a trout

This section will explore another maneuvering motion of great interest and potential for application, the fast-start. Fast-starts are sudden, short-duration accelerations used by fish mainly for prey capture. While they are common to many species of fish, their hydrodynamic origin is not well-known, and the maximum reported accelerations of fast-starting fish exceed most engineered propulsion systems in air, where the resistance to motion is negligible compared to a fluid. Recently, the fast-start capabilities of autonomous underwater robotic flexible-hull vehicles have been investigated on a model of the northern pike [118], known for its astounding reported maximum strike accelerations of 25 g [81].

The mechanisms of fluid control which the fish utilizes to obtain such performance result from the local backbone motions and tail motions; their relationship to the flow actuation and vorticity control mechanisms utilized in the turning maneuver is the subject of the present investigation. As a consequence, the limitations of the three-dimensional numerical scheme will be highlighted, and the validity its applicability to the problem investigated will be explored under the assumptions given.

5.2.1 Experimental evidence

Weihs (1973) [226] presented detailed experimental results for the starting motions of a trout (*Salmo trutta*) from rest, which generated body accelerations of 40 m/s^2 in shallow water. Film sequences taken of the motion on a scaled background grid

allowed for the discretizations of the backbone profiles at eight discrete intervals over the course of the lunging motion. Detailed analysis of the kinematics is presented in the original paper, with an extension of Lighthill's large amplitude elongated body theory to predict the forces during the transient starting motion.

Three stages of the motion are identified: *(i)* the preparatory stage, in which the fish contorts its body into an "L"-shape from its unstretched starting orientation; *(ii)* the propulsive stroke, which is characterized by the rapid sweeping motion of the tail perpendicular to the direction of the starting motion to conclude again with the body in an "L"-shape with the tail pointing in the opposite direction; *(iii)* the final stage in which the tail resumes moderate lateral heaving motions which drive the straight-line swimming motion.

Eight images of the starting trout were captured at intervals of $dt = 0.025\ s$, such that the duration of the entire transient motion was slightly less than $t = 0.20\ s$. The length of the body was just over 33 *cm* long from the nose to the trailing edge of the tail fin. Reconstruction of the original backbone data from Weihs is shown in Figure 5-11(a). The length scales are altered in the reproduction based on the manner in which the backbone profiles were discretized.

The original backbone images were discretized into 20 equal arc length segments. Then the local backbone undulations were represented by Fourier temporal and spatial expansions about the instantaneous nose-tail line. Ten temporal and spatial modes were utilized. The global trajectory was expanded similarly, again utilizing Fourier temporal expansions of ten modes. The backbone locations were then determined at 80 locations over the duration of the starting motion, separated by time segments $dt = 0.002$. This continuous representation of the motion is shown in Figure 5-11(b). These backbone locations were used as simulation input for the three-dimensional numerical scheme, in the manner described previously for the Giant Danio turn.

5.2.2 Simulation results

The starting motion of the trout is simulated using the three-dimensional unsteady numerical method. The computational geometry is developed to resemble the mor-

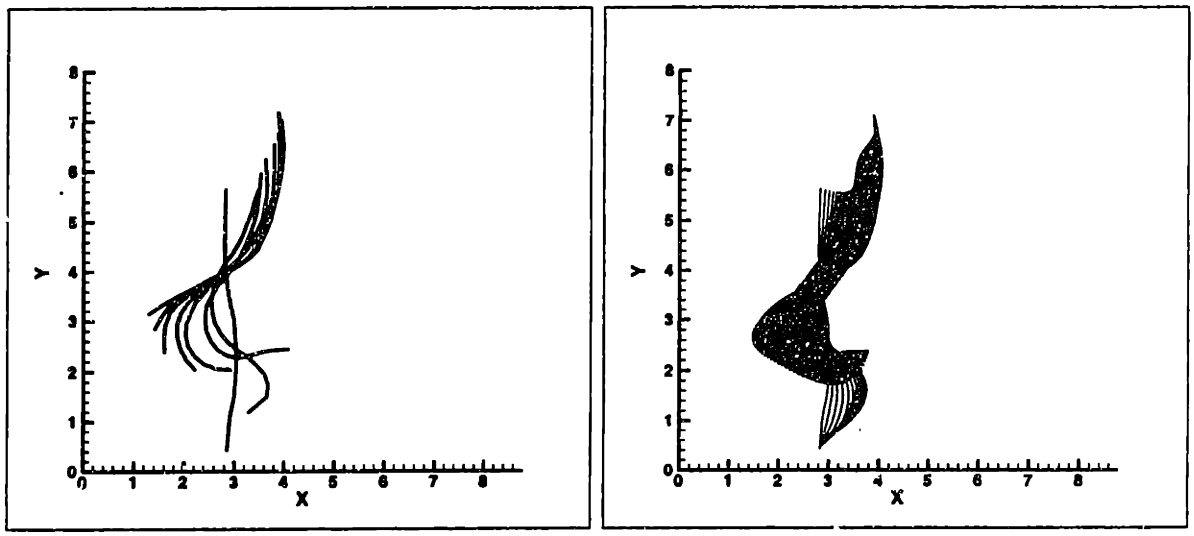

(a) Experiment (b) Computation

Figure 5-11: Trajectory of fast-starting trout (*Salmo trutta*). (a) Experimental data from Weihs (1973) [226] showing the backbone profiles at eight discrete intervals of the 0.175 s starting motion, separated by $dt = 0.025$ s. (b) Simulation input: the fish backbone trajectory is shown during the numerical simulation at intervals of $dt = 0.002s$. Both images are not to scale.

phology of the trout (*Salmo gairdneri*) described in detail in Webb (1975) [221] and Yates (1983) [247], a similar species to the trout *Salmo trutta* considered herein. The main body was represented by $O(1200)$ quadrilateral panels, and the caudal fin was represented by $O(600)$ quadrilateral panels. The smaller fins, such as the dorsal, pectoral, and anal fins, are ignored in this analysis due to the complex body motions and subsequent wake dynamics which result from merely considering one separation line. The wake desingularization radius was selected as $\delta_w = 0.025\ell$ based on body length ℓ. Similarly, the body desingularization radius was chosen to be $\delta_b = 0.025\ell$. The backbone motions are imposed based on the series expansion representation, and the body is scaled at each time to eliminate the influence of an unmodelled source potential. The results of the simulation are shown at six discrete time instants in Figure 5-12 over the duration the turn.

Referring to Figure 5-12, at time $t = 0.0$, the fish is shown in its initial condition, with no ramping-up motion as the trout observed in experiments commenced its

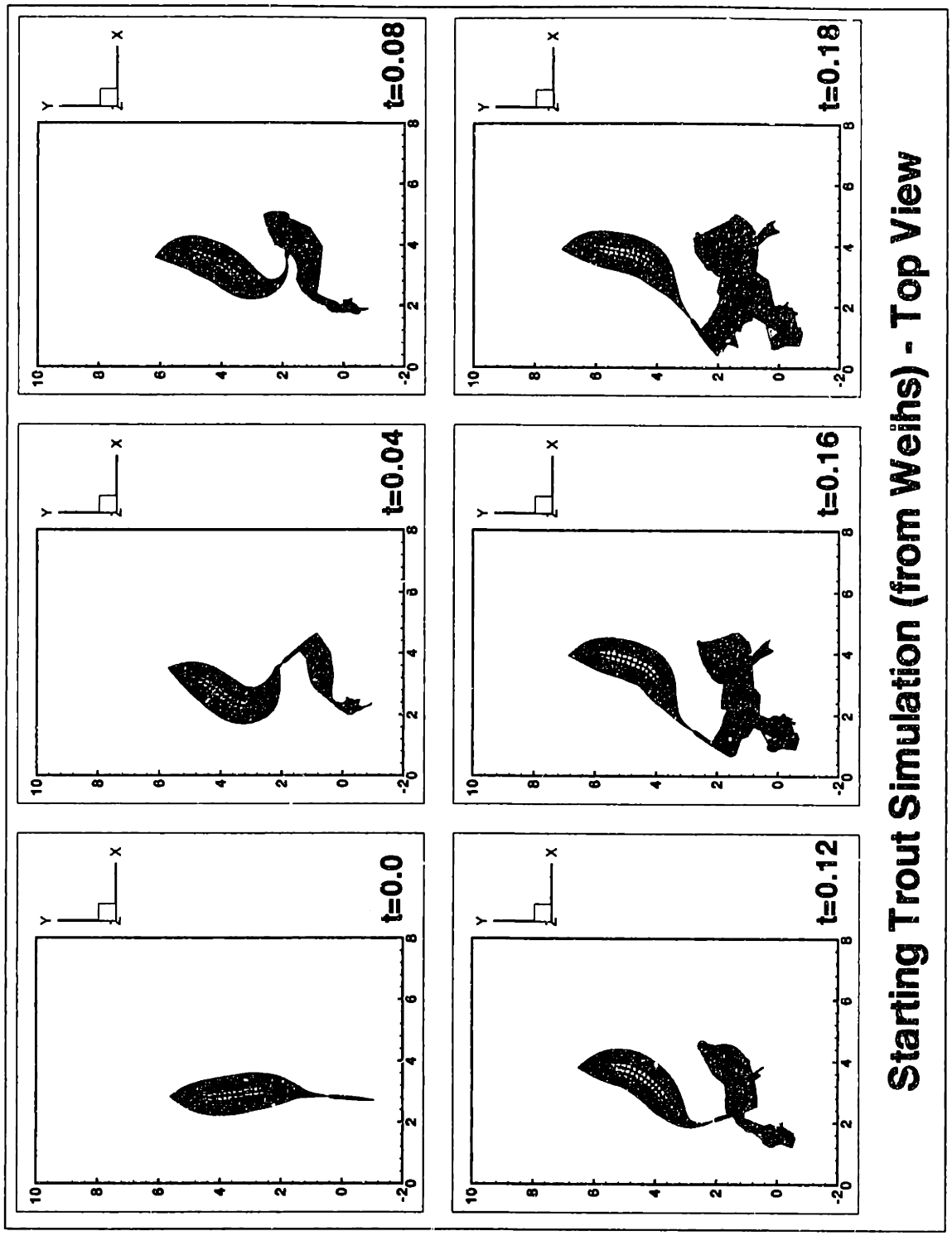

Figure 5-12: Simulation results of the fast-starting motions of a trout (*Salmo trutta*) from Weihs (1973) [226] showing the wake generation from the caudal fin over time (top view). The wake dipole strength is superimposed on the wake computational grid. Blue indicates a counterclockwise induced fluid rotation in the xy-plane, and red indicates a clockwise induced fluid rotation in the xy-plane, when viewed from the top.

lunge from rest. The fish then initiates the preparatory stage, which is shown in mid-motion at time $t = 0.04$. At this time, the starting vorticity is clearly visible as the red portion of the dipole sheet shed from the entire swept span of the caudal fin. Also, the blue-colored wake surface shed from the trailing edge of the caudal fin during the backbone contraction is evident, and this change in dipole strength produces small starting vortex which induces a clockwise fluid rotation in the xy-plane viewed from above, forming the first patch of vorticity which will comprise the strong thrust jet. At the next time shown $t = 0.08$, the fish has concluded the preparatory stage and initiates the propulsive stroke. The change in sign of the dipole wake sheet surface shed from the caudal fin trailing edge is seen to have occurred at the point of extreme backbone curvature, with a red-colored wake sheet being shed with the downward motion of the tail fin. This abrupt change in the sign of the wake dipole sheet produces a strong vortex, inducing a counterclockwise fluid rotation which is responsible for the formation of a significant component of the thrust jet structure.

At time $t = 0.12$ shown in Figure 5-12, the tail is in mid-propulsive stroke. The caudal fin must pass through the wake previously shed during the preparatory stage, and the two oppositely-signed dipole sheets intermingle through self-induced deformations as well as through the rotations induced by the strong vortex produced at the height of the preparatory contraction sand by the weaker starting vortex. At time $t = 0.16$, the propulsive stroke motion of the tail begins to decelerate, and the rotational motions induced by the strong thrust jet vortex to the right of the body has caused strong wake interactions evidenced by the tight roll-up of the shed wakes. It should be noted that some non-physical panel endpoint accelerations are evidenced at this point by the sharp protruding areas of the wake sheet. At time $t = 0.18$, the tail propulsive stroke has concluded, and the dipole sheet strength being shed from the trailing edge of the caudal fin weakens. This change in dipole strength forms an additional strong wake vortex which will induce a clockwise rotation in the xy-plane when viewed from above. This strong vortex will pair with the strong vortex formed at the outset of the propulsive stroke to form a jet of fluid directing momentum in the negative y-direction, countered by the propelling of the body forward in the pos-

itive y-direction. The mechanics of this second clockwise vortex formation are not completely apparent by $t = 0.18$ but are inferred from the wake interactions seen over the course of the propulsive stroke and from the obvious decay in the strength of the wake dipole sheet. The extremes of the experimental dataset have been reached at $t = 0.18$, beyond which no more simulation is possible without the assumption of a swimming motion or more experimental backbone trajectory data, as a Gibbs phenomena is rapidly encountered and results in simulation breakdown.

Further attempts to visualize the wake and near-body flow dynamics were unsuccessful for the reasons outlined in the following section, which highlights the limitations of this three-dimensional numeric scheme to simulate the unsteady flow about arbitrary starting motions of the flexible body.

5.2.3 Applicability of the computational scheme

The computational scheme has been shown to be an effective tool for visualization of the near-body flow and wake dynamics around the steady straight-line swimming motions of a three-dimensional flexible body with an arbitrary distribution of lifting surfaces. In some cases, the unsteady motions of the body, such as turning within a fraction of the body length, are similarly well-suited to simulation. The validity and suitability of the numerical scheme to studying unsteady motions are questionable, however, when the imposed body motions may induce physics which violate the assumptions of the method formulation. This has been evidenced through repeated simulations of the trout starting motion presented in the previous section, where the applicability of the computational scheme comes into doubt.

Physics factors which may render this numerical scheme insufficient include the continuous representation of the wake dipole sheet and the lack of additional modeled separation. During the preparatory stage, the instantaneous angle of attack of the caudal fin would likely cause widespread separation from the leading and trailing edges of the caudal fin, in addition to backbone ridge and bluff body separation over the contraction region and nose, respectively. As the caudal fin passes through the previously shed preparatory wake during the propulsive stroke, the validity of the

trailing-edge separation line assumption is also questionable. Stall vortices would likely be attached to the back-sides of the leading and trailing edge, whose strength and behavior would be strongly influenced by the turbulent fluctuations inherent in the wake encountered from the preparatory motions, assuming that this preparatory wake was a valid approximation to begin with. Finally, assuming that the separation schemes as imposed were valid representations of the vorticity released into the fluid, the wakes should not penetrate the body, and shed wake shear layers would likely combine and connect to form strong discrete patches of vorticity, as seen in the Giant Danio turning simulations.

Factors contributing to the non-physical wake behavior observed likely include intermingling of two desingularized wake sheets of such strong dipole strength and the passing of the body geometry and the continued separation from the trailing edge through the path of prior wake release. These issues can be addressed computational, and indeed, the body and wake desingularization parameters can be tuned to produce a more reasonable "looking" wake picture [166]. However, the poor representation of the physics of the problem are exacerbated by this decision as wake panels will frequently convect to within the body surface enclosure and must be dealt with specially, unless an extremely small time step is used during time integration of the solution which yields numerical instabilities addressed in depth in *Chapter 2*. Thus, a smaller desingularization radius is favored for more accurate representation of the continuous solution, but result in spurious panel endpoint convections, especially during the propulsive stroke.

In order for this numeric scheme to be a valid approach to simulate the unsteady hydrodynamic mechanisms of transient maneuvering motions, careful criteria of the unsteady motion considered must be satisfied. The tail must follow a smooth path through the fluid, i.e. under the assumption of quiescent ambient fluid in the vicinity of the tail throughout the maneuvering motions, the possibility of cross-flows and leading edge separation must be eliminated. In reality, some separation may occur, which can only be effectively handled by a fully viscous approach. Also, the tail should not pass through the path of previously shed dipole sheet wakes, as the solution of the

potential distribution around the tail and thus the strength of the shed wake dipole sheet from the trailing edge becomes suspect. In contrast, the caudal fin may pass perpendicularly through previously shed wakes sheets, such as those release upstream by thin fins surfaces, as non-physical wake accelerations and body penetrations can be alleviated and the upstream shed wakes are generally much weaker shear layers than that shed from the caudal fin, especially for steady straight-line swimming motions. Possible improvements to the numeric scheme, which will be outlined in detail in *Chapter 7*, would include a more robust wake representation, such as a vortex particle method, which can account for vortex strength redistribution [110, 111, 112] and vorticity field diffusion [231, 232].

Chapter 6

Flow and vorticity control swimming mechanisms

6.1 Principles of vorticity and flow control

In this chapter, vorticity control mechanisms utilized by the swimming fish to enhance performance are identified, which allow it to produce a strong thrust, to recapture energy in the flow for higher efficiency, or to generate a strong drag force. The relationships between the kinematics of the swimming motions and the vorticity control mechanisms for several separation models are identified as different modes of wake-wake and wake-body interactions which dramatically influence the performance of the fish. In addition, the mechanisms of the generation and the controlled release of body-bound vorticity are identified which elucidate the manner in which the fish is able to control the wake-body flow interactions and to exploit the two-dimensional thrust and drag jet instabilities to enhance its dynamical performance.

Vorticity control is the process of altering the position and strength of vortices to affect the load distribution on a body, so as to enhance propulsive efficiency for instance, or the dynamics of the unsteady fluid, so as to reduce wake signature for example. This control of vorticity is simply accomplished through the unsteady motion of a body in a fluid or the unsteady forcing of the flow [56, 202].

Unsteady propulsion may offer certain advantages over to conventional propulsors.

Gursul and Ho (1992) [80] demonstrated that unsteady motion of airfoils can cause a very high lift coefficient, and recent work by Anderson *et al.* (1998) [10] shows that oscillating foils are able to produce propulsive thrust very efficiently. Additionally, an oscillating foil can be used to alter and reposition oncoming vorticity [114, 9] and recapture energy contained in the eddies of an oncoming flow [68, 190, 191]. The interactions of oncoming vorticity with an oscillating lifting surface are shown to produce thrust in three distinct ways, including the strengthening of vortices shed from the oscillating foil forming a strong reverse Kármán street, weakening the vortices shed by the oscillating foil forming a weakened reverse Kármán street, and pairing with oppositely-signed vortices shed from the oscillating foil creating vortex pairs which widen the wake. As found theoretically and confirmed experimentally, a foil may extract energy from the oncoming vorticity when destructive interference is observed, increasing its efficiency substantially [191].

Through detailed flow visualization of the simulated fish straight-line swimming motions, the interactions of the body-generated vorticity with the oscillating caudal fin will be studied. The need to actuate the articulated tail to generate thrust on the fish causes the body to undulate. These undulations contribute to the propulsion mechanics by generating a suction force around the low aspect ratio body as the body generates a circulation and body-bound vorticity. As the vorticity generated by the body is shed into the wake, it is manipulated by the oscillating tail in order to enhance the performance. Similarly, the control of these packets of body-generated vorticity is a mechanism by which the vorticity present in the boundary layer of the real fish can be efficiently gathered and controlled to contribute to the production of useful thrust rather than drag.

The geometric and separation model dependencies of the performance will be considered in the following section, which reveals the vorticity control mechanisms of live fish. Later, treatment of the kinematic dependencies of the wake structures and vorticity control performance will be presented, with generalized models of the types of wake-wake-body interaction modes observed in fish swimming motions, for both steady straight-line swimming and unsteady maneuvering.

6.2 Vorticity control mechanisms of live fish

6.2.1 Geometric influences

Two different body geometries are chosen to simulate the straight-line swimming and the maneuvering of the Giant Danio, with emphasis on studying the effects of secondary fin modeling on the vorticity control mechanisms utilized in the swimming motions. In addition, two different separation schemes are chosen in conjunction with the geometric modeling differences to determine the effects of upstream vorticity generation on the performance of the fish. From experience gained in the studies of *Chapter 4* and *Chapter 5*, only simulations which employed some form of upstream vorticity shedding was employed, as the importance of these wake-wake interactions on both the accuracy of the solution and on the comparison to experiments is easily gleaned from the detailed simulation results already presented with analysis. As described previously in *Chapter 4*, the body of the fish and the caudal fin comprise Body I, and the addition of dorsal and anal fins to this simple geometry comprise Body II (see Figure 4-15). For Body I, Separation Scheme B, caudal and backbone shedding was considered, and Separation Scheme C, caudal and thin fin shedding, was considered for the Body II geometry.

For the straight-line swimming motions examined in *Chapter 4*, the same motions captured using DPIV in the live fish experiments are simulated to study the dynamics associated with each of the shedding models. The effects of multiple-vortex sheet wake-body and wake-wake interactions may have considerable influence on the performance realized by straight-line swimming motions, and they may also explain morphological features and kinematic behaviors developed independently by various species of fish for energy recapture and vorticity control.

Backbone ridge wake shedding

Separation Scheme B is employed in the straight-line fish swimming simulations of the Giant Danio, and it is assumed that this model will produce wake dynamics of backbone-shed vorticity which will not differ greatly from the dynamics of the vorticity

shed from the actual dorsal and anal fins, for straight-line swimming of moderate tail excursions [127]. Detailed visualizations of the wake roll-up and interactions with the caudal fin and the main caudal wake were performed to corroborate these assumptions and to gain understand about how these wakes actually behave. A sequence of images is shown in Figure 6-1 which highlights the interaction of the backbone shed vorticity with the oscillation of the caudal fin.

As can be seen from Figure 6-1, the unsteady motion of the body significantly affects the behavior of the shed backbone wakes. The wake sheets shed from the backbone roll-up and tighten into tubes under the self-influence of the wake sheet vorticity and the perturbation velocity influence of the undulations of the contraction region of the body. These packets of vorticity, represented by the rolled-up dipole sheet of variable strength, are intercepted by the oscillations of the tail such that the smaller backbone wakes are rolled-up into the caudal wake sheets of an opposite sign. In this way, vertical vorticity shed from the backbone is paired with vertical vorticity of opposite sign from the caudal fin as the thrust jet wake develops. This will be examined in greater detail in the coming section, but it is interesting to note that the leading edge of the caudal fin passes through these smaller wakes before the upstream vorticity has had a chance to significantly into tubes of vorticity, likely affecting the loading on the caudal fin and the strength of the caudal wake, as the leading edge suction force and thus the circulation distribution along the span is altered due to the perturbation influence of the shed upstream wakes.

Thin fin shedding

Through straight-line swimming and maneuvering simulation visualizations of *Chapter 4* and *Chapter 5*, the geometric modeling of the dorsal and anal fins of the body with consequent wake shedding was demonstrated to provide the best results of the thrust jet structure in comparison to experiment. In order to visualize how the tail is manipulating the wakes shed from these smaller thin fins, Figure 6-2 shows a sequence of simulation results for straight-line swimming motions of the Giant Danio, modeled with Body II and the associated Separation Scheme C. The images depict the

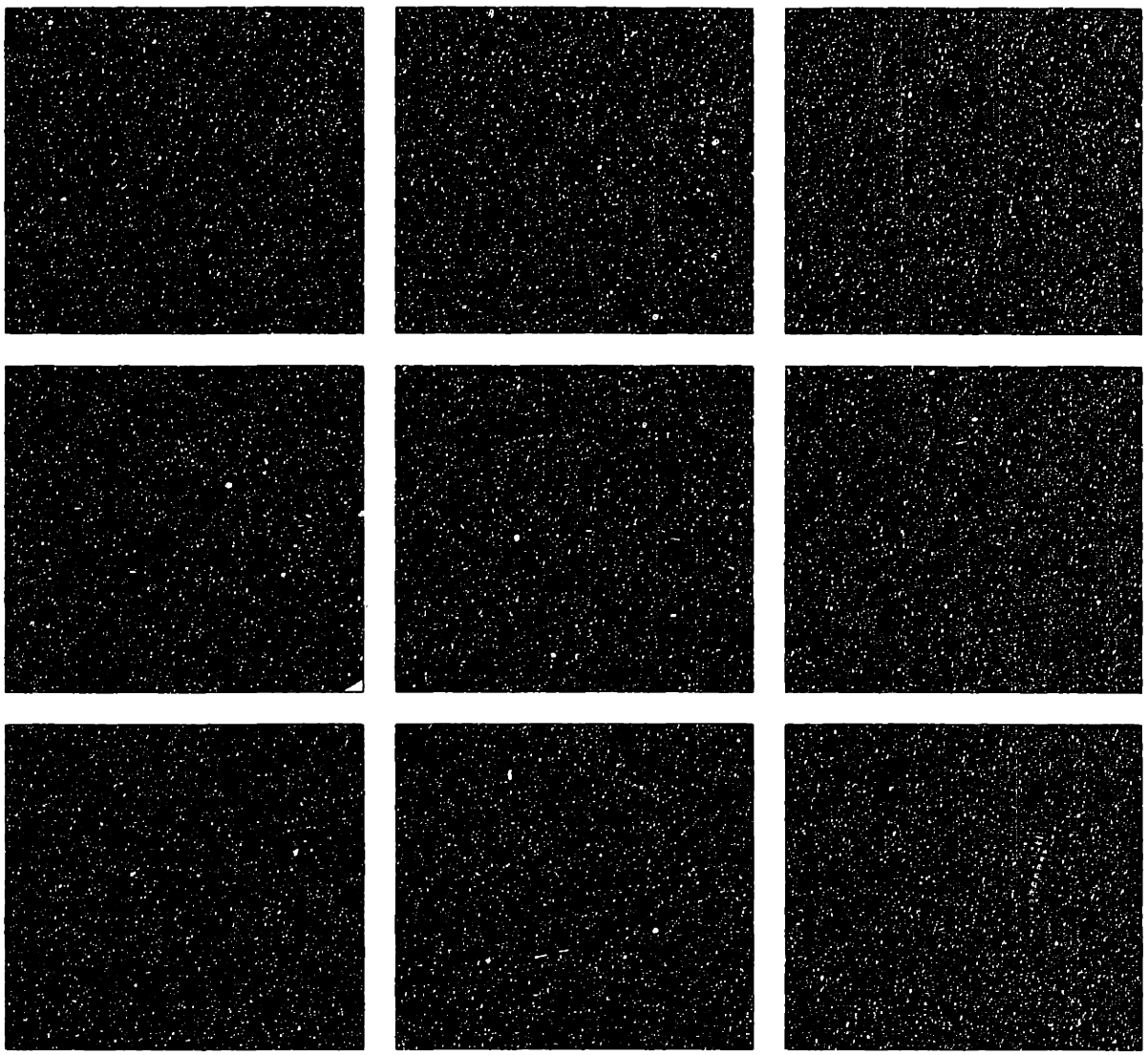

Figure 6-1: Wake-wake and wake-body interactions over one period T of Giant Danio straight-line swimming motions, highlighting the interaction effects of upstream shed vorticity with the oscillating caudal fin and strong caudal wake. Separation Scheme B, backbone ridge and caudal fin shedding, is shown applied to Body I. Color contours of the dipole strength of the multiple wake sheets are superimposed on the wake computational grid. Sequence is shown from left to right, top row first to bottom row at intervals of $T/8$.

motions of the flexible swimming body, taken at equal intervals over one swimming period, with wakes separating from the three prescribed trailing edges. The wakes are each shown in their own individual color scheme, rather than in contours of dipole strength, for clarity in visualization of the wake-wake and wake-body interactions.

This sequence of eight images in Figure 6-2 clearly presents evidence of the importance of wake-wake and wake-body interaction dynamics for straight-line swimming with upstream vorticity release. The motion of the caudal fin is phased such that the leading edge of the oscillating tail intercepts vorticity packets released by thin fins upstream. These packets of upstream shed vorticity, where the smaller wakes are beginning to tightly curl, correspond to peaks in the vorticity strength shed by oscillation of the thin fins, of a strength opposite to that of the vorticity present in the subsequently shed caudal fin wake. Through this type interaction with the tail fin, it is possible that the body may reclaim some of the energy lost to wake generation upstream and more efficiently generate thrust with the tail. Such constructive interaction of a lifting surface with upstream vorticity packets was shown by Streitlien, *et al.* (1996) [191] to recover energy and improve propulsive efficiency.

From these visualizations of caudal fin interaction with wakes shed from the body dorsal and anal fins, the morphology of the body fins with nearly vertical trailing edges may be explained. The numerical simulations reveal that the relationship between the oscillation frequency f of the fish backbone wave and the corresponding backbone wavelength λ during the natural straight-line swimming motions of the Giant Danio body allow strong interaction of the wakes shed from the smaller thin fins with the caudal fin wakes. Additionally, the near-vertical trailing edge of the thin fins allows the deforming upstream wakes to affect the flow around the oscillating caudal fin for much of the span, allowing for significant alteration of spanwise circulation distribution, leading edge suction force, and loading on the caudal fin, due to the perturbation velocities induced by the upstream-shed wakes. Lack of these side fins, or a variation in their placement or shape, would alter the interaction dynamics and may result in a reduced swimming performance. In fact, as previous shown the replacement of the thin fins by smaller wakes shedding from the dorsal and ventral

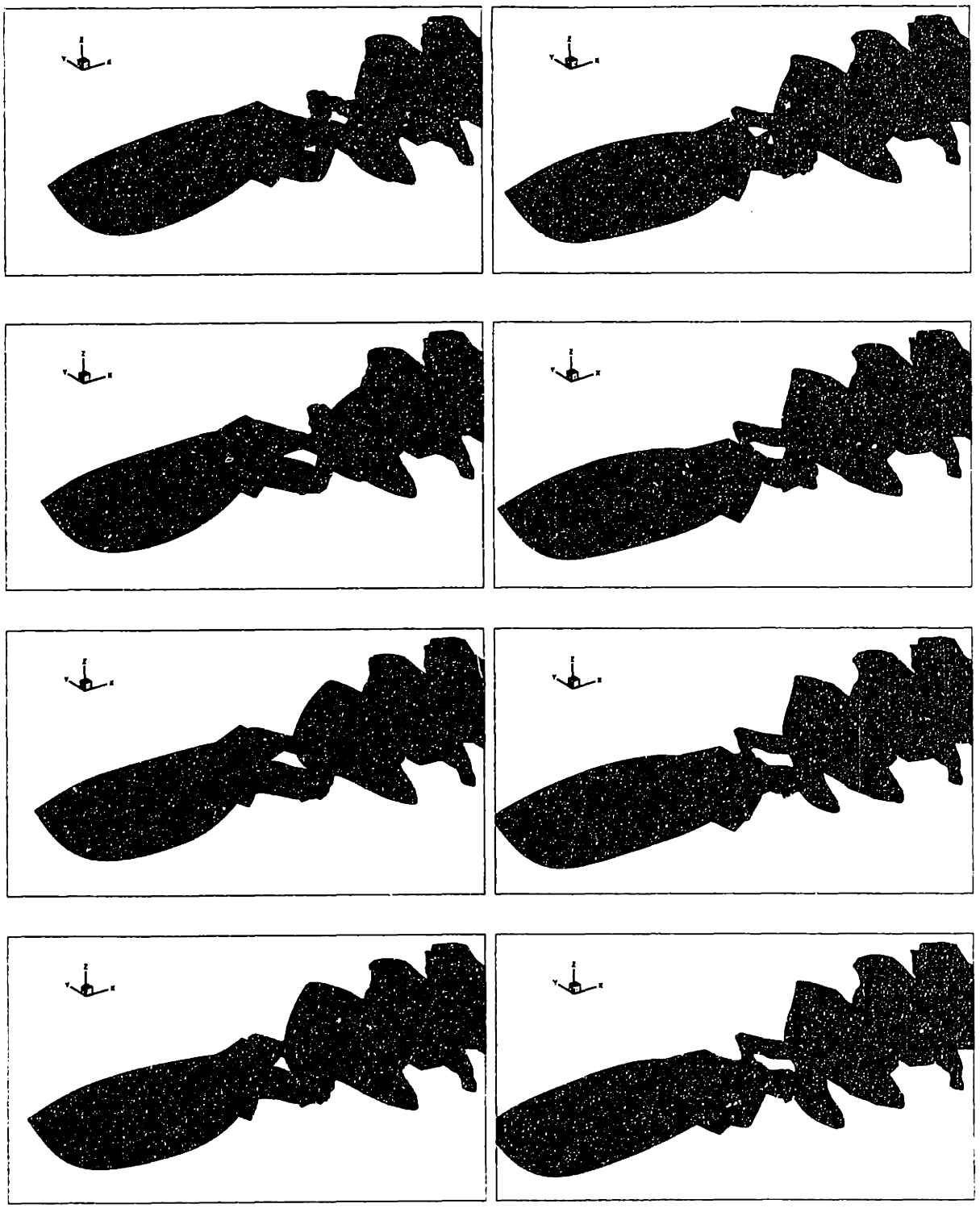

Figure 6-2: Interaction of the caudal fin with upstream shed vorticity from thin fins and corresponding wake-wake influence and dynamics. Giant Danio straight-line swimming numerical simulation. Sequence is shown from top to bottom, first left then right column, at $T/8$ intervals.

ridges results in separation lines with greatly reduced slope, whose wakes then tightly roll up into tubes, diminishing the extent of significant favorable interaction with the caudal fin in comparison to the thin fin wake interactions. Changes in kinematics in addition would significantly alter the interaction dynamics and thus the loading on the body, but this will be examined in the context of the *RoboTuna* simulations in Sections 6.3 through 6.5.

6.2.2 Dynamical consequences

Figure 6-3 illustrates the thrust and sideforces as functions of time achieved by the Giant Danio during the straight-line swimming cycle. In addition, the time history of these forces is plotted for each of the three wake separation schemes applied to the simulation model. As expected, the thrust forces have a net positive temporal mean, although at any given time, the thrust force may be positive or negative. The sideforces have a net of zero as the mean fish trajectory is a straight-line. In actuality, the forward speed of the fish is not a constant U as described by the numerical model, but the second-order periodic surge of the body is neglected and is not expected to significantly affect the body dynamics or the wake-body and wake-wake interactions. In general, the side force on the body geometry is evenly distributed between the caudal fin and the rest of the body, whereas the caudal fin typically sustains over 90% of the thrust force.

As can be seen from the thrust time histories given in Figure 6-3, higher peak forces are realized when Separation Schemes B and C are employed than when only the caudal fin separates in Separation Scheme A. However, for comparable surface areas, a lower mean thrust force is realized for Separation Scheme B with the backbone ridge wake separations than for Separation Scheme A with just caudal fin separation, suggesting a diminished thrust jet strength caused by the interaction of the upstream wakes with the caudal fin and caudal fin wake. Utilization of Separation Scheme C, with separation from the thin dorsal and anal fins in addition to the caudal fin, results in the highest mean thrust force. The load distribution on the body for this simulation implies a favorable interaction between upstream shed vorticity and the

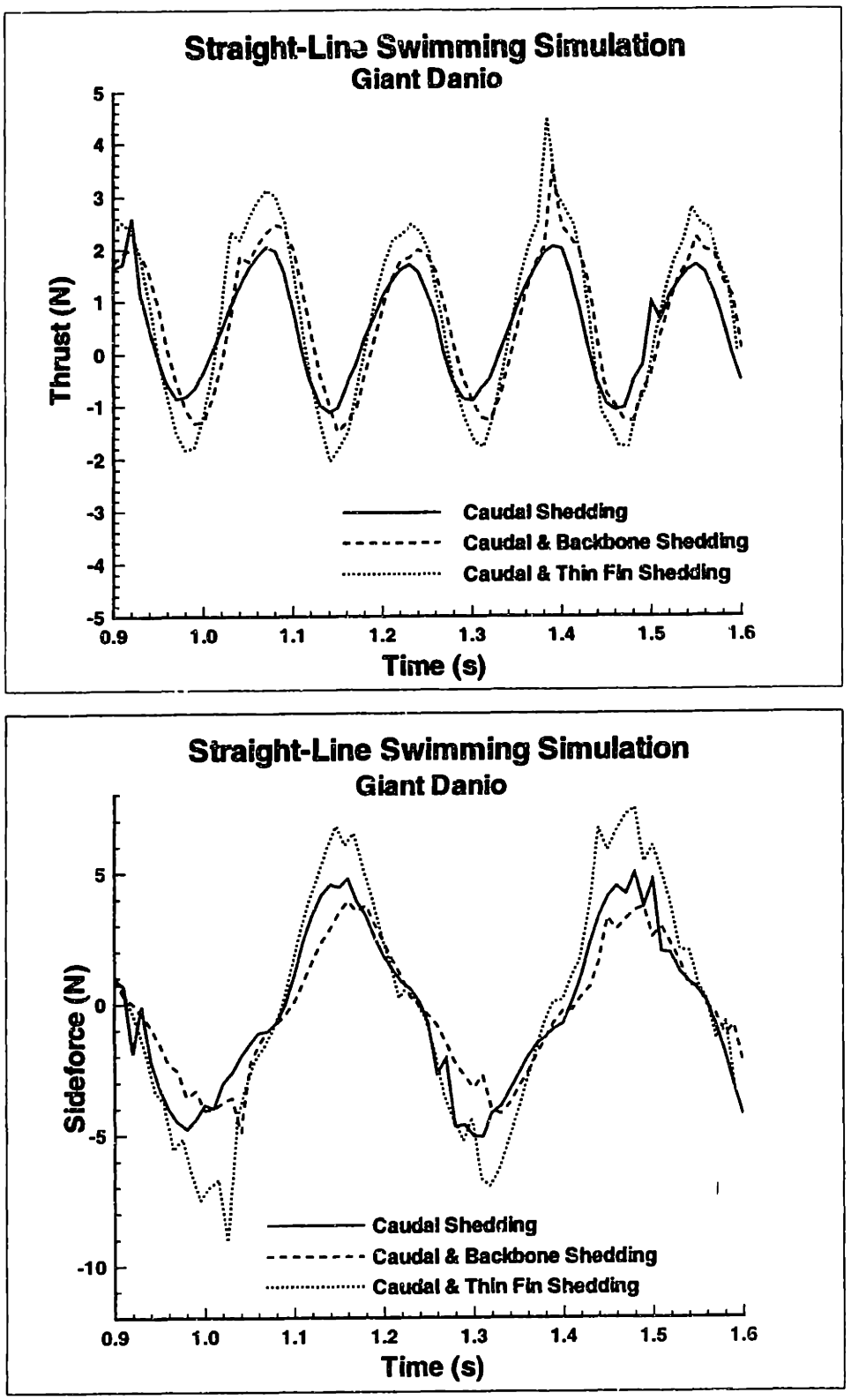

Figure 6-3: Thrust and sideforces on the body during straight-line swimming simulation as functions of time. The three different separation schemes are superimposed on each plot: (—) Scheme A, caudal shedding, (- - -) Scheme B, caudal and backbone shedding, (···) Scheme C, caudal and thin fin shedding.

oscillating caudal fin.

Similarly, as can be seen from the time histories of the side forces in Figure 6-3, the lowest peak side force magnitudes are realized for straight-line swimming motions employing the caudal and backbone separation model, Separation Scheme B. Employing Separation Scheme A results slightly higher side forces than Scheme B, and the addition of dorsal and anal fins for the application of Separation Scheme C realizes the highest peak side force magnitudes. This evidence suggests a similar favorable interaction of upstream shed vorticity with the body and caudal fin, and for comparable surface areas, upstream vorticity shedding decreases the peak magnitudes of the side forces realized during straight-line swimming.

From Figure 6-3, it is clear that the swimming Giant Danio is able to generate a lower thrust and lower sideforces for the same imposed motion and same surface area when upstream wakes are permitted to be released and to interact with the oscillating caudal fin and its strong wake. The larger forces with thin fins added to the geometry are to be expected with the larger surface area, but from qualitative observation of the same types of wake interactions occurring for both types of upstream wake shedding models, it can be construed that these wake interactions resulting from the addition of thin dorsal and anal fins to the body will have a positive affect on the swimming performance. Thus, for this natural swimming motion imposed on the various wake shedding models, the Giant Danio appears to have optimized its kinematic behavior to maximize performance within its morphological constraints.

6.2.3 Details of flow structure actuation and vorticity control

To understand more clearly why Separation Scheme B might result in an improved performance over the caudal fin wake shedding model, the interactions of the vorticity structures and the regions of high momentum accelerated by the undulating body which are directed to form a thrust jet are visualized. From the desingularized dipole sheet representation of the wake surfaces and the desingularized source-dipole distribution representation of body surfaces, a fluid velocity field can be constructed with distributed vorticity components. These vortex structures, while not calculated by a

surface production of vorticity mechanism [238], are representative of vortical structures which are modeled through the dipole sheet wake representations. They more clearly illustrate wake interactions which are obviated by the complex deformations of multiple, nonlinear, desingularized wake sheets. In this manner, the wake structures formed upstream are distinguishable from those structures formed by the oscillating caudal fins, and although this wake vorticity cannot merge or annihilate each other, the wake vorticity components formed upstream can be observed to become closely intertwined and entrained in larger structures from the caudal fin wake. These interactions will enable the abstraction of several vorticity control modes employed in fish swimming, presented in Section 6.5.

Figure 6-4 shows the interaction of vorticity structures over one-half of the straight-line swimming cycle of the Giant Danio. The images were generated with high resolution of the velocity field from the desingularized surface perturbation velocity influences, revealing fine features of the isosurfaces of the resulting vorticity structures.

The interaction of the wake vorticity structures alone is shown in Figure 6-4. Isosurfaces of total vorticity magnitude are shown on the left of the figure, while isosurfaces of the vertical component of vorticity are visible on the right. Several features of the wake structure are immediately striking. The wake vorticity structures become smaller as they evolve in the wake far away from the body, due to the desingularization effects of the evolving wake sheet which is tightly rolling up into vortex tubes of vertical orientation, but which may qualitatively capture the dissipative and diffusive effects of the actual wake structures. The total vorticity magnitude also shows the interconnectedness of the vortex wake ring-like structures which are shed from the body and caudal fin, with horizontal vorticity components in the xy-plane bridging the large vertical vorticity structures visible on the right of the figure.

Through examination of Figure 6-4, it is also evident that the wake is largely composed of vertical vorticity structures, as opposed to strong longitudinal structures predicted by three-dimensional linear swimming theory [126]. Most of the area obscured by total vorticity magnitude structures on the left of the figure is similarly obscured by the vertical vorticity structures on the right, except in regions close to the

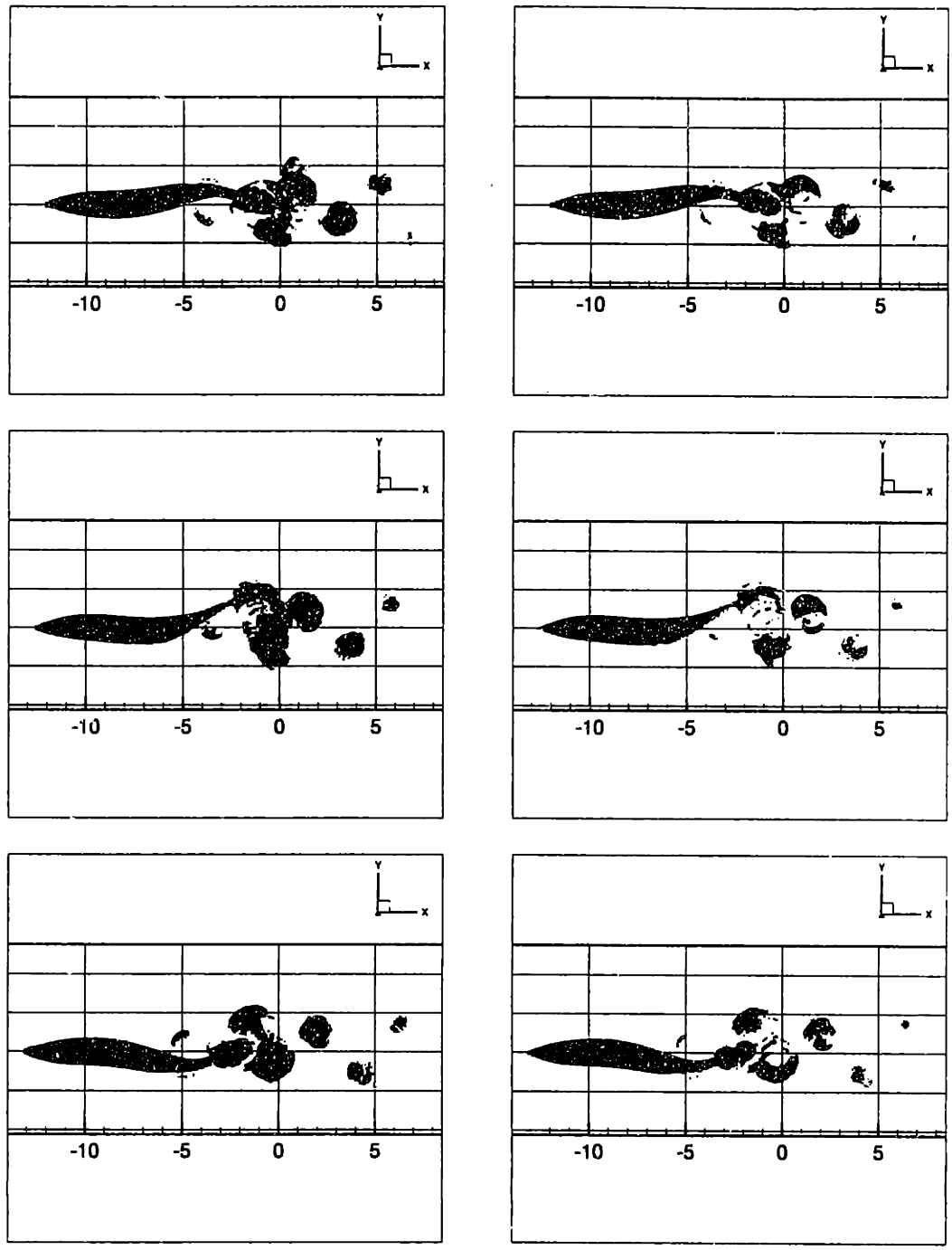

(a) Total vorticity magnitude $|\vec{\omega}|$ (b) Vertical vorticity ω_z components

Figure 6-4: Interaction of the caudal fin with upstream shed vorticity and corresponding wake-wake influence and dynamics. Giant Danio straight-line swimming numerical simulation employing backbone ridge shedding model is shown through a top view with (a) isosurfaces of total vorticity magnitude $|\vec{\omega}| = 7.0\ s^{-1}$, (b) isosurfaces of vertical vorticity magnitude $|\omega_z| = -7.0\ s^{-1}$ (red) and $|\omega_z| = 7.0\ s^{-1}$ (blue). Red patches induce a counterclockwise fluid rotation, blue clockwise, in this view. One-half period of motion sequence is shown from top to bottom at $T/4$ intervals.

body where tip vortices shed from the body and the caudal fin connect the vertical structures. Finally, the plot of vertical vorticity structures is particularly revealing in that it shows pairing of opposite signed vorticity in the thrust jet wake which would tend to diminish the strength of the total thrust jet. These pairings occur when strong vortical structures in a thrust jet orientation shed from the tail interact with smaller vortical structures released by the body upstream of the caudal fin. These smaller structures as they appear in the figure would alone form a small drag jet in the wake. However, the caudal fin has manipulated these smaller vortical structures in such a way that they merely diminish the strength of the thrust jet. In the of top Figure 6-4, a region of red (negative) vorticity inducing a counterclockwise fluid rotation is released from the body in at a point in the oscillation cycle which would allow this structure to contribute to the thrust jet wake. However, the tail is seen to be intercepting this vortical structure and forcing below the path which the tail is tracing. This allows this upstream shed negative vortical structure to interact with the strong positive vortical structure at the bottom extreme of the thrust jet wake shed one-half cycle previously by the caudal fin. As seen in the middle of Figure 6-4, the caudal fin sheds a strong negative vortical structure in the wake at the top of the cycle, where a small blue vortical structure begins to be released upstream by the body which would normally contribute to the formation of the total thrust jet. The previous wake pairings are evident in this figure, including the one discussed previously which initiated in the top of Figure 6-4. At the bottom of the Figure 6-4, the caudal fin is again seen to intercept the smaller positive vortical structure shed upstream which by this point has gained considerable strength through continued peduncular shedding. This vortical is again passed over the peduncular region of the body in front of the leading edge of the caudal fin, such that the path traced by the caudal fin forces the body-generated vorticity to the other side of the wake, where it will no longer contribute to the thrust jet total strength and will pair with the strong negative vorticity shed at the top of the caudal fin oscillation cycle, shown in Figure 6-4.

In this manner, the fish may generate thrust with its undulating body, and

then through controlled release of body-generated vorticity upstream of the tail and through controlled timing and oscillation of the tail, decrease the total strength of the thrust jet bounded by the strong vortical structures released by the caudal fin. This wake-wake-body interaction process is indicative of vorticity control mechanisms employed by the fish to reclaim energy lost to thrust production by the upstream undulations of the body, thereby improving the total propulsive efficiency.

Figure 6-5 shows the interactions of the vertical vorticity structures with the high fluid momentum regions comprising the thrust jet wake with the same high resolution over one-half straight-line swimming cycle. Two orthogonal views of the same time instances are shown for three discrete times separated by $T/4$, corresponding to the same times shown in Figure 6-4. It can be seen that these low pressure regions similarly decrease in size as the wake becomes farther from the fish, indicating the expansion of the fluid jet in a cylindrical fashion as the desingularized wake sheets evolve. Figure 6-5 illustrates how low pressure regions are formed upstream by the undulating body, are then manipulated by the oscillating caudal fin to become stronger, and are then bounded by the strong vertical vorticity structures in the wake. Although the velocities induced by the wake vorticity contribute to the strength of these low pressure regions, as evidenced by the overlap of vortical and pressure structure isosurfaces, the interaction of the low pressure regions actuated through upstream and caudal fin motions with the low pressure regions induced by the wake vorticity augments the strength of the shed wake vertical vorticity structures and smoothes the total momentum distribution of the wake. It is remarkable that no high momentum regions exist outside of the bounding vertical vorticity in the wake, further suggesting the efficiency with which the swimming fish actuates near-body and near-caudal high fluid momentum regions to produce useful thrust. It should be noted that the desingularized nature of the wake representations prohibits large core velocities which reconciles the lack of total overlap between the low pressure structures and the wake vorticity structures.

A more detailed sequence of these wake structure interactions is shown over the entire cycle of the straight-line swimming motions of the Giant Danio in Figures 6-6

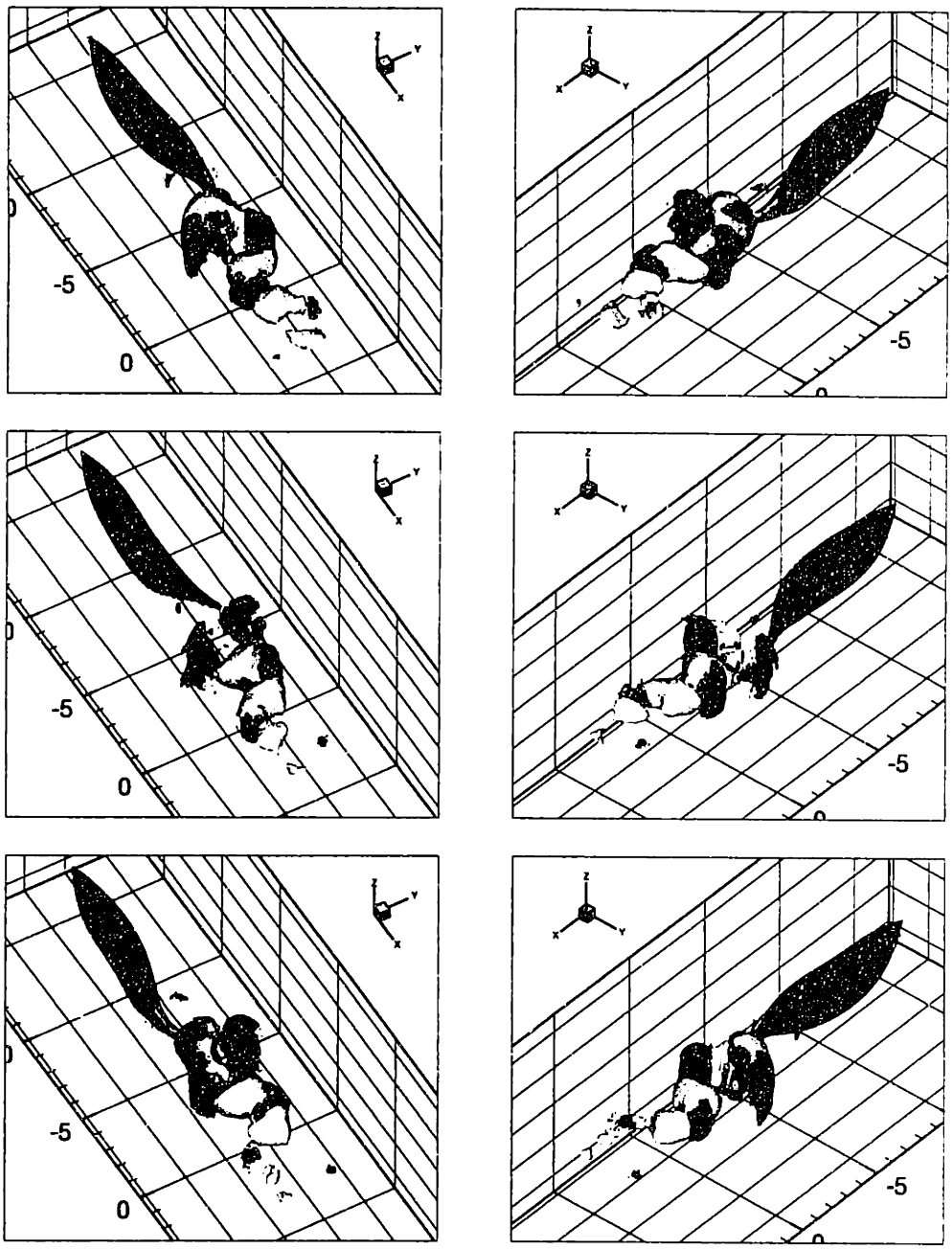

(a) Orthogonal View 1 (b) Orthogonal View 2

Figure 6-5: Interaction of the caudal fin with upstream shed vorticity, regions of high fluid momentum, and the subsequent wake-wake dynamics. Giant Danio straight-line swimming numerical simulation employing backbone ridge shedding model is shown with isosurfaces of vertical vorticity magnitude $\omega_z = -7.0\ s^{-1}$ (red) and $\omega_z = 7.0\ s^{-1}$ (blue) and pressure coefficient $|C_P| = 0.8$ (yellow) based on swimming speed U. Red patches induce a counterclockwise fluid rotation, blue clockwise, when viewed from above. Yellow patches are low pressure regions near the body and in the thrust jet. One-half period of the motion is shown for two orthogonal vantage points. Sequence is shown from top to bottom at $T/4$ intervals.

and 6-7. Figure 6-6 illustrates the interaction of the low pressure structures, shown as yellow isosurfaces of dynamic pressure coefficient $C_P = 0.7$ based on forward swimming speed U, with isosurfaces of total vorticity magnitude, shown as green structures with magnitude $|\vec{\omega}| = 5.0\ s^{-1}$. A lower resolution of the velocity field was used to obtain these images due to the large computational burden consequent of obtaining the unsteady velocity field at several discrete times during the swimming cycle. The formation of the low pressure regions upstream of the caudal fin can be seen from the sequence, whose strength is amplified by the oscillation of the caudal fin which contains the upstream-generated high momentum regions within the bounds of the expanding thrust jet. The ring structure of the wake vorticity is less evident in this series of images, as the computational resolution was too low to effectively capture the longitudinal tip vortices connecting strong vertical structures released by the oscillating caudal fin.

Figure 6-7 shows a similar interaction of the high momentum regions formed by the undulations of the body and the oscillations of the caudal fin with the vertical vorticity structures released into the wake by the backbone separation scheme and the caudal fin. The lower resolution of these images again obscures the vortical structure wake pairings evident in Figures 6-4 and 6-5. However, it can be more easily seen in Figure 6-7 the manner in which the caudal fin releases a strong vortical structure at the extreme location of its oscillation cycle, which then affects the actuation of the body-generated and caudal-generated low pressure regions to form the wake thrust jet. The expansion of the thrust jet is again evident as the size of the strong vertical vorticity structures decreases as the wake develops and as the size of the high momentum regions decreases downstream, indicating transfer and diffusion of momentum from the strong low pressure structures to the bounds of the thrust jet.

From these simulations, the ability of the live fish to recover energy imparted to the fluid through its body undulations is likely an evolutionary convergence of both kinematic and morphological adaptations. The Giant Danio would like to oscillate its tail in a manner which produces as much useful thrust as possible for a minimum momentum imparted to the fluid, by exploiting the natural instability dynamics of

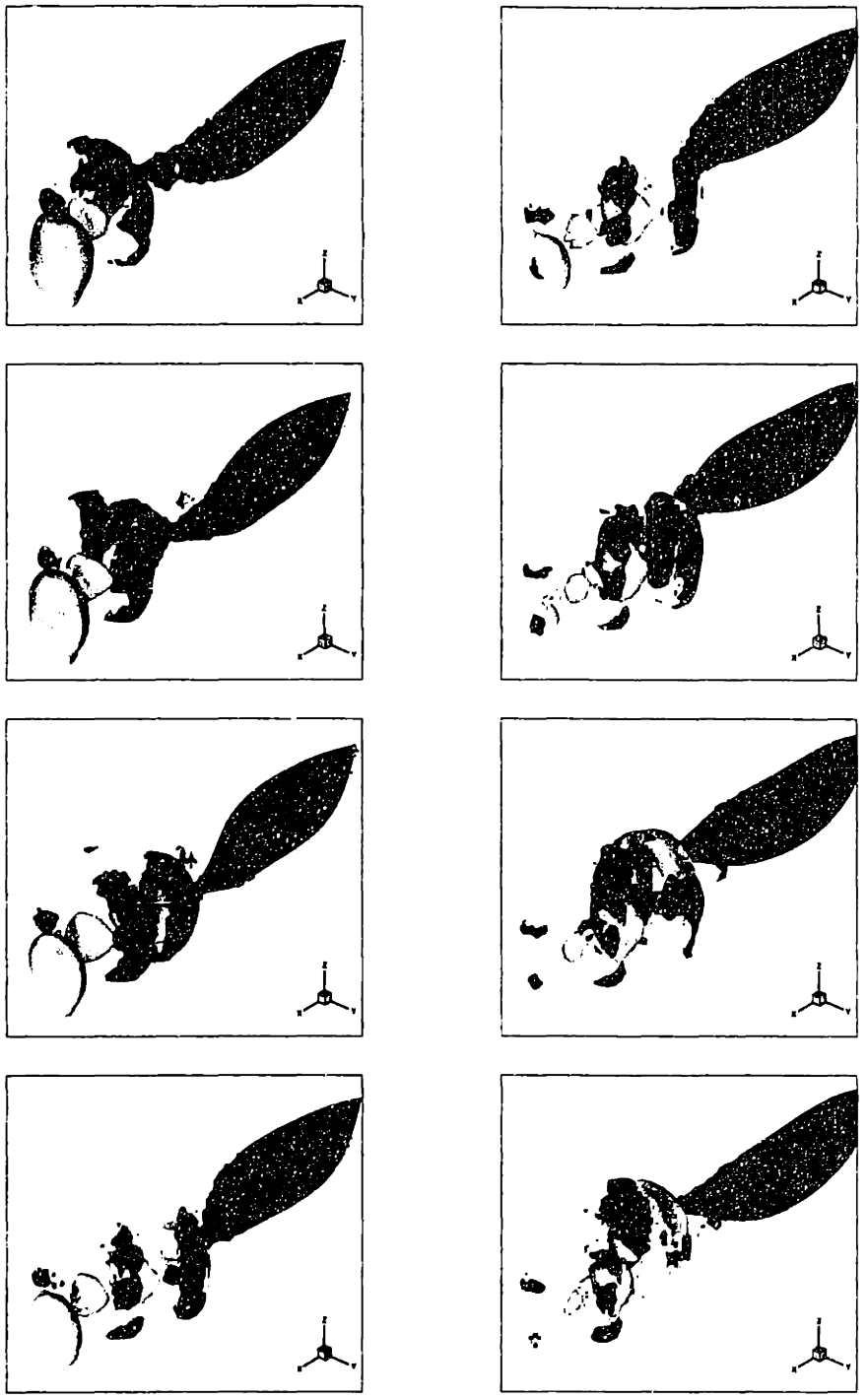

Figure 6-6: Interaction of the caudal fin with upstream shed vorticity, regions of high fluid momentum, and the subsequent wake-wake dynamics. Giant Danio straight-line swimming numerical simulation employing backbone ridge shedding model is shown with isosurfaces of vorticity magnitude $|\vec{\omega}| = 5.0\ s^{-1}$ (green) and pressure coefficient $|C_P| = 0.7$ (yellow) based on swimming speed U. Green patches induce a rotational flow, and yellow patches are low pressure regions near the body and in the thrust jet. One period of the motion sequence is shown from top to bottom, first left then right column, at $T/8$ intervals.

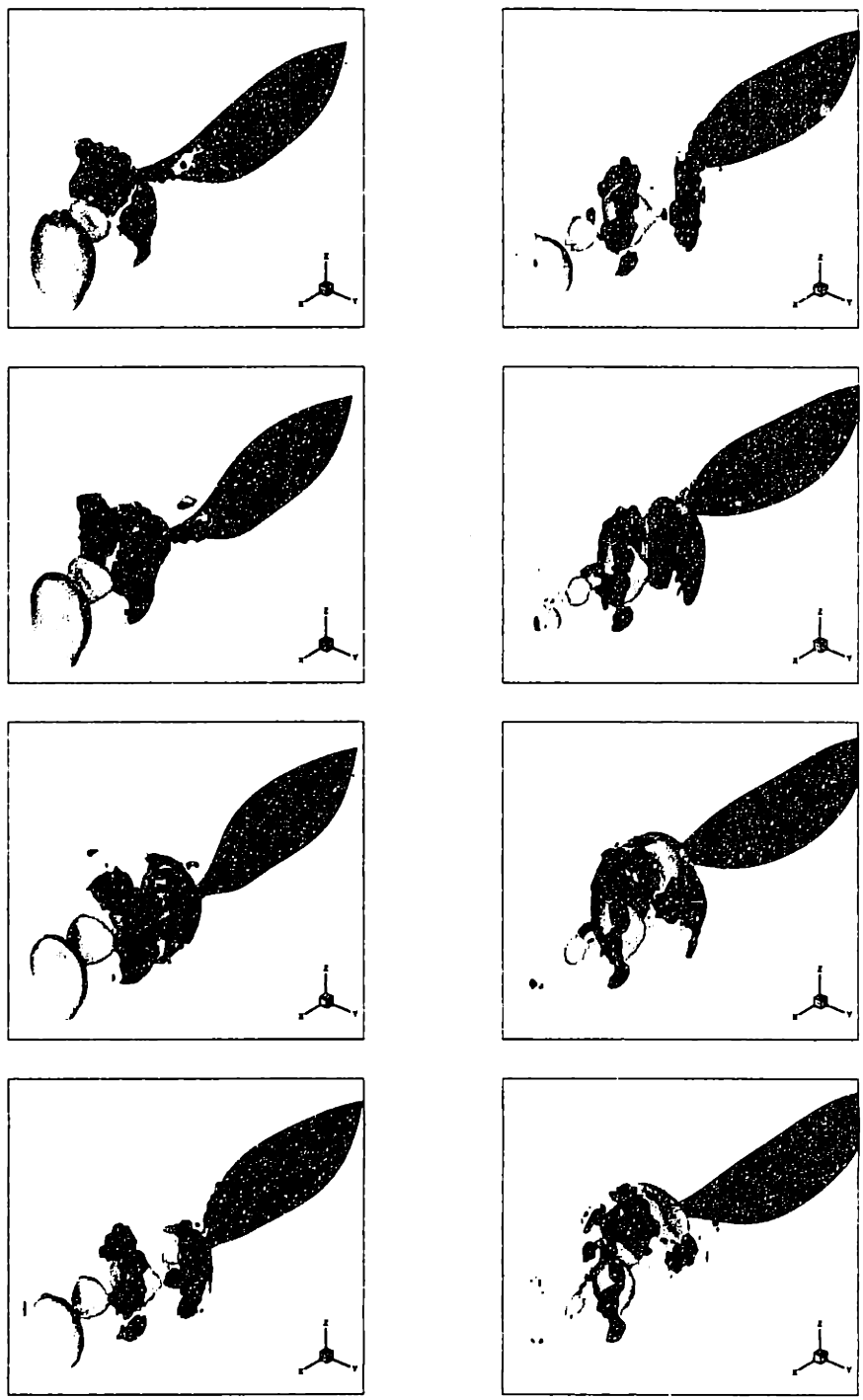

Figure 6-7: Interaction of the caudal fin with upstream shed vertical vorticity, regions of high fluid momentum, and the subsequent wake-wake dynamics. Giant Danio straight-line swimming numerical simulation employing backbone ridge shedding model is shown with isosurfaces of vertical vorticity magnitude $\omega_z = -5.0\ s^{-1}$ (red) and $\omega_z = 5.0\ s^{-1}$ (blue) and pressure coefficient $|C_P| = 0.7$ (yellow) based on swimming speed U. Red patches induce a counterclockwise motion, blue clockwise, when viewed from above, and yellow patches are low pressure regions. One period of the motion is shown: top to bottom, first left then right column, $T/8$ intervals.

the two-dimensional thrust jet. In doing so, it undulates its body to actuate the oscillations of the caudal fin, and the fish has learned to produce thrust through these body undulations much like a low-aspect-ratio wing. The vortical energy delivered to the fluid consequent to these body motions can be recaptured through tuning of the body kinematics; to pair body-generated vortices which would originally produce a thrust wake with oppositely-signed thrust vortices produced by the caudal fin, the caudal fin must intercept these upstream-generated vortices and transfer them to the opposite side of the wake. This interaction decreases the strength of the total thrust jet produced, minimizing the momentum in the wake for a given produced thrust, thus increasing the efficiency of the motion. This motion of transferring the body-generated vortices from one side of the wake to the other affects the leading-edge flow of the caudal fin such that the strength of the caudal wake shed is decreased for the same the total loading on the tail, thus recovering energy from the vorticity delivered to the fluid through upstream shedding. For a given morphology, the effects of adding upstream vorticity release mechanisms on the performance will be examined again in the following section, Section 6.3, and by simulating the motions of the *RoboTuna*, which closely emulate the motions of the live bluefin tuna, the effects of altering the kinematics on the performance of swimming will also be examined. This investigation will illustrate how these wake-wake-body interactions can be tuned to achieve a desired performance.

6.3 Kinematic mechanisms of vorticity control

In this section, the investigation of fish swimming vorticity control mechanisms returns to the geometry of the *RoboTuna*. In *Chapter 4*, a kinematic parametric investigation of swimming performance with comparison to experimental results was conducted for a *RoboTuna* geometry and a caudal fin wake shedding model which closely paralleled a genetic optimization series performed by Barrett (1996) [19]. In some cases, the comparison of the power delivered to the fluid computationally to the experimental power consumed by the motors of the *RoboTuna* was quite good. Also,

some cases resulted in high computed propulsive efficiencies, although these simulation results could not be corroborated by experimental measurements of the thrust produced by the swimming robotic mechanism. Some cases resulted in both good comparison and high propulsive efficiencies for the caudal fin wake shedding model, and these were presented in detail in *Chapter 4* and usually correlated to experimental conditions which resulted in significant apparent drag reduction. Other cases resulted in only high thrust with mediocre comparison to experiments, and occasionally no thrust was produced at all through simulation of the imposed motions.

To understand why specific swimming cases resulted in high propulsive efficiencies, high thrusts, or even drag, the wake interactions are shown in detail in this section through visualization. In addition, a backbone ridge wake shedding model is adopted, similar to the Separation Scheme B of the Giant Danio swimming simulations, for comparison to the original caudal fin wake shedding model, in order to elucidate vorticity control mechanisms which the fish may be utilizing to enhance its performance. In reality, the transversely oscillating elliptic cross sections of the *RoboTuna* may induce some backbone separation, although the separation location around the circumference of the section may vary throughout the swimming cycle and for different kinematics. In addition, the *RoboTuna* was often operated with small dorsal and anal fins which would shed a wake during swimming motions. Thus, while this fixed separation line of the computational model may be a first approximation to separation which may occur along *RoboTuna* sections, the upstream wake shedding properties is more intended to model the effects of backbone finlets present on the live bluefin tuna. These finlets may be actively controlled by the tuna during swimming to rotate to a desired orientation to the cross-flow or oncoming flow, but for this simulation, it is assumed that they remain locally parallel to the undulations of the backbone mean line.

In this way, both the geometric dependencies and the kinematic dependencies of the swimming motions may be concurrently investigated. Several types of motions are investigated, to understand how the tuna can tune its kinematics for a given morphology to obtain the range of performance observed in live fish. In Table 6.1, the

Barrett Run Code		Case 1 j702_01b	Case 2 j705_03	Case 3 j702_06	Case 4 j701_01b
Strouhal number St	(–)	0.310	0.182	0.198	0.102
Swimming speed	(BL/s)	0.656	0.656	0.656	0.656
Wavelength λ	(BL)	1.316	0.936	0.936	1.316
Oscillation frequency ω	(rad/s)	9.534	6.278	6.830	3.137
Angle of attack α	(deg.)	28.4	24.8	19.0	11.5
Tail phase ϕ	(deg.)	90.0	80.0	97.7	77.0
Amplitude coefficient c_1	(–)	0.00236	0.00294	0.00294	0.00236
Amplitude coefficient c_2	(1/BL)	0.15501	0.13693	0.13693	0.15501
Tail excursion A	(BL)	0.134	0.120	0.120	0.134
Experimental drag reduction	(%)	40.6	47.7	47.8	−282.9
Mean power input (experiment)	(W)	4.44	1.07	1.08	4.58
Mean power input (computation)	(W)	4.89	1.15	1.29	−0.45
Mean power input error	(%)	10.1	7.48	19.4	109.9
Mean thrust force (computation)	(N)	5.19	1.50	1.67	−0.92
Computed propulsive efficiency	(η)	74.3%	91.4%	90.4%	—

Table 6.1: Summary of kinematic and performance data from Tables 4.2 and 4.3 for the cases to be considered in vorticity control investigations, showing comparison between experimental measurements from *RoboTuna*, and the simulation results for caudal fin wake shedding model only.

kinematic details of cases considered in this section are summarized, with performance data from experiments and from computation with a caudal fin wake shedding model as in *Chapter 4*. These cases span the range of "good" and "bad" performance of the *RoboTuna* motions.

For each of the four cases listed in Table 6.1, the motions are simulated with caudal fin wake shedding only and with caudal fin wake plus dorsal and ventral ridge wake shedding for comparison, denoted hereafter by the suffix `A` or `B`, respectively. Thus, through each simulation, the unsteady behavior of the main vortical structures will be examined for varying geometric assumptions. Additionally, by comparing the visualization results for varying kinematic parameters, optimal vortical structure-body interaction modes may be identified for both caudal wake shedding only as well as upstream wake shedding considerations. The intention of the comprehensive visual study to follow that both "good" and "bad" modes of wake-body and wake-wake-body interactions can be identified, with their corresponding effects on the efficiency of the

swimming motions or on the overall desired performance.

6.3.1 Case 1: Run j702_01b

A simulation is chosen with kinematic parameters which resulted in excellent performance of the *RoboTuna* under conditions of self-propulsion. Additionally, the simulated motion with caudal separation scheme employed resulted in large values of mean power delivered to the fluid and mean thrust generated, with a mean power comparison of around 10% error and with a computed propulsive efficiency of 74.3%. This motion experimentally resulted in a reduction of the drag on the actively-swimming body to 40.6% below the rigid body drag (Barrett 1996) [19]. Kinematic parameters for this run: Strouhal number $St = 0.310$, swimming speed $U = 0.656\ BL/s$, tail circular frequency $\omega = 9.534\ rad/s$, wavelength $\lambda = 1.316\ BL$, tail tip double amplitude $A = 0.134\ BL$, angle of attack $\alpha = 28.4^o$, and tail phase between pitch and heave $\phi = 90.0^o$.

Figures 6-8 and 6-9 show the simulated motions over one complete swimming cycle. The two different wake separation schemes are shown for comparison in the two figures, illustrating the self- and body-interaction effects of the deforming wakes. For caudal shedding only, shown in Figure 6-8, the case is referred to as case j702_01bA to distinguish it from the plots in Figure 6-9 of caudal and backbone ridge shedding, hereafter referred to as case j702_01bB. As can be seen from the color contours of wake dipole strength superimposed on the computational grid of the shed wake surfaces, the phase of encounter between the oscillating caudal fin and the body-generated vorticity released upstream through backbone ridge separation significantly affects subsequent wake-wake interaction dynamics. This phase of encounter is dependent on the wavelength of the backbone wave λ, the longitudinal distance between the backbone ridge and the leading edge of the caudal fin, and the phase speed of the backbone wave with respect to the swimming speed c_p/U. From Figure 6-9, as the tail sweeps from side-to-side, a wake of oscillating strength separates from the caudal fin trailing edge. When the tail encounters the wake sheets shed upstream from the backbone ridge, the caudal fin wake induces a rotational velocity which is in the same

		RoboTuna	Scheme A j702_01bA	Scheme B j702_01bB
Mean power input	(W)	4.44	4.89	5.38
Mean power input difference	(%)	—	10.1	21.2
Peak power input	(W)	7.98	9.02	11.3
Peak power input difference	(%)	—	13.0	41.6
Mean thrust force (computation)	(N)	—	5.19	5.47
Computational propulsive efficiency	(η)	—	74.3%	71.2%

Table 6.2: Summary of performance data, showing comparison between experimental measurements from *RoboTuna*, wake Separation Scheme A `j702_01bA` (caudal fin shedding only), and wake Separation Scheme B `j702_01bB` (caudal fin and backbone ridge shedding).

direction of the fluid rotation induced by the upstream-shed vorticity. In this manner, the tail may reinforce the strength of the shed propulsive thrust jet wake, increasing the thrust generated for given kinematics.

The simulation results are compared to the integrated performance dynamics obtained by the *RoboTuna*, in order to understand further the impact of these fluid-body interactions revealed through our flow visualizations on the body dynamics. Figure 6-10(a) shows the power required for swimming by the experimental robotic vehicle under conditions of self-propulsion, compared to the power delivered to the fluid through simulation utilizing the two wake separation schemes. In addition, while thrust and drag cannot be measured separately in the experimental mechanism (Barrett, *et al.* 1999) [21], the thrust force computed during simulation is shown in Figure 6-10(b) for both wake separation schemes. A summary of these results is given in Table 6.2. The caudal fin wake separation scheme shows good comparison to the experimental results and moderate propulsive efficiencies $\eta = \bar{T}U/\bar{P}$. The caudal fin and backbone ridge wake separation scheme also shows moderate propulsive efficiency, although slightly lower than the caudal shedding simulation only, with higher values for the thrust produced and the power required for swimming. This suggests that the interactions of the oscillating tail with upstream-generated vorticity greatly enhances the thrust produced by the tail and the overall performance of the motions.

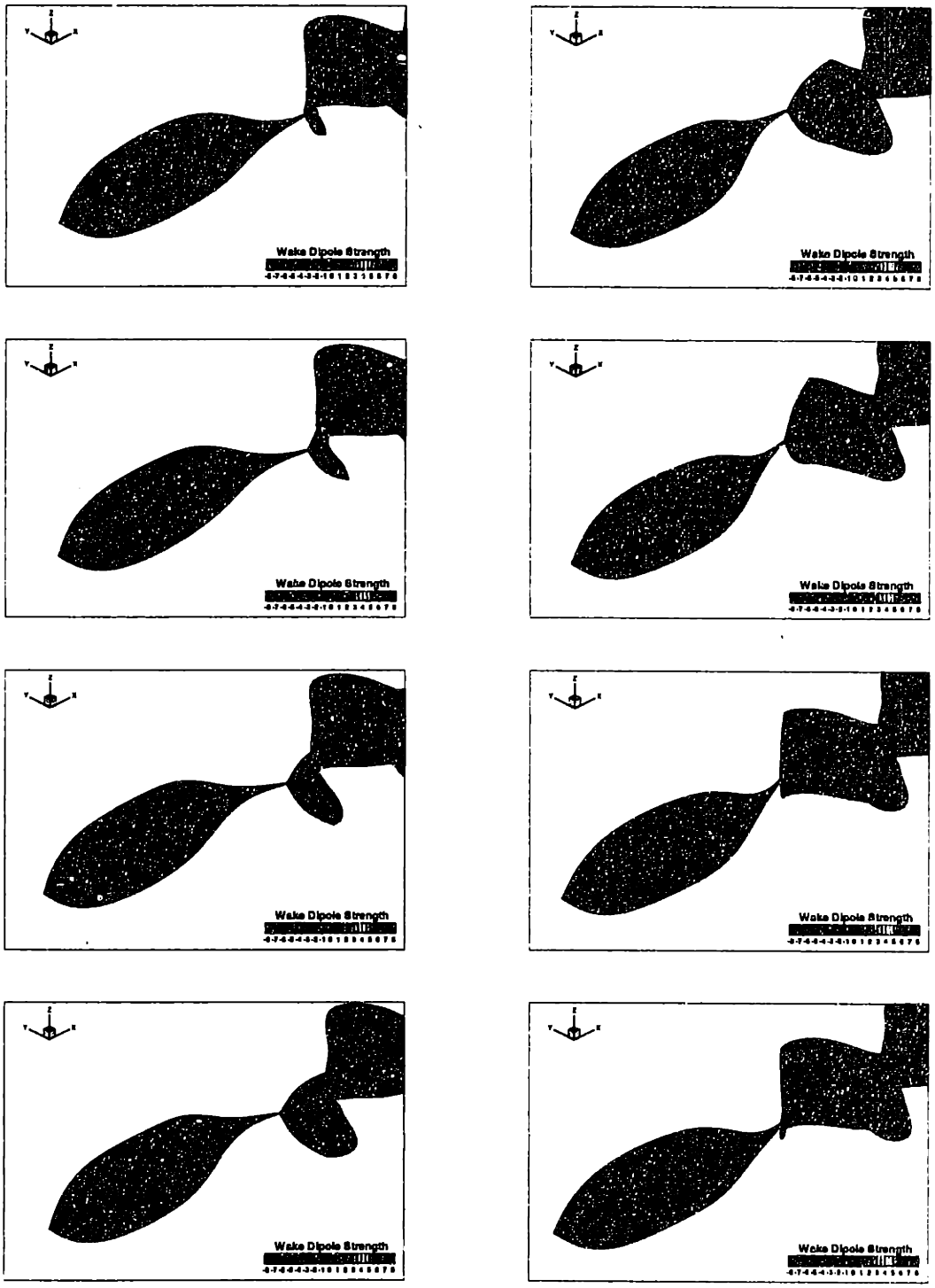

Figure 6-8: Straight-line swimming motion simulation results for one swimming cycle of the *RoboTuna* showing wake development for caudal fin shedding, case `j702_01bA`. The computational grid is superimposed on the tuna geometry and the wake surface. Wake surface color is scaled by strength of the wake dipole sheet. Sequence is shown top to bottom, first left then right column, at intervals of $T/8$.

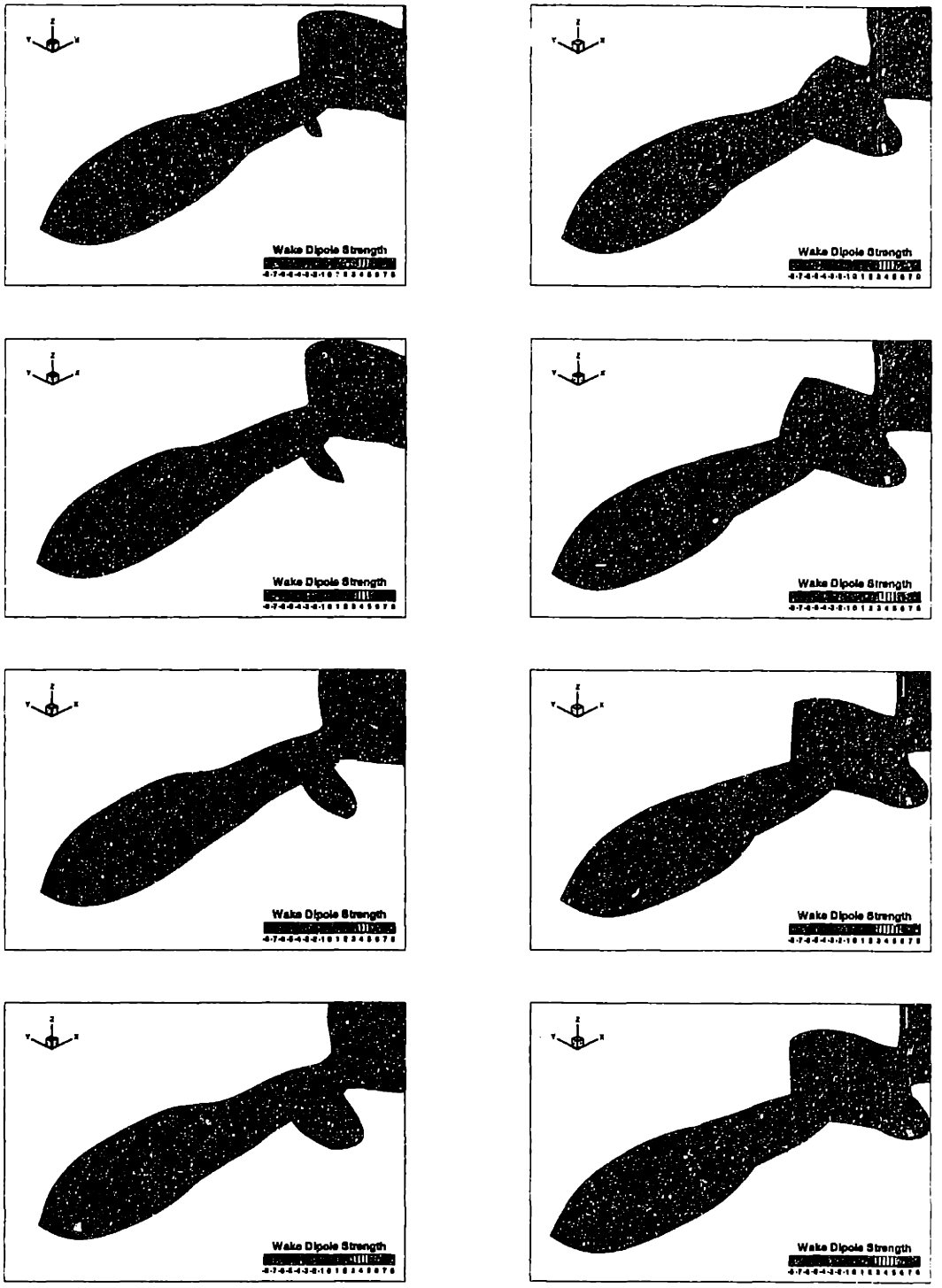

Figure 6-9: Straight-line swimming motion simulation results for one swimming cycle showing wake development and interactions for caudal fin and backbone ridge wake separation scheme, case j702_01bB. The computational grid is superimposed on the tuna geometry and the wake surfaces. Wake surface color is scaled by strength of the wake dipole sheet. Sequence is shown top to bottom, first left then right column, at intervals of $T/8$.

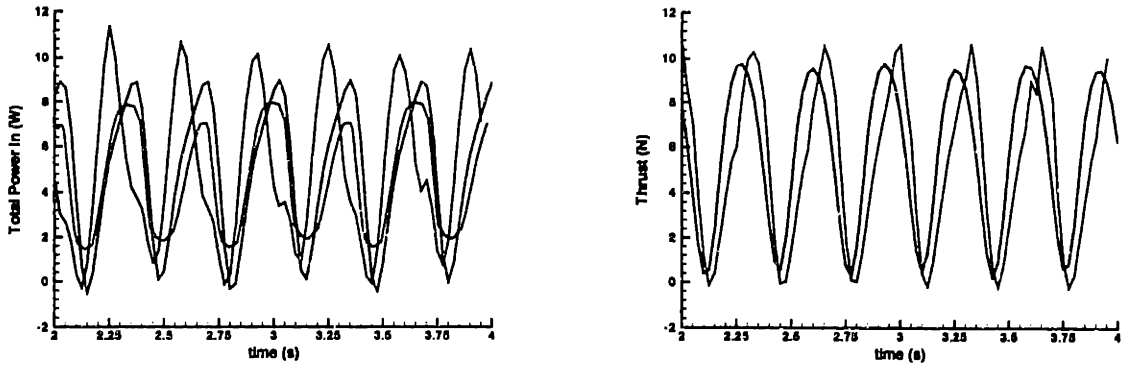

(a) Power

(b) Thrust

Figure 6-10: Time records of (a) the total power into the fluid and (b) the total thrust. Comparison of the various methods: *(i)* caudal fin shedding only, case `j702_01bA` (black); *(ii)* caudal fin and backbone ridge shedding, case `j702_01bB` (red); *(iii)* experimental measurements of total power from *RoboTuna* (blue). Summary of principal performance measures is given in Table 6.2.

6.3.2 Case 2: Run `j705_03`

A simulation is chosen with kinematic parameters which resulted in excellent performance of the *RoboTuna* under conditions of self-propulsion. This motion experimentally resulted in a reduction of the drag on the actively-swimming body to 47.7% below the rigid body drag (Barrett, *et al.* 1999) [21]. Kinematic parameters for this run: Strouhal number $St = 0.182$, swimming speed $U = 0.656\ BL/s$, tail circular frequency $\omega = 6.278\ rad/s$, wavelength $\lambda = 0.936\ BL$, tail tip double amplitude $A = 0.120\ BL$, angle of attack $\alpha = 24.8^o$, and tail phase between pitch and heave $\phi = 80.0^o$.

Figures 6-11 and 6-12 show the simulated motions over one complete swimming cycle. The two different wake separation schemes are shown for comparison in the two figures, illustrating the self- and body-interaction effects of the deforming wakes. For caudal shedding only, shown in Figure 6-11, the case is referred to as case `j705_03A` to distinguish it from the plots in Figure 6-12 of caudal and backbone ridge shedding, hereafter referred to as case `j705_03B`. As can be seen from the color contours of wake dipole strength superimposed on the computational grid of the shed wake surfaces,

the phase of encounter between the oscillating caudal fin and the body-generated vorticity released upstream through backbone ridge separation significantly affects subsequent wake-wake interaction dynamics. This phase of encounter is dependent on the wavelength of the backbone wave λ, the longitudinal distance between the backbone ridge and the leading edge of the caudal fin, and the phase speed of the backbone wave with respect to the swimming speed c_p/U. From Figure 6-12, as the tail sweeps from side-to-side, a wake of oscillating strength separates from the caudal fin trailing edge. When the tail encounters the wake sheets shed upstream from the backbone ridge, the caudal fin wake induces a rotational velocity which is in the *opposite* direction of the fluid rotation induced by the upstream-shed vorticity. In this manner, the tail may recover energy released into fluid upstream and enhance the loading on the tail.

Figures 6-13 and 6-14 illustrate the interaction of fluid structures produced during the swimming motions for the two different separation schemes. Isosurfaces of vertical vorticity ω_z and dynamic pressure coefficient C_P are shown over half of a swimming cycle. The red and blue patches of vertical vorticity ω_z induce counter-rotating fluid velocity regions which define the boundaries of a reverse Kármán street thrust jet in the wake of the swimming fish. The regions of low pressure are formed upstream of the wake through the undulation of the body and the oscillation of the tail. These low pressure regions are then enhanced and manipulated by the tail, interacting with low pressure regions formed by the alternating-strength patches of wake vorticity ω_z. This further amplifies the fluid jet defined by the reverse Kármán street in the wake. The vertical vorticity ω_z are generally of constant diameter over the depth of the fish, reinforcing the predisposition of fish to swim at a Strouhal number St corresponding to the maximum spatial amplification of the two-dimensional thrust jet instability (Triantafyllou, *et al.* 1993) [204]. However, for the backbone ridge wake and caudal fin wake separation scheme shown in Figure 6-14, the vertical vorticity structures lose strength as the wake evolves, indicating that the effects of the pairing of opposite strength wake structures due to vorticity control by the tail gradually diminishes the strength of the overall thrust jet.

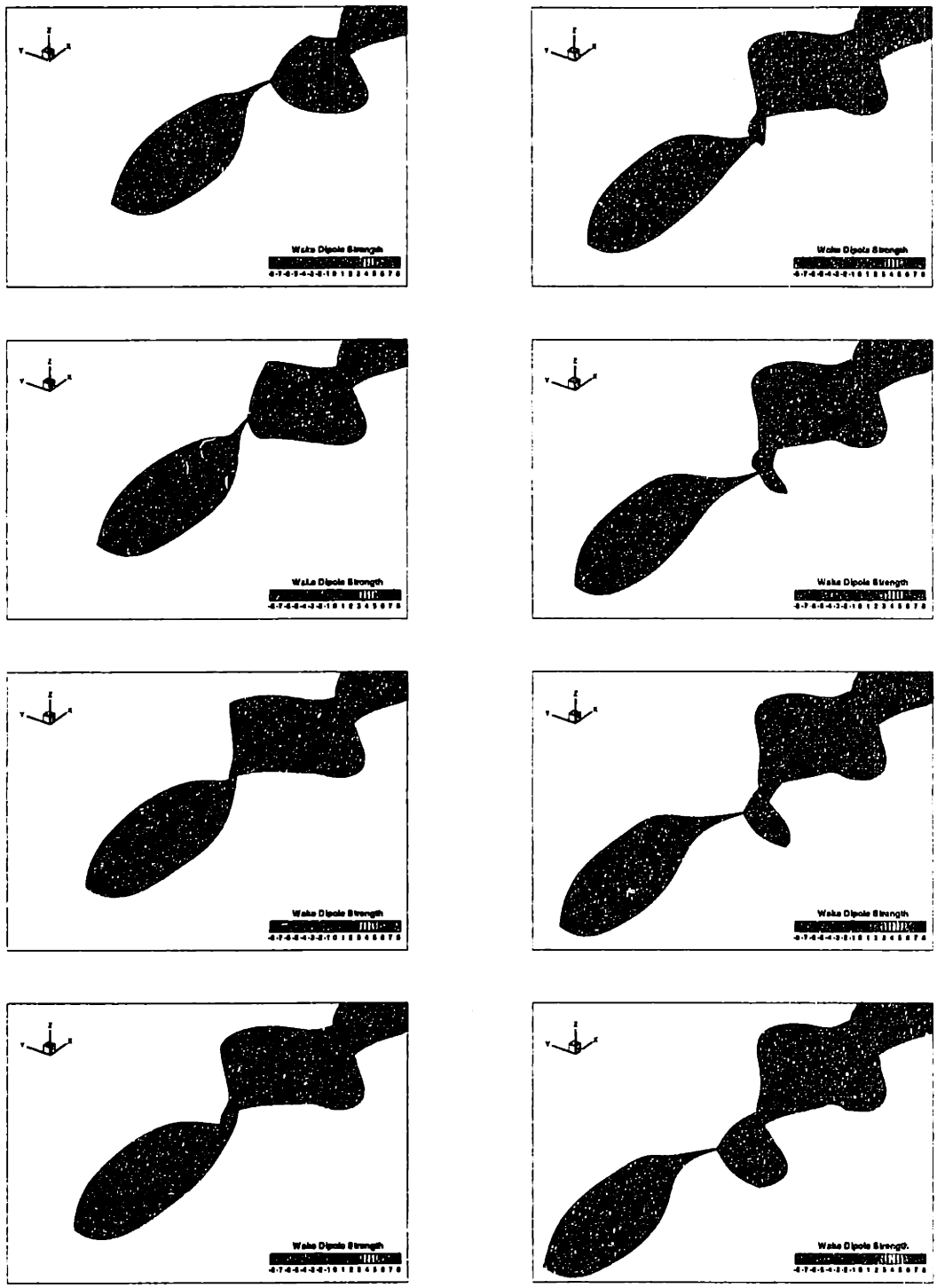

Figure 6-11: Straight-line swimming motion simulation results for one swimming cycle of the *RoboTuna* showing wake development for caudal fin shedding, case `j705_03A`. The computational grid is superimposed on the tuna geometry and the wake surface. Wake surface color is scaled by strength of the wake dipole sheet. Sequence is shown top to bottom, first left then right column, at intervals of $T/8$.

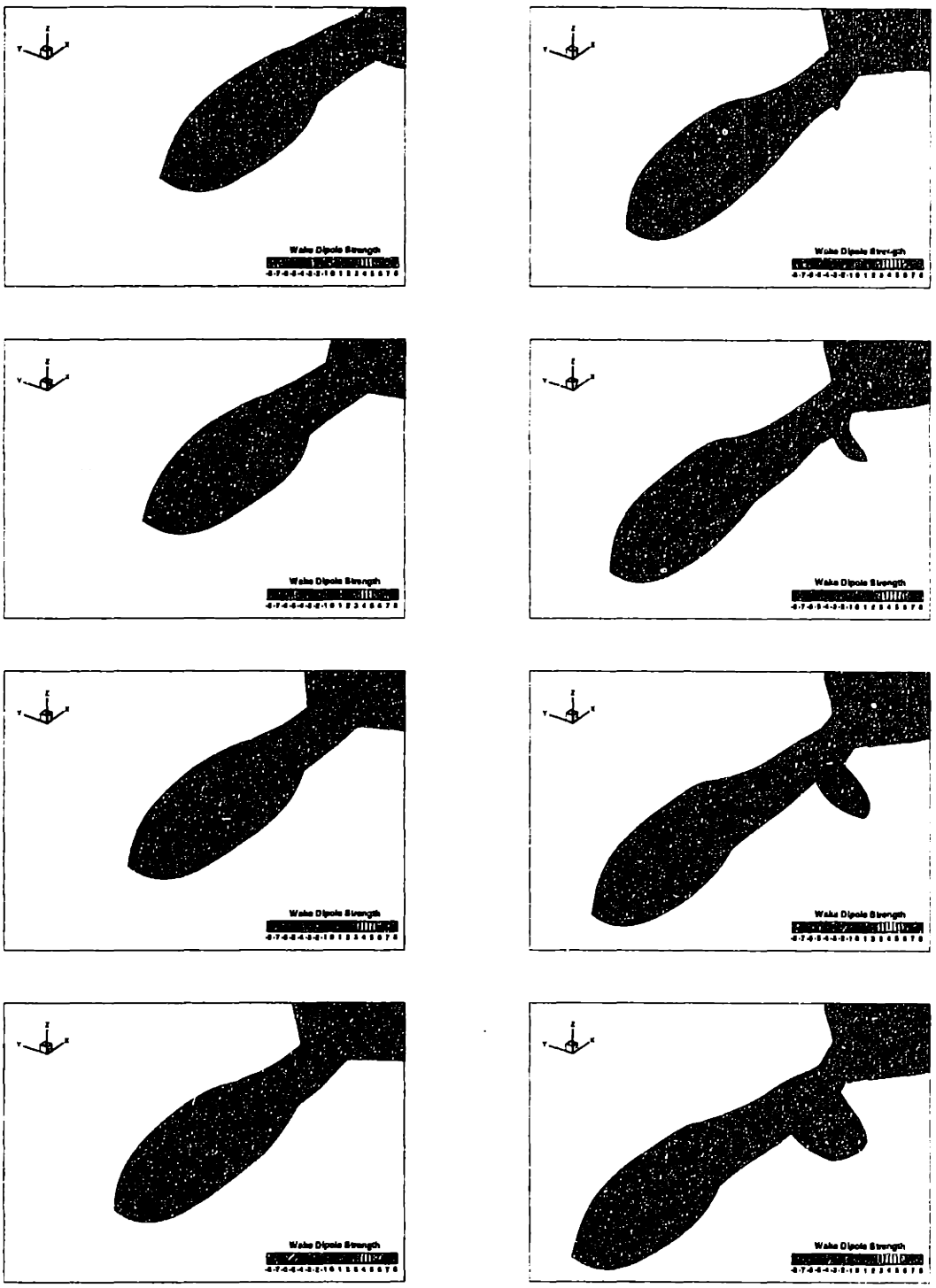

Figure 6-12: Straight-line swimming motion simulation results for one swimming cycle showing wake development and interactions for caudal fin and backbone ridge wake separation scheme, case j705_03B. The computational grid is superimposed on the tuna geometry and the wake surfaces. Wake surface color is scaled by strength of the wake dipole sheet. Sequence is shown top to bottom, first left then right column, at intervals of $T/8$.

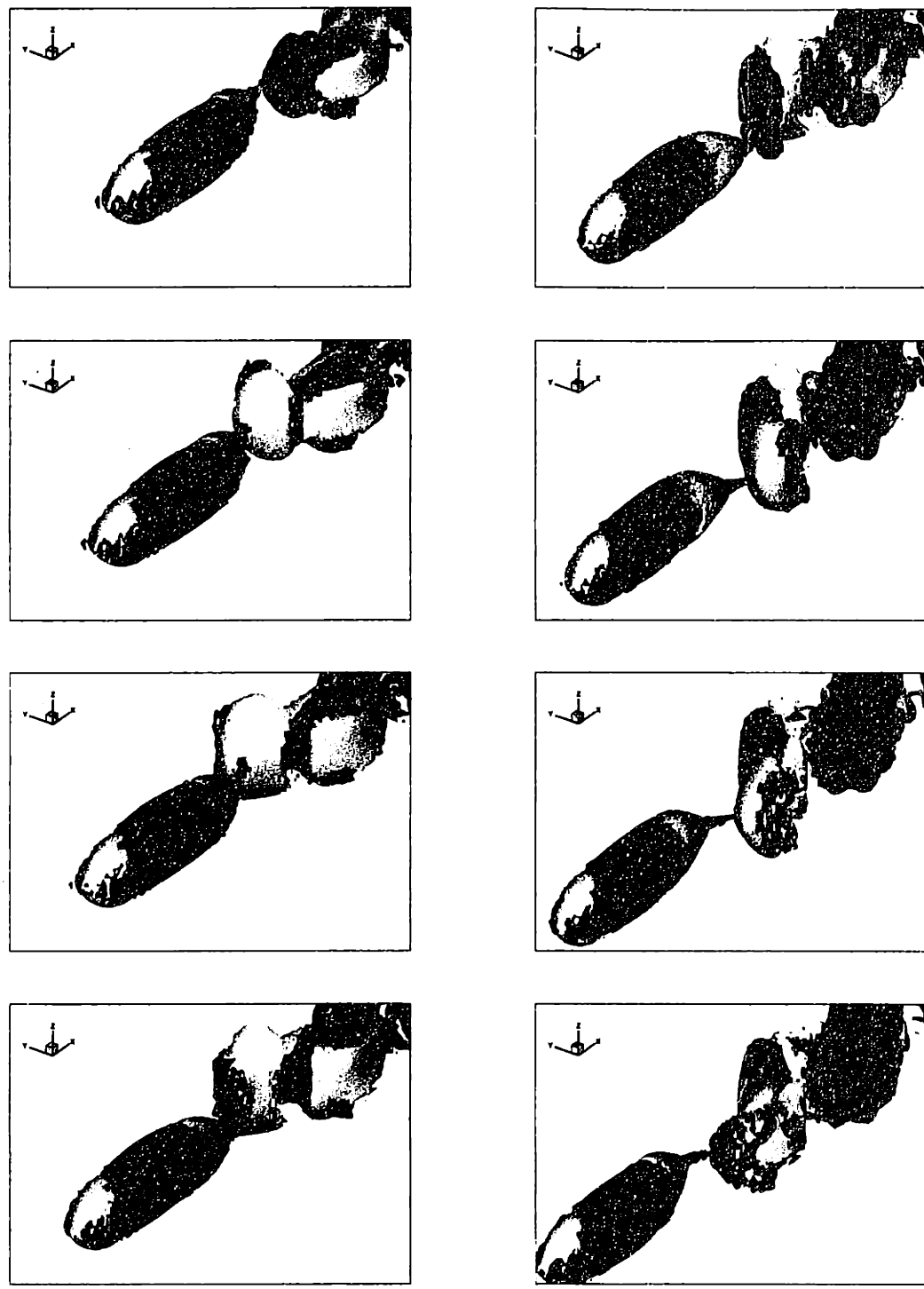

Figure 6-13: Straight-line swimming motion simulation results for one swimming cycle showing flow structure interactions, employing caudal fin wake separation scheme, case j705_03A. Isosurfaces of vertical vorticity ω_z are shown in red ($\omega_z = 1.0\ s^{-1}$) and blue ($\omega_z = -1.0\ s^{-1}$), and an isosurface of dynamic pressure coefficient is shown in yellow ($C_P = 0.8$), nondimensionalized by the swimming speed U. The computational grid is superimposed on the tuna geometry. Sequence is shown top to bottom, first left then right column, at intervals of $T/8$.

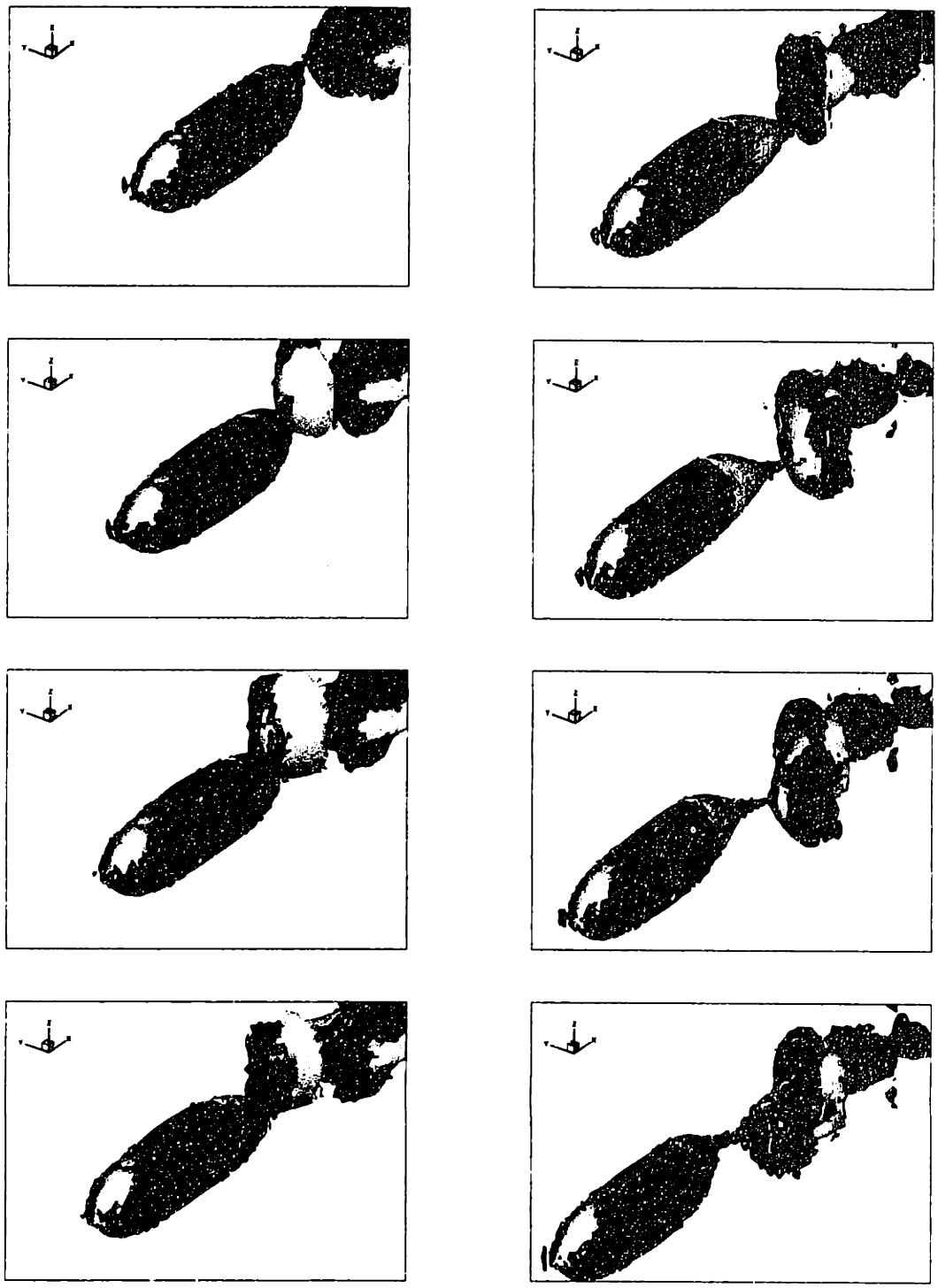

Figure 6-14: Straight-line swimming motion simulation results for one swimming cycle showing flow structure interactions, employing caudal fin and backbone ridge wake separation scheme, case j705_03B. Isosurfaces of vertical vorticity ω_z are shown in red ($\omega_z = 1.0\ s^{-1}$) and blue ($\omega_z = -1.0\ s^{-1}$), and an isosurface of dynamic pressure coefficient is shown in yellow ($C_P = 0.8$), nondimensionalized by the swimming speed U. The computational grid is superimposed on the tuna geometry. Sequence is shown top to bottom, first left then right column, at intervals of $T/8$.

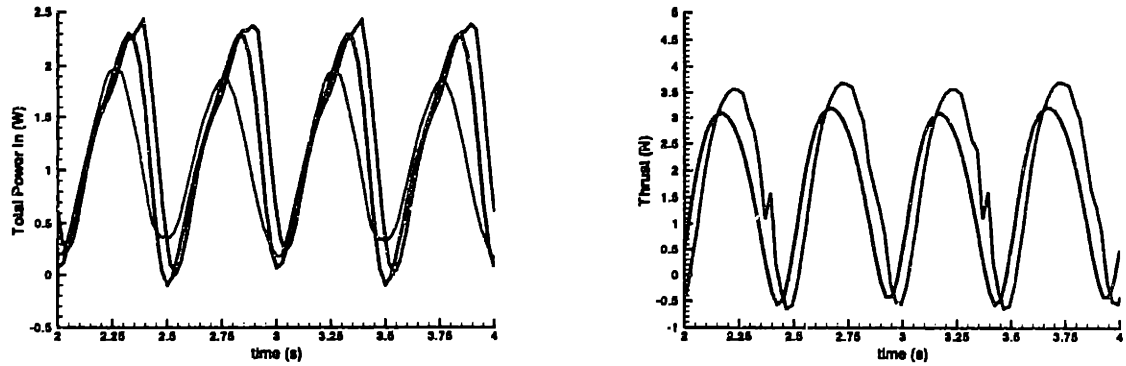

(a) Power

(b) Thrust

Figure 6-15: Time records of (a) the total power into the fluid and (b) the total thrust. Comparison of the various methods: *(i)* caudal fin shedding only, case j705_03A (black); *(ii)* caudal fin and backbone ridge shedding, case j705_03B (red); *(iii)* experimental measurements of total power from *RoboTuna* (blue). Summary of principal performance measures is given in Table 6.3.

To understand the impact of these fluid-body interactions revealed through our flow visualizations on the body dynamics, the simulation results are again compared to the integrated performance dynamics obtained by the *RoboTuna*. Figure 6-15(a) shows the power required for swimming by the experimental robotic vehicle under conditions of self-propulsion, compared to the power delivered to the fluid through simulation utilizing the two wake separation schemes. The thrust force computed during simulation is shown in Figure 6-15(b) for both wake separation schemes. A summary of these results is given in Table 6.3. The caudal fin wake separation scheme shows good comparison to the experimental results and high propulsive efficiency η. The caudal fin and backbone ridge wake separation scheme also shows high propulsive efficiency, with slightly higher values for the thrust produced and the power required for swimming. This suggests that the favorable interactions of the oscillating tail with upstream-generated vorticity enhances the thrust produced by the tail and the overall performance of the motions.

		RoboTuna	Scheme A j705_03A	Scheme B j705_03B
Mean power input	(W)	1.07	1.15	1.30
Mean power input difference	(%)	—	7.48	21.5
Peak power input	(W)	2.04	2.30	2.42
Peak power input difference	(%)	—	12.7	22.2
Mean thrust force (computation)	(N)	—	1.50	1.71
Computational propulsive efficiency	(η)	—	91.4%	91.8%

Table 6.3: Summary of performance data, showing comparison between experimental measurements from *RoboTuna*, wake Separation Scheme A j705_03A (caudal fin shedding only), and wake Separation Scheme B j705_03B (caudal fin and backbone ridge shedding).

6.3.3 Case 3: Run j702_06

Another simulation is chosen with kinematic parameters which resulted in excellent performance of the *RoboTuna* under conditions of self-propulsion, but which has kinematic parameters which differ slightly from Case 2, specifically the motion of the tail. The Strouhal numbers, backbone wavelengths, oscillation frequencies, and tip amplitudes are similar. This motion experimentally resulted in a reduction of the drag on the actively-swimming body to 47.8% below the rigid body drag (Barrett, *et al.* 1999) [21]. Kinematic parameters for this run: Strouhal number $St = 0.198$, swimming speed $U = 0.656\ BL/s$, tail circular frequency $\omega = 6.830\ rad/s$, wavelength $\lambda = 0.936\ BL$, tail tip double amplitude $A = 0.120\ BL$, angle of attack $\alpha = 19.0^o$, and tail phase between pitch and heave $\phi = 97.7^o$.

Figures 6-16 and 6-17 show the simulated motions over one complete swimming cycle for the two wake separation schemes, caudal shedding only case j702_06A and caudal and backbone ridge shedding case j702_06B, respectively. As can be seen from the color contours of wake dipole strength superimposed on the computational grid of the shed wake surfaces, the wake-wake interaction dynamics of case j702_06B are similar to those for case j705_03B. The phase of encounter of the oscillating tail with the backbone wakes released by the undulating body upstream causes an interaction between the body-generated and caudal-generated wake structures which

may decrease the strength of the total thrust jet. Again, when the tail encounters the wake sheets shed upstream from the backbone ridge, the caudal fin wake induces a rotational velocity which is in the *opposite* direction of the fluid rotation induced by the upstream-shed vorticity. In this manner, the tail may recover energy released into fluid upstream and enhance the loading on the tail. The differences in the wake structures between these cases and cases j705_03 are not readily apparent because the kinematics of the two swimming motions are so similar, with some subtle tail motion phasing variations.

To understand the impact of the wake-wake-body interactions revealed through our flow visualizations on the body dynamics and to uncover the subtle kinematics dependencies of the performance, the simulation results are again compared to the integrated performance dynamics obtained by the *RoboTuna*. Figure 6-18(a) shows the power required for swimming by the experimental robotic vehicle under conditions of self-propulsion, compared to the power delivered to the fluid through simulation utilizing the two wake separation schemes. The thrust force computed during simulation is shown in Figure 6-18(b) for both wake separation schemes. A summary of these results is given in Table 6.4. The caudal fin wake separation scheme shows decent comparison to the experimental results and high propulsive efficiency η. The caudal fin and backbone ridge wake separation scheme also shows a much propulsive efficiency, with slightly lower values for the thrust produced and the slightly higher power required for swimming. This suggests that the interactions of the oscillating tail with upstream-generated vorticity diminishes the overall thrust produced and the subsequent performance of the motions for a given input power. These interaction dynamics differ slightly than those revealed in cases j705_03A and j705_03B, which showed that the wake-wake-body interaction dynamics can increase thrust, power, and efficiency. By decreasing thrust and keeping power roughly constant, these kinematics with a larger phase angle between tail fin pitch and heave and a lower angle of attack result in a less efficient motion. However, the ability of the tail fin to control wake interactions to diminish the strength of the total thrust jet is clear, and in nature, the fish may slightly adjust its kinematics further to decrease the power required

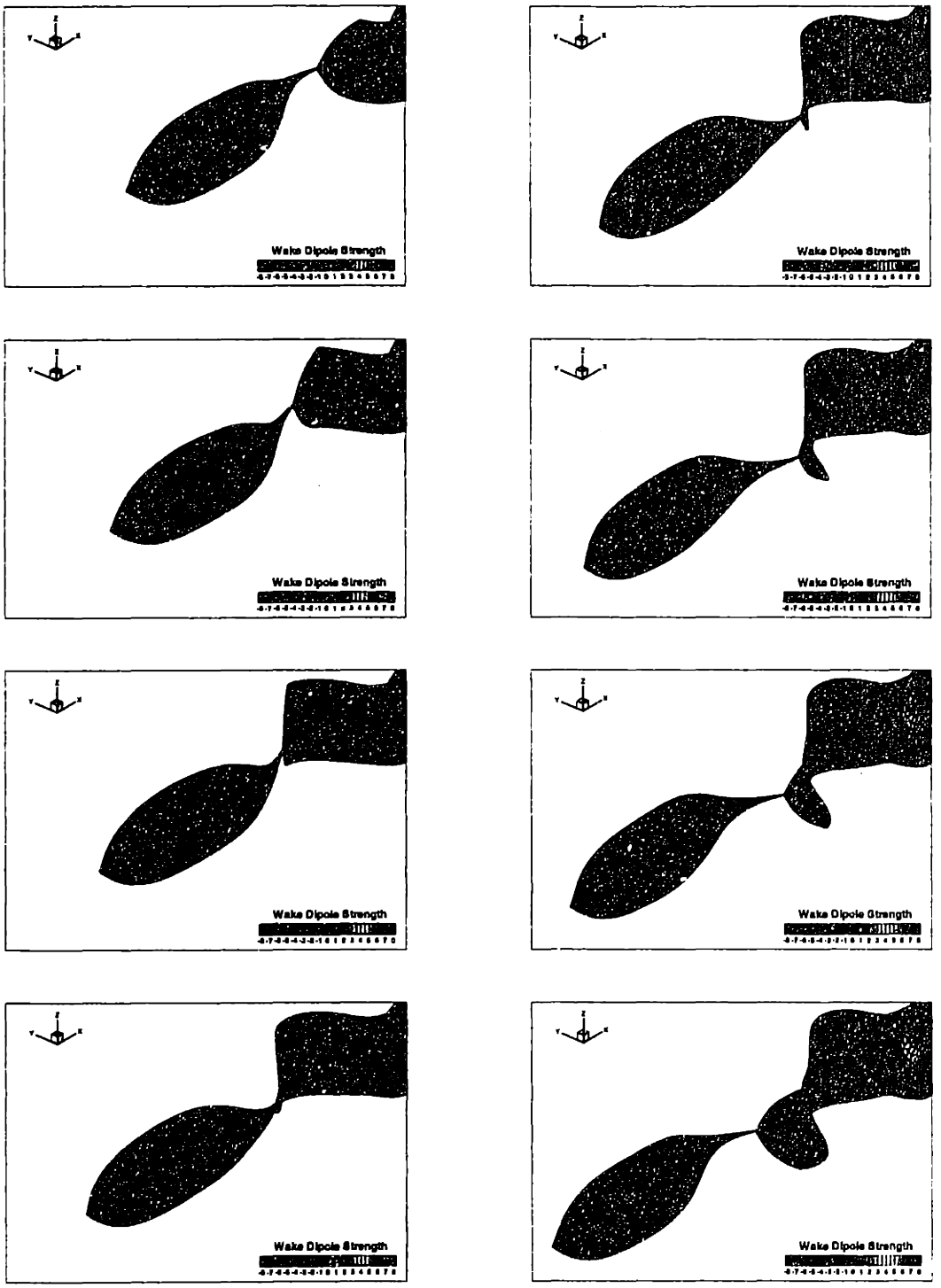

Figure 6-16: Straight-line swimming motion simulation results for one swimming cycle of the *RoboTuna* showing wake development for caudal fin shedding, case j702_06A. The computational grid is superimposed on the tuna geometry and the wake surface. Wake surface color is scaled by strength of the wake dipole sheet. Sequence is shown top to bottom, first left then right column, at intervals of $T/8$.

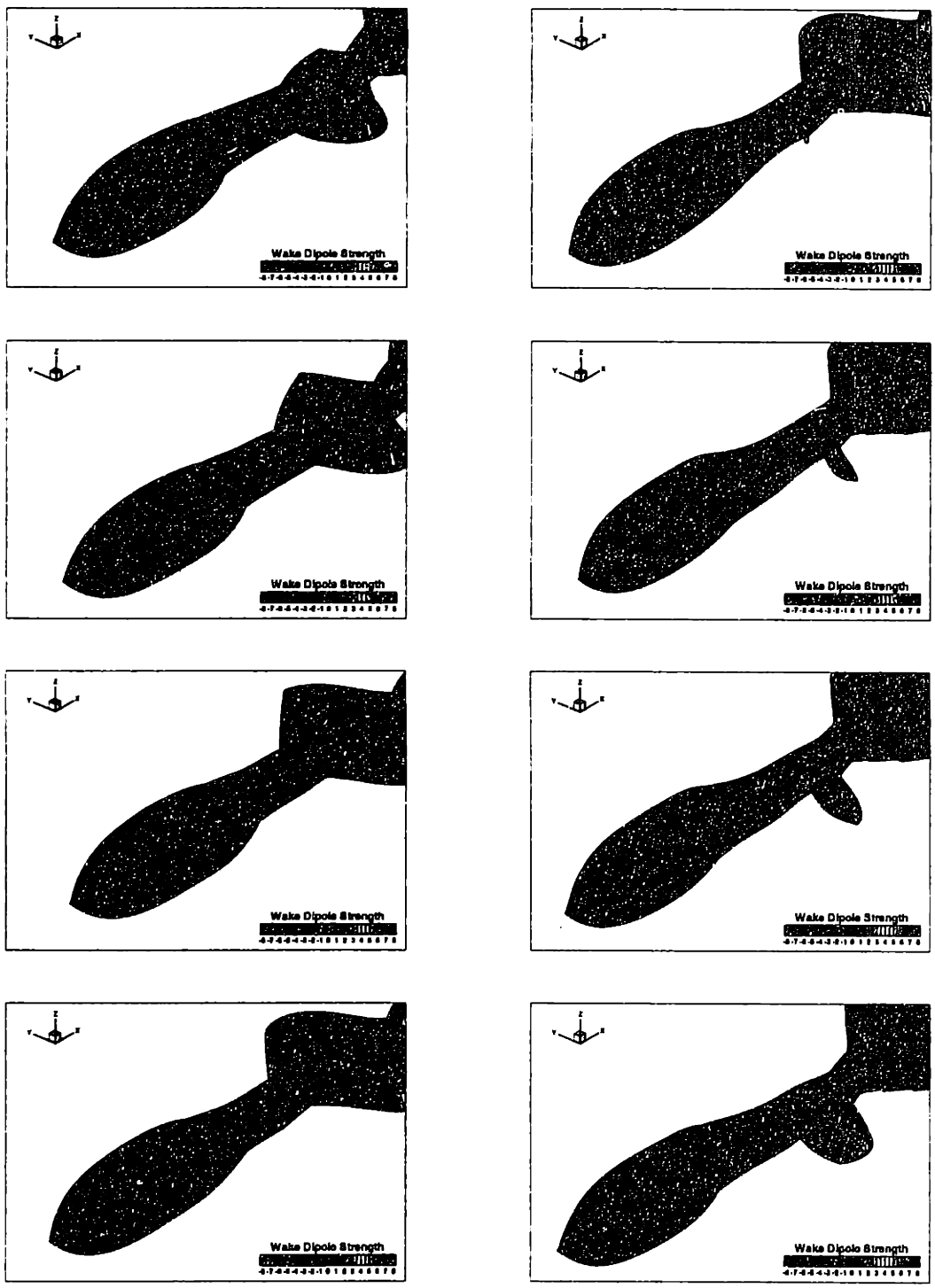

Figure 6-17: Straight-line swimming motion simulation results for one swimming cycle showing wake development and interactions for caudal fin and backbone ridge wake separation scheme, case j702_06B. The computational grid is superimposed on the tuna geometry and the wake surfaces. Wake surface color is scaled by strength of the wake dipole sheet. Sequence is shown top to bottom, first left then right column, at intervals of $T/8$.

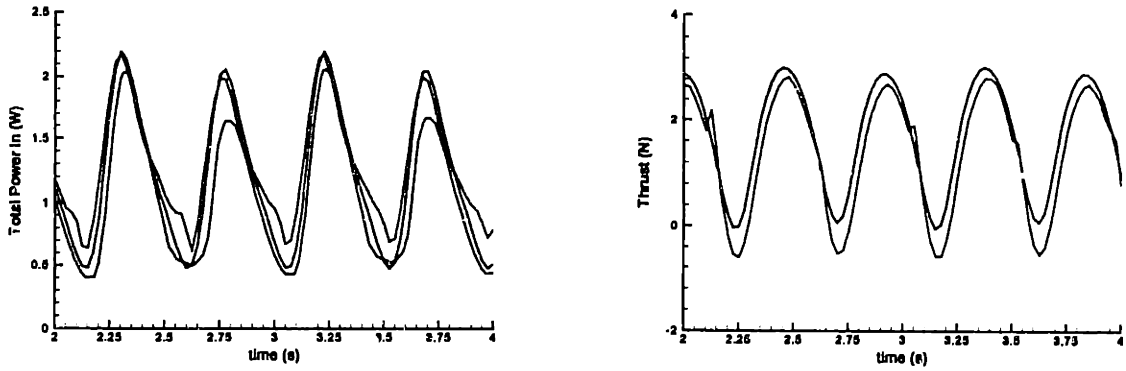

(a) Power

(b) Thrust

Figure 6-18: Time records of (a) the total power into the fluid and (b) the total thrust. Comparison of the various methods: *(i)* caudal fin shedding only, case j702_06A (black); *(ii)* caudal fin and backbone ridge shedding, case j702_06B (red); *(iii)* experimental measurements of total power from *RoboTuna* (blue). Summary of principal performance measures is given in Table 6.4.

for the motions. In this way, efficient motion can be obtained while exploiting the wake release phasing and interaction dynamics to recover energy.

6.3.4 Case 4: Run j701_01b

Finally, a simulation is chosen with kinematic parameters which resulted in poor performance of the *RoboTuna*. This motion experimentally resulted in drag amplification on the actively-swimming body to 282.9% above the rigid body drag (Barrett 1996) [19]. The numerical simulation of the power input to the fluid for this run did not compare well to the experimental power required by the motors, and in addition, a mean drag force was simulated, rather than thrust. Kinematic parameters for this run: Strouhal number $St = 0.102$, swimming speed $U = 0.656\ BL/s$, tail circular frequency $\omega = 3.137\ rad/s$, wavelength $\lambda = 1.316\ BL$, tail tip double amplitude $A = 0.134\ BL$, angle of attack $\alpha = 11.5^o$, and tail phase between pitch and heave $\phi = 77.0^o$.

Figures 6-19 and 6-20 show the simulated motions over one complete swimming cycle for the two different wake separation schemes, for caudal shedding only case

		RoboTuna	Scheme A j702_06A	Scheme B j702_06B
Mean power input	(W)	1.08	1.29	1.33
Mean power input difference	(%)	—	19.4	26.7
Peak power input	(W)	1.99	2.20	2.18
Peak power input difference	(%)	—	10.7	9.55
Mean thrust force (computation)	(N)	—	1.67	1.54
Computational propulsive efficiency	(η)	—	90.4%	81.1%

Table 6.4: Summary of performance data, showing comparison between experimental measurements from *RoboTuna*, wake Separation Scheme A j702_06A (caudal fin shedding only), and wake Separation Scheme B j702_06B (caudal fin and backbone ridge shedding).

j705_03A and caudal and backbone ridge shedding case j705_03B, respectively. From the sequence of images shown in Figure 6-19, it can be seen that the motion of the tail alone releases a series of drag wakes behind the tail fin. Much like the wakes released behind an impulsively-started airfoil, these wake structures oscillate in strength and position behind the fish due to the slow motion of the oscillating tail relative to the speed of swimming. This series of drag wake structures forms a drag jet, and the body absorbs power through its imposed motions due to the induced drag of its wake. As can be seen from the color contours of wake dipole strength superimposed on the computational grid of the shed wake surfaces, the phase of encounter shown in Figure 6-20 between the oscillating caudal fin and the body-generated vorticity released upstream through backbone ridge separation significantly affects subsequent wake-wake interaction dynamics. From Figure 6-20, as the tail sweeps from side-to-side, a drag jet of oscillating strength wake components separates from the caudal fin trailing edge. When the tail encounters the wake sheets shed upstream from the backbone ridge also in the form of a drag jet, the caudal fin wake pairs with the same-signed vortical structures released from upstream, inducing a rotational velocity which is in the *same* direction of the fluid rotation induced by the upstream-shed vorticity. In this manner, the drag realized by the body may be increased in the absence of unsteady bluff-body or leading edge separation or stall of the tail fin.

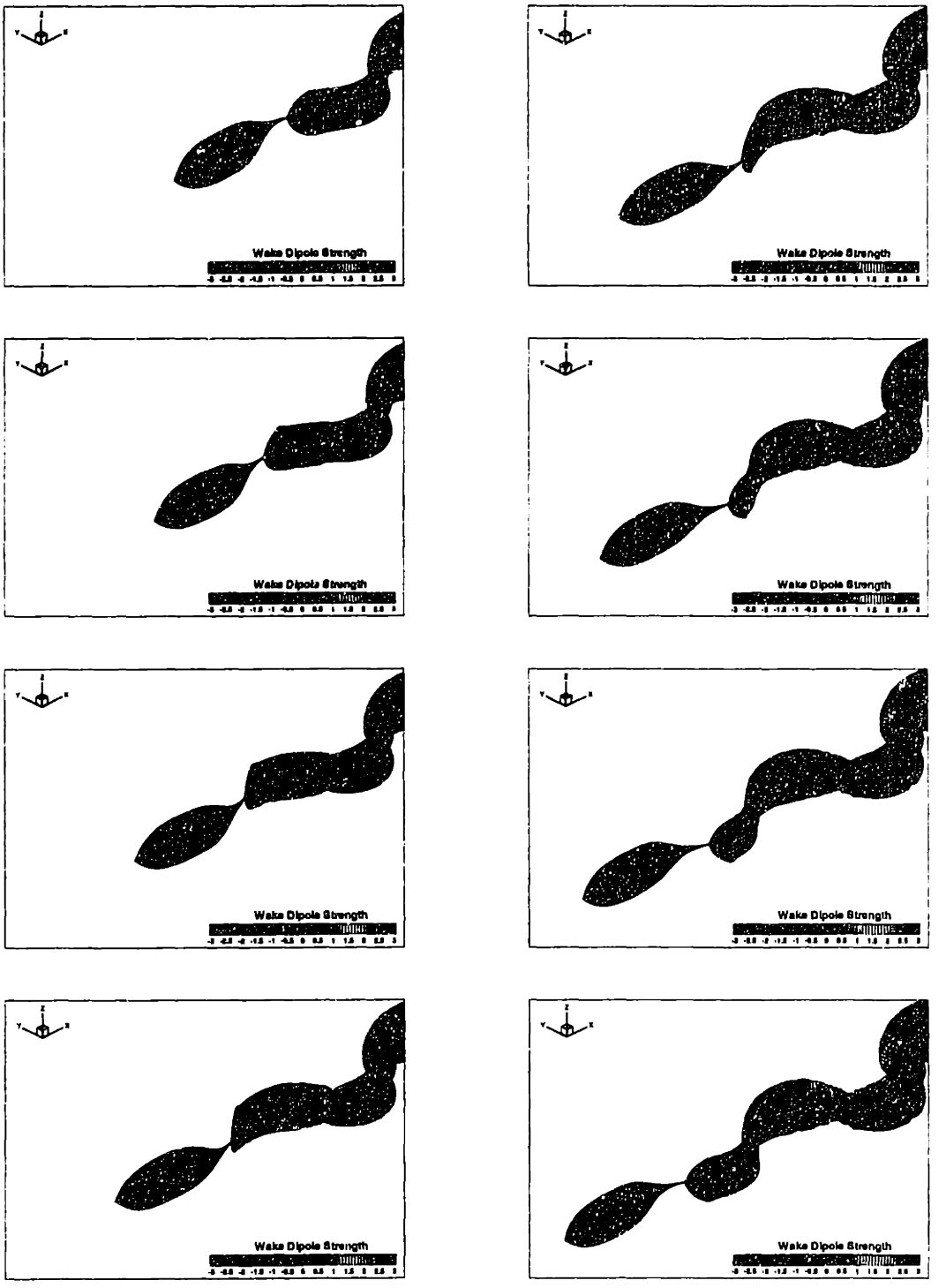

Figure 6-19: Straight-line swimming motion simulation results for one swimming cycle of the *RoboTuna* showing wake development for caudal fin shedding, case `j701_01bA`. The computational grid is superimposed on the tuna geometry and the wake surface. Wake surface color is scaled by strength of the wake dipole sheet. Sequence is shown top to bottom, first left then right column, at intervals of $T/8$.

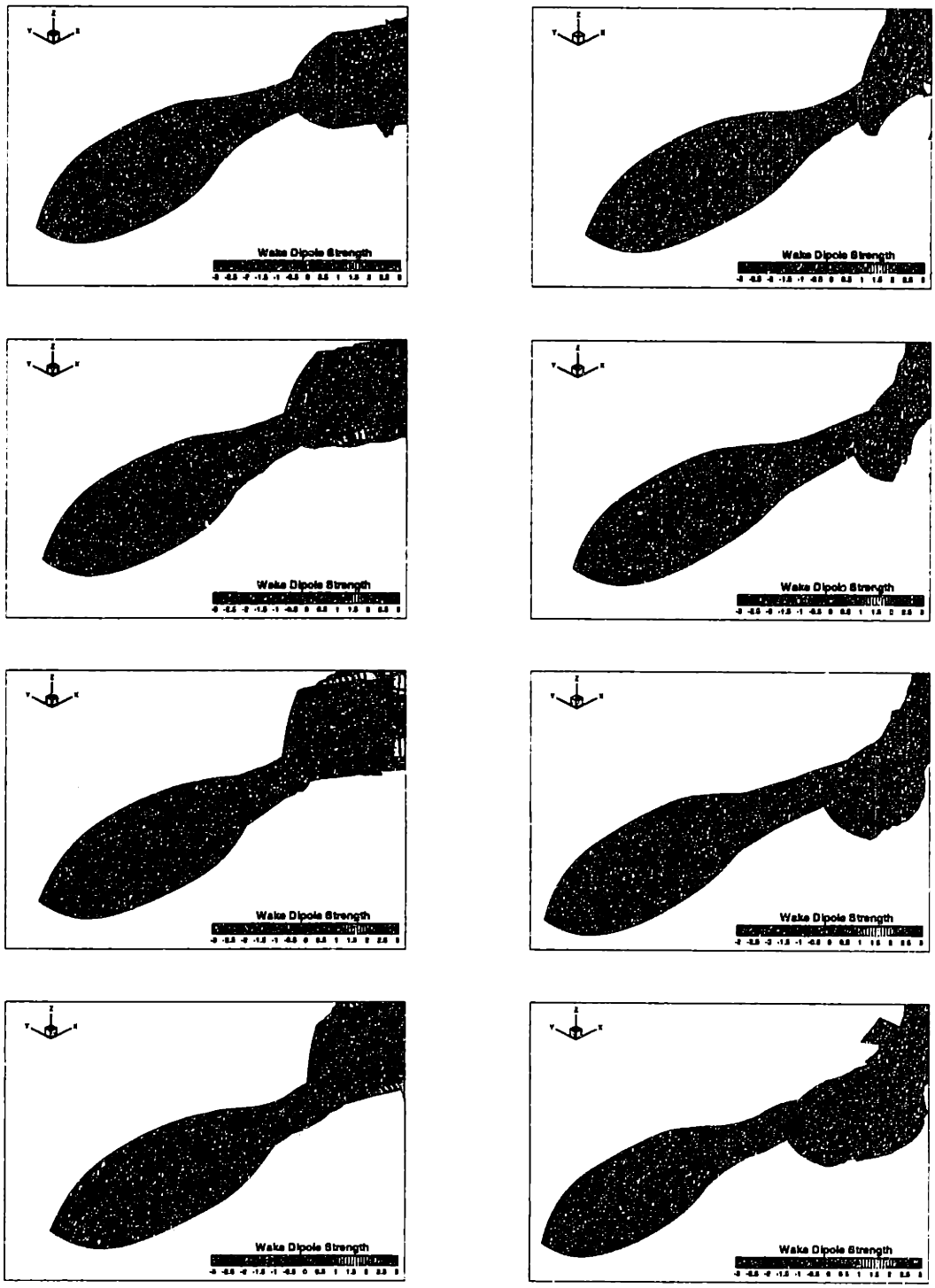

Figure 6-20: Straight-line swimming motion simulation results for one swimming cycle showing wake development and interactions for caudal fin and backbone ridge wake separation scheme, case j701_01bB. The computational grid is superimposed on the tuna geometry and the wake surfaces. Wake surface color is scaled by strength of the wake dipole sheet. Sequence is shown top to bottom, first left then right column, at intervals of $T/8$.

		RoboTuna	Scheme A j701_01bA	Scheme B j701_01bB
Mean power input	(W)	4.58	−0.45	−1.04
Mean power input difference	(%)	—	109.9	122.7
Peak power input	(W)	8.21	0.61	0.83
Peak power input difference	(%)	—	92.6	89.9
Mean thrust force (computation)	(N)	—	−0.92	−1.73
Computational propulsive efficiency	(η)	—	—	—

Table 6.5: Summary of performance data, showing comparison between experimental measurements from *RoboTuna*, wake Separation Scheme A `j701_01bA` (caudal fin shedding only), and wake Separation Scheme B `j701_01bB` (caudal fin and backbone ridge shedding).

To understand the impact of these fluid-body interactions revealed through our flow visualizations on the body dynamics, the simulation results are again compared to the integrated performance dynamics obtained by the *RoboTuna*. Figure 6-21(a) shows the power required for swimming by the experimental robotic vehicle compared to the power delivered to the fluid through simulation utilizing the two wake separation schemes. The thrust force computed during simulation is shown in Figure 6-21(b) for both wake separation schemes. A summary of these results is given in Table 6.5.

The caudal fin wake separation scheme shows poor comparison to the experimental results, with a negative thrust produced and power absorbed from the local integrated product of the body force and imposed body velocity. It should be noted that the experimental mechanism may realize such similar power absorption qualities if it did not have to overcome any viscous separation effects to produce the imposed motion, which may cause the great discrepancy between experimental and computational results. The caudal fin and backbone ridge wake separation scheme also realizes a mean drag force and power absorbed, with slightly higher values for the drag produced and the power absorbed during swimming. This suggests that the interactions of the oscillating tail with upstream-generated vorticity enhances the total drag wake produced by the swimming body.

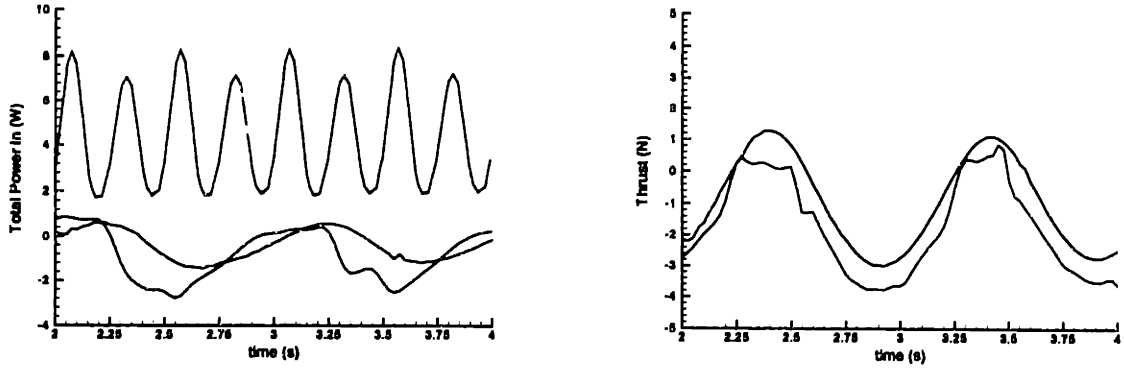

(a) Power

(b) Thrust

Figure 6-21: Time records of (a) the total power into the fluid and (b) the total thrust. Comparison of the various methods: *(i)* caudal fin shedding only, case `j701_01bA` (black); *(ii)* caudal fin and backbone ridge shedding, case `j701_01bB` (red); *(iii)* experimental measurements of total power from *RoboTuna* (blue). Summary of principal performance measures is given in Table 6.5.

6.4 Flow actuation mechanisms of efficient swimming modes

As seen in the previous sections, the fish is effectively able to generate body-bound vorticity, through propagation of a traveling backbone wave, and release it in a controlled manner to favorably interact with the oscillating tail. However, the mechanisms of this body-bound vorticity generation has been the subject much controversy. In this section, the near-body flow around the *RoboTuna* for an efficient swimming motion considered previously will be examined in detail. The objective is to identify the structure of the near body flow and the mechanisms of its actuation, which affects the production of body-generated vorticity which can be released by the backbone and controlled by the tail as well as the production and manipulation of a thrust jet with strong two-dimensional components.

Although the wake vorticity defining the thrust jet appears to have a two-dimensional structure with large vertical vortices bounding the region of the jet, the near-body flow around the fish is much more complex. Linear theory would suggest that the

streamlines of the velocity field would remain in-plane. Two-dimensional predictions for fish swimming dynamics require the flow velocities to remain in the longitudinal plane for all depths (Wu 1961, 1971) [239, 241], whereas slender-body theory requires that the fluid velocity vectors remain entirely transverse in sectional planes along the body length (Wu 1971; Lighthill 1975) [242, 243].

Considering the "good" case from the *RoboTuna* experiments j705_03, it can be seen that the actual flow along the fish length is quite complex. As shown in Figure 6-22, the flow profiles around the fish are shown at two depth planes, near the top of the body $z/D = 0.2$ and along the mid-body depth $z/D = 0.5$ for total body depth D, for the two wake separation schemes, case j705_03A and j705_03B. The in-plane velocity vector streamlines are superimposed on a contour plot of the vertical vorticity ω_z component in that plane. Again, the two-dimensional nature of the wake vorticity structures can be seen from identification of the red and blue regions of alternating-strength vorticity at different depths, which induce the counter-rotating fluid velocity regions forming the reverse Kármán street thrust jet. Streamlines in the wake further identify the thrust jet of fluid, although wake-wake interactions resulting from implementation of the backbone ridge shedding model may make this less clear, as the strength of the overall jet is altered as discussed in Section 6.3. However, while the flow around the body is characterized by the longitudinal patterns predicted by two-dimensional swimming theory, the confluence of the streamlines in some regions indicates a strong out-of-plane transverse velocity component, suggesting a highly three-dimensional fluid actuation process affected by the fish motions.

To determine the extent of the transverse flow patterns suggested by the confluence of streamlines in the two-dimensional longitudinal cuts, sectional planes around the *RoboTuna* are examined in Figure 6-23. The body position considered is from the identical time instant as in Figure 6-22 for both separation schemes. While linear three-dimensional slender body theory would predict entirely transverse flow patterns, with circular, dipole-like cross-flows at the depth extremes of the elliptic body sections, the actual flow patterns appear primarily two-dimensional in nature along the body length in Figure 6-23. Sectional planes reveal the in-plane streamlines from

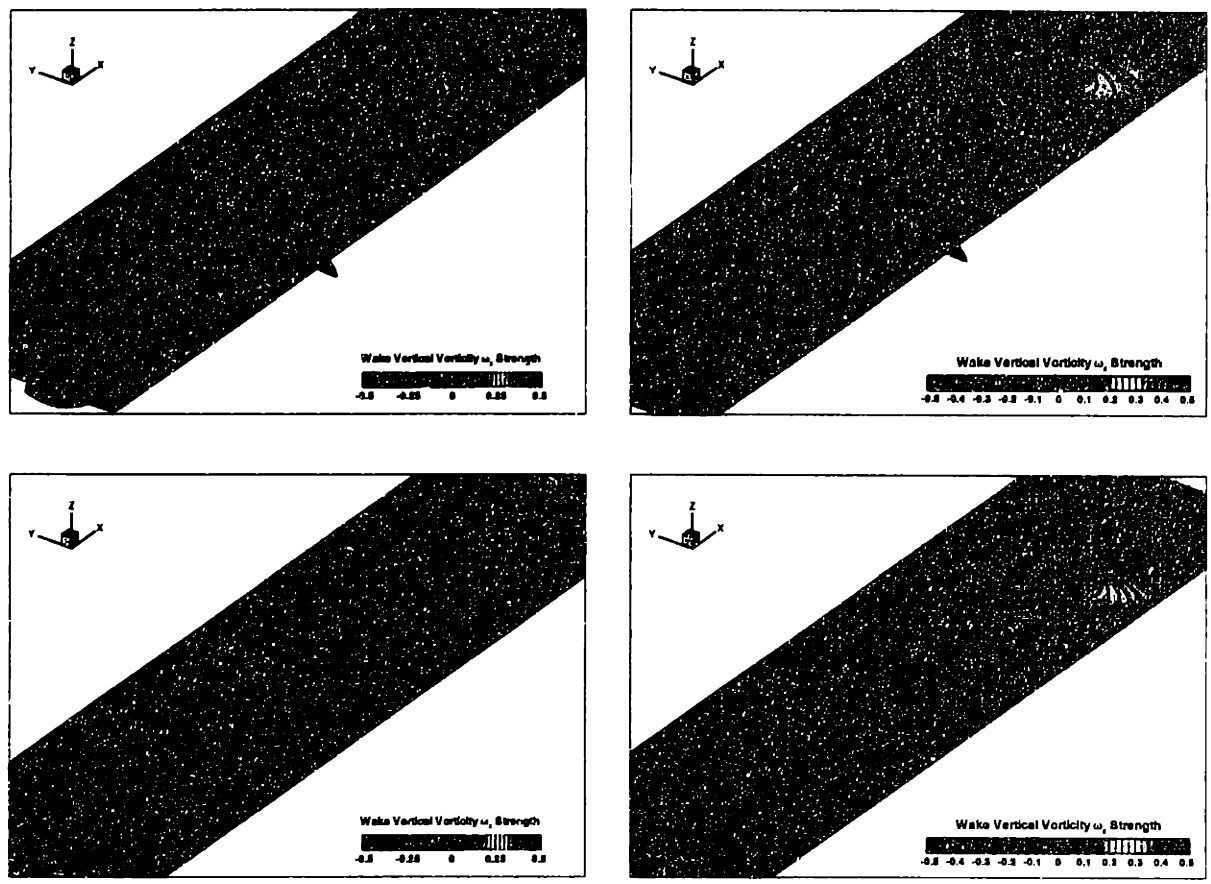

(a) Caudal shedding

(b) Caudal + backbone shedding

Figure 6-22: Flow profiles at two vertical locations along the body of total depth D for (a) case j705_03A caudal fin shedding and (b) j705_03B caudal fin and backbone ridge shedding. Top row: $z/D = 0.2$ measured from the top. Bottom row: $z/D = 0.5$. In-plane velocity vector streamlines (black) are superimposed on a contour plot of the vertical vorticity ω_z component in the plane (Range:[$-0.5\ s^{-1}$,$0.5\ s^{-1}$]). Viewed from above, red vorticity indicates clockwise fluid rotation, blue vorticity indicates counterclockwise rotation, and green regions are irrotational. Time shown corresponds to the body position on the bottom right of Figures 6-11 and 6-12.

the expanding region in the forebody through the contraction region anterior to the caudal peduncle, separated by distances of 20% of the body length. Only in the mid-body region, which corresponds to a node in the propagation of the backbone wave for the time instant shown, does the flow appear to have a dipole-like quality with circular cross-flow streamlines at the top and bottom extremes of the fish depth. At the other cuts, the flow appear to be actuated in a lateral direction over the majority of the fish depth, as suggested by two-dimensional swimming theory.

The color contours in the sectional planes of Figure 6-23 correspond the the dynamic pressure coefficient based on swimming speed. Comparison of the pressure profiles at the various sections along the length of the fish illustrate how the localized body undulations formed by the progressive backbone wave contribute to the production of near-body low pressure regions. These low pressure regions are then actuated by the oscillations of the tail to form the thrust jet in the wake and similarly enhance the strength of the caudal fin wake vorticity as these low pressure regions pass over the leading edge of the caudal fin. Additionally, comparison of the pressure contours in the peduncular region (the posterior section cut) for the different shedding schemes in Figure 6-23 illustrates how the release of body-generated vorticity contributes to the strength of these low pressure regions. This mechanism of high momentum region reinforcement has been observed previously through visualization of the wake vortical and pressure structures in the swimming Giant Danio and *RoboTuna*, which overlap in certain regions comprising the wake thrust jet.

Consideration of the combined flows visualized in Figures 6-22 and 6-23, the formation mechanism of the body-generated vortical structures through localized backbone actuation can be explained. Based on observations in these and all other visualization of the near-body flow profiles for the fish swimming motions considered in this investigation, a summary of flow profiles around the fish body for $c_p/U > 1$ showing transverse and longitudinal components of fluid velocity can be seen in Figure 6-24. The backbone wave is progressing from head to tail. Top figure is shows a schematic with sectional cuts at the crest and trough of the backbone wave when viewed from above. Flow is longitudinal in nature in the yz-plane at the backbone wave nodes, as

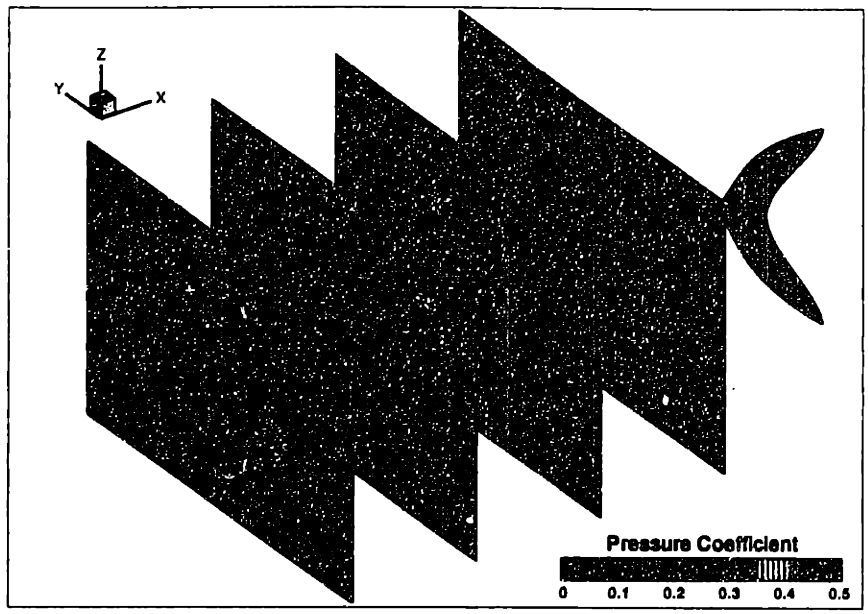

(a) Caudal shedding

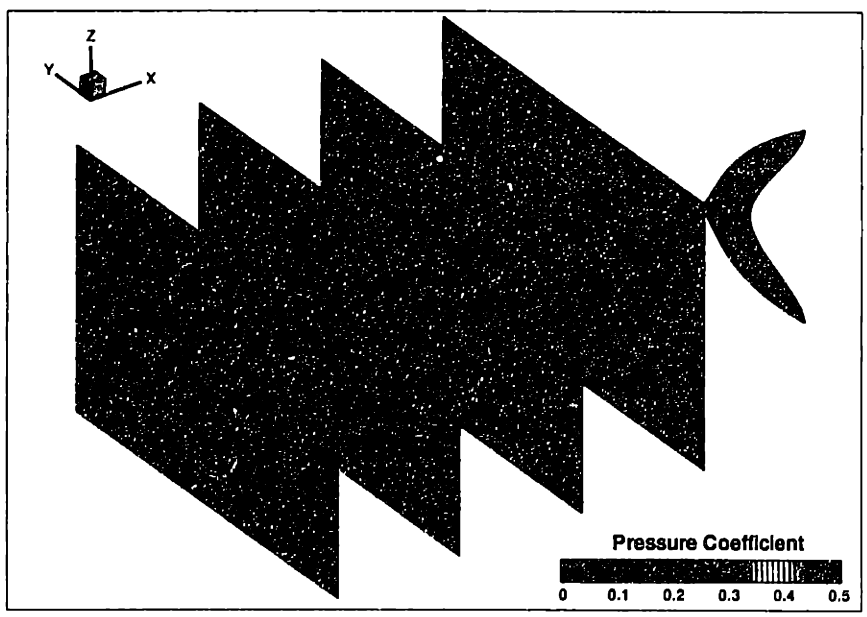

(b) Caudal + backbone shedding

Figure 6-23: Flow section flow profiles at four longitudinal locations along the body length ℓ for (a) case j705_03A caudal fin shedding and (b) case j705_03B caudal fin and backbone ridge shedding. Sections are separated by 0.2 ℓ, with forward section 0.2 ℓ from the nose. In-plane velocity vector streamlines (black) are superimposed on a contour plot of the dynamic pressure coefficient (Range:[0.0,0.5]). Red contours indicate high fluid velocity, blue indicates low fluid velocity. Time shown corresponds to the body position on the bottom right of Figures 6-11 and 6-12.

evidenced by the red streamlines in the plane of the sectional cuts. The flow along the body between the two section cuts is more transverse in the xy-plane, especially in the regions of the troughs of the backbone wave as evidenced by the blue streamlines. This is more simply shown in a top view in the bottom figure. At the top and bottom edges of the fish, cross flow reverses the longitudinal direction of the perturbation velocity from one side of the fish to the other, as evidenced by the purple streamlines, strengthening the longitudinal vorticity which connects the body-generated vertical vorticity at the backbone wave maxima to form a lattice of vortex rings.

The fish swims with a motion which exploits the natural stability properties of the vortical structures which it creates, with Strouhal numbers with an optimal range for a two-dimensional thrust jet instability identified by Triantafyllou *et al.* (1993) [204]. The two-dimensional quality of the wake structure over a depth equivalent to that of the fish corroborates these observations of the kinematics of live fish. While the near-body actuated flow has a strong two-dimensional quality as well, the body-generated vortical system, like the caudal wake, preserves connectivity through longitudinal vortices shed at the tips of the body separation points or the caudal tips. These three-dimensional ring-like systems disrupt the purely two-dimensional quality of the thrust jet, but the fish may similarly exploit the secondary three-dimensional wake structure instability through its swimming motions.

The Strouhal number instability properties of the two-dimensional thrust jet have an analogy in the universal "formation time" for laminar vortex rings studied by Rosenfeld, *et al.* (1998) [174] and Gharib, *et al.* (1998) [64]. Laminar vortex rings have been shown to achieve their maximum circulation at a nondimensional formation time Ut/D of approximately 4, where U is the velocity of the jet forming the vortex ring, t is the time, and D is the diameter of the jet. This nondimensional formation time can be considered within the context of fish swimming. The Giant Danio has been observed to swim at a forward speed of $U = 0.7\ BL/s$, oscillating its caudal fin at $\omega = 19.6 rad/s$ with a total peduncle excursion of $D = 0.23\ BL$. If the time to form a ring-like vortical structure by the body and the tail t is assumed to be equivalent to one-half a swimming period $T = 0.32\ s$, then the formation time of the

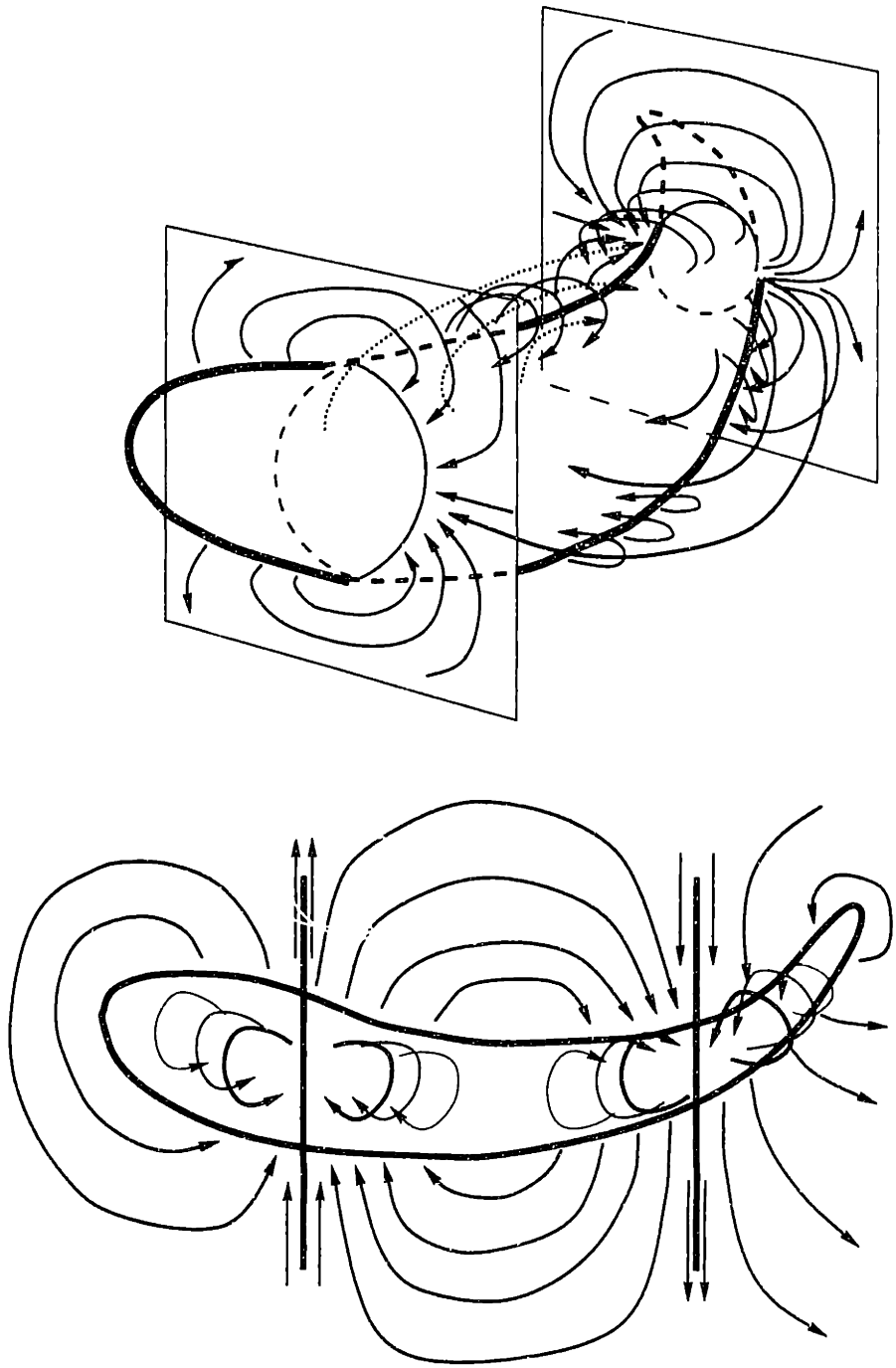

Figure 6-24: Summary of flow profiles around the fish body for $c_p/U > 1$ showing transverse and longitudinal components at the maxima and nodes of the backbone wave which is progressing from head to tail. Top figure is shows an orthogonal schematic with sectional cuts at the nodes of the backbone wave when viewed from above. Red streamlines indicate flow in the plane of the sectional cuts. Blue streamlines indicate flow along the body between the two section cuts. At the top and bottom edges of the fish, purple streamlines indicate a cross flow reversing the longitudinal direction of the perturbation velocity on either side of the fish. Bottom figure is a top view of the orthogonal schematic.

vortex ring system developed by the oscillating tail is approximately $Ut/D = 4.8$. This formation time may slightly higher for the ring-like vortices shed by the body thin fins and slightly lower for the ring-like vortices shed by the trailing edge of the caudal fin, with slightly lower and higher total lateral excursions, respectively. This formation time is in good agreement with the formation time of vortex ring structures in a thrust jet observed through experiments and computations over a range of Reynolds numbers. Thus, the predisposition of the fish to swim at frequencies which correspond to natural vortical flow instabilities has been extended to account for the three-dimensional quality of the vortex structure formed by the undulations of the body and the tail.

It should be noted that the effect of the Rankine ellipsoidal body flow has been neglected in this interpretation of the mechanisms of bound-vorticity generation, and only circular perturbation flows are considered, i.e. the lifting rather than the thickness problem is the essence of the model presented in Figure 6-24. For the elliptical body sections of moderate aspect ratio $AR > 1.5$ considered in this investigation, the perturbation velocity contributions appear longitudinal in nature over the majority of the body depth. This longitudinal Rankine body perturbation flow results in an overall flow picture which might appear to have components directed to both lateral sides of the body at the same longitudinal section in Figure 6-22. Much like the circulation flow about an airfoil, though, the body-generated vorticity perturbs the local flow velocities near the body to generate circular flow patterns and corresponding regions of suction, which contribute to the propulsion of the undulating body; however, these circular flows are difficult to identify visually in the composite images of three-dimensional flow simulation results.

6.5 Vorticity control modes of fish swimming

The unsteady propulsion vorticity control mechanisms utilized by fish are elucidated through the visualization of the near-body and wake structure dynamics. The steadily-swimming fish generates vorticity through the body undulations described by a progressive backbone wave. This body-generated vorticity interacts with the strong wake shed from the oscillating caudal fin to affect the efficient generation of a thrust jet in the form of a reverse Kármán vortex street. Low pressure regions formed by the acceleration of the near-body fluid by the backbone wave are manipulated by the oscillating tail to enhance the strength of the thrust jet, as well as to recover energy from the flow through increased localized lift around the tail. These fluid actuation and transport processes are significantly affected by variation of the prescribed body kinematics; uniquely lending this investigation of unsteady propulsion schemes to comprehensive visual study, and is presented in a concise format in Wolfgang *et al.* (1999) [237].

Many of the interaction modes which can be seen through simulation of the fish motions are evidence of mechanisms utilized by the swimming fish to recapture energy, generate large thrusts, or even generate large drags. In this section, simple models are presented which describe the main fluid structure-body interactions and manipulations, highlighting the vorticity control mechanisms of both "efficient" and "bad" modes of straight-line swimming, as well as the unsteady maneuvering vorticity control mechanisms elucidated through the flow visualizations of *Chapter 5*. These mechanisms of vorticity control are similar to those observed by an oscillating foil which encounters upstream-released vorticity in a shear layer, studied in detail through experiments and computation by Gopalkrishnan, *et al.* (1994) [68], Streitlien (1994) [190], and Anderson (1996) [9].

6.5.1 Mode 1: *Burst swim* - Constructive interference thrust wake

The first mode considered is that seen through simulation of the *RoboTuna* swimming motions at a high Strouhal number St, such as observed in Case j702_01. With this burst swimming motion, the fish generates a strong thrust jet in its wake. Utilization of an upstream wake-shedding model elucidates the mechanism by which the undulations of the body produces thrust, which is then amplified by the oscillation of the tail. This amplification is further aided by the interaction of body-generated low pressure regions with the oscillating tail, which are "pumped" into the wake by the movement of the progressive wave towards the tail. As these low pressure regions pass over the tail, an increased leading-edge flow and stronger circulation is realized, thus increasing the strength of the shed wake.

Figure 6-25 illustrates the mechanisms by which the vorticity shed from the oscillating tail pairs with the body-generated vorticity shed from the undulating body, amplifying the thrust jet in the wake. The effects of pressure structures, while described above, are not shown in detail herein, as the qualitative behavior is identical to that described in Figure 4-32 of *Chapter 4*.

The top illustration in the sequence of Figure 6-25 shows two pairs of wake vortices P1 and P2. The vortices of each pair are of the same circulation orientation, comprising a strong wake thrust jet. Another vortex with counterclockwise circulation c1 is released by the caudal fin at the top of its stroke as it begins its downward path, and a body-generated vortex b1 propagates towards the tail. In the second illustration of the series, vortex b1 is released through separation from the backbone ridge as the caudal fin begins to develop a clockwise circulation. In the third illustration, body-generated free vortex b1 pairs with same-signed caudal generated vortex c1 to contribute to the thrust jet. At the same time, the caudal fin begins to release clockwise vorticity c2 into the wake at the bottom of the tail stroke, while a new body-generated vortex b2 forms with the trough of the backbone wave at the head of the fish. In the final image of the series, body-generated vortex b2 is released through

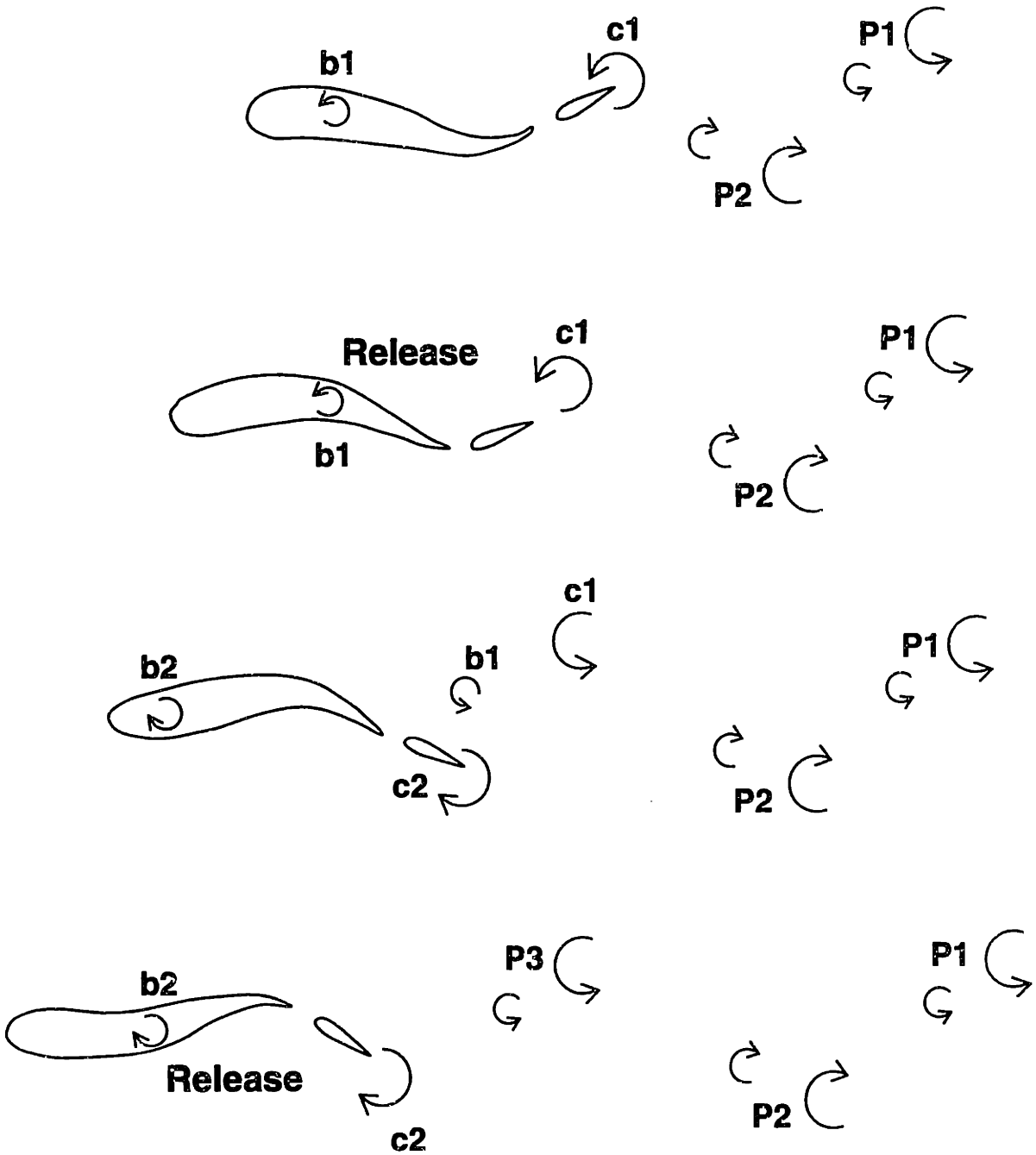

Figure 6-25: Vorticity Control Mode 1 - *Burst Swim.* This series shown top to bottom illustrates the manner in which vortices shed from upstream separation lines are manipulated by the oscillation of the articulated caudal fin to amplify the strength of the thrust jet in a constructive interference pattern.

separation from the backbone, and the caudal fin has completely released c2 into the wake, concluding the swimming cycle.

6.5.2 Mode 2: *Cruising* - Destructive interference thrust wake

Experimental observations of the kinematics of live tuna [57, 47] established the baseline of parametric swimming modes employed by the *RoboTuna*. Through the simulation of these motions without considering vorticity shed into the wake through upstream separation lines, the computed power imparted to the fluid compares well to that utilized by the motors in the generating the flexible-hull robotic vehicle motions, particularly for motions which experimentally realized large drag reductions, characteristic of live tuna steady-state straight-line swimming kinematics.

Through investigation of the influence of vorticity shed from the backbone motions on the evolving wake structure and the near-body flows, the hydrodynamic mechanisms employed by live tuna with dorsal and ventral finlet ridges may be studied. By simulating the imposed motions of the swimming tuna which resulted in good previous experimental comparisons, the interactions of this body-generated vorticity with the wake shed from the caudal fin reveal how the body may recover energy from its upstream-generated disturbances, such as observed in Case j705_03. This energy recovery is affected by the pairing of vorticity shed from the backbone with oppositely-signed vorticity shed from the tail, through the manipulation of this free body-generated vorticity by the tail motions, as seen in Figure 6-26.

The top illustration in the sequence of Figure 6-26 shows two pairs of wake vortices P1 and P2. Each pair of vortices is composed of a strong vortex on the outside on the wake width which contributes to the thrust jet and a smaller, oppositely-signed vortex closer to the jet centerline which is in a drag jet orientation. The net result of the vortex pairings shown is a diminished thrust jet strength than the one observed in the *Burst Swim* mode of Figure 6-25. Also in the top of Figure 6-26, another strong vortex with counterclockwise circulation c1 is released by the caudal fin at the top

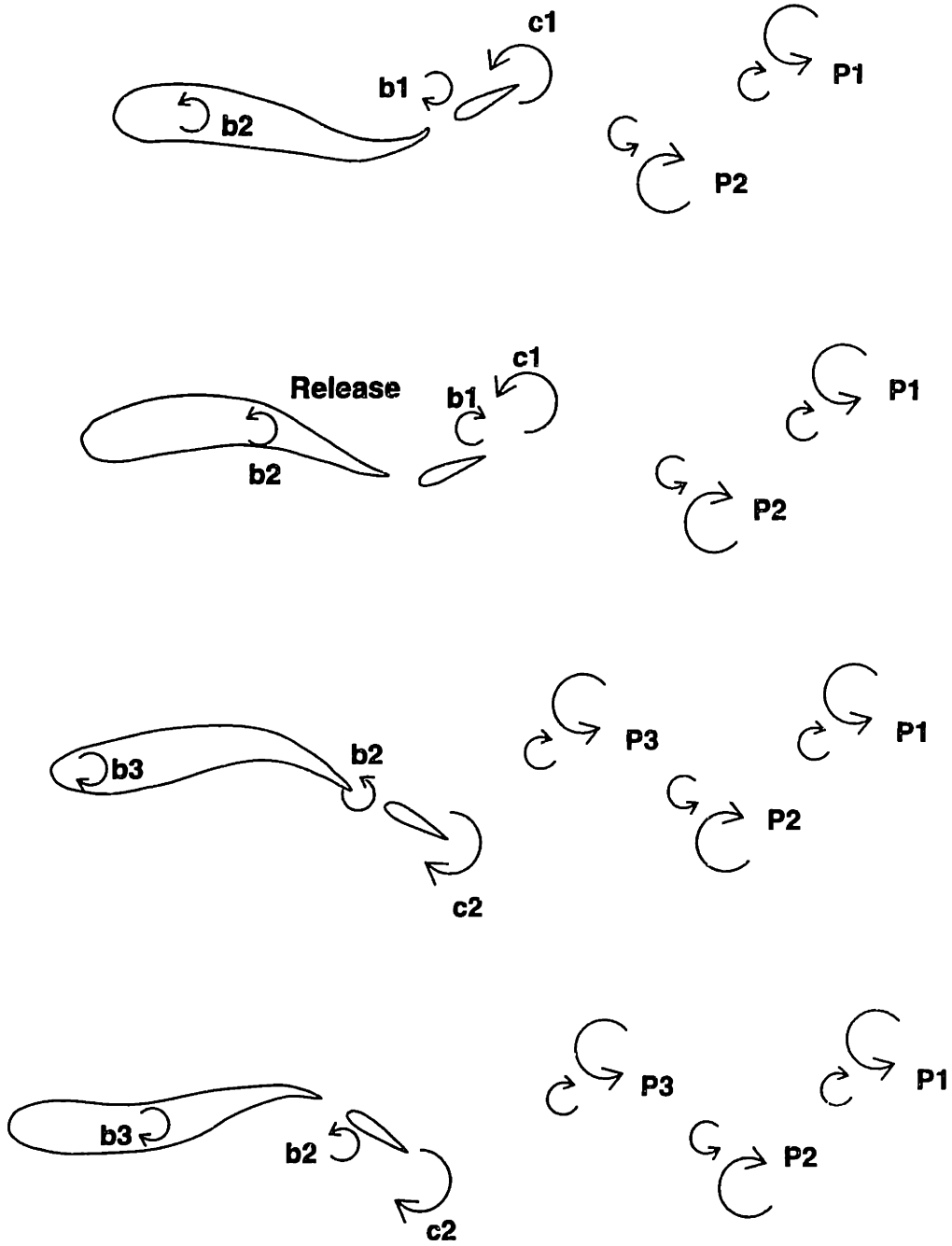

Figure 6-26: Vorticity Control Mode 2 - *Cruising.* This series shown top to bottom illustrates the manner in which vortices shed from upstream separation lines are manipulated by the oscillation of the articulated caudal fin to decrease the strength of the total thrust jet produced. This destructive interference pattern allows the oscillating tail to recapture energy imparted to the flow through the body undulations necessary to actuate the high-aspect-ration caudal fin.

of its stroke as it begins its downward path, and a free body-generated vortex b1, with a circulation direction opposite that of vortex c1, passes on the inside of the tail's motion. A second body-generated vortex b2 is formed at the crest of the body backbone wave, in an orientation where it is contributing to the thrust of the body and the net thrust jet wake. In the second illustration of the series, vortex b2 of counterclockwise circulation is released through separation from the backbone ridge as the caudal fin begins to develop a clockwise circulation. Oppositely-signed vortices b1 and c1 pair to form P3, delivering a positive net contribution to the thrust jet. In the third illustration, the caudal fin begins to release clockwise vorticity c2 into the wake at the bottom of the tail stroke, while the free body-generated vortex b2 passes over the peduncle region and is forced below the tail. This tail motion effectively transfers the body-generated vortex from a side of the wake where it was originally strengthening the thrust jet to the other side of the wake where it detracts from the thrust jet strength. A new body-generated vortex b3 forms with the trough of the backbone wave at the head of the fish, again in an orientation which would contribute to the thrust jet based on the side of the wake where it is developing. In the final image of the series, body-generated vortex b2 has been completed transfered to the opposite side of the wake and pairs with oppositely-signed caudal-generated vortex c2 to form a net contribution to the thrust jet, concluding the swimming cycle.

This same pattern of destructive wake interference is seen in the naturally-observed swimming motions of the Giant Danio, and is corroborated through the numerical simulation results presented in Figures 6-4 through 6-6 in which wake vorticity pairing is evident. This type of destructive interference is also shown to cause drag wake jet annihilation through the destructive interaction of thrust jet vortices produced by an oscillating foil with the shear layer drag wake vortices produced by an upstream bluff body [68, 190, 191, 9]. The interaction observed here is qualitatively similar but allows for an improvement in swimming efficiency of the *RoboTuna* in Section 6.3, an efficiency improvement of the whole system as opposed to just an oscillating foil reclaiming energy from an upstream-generated unsteady shear layer forming a drag wake.

6.5.3 Mode 3: *Braking* - Constructive interference drag wake

As seen through the simulation results of Case j701_01b, a drag wake is produced when the $c_p/U < 1$, and the body appears more rigid to the fluid which it observes. In this manner, the fish may stiffen its body and coast to a stop. This behavior is exhibited by the Giant Danio just before it begins its turning maneuver: experimental DPIV images show that the body backbone stiffens into a rigid curve as straight-line swimming motions cease, which is corroborated by the drag wake produced during the numerical simulation ramping-up interval coasting motion.

When a backbone shedding model is implemented for the drag producing case, this drag may be amplified by vortex pairing. This pairing is evident from the unsteady wake records of Figure 6-20 for Case j701_01b, and is similar to the two-dimensional constructive vortex interactions seen in experiments by Gopalkrishnan *et al.* (1994) [68] and Anderson [9]. The generation of low pressure regions actuated by body undulations are minimal, unlike the steady-swimming cases analyzed for $c_p/U > 1$, and this the drag wake is amplified mainly through the appearance of the body to the local flow as a quasi-steady lifting surface.

Figure 6-27 illustrates the mechanisms by which body-generated lift pairs with the drag wake released from the caudal fin, to form a stronger drag wake.

The top illustration in the sequence of Figure 6-27 shows two pairs of wake vortices P1 and P2. The vortices of each pair are of the same circulation orientation, comprising a strong wake drag jet. Another vortex with counterclockwise circulation c1 is forming around the caudal fin at the top of its stroke as it begins its downward path, and a body-generated vortex b1 propagates towards the tail. In the second illustration of the series, vortex b1 is released through separation from the backbone ridge as the caudal fin begins to release counterclockwise vortex c1 into the wake at the bottom of its downstroke. In the third illustration, the strong downwash induced by caudal-generated vortex c1 forces body-generated free vortex b1 to pass on the outside of the tail motion to pair with same-signed caudal generated vortex c1 to contribute to the drag jet. In the final image of the series, a new body-generated vortex b2 is forming

at the trough of the propagating backbone wave, and the caudal fin is developing vortex c2 with clockwise circulation and transferring it to the upper side of the wake, where it will contribute to the drag jet, concluding the swimming cycle.

Mode 3a: *Drifting*

The symmetry of the wake structure interactions motivate the hypothesis that a fourth vortex pairing mode must exist which would destructively interfere with drag wake production. This mode would involve a smaller body-generated thrust wake vortex pairing with a strong caudal-generated drag vortex, decreasing the strength of the overall drag jet. This was not observed through simulation, but is likely to be employed in swimming motions where the fish is trying to slowly decrease its swimming speed.

6.5.4 Mode 4: *Turning*

This interaction mode is considered in detail in *Chapter 5.* However, the interaction of body-generated and tail-generated vorticity was not specifically discussed previously, and the basic mechanisms of vorticity control utilized by the fish during turning is qualitatively similar to those interactions observed for straight-line swimming. Figure 6-28 illustrates more clearly the vorticity control mechanisms which are crucial to turning performance. Five body images, read from left to right, show the generation, release, and control of body-generated and caudal-generated vorticity.

As the body ceases straight-line swimming and begins to tighten into a "C"-curve, the two near-body circular flows which form are caused by bound vortices b1 and b2, which move from the center of the body towards either end with the contraction motion. The initiation of the motion also causes a small "starting" vortex to be shed from the caudal fin c1. As the tightening motion continues in the middle cartoon of Figure 6-28, the posterior body-generated vortex b1 is released into the flow through backbone separation, while a second strong vortex of the same sign c2 forms bound in the caudal fin.

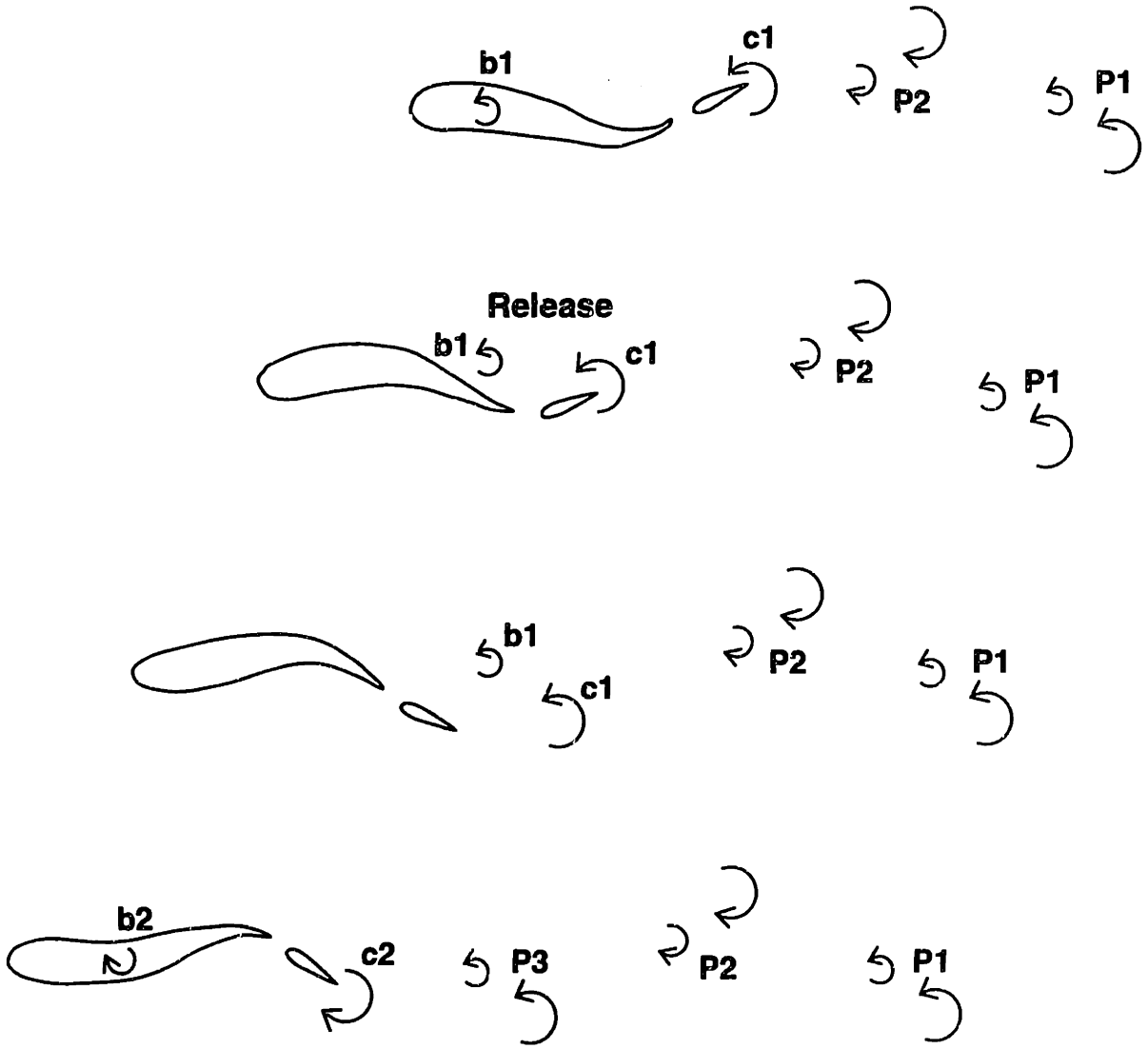

Figure 6-27: Vorticity Control Mode 3 - *Braking.* This series shown top to bottom illustrates the manner in which vortices shed from upstream separation lines constructively pair with the drag profile created by the flow over the articulated tail to increase the strength of the total drag jet produced.

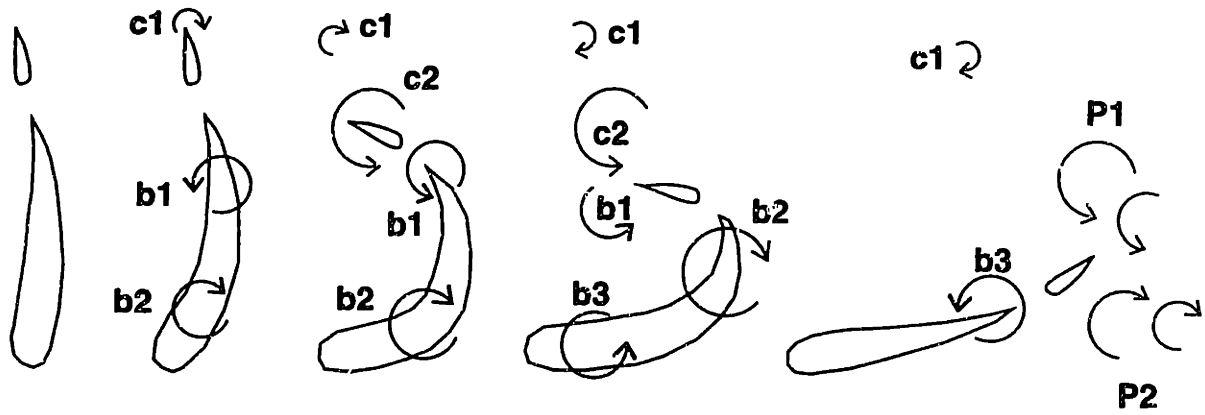

Figure 6-28: Vorticity Control Mode 4 - *Turning.* This series shown left to right illustrates the manner in which vortices shed from upstream separation constructively pair with the vortices shed by the sweeping articulated caudal fin to increase the strength of the total turning thrust jet produced.

The fourth image of Figure 6-28 shows the release of this strong caudal vortex c2, which pairs with body-generated vortex of the same sign b1 which has passed inside the sweep of the tail fin to the right. These two vortices of counterclockwise circulation induce a strong flow to the right between the fish body and the vortex pair, and above the vortex pair, a smaller jet to the left is formed with the aid of velocities induced by c1, which is corroborated by experimental observations. Also at this time, body-generated vortex b2 moves towards the posterior end of the body as the tail begins the downstroke, while a new body-generated vortex forms at the head of the fish.

Between the fourth and fifth images, the tail continues its downstroke and forms a caudal vortex c3 of the same clockwise circulation as body-generated vortex b2. As b2 is released from the body and passes over the sweeping caudal fin, it is paired with the caudal vortex c3 to form a second pair of vortices P2, inducing a circulation opposite to that induced by the c2 and b1 pair P1. These two counter-rotating pairs form the strong turning thrust jet to the right seen in the last image of Figure 6-28. In this last image, the third body-generated vortex b3 is also released from the body, where it will pass over the caudal fin to help bound the straight-line swimming thrust jet to be created as the fish swims off to the left. While this vorticity control sequence details the strong constructive interactions of the body-generated and tail fin vortical

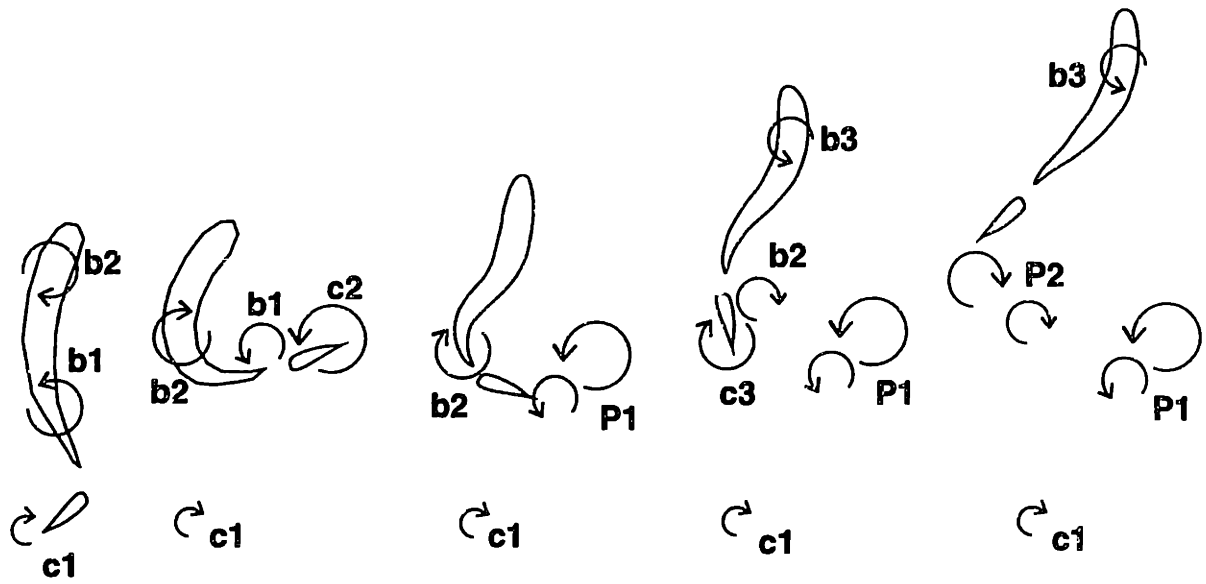

Figure 6-29: Vorticity Control Mode 5 - *Fast-starting.* This series shown left to right illustrates the manner in which vortices shed from upstream separation constructively pair with the vortices shed by the sweeping articulated caudal fin to increase the strength of the total starting thrust jet produced.

structures, it is qualitatively similar to the maneuvering flow actuation model given in Figure 5-10.

6.5.5 Mode 5: *Fast-starting*

This interaction mode is considered briefly in *Chapter 5* with reference to Weihs starting trout. However, the interaction of body-generated and tail-generated vorticity was not specifically discussed previously, and the basic mechanisms of vorticity control utilized by the fish during rapid-starting is qualitatively similar to those interactions observed for straight-line swimming and turning. Figure 6-29 illustrates more clearly the vorticity control mechanisms which are crucial to starting performance. Five body images, read from left to right, show the generation, release, and control of body-generated and caudal-generated vorticity.

In the first position of Figure 6-29, the fish body begins to contract into an "L"-shape, affecting the formation of two near-body circular flows and body-generated vortices b1 and b2. In addition, a "starting" vortex c1 is shed from the caudal fin as the leading edge follows a smooth path into the flow as the body contracts. In the

second image of the sequence at the conclusion of the preparatory stroke, a strong vortex has been formed in the caudal fin c2 with a counterclockwise circulation, inducing a rotational velocity in the same direction as body-generated vortex b1, which has propagated toward the contraction region of the body. Body-generated vortex b1 is released through separation into the fluid within the included angle of the body curvature, and vortex b2 has progressed towards the mid-body region.

The third image in the sequence shown in Figure 6-29 shows the beginning of the propulsive stroke, and the strong vortex generated by the tail c2 has paired with the body-generated vortex b1 to form a pair P1 which has a strong net counterclockwise circulation. Body-generated vortex b2 has progressed to the peduncle region and is released through separation into the flow on the inside of the tail sweep. The fourth image in the sequence shown in Figure 6-29 shows the generation of a strong vortex around the caudal fin c3 which has a clockwise circulation, in the same direction as the circulation of free body-generated vortex b2. Additionally, a body-generated circular flow and vortex b3 forms near the head as the body bends toward the direction in which it will eventually swim.

The final image in the sequence shown in Figure 6-29 shows the conclusion of the propulsive stroke as the fish begins to translate rapidly in the direction of swimming. The clockwise circulation vortex c3 formed by the caudal fin during the sweeping propulsive stroke has been released into the fluid, where it interacts with body-generated vortex b2 to form a second pair of vortices P2 with a strong net clockwise circulation. Body-generated vortex b3 moves towards the mid-body region as straight-line swimming motions resume. The strong counter-rotating pairs P1 and P2 of same-signed vortices form a strong thrust jet, forcing fluid downwards in this view and propelling the fish upwards (forwards). This vorticity control sequence highlights the strong constructive interactions of the body-generated and caudal-generated vortical structures, and the actuation mechanisms are analogous to those analyzed for the turning fish in the *Turning* vorticity control mode.

Chapter 7

Conclusion

7.1 Summary of Results

The results presented in this thesis demonstrate the numerous issues involved in the simulation and the study of flexible-body hydrodynamics and vorticity control. Furthermore, the simulation scheme has elucidated many of the details of the vortical flow actuation which enables swimming fish to achieve remarkable straight-line swimming and maneuvering performance.

The development of a three-dimensional numerical method for simulation of coupled-IBVPs of a multiple-finned body of arbitrary flexibility with multiple, interacting, desingularized wakes has been presented, and is of fundamental significance to enable the study of fish swimming hydrodynamics. Validation of the simulation scheme developed has provided corroborative evidence of experimental drag reduction achieved through unsteady propulsive mechanisms with the *RoboTuna*. In addition, the details of the flow structures revealed through application of the numeric scheme to live fish geometries has elucidated the mechanisms of thrust jet wake actuation, and compares well to existing experimental flow visualizations using DPIV.

Combining insight gleaned from flow simulation details with records of the performance of the swimming motions, quantification of the importance of linear theory in estimation of swimming performance is achieved. The effects of wake, motion, and geometric nonlinearities on the relevance of linear theory in prediction of swim-

ming performance is also realized. Through visualization of near-body flow structure actuation dynamics and the correlation of these flow dynamics to those predicted by linear theory, the "2D"/"3D"-nature of the near-body flow around live fish is revealed, which is far more complex than the linear theory would suggest. Through these studies of the flow around live fish and the *RoboTuna*, a new methodology is presented to describe the flow actuation and vorticity control mechanisms of straight-line steady swimming, as well as unsteady swimming and maneuvering. Details of the mechanisms of the regulated release of body-generated vorticity and the optimized actuation of near-body flow structures have been elucidated through visualizations of the wake and near-body unsteady flows.

Similarly, the relevance of two-dimensional swimming simulations and theory to describe complex three-dimensional swimming processes is demonstrated over a range of kinematic parameters. While the near-body flow actuation by the oscillating tail and peduncle region is not well-treated through two-dimensional simulation alone, the dynamics of the large caudal fin wake are modeled adequately, and the effects of large amplitude and high frequency motions of the actual fish demonstrate the inadequacies of the two-dimensional swimming theory to predict performance in a consistent manner.

Investigation of vorticity control mechanisms utilized by fish to achieve superior performance provides further insight into the manner in which fish manipulate the vorticity shed from anterior body regions to their advantage, supporting explanation of the range of motions achievable by the fish. The fish uses its oscillating tail to generate the majority of the thrust for propulsion. As a result, nature has uniquely adapted each species to minimize the recoil effects of oscillating this lifting surface through the necking of the body region anterior to the tail to form the caudal peduncle; this also minimizes the body mass which the fish must oscillate, and the undulations of significant amplitude are mainly confined to the tail region. However, this necking of the caudal peduncle causes lift generated through local undulations of the backbone in the main body of the fish to be released into the wake as the body lift strength changes with movement. This energy might be wasted, if the fish did

not control it. Through the analysis of several "good" and "bad" performance modes of the *RoboTuna*, this work identifies the manner in which the fish actively controls its wake-body and wake-wake interactions to achieve a desired performance. The development of simple models in this thesis of the wake-body and wake-wake interactions observed during straight-line swimming uncover methods of energy storage and recovery, as well as drag enhancement, for optimized performance. Investigation of the effects of modifying geometric and wake shedding parameters on achieving swimming performance, including the effects of multiple fins and wake separation models, is presented, motivating the necessity of specific morphological adaptations observed on live fish. This study has provided unique insight into the tuning of unsteady fluid-structure interactions to achieve robust performance and improved propulsive efficiency.

Finally, the derivation of a robust, nonlinear, adaptive control algorithm for physical systems with unsteady, unknown fluid dynamic load parameters is presented in *Appendix B*. This control system design allows for the estimation of unsteady fluid dynamic loads associated with oscillatory lifting surfaces, which might be constructed from parametric data, simulation, or past performance. Preliminary application of this control system design to the investigation of energy recovery of an two-dimensional oscillating hydrofoil for fish-like vehicle maneuvering is demonstrated. Further study may elucidate kinematic ranges which allow for the minimization of control input power for achieving a desired performance.

7.2 Future work recommendations

Several extensions of the methods developed in this thesis may further elucidate the details of the vorticity control mechanisms utilized by swimming fish but exceeded the scope of the present investigation.

Recent advancements in panel methods [142] may allow for the validation of model assumptions through the incorporation of real flow parameters, such as leading edge and unsteady boundary layer separation, into a boundary layer-potential flow coupling

scheme. Unsteady vorticity control mechanisms such as leading edge separation and manipulation can not be easily modeled by the present method, and the application of an unsteady boundary layer coupling scheme may provide the first extension which will handle this unsteady dynamics. In addition, the validity of the separation model is questionable for extreme unsteady motions in this numeric representation, which may be handled by a robust boundary layer model. Alternatively, full extension to three-dimensional DNS may elucidate these processes through careful simulation, but the computational burden of such an investigation may be prohibitive for the unsteady flexing body at Reynolds numbers of practical interest [134]. This is likely to change as the fast pace of technology continues to develop more rapid computational capabilities, so the feasibility of a fully three-dimensional viscous approach at high Reynolds numbers, such as those experienced by live tuna swimming $R_e \sim O(10^7)$, may not be far off.

Coupling of inviscid model to viscous & separation drag estimates or the extension of the method to fully viscous CFD will allow for the simulation of unconstrained self-propelled rigid body swimming and maneuvering. This will advance the understanding of the importance of recoil motions, the optimal steady-state swimming motions for a given geometry, and the optimal geometry for given kinematics with optimal mass distribution and energy storage and absorption properties.

The extension of the two-dimensional numeric scheme to allow for the investigation of multiple, wake-shedding, flexible bodies may more simply elucidate the modes of vorticity control identified in this dissertation. The canonical problem to be investigated which may uncover these hydrodynamic mechanisms would involve the simulation of a flexible body with a progressive backbone wave of small amplitude, shedding a wake in a free stream which interacts with a rigid foil section downstream, oscillating in pitch and heave, also shedding a wake. The resulting wake dynamics can be investigated over a range of kinematic parameters and nondimensional scaling parameters, such as foil section leading-edge spatial phasing with the trailing edge of the undulating body, the temporal phasing of the foil pitch and heave motions, the amplitude ratio of the undulating streamlined body trailing edge and the amplitude

of the foil heave, and the wavelength λ and phase speed c_p/U of the backbone wave, and Strouhal number St. In this manner, the effects of vertical vorticity ω_z shed from the backbone ridge in the three-dimensional model interacting with the oscillating caudal fin may be modeled, and the optimal spacing of the tail and the streamlined undulating body trailing edge can be correlated to that observed in live fish. This model will provide additional insight into the applicability of the two-dimensional simulation method to the prediction of three-dimensional swimming performance.

A powerful and simple extension to the present three-dimensional model will involve the modification of the wake representation scheme to discrete vortex particle methods to allow for complex wake-body interactions and wake-wake interactions. The present method breaks down after long simulation time as the sheets continue to roll up, and the interactions of multiple wakes sheets will not allow for the elucidation of vortex diffusion, breakdown, and reconnection, such as those shown for the tip vortices shed from an oscillating rectangular lifting surface [83]. Vortex particle methods will also allow for the modeling of diffusive and dissipative viscous effects, and the subsequent investigation of the time-scales of the wake evolution and interaction. In addition, the present wake representation model does not allow for wakes to be shed on top of each other. Although of wake interactions modeled appear to be robust, the solution of the strength of the shed wake in the linear system for the body perturbation potential is sensitive to strong dipole influences, such as cusped trailing edges and nearby wake panels. This limitation may be alleviated through more robust wake handling methods.

Advances in the implementation of the present method will include the parallelization of the code to lighten the burden of this computationally-intensive investigation. Run times on a DEC ALPHA for ten periods of a typical *RoboTuna* motion may take up to eight hours if only performance quantities requiring a boundary integral of the pressure are desired. The computational time required to store complete flow field data for one period of the same *RoboTuna* simulations may exceed one week, if the relevant grid length of the flow field is less than 1% of the body length. In addition, the storage space required to save the unsteady flow field data is prohibitively large

to allow for a comprehensive investigation of the complete experimental parametric space previously examined for performance only.

The extension of the adaptive control scheme to three-dimensional complex geometry with mass-spring-damper distributions will allow for its first practical marine engineering application where it can be employed on a fish-like robotic underwater vehicle. Experimental application of the simple straight-line swimming and maneuvering generalized mechanisms will correlate the desired trajectory kinematics to the realized performance, trajectories, and localized load distributions . Unsteady near-body pressure and flow field data gathered from the implementation of a desired trajectory scheme will allow for a phase plane representation of the relationship between kinematic input to hydrodynamic load distribution. In a sense, this would constitute a level of lateral line intelligence, and the subsequent development of a vortical flow sensing algorithm and its coupling to the adaptive control algorithm may allow for the extension of the minimization of tracking error with respect to a desired integrated performance, as opposed to a desired trajectory, and further hydrodynamic optimization.

Appendix A

Convergence of the unsteady two-dimensional numeric scheme

A.1 Without desingularization

Before desingularization was included in the model, the code was tested for convergence using the cusped Joukowski foil for discrete point vortices with infinite core velocities as described by Batchelor [23]. Such a wake description yielded adequate results for moderate panel numbers and time step sizes, as are used in typical propeller codes, for example [105]. However, when the number of panels describing the body was continually increased or when the time step was systematically decreased, numerical errors and unsteady solution instability dominated the steady-state foil lift results. In addition, when employing a Runge-Kutta time integration scheme, these instabilities and errors are exacerbated for a given time step size and panel number over a simple Euler time integration scheme, a consequence of solving the boundary value problem at intermediate times. These findings are presented herein and motivate the use of desingularized vortex wake descriptions for both two-dimensional and three-dimensional analysis in all further studies.

A Euler time integration scheme is employed at the outset for the study of the impulsively-started flow about a Joukowski foil with a cusped trailing edge. The value of the lift coefficient is computed over the course of the simulation from impulsive

start to time $Ut/c = 100$. Figures A-1 and A-2 show the effect of increasing the panel number k and decreasing the time step size dt on the asymptotic approach to the steady-state lift coefficient with time, employing a simple Euler time integration scheme.

Figure A-1 illustrates how increasing the panel number k can cause solution error as time progresses for the impulsively-started flow problem. The lift coefficient is shown as a function of time, in addition to the corresponding time record of the absolute error of the instantaneous lift coefficient in comparison to its analytic steady-state value. The sharp minima in the lift coefficient error correspond to the time at which the calculated lift coefficient surpasses the analytic steady-state value for the two-dimensional foil. Ideally, this error norm should continue to decrease at a steady rate with time. Figure A-2 similarly illustrates how decreasing the time step size dt can introduce solution inaccuracy for the steady-state lift after long simulation times. In general, a smaller time step size dt would tend to describe the time-varying strength of the wake more accurately for the impulsively-started flow problem and thus lead to a more rapid convergence to the steady-state lift. However, as can be seen in the plot of instantaneous lift coefficient error versus time, a smaller time step may lead to a faster convergence to the steady-state lift, but it is quickly surpassed as the load on the foil continues to increase. The smaller the time step size dt, the more rapid this process of convergence and overshoot.

The choice to employ a fourth-order Runge-Kutta time integration scheme instead of the simple Euler time integration scheme was made in an attempt to alleviate these overshoot errors in the steady-state lift convergence. As can be seen in Figures A-3 and A-4, the lift coefficient convergence for the impulsively-started flow about a Joukowski foil for varying panel number k and time step size dt is demonstrated for the fourth-order Runge-Kutta time integration scheme to a simulation time of $Ut/c = 100.0$. Both pressure integration and use of the Kutta-Joukowski theorem are used to find the instantaneous lift and the instantaneous absolute error norm with respect to the analytic steady-state lift. In Figure A-3, the lift convergence is shown over a range of increasing panel number k for a constant time step size $dt = 0.25$.

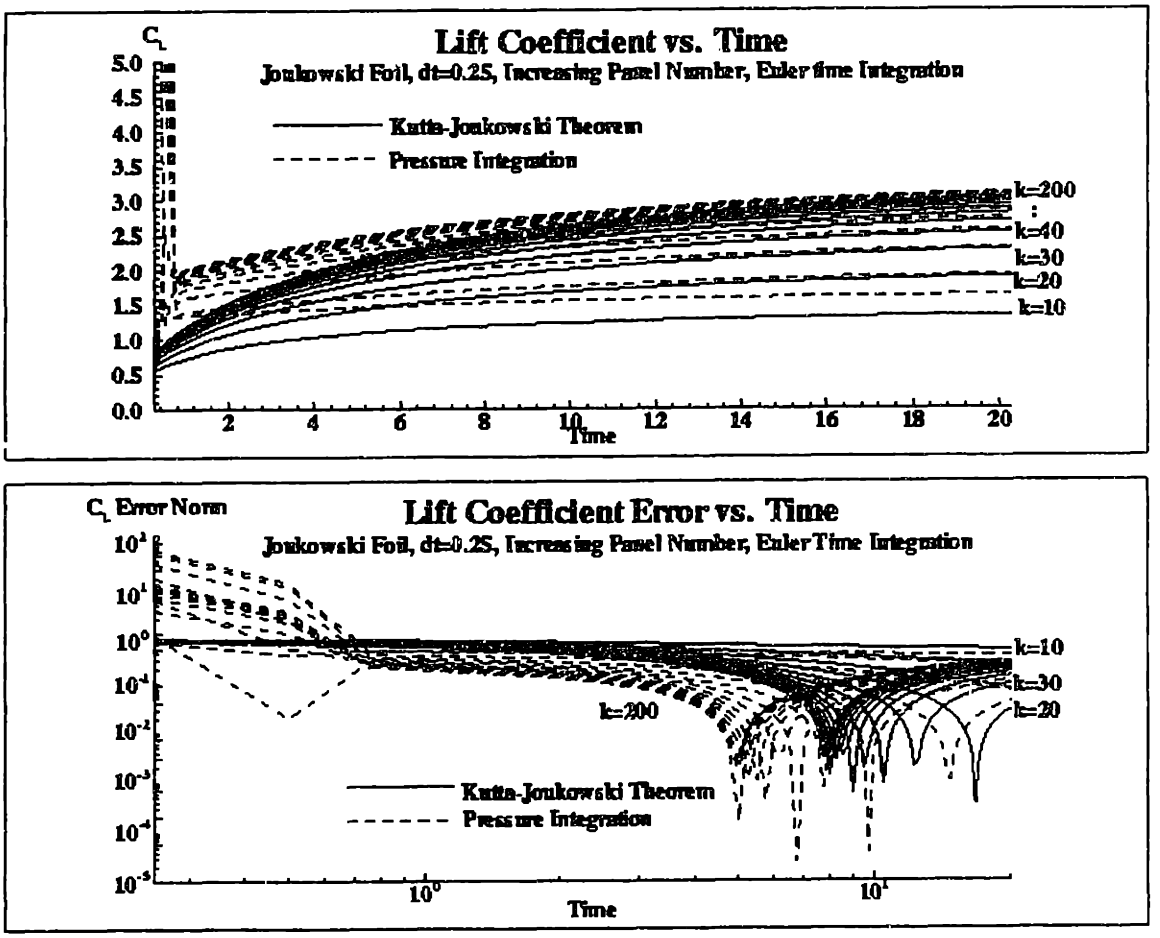

Figure A-1: Lift coefficient convergence behavior versus time for a Joukowski foil two-dimensional section with varying number of panels k. Euler time integration scheme is employed for unsteady wake convection. Top figure of pair shows the computed value of the lift coefficient as found by pressure integration and by employing the Kutta-Joukowski theorem. Bottom figure of pair shows the absolute error norm of the instantaneous lift coefficient with respect to the analytic steady-state value of the lift.

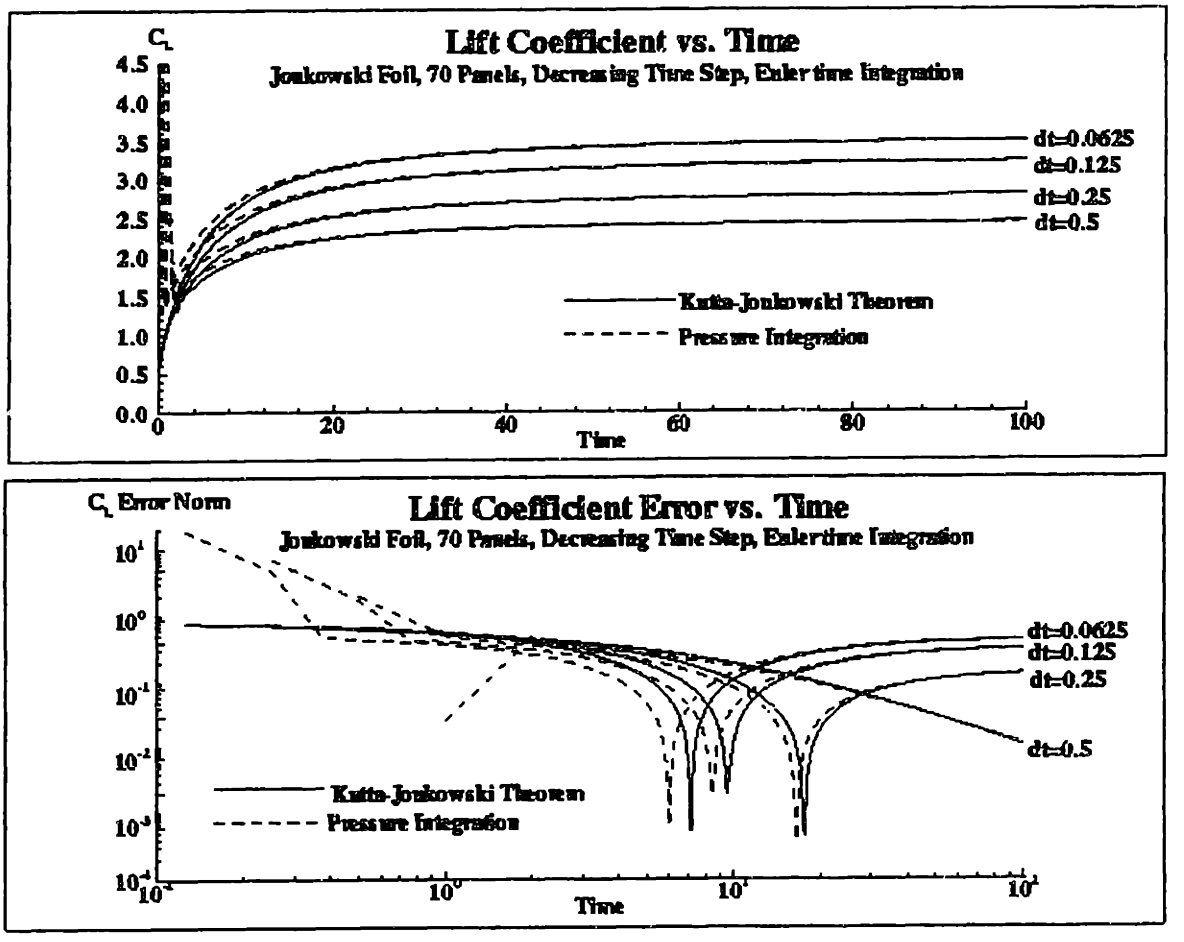

Figure A-2: Lift coefficient convergence behavior versus time for a Joukowski foil two-dimensional section with varying time step size dt. Euler time integration scheme is employed for unsteady wake convection. Top figure of pair shows the computed value of the lift coefficient as found by pressure integration and by employing the Kutta-Joukowski theorem. Bottom figure of pair shows the absolute error norm of the instantaneous lift coefficient with respect to the analytic steady-state value of the lift.

Again, it can bee seen from the absolute error norm plots that an increase in the panel number leads to a more rapid convergence to the analytic value of the steady-state lift, the but the lift continues to increase with time. Consistency of the scheme is evident from the convergence of the lift records to an asymptotic slope with time. These inaccuracies associated with an increasing panel number are compounded with solution instability when the time step size is decreased, as can be seen in Figure A-4. For a constant number of body panels $k = 70$, convergence of the numeric scheme is studied by decreasing the size of the time step dt. When the time step continues to decrease, although the analytic steady-state value of lift is more rapidly achieved, the overshoot is more dramatic. Indeed for the case of $dt = 0.0625$, the time record of actual lift is not even shown due to its erratic appearance, which make the other time records unreadable. This instability causing wild oscillation of the solution at $dt = 0.0625$ is evident from the time record of the error norm, where the previously-smooth solution is seen to break down not long after overshoot occurs.

It should be noted that the time step size dt is defined at the time between recorded solutions of the boundary value problem, and intermediate solutions of the boundary value problem during the course of the fourth-order Runge-Kutta time integration utilize time stepping intervals smaller than the reported dt. It should also be noted that even when the solution is smooth for a moderate number of panels k and time step size dt, the overshoot of the analytic steady-state lift of the Joukowski foil occurs more rapidly for the Runge-Kutta time integration scheme than for the Euler time integration scheme. Similarly, the total absolute error at time $Ut/c = 100.0$ is larger for the Runge-Kutta scheme than for the Euler scheme. This behavior is evident upon close comparison of Figure A-1 with Figure A-3 and Figure A-2 with Figure A-4.

The Euler and Runge-Kutta time integration schemes are also compared for the convergence of the steady-state drag coefficient around the foil. Initially, the starting vorticity shed by the foil will cause some force in the x-direction, drag in the case of steady foil about a rigid fixed foil. As the strength of the wake sheet stabilizes to a constant value and the starting vorticity convects away from the foil, however, the x-components of the force on the foil should disappear [105]. Thus, for the steady

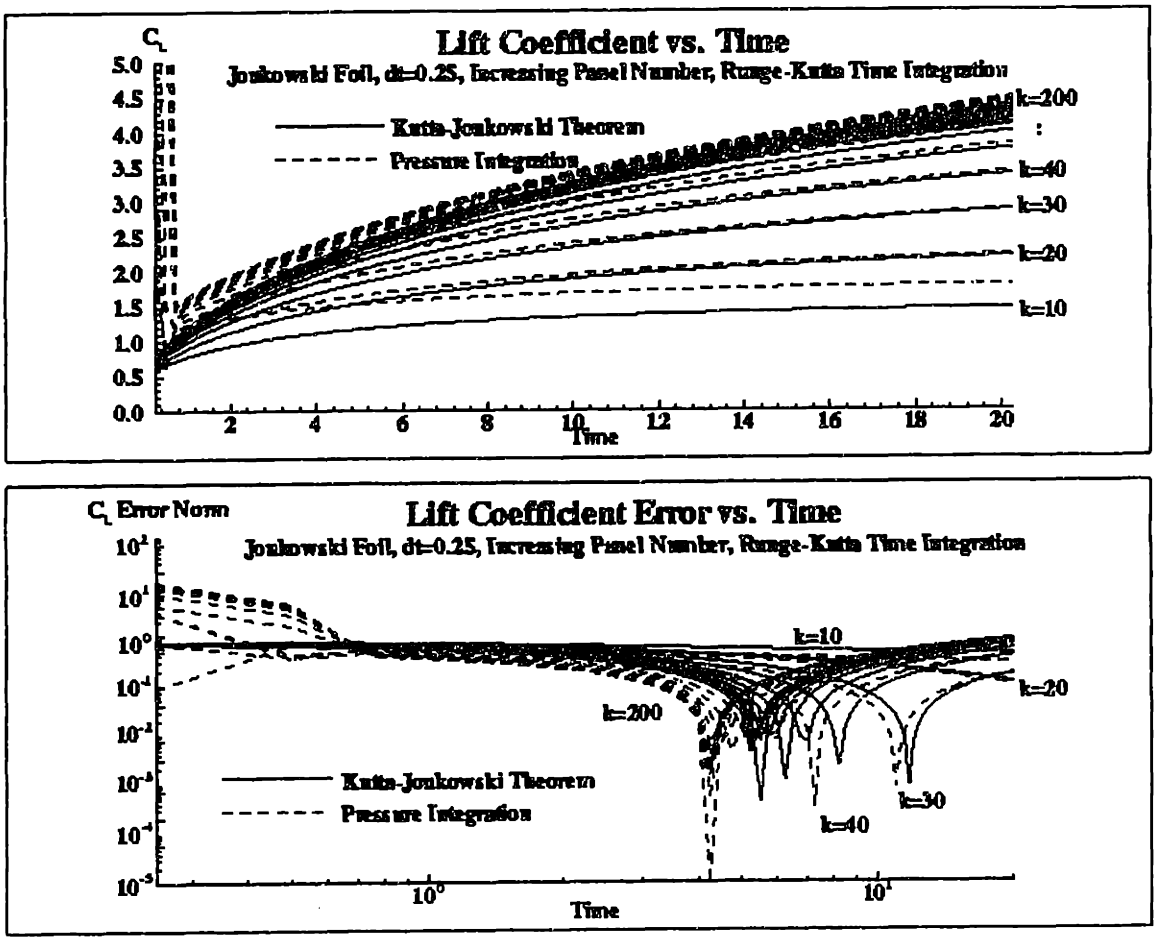

Figure A-3: Lift coefficient convergence behavior versus time for a Joukowski foil two-dimensional section with varying number of panels k. A fourth-order Runge-Kutta time integration scheme is employed for wake convection. Top figure of pair shows the computed value of the lift coefficient as found by pressure integration and by employing the Kutta-Joukowski theorem. Bottom figure of pair shows the absolute error norm of the instantaneous lift coefficient with respect to the analytic steady-state value of the lift.

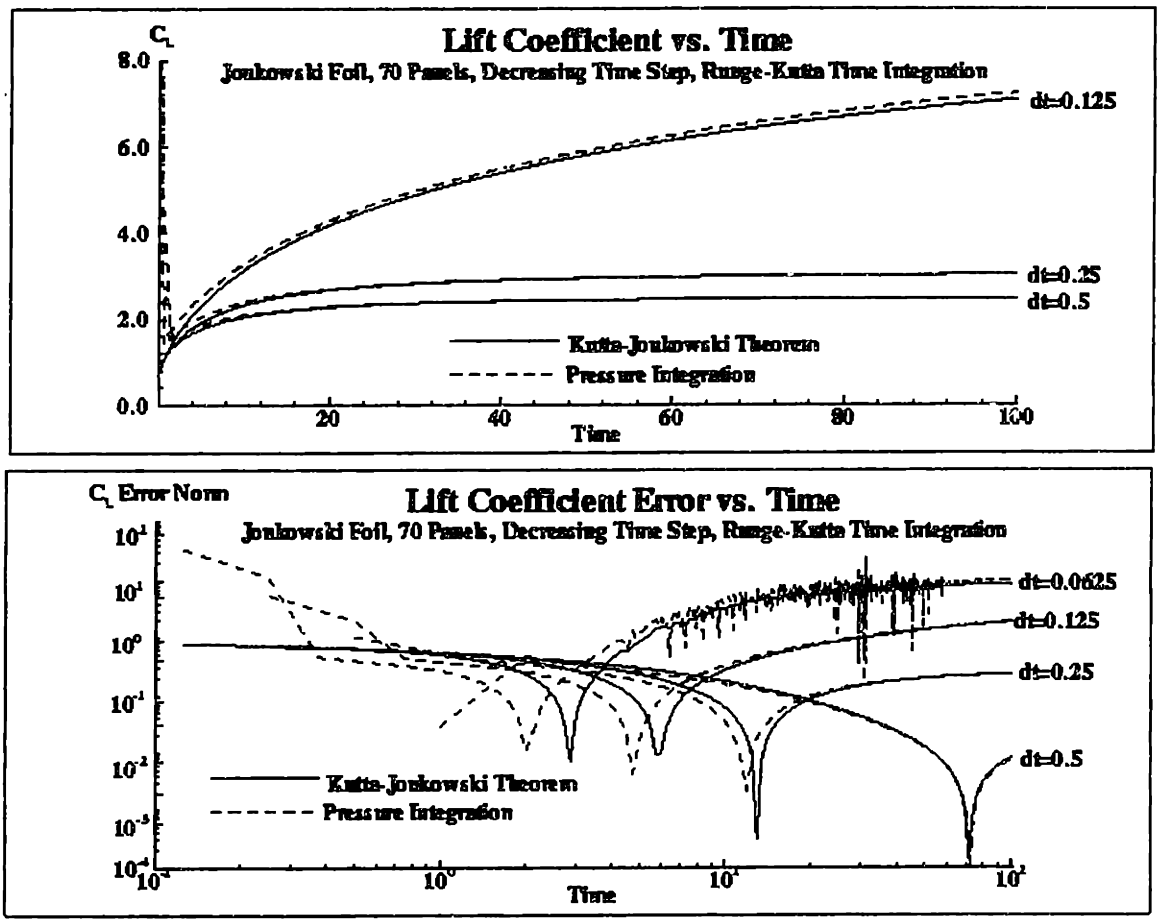

Figure A-4: Lift coefficient convergence behavior versus time for a Joukowski foil two-dimensional section with varying time step size dt. A fourth-order Runge-Kutta time integration scheme is employed for wake convection. Top figure of pair shows the computed value of the lift coefficient as found by pressure integration and by employing the Kutta-Joukowski theorem. Bottom figure of pair shows the absolute error norm of the instantaneous lift coefficient with respect to the analytic steady-state value of the lift.

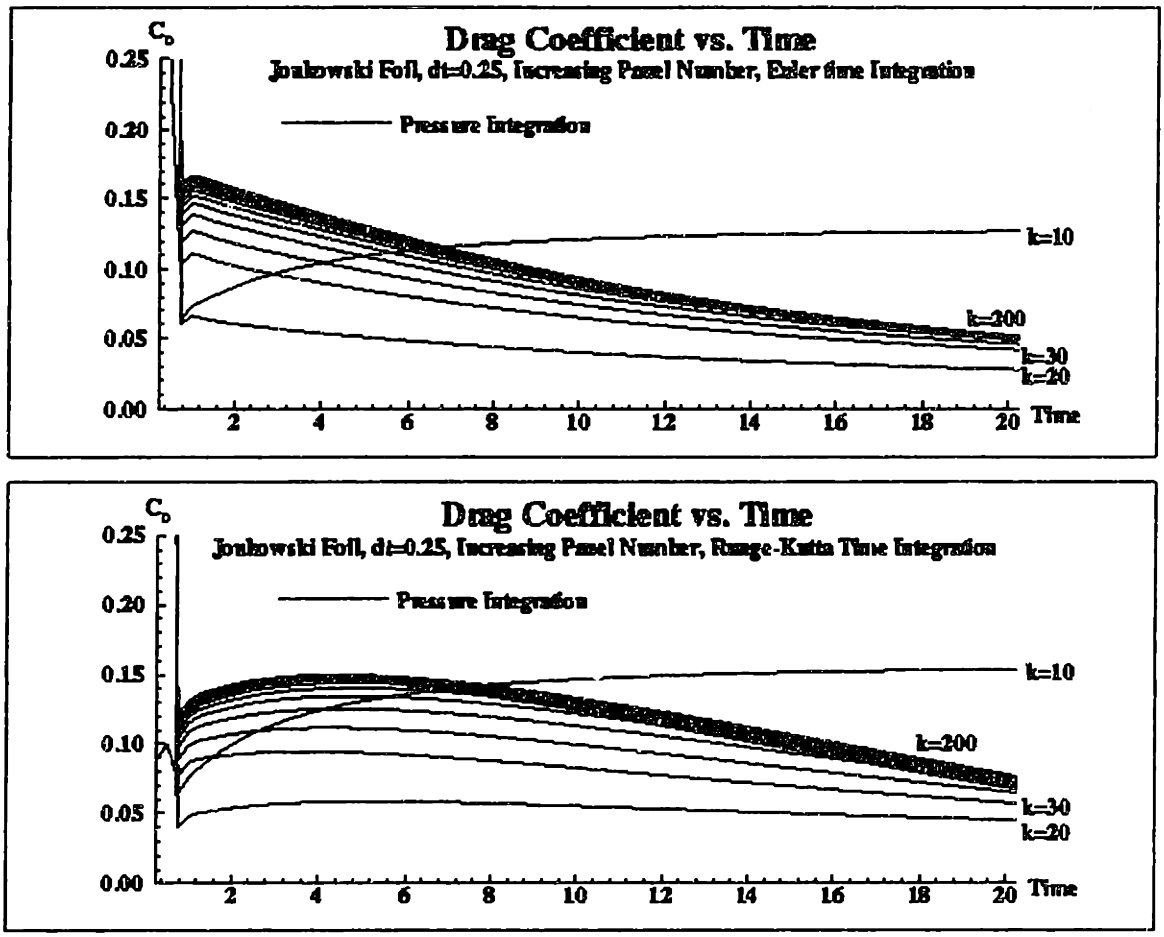

Figure A-5: Induced drag coefficient convergence behavior versus time for a Joukowski foil profile two-dimensional section with varying number of panels k. A simple Euler time integration scheme (top) is shown for comparison to a fourth-order Runge-Kutta time integration scheme (bottom) for unsteady wake convection. Drag coefficient is found by pressure integration.

force, only lift acts on the foil, expressed through the Kutta-Joukowski law. The convergence of the drag coefficient on the foil is shown as a function of time for varying panel numbers in Figure A-5. The impulsively-started flow simulation is again allowed to run to a time $Ut/c = 100.0$. The top plot illustrates the convergence properties with increasing panel number k for the simple Euler time integration scheme, and the bottom figure shows similar convergence for the fourth-order Runge-Kutta time integration scheme. Again, the choice of a higher order time integration scheme does not improve the convergence properties of the numerical scheme.

The low order of Euler time integration scheme was concluded to not be the source

of the overshoot error for the unsteady problem, and in fact, increasing the accuracy of the time-stepping model by employing a fourth-order Runge-Kutta scheme contributed to the source of error and induced solution instability. It was hypothesized that geometric influence of the cusped trailing edge, and the associated geometric influence of the small wake panel of unknown strength, was causing the solution breakdown. With smaller time step sizes dt and larger number of panels k, both the length of the unknown-strength shed wake panel and the length of the body panels was decreasing, particularly so for cosine-spaced body panels where the trailing edge panel lengths became minute for large numbers of panels. This disparity between the length of the smallest and the largest panels, as well as the proximity and geometric relationship of trailing edge panels with small included angles, increases the condition number of the matrix equations for solution of the boundary value problem. This growing condition number was hypothesized to cause instability inception.

For these reasons, a Kármán-Trefftz foil was studied instead of a Joukowski foil, for both the Euler and Runge-Kutta time integration schemes previously considered. The impulsively-started flow around the foil was investigated for geometry with a trailing edge included angle of $\lambda = 27.5^o$, a flow velocity of $U = 1.0$, and a chord of $c = 1$. The unsteady simulations were run to a time of $Ut/c = 100.0$. The convergence of the solution with time for an increasing number of body panels k and a decreasing time step size dt is shown in Figures A-6 and A-7, respectively, employing the simple Euler time integration scheme. Again, both pressure integration and employing the Kutta-Joukowski theorem are used to find the instantaneous lift on the foil section. The improvement in the convergence properties is dramatic, as a comparison with Figures A-1 and A-2 reveals. For an increase in the panel number k for a constant time step size, shown in Figure A-6, the analytic value of the steady-state lift is approached but not exceeded, and the instantaneous absolute error continues to decrease with time, as expected and desired. Similarly, for a decreasing time step size dt for a constant number of panels, as shown in Figure A-7, the error in the lift coefficient does not overshoot the analytic steady-state value. However, in contrast to the behavior of the Joukowski foil illustrated in Figure A-2, the decreasing time step size causes a

slower convergence to the analytic value of steady-state lift. For the Kármán-Trefftz foil, it appears that a larger time step is desirable to obtain a more accurate solution for a given number of panels. The overall predictions for the Kármán-Trefftz foil shown in Figure A-7 are much better than the behavior of cusped-foil Figure A-2, with no overshoot in the steady-state lift prediction. However, as the condition number increases with decreasing time step size dt, the solution does not converge in the classical fashion with the approach to the continuous representation.

The simple Euler time integration scheme is abandoned for the fourth-order Runge-Kutta scheme in Figures A-8 and A-9. Similar to the Euler scheme behavior shown in Figures A-6 and A-7, the solution continues to approach the analytic steady-state lift value with time, as expected, for both increasing panel number k and decreasing time step dt. Comparison of Figure A-6 and Figure A-8 reveals that the Runge-Kutta time integration scheme yields superior lift convergence properties, as the number of panels increases for a constant time step size. In Figure A-9, a pattern of decreasing solution accuracy with decreasing time step size dt, similar to that shown in Figure A-7, is evident, with the largest time steps exhibiting the best convergence properties. In fact, neither time integration scheme is superior with respect to convergence as the time step size is decreased, with no discernible differences in the error records.

A.2 With desingularization

A desingularization technique, as described in Section 2.1.4, was adopted to improve the numeric convergence properties of the two-dimensional computational method. A systematic convergence investigation of the numerical method was completed by varying the time step and the panel size around the Kármán-Trefftz foil. In addition, the desingularization parameter δ_w for the vortex core was varied, to illustrate the convergence of the numerical solution to the theoretical solution as δ_w is decreased, while not encountering the short wavelength instability of the $\delta_w = 0$ case, as illustrated by Krasny [116]. Figures A-10 and A-11 illustrate the systematic convergence study for the two-dimensional desingularized Kármán-Trefftz foil.

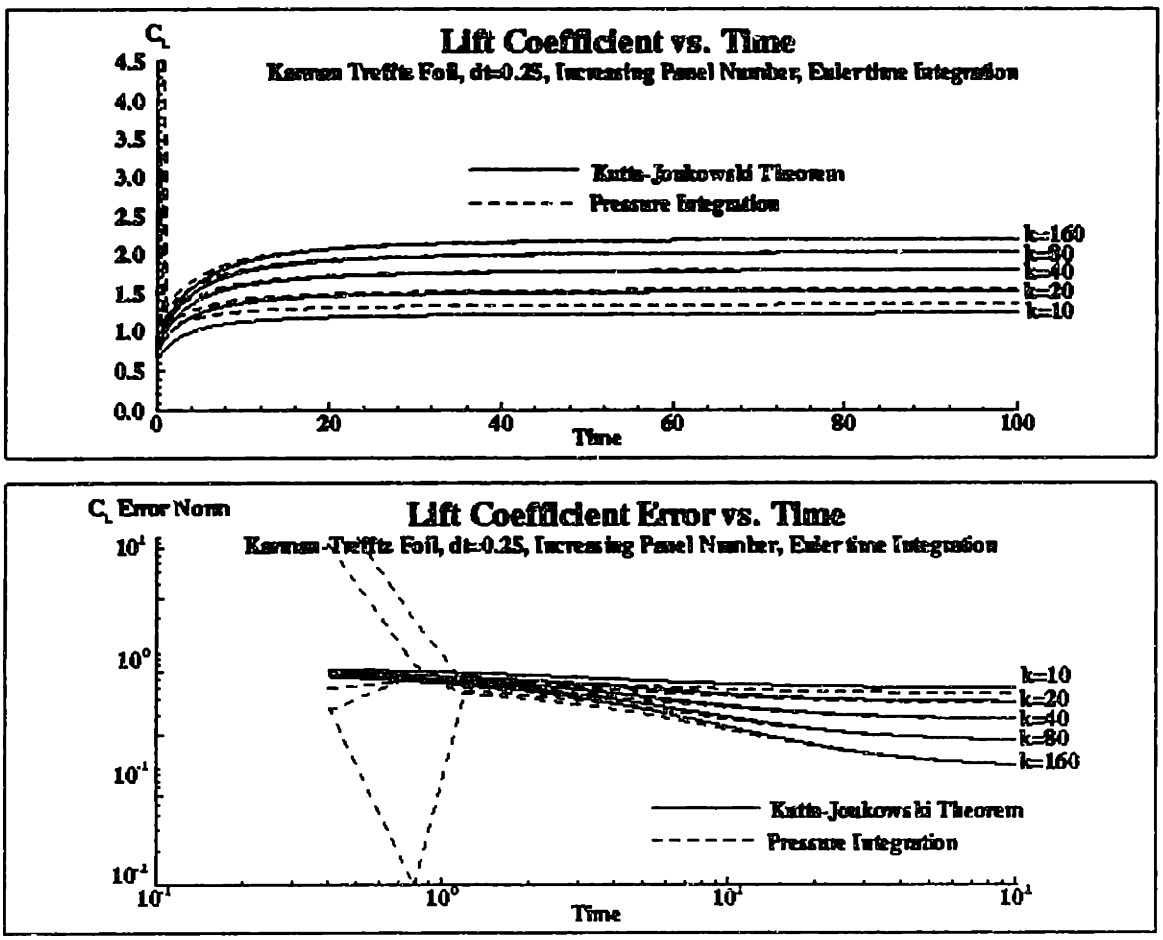

Figure A-6: Lift coefficient convergence behavior versus time for a Kármán-Trefftz foil two-dimensional section (trailing edge angle $\lambda = 27.5°$) with varying number of panels k. Euler time integration scheme is employed for unsteady wake convection. Top figure of pair shows the computed value of the lift coefficient as found by pressure integration and by employing the Kutta-Joukowski theorem. Bottom figure of pair shows the absolute error norm of the instantaneous lift coefficient with respect to the analytic steady-state value of the lift.

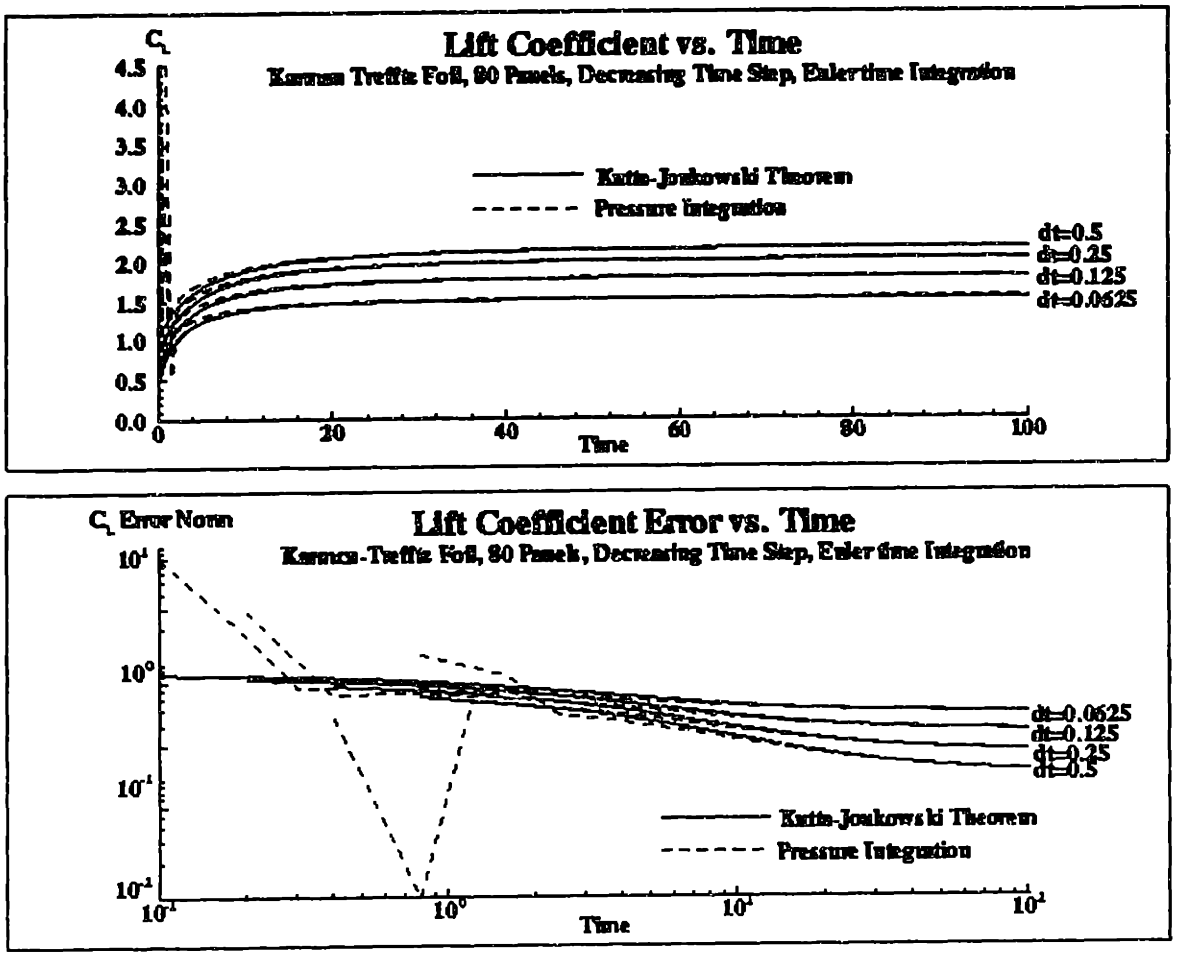

Figure A-7: Lift coefficient convergence behavior versus time for a Kármán-Trefftz foil two-dimensional section (trailing edge angle $\lambda = 27.5^o$) with varying time step size dt. Euler time integration scheme is employed for unsteady wake convection. Top figure of pair shows the computed value of the lift coefficient as found by pressure integration and by employing the Kutta-Joukowski theorem. Bottom figure of pair shows the absolute error norm of the instantaneous lift coefficient with respect to the analytic steady-state value of the lift.

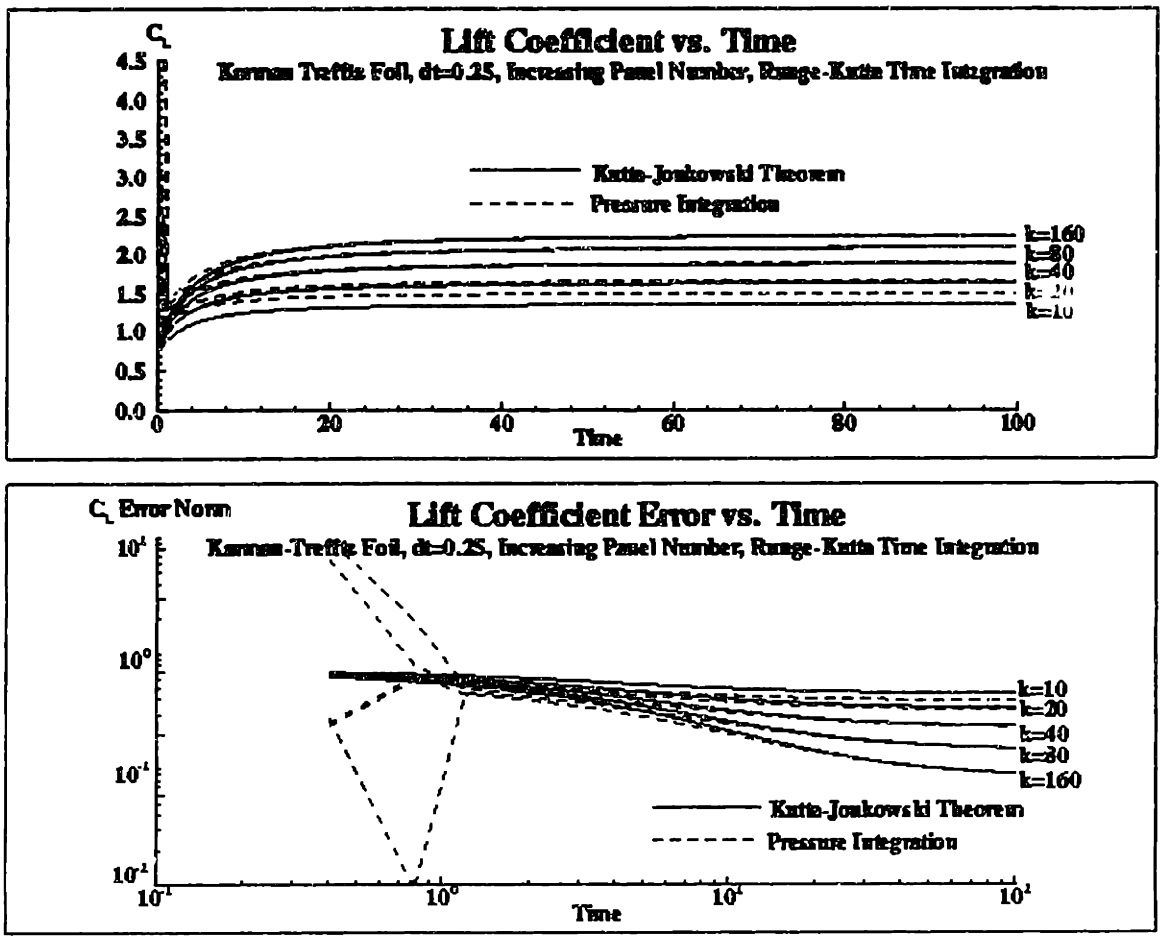

Figure A-8: Lift coefficient convergence behavior versus time for a Kármán-Trefftz foil two-dimensional section (trailing edge angle $\lambda = 27.5°$) with varying number of panels k. A fourth-order Runge-Kutta time integration scheme is employed for wake convection. Top figure of pair shows the lift coefficient as calculated by pressure integration and by employing the Kutta-Joukowski theorem. Bottom figure of pair shows the absolute error norm of the instantaneous lift coefficient with respect to the analytic steady-state value of the lift.

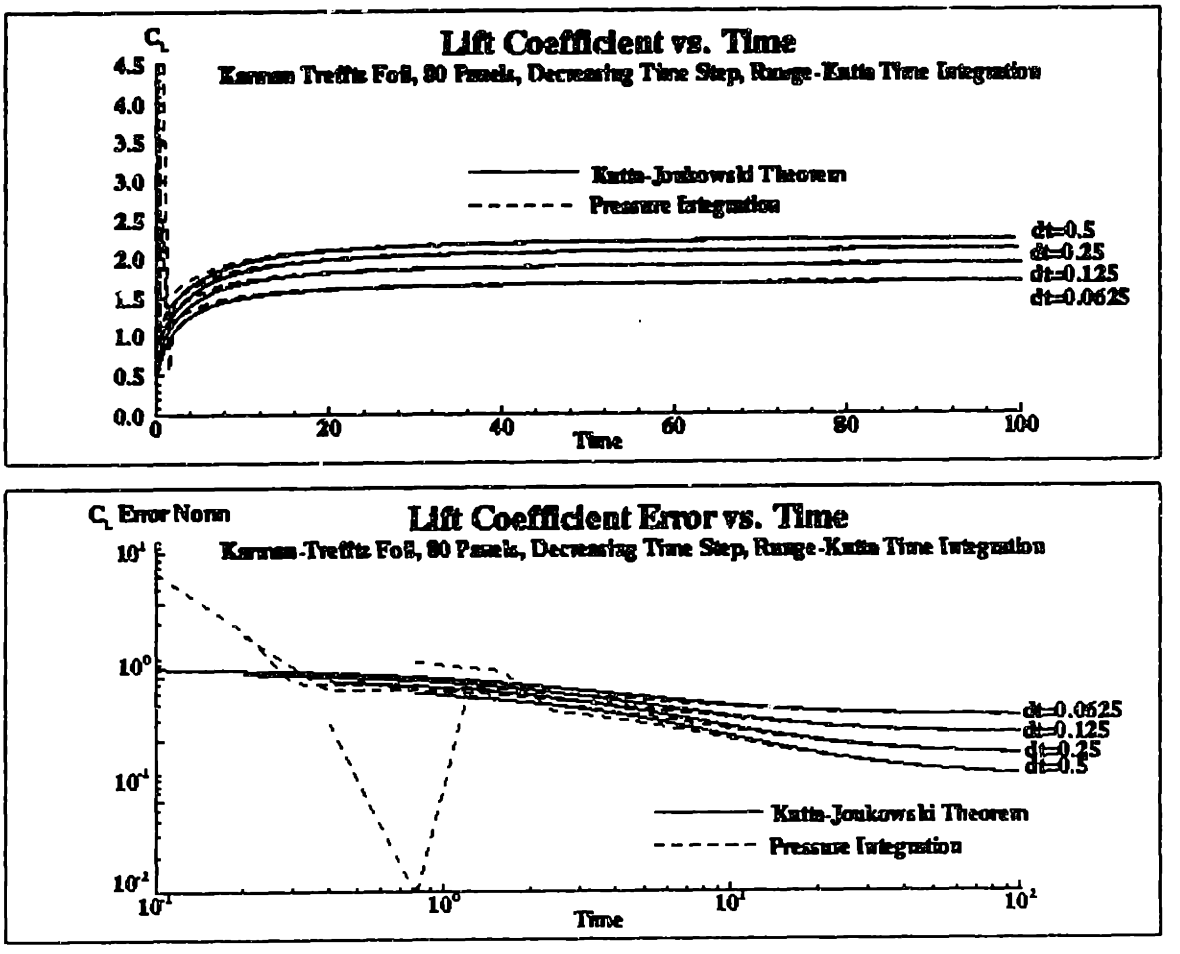

Figure A-9: Lift coefficient convergence behavior versus time for a Kármán-Trefftz foil two-dimensional section (trailing edge angle $\lambda = 27.5°$) with varying time step size dt. A fourth-order Runge-Kutta time integration scheme is employed for wake convection. Top figure of pair shows the lift coefficient as calculated by pressure integration and by employing the Kutta-Joukowski theorem. Bottom figure of pair shows the absolute error norm of the instantaneous lift coefficient with respect to the analytic steady-state value of the lift.

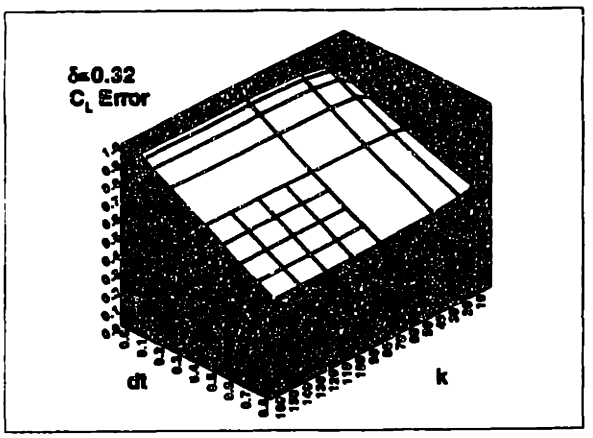

(a) $\delta_w = 0.32$

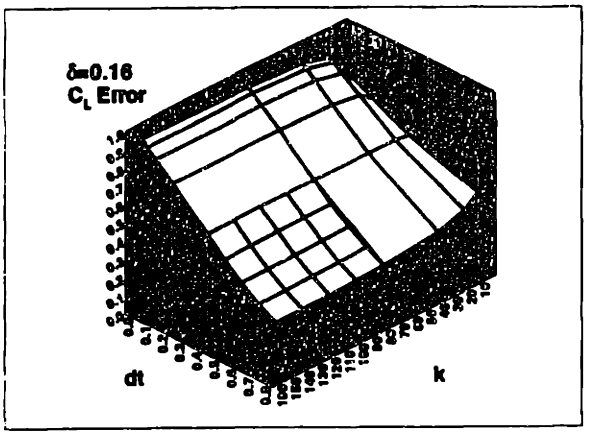

(b) $\delta_w = 0.16$

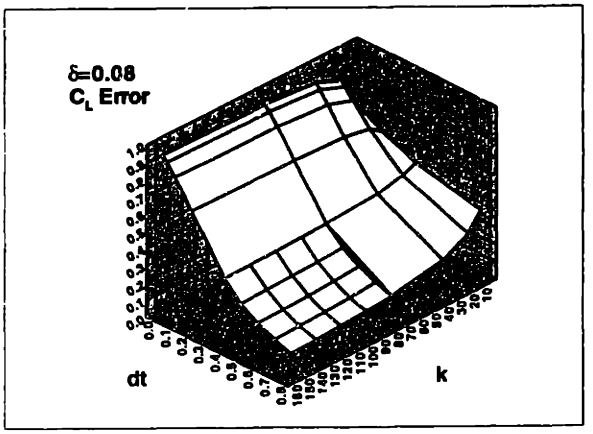

(c) $\delta_w = 0.08$

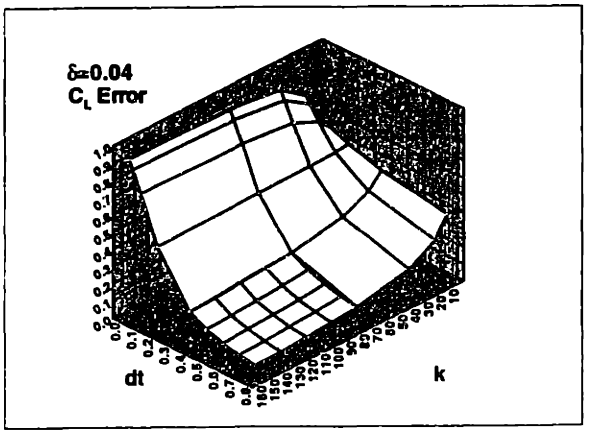

(d) $\delta_w = 0.04$

Figure A-10: Error isosurfaces for the steady state lift coefficient convergence of an impulsively-started Kármán-Trefftz foil (22.5° trailing-edge angle) after $Ut/c = 100$ for a range of time step size dt and panel number k. The value of the vortex desingularization parameter δ_w is fixed for each of the above graphs.

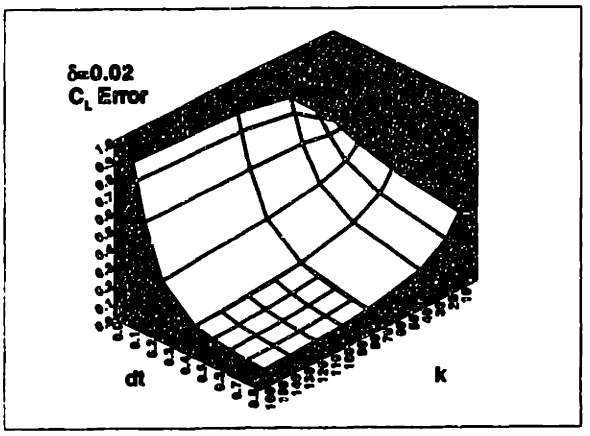

(a) $\delta_w = 0.02$

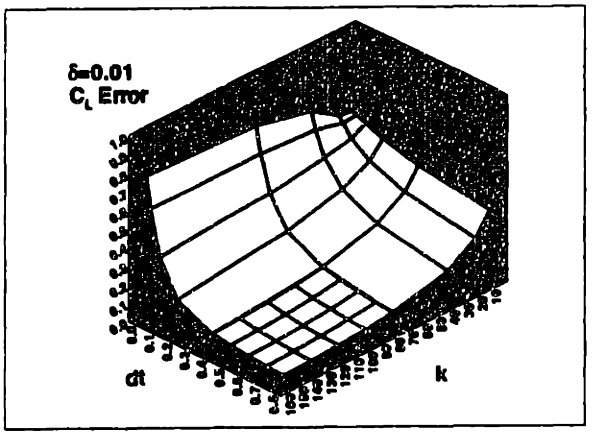

(b) $\delta_w = 0.01$

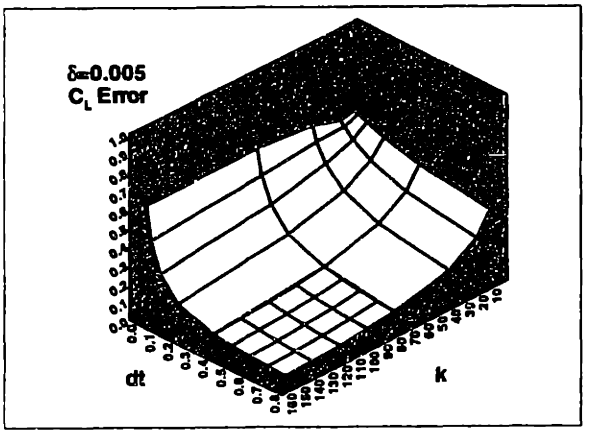

(c) $\delta_w = 0.005$

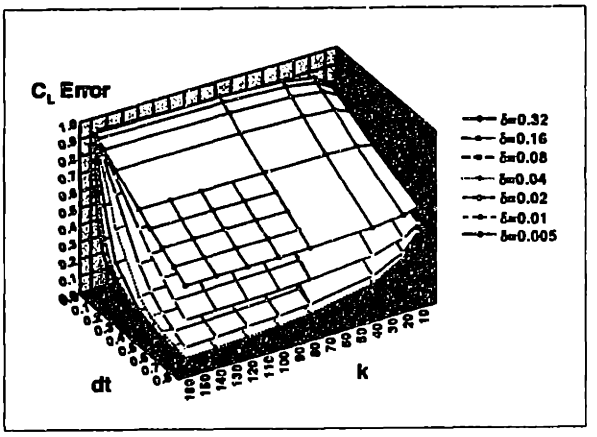

(d) Range of δ_w

Figure A-11: Error isosurfaces for the steady state lift coefficient convergence of an impulsively-started Kármán-Trefftz foil (22.5° trailing-edge angle) after $Ut/c = 100$ for a range of time step size dt and panel number k. The value of the vortex desingularization parameter δ_w is fixed for each of the above graphs. In (d), comparison of the various error isosurfaces is shown for all values of δ_w.

Isosurfaces of error at $Ut/c = 100$ are shown in Figures A-10 and A-11 for various values of δ_w. Force convergence tests shown in Figures A-10 and A-11 were performed by pressure integration. For a given value of δ_w and the time step dt, the error generally decreases for increasing panel number k. However, this same trend is not realized with fixed k and δ_w for a decreasing time step size dt. In general, it can be seen that the error increases as a smaller time step is employed, which is contrary to convergence principles in numerical methods. Similar trends are observed in the convergence of steady-state drag coefficient, shown in Figure A-12 for $\delta_w = 0.32$ and $\delta_w = 0.02$. This behavior illustrates a unique form of numerical instability, and considerable efforts have been made to shed light on these phenomena. It can be shown that the error exponentially increases as the time step is decreased, and that the error is highly geometry dependent, with a Joukowski foil exhibiting the worst convergence results.

Again, this numerical instability results from the proximity of the shed wake dipole to the smallest trailing edge panels being too close or from the included angle of the trailing edge geometry approaching 0°. As these convergence tests illustrate, a smooth increase in error as time step is reduced is realized for all fixed values of all other parameters. Thus, a simple instability criterion or Courant number does not exist which separates the convergent from the non-convergent simulations.

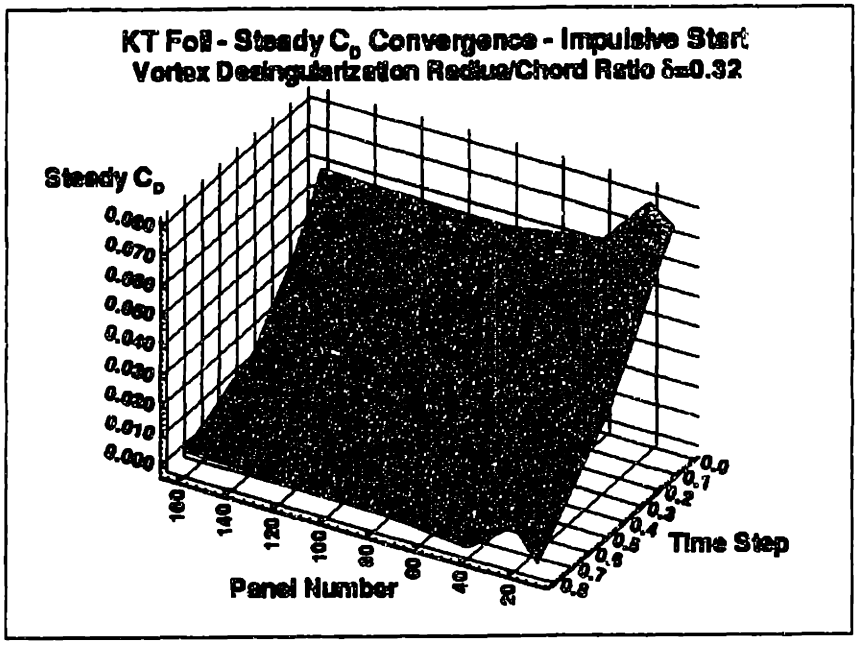

(a) $\delta_w = 0.32$

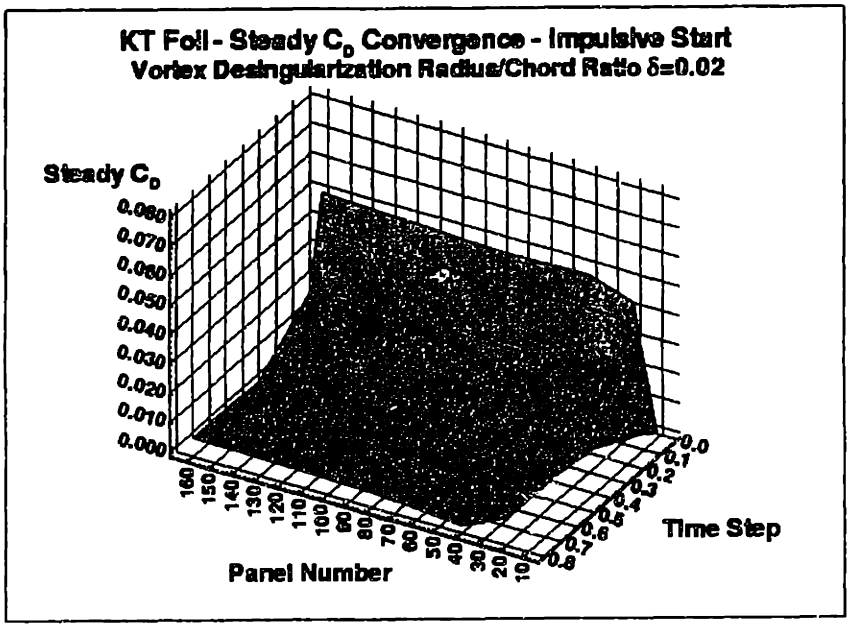

(b) $\delta_w = 0.02$

Figure A-12: Error isosurfaces for the steady-state drag coefficient convergence of an impulsively-started Kármán-Trefftz foil (22.5° trailing-edge angle) after $Ut/c = 100$ for a range of time step size dt and panel number k. The value of the vortex desingularization radius δ_w, based on chord length c, is fixed for each of the above graphs (a) $\delta_w = 0.32$ (b) $\delta_w = 0.02$.

Appendix B

Adaptive control of an oscillatory lifting surface

B.1 Introduction

Fluid-mechanical systems present unique challenges for control system design, due to the strongly nonlinear nature of the fluid dynamics and the resulting structural interaction forces. Even when simplifications to the Navier-Stokes momentum equations result in more tractable physics from a simulation point-of-view, the optimization of the fluid-structure interactions to obtain a desired performance is subject to a variety of parametric dependencies. Several computational tools have been previously developed to simulate the hydrodynamics of oscillating lifting surfaces, with careful treatment of wake modeling and self-interaction. These tools can be adapted and modified, through the development of rigid body motion time integration techniques with control inputs, to study control of these lifting surfaces to obtain an optimal desired performance.

The types of optimal performance of oscillatory lifting surfaces which the fluid dynamicist might seek include:

- Maximization of time-averaged thrust coefficient $\bar{C}_T$.
- Maximization of instantaneous lift coefficient C_L.

- Maximization of propulsive efficiency $\eta = \bar{T}U/\bar{P}$.

The computational model developed to study oscillatory lifting surfaces assumes that the flow is inviscid, with the exception of a thin region of vorticity confined to a wake sheet and to a thin layer on the body. This is a close approximation to high Reynolds number flows around the lifting surface. This investigation considers the problem of the optimization of power absorbed by a pitching and heaving hydrofoil in a steady stream of velocity U.

The system has two-degrees of freedom, which exhibit strong mechanical dynamic coupling if the distance between the pivot point and the center of mass, cm, is not negligible. The hydrodynamic forcing which results from the motions is similarly coupled. Based on the assumptions inherent in the computational model, the fluid dynamics are governed mainly by the nondimensional Strouhal number $St = Af/U$, where A is the double amplitude of the trailing edge motion, f is the frequency of oscillation, and U is the free stream speed.

The adaptive control of a given lifting surface to achieve optimal mean power absorption performance will be examined, based on the assumptions implicit in the numerical modeling. Parametric dependence of performance on the spring constant k, damping coefficient b, frequency and magnitude of imposed torque τ, and the resulting Strouhal number St will be investigated.

B.2 System Dynamics

The problem of a hydrofoil with a sharp trailing edge in a steady free stream of velocity U is considered. The hydrofoil has minimal thickness, no camber, and a rounded leading edge. A thin shear layer develops over the surface of the lifting surface and separates at the trailing edge of the foil, forming a smooth wake sheet. The hydrofoil is forced to undergo angular pitching motions, through the application of an external torque $\tau(t)$, about an arbitrary point P, which lies along the chord c. The hydrofoil is allowed to heave vertically constrained at this pitch point. The location of P is generally independent of the location of the center of mass cm of the

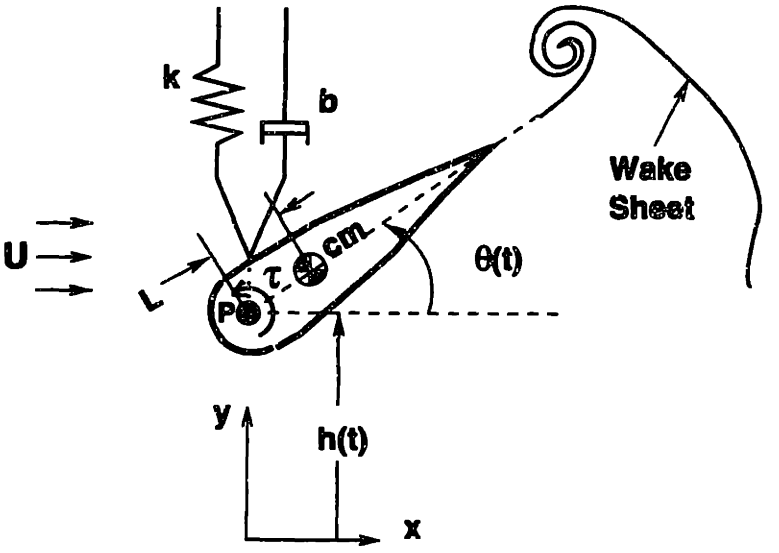

Figure B-1: Geometry definition of power absorption mechanism.

hydrofoil, with linear separation distance L. A system of linear springs and dampers attached to the hydrofoil at P are capable of storing and absorbing energy as the foil heaves (See Figure B-1).

The system dynamics are governed by two degrees of freedom. A coordinate system is chosen as detailed in Figure B-1, with $\theta(t)$ describing the instantaneous angle of attack of the foil and $h(t)$ describing the heave amplitude of the foil from a $y = 0$ equilibrium position.

The equations of motion are derived by Lagrangian analysis. Generalized coordinates δ_i are chosen to be $\delta_1 = \delta_\theta$ and $\delta_2 = \delta_h$, corresponding to the two degrees of freedom $\theta(t)$ and $h(t)$ illustrated above. The location of the center of mass cm can be written in terms of θ and h.

$$x_{cm} = L\cos\theta \tag{B.1}$$

$$y_{cm} = L\sin\theta + h \tag{B.2}$$

The Lagrangian $\mathcal{L}$ can be written:

$$\mathcal{L} = \frac{1}{2}(I + mL^2)\dot{\theta}^2 + mL\dot{h}\dot{\theta}\cos\theta + \frac{1}{2}m\dot{h}^2 - \frac{1}{2}kh^2 \tag{B.3}$$

Equations of motion can be derived from the Lagrangian $\mathcal{L}$ with generalized forces Ξ_θ and Ξ_h acting in the θ and h directions, respectively.

$$(I + mL^2)\ddot{\theta} + mL\ddot{h}\cos\theta = \Xi_\theta \tag{B.4}$$

$$m\ddot{h} + mL\ddot{\theta}\cos\theta - mL\dot{\theta}^2\sin\theta + kh = \Xi_h \tag{B.5}$$

Generalized forces Ξ_i are comprised of the external applied forces and torque τ, the heave damping force, and the resultant hydrodynamic forcing. At any instant, the hydrodynamic force F_H acts through the aerodynamic center of the hydrofoil AC, which is dynamically positioned for unsteady foil motion. The hydrodynamic force vector is inclined at an angle ψ to the x-axis, as shown in Figure B-2. The hydrodynamic center lies along the chord a linear distance γ from the pivot point P. The components of F_H acting in the θ and h directions are $F_{H\theta} = F_H \sin(\psi - \theta)$ and $F_{Hy} = F_H \sin\psi$, respectively.

Expanding the components of the generalized forces, the equations of motion can be expressed more completely. The equations are coupled through the resultant hydrodynamics forcing components, and through the arbitrary distance L between the pivot point P and the center of mass of the foil cm. If $L = 0$, the nonlinear dynamic coupling terms would vanish, but nonlinear hydrodynamic coupling associated with the generation of a vorticity in the wake would still be present. The general equations are expanded as follows:

$$(I + mL^2)\ddot{\theta} + mL\ddot{h}\cos\theta = \tau_\theta + \gamma F_H \sin(\psi - \theta) \tag{B.6}$$

$$m\ddot{h} + mL\ddot{\theta}\cos\theta - mL\dot{\theta}^2\sin\theta + b\dot{h} + kh = F_H \sin\psi \tag{B.7}$$

The hydrodynamic effects of lift and drag cause both heaving and rotational forces. The forces are the result of the kinematics and the imposition of a Kutta condition,

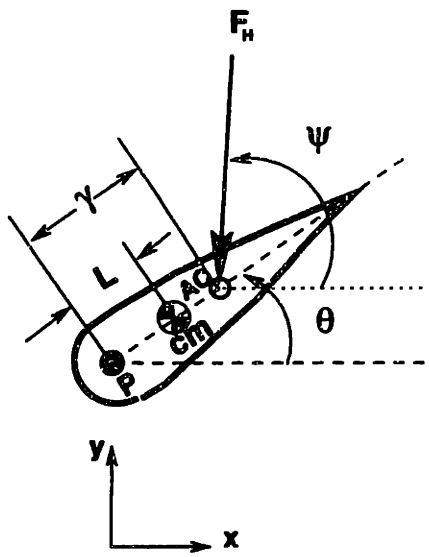

Figure B-2: Hydrodynamic force F_H convention.

requiring smooth flow from the trailing edge, thereby inducing a circulation around the foil. Therefore, the trajectory of the foil will determine the hydrodynamic forces and thus the performance.

B.3 Control System Design

B.3.1 General algorithm - robust adaptive control

We seek to optimize the performance of the foil by imposing a known trajectory *a priori*. Experimental attempts to achieve a desired trajectory in the presence of unsteady flows with large-scale vorticity are often thwarted by unmodelled dynamics resulting from high-order fluid-structure interactions and vibrations. To do this, an adaptive control algorithm can be designed which attempts to achieve the desired trajectory through adaption of the estimates of the physical parameters governing the unsteady dynamics. The free stream strength U is assumed to be fixed and constant. The remaining independent parameters include the damping coefficient b, the spring constant k, the frequency of the pitching and heaving motions ω, and the phase angle between pitch and heave motions ϵ, all assumed to be unknown to the

controller, along with the mass and inertial properties of the foil.

A control architecture is designed to achieve optimal performance, by adaptation of estimates of the physical parameters governing the dynamics [185]. Analysis of the forces on the foil subsequent to achieving a desired motion enable assessment of the performance. Performance measures for the hydrofoil dynamical behavior include propulsive efficiency η, power absorbed to power input ratio $\bar{P}_a$, and mean thrust coefficient $\bar{C}_T$, each specific for a desired application. In this case, the performance of power absorption characteristics of the oscillating foil will be considered for a known magnitude of input torque, so as to maximize the power absorbed by damping as compared to the power input to the system. Ideally, this ratio $\bar{P}_a$ should be greater than 1.0 for energy extraction from the free stream to take place.

The desired trajectories of pitch at an angle $\theta_d(t)$ and heave $h_d(t)$ are defined as simple sinusoids, with a phase angle ϵ separating the temporal occurrence of their maxima.

$$h_d(t) = H_o \sin \omega t \tag{B.8}$$

$$\theta_d(t) = \Theta_o \sin(\omega t + \epsilon) \tag{B.9}$$

A phase angle $\epsilon = \pi/2$ will result in maximum angle of attack at the time of heave $h_d(t) = 0$. The differences between the actual heave h and pitch θ and the desired heave h_d and pitch θ_d are the trajectory errors $\tilde{h}$ and $\tilde{\theta}$, respectively. These coordinates can be incorporated into a column vector q.

$$q = [\theta \;\; h]^T \tag{B.10}$$

$$\tilde{q} = [\tilde{\theta} \;\; \tilde{h}]^T = [(\theta - \theta_d) \;\; (h - h_d)]^T \tag{B.11}$$

The tracking error s is then defined, in the usual manner for robust trajectory control:

$$s = \dot{\tilde{q}} + \Lambda \tilde{q} = \dot{q} - \dot{q}_r \tag{B.12}$$

where $\dot{q}_r$ is the reference velocity vector,

$$\dot{q}_r = \dot{q}_d - \Lambda\tilde{q} \tag{B.13}$$

The matrix form of the equations of motion (B.6) and (B.7) can be written:

$$\begin{bmatrix} H_{11} & H_{12} \\ H_{21} & H_{22} \end{bmatrix} \ddot{q} + \begin{bmatrix} 0 & 0 \\ C_{21} & C_{22} \end{bmatrix} \dot{q} + \begin{bmatrix} G_1 \\ G_2 \end{bmatrix} = \begin{Bmatrix} \tau_\theta \\ 0 \end{Bmatrix} \tag{B.14}$$

or in simplified matrix notation,

$$H\ddot{q} + C\dot{q} + G = \tau \tag{B.15}$$

A vector a is then defined to be a column vector of parameters governing the physical properties of the system. The unknown physical parameters are estimated as $\hat{a}$, leading to an error in parameter estimation $\tilde{a} = \hat{a} - a$. The Lyapunov function V is considered, in the form of a basic robust adaptive control algorithm Lyapunov function [185],

$$V(t) = \frac{1}{2}[s^T H s + \tilde{a}^T \Gamma^{-1} \tilde{a}] \tag{B.16}$$

with Γ a positive definite gain matrix. Differentiating yields:

$$\dot{V}(t) = s^T(\tau - H\ddot{q}_r - C\dot{q}_r - G) + \dot{\hat{a}}^T \Gamma^{-1} \tilde{a} \tag{B.17}$$

The left-hand side of the matrix form of the equations of motion (B.15) is then decomposed as the product of a known matrix Y and the unknown physical parameter matrix a,

$$H(q)\ddot{q}_r + C(q,\dot{q})\dot{q}_r + G(q) = Y(q,\dot{q},\dot{q}_r,\ddot{q}_r)\ a \tag{B.18}$$

Taking the control law to be

$$\tau = Y\hat{a} - K_d s \tag{B.19}$$

allows the time rate of change of energy described by $\dot{V}(t)$ to be written

$$\dot{V}(t) = s^T Y\tilde{a} - s^T K_d s + \dot{\hat{a}}^T \Gamma^{-1}\tilde{a} \tag{B.20}$$

An adaptation law is then implemented, such that the $\dot{V}(t)$ stability of the global system and the convergence of the tracking error are assured.

$$\dot{\hat{a}} = -\Gamma Y^T s \tag{B.21}$$

which, substituted into (B.20), yields

$$\dot{V}(t) = -s^T K_d s \leq 0 \tag{B.22}$$

B.3.2 Detailed decomposition

The matrix equations of motion (B.14) contain entries in the H, C, and G matrices which are expanded below:

$$H_{11} = I + mL^2 \tag{B.23}$$

$$H_{12} = mL\cos\theta \tag{B.24}$$

$$H_{21} = H_{12} \tag{B.25}$$

$$H_{22} = m \tag{B.26}$$

$$C_{21} = -mL\dot{\theta}\sin\theta \tag{B.27}$$

$$C_{22} = b \tag{B.28}$$

$$G_1 = \gamma F_H \sin\psi\cos\theta - \gamma F_H \cos\psi\sin\theta \tag{B.29}$$

$$G_2 = kh - F_H \sin\psi \tag{B.30}$$

When the left-hand side of these equations modified in (B.18) is redefined as the product of Y and a, the physical parameters which must be estimated must first be

identified. In this case, eight parameters for estimation are defined as follows:

$$a = [a_1 \;\; a_2 \;\; a_3 \;\; a_4 \;\; a_5 \;\; a_6 \;\; a_7 \;\; a_8]^T \tag{B.31}$$

where

$$a_1 = I + mL^2 \tag{B.32}$$

$$a_2 = mL \tag{B.33}$$

$$a_3 = m \tag{B.34}$$

$$a_4 = b \tag{B.35}$$

$$a_5 = \gamma F_H \sin\psi \tag{B.36}$$

$$a_6 = \gamma F_H \cos\psi \tag{B.37}$$

$$a_7 = k \tag{B.38}$$

$$a_8 = F_H \sin\psi \tag{B.39}$$

which yields a Y matrix:

$$Y = \begin{bmatrix} \ddot{\theta}_r & \ddot{h}_r \cos\theta & 0 & 0 & \cos\theta & -\sin\theta & 0 & 0 \\ 0 & \ddot{\theta}_r \cos\theta - \dot{\theta}\dot{\theta}_r \sin\theta & \ddot{h}_r & \dot{h}_r & 0 & 0 & h & -1 \end{bmatrix} \tag{B.40}$$

Again, the relative velocity and acceleration terms are expanded as:

$$\dot{\theta}_r = \dot{\theta}_d - \Lambda_\theta(\theta - \theta_d) \tag{B.41}$$

$$\ddot{\theta}_r = \ddot{\theta}_d - \Lambda_\theta(\dot{\theta} - \dot{\theta}_d) \tag{B.42}$$

$$\dot{h}_r = \dot{h}_d - \Lambda_h(h - h_d) \tag{B.43}$$

$$\ddot{h}_r = \ddot{h}_d - \Lambda_h(\dot{h} - \dot{h}_d) \tag{B.44}$$

These results are then used to implement the control system design and the rigid body motion equations time integration into a previously existing hydrodynamics simulation package.

B.4 Numerical Method & Control Implementation

B.4.1 Overview of the hydrodynamic model

A numerical method has been developed to simulate the hydrodynamics surrounding the prescribed motions of an oscillating foil in *Chapter 2.* Unlike traditional analytic studies or more recent numerical works, this formulation allows for the satisfaction of the exact body boundary conditions and the improved modeling of highly nonlinear self-induced wake dynamics. The fluid is assumed to be inviscid and the free shear layer wake confined to an infinitesimal dipole sheet, outside of which the flow is irrotational, allowing for the existence of a velocity potential $\Phi(\vec{x},t)$. The foil shape is discretized into a number of linear, piecewise panels. The flow around the body is assumed to be impulsively-started from rest, and an initial-boundary-value problem for the body perturbation velocity potential is solved using the boundary integral previously described, with the wake is represented by desingularized discrete point vortices.

B.4.2 Hydrodynamic boundary conditions and solution algorithm

The boundary value problem is formulated for the body perturbation velocity potential $\Phi_b(\vec{x},t)$, as at any time the strength of the wake is known, and thus the wake perturbation velocity potential $\Phi_w(\vec{x},t)$ is known. Both velocity potentials satisfy the Laplace's field equation for the conservation of mass. The prescribed body motions $\vec{V}_b(\vec{x},t)$ gives the Neumann body boundary condition in terms of the body perturbation potential for a body normal vector $\hat{n}_b$:

$$\frac{\partial\Phi_b(\vec{x},t)}{\partial n_b} = \left\{\vec{V}_b(\vec{x},t) - \vec{\nabla}\Phi_w(\vec{x},t)\right\}\cdot\hat{n}_b \tag{B.45}$$

A radiation condition requires that the perturbation potential influence decay rapidly to zero in the far field:

$$\vec{\nabla}\Phi_b = 0 \tag{B.46}$$

The unsteady Kutta condition states that the flow must leave the trailing edge smoothly. This condition is a physical restriction which limits velocities and prevents pressure jumps. To that end, we set the body perturbation velocity potential jump at the trailing edge at any time to equal the strength of the shed wake perturbation velocity potential.

$$\Delta\Phi_b(\vec{x}_{TE}, t) = \Phi_w(\vec{x}_{TE}, t) \tag{B.47}$$

From Green's theorem, it can be then easily shown that perturbation velocity potential at any point on the body can be described in terms of the integral around the boundaries.

$$-\pi\Phi_b(\vec{x}) \;=\; -\oint_{S_B}(\Phi_b\frac{\partial ln|r|}{\partial n_B})\,ds \;+\; \int_{S_B}(ln|r|\frac{\partial\Phi_b}{\partial n_B})\,ds \tag{B.48}$$

where $ln|r|$ is the two dimensional Green's function, and r represents the distance between the body observation point and any field point along the contour of integration.

The wake surface is a material surface, and can thus be represented by a smoothly-varying strength dipole sheet. The body boundary and wake are then divided into linear panels. The local perturbation potential is assumed to be constant across each panel. As Green's Theorem again allows us to treat a linear dipole sheet of constant strength as two point vortices, the entire wake can be transformed from a variable-strength dipole sheet into a distribution of discrete point vortices.

The panelization technique results in a linear system of equations results for Φ_b, the body perturbation velocity potential, at each panel. The no-flux condition on the body surface gives the normal velocity at each panel, and is comprised of contributions from the imposed velocity of the body, any free stream present, and the velocities induced at each panel by the vortices. At any time, the strength of the newly-shed

wake panel is unknown and is solved for in the system of equations for Φ_b. A fourth-order Runge-Kutta scheme was adopted for time integration, although the boundary-integral equation must be solved as intermediate steps in the time integration in order to satisfy the kinematic body boundary condition, resulting in dramatically increased time integration computational burden.

B.4.3 Rigid body motion and control implementation

From the vector form of the equations of motion given in (B.14), the expressions for the acceleration terms can be rearranged in vector form as

$$\begin{Bmatrix} \ddot{\theta} \\ \ddot{h} \end{Bmatrix} = \begin{bmatrix} H_{11} & H_{12} \\ H_{21} & H_{22} \end{bmatrix}^{-1} \left(Y\hat{a} - K_d s - \begin{bmatrix} 0 & 0 \\ C_{21} & C_{22} \end{bmatrix} \begin{Bmatrix} \dot{\theta} \\ \dot{h} \end{Bmatrix} - \begin{bmatrix} G_1 \\ G_2 \end{bmatrix} \right) \quad \text{(B.49)}$$

or more simply

$$\frac{d}{dt} \begin{Bmatrix} \dot{\theta} \\ \dot{h} \end{Bmatrix} = H^{-1}(Y\hat{a} - K_d s - C\dot{q} - G) \quad \text{(B.50)}$$

which can be integrated by Runge-Kutta fourth-order algorithm. The full equations of motion must not only update velocities, but the positions as well. In addition, the parameter estimates must be updates throughout the time integration scheme to reflect the adaptation law which enforces convergence of the Lyapunov function V and the tracking error s. Thus, the full system of time-integrable equations is expressed in the following form:

$$\frac{d}{dt} \begin{Bmatrix} \theta \\ h \\ \hline \dot{\theta} \\ \dot{h} \\ \hline \hat{a} \end{Bmatrix} = \begin{Bmatrix} \dot{\theta} \\ \dot{h} \\ \hline H^{-1}(Y\hat{a} - K_d s - C\dot{q} - G) \\ \hline -\Gamma Y^T s \end{Bmatrix} \quad \text{(B.51)}$$

Such fourth-order Runge Kutta time integration is far from trivial, for reasons dependent on the hydrodynamic model described previously. The boundary-integral equation must be solved as intermediate steps in the time integration. At each intermediate time step, the vortices comprising the continuous wake model are convected to intermediate locations, and new induced velocities must be found at these vortex locations based on the strengths of all other vortices and the gradient of the body perturbation potential. In addition, the body location must be updated, as well as the imposed forces and torques during intermediate times. If the boundary-value problem is not solved as an intermediate step, the boundary conditions on the foil and in the wake will be violated, and the induced velocities and estimated torques would be invalid. Therefore, at each intermediate Runge-Kutta step, the boundary-value problem is solved, a new vortex is shed, the new induced velocities are determined at each intermediate vortex location, the body position is updated, and the torques are recomputed by updating the parameter estimates $\hat{a}$. Then, the shed vortex is removed, and the vortices return to their original locations for the next intermediate step. At the final stage of convection, the vortices are moved from their original locations at the high-order Runge-Kutta velocity to the new locations, as are the body positions $\theta(t)$ and $h(t)$ and the body velocities $\dot{\theta}(t)$ and $\dot{h}(t)$. Thus, the entire problem will be solved again with one vortex shed in the wake. The net result of implementing this higher-order scheme is approximately the same computational load as a traditional Euler scheme as a larger time step can be used, but with less wake instability, less trajectory instability, and higher accuracy as validated by a Richardson extrapolation scheme.

B.5 Results

The performance of the controller design is evaluated in the following ways:

- Investigate the convergence of the tracking error s, the desired trajectory q_d, and the parameter estimates $\hat{a}$ on the controller gains Γ, Λ, and K_d.

- Investigate the convergence of s, q_d, and $\hat{a}$ on the intentional omission of the heave "torque" control input τ_h.

- Investigate the power absorption characteristics of the hydrofoil for this controller input power as functions of damping coefficient b, spring constant k, and Strouhal number St (a consequence of the desired trajectory q_d.

The wake profiles which result from these rigid body controlled motions are also examined.

B.5.1 Gain dependency

Both input torques are allowed for this numerical experiment, so the hydrofoil is forced in both heave and pitch through the application of a control torque in θ and a control force in h. Arbitrarily gains are chosen as follows:

$$K_d = \text{diag}[100 \;\; 100] \tag{B.52}$$

$$\Lambda = \text{diag}[20 \;\; 20] \tag{B.53}$$

$$\Gamma_1 = \text{diag}[0.5 \;\; 0.5 \;\; 0.5 \;\; 0.5 \;\; 0.5 \;\; 0.5 \;\; 0.5 \;\; 0.5] \tag{B.54}$$

A desired trajectory is selected corresponding to a Strouhal Number $St = 2.0$, with spring constant $k = 10$ and damping coefficient $b = 10$:

$$\theta_d = 10^o \sin(2\pi t + 2\pi/3) \tag{B.55}$$

$$h_d = 1.0 \sin(2\pi t) \tag{B.56}$$

The other physical parameters for the hydrofoil with a NACA0012 symmetric section shape and a chord length $c = 1.0$ are actually:

$$a_1 = I + mL^2 = 43.575 \tag{B.57}$$

$$a_2 = mL = 24.5 \tag{B.58}$$

$$a_3 = m = 70 \tag{B.59}$$

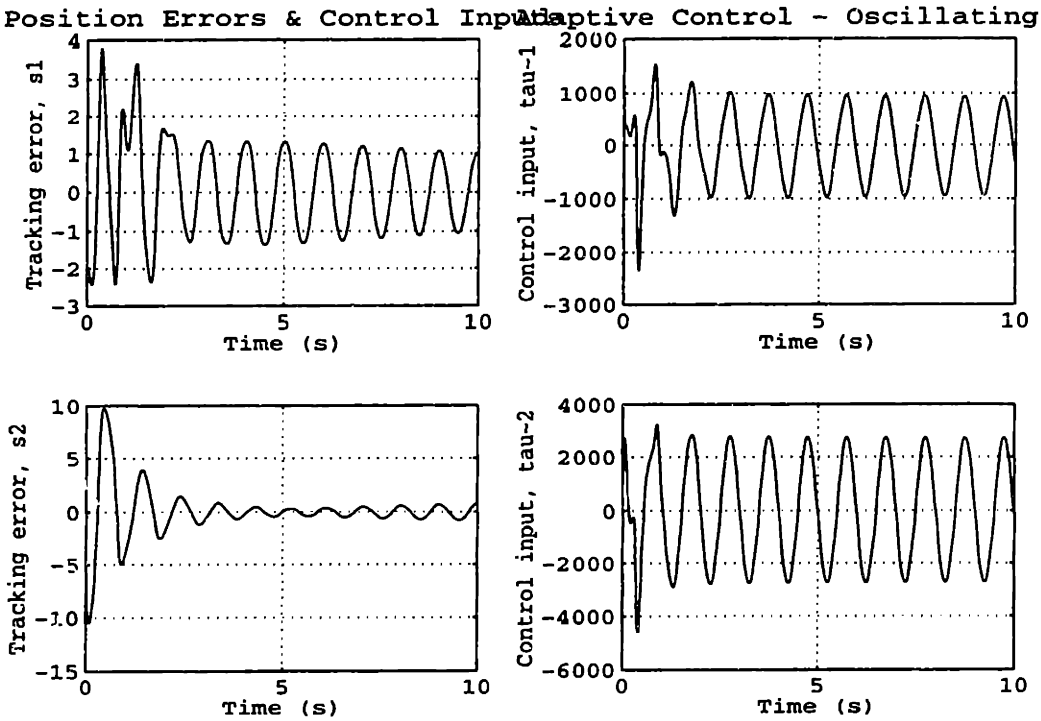

Figure B-3: Tracking error and input torques for $\Gamma = \Gamma_1$.

with appropriate units, corresponding to a distance between the pitch point P and the center of mass cm of $L = 0.35c$. Initial conditions on parameters estimates are $\hat{a} = 0$.

Figure B-3 shows the tracking errors and input torques for this simulation. This is a particularly high Strouhal number St, resulting in a strong drag wake configuration. The tracking errors s are driven to zero, but strongly nonlinear wake interaction prohibits the angular position from achieving its desired trajectory, as can be seen in Figure B-4. The parameter estimates, shown in Figure B-5, show steady convergence, and the estimates for a_5, a_6, and a_8 exhibit some oscillatory behavior as expected, due to the oscillatory nature of the lift and drag forces on the foil.

Then, the same case is simulated with a stronger adaptation gain Γ to illustrate dependencies of the convergence of the parameter estimates $\hat{a}$ and the tracking error s. The new, symmetric gain matrix $\Gamma = \Gamma_2$ are increased tenfold from the Γ_1 gains

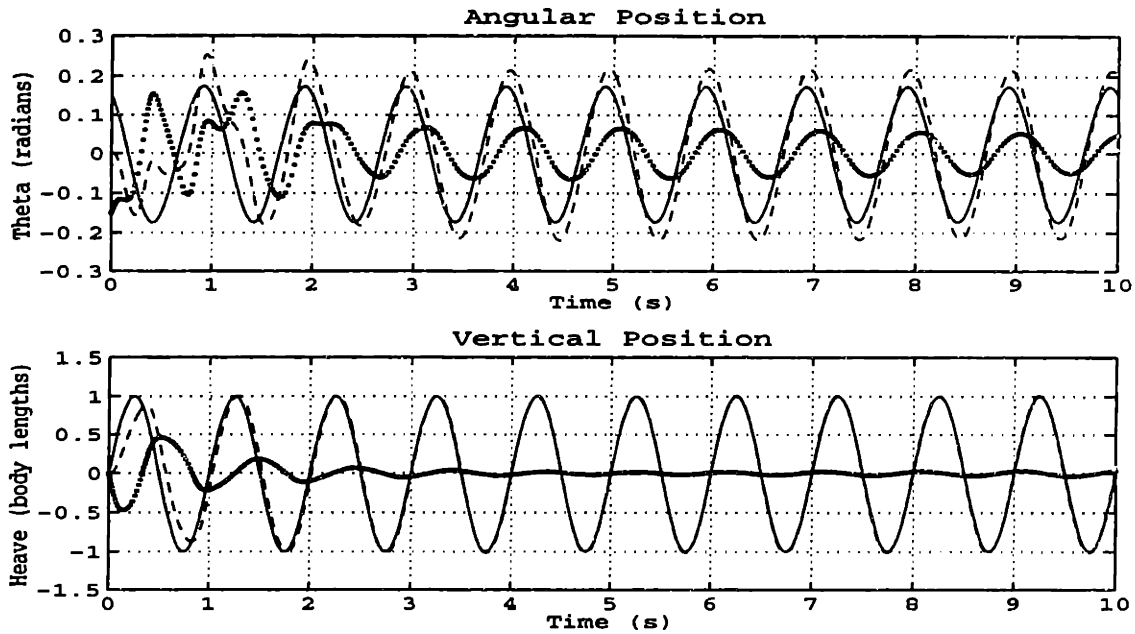

Figure B-4: Trajectories for $\Gamma = \Gamma_1$. (—) desired trajectory q_d, (- -) actual trajectory q, (· ·) error $\tilde{q}$.

while leaving the tracking error gains K_d and Λ constant:

$$K_d = \text{diag}[100 \;\; 100] \tag{B.60}$$

$$\Lambda = \text{diag}[20 \;\; 20] \tag{B.61}$$

$$\Gamma_1 = \text{diag}[5.0 \;\; 5.0 \;\; 5.0 \;\; 5.0 \;\; 5.0 \;\; 5.0 \;\; 5.0 \;\; 5.0] \tag{B.62}$$

Figure B-6 shows the tracking errors and input torques for this high Γ_2 gain simulation. As can be easily seen, the tracking errors s are driven to zero much more quickly, despite strongly nonlinear wake interaction. In addition, as can be seen in Figure B-7, both the angular position and the heave position converge rapidly on their desired trajectories. The parameter estimate $\hat{a}$ convergence, shown in Figure B-8, is evident, although the limits of the parameter estimate convergence are generally slightly different than that shown in Figure B-5. Here, the oscillatory nature of the hydrodynamic forcing, which should be evident in the estimates for a_5, a_6, and a_8, is not modeled, due to the high adaptation gains, which allows little time for the

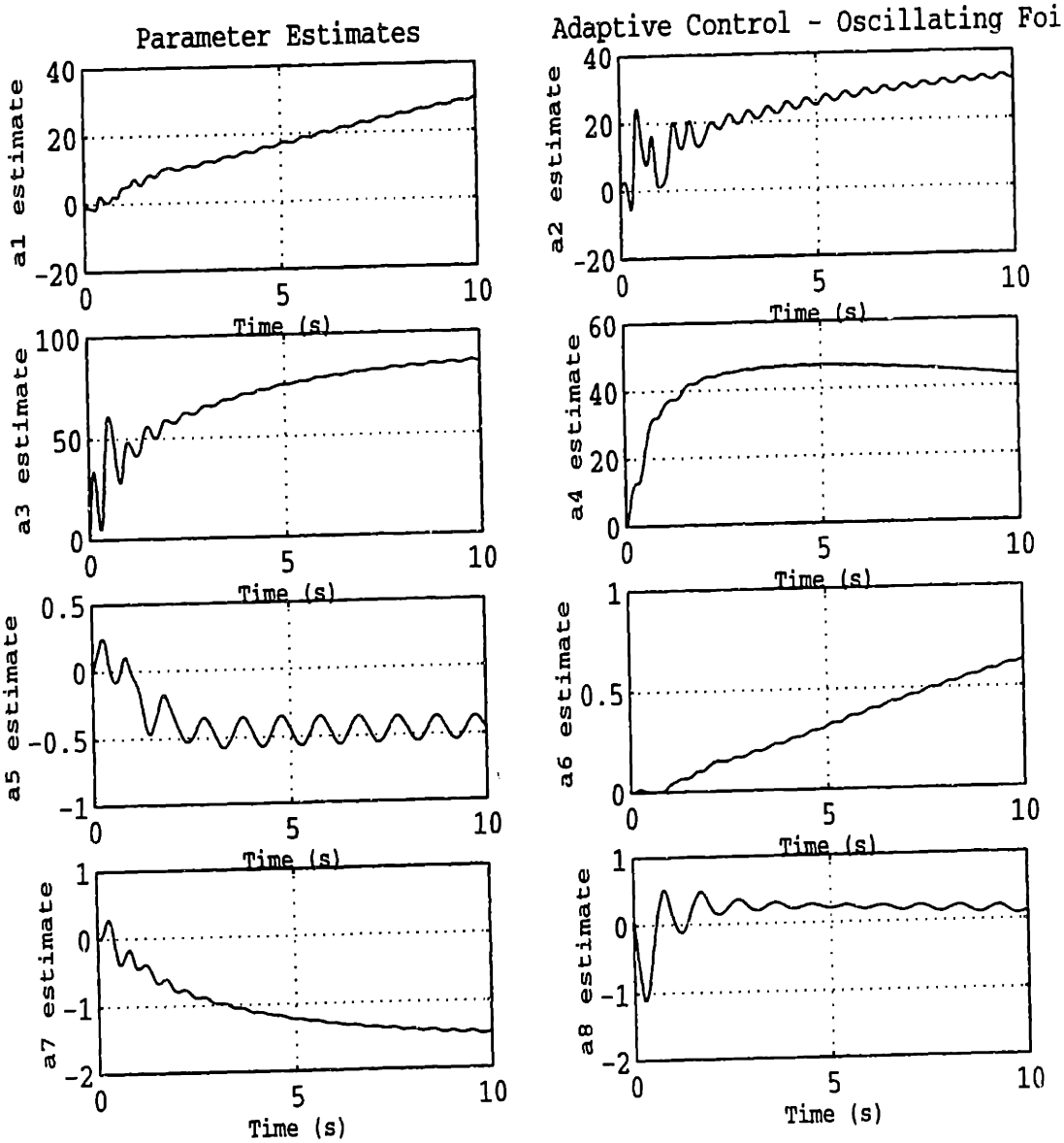

Figure B-5: Time histories of parameter estimates $\hat{a}$ for $\Gamma = \Gamma_1$.

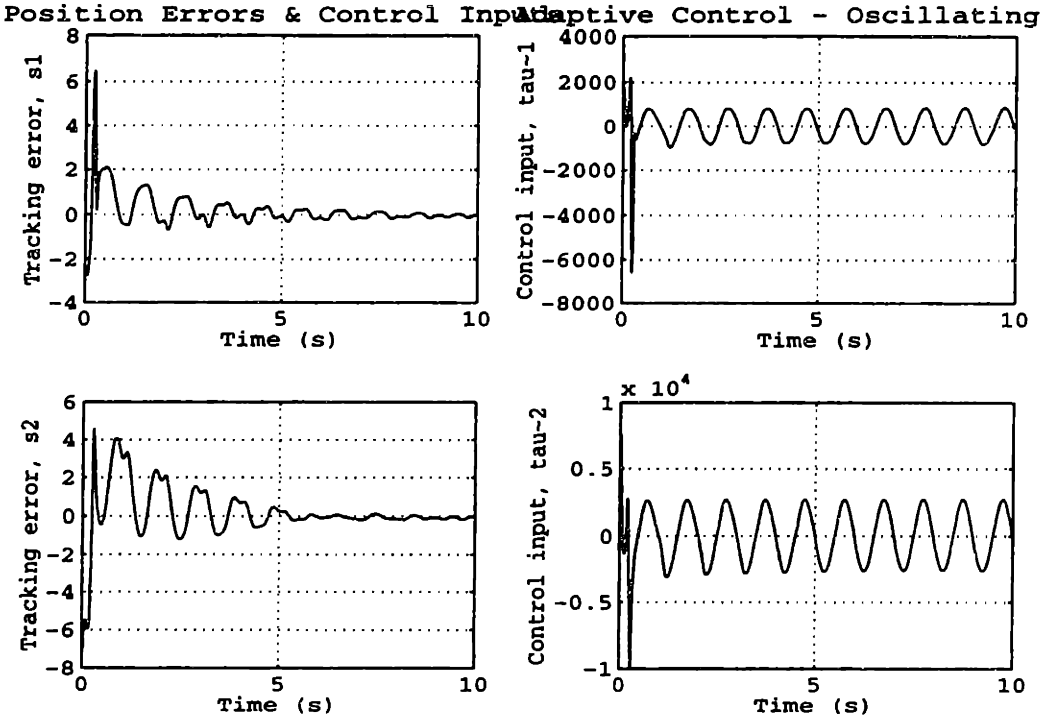

Figure B-6: Tracking error and input torques for $\Gamma = \Gamma_2$.

controller to absorb the effects of the actual physically changing parameters.

Changes in other gain levels result in expected performance tradeoffs in accuracy, convergence time and parameter estimation. A higher Λ matrix places more emphasis on the position error than the velocity error, leading to increased performance convergence and lower trajectory errors. Similarly, a higher K_d increases the control input significantly and results in rapid convergence of the tracking errors and the trajectories, while not significantly affecting the parameter estimation convergence. For the sake of brevity, the details of these results are not included in the present work.

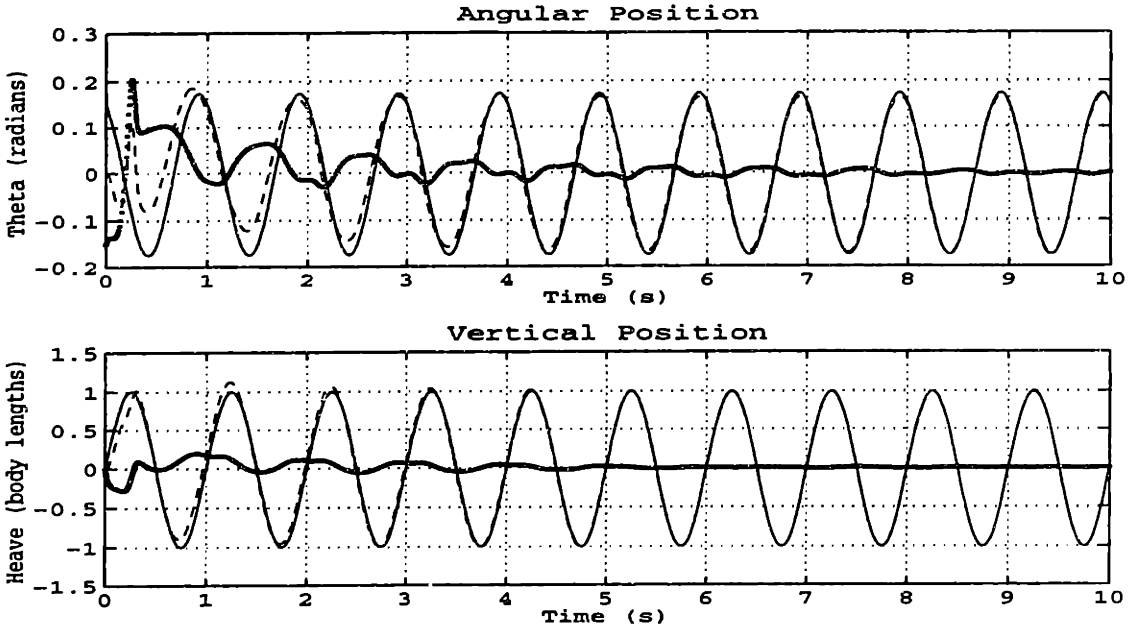

Figure B-7: Trajectories for $\Gamma = \Gamma_2$. (—) desired trajectory q_d, (- -) actual trajectory q, $(\cdot\ \cdot)$ error $\tilde{q}$.

B.5.2 Elimination of dual control inputs

For practical applications of this system, a rotational torque may only be able to be applied. For instance, the tail of a highly efficient swimming fish appears as a high aspect ratio hydrofoil, which is connected to the body through a fine caudal peduncle. The caudal peduncle is a joint which delivers rotational motion to the tail and sustains and transmits the tail lifting force to the center of mass of the fish to produce a useful thrust force. In that sense, the fish tail may be capable of limited "heave" control input, with the bulk of the actuation of the tail controlled through rotational torque.

To that end, the robust adaptive control of the two-dimensional hydrofoil trajectory is examined with the omission of the heave control input $\tau_2 = \tau_h$, such that the applied torque vector now receives its rotational input from the adaptive control law expressed in (B.19), but imposes a heave control input $\tau_h = 0$, neglecting the adaptive control inputs based on parameter estimates and current tracking error levels. The

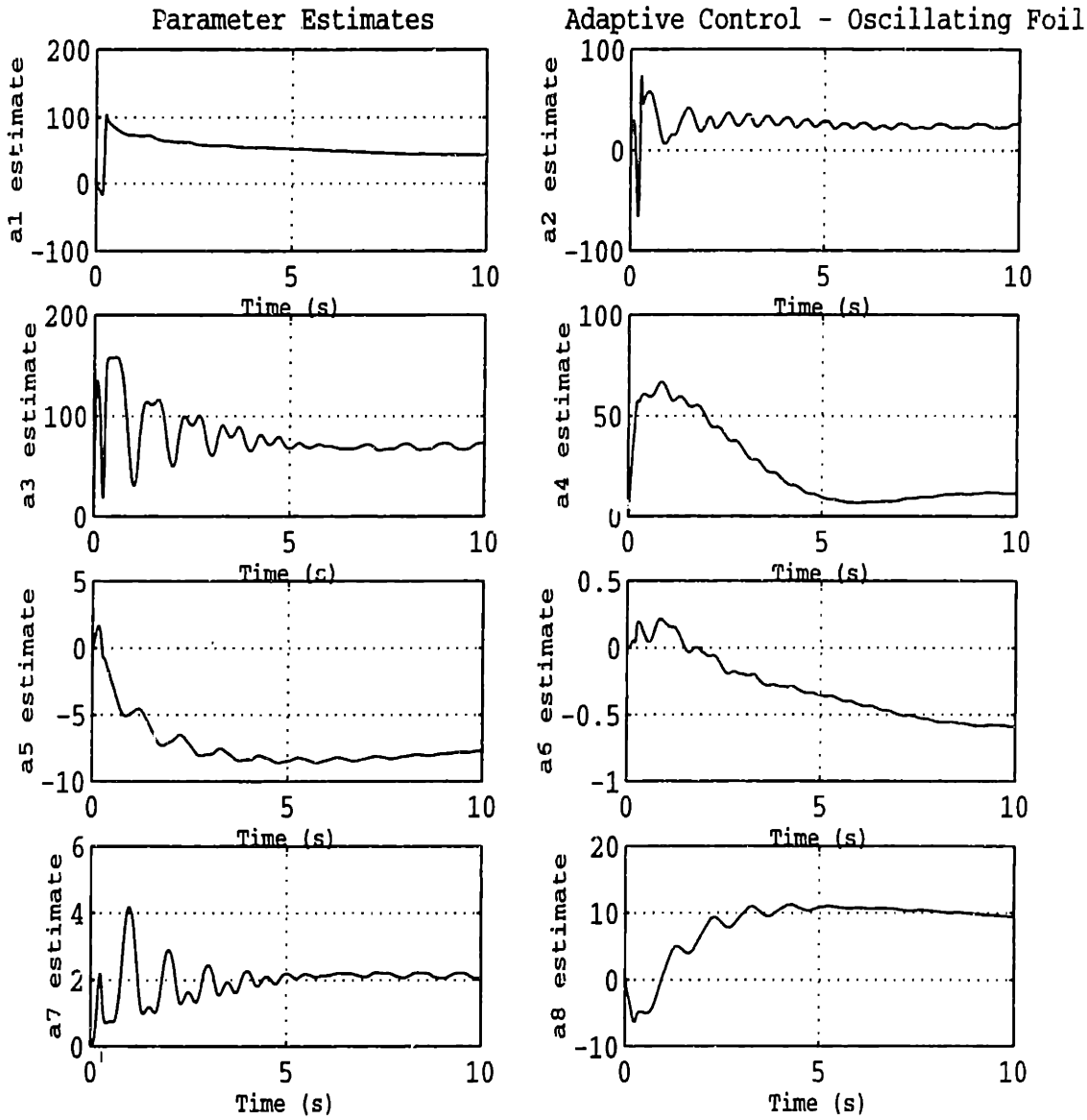

Figure B-8: Time histories of parameter estimates $\hat{a}$ for $\Gamma = \Gamma_2$.

artificially imposed control law now reads:

$$\tau = \begin{Bmatrix} \tau_\theta \\ 0 \end{Bmatrix} \tag{B.63}$$

All parameters continue to be updated by the adaptation law (B.21), and the effects of the mechanical and hydrodynamic coupling on the performance and achievement of desired trajectories are studied through simulation.

Simulation parameters are the same as the original case for Strouhal number $St = 2.0$. The desired trajectories are identical to those expressed in (B.55) and (B.56). Similarly, the gains are returned to the original levels for K_d, Λ, and Γ, expressed in (B.52), (B.53), and (B.54), respectively.

Figure B-9 shows the tracking errors and input torques for this artificial control law simulation. The tracking error s_1 for the rotational motion reaches a steady-state oscillatory level after short time, but the tracking error s_2 for the vertical heave motion does not converge and oscillates wildly, corresponding to the oscillatory trajectory error incurred through the exclusion of τ_h. Strong coupling between the heave and pitch motions result in a steady-state error in the angular position's attempt to achieve its desired trajectory, as can be seen in Figure B-10. In addition, it can be seen that heave motion achieved h differs greatly from its oscillatory desired trajectory h_d, drifting to some steady-state offset observed through the tracking error convergence graph of s_2 in Figure B-9. However, the mild oscillations in the time record for h suggest that tuning the physical system parameters, such as k, b, the mass and inertia, as well as the desired trajectory of the system and the corresponding Strouhal number St, will result in natural frequency oscillations of the sort which achieve the desired heave trajectories with only rotational motion control input, as exhibited in marine systems. The parameter estimates, shown in Figure B-11, show poor convergence, as would be expected due to the artificial control law applied and the resulting tracking error. It should be noted that those parameters associated with the adaptation of the rotational motions dependencies, a_1, a_2, a_5, and a_6 do converge to a steady-state value, while those parameters associated with the adaptation of heave motion dependencies,

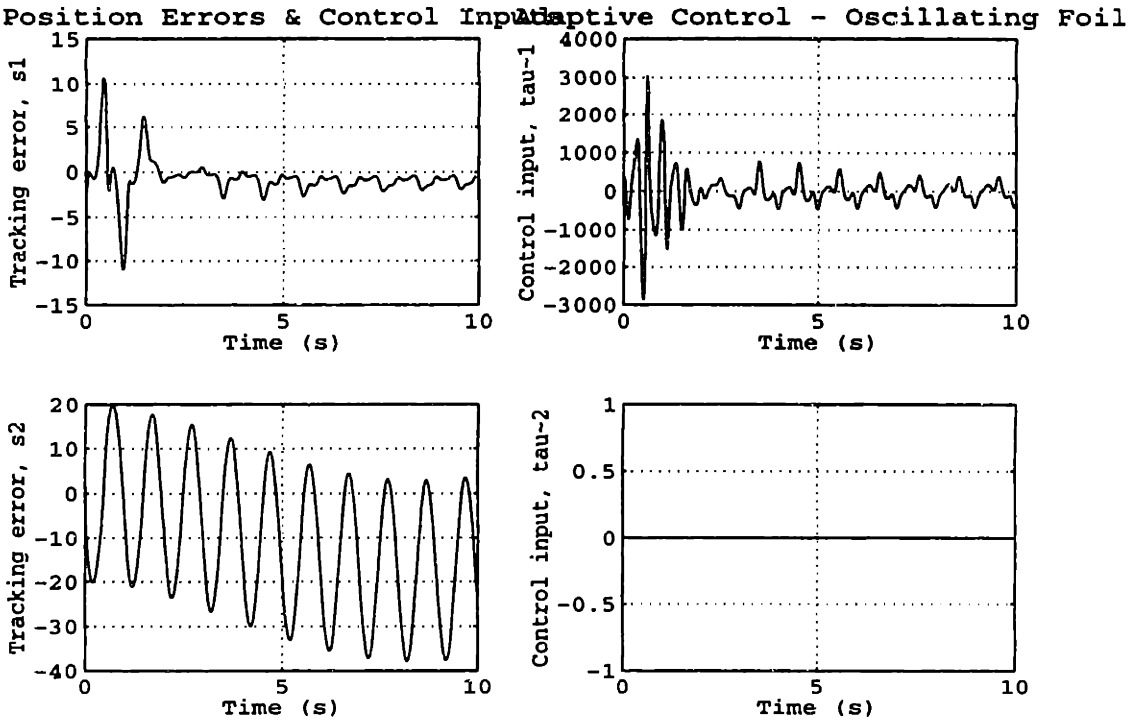

Figure B-9: Tracking error and input torques for $\Gamma = \Gamma_1$. Heave control input set to $\tau_2 = \tau_h = 0$.

a_3, a_4, a_7, and a_8 do not converge and exhibit wild errors and oscillations.

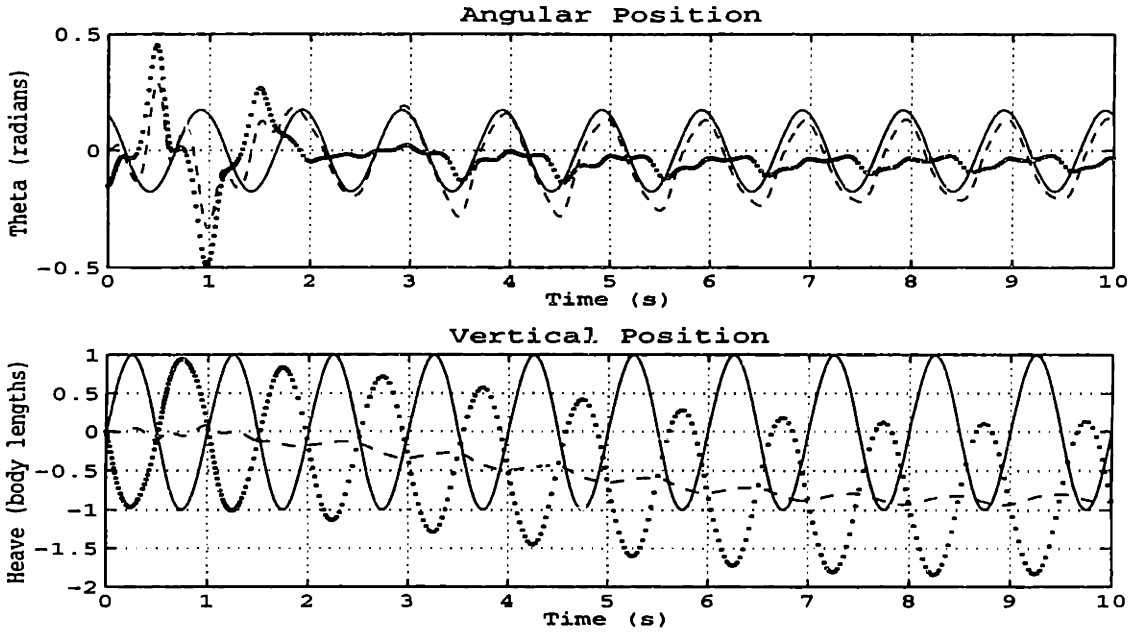

Figure B-10: Trajectories for $\Gamma = \Gamma_1$. (—) desired trajectory q_d, (- -) actual trajectory q, $(\cdot\ \cdot)$ error $\tilde{q}$. Heave control input set to $\tau_2 = \tau_h = 0$.

B.5.3 Analysis of power absorption mechanisms

It is hypothesized that when fish swim, they are able to control vorticity shed from their tail fin in such a way that the drag characteristics of the body can be altered. This mechanism of vorticity control is believed to alter the body's pressure distribution in such a way so as to generate favorable pressure gradients around the lifting surface throughout the entirety of its oscillation cycle, producing a powerful net thrust while suppressing separation over the rest of the body. Indeed, by aligning the counter-rotating vortical wake structures to produce a net thrust jet as opposed to a net drag wake, the foil is able to minimize the amount of energy delivered to the fluid (which is wasted) for a given momentum imparted (or absorbed) from the fluid.

In addition, by allowing for some damping mechanism to be modeled in our simplified system, the absorption of energy by the muscular tissues and mechanical linkages in the fish can be approximated. This is the focus of the present investigation. If the inherent energy of the free stream can be absorbed by a swimming fish through

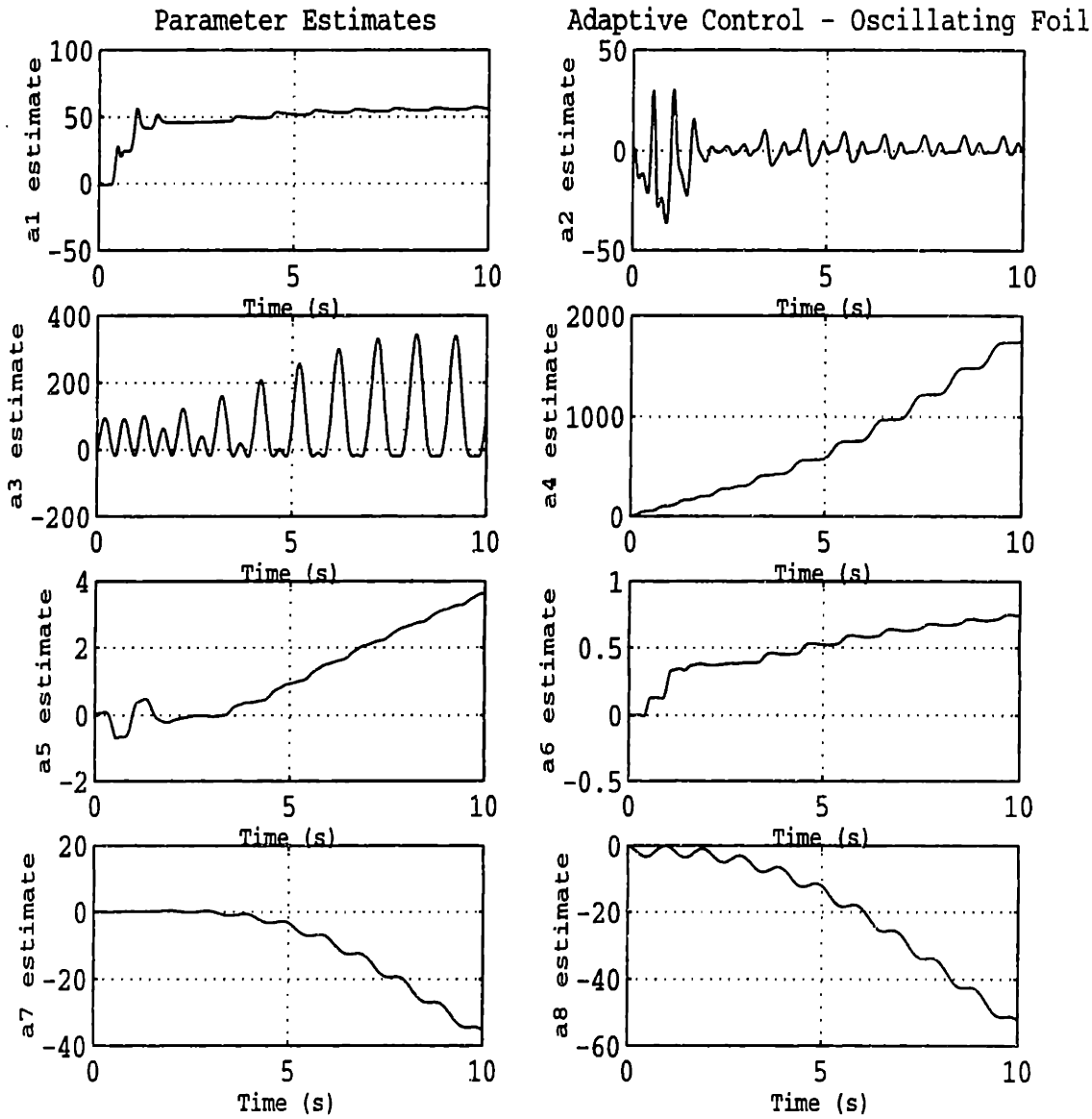

Figure B-11: Time histories of parameter estimates $\hat{a}$ for $\Gamma = \Gamma_1$. Heave control input set to $\tau_2 = \tau_h = 0$.

its musculature and skeletal harmonics, The parameters of this absorption can be modeled by investigating the power required to produce a prescribed or desired trajectory, and then comparing that to the time rate of change of positive definite energy absorbed by the damper model.

To do this, a desired trajectory is specified as before, given in (B.55 and (B.56), and simulate the system under the same physical conditions as originally investigated, with the corresponding gains given by (B.52), (B.53), and (B.54). Both control inputs for the rotational motion θ and the heave motion h are utilized in these simulations to determine the power into the system, although the actual system would be devoid of τ_h. Subsequent investigation into the tuning of the physical parameters may allow for the exclusion of the τ_h and still achieve desired trajectory performance, but such a search would be exhaustive for the scope of this project and will be ignored for the time.

Below, Figure B-12 shows the power absorption characteristics of the original system upon simulation. Due to the drops in power delivered to the system to a low level, spikes appear in the time record of the power absorption ratio P_a, which is defined,

$$P_a = \frac{\text{Power delivered to the system}}{\text{Power absorbed by damping}} = \frac{\tau_\theta \dot{\theta} + \tau_h \dot{h}}{b\dot{h}^2} \tag{B.64}$$

For the case illustrated in Figure B-12, the time averaged mean power absorption ratio is $\bar{P}_a = 0.3826$, relatively low as would be expected from the high Strouhal number, resulting in large power inputs to achieve the desired trajectory.

The power absorption mechanisms are investigated for the dual control inputs as a function of different prescribed trajectories and physical parameters, such as the damping coefficient b and the spring constant k. Trajectories are chosen resulting in a range of discrete Strouhal Numbers St. In addition, several different values of k and b are chosen to arrive at 80 simulations to find peak $\bar{P}_a$ values and dependencies. Results are shown in Figure B-13. Each simulation took approximately 5 to 10 minutes on an SGI R8000 workstation, with variability due to dynamic time stepping, to satisfy Courant conditions for numerical stability. Wake structure profiles for three Strouhal

Numbers are given in Figure B-14.

B.6 Discussion

A robust adaptive control system has been designed for the problem of a two-dimensional hydrofoil situated in a free stream of velocity U, allowed to pitch about and heave along a pivot axis P, attached to a system of linear springs k and dampers b. The nonlinearity of the system arises from the dynamic coupling between the pitch θ and heave h motions when the distance between the pivot point P and the center of mass cm is non-zero, and nonlinear effects are dominant due to the hydrodynamic forcing F_H, which is inherently nonlinear to begin with based on considerations of the wake modeling and evolution.

The robust adaptive control system was implemented by estimation of the physical parameters governing the system. Most of these parameters are constant, but some containing the hydrodynamic forcing term vary over the oscillation cycle. Nonetheless, decent performance of the tracking error convergence and trajectory following are obtained despite this assumption.

The control system was then tested to determine if the heave control input could be omitted while still obtaining decent heave trajectory following and tracking error convergence. The heave trajectory is found to drift to a constant steady value, resulting in a large tracking and trajectory error for the desired oscillatory behavior of the heave. However, slight oscillations in this steady value of heave suggest that tuning of system parameters may result in better performance for a single input of rotational control torque.

Finally, the control system application was used to study the mean power absorption ratio for the linear damper b installed. The implication of this study is the modeling of possible energy recovery from the fluid by a lifting surface with energy absorption capability, such as musculature and harmonically tuned linkages. The dependencies revealed through simulations are the following:

- The mean power absorption ratio $\bar{P}_a$ is found to be relatively insensitive to

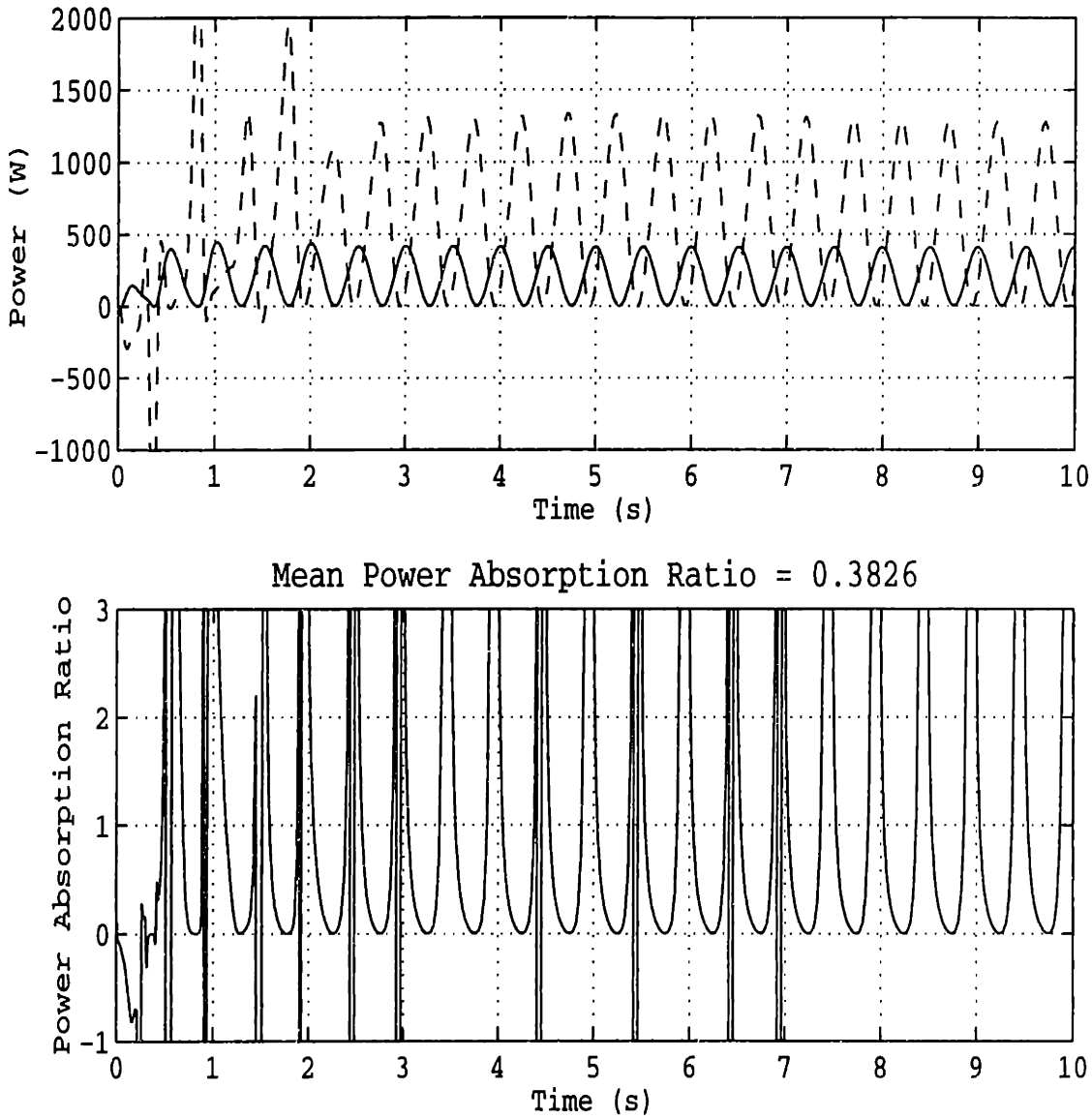

Figure B-12: Power input through control torques and power absorbed through damping: (- -) power input, (—) power absorbed. Power absorption ratio P_a is power absorbed/power in. Mean power absorption ratio for this original case with $\Gamma = \Gamma_1$ and both control inputs is $\bar{P}_a = 0.3826$.

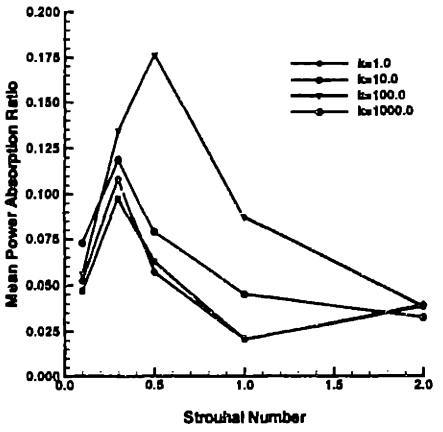

(a) Damping coefficient $b = 1$.

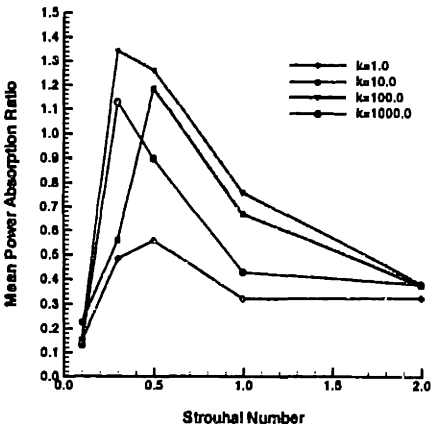

(b) Damping coefficient $b = 10$.

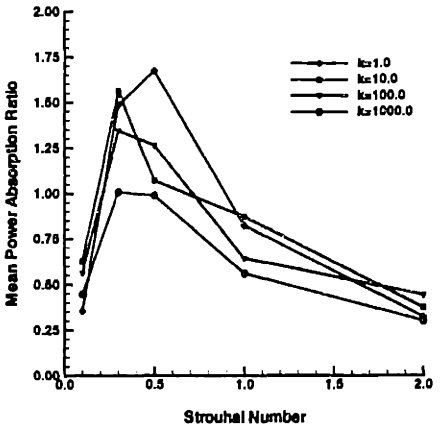

(c) Damping coefficient $b = 100$.

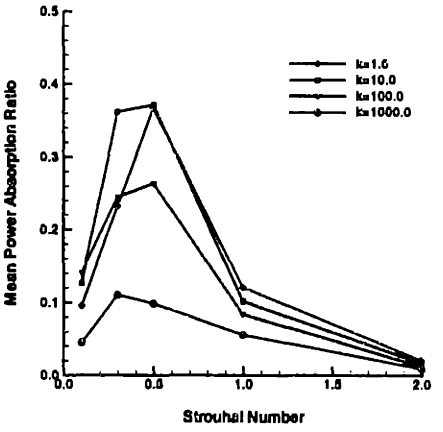

(d) Damping coefficient $b = 1000$.

Figure B-13: Mean power absorption ratio $\bar{P}_a$ for a range of Strouhal Numbers St, damping coefficients b and spring constants k. Strouhal Number St was altered by varying the amplitude of desired heave oscillation h_d, keeping desired rotational amplitude or angle or attack small at $\theta_d = 10^o$. Oscillation frequency $\omega = 2\pi$ and free stream velocity $U = 1.0$ were fixed.

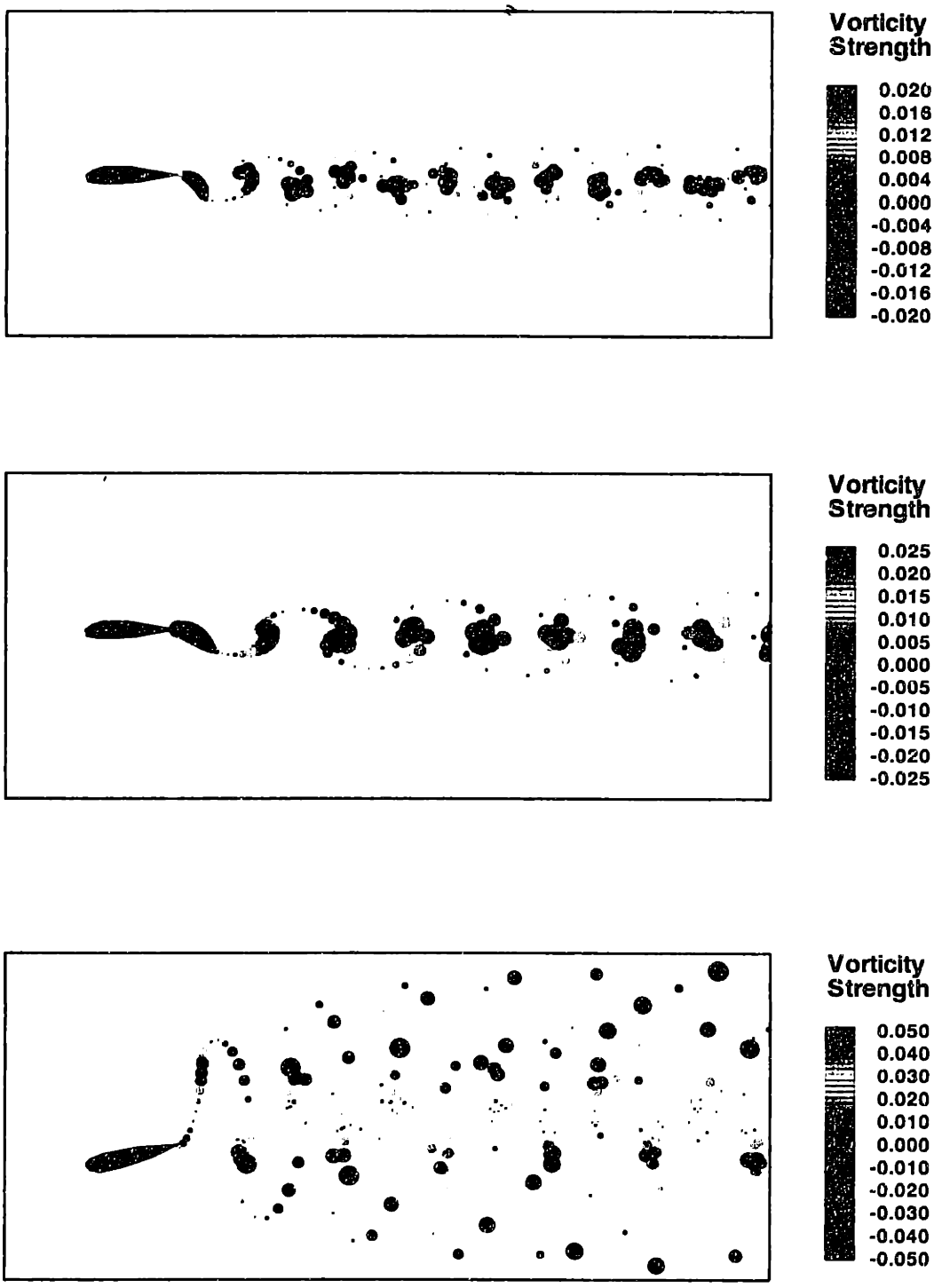

Figure B-14: Wake structure dependence on Strouhal Number St: Top simulation $St = 0.1$, middle simulation $St = 0.3$, bottom simulation $St = 2.0$.

spring constant k, although the k corresponding to the natural frequency of the fluid-mechanical system tended to have slightly improved performance.

- The dependence of $\bar{P}_a$ on the damping coefficient b is illustrated in Figure B-13, indicating an optimal range for the damping coefficient for peak energy recovered from the free stream.

- The dependence of $\bar{P}_a$ on the Strouhal Number reveals a strong peak within a narrow range of low Strouhal Numbers. This range is hypothesized to relate to the range of Strouhal Numbers which correspond to the maximum spatial amplification of the vortical wake instabilities, which is accepted to fall within a range of $St = 0.2$–0.5 [203, 204].

Future work on these areas might include a thorough investigation of the phenomena which has been preliminarily revealed above, including an exhaustive optimization routine to tune physical parameters to obtain adequate performance with a single control input. A broader investigation of energy recapture mechanisms of vorticity control will allow for advancements in many areas of fluid dynamics engineering, from propulsion systems to drag reduction, from manufacturing process design to environmental architectural synergy.

Specific application of this particular control system design might include sheathing attachments for deep-water drilling riser cables. Such a sheathing might consist of rectangular foil sections, of a length corresponding to the correlation length of shedding along the riser, attached to prior-tuned or dynamically-tuned rotational springs and dampers. In this manner, the rotational and translational oscillations of the foil, caused by the vorticity packets of oscillatory strength shed from the risers in a current which then impinge on the leading edge of the sheathing foils, can be tuned to annihilate the large separation vortices shedding from the risers, thus remediating vortex-induced-vibration problems.

Appendix C

Two-dimensional rigid body equations of motion for a wake-shedding flexible body

C.1 Definitions

For the two-dimensional flexible foil to experience free swimming, we formulate the equations of motion for a rigid-body with time-dependent added mass. For this problem, we define two coordinate systems, an inertial coordinate system fixed in space $OXYZ$, and a local coordinate system $o'x'y'z'$, at any time fixed at the body center of mass, about which the mean body undulations are defined. Although the variations in z for the two-dimensional problem are neglected in the application of these rigid body equations of motion for time integration, the equations will be expanded in general form for three-dimensions for the ease of extension in future investigations. The two coordinate systems are related by a translation by position vector $\vec{R} = \overrightarrow{Oo'}$, and by an orthogonal coordinate transformation for a rotation by angle θ.

Unit vectors in the global and local coordinate systems are defined as $\tilde{x}_u^T = [\hat{i} \;\; \hat{j} \;\; \hat{k}]$ and $\tilde{x'}_u^T = [\hat{i'} \;\; \hat{j'} \;\; \hat{k'}]$, respectively. Any free vector $\vec{V}$ can be related to a specific coordinate system by the relation $\vec{V} = \tilde{x}_u^T \tilde{V}$ or $\vec{V} = \tilde{x'}_u^T \tilde{V'}$. Components of vectors

expressed with respect to either coordinate system are related by the orthogonal coordinate transformation matrix $\tilde{L}$, such that $\tilde{v}' = \tilde{L}\tilde{v}$ and $\tilde{v} = \tilde{L}^{-1}\tilde{v}'$, where

$$\tilde{L} = \begin{bmatrix} cos\theta & -sin\theta \\ sin\theta & cos\theta \end{bmatrix} \tag{C.1}$$

The general forces and moments at any instant on the body can be categorized as hydrodynamic forces due to unsteady inviscid flow with a time dependent wake, $\vec{F}_{H_O}$ and $\vec{M}_{H_O}$, and forces due to viscous drag and separation, $\vec{F}_{D_O}$ and $\vec{M}_{D_O}$, applied at O in the global reference frame. For the implementation of the rigid body equations of motion for a steadily-swimming two-dimensional foil section, it is necessary to make some approximation of the viscous forces and moment on the body, in order to prevent immediate solution instability and non-physical body dynamics, although this approximation may be based on parametization of empirical results.

To smooth out the numerical solution, it is advantageous to solve the equations of motion with all momentum linearly proportional to velocity on the left-hand side. For that reason, we can define an added momentum term, $\tilde{P}_{A_O}$, proportional to the inviscid added mass of the foil shape at any time.

$$\tilde{P}_{A_O} = \tilde{A}_O \tilde{V}_O \tag{C.2}$$

$\tilde{A}_O$ is a global 6x6 added mass matrix, $\tilde{V}_O$ is generalized 6x1 velocity vector for translational and rotational body velocities in three-dimensions, and the added momentum $\tilde{P}_{A_O}$ is the global 6x1 added momentum matrix, linear and angular, referred to O.

The concept of added mass is only truly valid for a body in an irrotational unbounded fluid domain. However, the numerical nature of the unsteady foil problem makes it advantageous to identify these terms proportional to the body velocity. To find these approximate added mass coefficients, the boundary value problem for the two-dimensional foil is solved at each time for a unit velocity in each direction. From the solution of the unit potential problem, the added mass coefficients can be determined in the usual way [157] as the integral of this unit potential around the body.

Although the coefficients determined are not the exact approximation of the body's added mass coefficients, the stability this method brings to the numerical solution justifies its implementation. Systematic convergence tests of the unit potential boundary value problem solution to find the added mass of a variety of lifting and non-lifting bodies confirm the accuracy of the approximation.

Thus, the global added mass matrix can be written simply as

$$\tilde{A}_O = \begin{bmatrix} \tilde{A}_{11} & \tilde{A}_{12} \\ \tilde{A}_{21} & \tilde{A}_{22} \end{bmatrix} \tag{C.3}$$

where $\tilde{A}_{11}$ is the 3x3 added mass matrix, $\tilde{A}_{12}$ and $\tilde{A}_{21}$ are the 3x3 added moment of mass matrices, and $\tilde{A}_{22}$ is the added moment and product of inertia matrix. The added momentum can then be rewritten for clarity as

$$\begin{Bmatrix} \tilde{p}_{A_O} \\ \tilde{h}_{A_O} \end{Bmatrix} = \begin{bmatrix} \tilde{A}_{11} & \tilde{A}_{12} \\ \tilde{A}_{21} & \tilde{A}_{22} \end{bmatrix} \begin{Bmatrix} \tilde{v}_O \\ \tilde{\omega}_O \end{Bmatrix} \tag{C.4}$$

where $\tilde{p}_{A_O}$ and $\tilde{h}_{A_O}$ are the global linear and angular added momentum, respectively, and $\tilde{v}_O$ and $\tilde{\omega}_O$ are the general global translational and angular velocity vectors in three dimensions.

C.2 Translations

Translational motions are considered in a global reference frame, with respect to O. The general equation of translational motion is

$$\frac{d}{dt}[\tilde{m}\tilde{v}_O] = \tilde{F}_O \tag{C.5}$$

where the generalized mass matrix $\tilde{m}$ is defined

$$\tilde{m} = m\tilde{I}_D = m\begin{bmatrix} 1 & 0 & 0 \\ 0 & 1 & 0 \\ 0 & 0 & 1 \end{bmatrix} \tag{C.6}$$

Removing the added mass forces, $\tilde{F}_{A_O}$ from the general applied forces, and substituting the inviscid hydrodynamic forces and the viscous drag forces for $\tilde{F}_O$, we have

$$\frac{d}{dt}[\tilde{m}\tilde{v}_O + \tilde{p}_{A_O}] = \tilde{F}_{H_O} + \tilde{F}_{D_O} - \tilde{F}_{A_O} \tag{C.7}$$

Substituting the global linear added momentum and taking the time derivative, we arrive at the final equation of translational motion in vector form.

$$\frac{d}{dt}[\tilde{m}\tilde{v}_O + \tilde{A}_{11}\tilde{v}_O + \tilde{A}_{12}\tilde{\omega}_O] = \tilde{F}_{H_O} + \tilde{F}_{D_O} - \tilde{F}_{A_O} \tag{C.8}$$

$$\tilde{F}_{H_O} + \tilde{F}_{D_O} - \tilde{F}_{A_O} = (\tilde{m} + \tilde{A}_{11})\dot{\tilde{v}}_O + \tilde{A}_{12}\dot{\tilde{\omega}}_O + \dot{\tilde{A}}_{11}\tilde{v}_O + \dot{\tilde{A}}_{12}\tilde{\omega}_O \tag{C.9}$$

C.3 Rotations

Rotational motions are considered in a local reference frame, with respect to o'. The general equation of rotational motion is

$$\frac{d}{dt}[\tilde{I}\tilde{\omega}] = \tilde{M} \tag{C.10}$$

where the inertia matrix $\tilde{I}$ is defined for the time-dependent body shape with respect to o'. Removing the added mass moment $\tilde{M}_A$ from the general applied moments, and substituting the inviscid hydrodynamic moment and the viscous drag moment for $\tilde{M}$, we have

$$\frac{d}{dt}[\tilde{I}\tilde{\omega} + \tilde{h}_A] = \tilde{M}_H + \tilde{M}_D - \tilde{M}_A \tag{C.11}$$

Moments in the local reference frame can be defined in terms of the global reference frame by

$$\tilde{M} = \tilde{M}_O - \tilde{R} \times \tilde{F}_O \tag{C.12}$$

So the local applied moments can be expressed

$$\tilde{M}_H + \tilde{M}_D - \tilde{M}_A = \tilde{M}_{H_O} + \tilde{M}_{D_O} - \tilde{M}_{A_O} - \tilde{R} \times \tilde{F}_{D_O} - \tilde{R} \times \tilde{F}_{H_O} + \tilde{R} \times \tilde{F}_{AO} \tag{C.13}$$

Thus, the rotational equation of motion can be rewritten in terms of forces which are considered with respect to O

$$\tilde{M}_H + \tilde{M}_D - \tilde{M}_A = \frac{d}{dt}[\tilde{I}_O \tilde{\omega}_O + \tilde{h}_{A_O}] - \tilde{R} \times \frac{d}{dt}[\tilde{m}\tilde{v}_O + \tilde{p}_{A_O}] \tag{C.14}$$

Substituting the global added momentum terms and taking the time derivative, we have

$$\begin{aligned} \tilde{M}_H + \tilde{M}_D - \tilde{M}_A = {} & \tilde{A}_{21}\dot{\tilde{v}}_O + (\tilde{A}_{22} + \tilde{I}_O)\dot{\tilde{\omega}}_O + \dot{\tilde{A}}_{21}\tilde{v}_O + (\dot{\tilde{A}}_{22} + \dot{\tilde{I}}_O)\tilde{\omega}_O \\ & - \tilde{R} \times \{(\tilde{m} + \tilde{A}_{11})\dot{\tilde{v}}_O + \tilde{A}_{12}\dot{\tilde{\omega}}_O + \dot{\tilde{A}}_{11}\tilde{v}_O + \dot{\tilde{A}}_{12}\tilde{\omega}_O\} \end{aligned} \tag{C.15}$$

C.4 Time integration

Rewriting the translational and rotational equations of motion:

$$\tilde{F}_{H_O} + \tilde{F}_{D_O} - \tilde{F}_{A_O} = (\tilde{m} + \tilde{A}_{11})\dot{\tilde{v}}_O + \tilde{A}_{12}\dot{\tilde{\omega}}_O + \dot{\tilde{A}}_{11}\tilde{v}_O + \dot{\tilde{A}}_{12}\tilde{\omega}_O \tag{C.16}$$

$$\begin{aligned} \tilde{M}_H + \tilde{M}_D - \tilde{M}_A = {} & \tilde{A}_{21}\dot{\tilde{v}}_O + (\tilde{A}_{22} + \tilde{I}_O)\dot{\tilde{\omega}}_O + \dot{\tilde{A}}_{21}\tilde{v}_O + (\dot{\tilde{A}}_{22} + \dot{\tilde{I}}_O)\tilde{\omega}_O \\ & - \tilde{R} \times \{(\tilde{m} + \tilde{A}_{11})\dot{\tilde{v}}_O + \tilde{A}_{12}\dot{\tilde{\omega}}_O + \dot{\tilde{A}}_{11}\tilde{v}_O + \dot{\tilde{A}}_{12}\tilde{\omega}_O\} \end{aligned} \tag{C.17}$$

We wish to formulation the equations for time integration as

$$\tilde{E}\left\{ \begin{array}{c} \dot{\tilde{v}}_O \\ \dot{\tilde{\omega}}_O \end{array} \right\} = \tilde{q} \tag{C.18}$$

where

$$\tilde{E} = \left(\begin{array}{cc} \{\tilde{m} + \tilde{A}_{11}\} & \{\tilde{A}_{12}\} \\ \{\tilde{A}_{21} - (\tilde{R} \times (\tilde{m} + \tilde{A}_{11}))\} & \{(\tilde{A}_{22} + \tilde{I}_O) - (\tilde{R} \times \tilde{A}_{12})\} \end{array} \right) \tag{C.19}$$

and

$$\tilde{q} = \left\{ \begin{array}{l} \tilde{F}_{H_O} + \tilde{F}_{D_O} - \tilde{F}_{A_O} - \dot{\tilde{A}}_{11}\tilde{v}_O - \dot{\tilde{A}}_{12}\tilde{\omega}_O \\ \tilde{M}_H + \tilde{M}_D - \tilde{M}_A - \{\dot{\tilde{A}}_{21} - (\tilde{R} \times \dot{\tilde{A}}_{11})\}\tilde{v}_O - \{(\dot{\tilde{A}}_{22} + \dot{\tilde{I}}_O) - (\tilde{R} \times \dot{\tilde{A}}_{12})\}\tilde{\omega}_O \end{array} \right\} \tag{C.20}$$

then

$$\left\{ \begin{array}{c} \dot{\tilde{v}}_O \\ \dot{\tilde{\omega}}_O \end{array} \right\} = \tilde{E}^{-1}\tilde{q} \quad \Longrightarrow \quad \frac{d}{dt}\left\{ \begin{array}{c} \tilde{v}_O \\ \tilde{\omega}_O \end{array} \right\} = \tilde{E}^{-1}\tilde{q} \tag{C.21}$$

which can be integrated by Runge-Kutta fourth-order algorithm. The full equations of motion must not only update velocities, but the positions as well, so the full time integrable equation is of the form

$$\frac{d}{dt}\left\{ \begin{array}{c} \tilde{x}_O \\ \tilde{\theta}_O \\ \hline \tilde{v}_O \\ \tilde{\omega}_O \end{array} \right\} = \left\{ \begin{array}{c} \tilde{v}_O \\ \tilde{\omega}_O \\ \hline \\ \tilde{E}^{-1}\tilde{q} \end{array} \right\} \tag{C.22}$$

where all of the three-dimensional vectors and matrices are greatly simplified to two dimensions.

C.5 Added mass forces and moments

Added mass is defined for a rigid body in an unbounded inviscid fluid. For a moving or flexible body shedding a wake due to the presence of a sharp trailing edge, no such concept is defined. However, it is acceptable to describe that external applied momentum which is linearly proportional to the velocity of the body. Thus, some mass of fluid is entrained with the body such that forces acting on the body are caused by the momentum change of this fluid.

The added mass forces and moments have been previously defined to be

$$\tilde{F}_{A_O} = -\frac{d}{dt}\tilde{p}_{A_O} = -(\tilde{A}_{11}\dot{\tilde{v}}_O + \tilde{A}_{12}\dot{\tilde{\omega}}_O + \dot{\tilde{A}}_{11}\tilde{v}_O + \dot{\tilde{A}}_{12}\tilde{\omega}_O) \tag{C.23}$$

$$\tilde{M}_A = -\frac{d}{dt}\tilde{h}_{A_O} + \tilde{R} \times \frac{d}{dt}\tilde{p}_{A_O} \tag{C.24}$$

$$= -(\tilde{A}_{21}\dot{\tilde{v}}_O + \tilde{A}_{22}\dot{\tilde{\omega}}_O + \dot{\tilde{A}}_{21}\tilde{v}_O + \dot{\tilde{A}}_{22}\tilde{\omega}_O)$$

$$+ \tilde{R} \times \{\tilde{A}_{11}\dot{\tilde{v}}_O + \tilde{A}_{12}\dot{\tilde{\omega}}_O + \dot{\tilde{A}}_{11}\tilde{v}_O + \dot{\tilde{A}}_{12}\tilde{\omega}_O\}$$

Substituting these expressions into the expressions for $\tilde{q}$

$$\tilde{q} = \left\{ \begin{array}{l} \tilde{F}_{H_O} + \tilde{F}_{D_O} + \tilde{A}_{11}\dot{\tilde{v}}_O + \tilde{A}_{12}\dot{\tilde{\omega}}_O \\ \tilde{M}_H + \tilde{M}_D + \{\tilde{A}_{21} - (\tilde{R} \times \tilde{A}_{11})\}\dot{\tilde{v}}_O + \{\tilde{A}_{22} - (\tilde{R} \times \tilde{A}_{12})\}\dot{\tilde{\omega}}_O \end{array} \right\} \tag{C.25}$$

Thus, a new system of time integrable equations of motion for the two-dimensional foil is derived. The time derivatives of the velocities are found using a second-order backward difference method, and the time derivatives of the global added mass matrices have been eliminated. The validity of this numeric scheme is assessed through systematic convergence tests employing a variety of lifting and non-lifting bodies in prescribed conservative potential fields.

Appendix D

Constant-dipole panel/vortex ring self-influence equivalence

For a quadrilateral element in arbitrary orientation with a constant doublet strength μ distribution over the surface, the velocity potential at any field point $\phi(x, y, z)$ can be written as an integral over the surface element geometry S as

$$\phi(x,y,z) = \frac{-\mu}{4\pi} \int_S \frac{(z - z_0)\, dS}{[(x - x_0)^2 + (y - y_0)^2 + (z - z_0)^2]^{3/2}} \tag{D.1}$$

The integral for this potential is the same integral as the normal velocity component for the quadrilateral source [99]. If the quadrilateral panel is assumed to lie in the xy-plane, by integrating over S and then differentiating to find the vertical velocity w, we obtain:

$$\begin{aligned} w \;=\; & \frac{\mu}{4\pi}\Bigg[\frac{[(x-x_2)(y-y_1)-(x-x_1)(y-y_2)](r_1+r_2)}{r_1 r_2\{r_1 r_2 - [(x-x_1)(x-x_2)+(y-y_1)(y-y_2)+z^2]\}} \\ & + \frac{[(x-x_3)(y-y_2)-(x-x_2)(y-y_3)](r_2+r_3)}{r_2 r_3\{r_2 r_3 - [(x-x_2)(x-x_3)+(y-y_2)(y-y_3)+z^2]\}} \\ & + \frac{[(x-x_4)(y-y_3)-(x-x_3)(y-y_4)](r_3+r_4)}{r_3 r_4\{r_3 r_4 - [(x-x_3)(x-x_4)+(y-y_3)(y-y_4)+z^2]\}} \\ & + \frac{[(x-x_1)(y-y_4)-(x-x_4)(y-y_1)](r_4+r_1)}{r_4 r_1\{r_4 r_1 - [(x-x_4)(x-x_1)+(y-y_4)(y-y_1)+z^2]\}}\Bigg] \end{aligned}$$

where x_i refers to corner i of the quadrilateral panel, and r_i is the linear distance between the field point x and the corner x_i. As $z \to 0$, and field point approaches the panel, much in the manner a collocation point is determined, and the tangential velocity components u and v vanish. In this case, w simplifies to

$$\begin{aligned} w &= \frac{\mu}{4\pi}\Big[\frac{[(x-x_2)(y-y_1)-(x-x_1)(y-y_2)](r_1+r_2)}{r_1r_2\{r_1r_2-[(x-x_1)(x-x_2)+(y-y_1)(y-y_2)]\}} \\ &+ \frac{[(x-x_3)(y-y_2)-(x-x_2)(y-y_3)](r_2+r_3)}{r_2r_3\{r_2r_3-[(x-x_2)(x-x_3)+(y-y_2)(y-y_3)]\}} \\ &+ \frac{[(x-x_4)(y-y_3)-(x-x_3)(y-y_4)](r_3+r_4)}{r_3r_4\{r_3r_4-[(x-x_3)(x-x_4)+(y-y_3)(y-y_4)]\}} \\ &+ \frac{[(x-x_1)(y-y_4)-(x-x_4)(y-y_1)](r_4+r_1)}{r_4r_1\{r_4r_1-[(x-x_4)(x-x_1)+(y-y_4)(y-y_1)]\}}\Big] \end{aligned}$$

Considering now a vortex ring bounding a region along the perimeter C of the area occupied by the same doublet panel S. The four vortex segments constituting this ring are assigned constant circulation Γ. The velocity $\vec{v}(\vec{x})$ distribution due to this vortex ring can be found by the Biot-Savart Law:

$$\vec{x}(\vec{x}) = \frac{\Gamma}{4\pi}\int_C \frac{d\vec{\ell}\times\vec{r}}{r^3} \tag{D.2}$$

For $d\vec{\ell} = [dx_0, dy_0]$ and $\vec{r} = [x-x_0, y-y_0, z]$, this can be rewritten

$$\vec{v}(\vec{x}) = \frac{\Gamma}{4\pi}\int_C \Big\{\hat{i}\frac{z}{r^3}dy_0 - \hat{j}\frac{z}{r^3}dx_0 + \hat{k}[(y-y_0)dx_0 - (x-x_0)dy_0]\Big\} \tag{D.3}$$

Then using Stokes' theorem on the above expression and allowing $z \to 0$, we can show that the expression reduces to the identical normal velocity expression as for the constant-strength dipole panel.

$$\vec{v}(\vec{x}) = \frac{\Gamma}{4\pi}\int_S -\hat{k}\Big(\frac{\partial}{\partial x_0}\frac{x-x_0}{r^3} + \frac{\partial}{\partial y_0}\frac{y-y_0}{r^3}\Big)\,dS \tag{D.4}$$

leading to

$$
\begin{aligned}
w \;=\; & \frac{\mu}{4\pi}\Bigg[\frac{[(x-x_2)(y-y_1)-(x-x_1)(y-y_2)](r_1+r_2)}{r_1r_2\{r_1r_2-[(x-x_1)(x-x_2)+(y-y_1)(y-y_2)]\}} \\
& + \frac{[(x-x_3)(y-y_2)-(x-x_2)(y-y_3)](r_2+r_3)}{r_2r_3\{r_2r_3-[(x-x_2)(x-x_3)+(y-y_2)(y-y_3)]\}} \\
& + \frac{[(x-x_4)(y-y_3)-(x-x_3)(y-y_4)](r_3+r_4)}{r_3r_4\{r_3r_4-[(x-x_3)(x-x_4)+(y-y_3)(y-y_4)]\}} \\
& + \frac{[(x-x_1)(y-y_4)-(x-x_4)(y-y_1)](r_4+r_1)}{r_4r_1\{r_4r_1-[(x-x_4)(x-x_1)+(y-y_4)(y-y_1)]\}}\Bigg]
\end{aligned}
$$

This expression contains no singular terms as long as the field point does not approach the perimeter or corners of the panel area S. Thus, for centrally-located collocation points and a sufficiently robust numerical algorithm, self-influence coefficients for the velocity influence of a normal dipole sheet should not cause solution instability.

By similar analysis, it can be easily shown that a semi-infinite constant dipole panel of strength μ with width s is equivalent to a "horseshoe" vortex with width s on the perimeter of the semi-infinite constant dipole panel, with circulation $\Gamma = \mu$. Hess [85] presents a derivation to relate a general surface doublet distribution to the corresponding surface vortex distribution, effectively reducing the order of the singularity distribution. However, care must be taken in determining the self-influence for the general doublet distribution, as explained previously, and explored in detail by various other investigators [144, 79, 143].

Appendix E

Vorticity impulse

E.1 Derivation

Lamb [119] described the impulse of a fluid in Article **8** and the impulse and energy of a vorticity field $\vec{\omega} = [\xi, \eta, \zeta]$ in Article **152**. The individual components of impulse $\vec{P} = [P, Q, R]$ can be written:

$$P = \frac{1}{2}\rho \iiint_V (y\zeta - z\eta)\, dx\, dy\, dz \tag{E.1}$$

$$Q = \frac{1}{2}\rho \iiint_V (z\xi - x\zeta)\, dx\, dy\, dz \tag{E.2}$$

$$R = \frac{1}{2}\rho \iiint_V (x\eta - y\xi)\, dx\, dy\, dz \tag{E.3}$$

This was generalized by Batchelor [23] in §**7.2** for flow in an unbounded fluid at rest in the far field.

$$\vec{P} = \frac{1}{2}\rho \iiint_V \vec{x} \times \vec{\omega}\, dV(\vec{x}) \tag{E.4}$$

The force required to generate this motion from rest is

$$\frac{d\vec{P}}{dt} = \frac{1}{2}\rho \frac{D}{Dt} \iiint_V \vec{x} \times \vec{\omega}\, dV(\vec{x}) \tag{E.5}$$

Defining the fluid volume as two simply-connected regions, R_1 and R_2, with R_2 completed contained in R_1, we can express the total change in momentum in the fluid

volume as the sum of the contribution from the two regions:

$$\frac{d\vec{P}}{dt} = \frac{1}{2}\rho\frac{D}{Dt}\iiint_{R_1} \vec{x}\times\vec{\omega}\,dV(\vec{x}) \;+\; \frac{1}{2}\rho\frac{D}{Dt}\iiint_{R_2} \vec{x}\times\vec{\omega}\,dV(\vec{x}) \tag{E.6}$$

Expand the expression for vorticity ω in terms of velocity $\vec{v}$ in the smaller region R_2:

$$\frac{1}{2}\rho\frac{D}{Dt}\iiint_{R_2} \vec{x}\times\vec{\omega}\,dV(\vec{x}) \;=\; \frac{1}{2}\rho\frac{D}{Dt}\iiint_{R_2} \vec{x}\times(\vec{\nabla}\times\vec{v})\,dV(\vec{x}) \tag{E.7}$$

Using a vector identity listed in Hildebrand [88] §**6.9**, Green's First Identity can be employed in the region R_2 to transform the volumetric integral into an integral over the boundary S_2 of region R_2 with outward pointing normal $\hat{n}$.

$$\frac{1}{2}\rho\frac{D}{Dt}\iiint_{R_2} \vec{x}\times(\vec{\nabla}\times\vec{v})\,dV(\vec{x}) \;=\; -\frac{1}{2}\rho\frac{D}{Dt}\iint_{S_2} \vec{x}\times(\hat{n}\times\vec{v})\,dS(\vec{x}) \tag{E.8}$$

Thus, the total time rate change of momentum in the fluid volume can be written as:

$$\frac{d\vec{P}}{dt} = \frac{1}{2}\rho\frac{D}{Dt}\iiint_{R_1} \vec{x}\times\vec{\omega}\,dV(\vec{x}) \;-\; \frac{1}{2}\rho\frac{D}{Dt}\iint_{S_2} \vec{x}\times(\hat{n}\times\vec{v})\,dS(\vec{x}) \tag{E.9}$$

The force sustained on the body, which is now defined to be occupying the smaller region R_2, is opposite to that force applied to the fluid; this is the generalized force presented by Wu & Wu [238] in §**6.A**:

$$F_B = -\frac{\rho}{d-1}\frac{D}{Dt}\iiint_{R_1} \vec{x}\times\vec{\omega}\,dV(\vec{x}) \;+\; \frac{\rho}{d-1}\frac{D}{Dt}\iint_{S_2} \vec{x}\times(\hat{n}\times\vec{v})\,dS(\vec{x}) \tag{E.10}$$

where $d = 2$ for a two-dimensional flow and $d = 3$ for a three-dimensional flow, reproducing the form above. Note that the second term would vanish for a "no-slip" kinematic boundary condition on the body.

E.2 Evaluation

To simplify the expression, Batchelor citebatchelor:67 in §**7.1** notes that the curl of the inviscid Euler equations leads to a form of the vorticity equation:

$$\frac{\partial \vec{\omega}}{\partial t} = \vec{\nabla} \times (\vec{v} \times \vec{v}) \tag{E.11}$$

So, if the volumes are rigid and not moving, the force can be rewritten:

$$F_B = -\frac{\rho}{d-1} \iiint_{R_1} \vec{x} \times (\vec{\nabla} \times (\vec{v} \times \vec{\omega}))\, dV(\vec{x}) + \frac{\rho}{d-1} \iint_{S_2} \vec{x} \times (\hat{n} \times \frac{\partial \vec{v}}{\partial t})\, dS(\vec{x}) \tag{E.12}$$

In a fluid where a distribution of vorticity $\vec{\omega}$ is the known variable, evaluation of the above expression requires knowledge of the Eulerian fields describing fluid velocity and fluid acceleration. These can be found from the Biot-Savart Law. Assuming an incompressible fluid, the vorticity can be written as the curl of the velocity field, $\vec{\omega} = \vec{\nabla} \times \vec{v}$, and the velocity field can be described as the curl of a stream function, $\vec{v} = \vec{\nabla} \times \vec{\psi}$. Thus, the stream function $\vec{\psi}$ satisfies the Poisson operator for the vorticity vector $\vec{\omega}$.

$$-\vec{\nabla}^2 \vec{\psi} = \vec{\omega} \tag{E.13}$$

and the stream function $\vec{\psi}$ can be written as a integral of the vorticity $\vec{\omega}$ times a Green's function kernel, from which the velocity $\vec{v}$ and Eulerian fluid acceleration $\partial \vec{v}/\partial t$ can be found.

$$\vec{\psi}(\vec{\zeta}) = \frac{1}{4\pi} \iiint_V \frac{\vec{\omega}(\vec{\zeta}')}{|\vec{\zeta} - \vec{\zeta}'|}\, dV(\vec{\zeta}') \tag{E.14}$$

$$\vec{v}(\vec{\zeta}) = \frac{1}{4\pi} \iiint_V \vec{\nabla} \times \frac{\vec{\omega}(\vec{\zeta}')}{|\vec{\zeta} - \vec{\zeta}'|}\, dV(\vec{\zeta}') \tag{E.15}$$

$$\frac{\partial \vec{v}(\vec{\zeta})}{\partial t} = -\frac{1}{4\pi} \iiint_V \frac{(\vec{\zeta} - \vec{\zeta}') \times \partial \vec{\omega}(\vec{\zeta}')/\partial t}{|\vec{\zeta} - \vec{\zeta}'|^3}\, dV(\vec{\zeta}') \tag{E.16}$$

and letting $\vec{r} = \vec{\zeta} - \vec{\zeta}'$, these expressions for $\vec{v}$ and $\partial\vec{v}/\partial t$ can be simplified

$$\vec{v}(\vec{\zeta}) = -\frac{1}{4\pi}\iiint_V \frac{\vec{r}\times\vec{\omega}(\vec{\zeta}')}{|\vec{r}|^3}\,dV(\vec{\zeta}') \tag{E.17}$$

$$\frac{\partial\vec{v}(\vec{\zeta})}{\partial t} = -\frac{1}{4\pi}\iiint_V \frac{\vec{r}\times(\vec{\nabla}\times(\vec{v}(\vec{\zeta}')\times\vec{\omega}(\vec{\zeta}')))}{|\vec{r}|^3}\,dV(\vec{\zeta}') \tag{E.18}$$

These expressions for $\vec{v}$ and $\partial\vec{v}/\partial t$ are substituted into the equation (E.12) for the force on the body F_B. Calculation of this force therefore relies on knowledge of the velocity, vorticity, and acceleration vector fields in order to evaluate the integrals over the entire fluid. Indeed, the calculation first requires an integral over the *entire* fluid for *each* point at which the velocity and acceleration are to be found, and then an integral again over the entire fluid to find the force. Numerical evaluation of equations (E.12) and (E.18) may be simplified if the following vector identity is employed:

$$\vec{\nabla}\times(\vec{v}\times\vec{\omega}) = (\vec{\omega}\cdot\vec{\nabla})\vec{v} - (\vec{v}\cdot\vec{\nabla})\vec{\omega} \tag{E.19}$$

E.3 Coordinate System Invariance

From equation (E.5) we can examine the dependence of the value of the integral on the location of the origin with respect to the volume of integration. Let

$$\vec{X} = \vec{x} + \vec{x_o} \tag{E.20}$$

where x_o is some constant. Then the total force on the fluid to bring it to some motion from rest can be written

$$\frac{d\vec{P}}{dt} = \frac{1}{2}\rho\frac{D}{Dt}\iiint_V \vec{X}\times\vec{\omega}\,dV(\vec{x}) \tag{E.21}$$

and we can write out the expressions for $\vec{X}\times\vec{\omega}$ as

$$\vec{X}\times\vec{\omega} = [(x+x_o),(y+y_o),(z+z_o)]\times[\omega_x,\omega_y,\omega_z] \tag{E.22}$$

$$\vec{X} \times \vec{\omega} = [(\omega_z(y+y_o) - \omega_y(z+z_o)), (\omega_x(z+z_o) - \omega_z(x+x_o)), (\omega_y(x+x_o) - \omega_x(y+y_o))] \tag{E.23}$$

Therefore, the two position vector cross products can be separated.

$$\vec{X} \times \vec{\omega} = (\vec{x} \times \vec{\omega}) + (\vec{x_o} \times \vec{\omega}) \tag{E.24}$$

If we now examine the integral over the fluid employing the constant vector x_o, we would like this contribution to go to zero for arbitrary variance.

$$\frac{D}{Dt}\int\int\int_V \vec{x_o} \times \vec{\omega}\, dV(\vec{x}) \;=\; \frac{D}{Dt}\int\int\int_V \vec{x_o} \times (\vec{\nabla} \times \vec{v})\, dV(\vec{x}) \tag{E.25}$$

Using the same vector identity employed for equation (E.9) from Hildebrand [88]§**6.9**, Green's First Identity allows the above equation to be rewritten

$$\frac{D}{Dt}\int\int\int_V \vec{x_o} \times (\vec{\nabla} \times \vec{v})\, dV(\vec{x}) \;=\; \frac{D}{Dt}\int\int_S \vec{x_o} \times (\hat{n} \times \vec{v})\, dS(\vec{x}) \tag{E.26}$$

If we take the velocity vector to have normal, tangential, and bi-normal components

$$\vec{v} = [V_n\hat{n}, V_t\hat{t}, V_b\hat{b}] \tag{E.27}$$

we can rewrite the integral as

$$\frac{D}{Dt}\int\int_S \vec{x_o} \times (\hat{n} \times \vec{v})\, dS(\vec{x}) \;=\; \frac{D}{Dt}\int\int_S \vec{x_o} \times [V_t(\hat{n} \times \hat{t}) + V_b(\hat{n} \times \hat{b})]\, dS(\vec{x}) \tag{E.28}$$

Noting that the cross product of two unit vectors yields the third, and that $\vec{x_o}$ is constant and may be pulled out of the integral, we can rewrite the expression as

$$\frac{D}{Dt}\int\int_S \vec{x_o} \times [V_t\hat{b} + V_b\hat{t}]\, dS(\vec{x}) \;=\; \frac{D}{Dt}\left[\vec{x_o} \times C_1 + \vec{x_o} \times C_2\right] \tag{E.29}$$

$$C_1 \;=\; \int\int_S V_t\hat{b}\, dS(\vec{x}) \tag{E.30}$$

$$C_2 \;=\; \int\int_S V_b\hat{t}\, dS(\vec{x}) \tag{E.31}$$

Thus, if C_1 and C_2 are invariant with time:

$$\frac{D}{Dt}\left[\vec{x_o} \times (C_1 + C_2)\right] = 0 \tag{E.32}$$

$$\frac{d\vec{P}}{dt} = \frac{1}{2}\rho\frac{D}{Dt}\iiint_V \vec{x_o} \times \vec{\omega}\, dV(\vec{x}) = 0 \tag{E.33}$$

So, in order for the vortex impulse force calculation to be coordinate system invariant, C_1 and C_2 must be temporally invariant, or must be subject to the conditions Kelvin's Theorem, i.e. the flow must be an ideal fluid which is subject only to conservative body forces, and the contours of integration must be material surfaces.

Bibliography

[1] I. Abbott and A. von Doenhoff. *Theory of wing sections: Including a summary of airfoil data.* Dover Publications, Inc., New York, 1959.

[2] M. Acharya and M. Metwally. Unsteady pressure field and vorticity production over a pitching airfoil. *AIAA Journal*, 30(2):403–411, 1992.

[3] R. Adrian. Multi-point optical measurements of simultaneous vectors in unsteady flow: A review. *International Journal of Heat Fluid Flow*, 7:127–145, 1986.

[4] R. Adrian. Particle-imaging techniques for experimental fluid mechanics. *Annual Review of Fluid Mechanics*, 23:262–304, 1991.

[5] B. Ahlborn, S. Chapman, R. Stafford, R. Blake, and D. Harper. Experimental simulation of the thrust phases of fast-start swimming of fish. *Journal of Experimental Biology*, 200:2301–2312, 1997.

[6] B. Ahlborn, D. Harper, R. Blake, D. Ahlborn, and M. Cam. Fish without footprints. *Journal of Theoretical Biology*, 148:521–533, 1991.

[7] Y. Aleyev. *Nekton.* Dr. W. Junk b.v., Publishers, The Hague, Netherlands, 1977.

[8] D. Ames. Shear flow visualization at high Reynolds numbers. Master's thesis, Massachusetts Institute of Technology, Department of Ocean Engineering, Cambridge, MA, 1998.

[9] J. Anderson. *Vorticity control for efficient propulsion.* PhD dissertation, Massachusetts Institute of Technology and the Woods Hole Oceanographic Institution, Department of Ocean Engineering, 1996.

[10] J. Anderson, K. Streitlien, D. Barrett, and M. Triantafyllou. Oscillating foils of high propulsive efficiency. *Journal of Fluid Mechanics*, 360:41–72, 1998.

[11] H. Aref. Motion of three vortices. *Physics of Fluids*, 22(3):393–400, 1979.

[12] H. Aref. Integrable, chaotic, and turbulent vortex motion in two-dimensional flows. *Annual Review of Fluid Mechanics*, 15:345–389, 1983.

[13] H. Asada and J. Slotine. *Robot analysis and control.* Wiley-Interscience Publication, John Wiley and Sons, New York, 1986.

[14] H. Ashley and M. Landahl. *Aerodynamics of wings and bodies.* Dover Publications, New York, 1965.

[15] E. Atta, O. Kandil, D. Mook, and A. Nayfeh. Unsteady aerodynamics loads on arbitrary wings including wing-tip and leading-edge separation. Technical Paper 77-156, AIAA, 1977.

[16] R. Bainbridge. Caudal fin and body movement in the propulsion of some fish. *Journal of Experimental Biology*, 40:23–56, 1963.

[17] P. Bandyopadhyay, J. Castano, J. Rice, R. Philips, W. Nedderman, and W. Macy. Low-speed maneuvering hydrodynamics of fish and small underwater vehicles. *ASME Journal of Fluids Engineering*, 119:136–144, 1997.

[18] D. Barrett. The design of a flexible hull undersea vehicle propelled by an oscillating foil. Master's thesis, Massachusetts Institute of Technology, Department of Ocean Engineering, 1994.

[19] D. Barrett. *Propulsive efficiency of a flexible hull underwater vehicle.* PhD dissertation, Massachusetts Institute of Technology, Department of Ocean Engineering, 1996.

[20] D. Barrett and M. Triantafyllou. The design of a flexible hull undersea vehicle propelled by an oscillating foil. In 9th *International Symposium on Unmanned Untethered Submersible Technology*, 1995.

[21] D. Barrett, M. Triantafyllou, D. Yue, M. Grosenbaugh, and M. Wolfgang. Drag reduction in fish-like locomotion. *Journal of Fluid Mechanics*, 1999. In press.

[22] B. Basu and G. Hancock. The unsteady motion of a two-dimensional aerofoil in incompressible inviscid flow. *Journal of Fluid Mechanics*, 87:159–178, 1978.

[23] G. Batchelor. *An introduction to fluid dynamics.* Cambridge University Press, Cambridge, U.K., 1967.

[24] R. Bisplinghoff and H. Ashley. *Principles of Aeroelasticity.* Dover Publications, New York, 1962.

[25] S. Black. *Integrated lifting-surface/Navier-Stokes design and analysis methods for marine propulsors.* PhD dissertation, Massachusetts Institute of Technology, Department of Ocean Engineering, 1997.

[26] R. Blake. *Fish locomotion.* Cambridge University Press, Cambridge, U.K., 1983.

[27] N. Bose and J. Lien. Propulsion of a fin whale (*balaenoptera physalus*): Why the whale is a fast swimmer. *Proceedings of the Royal Society of London* **B**, 237:175–200, 1989.

[28] N. Bose and J. Lien. Energy absorption from ocean waves: A free ride for cetaceans. *Proceedings of the Royal Society of London* **B**, 240:591–605, 1990.

[29] C. Breder. The locomotion of fishes. *Zoologica*, 4:159–256, 1926.

[30] C. Brown and W. Michael. Effect of leading edge separation on the lift of a delta wing. *Journal of Aeronautical Sciences*, pages 690–694, 1954.

[31] C. Brown and W. Michael. On delta wings with leading-edge separation. Technical Note 3430, NACA, 1955.

[32] A. Bryson and Y. Ho. *Applied optimal control: Optimization, estimation, and control.* Hemisphere Publishing Corporation, Washington, D.C., 1975.

[33] J. Carling, T. Williams, and G. Bowtell. Self-propelled anguilliform swimming: Simultaneous solution of the two-dimensional Navier-Stokes equations and Newton's laws of motion. *Journal of Experimental Biology*, 201:3143–3166, 1998.

[34] H. Cheng and L. Murillo. Lunate-tail swimming propulsion as a problem of curved lifting line in unsteady flow. Part 1. Asymptotic theory. *Journal of Fluid Mechanics*, 143:327–350, 1984.

[35] J. Cheng and R. Blickhan. Note on the calculation of propeller efficiency using elongated body theory. *Journal of Experimental Biology*, 192:169–177, 1994.

[36] J. Cheng, L. Zhuang, and B. Tong. Analysis of swimming of three-dimensional waving plates. *Journal of Fluid Mechanics*, 232:341–355, 1991.

[37] S. Childress. *Mechanics of swimming and flying.* Courant Institute of Mathematical Sciences, New York University, New York, NY, 1977.

[38] M. Chopra. Hydromechanics of lunate-tail swimming propulsion. *Journal of Fluid Mechanics*, 64:375–391, 1974.

[39] M. Chopra. Large-amplitude lunate-tail theory of fish locomotion. *Journal of Fluid Mechanics*, 74:161–182, 1976.

[40] M. Chopra and T. Kambe. Hydromechanics of lunate-tail swimming propulsion. Part 2. *Journal of Fluid Mechanics*, 79:49–69, 1977.

[41] C. Chow and M. Huang. The initial lift and drag of an impulsively started airfoil of finite thickness. *Journal of Fluid Mechanics*, 118:393–409, 1982.

[42] K. Chua and T. Quackenbush. Fast three-dimensional vortex methods for unsteady wake calculations. *AIAA Journal*, 31(10):1957–1958, 1993.

[43] R. Coene. The swimming of slender fish-like bodies in waves. In T. Wu, C. Brokaw, and C. Brennan, editors, *Proceedings of the symposium on swimming and flying in nature: Volume 2*, pages 673–686. Plenum Press, New York, July 1975.

[44] L. Cortelezzi. On the unsteady separated flow past a semi-infinite plate: Exact solution of the Brown and Michael model, scaling, and universality. *Physics of Fluids*, 7(3):526–529, 1995.

[45] B. Culik, R. Wilson, and R. Bannasch. Underwater swimming at low energetic cost by pygoscelid penguins. *Journal of Experimental Biology*, 197:65–78, 1994.

[46] J. Czarnowski. Exploring the possibility of placing traditional marine vehicles under oscillating foil propulsion. Master's thesis, Massachusetts Institute of Technology, Department of Ocean Engineering, Cambridge, MA, 1997.

[47] H. Dewar. *Studies of tropical tuna swimming performance: thermoregulation, swimming mechanics, and energetics.* PhD dissertation, University of California, San Diego, Physiological Research Laboratory, Scripps Institute of Oceanography, 1993.

[48] H. Dewar and J. Graham. Studies of tropical tuna swimming performance in a large water tunnel. III. Kinematics. *Journal of Experimental Biology*, 192:45–59, 1994.

[49] H. Dewar and J. Graham. Studies of tropical tuna swimming performance in a large water tunnel. I. Energetics. *Journal of Experimental Biology*, 192:13–31, 1994.

[50] H. Dewar, J. Graham, and R. Brill. Studies of tropical tuna swimming performance in a large water tunnel. II. Thermoregulation. *Journal of Experimental Biology*, 192:33–44, 1994.

[51] P. Domenici and R. Blake. Review: The kinematics and performance of fish fast-start swimming. *Journal of Experimental Biology*, 200:1165–1178, 1997.

[52] E. Dowell, E. Crawley, H. Curtiss, D. Peters, R. Scanlan, and F. Sisto. *A modern course in aeroelasticity.* Kluwer Academic Publishers, Boston, 1995.

[53] C. Ellington. The aerodynamics of hovering insect flight. IV. Aerodynamic mechanisms. *Phil. Tran. Royal Society of London* **B**, 305:79–113, 1984.

[54] C. Ellington, C. van den Berg, and A. Thomas. Leading edge vortices in insect flight. *Nature*, 384:626, 1996.

[55] J. Fein. Dolphin drag reduction: Myth or magic. In *Proceedings of the International Symposium on Seawater Drag Reduction*, pages 429–433, Newport, RI, July 1998. ONR, NSSC, DARPA, NSWC, ASME, and NUWC.

[56] J. Ffowcs-Williams and B. Zhao. The active control of vortex shedding. *Journal of Fluids and Structures*, 3:115–122, 1989.

[57] H. Fierstine and V. Walters. Studies in locomotion and anatomy of scombroid fishes. *Memoir of the Southern California Academy of Sciences*, 6:1–31, 1968.

[58] P. Fink and W. Soh. Calculation of vortex sheets in unsteady flow and applications in ship hydrodynamics. In *Proceedings of the* 10^{th} *symposium on naval hydrodynamics*, pages 463–488, Cambridge, MA, 1974.

[59] F. Fish. Power output and propulsive efficiency of swimming bottlenose dolphins (*tursiops truncatus*). *Journal of Experimental Biology*, 185:179–193, 1993.

[60] F. Fish. Comparative kinematics and hydrodynamics of odontocete cetaceans: Morphological and ecological correlates with swimming performance. *Journal of Experimental Biology*, 201:2867–2877, 1998.

[61] H. Frith and R. Blake. The mechanical power output and hydromechanical efficiency of northern pike (*esox lucius*) fast-starts. *Journal of Experimental Biology*, 198:1863–1873, 1995.

[62] M. Gad-el-Hak and D. Bushnell. Separation control: Review. *ASME Journal of Fluids Engineering*, 113:5–30, 1991.

[63] M. Gad-el-Hak and C. Ho. Unsteady vortical flow around three-dimensional lifting surfaces. *AIAA Journal*, 24:713–721, 1986.

[64] M. Gharib, E. Rambod, and K. Shariff. A universal time scale for vortex ring formation. *Journal of Fluid Mechanics*, 360:121–140, 1998.

[65] J. Giesing. Nonlinear two-dimensional unsteady potential flow with lift. *Journal of Aircraft*, 5(3):135–143, 1968.

[66] H. Glauert. The force and moment on an oscillating aerofoil. Technical Report 1242, Aerospace Research Commission, 1929.

[67] D. Goldberg. *Genetic algorithms in search, optimization, and machine learning.* Addison-Wesley, Reading, MA, 1989.

[68] R. Gopalkrishnan, M. Triantafyllou, G. Triantafyllou, and D. Barrett. Active vorticity control in a shear flow using a flapping foil. *Journal of Fluid Mechanics*, 274:1–21, 1994.

[69] J. Graham. Vortex shedding from sharp edges. I.C. Aero Report 77-06, Imperial College of Science and Technology, 1977.

[70] J. Graham. The forces on sharp-edged cylinders in oscillatory flow at low Keulegan-Carpenter numbers. *Journal of Fluid Mechanics*, 97:331–346, 1980.

[71] J. Graham. The lift on an aerofoil in starting flow. *Journal of Fluid Mechanics*, 133:413–425, 1983.

[72] J. Gray. Studies in animal locomotion: I. The movement of fish with special reference to eel. *Journal of Experimental Biology*, 10(1):88–104, 1933.

[73] J. Gray. Studies in animal locomotion: II. The relationship between waves of muscular contraction and the propulsive mechanism of the eel. *Journal of Experimental Biology*, 10(4):386–400, 1933.

[74] J. Gray. Studies in animal locomotion: IV. The neuromuscular mechanism of swimming in the eel. *Journal of Experimental Biology*, 13(2):170–180, 1936.

[75] J. Gray. Studies in animal locomotion: V. Resistance reflexes in the eel. *Journal of Experimental Biology*, 13(2):181–190, 1936.

[76] J. Gray. Studies in animal locomotion: VI. The propulsive powers of the dolphin. *Journal of Experimental Biology*, 13(2):192–199, 1936.

[77] J. Gray. *Animal locomotion.* Weidenfield and Nicolson, London, 1968.

[78] J. Gray and A. Sand. The locomotory rhythm of the dogfish *scyllium canicula*. *Journal of Experimental Biology*, 13(2):200–209, 1936.

[79] M. Guiggiani, G. Krishnasamy, T. Rudolph, and F. Rizzo. A general algorithm for the numerical solution of hypersingular boundary integral equations. *Journal of Applied Mechanics*, 59:604–614, 1992.

[80] I. Gursul and C. Ho. High aerodynamic loads on an airfoil submerged in an unsteady stream. *AIAA Journal*, 30:1117–1119, 1992.

[81] D. Harper and R. Blake. Fast start performance of rainbow trout *salmo gairdneri* and northern pike *esox lucius* during escapes. *Journal of Experimental Biology*, 150:321–342, 1990.

[82] D. Harper and R. Blake. Prey capture and the fast-start performance of northern pike (*esox lucius*). *Journal of Experimental Biology*, 155:175–192, 1991.

[83] D. Hart, A. Acosta, and A. Leonard. Observation of cavitation and wake structure of unsteady tip vortex flows. In *Proceedings of the international STG symposium on propulsors and cavitation*, pages 121–127, Hamburg, Germany, June 1992.

[84] H. Hertel. *Structure, form, and movement.* Reinhold Publishing Corporation, New York, 1966.

[85] J. Hess. Calculation of potential flow about arbitrary three-dimensional lifting bodies. Final Technical Report MDC J5679-01, McDonnell Douglas, Long Beach, CA, 1972.

[86] J. Hess and A. Smith. Calculation of non-lifting potential flow about arbitrary three-dimensional bodies. *Journal of Ship Research*, 8(2):22–42, 1964.

[87] J. Hess and A. Smith. Calculation of potential flow about arbitrary bodies. *Progress in Aeronautical Sciences*, 8:1–138, 1967.

[88] F. Hildebrand. *Advanced calculus for applications.* Prentice-Hall, Inc., Englewood Cliffs, NJ, 1976.

[89] C. Hirsch. *Numerical Computation of internal and external flows. Volume 1: Fundamentals of numerical discretization.* Wiley-Interscience Series in Numerical Methods in Engineering. John Wiley and Sons, Chichester, U.K., 1988.

[90] C. Hirsch. *Numerical Computation of internal and external flows. Volume 2: Computational methods for inviscid and viscous flows.* Wiley-Interscience Series in Numerical Methods in Engineering. John Wiley and Sons, Chichester, U.K., 1990.

[91] H. Hoeijmakers and W. Vaatstra. A higher order panel method applied to vortex sheet roll-up. *AIAA Journal*, 21:516–523, 1983.

[92] S. Hoerner. *Fluid-dynamic drag.* Hoerner Fluid Dynamics, Vancouver, Washington, 1965.

[93] S. Hoerner. *Fluid-dynamic lift.* Hoerner Fluid Dynamics, Vancouver, Washington, 1985.

[94] J. Hoyt. Hydrodynamic drag reduction due to fish slimes. In T. Wu, C. Brokaw, and C. Brennan, editors, *Proceedings of the symposium on swimming and flying in nature: Volume 2*, pages 653–672, New York, July 1975. Plenum Press.

[95] C. Hsin. *Development and analysis of panel methods for propellers in unsteady flow.* PhD dissertation, Massachusetts Institute of Technology, Department of Ocean Engineering, Cambridge, MA, 1990.

[96] H. Kagemoto. Design of an artificial fish. Department of ocean engineering technical report, Massachusetts Institute of Technology, 1997.

[97] H. Kagemoto, M. Wolfgang, D. Yue, and M. Triantafyllou. Force and power estimation in fish-like locomotion using a vortex-lattice method. *Journal of Fluids Engineering*, 1999. *Sub judis.*

[98] G. Karpouzian, G. Spedding, and H. Cheng. Lunate-tail swimming propulsion. Part 2. Performance analysis. *Journal of Fluid Mechanics*, 210:329–354, 1990.

[99] J. Katz and A. Plotkin. *Low-speed aerodynamics: From wing theory to panel methods.* Aeronautical and Aerospace Engineering. McGraw-Hill, Inc., New York, NY, 1991.

[100] J. Katz and D. Weihs. Behavior of vortex wakes from oscillatory airfoils. *Journal of Aircraft*, 15(12), 1978.

[101] J. Katz and D. Weihs. Hydrodynamic propulsion by large amplitude oscillation of an airfoil with chordwise flexibility. *Journal of Fluid Mechanics*, 88(3):485–497, 1978.

[102] J. Katz and D. Weihs. Large amplitude unsteady motion of a flexible slender propulsor. *Journal of Fluid Mechanics*, 90(4):713–723, 1979.

[103] J. Katz and D. Weihs. Wake rollup and the Kutta condition for airfoils oscillating at high frequency. *AIAA Journal*, 19(12):1604–1606, 1981.

[104] J. Katz and D. Weihs. The effect of chordwise flexibility on the lift of a rapidly accelerated airfoil. *Aeronautical Quarterly*, pages 360–369, February 1989.

[105] J. Kerwin. Hydrofoils and propellers. Lecture Notes 13.04, Massachusetts Institute of Technology, Department of Ocean Engineering, 1995.

[106] H. Khalil. *Nonlinear systems.* Macmillan Publishing Company, New York, 1992.

[107] S. Kinnas and C. Hsin. Boundary element method for the analysis of the unsteady flow around extreme propeller geometries. *AIAA Journal*, 30(3):688–696, 1992.

[108] S. Kinnas and C. Hsin. The local error of a low-order boundary element method at the trailing edge of a hydrofoil and its effect on the global solution. *Computers and Fluids*, 23(1):63–75, 1994.

[109] J. Kitchell, W. Neill, A. Dizon, and J. Magnuson. Bioenergetic spectra of skipjack and yellowfin tunas. In G. Sharp and A. Dizon, editors, *The physiological ecology of tunas*, pages 357–368. Academic Press, New York, 1978.

[110] O. Knio and A. Ghoniem. Numerical study of a three-dimensional vortex method. *Journal of Computational Physics*, 86(1):75–106, 1990.

[111] O. Knio and A. Ghoniem. Three-dimensional vortex simulation of rollup and entrainment in a shear layer. *Journal of Computational Physics*, 97(1):172–223, 1991.

[112] O. Knio and A. Ghoniem. The three-dimensional structure of periodic vorticity layers under non-symmetric conditions. *Journal of Fluid Mechanics*, 243:353–392, 1992.

[113] M. Koochesfahani. Vortical patterns in the wake of an oscillating airfoil. *AIAA Journal*, 27:1200–1205, 1989.

[114] M. Koochesfahani and P. Dimotakis. A cancellation experiment in a forced turbulent shear layer. Technical Paper 88-3713-CP, AIAA, 1988.

[115] M. Kramer. Boundary layer stabilization by distributed damping. *American Society of Naval Engineers Journal*, pages 25–33, 1957.

[116] R. Krasny. Desingularization of periodic vortex sheet roll-up. *Journal of Computational Physics*, 65:292–313, 1986.

[117] R. Krasny. Computation of vortex sheet roll-up in the trefftz plane. *Journal of Fluid Mechanics*, 184:123–155, 1987.

[118] J. Kumph and M. Triantafyllou. A fast-starting and maneuvering vehicle, the RoboPike. In *Proceedings of the International Symposium on Seawater Drag Reduction*, pages 485–490, Newport, RI, July 1998. ONR, NSSC, DARPA, NSWC, ASME, and NUWC.

[119] H. Lamb. *Hydrodynamics*. Dover Publications, New York, 1945.

[120] C. Lan. A quasi-vortex-lattice method in thin-wing theory. *Journal of Aircraft*, 11(9):518–527, 1974.

[121] C. Lan. The unsteady quasi-vortex-lattice method with applications to animal propulsion. *Journal of Fluid Mechanics*, 93:747–765, 1979.

[122] T. Lang. Speed, power, and drag measurements of dolphins and porpoises. In T. Wu, C. Brokaw, and C. Brennan, editors, *Proceedings of the symposium on swimming and flying in nature: Volume 2*, pages 553–572, New York, July 1975. Plenum Press.

[123] T. Lang and A. Daybell. Porpoise performance tests in a sea-water tank. NAVWEPS Report 8060, United States Naval Ordnance Test Station, China Lake, CA, 1963.

[124] M. Lighthill. Note on the swimming of slender fish. *Journal of Fluid Mechanics*, 9:305–317, 1960.

[125] M. Lighthill. Aquatic animal propulsion of high hydromechanical efficiency. *Journal of Fluid Mechanics*, 44:265–301, 1970.

[126] M. Lighthill. Large-amplitude elongated-body theory of fish locomotion. *Proceedings of the Royal Society of London* **B**, 179:125–138, 1971.

[127] M. Lighthill. *Mathematical Biofluiddynamics*. Society for Industrial and Applied Mechanics, Philadelphia, Pennsylvania, 1975.

[128] M. Lighthill. Fundamentals concerning wave loading on offshore structures. *Journal of Fluid Mechanics*, 173:667–681, 1986.

[129] M. Lighthill. Biofluiddynamics of balistiform and gymnotiform locomotion. Part 2. The pressure distribution arising in two-dimensional irrotational flow from a general symmetrical motion of a flexible flat plate normal to itself. *Journal of Fluid Mechanics*, 213:1–10, 1990.

[130] M. Lighthill. Biofluiddynamics of balistiform and gymnotiform locomotion. Part 3. Momentum enhancement in the presence of a body of elliptic cross-section. *Journal of Fluid Mechanics*, 213:11–20, 1990.

[131] M. Lighthill. Biofluiddynamics of balistiform and gymnotiform locomotion. Part 4. Short-wavelength limitations on momentum enhancement. *Journal of Fluid Mechanics*, 213:21–28, 1990.

[132] M. Lighthill and R. Blake. Biofluiddynamics of balistiform and gymnotiform locomotion. Part 1. Biological background and analysis by elongated-body theory. *Journal of Fluid Mechanics*, 212:183–207, 1990.

[133] J. Lin and D. Rockwell. Force identification by vorticity fields: Techniques based on flow imaging. *Journal of Fluids and Structures*, 10(6):663–668, August 1996.

[134] H. Liu, C. Ellington, K. Kawachi, C. van den Berg, and A. Willmott. A computational fluid dynamic study of hawkmoth hovering. *Journal of Experimental Biology*, 201:461–477, 1998.

[135] H. Liu, R. Wassenberg, and K. Kawachi. A computational fluid dynamics study of tadpole swimming. *Journal of Experimental Biology*, 199:1245–1260, 1996.

[136] H. Liu, R. Wassenberg, and K. Kawachi. The three-dimensional hydrodynamics of tadpole swimming. *Journal of Experimental Biology*, 200:2807–2819, 1997.

[137] P. Liu. *A time domain panel method for oscillating propulsors with both chordwise and spanwise flexibility.* PhD dissertation, Memorial University of Newfoundland, Faculty of Engineering and Applied Science, St. John's, Newfoundland, 1996.

[138] L. Lourenco and A. Krothapalli. On the accuracy of velocity and vorticity measurements with PIV. *Experiments in Fluids*, 18:421–428, 1995.

[139] E. Lurie. Private communication and permission to use propeller code PAN2D, 10/19/94.

[140] E. Lurie. *Investigation of high reduced frequency, separated trailing edge flows.* ScD dissertation, Massachusetts Institute of Technology, Department of Ocean Engineering, 1996.

[141] H. Maniar. *A three dimensional higher order panel method based on B-splines.* PhD dissertation, Massachusetts Institute of Technology, Department of Ocean Engineering, Cambridge, MA, 1995.

[142] D. Mantzaris. *A Rankine panel method as a tool for the hydrodynamic design of complex marine vehicles.* PhD dissertation, Massachusetts Institute of Technology, Department of Ocean Engineering, Cambridge, MA, 1998.

[143] P. Martin. Mapping flat cracks onto penny-shaped cracks, with application to somewhat circular tensile cracks. *Quarterly of Applied Mathematics*, 54(4):663–675, 1996.

[144] P. Martin and F. Rizzo. On boundary integral equations for crack problems. *Proceedings of the Royal Society of London* **A**, 421:341–355, 1989.

[145] E. Maskell. Unpublished note on the Kutta-Joukowski condition in unsteady flow, 1972.

[146] B. Maskew. Subvortex technique for the close approach to a discretized vortex sheet. *Journal of Aircraft*, 14(2):188–193, 1977.

[147] T. Maxworthy. Some experimental studies of vortex rings. *Journal of Fluid Mechanics*, 81(3):465–495, 1977.

[148] W. McCroskey. The fluid dynamics of insect flight. *Annual Review of Fluid Mechanics*, 13:329–350, 1981.

[149] W. McCroskey. Unsteady airfoils. *Annual Review of Fluid Mechanics*, 14:285–311, 1982.

[150] C. McCutchen. Flow visualization with stereo shadowgraphs of stratified flow. *Journal of Experimental Biology*, 65:11–20, 1976.

[151] L. Milne-Thomson. *Theoretical Hydrodynamics.* Dover Publications, New York, 1938.

[152] L. Milne-Thomson. *Theoretical Aerodynamics.* Dover Publications, New York, 1958.

[153] U. Müller, B. van den Heuvel, E. Stamhuis, and J. Videler. Fish foot prints: Morphology and energetics of the wake behind a continuously swimming mullet (*chelon labrosus* Risso). *Journal of Experimental Biology*, 200:2893–2906, 1997.

[154] T. Nakaoka and Y. Toda. Laminar flow computation of fish-like motion wing. In *Proceedings of the Fourth International Offshore and Polar Engineering Conference*, pages 530–538, Osaka, Japan, April 1994. International Society of Offshore and Polar Engineers.

[155] A. Nayfeh and D. Mook. *Nonlinear Oscillations.* Wiley-Interscience Publication, John Wiley and Sons, New York, 1979.

[156] J. Newman. The force on a slender fish-like body. *Journal of Fluid Mechanics*, 58(4):689–702, 1973.

[157] J. Newman. *Marine hydrodynamics.* MIT Press, Cambridge, MA, 1977.

[158] J. Newman. Distributions of sources and normal dipoles over a quadrilateral panel. *Journal of Engineering Mathematics*, 20:113–126, 1986.

[159] J. Newman and T. Wu. A generalized slender-body theory for fish-like forms. *Journal of Fluid Mechanics*, 57(4):673–693, 1973.

[160] J. Newman and T. Wu. Hydromechanical aspects of fish swimming. In T. Wu, C. Brokaw, and C. Brennan, editors, *Proceedings of the symposium on swimming and flying in nature: Volume 2*, pages 615–634, New York, July 1975. Plenum Press.

[161] M. Osborne. Aerodynamics of flapping flight with application to insects. *Journal of Experimental Biology*, 28:221–245, 1951.

[162] M. Osborne. The hydromechanical performance of migratory salmon. *Journal of Experimental Biology*, 38:365–390, 1961.

[163] D. Pullin. The large-scale structure of unsteady self-similar rolled-up vortex sheets. *Journal of Fluid Mechanics*, 88:401–430, 1978.

[164] D. Pullin and A. Perry. Some flow visualization experiments on the starting vortex. *Journal of Fluid Mechanics*, 97:239–255, 1980.

[165] D. Pullin and W. Philips. On a generalization of Kaden's problem. *Journal of Fluid Mechanics*, 104:45–53, 1981.

[166] W. Ramsey. *Boundary integral methods for lifting bodies with vortex wakes.* PhD dissertation, Massachusetts Institute of Technology, Department of Ocean Engineering, Cambridge, MA, 1996.

[167] J. Rayner. A vortex theory of animal flight. Part 1. The vortex wake of a hovering animal. *Journal of Fluid Mechanics*, 91:697–730, 1979.

[168] J. Rayner. A vortex theory of animal flight. Part 2. The forward flight of birds. *Journal of Fluid Mechanics*, 91:731–763, 1979.

[169] D. Read. Design, construction, and testing of a biomimetic flapping foil device. Master's thesis, Massachusetts Institute of Technology, Department of Ocean Engineering, Cambridge, MA, 1999.

[170] F. Roberts and A. Roshko. Effects of periodic forcing on mixing in turbulent shear layers and wakes. In *Proceedings of the AIAA shear flow control conference*, Boulder, CO, 1985. AIAA paper 85-0570.

[171] L. Rome, D. Swank, and D. Corda. How fish power swimming. *Science*, 261:340–343, 1993.

[172] M. Rosen. Water flow about a swimming fish. NAVWEPS Report 2298, United States Naval Ordnance Test Station, China Lake, CA, 1959.

[173] M. Rosen. Flow visualization experiments with a dolphin. NAVWEPS Report 8062, United States Naval Ordnance Test Station, China Lake, CA, 1963.

[174] M. Rosenfeld, M. Gharib, and E. Rambod. Circular and formation number of laminar vortex rings. *Journal of Fluid Mechanics*, 376:297–318, 1998.

[175] N. Rott. Diffraction of a weak shock with vortex generation. *Journal of Fluid Mechanics*, 1:111–128, 1956.

[176] P. Saffman. *Vortex dynamics.* Cambridge University Press, Cambridge, U.K., 1992.

[177] P. Saffman and J. Schatzman. An inviscid model for the vortex-street wake. *Journal of Fluid Mechanics*, 122:467–486, 1982.

[178] P. Saffman and J. Schatzman. Stability of a vortex street with finite vortices. *Journal of Fluid Mechanics*, 117:171–185, 1982.

[179] T. Sarpkaya. An inviscid model of two-dimensional vortex shedding for transient and asymptotically steady separated flow over an inclined plate. *Journal of Fluid Mechanics*, 68:109–128, 1975.

[180] T. Sarpkaya. Computational methods with vortices: The 1988 freeman scholar lecture. *Journal of Fluids Engineering*, 111:5–52, 1989.

[181] T. Sarpkaya. Vortex element methods for flow simulation. *Advances in Applied Mechanics*, 21:113–247, 1994.

[182] T. Sarpkaya and R. Schoaff. Inviscid model of two-dimensional vortex shedding by a circular cylinder. *AIAA Journal*, 17(11):1193–1200, 1979.

[183] J. Scherer. Experimental and theoretical investigation of large amplitude oscillating foil propulsion systems. United States Army Engineering Research and Development Laboratories Report 80841, Hydronautics, Inc., Washington, D.C., 1968.

[184] W. Schultz, R. Zhou, and P. Webb. A numerical study of fish swimming. *Journal of Fluid Mechanics*, 1993. unpublished submission.

[185] J. Slotine and W. Li. *Adaptive nonlinear control.* Prentice Hall, Englewood Cliffs, NJ, 1991.

[186] E. Stamhuis and J. Videler. Quantitative flow analysis around aquatic animals using laser sheet particle image velocimetry. *Journal of Experimental Biology*, 198:283–294, 1995.

[187] E. Stamhuis and J. Videler. Burrow ventilation in the tube-dwelling shrimp *callianassa subterranea* (Decapoda:Thalassinidea). I. Morphology and motions of the pleopods, uropods and telson. *Journal of Experimental Biology*, 201:2151–2158, 1998.

[188] E. Stamhuis and J. Videler. Burrow ventilation in the tube-dwelling shrimp *callianassa subterranea* (Decapoda:Thalassinidea). II. The flow in the vicinity of the shrimp and the energetic advantages of a laminar non-pulsating ventilation current. *Journal of Experimental Biology*, 201:2159–2170, 1998.

[189] E. Stamhuis and J. Videler. Burrow ventilation in the tube-dwelling shrimp *callianassa subterranea* (Decapoda:Thalassinidea). III. Hydrodynamic modelling and the energetics of pleopod pumping. *Journal of Experimental Biology*, 201:2171–2181, 1998.

[190] K. Streitlien. *Extracting Energy from unsteady flows through vortex control.* PhD dissertation, Massachusetts Institute of Technology, Department of Ocean Engineering, 1994.

[191] K. Streitlien, G. Triantafyllou, and M. Triantafyllou. Efficient foil propulsion through vortex control. *AIAA Journal*, 34(11):2315–2319, 1996.

[192] K. Streitlien and M. Triantafyllou. Force and moment on a joukowski profile in the presence of point vortices. *AIAA Journal*, 33(4):603–610, 1995.

[193] P. Sverdrup. Analysis of harmonically flapping wing in a steady stream. Sivilingenior thesis, Norwegian University of Science and Technology and the Massachusetts Institute of Technology, Department of Marine Hydrodynamics, Trondheim, Norway, 1997.

[194] S. Taneda. Experimental investigation of vortex streets. *Journal of the Physical Society of Japan*, 20(9):1714–1721, 1965.

[195] S. Taneda. Visual study of unsteady separated flows around bodies. *Progress in Aerospace Science*, 17:287–348, 1977.

[196] S. Taneda. Visual observations of the flow past a circular cylinder performing a rotary oscillation. *Journal of the Physical Society of Japan*, 45:1038–1043, 1978.

[197] S. Taneda and Y. Tomonari. An experiment on the flow around a waving plate. *Journal of the Physical Society of Japan*, 36(6):1683–1689, 1974.

[198] G. Taylor. Analysis of the swimming of microscopic organisms. *Proceedings of the Royal Society of London* **A**, 209:447–461, 1951.

[199] G. Taylor. The action of waving cylindrical tails in propelling microscopic organisms. *Proceedings of the Royal Society of London* **A**, 211:225–239, 1952.

[200] G. Taylor. Analysis of the swimming of long and narrow animals. *Proceedings of the Royal Society of London* **A**, 214:153–183, 1952.

[201] D. Thrasher, D. Mook, O. Kandil, and A. Nayfeh. Application of the vortex-lattice concept to general, unsteady lifting surface problems. Technical Paper 77-1157, AIAA, 1977.

[202] P. Tokomaru and P. Dimotakis. Rotary oscillation control of a cylinder wake. *Journal of Fluid Mechanics*, 224:77–90, 1991.

[203] G. Triantafyllou, M. Triantafyllou, and C. Chryssostomidis. On the formation of vortex streets behind stationary cylinders. *Journal of Fluid Mechanics*, 170:461–477, 1986.

[204] G. Triantafyllou, M. Triantafyllou, and M. Grosenbaugh. Optimal thrust development in oscillating foils with application to fish propulsion. *Journal of Fluids and Structures*, 7:205–224, 1993.

[205] M. Triantafyllou, D. Barrett, D. Yue, J. Anderson, M. Grosenbaugh, K. Streitlien, and G. Triantafyllou. A new paradigm of propulsion and maneuvering for marine vehicles. *Transactions of the Society of Naval Architects and Marine Engineers*, 104:81–100, 1996.

[206] M. Triantafyllou and G. Triantafyllou. An efficient swimming machine. *Scientific American*, 272(3):64–70, 1995.

[207] M. Triantafyllou, G. Triantafyllou, and R. Gopalkrishnan. Wake mechanics for thrust generation in oscillating foils. *Physics of Fluids A*, 3:2835–2837, 1991.

[208] M. Triantafyllou, G. Triantafyllou, and D. Yue. Hydrodynamics of fish-like swimming. *Annual Review of Fluid Mechanics*, 32, 1999. In press.

[209] W. Tsai. *I. Regular and chaotic motions in a wave tank. II. Interactions between a free surface and a shed vortex sheet.* PhD dissertation, Massachusetts Institute of Technology, Department of Ocean Engineering, 1991.

[210] W. Tsai and D. Yue. Interactions between a free surface and a vortex shed in the wake of a surface-piercing plate. *Journal of Fluid Mechanics*, 257:691–721, 1993.

[211] J. Videler. Swimming movements, body structure and propulsion in cod *gadus morhua*. *Symposium of the Zoological Society of London*, 48:1–27, 1981.

[212] J. Videler. *Fish Swimming.* Chapman and Hall, London, U.K., 1993.

[213] J. Videler and F. Hess. Fast continuous swimming of two pelagic predators, saithe *pollachius virens* and mackerel *scomber scombrus*: A kinematic analysis. *Journal of Experimental Biology*, 109:209–228, 1984.

[214] S. Vogel. *Life in moving fluids: The physical biology of flow.* Princeton University Press, Princeton, NJ, 1994.

[215] T. von Kármán and J. Burgess. General aerodynamic theory - Perfect fluids. In W. Durand, editor, *Aerodynamic theory: Volume 2*, pages 346–349. Springer-Verlag, Berlin, 1935.

[216] J. Walker and M. Westneat. Labriform propulsion in fishes: Kinematics of flapping aquatic flight in the bird wrasse *gomphosus varius* (Labridae). *Journal of Experimental Biology*, 200:1549–1569, 1997.

[217] Z. Wang. Unsteady aerodynamics of insect flight. I: Optimal flapping. *Journal of Fluid Mechanics*, 1999. *Sub judis.*

[218] C. Wardle, J. Videler, and J. Altringham. Tuning in to fish swimming waves: Body form, swimming mode, and muscle function. *Journal of Experimental Biology*, 198:1629–1636, 1995.

[219] P. Webb. The swimming energetics of trout I. Oxygen consumption and swimming efficiency. *Journal of Experimental Biology*, 55:521–540, 1971.

[220] P. Webb. The swimming energetics of trout I. Thrust and power at cruising speeds. *Journal of Experimental Biology*, 55:489–520, 1971.

[221] P. Webb. Hydrodynamics and energetics of fish propulsion. *Bulletin of the Fisheries Research Board of Canada*, 190:1–159, 1975.

[222] P. Webb. Fast-start performance and body form in seven species of teleost fish. *Journal of Experimental Biology*, 74:211–226, 1978.

[223] P. Webb. "Steady" swimming kinematics of tiger musky, an esociform accelerator, and rainbow trout, a generalist cruiser. *Journal of Experimental Biology*, 138:51–69, 1988.

[224] P. Webb. The high cost of body/caudal fin undulatory swimming due to increased friction drag or inertial recoil. *Journal of Experimental Biology*, 162:157–166, 1992.

[225] D. Weihs. A hydrodynamical analysis of fish turning manoeuvres. *Proceedings of the Royal Society of London* **B**, 182:59–72, 1972.

[226] D. Weihs. The mechanism of rapid starting of slender fish. *Biorheology*, 10:343–350, 1973.

[227] D. Weihs. Some hydrodynamical aspects of fish schooling. In T. Wu, C. Brokaw, and C. Brennan, editors, *Proceedings of the symposium on swimming and flying in nature: Volume 2*, pages 703–718. Plenum Press, New York, July 1975.

[228] D. Weihs and P. Webb. Optimization of locomotion. In P. Webb and D. Weihs, editors, *Fish Biomechanics*, Praeger Special Series, chapter 11, pages 339–371. Praeger, New York, 1983.

[229] C. Willert. *The interaction of modulated vortex pairs with a free surface.* PhD dissertation, The University of California, San Diego, 1992.

[230] C. Willert and M. Gharib. Digital particle image velocimetry. *Experiments in Fluids*, 10:181–193, 1991.

[231] G. Winckelmans. *Topics in vortex methods for the computation of three- and two-dimensional incompressible unsteady flows.* PhD dissertation, California Institute of Technology, 1989.

[232] G. Winckelmans and A. Leonard. Contributions to vortex particle methods for the computation of three-dimensional incompressible unsteady flows. *Journal of Computational Physics*, 109:247–273, 1993.

[233] M. Wolfgang, J. Anderson, M. Grosenbaugh, D. Yue, and M. Triantafyllou. Near-body flow dynamics in swimming fish. *Journal of Experimental Biology*, 1999. In press.

[234] M. Wolfgang, J. Anderson, M. Grosenbaugh, D. Yue, and M. Triantafyllou. Vortical flow actuation by flexible swimming bodies. *Journal of Fluids and Structures*, 1999. *Sub judis.*

[235] M. Wolfgang, S. Tolkoff, A. Techet, D. Barrett, M. Triantafyllou, D. Yue, F. Hover, M. Grosenbaugh, and W. McGillis. Drag reduction and turbulence control in swimming fish-like bodies. In *Proceedings of the International Symposium on Seawater Drag Reduction*, pages 463–469, Newport, RI, July 1998. ONR, NSSC, DARPA, NSWC, ASME, and NUWC.

[236] M. Wolfgang, M. Triantafyllou, and D. Yue. Visualization of complex near-body transport processes in flexible-body propulsion. *Journal of Visualization*, 2(2), 1999. In press.

[237] M. Wolfgang, D. Yue, and M. Triantafyllou. Vorticity dynamics and performance of fish swimming motions. *Journal of Fluid Mechanics*, 1999. To be submitted for publication.

[238] J.Z. Wu and J.M. Wu. Vorticity dynamics on boundaries. *Advances in Applied Mechanics*, 32:119–275, 1996.

[239] T. Wu. Swimming of a waving plate. *Journal of Fluid Mechanics*, 10:321–344, 1961.

[240] T. Wu. Hydromechanics of swimming fishes and cetaceans. *Advances in Applied Mathematics*, 11:1–63, 1971.

[241] T. Wu. Hydromechanics of swimming propulsion. Part 1. Swimming of a two dimensional flexible plate at variable forward speeds in an inviscid fluid. *Journal of Fluid Mechanics*, 46:337–355, 1971.

[242] T. Wu. Hydromechanics of swimming propulsion. Part 2. Some optimum shape problems. *Journal of Fluid Mechanics*, 46:521–544, 1971.

[243] T. Wu. Hydromechanics of swimming propulsion. Part 3. Swimming and optimum movements of slender fish with side fins. *Journal of Fluid Mechanics*, 46:545–568, 1971.

[244] T. Wu and A. Chwang. Extraction of flow energy by fish and birds in a wavy stream. In T. Wu, C. Brokaw, and C. Brennan, editors, *Proceedings of the symposium on swimming and flying in nature: Volume 2*, pages 687–702. Plenum Press, New York, July 1975.

[245] H. Yamaguchi and N. Bose. Oscillating foils for marine propulsion. In *Proceedings of the Fourth International Offshore and Polar Engineering Conference*, pages 539–544, Osaka, Japan, April 1994. The International Society of Polar and Offshore Engineers.

[246] G. Yates. *Finite amplitude unsteady slender body theory and experiments.* PhD dissertation, California Institute of Technology, 1977.

[247] G. Yates. Hydromechanics of body and caudal fin propulsion. In P. Webb and D. Weihs, editors, *Fish Biomechanics*, Praeger Special Series, chapter 6, pages 177–213. Praeger, New York, 1983.

[248] R. Yeung. A singularity-distribution method for free-surface flow problems with an oscillating body. Office of Naval Research Technical Report NA 73-6, College of Engineering, University of California, Berkeley, 1973.